Role of functional imaging in determining inflammation and extracellular matrix degradation in aortic aneurysms

Attia, Rizwan

Awarding institution:
King's College London

Role of functional imaging in determining inflammation and extracellular matrix degradation in aortic aneurysms

Rizwan Attia

Thesis submitted for the Degree of Doctor of Philosophy

King's College London

2014

Academic Department of Vascular Surgery

Cardiovascular Division, School of Medicine

St Thomas' Hospital

King's College London

London, SE1 7EH

Statement of originality

The work contained in this thesis is original work, except where acknowledged.

Acknowledgments

I would like to thank my supervisors, Professor Alberto Smith, Mr Matthew Waltham and Mr Bijan Modarai for their help, advice and support. I would also like to express my gratitude to Mr Christopher Young, Mr Vinnie Bapat and Professor Peter Taylor for their guidance in my clinical and academic development. They have provided continuous assistance in the clinical aspects of the study for patient recruitment and sample collection. I am indebted to Professor Rene Botnar for his advice, discussion and critical appraisal of the work. I would like to thank Professor Kevin Burnand for providing the opportunity to work in the laboratory. I would like to thank Dr Alkystis Phinikaridou and Marcelo Andia for all the help and input with the aortic magnetic resonance work and being there weekend after weekend always with a smile. I would like to thank Andrea Protti for all his advice and technical help with cardiac magnetic resonance imaging work. Many thanks for Dr Abdel Douiri for statistic advice. Professor Manuel Mayr for providing the miRNA antagomirs and Dr Richard Siow for providing the vascular smooth muscle cells. Dr Anna Zampataki for performing the RT-PCR and proteomics for the *in vivo* miR study. I would like to thank the NIHR Biomedical Research Centre, Royal College of Surgeons, Rosetrees Trust and British Heart Foundation for their financial support.

Mr Ashish Patel, Oliver Lyons, Prakash Saha and Steven Grover provided invaluable technical experimental advice and hours of discussion. They have been my colleagues and friends. I can't thank them enough for their input during the PhD. I would like to specially thank the students that have poured their heart and soul into the work. Miss Niovi Papalexopoulou for all the help and assistance especially for the immunohistochemistry. Miss Charlotte Lee was instrumental in performing cell culture and *in-vitro* work during her MSc.

Finally, I would like to thank my wife, friend and colleague Miss Victoria Asfour for always being there to urge me on. To continuously push after failed experiment or when the results did not make sense and when politics interfered with science and medicine. She has kept me sane and motivated to be the best that I can be.

Table of Contents

Chapter 1: General Introduction

Chapter 2: Optimisation of PET-CT, laser scintigraphy and creation of 3D masks for aortic aneurysm biopsy

Chapter 3: ^{18}F-FDG uptake in human aneurysms and biological correlates

Chapter 7: The effect of immune cells on vascular smooth muscle cell phenotype

Abstract

Aneurysmal disease of the aorta is a degenerative condition characterised by inflammation and extracellular protein loss, in particular, loss of cross-linked elastin. ^{18}F-FDG is currently the most widely available tracer used in assessing the metabolic activity of tissues and is known to be taken up in aneurysmal wall, but its biological correlates, other than metabolism, have yet to be evaluated. Other novel tracers for more specific functional imaging of proteins such as elastin in the aneurysm wall have also yet to be evaluated in the context of aneurysmal disease.

^{18}F-FDG uptake in aneurysms was characterised using a combination of laser scintigraphic 3D aortic masks generated from PET-CT that allowed precise aortic biopsy of areas of high and low tracer uptake. Positive correlations were obtained between ^{18}F-FDG uptake and total leukocyte, B-cell, T-cell and NK-cell content in human aneurysmal wall, while elastin and collagen content was reduced at sites of inflammatory cell infiltrate. B and T-cells had significant modulatory affects on vascular smooth muscle cell (VSMC) proliferation, survival and protein synthesis *in-vitro.*

^{18}F-FDG uptake and its inflammatory correlates were similarly characterised in ApoE$^{-/-}$-ATII model. There was a temporal, heterogeneous ^{18}F-FDG uptake in the aneurysms associated with increased immune cell content, but no correlation was found between uptake and aortic expansion or diameter.

Elastin-specific MR contrast agent (ESMA) uptake was characterised in the ApoE$^{-/-}$-ATII model and found to correlate with elastin, tropoelastin, immune cell content and extracellular matrix organisation, as well as aortic expansion. Treatment with elastin modulating antagomirs decreased aneurysm expansion and rupture. This was through modulated down-stream gene and protein expression of proteins and enzymes involved in elastin and collagen homeostasis namely TGFβ, LOX and MMP's.

It appears therefore that ^{18}F-FDG uptake correlates with specific immune cell infiltrates, in particular that of B- and T-cells that can modulate VSMC function. There are distinct cellular populations that are responsible for a pro-aneurysmal phenotype and B-T-regulatory cell populations that lead to aortic remodeling response. ESMA uptake was related to elastin remodelling and may provide a novel predictor of aneurysm behavior. Antagomir mediated alteration of VSMC phenotype might alter the natural history of aneurysmal disease.

Abbreviations

AAA	abdominal aortic aneurysm
AAV	adeno-associated virus
ACEi	angiotensin converting enzyme inhibitor
AD	aortic dissection
AKT	protein kinase B
ANOVA	analysis of variance
Ao	aorta
α-SMA	alpha-smooth muscle actin
AT1a	angiotensin II receptor 1a
ATII	angiotensin II
BSA	bovine serum albumin
$CaCL_2$	calcium chloride
CBA	cytokine bead array
CBR	cannabinoid receptor
CD	cluster of differentiation
Chek1	checkpoint kinase 1
COL	collagen
CT	computer Tomography
cT	threshold cycle
Cttk	cathepsin K
Ctts	cathepsin S
DAPI	4'6-diamidino-2-phenylindole
ECM	extracellular matrix
EDTA	ethylenediaminetetraacetic acid
EdU	5-ethynyl-2-deoxyuridine
ELISA	enzyme-linked immunosorbent assay
ELN	elastin
EP	elastin peptide
FACS	fluorescence-activated cell sorting
FBN	fibrillin

FBLN	fibulin
FDG	flurodeoxyglucose
FMO-1	florescence minus one
FSE	fast spin echo
HCL	hydrochloric acid
HR	heart rate
IFN-γ	interferon-gamma
IGF	insulin like growth factor
IHC	immunohistochemistry
Ig-	immunoglobulin
IL	interleukin
ISEL	*in situ* 3'-end-labelling
IL	interleukin
IMH	intramural haematoma
KO	knock out
LDS	Loeys-Dietz syndrome
LNA	locked nucleic acid
LRP-1	low-density lipoprotein 1
LOX	lysl oxidase
LV	left ventricle
LVEF	left ventricular ejection fraction
MAPK	mitogen activated protein-kinase
MCP-1	monocyte chemoattractant protein-1
MFS	marfans syndrome
miR	micro ribonucleic acid
mRNA	messenger ribonucleic acid
MMP	matrix metalloproteases
MRI	magnetic resonance imaging
NF-κB	nuclear factor kappa-light-chain-enhancer of activated B-cells
NGAL	neutrophil gelatinase associated lipocalin
NK	natural killer
OMe	2'-O-methyl-modified oligonucleotides

OxLDL	oxidized low-density lipoprotein
P4H	prolyl 4-hydroxylase
PAU	penetrating aortic ulcer
PBS	phosphate buffered saline
PBS-BA	phosphate buffered saline- bovine serum albumin
PBS-BE	phosphate buffered saline-bovine serum albumin-ethylenediaminetetraacetic acid
PET	positron emission tomography
PMA	phorbol myristate acetate
PPIB	peptidylprolyl isomerase B
PTEN	phosphatase and tensin
ROS	reactive oxygen species
RPLP0 50S	ribosomal subunit protein
RTPCR	reverse transcriptase polymerase chain reaction
siRNA	small interfering ribonucleic acid
SPECT	single photon emission photography
SRA	suprarenal aneurysm
SUV	standardised uptake value
SV	stroke volume
TAo	thoracic aorta
TAA	thoracic aortic aneurysm
TAAA	thoracoabdominal aortic aneurysm
TGF-β	transforming growth factor-beta
TIMPS	tissue Inhibitor matrix metalloproteinase
TNF-α	tumour necrosis factor-alpha
TRAIL	TNF-related apoptosis-inducing ligand
TUNEL	terminal deoxynucleotidyl transferase dUTP nick end labeling
TOE	transoesophageal echocardiography
US	ultrasound
VCAM	vascular cell adhesion molecule 1
VSMCs	vascular smooth muscle cells

Index of figures

Chapter 1

Chapter 2

Chapter 3

Chapter 4

Chapter 5

Chapter 6

Chapter 7

List of Tables

Chapter 1

Chapter 3

Chapter 4

Chapter 7

Chapter 1: General Introduction

1.1 Historical perspective

Arterial dilations were described as far back as ancient Egyptian times during 2000BC in the *Ebers Papyrus* medical scrolls. The first accurate descriptions were by Greek physicians such as Galen (A.D.126-c216)[1]. These were based on observations in the 2nd century A.D., of gladiators who were injured in battle and developed false aneurysms. Antyllus also described traumatic aneurysms and was the first person to attempt surgical correction with proximal and distal ligation, opening the aneurysm sac and evacuating the contents. The 1500's saw the description of syphilitic aneurysms by Pare (1510-1590)[1]. John Hunter made real surgical progress in 1800s when he popularised arterial ligation[2]. It was not till early twentieth century that Alexis Carrel and Charles Guthrie made advances using anastomotic techniques and the use of homografts as replacement conduits. Carrel won a Nobel Prize for his work and provided the basis for modern anastomotic techniques[3]. Innovative treatment options included aneurysm thrombosis by application of electric current (Fig 1.0) to wrapping aneurysms with cellophane. It was in 1944 that Ochsner performed the first open repair of a saccular aneurysm of the descending aorta with Denton Cooley (as an intern) performing an open repair of an ascending aortic false aneurysm a year later. In 1948 Rudolph Nissen operated on Albert Einstein at the Jewish Hospital in Brooklyn, New York by cellophane wrapping his aortic aneurysm. Due to this timely intervention the renowned physicist survived over 5-years before succumbing to aneurysm rupture. It was not till 1952 when Dubost repaired the first abdominal aortic aneurysm with an aortic homograft.

The balloon expandable stent was invented by Julio Palmaz and patented in 1985, but it was not until 1986 that the Ukrainian surgeon Nicholas Volodos performed the first endovascular repair of a traumatic thoracic aortic

aneurysm[4]. Parodi carried out the first infra-renal abdominal aortic aneurysm repair using an endograft in 1990. With the application of aortic screening programs and increasingly powerful imaging modalities available for aneurysm diagnosis, treatment and follow-up the outcomes for patients with this lethal condition should continue to improve.

The great physician Sir William Osler observed, “there is no condition more conductive to clinical humility than aneurysm of the aorta.” Although progress has been made since then, Osler’s observation regarding the challenge posed by aortic disease remains true to this day.

Fig 1.0 The historical treatment of aortic aneurysms

Electroshock therapy being used in Osler’s time to stop aortic aneurysm progression and rupture. It is likely our ‘modern therapy’ will look similarly archaic in 100 years time[5].

1.2 Aortic aneurysms

The aorta is anatomically described according to its location and relationships as it originates from the heart and ends by bifurcating into the iliac vessels (Fig 1.1). An aneurysm is an abnormal dilation of an artery to twice its normal diameter. In the case of adults, an abdominal aortic aneurysm (AAA) means an aortic diameter greater than 3cm and for the thoracic aortic aneurysm (TAA) greater than 4.5cm (Figs 1.2 and 1.3). Aneurysms are the 13th leading cause of death in the UK[6]. The incidence of TAA is around 5.9-10.4 per 100000 person years and this seems to be increasing with screening and better imaging techniques[7,8]. AAA affects 5.5% of men over the age of 65 and about 2.2% of women. It is estimated that around 8000 people die because of ruptured aortic aneurysm in the UK annually[9].

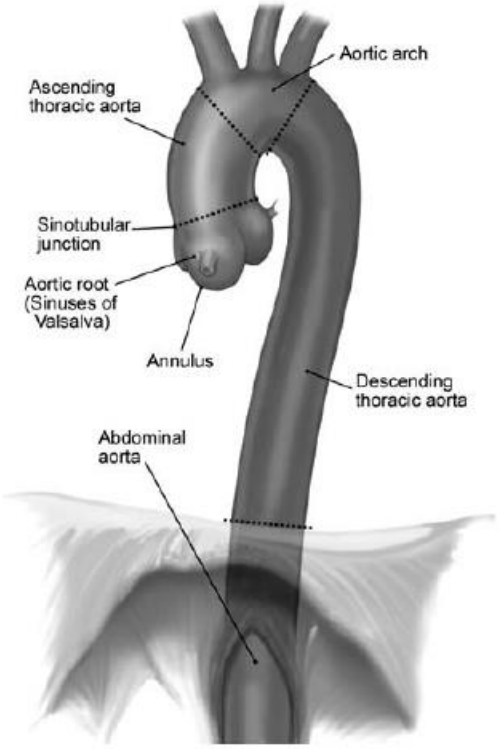

Fig 1.1 Aortic anatomy delineating the variously defined aortic segments[10]

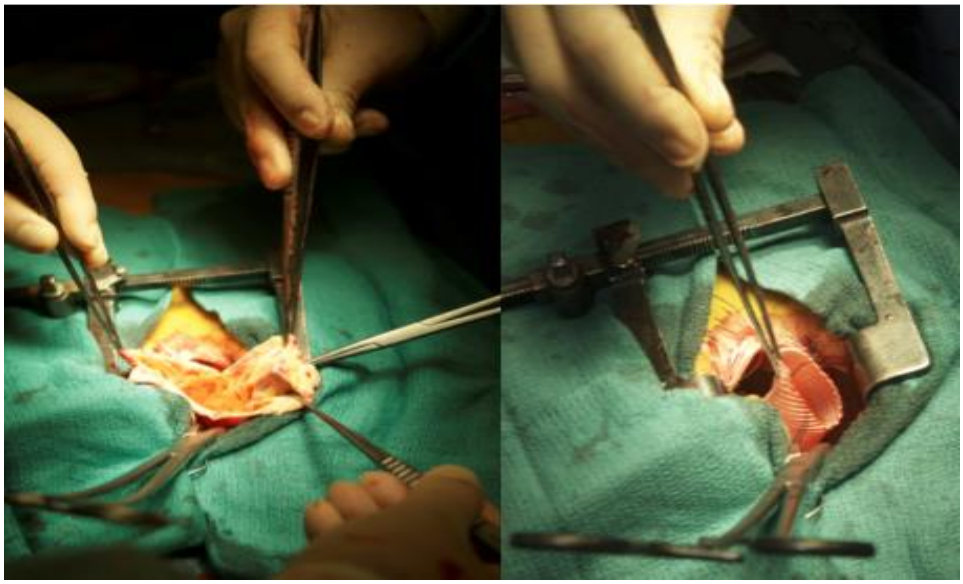

Fig 1.2 A thoracic aortic aneurysm in Marfans patient opened

The patient underwent replacement of the aortic root and ascending aorta with a Dacron graft. (Courtesy of C. Young)

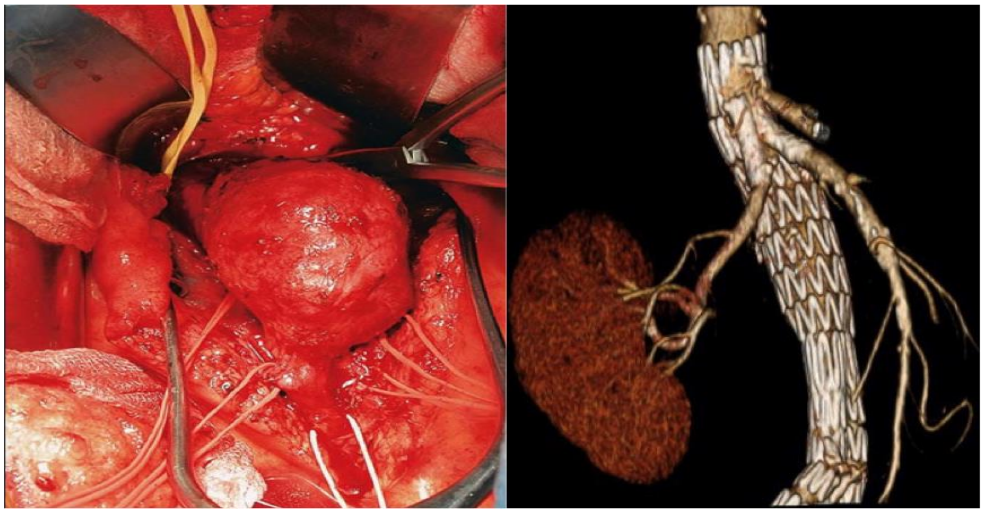

Fig 1.3 Degenerative abdominal aortic aneurysms

Open repair of a juxtarenal aortic aneurysm. A branch fenestrated endograft used for a suprarenal aneurysm. (Courtesy of P. Taylor)

1.3 Natural history of aortic aneurysms

Successful surgical treatment relies on understanding the risks of surgery balanced against the natural history of the disease. These data come from those aneurysm patients who did not have operative treatment. For thoracic aortic aneurysms overall 74% of patients rupture and of these 94% of patients will die from this[11]. For abdominal aortic aneurysms the average risk of rupture in men with 5-5.9cm aneurysms is 1% per year and in women with same sized aneurysms its around 3.9% per year[12-14]. Complications such as aortic rupture and dissection are determined by aortic diameter and underlying aortic pathology.

The diameter of the aneurysm increases the wall tension increases (T=PR, Laplace's law); where tension is proportional to pressure x radius. Increased systemic blood pressure and increased aneurysm diameter, therefore, markedly increase the risk of rupture. Logistic regression analysis has demonstrated over 4 fold increased rupture or dissection risk when aneurysm is 6.0-6.9cm in diameter compared with a 4.0-4.9cm[13,14]. Aneurysm size and growth rate are important clinical predictors for treatment decisions as they are know to determine aortic outcome. A 5cm thoracic aneurysm expands at an average rate of 0.08-0.12cm/year; whereas larger aneurysms grow at a greater rate: 8cm aneurysms grow at around 0.19-0.22cm/ year[14]. The growth rate varies depending on the site of aortic aneurysm independent of size. Ascending aortic aneurysms grow at 0.1cm annually compared to 0.29 for descending thoracic aneurysms. The mean growth is approximately 0.42cm per year[14]. This rate is accelerated in patients who smoke. Although hypertension is a risk factor for aneurysm development, none of the measures of hypertension are associated with abdominal aortic aneurysm expansion[15]. Similar data has been reported for thoracic aortic disease[16]. There are, however, indications that there is an association between diastolic blood pressure and the rate of aortic expansion[17].

Mechanical forces also contribute to aortic remodelling with three distinct influences on the aortic wall: i) pressure created by the hydrostatic forces ii) circumferential stretch exerting longitudinal forces and iii) shear stress caused by the blood flow[18]. The net resultant force comprises therefore of the pressure along the aortic wall, shear stress and the difference in the maximal pressure differences i.e. pulse pressure. Perturbation in the flow conditions leads to flow turbulence, contributing to aneurysm growth. Areas of oscillator and extremes in shear stress (high and low) correlate to sites of development of aneurysms[18,19]. Clinical studies have shown conflicting data where flow in aortic aneurysms can be smooth and laminar or irregular and turbulent with little information on the effects of wall shear stress in aneurysms[18-20]. The accelerated rate of aneurysm growth and lower mean death from rupture in patients with monogenetic causes of aneurysmal disease have provided the impetus for earlier aneurysm repair to be undertaken in these patients[21].

When lifetime risks of rupture and dissection are analysed there is a concept of aortic “hinge points”, when there is a sharp increase in risk of complications due to an aneurysms size (Fig 1.4). These hinge points occur at 6cm in the ascending aorta, 7cm in the descending aorta and 6cm in the abdominal aorta, in those without connective tissue disease[14,22,23]. It is also widely recognized that symptomatic aneurysms should be treated regardless of size as this heralds aortic rupture or dissection[24]. However 5% of patients are symptomatic before an acute aortic event. The first presenting symptom in 95% of cases is death. The overall 5-year survival for thoracic aortic aneurysms is 60-64%[14,22,25]. Survival is lower in descending aortic aneurysms (39% at 5 years) with an extremely poor outcome in patients who develop aortic dissection.

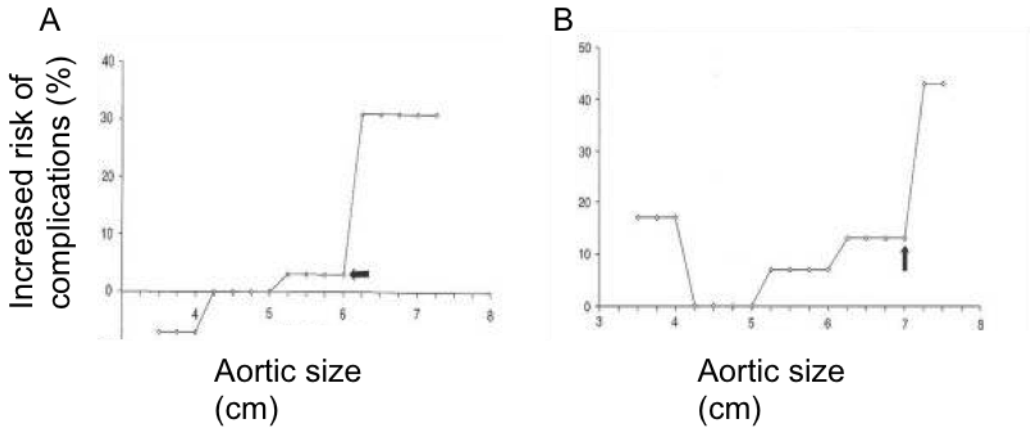

Fig 1.4 Risk of complications along the natural history of aortic aneurysms[23]

This depiction of 'hinge points' for lifetime natural history complications at various sizes of the aorta. The y-axis shows the likelihood of aortic dissection, rupture or death. The x-axis shows the aneurysm size. (A) Ascending aorta (B) Descending aorta[23].

Natural history data such as these have guided clinical trails that indicate that surveillance is a safe and effective tool in management of small AAAs[15,26-30]. Continued data collection on aortic aneurysms and multi-institutional pooling of outcomes data will enable analyses to improve our understanding and clinical decision making for managing aortic aneurysms. A better understanding of the pathophysiology of aneurysmal disease is, however, needed to facilitate the development of medical interventions that inhibit expansion.

1.3.1 Aetiology and pathophysiology

The risk factors for aneurysm development are male sex, hypertension, hypercholesterolemia, smoking and genetic predisposition. There are certain monogenetic conditions such as Marfan's, Ehlers-Danlos, Loeys-Dietz and other metabolic syndromes that predispose to early aneurysms[31]. There are certain familial polygenetic conditions that account for up to 10-15% of aneurysms with the remainder being classed as 'degenerative' occurring typically in those aged over 65yrs[21,32]. Recent genome wide association studies have shown that mutations in LDL receptor[33,34] and MMP3[35,36] might have a role in these 'degenerate aneurysm patients. The aortic wall expands and

contracts with the cardiac cycle. This is required to generate forward flow of pulsatile blood in the aorta. Aortic strength and elasticity is derived from the medial layer composed of collagen, elastin, vascular smooth muscle cells (VSMCs) and extracellular matrix (ECM) (Fig 1.5). As the aortic wall weakens and there is loss of elasticity, dilatation occurs and in some subjects there is elongation of the aorta. According to the law of Laplace, the dilatation leads to increased wall tension relative to intra-aortic pressure. This causes further progressive dilatation that is exacerbated by hypertension ultimately leading to dissection and or rupture.

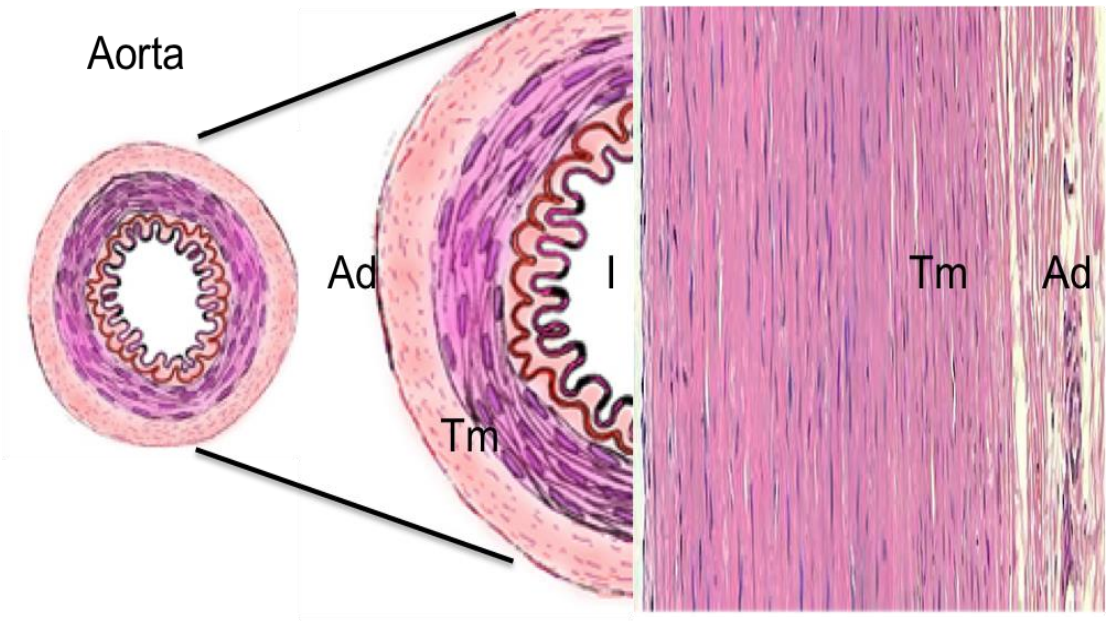

Fig 1.5 Aortic wall histology

The typical architecture of the aorta, composed of adventitia (Ad), tunica media (Tm) containing up to 60 elastic lamellae concentrated into bands (concentrated into internal and external elastic lamina) and intima (I) composed of endothelial cells. H&E attained human aorta demonstrating the aortic histology.

The aortic structure changes from ascending aorta (high in elastin) to descending thoracic and abdominal aorta (lower elastin content) where the media becomes thinner. The aortic wall is biologically active with VSMCs proliferating and producing elastin, collagen and proteoglycans. During

aneurysmal disease there is breakdown of the elastin and collagen with alterations in VSMC function and VSMC death[37-39]. Mucoid degeneration is a pathology of the thoracic aorta that is accelerated by smoking through increased levels of proteolytic enzymes[40]. Activation of the AMP-activated protein kinase ά2 by nicotine has is thought to be responsible for abdominal aortic aneurysm formation in mice[41].

Atherosclerosis is more commonly seen in the descending and abdominal aorta, rather than in the ascending aorta. It was thought atherosclerosis leads to damage of the elastic fibers and VSMCs leading to a weakened dilated aorta[42,43]. The causative role of atherosclerosis in aortic aneurysm has centered on aortic remodelling. There is some evidence to suggest that arterial stenosis leads to compensatory changes in the tunica media in response to the shear stress[43]. The extracellular matrix (ECM) remodelling promotes arterial expansion to normalise the aortic diameter and wall shear stress. This excessive aortic remodelling might lead to development of aortic aneurysms. Elastin breakdown in the tunica media caused by medial proteolysis through the action of matrix metalloproteinases[44-47] and other proteolytic enzymes such as cathepsins[48-50], and increased levels of pro-inflammatory cytokines could provide the stimulation for a chronic inflammatory response in the aortic wall[43]. This hypothesis has been scrutinised more carefully and it is now proposed that atherosclerosis is a concomitant process that infiltrates the diseased media[51-53]. It is postulated that chronic adventitial inflammation is the main contributor to aneurysm progression[54,55]. It is therefore shared environmental and genetic risk factors that promote the concurrent presence of atherosclerosis and aneurysms (Table 1.0). The mechanisms involved are, however, distinct. Another possibility is that that either atherosclerosis or aneurysms develop initially and both can then go on to stimulate the development of the other.

Table 1.0 Similarities and differences in between the pathogenesis of atherosclerosis and aortic aneurysms.

Characteristic	Similarity	Difference
Clinical	Increasing age Male Smoking Hypertension	Diabetes Obesity
Biomarker	CRP Fibrinogen	LDL/ VLDL
Genetic	Chromosome 9p21	Numerous genes only associated with aneurysms (e.g. FBN, TGFBR2, ACTA2)
Histology	Atheroma and thrombus in abdominal aneurysm	Elastin degradation and chronic inflammation
Animal models	$ApoE^{-/-}$ $ApoE^{-/-} \times eNOS^{-/-}$	LOX deficiency MMP3/ TIMP3 deficiency Elastase infusion $CaCl_2$ application

1.4 Genetic disorders

There are a variety of genetic disorders associated with aneurysmal disease. These range from autosomal dominant single gene defects, to multiple complex genetic polymorphisms that attribute a small cumulative risk to developing aortic aneurysms.

1.4.1 Marfan syndrome

Marfan syndrome is an autosomal dominant connective tissue disorder that manifests with a skeletal, ocular and life-threatening cardiovascular phenotype. It affects 0.2% of the overall population and, in a fifth of cases, occurs as a result of a new mutation. The cardiovascular complications include aortic dilatation, dissection (accounting for 5% of dissection patients) and rupture. The condition occurs as a result of defects in the fibrillin-1 *(FBN1)* gene that localises to chromosome 15q21.1[56]. *FBN1* encodes a 250kD cysteine-rich glycoprotein, which is an important component of the 10nm microfibrils that constitute elastic fibres[57,58]. Fibrillin-1 interacts with numerous components of the extracellular matrix, including fibrins, integrins, fibronectins, TGFβ binding proteins, insoluble elastin and collagens. In the aortic wall fibrillin provides a scaffold for the deposition of elastin and anchors smooth muscle cells by fibronectin[59]. Dilatation of the aorta is therefore, thought to be related to degradation of the insoluble extracellular matrix proteins within the arterial wall, in particular elastin and collagens. This results in mucoid degeneration (formerly misnamed cystic medial necrosis) which is characterised by the presence of alcianophilic glycosaminoglycans, vacuoles secondary to local loss of VSMCs, disorganised fibronectin and fibrillin and ruptured insoluble elastin and collagen.

A secondary locus for Marfans, *MFS2,* maps to chromosome 3p25-24.2. This accounts for heterogeneous mutations in the TGF-β receptor encoding sequence[60]. These include missense mutations and splicing errors in the serine-threonine kinase domain. TGF-β is a growth factor that plays an important part

in the control of anti-protease and matrix secretion. It is stored in an inactive form when associated with latent TGF-β binding protein and interacts with fibrillin, fibulins, fibronectin and extracellular matrix proteins. TGF-β is released in response to tissue injury and binds to receptors within the extracellular matrix where it has an important role in tissue repair. There is a relationship between TGF-β activity and the clinical features of Marfan syndrome[60]. High levels of TGF-β signaling has been reported in aneurysm samples and, although little is known about the precise pathogenesis of TGF-β mediated aneurysm formation, these data have lead to two multi-centre randomised control trials evaluating the role of angiotensin II receptor (AT1R) antagonists (such as Losartan) which can antagonise TFG-β activity to treat aneurysms[61,62] (Fig 1.6). Similarly there are ongoing trials looking at the role of angiotensin converting enzyme inhibitors in medically managing small infra-renal aortic aneurysms[63,64]. Recent evidence has also implicated intracellular cytokine signaling with P-Smad-2 in smooth muscle cells within the aortic wall, aortic and mitral valves, as well as with Smad independent pathways (Ras, Rhoa, TGF-β activated kinase 1)[57] (Fig 1.6). Although it is still unclear how these interact with TGF-β, they may also be putative pharmacological targets for the treatment of aneurysms.

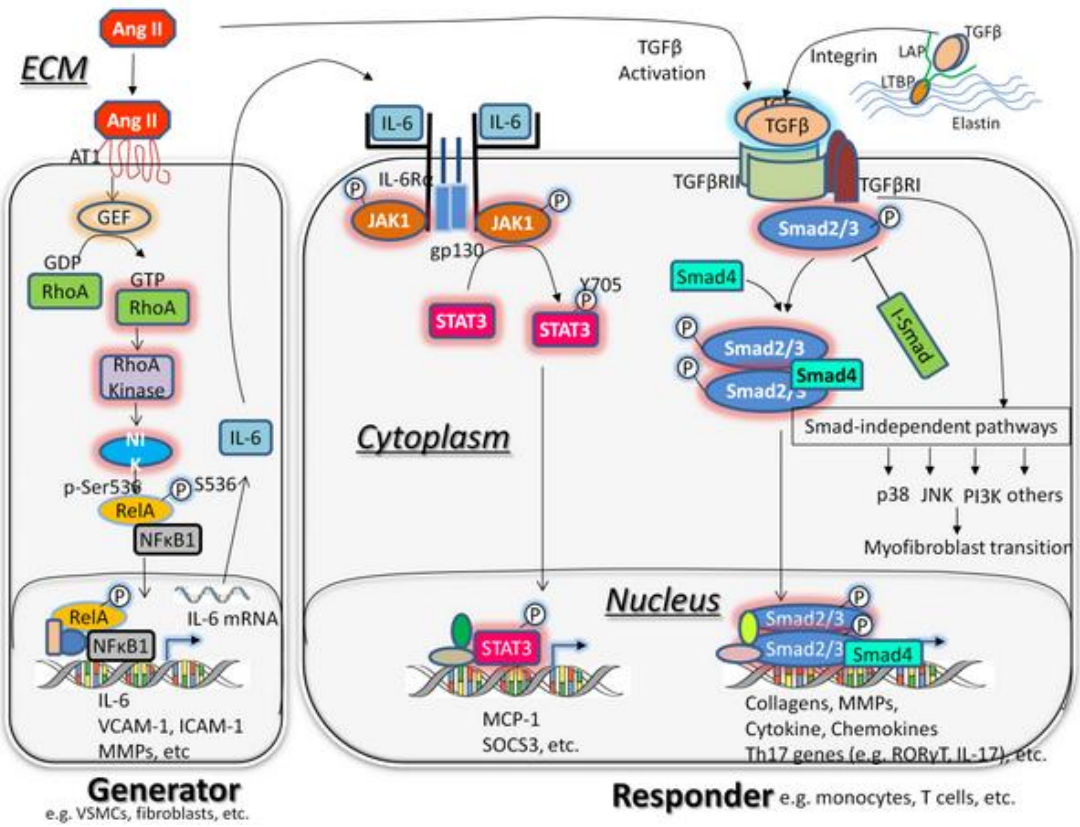

Fig 1.6 Angiotensin II mediated vascular inflammation[65]

Schematic diagrams depicting the cellular events implicated in angiotensin II mediated vascular inflammation. The vascular remodelling response is directly due to down stream signaling interactions between VSMCs and immune cells (lymphocytes, NK cells, mast-cells)[65].

1.4.2 Loeys-Dietz syndrome (LDS)

This is an autosomal dominant syndrome that has features that are similar to Marfan syndrome. It is characterised by mutations in genes encoding the TGF-β receptor 1 (TGFβR1) or 2 (TGFβR2)[66]. Characteristically, patients with type 1 LDS present with early, aggressive vascular disease, arterial tortuosity, aneurysms, hypertelorism, bifid uvula and craniosynostosis. Type 2 LDS patients have abnormalities of the skin, joint laxity, ectopia lentis and present with rupture of visceral organs as well as cardiovascular manifestations [67]. Aortic rupture and dissection occur at smaller aortic diameters in LDS patients, generally at an earlier age compared with patients with Marfan syndrome [68]. The aortic dilatation is maximal at the sinuses of Valsalva but is also observed throughout the arterial tree. The mean age of death in these patients is 26

years. Valve-sparing root replacement by graft implantation is the treatment of choice[69]. Open repair of thoracic and thoracoabdominal aneurysms is the treatment of choice[70].

1.4.3 Ehlers-Danlos syndrome

Ehlers-Danlos syndrome comprises a group of autosomal dominant conditions that arise as a result of mutations in the gene encoding collagen type III alpha 1 (COL3A1) and various enzymes that regulate collagen and elastin homeostasis (ADAMTs2, PLOD1, B4GALR7)[71]. Type IV Ehlers-Danlos syndrome can manifest with life-threatening cardiovascular complications, including spontaneous rupture of mesenteric vessels, development of thoracic and abdominal aneurysms and dissections.

1.4.4 Other genetic syndromes

Turner's syndrome is a condition that affects phenotypic females who lack all or part of the X-chromosome. Thoracic aortic aneurysm affects between 36-618/100,000 women with Turners syndrome per year[72,73]. The majority of these patients go onto develop type A aortic dissection (68%)[74]. The aneurysms occur at a younger age and are highest risk in those aged 30-39 years[72,73,75,76]. Numerous other conditions are associated with aneurysms, such as polycyctic kidney disease, scleroderma and osteogenesis imperfecta.

1.4.5 Familial aneurysms

Familial aggregation studies suggest that 11-19% of patients with thoracic aneurysms have a first degree relative with thoracic aortic disease. These patients with a family history of thoracic aortic disease present at a mean age of 56 years; this is significantly younger compared with non-familial, sporadic thoracic aneurysm cases that present at a mean age of 64 years[77]. In cases where multiple family members are affected, the disease behaves in an autosomal dominant inherited pattern with variable expression and penetration. The most frequently implicated genetic locus is TAAD1 at

chromosome 5q13-14[31]. Other putative loci are FAA1, mapped to 11q23-24, mutated NK (locus 5q13-14 – TAAD1), TGFBR2 (locus 3p24-25 - TAAD2), NK (locus 15q24-26 – TADD3), ACTA2 (locus 10q23-24 – TAAD4), and MYH11 (locus 16p12-13). Increased low-density lipoprotein receptor-related protein 1 (LRP-1) expression towards rs1466535 or the 12q13.3 locus significantly increased the risk of developing infra-renal abdominal aortic aneurysms[33].

Despite the identification of several genetic loci related to aneurysm formation there are multiple familial cases that have not been attributed to these, indicating the presence of additional and as yet unidentified gene mutations. The mode of the genetic inheritance of aneurysms is difficult to identify because of the considerable variation in clinical heterogeneity, variable penetration, age of onset and numerous associated features. It is recommended that all individuals in a 'at risk' family have aortic imaging throughout their lifetime.

It is also increasingly apparent that there are genetic mutations that increase the susceptibility of individuals to develop aortic aneurysms. These are phenotypically expressed with particular environmental insults such as smoking, aging and development of atherosclerosis[78-80]. It is also likely that individuals will acquire a set of mutations that are expressed in an increased number of cells and multiple mutations represent an increased disease burden to the acquisition and development of aneurysms.

1.4.6 Aneurysms associated with bicuspid aortic valves

Bicuspid aortic valves (BAV) are the commonest congenital cardiac defect with a prevalence estimated between 0.5 and 2%[83-85]. BAV is part of a large spectrum of structural developmental abnormalities involving the great vessels. The aortic valve and ascending aorta share the same embryonic origin from neural crest cells. BAV is associated with medial degeneration, increased MMP activity and decreased fibrillin-1 in the aorta. BAV is autosomal dominant with incomplete penetrance. The male-to-female ratio ≥3:1. BAV with Turner

syndrome suggests an X-linked aetiology. Heritability studies have found no X-linkage but linkage to chromosomal regions 5q, 13q, and 18q, including mutations in the NOTCH1 gene (chromosome 9q) that lead to signaling abnormalities that may be responsible not only for development of a bileaflet aortic valve but also accelerated valvular calcium deposition[81,82]. ACTA2 gene (chromosome 10q), which encodes VSMC α-actin are associated with familial thoracic aortic aneurysms and BAV. Deletions of chromosome 22q11.2 resulting in DiGeorge syndrome and velocardiofacial syndrome have demonstrated concomitant BAV, implying ubiquitin fusion degradation 1-like (UFD1L) gene downregulation. BAV thus encompasses a diverse large spectrum of conditions associated with aortic aneurysms that are discussed in following reviews[83-86].

1.4.7 Degenerate aneurysms

Fragmentation of elastin fibres is reported to have an immunological, infectious, inflammatory and/or idiopathic aetiology. Historically termed medial degeneration, it is characterised by the disruption and loss of elastin fibres and increased deposition of proteoglycans. VSMC in the media are also markedly reduced in aortic pathology associated with myosin heavy chain11, smooth muscle *(MYH11)* and actin, alpha2, smooth muscle aorta *(ACTA2)* defects[87]. Degenerated aneurysms are also associated with increased expression of matrix metalloproteinase's (MMPs) in the aortic media, in particular MMP2, 3, 9 and 13. The vasculitidies, including giant-cell arteritis and Takayasu's arteritis, are typified by T-cell clonal expansion, suggesting an antigenic trigger. Marked adventitial inflammatory cytokine and MMP production leads to granuloma formation and vascular destruction by fibrosis. Takayasu's arteritis results in obstructive arterial lesions with a dilatation in up to 15% of cases[88].

1.5 The role of inflammation in aneurysm development

Fragmentation of elastin fibres is reported to have an immunological, infectious, inflammatory and/or idiopathic aetiology (Fig 1.7). Aortic aneurysms are characterised by the presence of a pro-inflammatory cellular infiltrate. Historically termed medial degeneration, this is characterised by the disruption and loss of elastin fibres, increased collagen that is haphazardly arranged and increased deposition of proteoglycans. VSMC numbers in the media are also markedly reduced in aneurysms. There are numerous associated genetic mutations as discussed above (*MYH11, ACATA2*)[83], upregulation of MMPs that are produced by immune cells[41,47,89-93]. Marked adventitial inflammatory cytokine and MMP production leads to granuloma formation and vascular destruction by fibrosis. There is periadventitial inflammation with a host of immune cells infiltrating the aortic media. This involves lymphocytes, NK cells, monocyte recruitment and differention to macrophages all leading to an increased ECM turnover, increased vascularity and VSMC death[94].

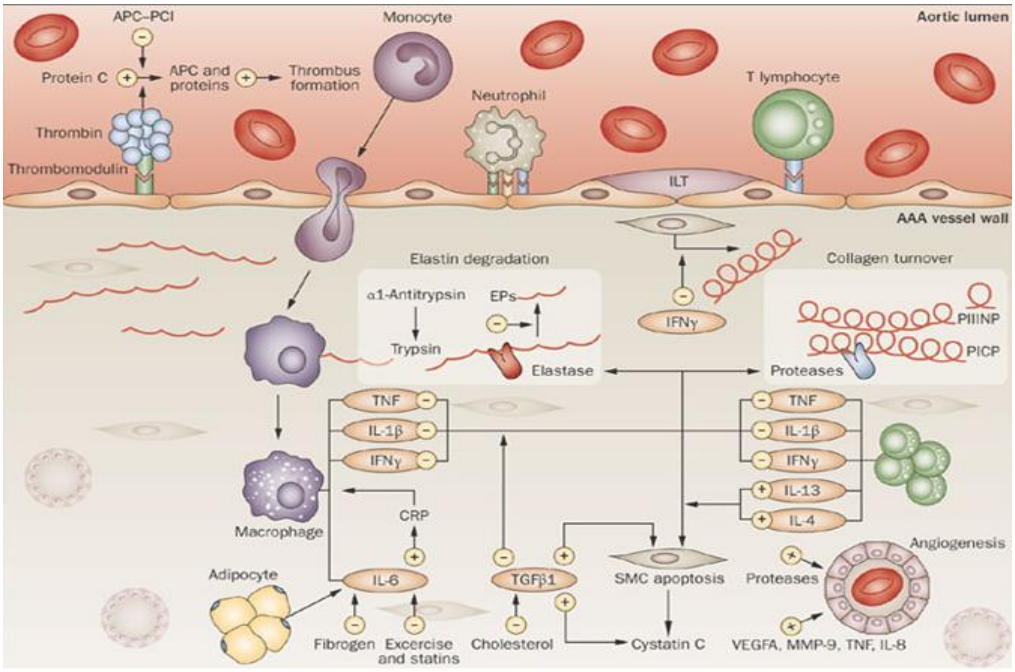

Fig 1.7 Schematic illustration of the mechanisms involved in aortic aneurysm development[94]

The most important processes involved are vascular inflammation and extracellular matrix breakdown[94].

1.5.1 Inflammatory mediators

The aneurysm wall produces cytokines, TNFα, interleukin (IL-1β), interferonγ (INFγ) and interleukin-6 (IL6)[94,95]. IL6 activates B and T lymphocytes, while INFγ stimulates B, T lymphocytes, macrophages, fibroblasts and endothelial cells to produce a pro-inflammatory response. These inflammatory cascades that are seen in *in-vitro* might have a role in the development of aortic wall dilatation, medial degeneration, VSMC apoptosis and loss of ECM[96-99]. Soluble mediators such as monocyte chemotactic protein-1 (MCP-1) and interleukin-8 (IL-8) are expressed in human aortic aneurysms and might be responsible for stimulation of early inflammatory responses[97,98]. There is a corresponding 40-fold more prostaglandin E_2 (PGE_2, produced by the infiltrating inflammatory cells) in aneurysmal wall compared with normal aortic wall[98]. PGE_2 suppresses VSMC proliferation and causes cell apoptosis. PGE_2 inhibition reduces expression of

pro-inflammatory IL1β and IL6 in the aneurysm wall and this might provide a potential therapeutic targets[98-102].

1.5.2 Modulation of inflammatory cell activity

The immune system is divided into the innate and the adaptive immune systems. There is strong evidence to suggest that numerous inflammatory cells have a key role in the pathogenesis of aneurysms. Unlike atherosclerosis, where monocytes/ macrophage cells predominate, aneurysmal disease is characterised by lymphocytes, dendritic cells, mast-cells[102-105]. These inflammatory cell subtypes infiltrate the tunica adventitia and the outer layer of the tunica media through the network of vasa vasora that are found in these regions[106-111]. Little is known regarding the immunogenic triggers for these cells, or what initiates and propagates these inflammatory responses. The key inflammatory cells involved are lymphocytes and NK cells (Fig 1.8).

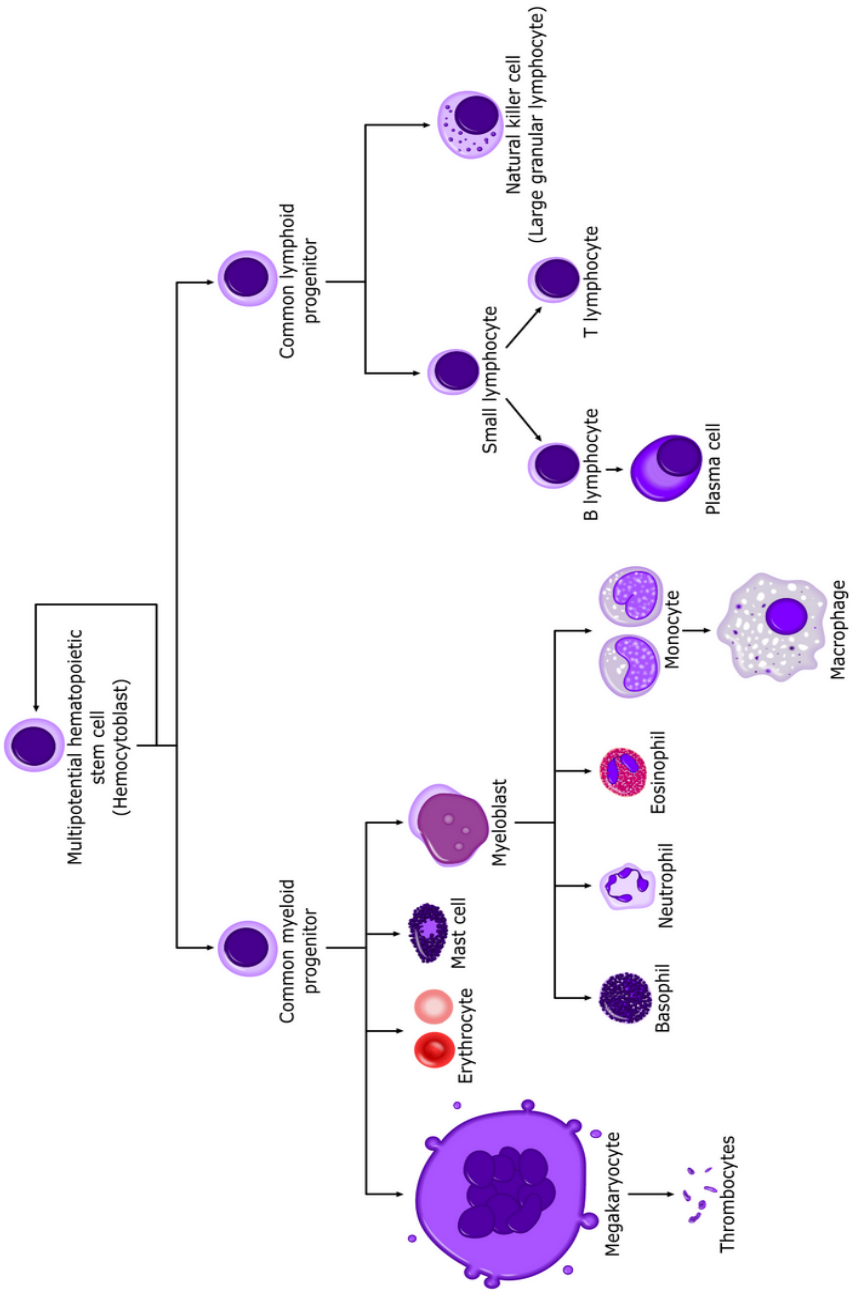

Fig 1.8 Haematopoietic cell lineage

The haemtopoietic stem cells give rise to two major progenitor cell lineages, namely myeloid and lymphoid progenitors. It is the lymphoid progenitor cell lineage that takes part in aneurysm development[109,110].

1.5.2.1 T-cells

T-cells account for over 50% of the $CD45^+$leucocytes present in aneurysmal tissue[37,101,111-113]. Most T-cell subtypes are present, including $CD8^+$ cytotoxic T-cells (Th1), helper $CD4^+$ (Th2), natural killer cells (NKT) and gamma delta T-cells[97,107,110,111]. The ratio of $CD8^+$:$CD4^+$ cells is increased in aneurysms compared with normal aorta suggesting increased antigen presentation, T-cell activation and interaction with B-cells[101, 102]. This would inturn promote a pro-inflammatory cascade with ECM degradation. The activation marker CD69 is present in all aneurysm related T-cells along with HLA-DR expression. T lymphocytes found in the aortic wall were $CD11a^+$, $CD11b^-$, $CD31^{+/-}$, $CD54^+$, $CD29^+$ (clone 4B4), $CD29act^{+/-}$, $CD49a^-$, $CD49d^+$, $CD49e^+$, $CD44^+$, and $CD103^{-}$[97]. This suggests expression of adhesion molecules such as β1, β2 integrins, selectins and the Ig-superfamily members in the aortic wall[102]. These molecules are responsible for cell-cell interaction of activated lymphocytes that are reacting to antigenic triggers in the aortic wall and likely to derive aortic ECM breakdown. This also suggests interaction with VSMCs with alteration of cell adhesion, proliferation and viability[114-116].

There are four subtypes of the T helper cell family (Th1, Th2, Th17 and iTreg cells) Fig1.9. Th1 and Th2 depending on the cytokine production[117]. Th1 cells produce INFγ that activates macrophages and dendritic cells, whereas Th2 produce IL-4, IL-5 and IL-13. The main effectors for these cytokines are eosinophils, basophils and mast cells along with IgE B-cells. Activation of Th2 responses therefore leads to release of histamine, serotonin and leukotrienes and typically mediates autoimmune phenomena such as allergic rhinitis, atopic dermatitis and asthma. This subset can also convert B-cells to become plasma cells and produce antibodies or form memory cells[113]. The presence of local pro-inflammatory cytokines such IL6 and IL21 can skew the differentiation of T-cells into a Th1 phenotype[113-115]. TGFβ, a cytokine associated with tissue repair [114-116] drives differentiation of native T helper cells into Th17 cells[118-121]. Th17 cells are responsible for host immunity against extracellular agents[122]. Once

triggered by IL-6 and TGFβ, their main effector cytokines are IL-6, IL-1 and TNFα. These cells inturn activate neutrophils, B-cells (IgM/ IgA producing) and other IL17 producing $CD4^+$ T-cells[119,121-124]. They derive the complement system of proteins and are implicated in autoimmune conditions such as rheumatoid arthritis[125].

Activation of the Foxhead box transcription factor, FoxP3, by TGFβ production and Th17 cells enhances the formation of Treg cells[124]. IL23 is required for the formation of Th17 cells, which are responsible for production of various chemokines (IL17A, IL17F, IL21, IL22 and IL17) that mediated recruitment of leucocytes and the interaction of T-cells with B and NK cells[124-125]. There is little literature published on the role that Th17 and Treg cells might have in the pathogenesis of aneurysmal disease, but the available data suggests that they might have a role in modulating the inflammatory response. Induced T regulatory cells (iTregs) are those expressing $CD3^+CD4^+CD25^+FoxP3^+$ and are involved in self-tolerance. These cells have been shown to suppress Th1/ Th2 cells. These cells are derived from mature $CD4^+$ cells outside the thymus and are different from the natural Tregs. Although they function in a similar manner, acute depletion of this population in murine studies has lead to active inflammation[125] .

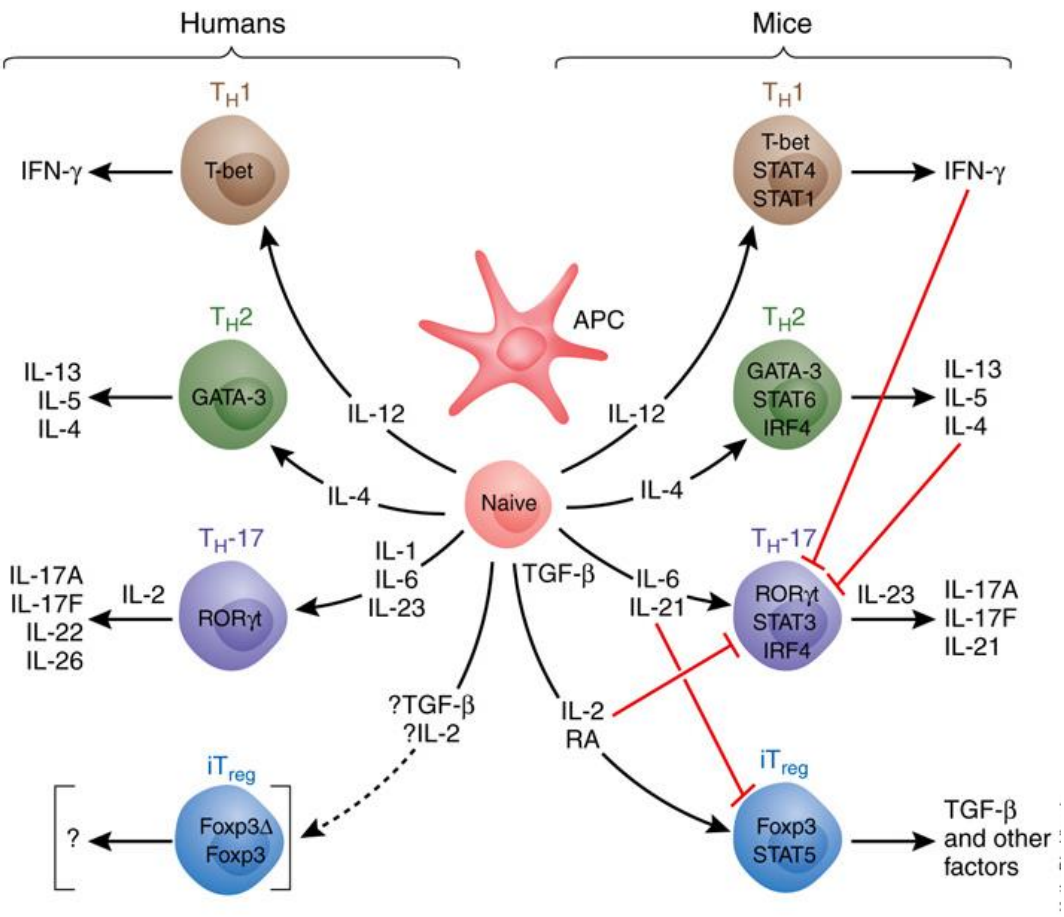

Fig 1.9 T-cell subtypes

After stimulation by antigen presenting cells (APCs) the T helper cells differentiate into variety of subsets, each defined by the cytokines that they secrete. TGFβ is a critical factor in differentiation of the two lineages with completely different attributes. Th1/Th2 are the inflammatory subset whereas the Th17/ Tregs are the anti-inflammatory cells. T-bet, T-box expressed in T-cells; RA, retinoic acid; iTreg, inducible Treg; Foxp3Delta, spliced Foxp3[126].

1.5.2.2 B-cells

B-cells account for up to 40% of the mononuclear cell infiltrate in the aneurysm wall. B-lymphocytes express the surface markers, $CD19^+$, $CD20^+$ and $CD40^+$, but also other markers suggestive of activation (Fig 1.10)[101]. B-cells might take part in formation of germinative centres of inflammation as histologically plasma cells have been demonstrated in the wall of aneurysms [127-129]. B-cell subpopulations produce immunoglobulins, but the significance of this within the aneurysm wall remains unknown. The activated B-cells and plasma cells in the aortic aneurysm wall express activation markers $CD69^+$ and $CD80^+$ [102, 129]. There is increased production of IgA^+ and IgG^+ B-cells in the aortic wall compared to the blood of patients with abdominal aortic aneurysms[102, 128]. Work from other authors has suggested B-cell rich infiltrate concentrated in the adventitia of AAA is an autoimmune response to specific tissue antigens[129]. Genetic analysis from the adventitia of the aortic wall demonstrated immunoglobulin heave chains genes from B-cells to be present in the tissue[129,130].

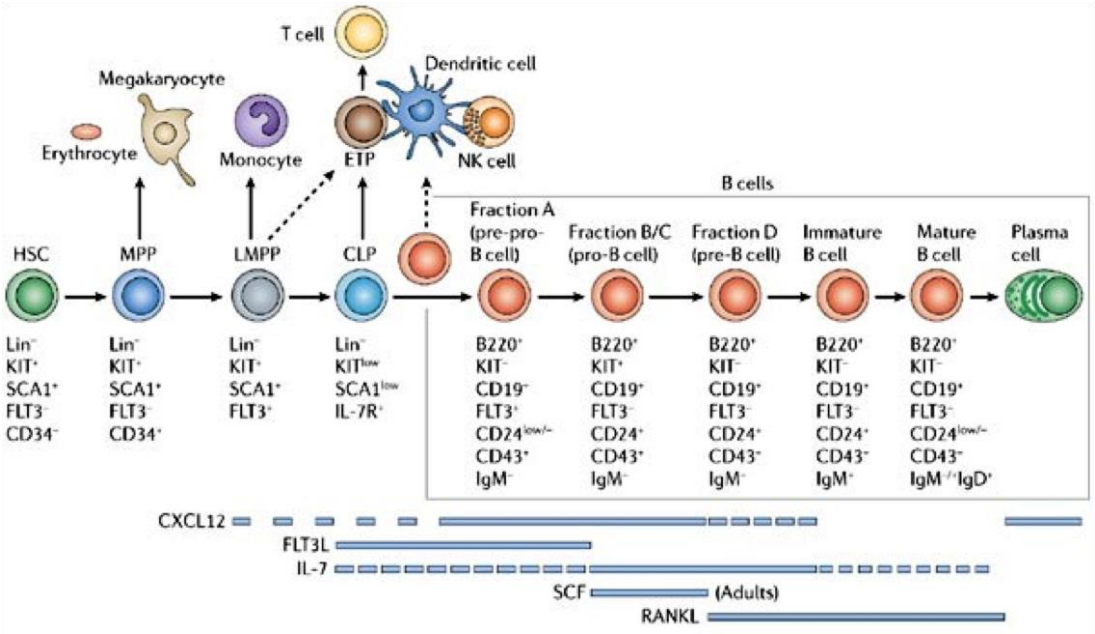

Fig 1.10 B-cell subtypes

Haematopoietic stem cells (HSCs) are $Lin^-B220^-KIT^+SCA1^+$ fms related tyrosine kinase 3 $(FLT3)^-$ $CD34^-$ cells. B-cells originate from lymphoid progenitors that are $Lin^-KIT^{low}SCA1^{low}$interleukin-7 receptor $(IL\text{-}7R)^+$ cells. B-cell subsets are pre-pro, pre and pro B-cells that are delineated as per their cell surface markers. The pre cells are released from the bone marrow and differentiate in response to antigenic stimulation and T-cell interaction. This in turn leads to phenotypic change. In adults the stem cell activation factor (SCF) and receptor activator of nuclear factor B ligand (RANKL) are involved in formation of pre-B and immature B-cells. ETP, early T-cell-lineage progenitor; NK, natural killer[130].

It is possible that the interaction of T and B-cells is important in monocyte recruitment, activation to macrophages and alteration of VSMC phenotype from elastogenic to elastolytic with increased breakdown of ECM (Fig 1.11). Of the immunoglobulin's produced, IgG1, 3 and 4 predominate and may be responsible for classical complement activation (*via* C3)[131,132]. The presence of Ig heavy chains indicates a polyclonal B-cell population resident in the aneurysm tissue that follows rather than initiates the inflammatory cascade.

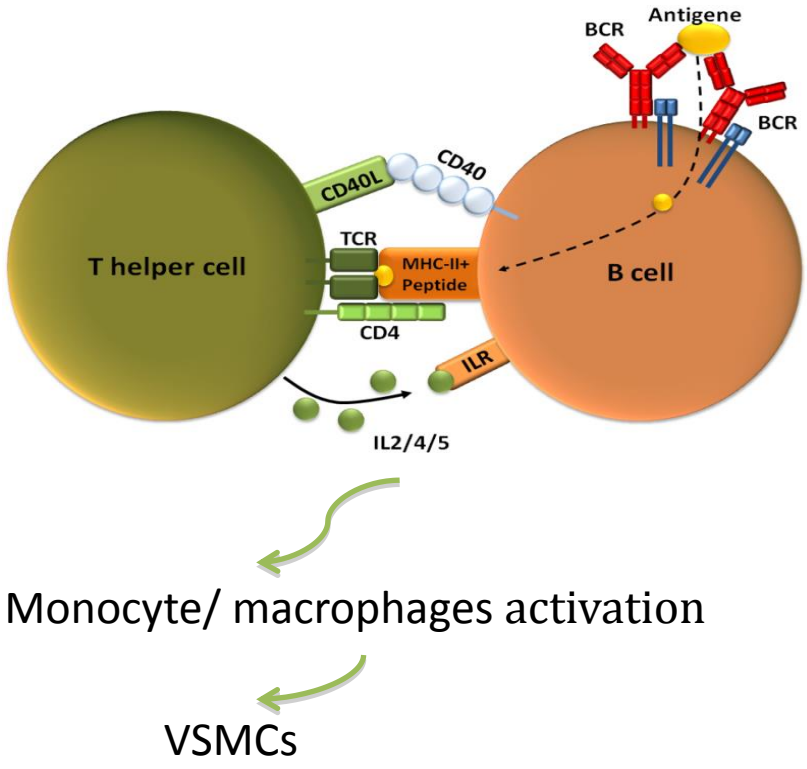

Fig 1.11 Mechanism of B-T-cells interaction

The interaction of B with T-cells is important in leading to monocyte recruitment, macrophage activation and alternation of VSMC phenotype. Modified from Janeway[127].

1.5.2.3 NK-cells

NK cells represent subset of T lymphocytes that express T-cell receptor (TCR$\alpha\beta$) and markers of NK cells (NK1.1), $CD122^+$ and $CD56^+$. These cells are $CD4^-/CD8^-$[133, 134]. These cells are able to produce gamma interferon and IL-4 and have been demonstrated in aneurysm wall[134, 135]. This might be the reason why Th1 T-cells predominate in aneurysms over Th2 phenotype. It is likely that these immune cells are responsible for effector action on VSMCs and through these actions influence the ECM in the aortic wall.

1.5.2.4 Macrophages

Monocytes and macrophage can infiltrate the aortic wall and release proteases, elastases and MMPs directly in the adventitia and tunica media and therefore compromise VSMC function, ECM production and hence wall integrity[136,137]. These cells also produce pro-inflammatory cytokines namely TNFα, INFγ and IL6[94,95,137-139] that recruit inflammatory lymphocytes into the aortic wall. These processes precede aortic wall dilatation and are involved in the growth and rupture of aneurysms in animal models[94,135-137]. It has been suggested that macrophage derived angiopoietin-like protein 2 accelerates development of AAA[138,139]. Additionally decreased *Notch1* protein protects against the formation of AAA by preventing macrophage recruitment and attenuating the inflammatory response in the aorta[140].

Macrophage infiltration appears in the adventitia and outer media of human AAA and correlate to aortic diameter[136]. In AAA with and without ILT macrophages are associated with a high degree of neovascularization[137,138]. In aortic ruptures there is increased propensity to find macrophages and T lymphocytes[139-143].

1.5.2.5 Neutrophils

Neutrophil polymorphs are found within the luminal layer of ILT that occurs in AAA at the interface with luminal blood. They are known to produce neutrophil elastases that are responsible for breakdown of ECM. The ILT rich in neutrophils are more likely to lead to aortic degradation with increased likelihood of aortic rupture[144-146]. ILT can store proteases[147,148] including neutrophil derived proteases and these can lead to inhibition of platelet aggregation or activation and aneurysm enlargement. Neutrophils produce neutrophil chemotactic factors, including IL8 and thus amplify its own recruitment[148].

1.5.2.6 Mast cells

Mast cells have been described in the adventitia of the aortic wall[149]. Although these cells are known for there involvement in chronic inflammatory and hypersensitivity allergic reactions there enumeration in the aortic wall might suggest a role in the development of aneurysms[149]. Mast cell deficiency has been associated to reduced aortic expansion in murine studies and infusion of bone marrow derived mast cells from WT subjects returned the aneurysm phenotype to TNF-α deficient animals[149]. Conversely mast cell deficient mice when infused with bone marrow derived mast cells from IL6 or IFNγ deficient mice did not form aneurysms[149]. There might be redundancy in cell phenotypes and it might be that mast cells act by producing IL6 and INFγ that inturn influences lymphocyte activity and function[97].

1.5.3 Inflammation and neovascularisation

Chronic inflammatory process in the aneurysm leads to an angiogenic response in the aortic wall[90]. The density of endothelial cells is 15-fold greater in aneurysms compared with the normal aorta and 3-fold greater compared with atherosclerotic aorta[99]. This is associated with histological medial neovascularisation, elastin degradation and chronic inflammatory cell infiltration. The increased aortic wall proteolysis, with caseinolytic serine proteinases and gelatinolytic MMPs and their inhibitors (TIMPs), are localised to the vasa vasorum[150,151]. It was suggested that aneurysm development occurs through progression of angiogenesis and inflammation from the base of the atherosclerotic plaque into the aortic media. It is likely, however, that the process starts peri-adventitialy and works its way down into the tunica media [147-149]. Neoangiogenesis might be important in allowing recruitment of activated inflammatory cell to the aortic wall[90,152-155] and has been associated with sites of rupture[151]. MMP 8 and 9, that are associated with angiogenesis, are located in the aortic adventitia[157,158]. It is probable that the MMP activity in the aneurysmal wall facilitates neovascularisation leading to inflammatory cell recruitment and further dysregulated proteolytic degradation of the ECM[145,153]. Exposure of integrin binding sites in the ECM in the aortic wall leads to endothelial-cadherin endothelial cell-cell adhesion interactions. The resulting positive feedback loop leads to the generation of proangiogenic cytokines and increased neovascularisation from the tunica adventitia into the tunica media[157,159]. B-T-macrophage interactions result in the generation of cytokines that induce the expression of molecules such as Ephrin B1 and its cognate receptor EphB2[160,161] effecting cell-cell interactions in the endothelium, and in this way mediating neovascularization[160,161].

1.6 Extracellular matrix proteins

1.6.1 Elastin

Elastin is a key extracellular matrix protein that is critical for the elasticity and strength of numerous biological tissues. This includes blood vessels, lung, skin, tendons and cartilage. Elastin enables the artery to stretch and recoil and maintain a consistent blood pressure and also has a critical role in supporting and maintaining cell health[162-167]. Tropoelastin is a soluble 70kDa protein, produced by VSMCs and fibroblasts that is the key building block of all elastin.

1.6.1.1 The elastin gene

There is one tropoelastin gene (ELN), in contrast to other connective tissue proteins such as the collagens that are expressed by complex gene families[165-167]. The human ELN gene possesses 34 exons, giving rise to multiple isoforms. The mRNA encodes for a 72kDA polypeptide depending on the splicing pattern[168]. Removal of a signal peptide leaves a 60kDa protein. There are at least 11 human tropoelastin variants dependent on alternative splice variants (domains 22, 23, 24, 26A and 33)[169,170]. ELN is expressed before birth with the vast majority of elastin synthesis and deposition occurring before birth and within the first few years of life[169-172]. From a young age there is a reduction in the elastin synthesis with extremely low-level expression by middle age. Thereafter, there is a slow turnover of elastin in tissues, with small amounts being deposited in response to degradation in various tissues. Elastin is therefore a highly durable and stable structural protein with a biological half-life of approximately 74-years in man[173].

ELN gene expression is variable and the primary transcripts can be spliced in different forms that contain various introns and exons giving rise to slightly different forms of tropoelastin varying in protein sequence and therefore composition[167,174]. Certain exons such as 26A are not transcribed in healthy

tissues, but highly expressed in damaged tissues (e.g. in skin following UV or thermal damage)[175, 176].

Decreased LOX levels have been reported in human hypertension. Thus defective elastin cross-linking might lead to decreased distensibility and compliance precipitating the development of hypertension[177]. In mice LOX inactivated phenotypes develop aortic aneurysms and perinatal death[178]. Genes associated with microfibrillar proteins; fibrillin-1 and fibrillin-2 are linked to Marfan syndromes.

The elastin content is decreased in aortic aneurysms from 35±3.2% to approximately 8%±3% of dry weight in the tunica media of the aorta[178,179]. The elastin fibres are disorganised with increased breaks and altered ratio of desmosines/isodesmosines. The serum elastin peptides and plasma alpha 1 antitrypsin levels are elevated, that are considered markers of elastin degradation[178,179]. The result of a decrease in elastin content leads to decreased ability of the aortic wall to deal with haemodynamic shear stress with low aortic distensibility[180].

1.6.1.2 Elastin fibre formation

Cross-linkage of tropoelastin molecules occurs through the action of lysyl oxidase (LOX), an amine oxidase catalysing the cross-linking process through oxidative deamination of the epsilon-amino group of specific Lys chains. Tropoelastin combines with other proteins including elaunin, oxytalan and Emilin1 to form elastin fibres [180,181]. Tropoelastin undergoes post-translational modification and cross-linkage in the cell cytoplasm followed by release into the extracellular environment with further cross-linking to create insoluble mature elastin [168,183-185]. Tropoelastin contains two domains that are important for its cross linkage. A hydrophilic domain consisting of lysine and alanine and a hydrophobic domain consisting of glycine, valine and proline. These alternate to form the cross-linked networks that comprise the elastin fibres. The splice

junctions and cross-linked regions are highly conserved, whilst the hydrophobic domains are variable. The C-terminus region is highly conserved being composed of two cystine residues joined by a disulphide bond. Disruption of this area leads to dramatically reduced ability of tropoelastin to form fibres. Elastin fibre formation also involves other molecules including microfibrils of fibrillin and fibulins-4 and -5[186].

Tropoelastin assembles into globules of several microns in diameter and is chaperoned from the endoplasmic reticulum to golgi apparatus and then to the cell membrane. The elastin binding protein (EBP) is responsible for this. Tropoelastin is rapidly assembled and cross-linked into fibres in the extracellular space. The monomers self assemble *via.* coacervation, aligning and concentrating the proteins into spheres prior to cross-linking[187]. The coacervate tropoelastin is attached to the cell surface collecting further tropoelastin units until released to nascent elastic fibre (Fig 1.12).

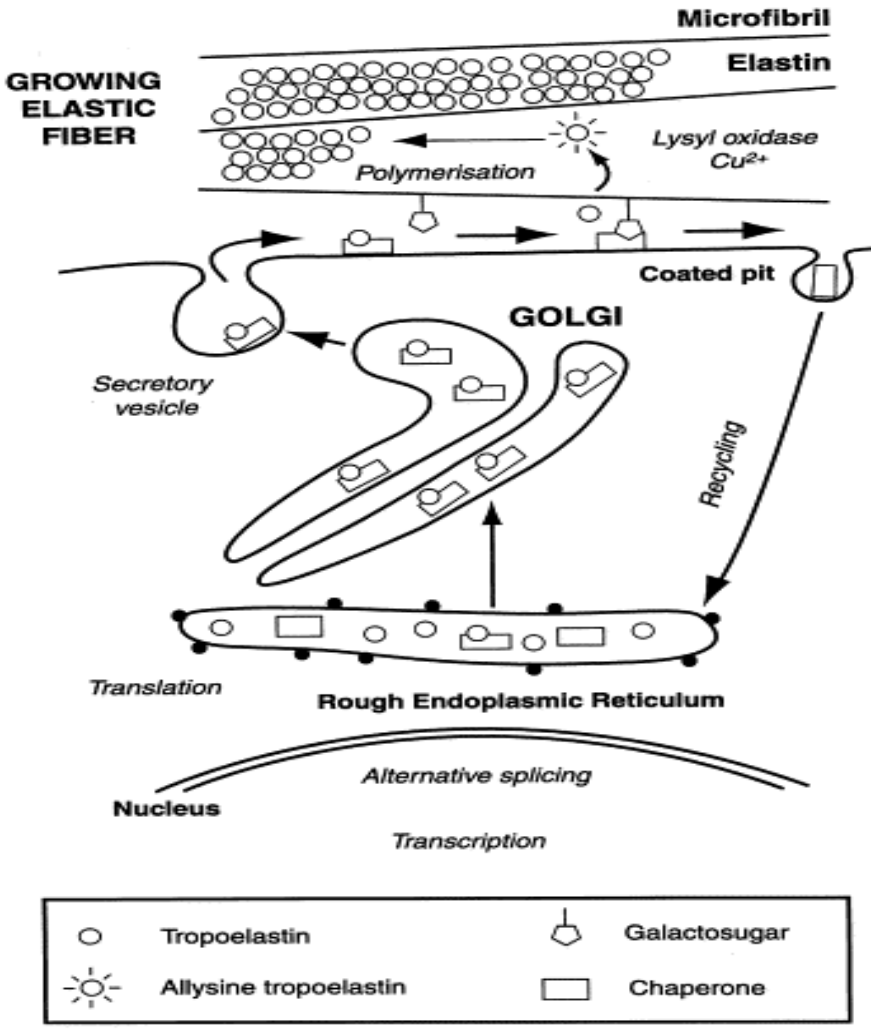

Fig 1.12 Elastin fibre synthesis

Tropoelastin is synthesised on the rough endoplasmic reticulum and captured by molecular chaperone proteins, preventing aggregation and its storage in the Golgi apparatus. It is released in vacuoles into the EC space. In contact with other elastin fibres the chaperone interacts with the galactosugars of microfibrils releasing the tropoelastin that is aligned and cross-linked by LOX. There is irreversible polymerisation between fibrillin, laminin, emilin and integrins to form elastin fibres[188].

1.6.1.3 Elastin protein composition

Once formed the tropoelastin amino acid sequence is divided into two major domains. The hydrophilic (lysine and alanine) and hydrophobic (glycine, valine and proline) residues. These alternate to form cross-linked networks composing elastin fibres. The splice junctions and cross-linked regions are highly preserved whilst the hydrophobic domains are variable. The C-terminus region is highly conserved being composed of two cystine residues joined by a

disulphide bond. Disruption of this area leads to dramatically reduced ability of tropoelastin to form fibres. Elastin fibre formation also involves other molecules including microfibrils of fibrillin and fibulins-4 and -5[186]. Recent studies have demonstrated further action of various other proteins, namely co-operativity between fibulin-2 and fibulin-5, emilin-1 regulating oxytalan fibre formation[186]. Emilin-1 is a prototype of a newly discovered family of glycoprotein, EMILIN[181,182]. Emilin-1 forms fibrillar network in vitro and in the ECM in tissues and co-distributes with elastin, forming an important component of elastic fibres[187]. Emilin-1 is localised to the interface between amorphous elastin and the surrounding microfibrils, and is required for the correct deposition of elastin[181,182]. Emilin-1 interacts in-vivo close to cell surface. It is likely that emilin-1 interacts with integrins and elastin fibres to form the ECM[188-190]. Integrins are widely present heterodimeric proteins that are essential in cell adhesion, migration, cell differentiation and ECM formation. Integrin $\alpha_v\beta_3$, a promiscuous RDG-dependent integrin is important in associations between fibrillin-1, 2, MAGP-2 and fibulin-5[191-194]. The protein folding leads to a structure including poly-proline II, compact ß turns and an organisation that produces a flexible protein configuration.

1.6.1.4 Elastin expression, activation and turnover

Tropoelastin is produced by VSMCs and fibroblasts. Tropoelastin assembles into globules of several microns in diameter and is chaperoned from the endoplasmic reticulum to golgi apparatus and then to the cell membrane. The elastin binding protein (EBP) is responsible for this. Once deposited the production of tropoelastin is reduced and little turnover of mature cross-linked elastin occurs over prolonged periods (Fig 1.12). Majority of elastin is laid in the late foetal and early neonatal periods[195].

In the event of injury the production of tropoelastin is recommenced. This is regulated by numerous cytokines and growth factors such as insulin like growth factor-1, interleukin 1ß, TNFα and TGF[196]. A set of proteases grouped

under elastases remodel elastin. MMP 2, 3, 9 and 12 are known to degrade elastin [91-93].

1.6.1.5 Elastin assembly

Tropoelastin is rapidly assembled and cross-linked into fibres in the extracellular space. The monomers self assemble *via.* coacervation, aligning and concentrating the proteins into spheres prior to cross-linking[187]. This process occurs optimally at 37°C at pH 7-8 in physiological electrolyte concentrations. The coacervate tropoelastin is attached to the cell surface collecting further tropoelastin units until released to nascent elastic fibre. There is interlinking of the tropoelastin with integrin proteins, cross-linking with LOX and deposition to form microfibrils incorporated into mature elastic fibres[188].

1.6.1.6 Elastin organisation and turnover in the vessel wall

Elastin represents 57% of the protein content of normal thoracic aorta and this decreases to 30% in abdominal aorta. Collagen represents 20% of the aortic extracellular matrix. Elastin is therefore responsible for providing resilience in the aortic wall, while collagen is characterised by its resistance to high pressure and provides tensile strength to the aortic wall. It is the lost of elastin from the aortic wall that leads to progressive aortic enlargement. The subsequent reduction in the tensile strength of the aorta relies increasingly on the collagen fibre mesh that comprises the adventitia. The increase strain of the expanded aorta exceeds the capacity of the elastin and collagen to resist expansion leading to rupture.

The quantity of elastin varies with age, aneurysm development and segment of aorta. It is thought to be VSMCs that are responsible for elastin production and fibroblasts, endothelial cells and inflammatory cells that are responsible for turnover of elastin and collagen. Histologically the aortic wall is arranged into three layers, namely intima, tunica media and tunica adventitia (Fig 1.5). There

are two dense condensations of elongated elastin fibres that are present in the media. These are the internal and external elastic laminae. Endothelial cells line the intimal lining, the media being composed of elastin fibres. Elastin is organised as 'lamellar units' of abundant organised elastin fibres that are cross-linked. VSMCs are also present in the media and interplay with the elastin in providing resilience and distensibility with cardiac cycle. There is a decrease in number of elastic lamellae in the infrarenal abdominal compared to the thoracic aorta. The tunica adventitia is the outer most layer that is composed of a thin network of collagen fibres with a minimal elastin content.

The durability of elastin has been demonstrated in *in-vivo,* and when extracted *in-vitro* to be decades[173,197,198]*.* Elastin is degraded in a variety of conditions in various tissues - aging in the skin, emphysema in lung parenchyma in and aneurysms in aortic wall. Once deposited the production of tropoelastin is reduced and little turnover of mature cross-linked elastin occurs over prolonged periods. The majority of elastin is laid in the late foetal and early neonatal periods[195], but in the event of injury the production of tropoelastin recommences. This is regulated by numerous cytokines and growth factors such as insulin like growth factor-1, interleukin 1ß, TNFα and TGF[196,197]. Enzymes with elastolytic activity such as MMP 2, 3, 9, 12, cathepsins K, H and S that are present in aneurysmal wall degrade and remodel elastin[91-95].

1.6.1.7 The relationship between inflammation and elastin remodeling

There is emerging evidence that elastin peptides might be responsible for immunomodulation in the aortic wall[198,199]. There is continuous degradation during the lifetime of elastin fibres. The elastin peptides (EP) that are produced might be able to exert chemotactic effects on neutrophils, monocytes and other immune cells by acting like chemoattractants such as C5a and formyl peptide (FMLP)[200,201]. Once at the site of EP degradation they are stimulated to produce oxygen free radicals, elastases and MMPs[91,196,201-203]. These interactions are balanced in the normal aortic wall, as there is extremely slow

degradation of elastin and therefore EP formation. There are also numerous protease inhibitors in the aortic wall such as α-1 antitrypsin, secretory leukocyte protease inhibitor-binding protein (SLPI), skin-derived antileukoproteinase (SKALP) and TGFβ that inhibits elastin degradation by increasing the expression of tissue inhibitors of metalloproteases (TIMPS)[204,205]. In aortic aneurysm wall this balance between synthesis and degrading enzymatic milieu is altered. The reason for this is not known and it is this chronic antigen stimulation of the immune system in the aortic wall that leads to aneurysm generation. In some cases this is measurable with increased pro-inflammatory cytokines such as IL-6, IL1β or TNFα[206,207]. It is also recognised that there is inverted CD4:CD8 ratio caused by expansion of the $CD8^+$ cells leading to a chronic low-grade inflammatory process[71,208]. EP strongly induces oxidised LDL and therefore influences neutrophil polymorphs, monocytes and lymphocytes[201,209].

Previous experiments on plaques have demonstrated EPs activate the elastin-laminin receptor and it is the $CD4^+$ T-cells that are attracted to the arterial wall[199,200]. This process is thought to be responsible for osteogenic response in VSMCs and lead to arterial wall calcification. The Th1 polarisation mediated by the EP binding on S-Gal leads towards a Th1 phenotype from previously non-orientated lymphocytes. This pre-orientation is preceded by production of IL-6, 12 and MMP9[202]. These cytokines might stimulate the secretion of proteolytic enzymes further contributing to the inflammatory process. This role of EP in maintaining and modulating the inflammatory process in the aortic wall has not been investigated in aneurysmal disease.

1.6.1.8 Elastin and aging

The elastin concentration decreases with age in the aorta, but the content remains the same[210-212]. This is due to increase in other components such as collagen[212]. Age can effect the amino acid structure of elastin[207]. The cross-linking amino acids desmosine and isodesmosine remain unchanged at 3/1000

amino acid residues, and start to decrease after the age of 63 reaching 2/1000 amino acid residues when aged 86[208]. Other studies have shown continuous decrease in amino acid residues with age throughout adult life and the content of histidinoalanine increases[208]. Histidinoalanine is an important residue in senescent elastin fibres and forms cross-links between neighbouring acidic proteins, collagen and elastin and might be responsible for age related changes in aortic wall elastin[208]. There is fragmentation of elastin fibres with aging and in atherosclerotic aortas[209-211]. This is explained as a consequence of mechanical fatigue failure due to pulsatile wall strain experienced by the aorta over the number of cardiac cycles over a lifetime[212-214]. There is a chemical proteolytic degradation of the aortic wall by MMPs with a decrease in the levels of TIMPs.

1.6.1.9 Distribution of elastin within the vasculature

The elastin content is higher in the thoracic aortic wall with 60 lamellar units, with a decrease to approximately 28 in infra-renal abdominal aorta. The most marked decline occurs between descending thoracic and supracoeliac aorta[214,215]. There is a 50% decrease in elastin content between the supra-renal and infra-renal aorta. This reflects a corresponding change in blood pressure with decrease in arterial compliance[216].

1.6.2 Collagen

Collagen is present in all tissues and provides a structural framework and strength. Collagen contains one or more domains of a triple helical structure composed of α-polypeptide chains that have a repetitive triplet sequence containing glycine (Gly-X-Y). There are more than 28 different collagen types that can be classified into five sub-families.

i) Fibril forming – Types I, II, III, V, XI

ii) Network forming – Types IV, VI, VIII, X

iii) FACIT (Fibril associated collagen with interrupted triple helices) – Types IX, XII, XIV, XVI, XIX, XX, XXI

iv) Multiplexin (Multiple triple helix domains and interruptions) - Types XV, XVIII

v) Transmembrane - XIII, XVII

Collagens that are involved in the basement membrane surrounding cells include collagen Type IV {[α1(IV)]$_3$}, XV {[α1(XV)]$_3$}, and XVIII {[α1(XVIII)]$_3$}. Aortic wall contains Type I and III collagen along with the basement membrane components[152,223,224]. The aortic wall tensile strength is drawn from discrete fibrillar bundles of collagen that range from 10-200nm in diameter[225-227]. The collagen fibres are present between the elastic lamellae and the SMC in the tunica media and the adventitia. Although the histological appearance of these fibres is loose they are highly effective and provide tensile strength under pulsatile blood flow[228,229].

1.6.3 Extracellular matrix degradation in aneurysmal disease

1.6.3.1 MMPs and their inhibitors

These are a family of zinc dependent endopeptidases that were first described by Busuttil in 1985[230] and have subsequently been implicated in the pathogenesis of aortic aneurysms[45,93,99,231-237].

MMP 2, 9, 13 are considered to be important peptides in aneurysm development [84,234,237,238]. The degradation of medial elastin in the aortic wall appears to be an initial step in the cascade of event leading up to aneurysm development. Elastases (MMP2, 7, 9, 12) and collagenases (MMP1, 8, 13) can degrade elastin and collagen [46,232-240]. MMP 13 is expressed in VSMCs in the aortic wall [71,72,234]. Elevated levels of MMP1 mRNA and an increased MMP1 to TIMP-1 ratio are found in aneurysm wall compared to normal aorta [234,240]. Real-time reverse transcriptase polymerase chain reaction (RT-PCR) quantification of gene expression has revealed MMP1 and 3 to be elevated in the aortic aneurysm wall compared to non-dilated regions of aorta [241].

Increased extracellular matrix degradation is characterised by increased gene expression ratio of MMP1 to TIMP1, 2, 3 and MMP3 mRNA to TIMP2 mRNA.

Tissue inhibitors of matrix metalloproteinases (TIMPS) are a family of 4 naturally occurring inhibitors of MMPs Cellular expression of TIMPs occurs at a transcriptional level with stimuli inducing concurrent MMP and TIMP production. As with MMPs, TIMP levels are increased in aortic aneurysms. Studies on normal and aneurysmal aortas have shown that MMPs are expressed in the presence of TIMPs[212,151,242-244]. TIMPs dampen the potential of widespread tissue damage of MMPs and enhancing their levels has been postulated for potential disease modulation (e.g. the adenoviral over expression of TIMP-1 in a mouse model of atherosclerosis leads to a reduction in lesion size[251,252]. Expression of TIMP-1 in rat aorta prevents aneurysm expansion and rupture[247-249]. TIMPs could therefore be specifically targeted in cardiovascular conditions such as aneurysms that involve excessive tissue remodelling[234,250,251]. TIMP3 is significantly up-regulated in aneurysm aortic wall and affect VSMC apoptosis[232]. It is likely it acts to inhibit the effects of MMP3 and stromolysin 1[232].

1.6.3.2 Cathepsins

These are a potent group of elastolytic enzymes that have also been implicated in aortic aneurysm development[252-254]. Most cathepsins are serine proteases, although some such as cathepsin D are aspartic proteases. Cathepsins work best in intra-cellular lysosomes that provide an acidic environment and are important in peptide degradation and antigen presentation. Macrophages are implicated in release of cathepsins in the extracellular space[254]. Cathepsins are inhibited by serine protease inhibitors, such as cystatin A, B and C[255-257]. Cystatins A and B are type I cystanins and are intracellular cathepsin inhibitors. Type II cystatins include cystatin C – that is the most potent cathepsin inhibitor[259]. Cystatin C shows the highest inhibiting properties to cathepsins L

and S, followed by B and H. Interestingly the proteolytic activity of some cathepsins is ten times more powerful than MMPs[47].

Aneurysmal wall is characterised by the up regulation of cathepsins and down regulation of cystatin C[253]. Cathepsins are involved in the formation of microvessels and VSMC apoptosis which characteristic of aortic aneurysm development. Levels of cathepsins B, D, and G are elevated in aortic aneurysms by 1.5 fold compared to normal aorta[253]. Levels of cathepsin C and L are also elevated in the aneurysm compared to the normal aorta[47,252,253]. Aneurysm tissue had less serine protease activity compared to thrombus that had high activity compared to clot[252]. Intimal VSMCs and macrophages express elastolytic cathepsins S and K. Cultured human VSMCs expresses cathepsin S and K on stimulation with IL-1β or γ-interferon. An important limitation of this work is that the cathepsins levels are compared between aneurysmal and normal aorta, however the presence of atherosclerosis would confound the results, as it is associated with significantly elevated cathepsin B, H, L and S levels[45,253,257,259].

Cystatin C deficiency is associated with progression of aneurysms[260]. Genetic polymorphisms in the cystatin C signal peptide and the signaling peptide (+148G>A and -82G>C, respectively) demonstrate a slower growth rate for aneurysms than compared to the +148AA and -82C genotype[48]. The deficiency of cystatin C in ApoE$^{-/-}$ mice leads to the thinning of the tunica media and aortic dilatation. These effects are thought to be mediated as a result of the effects on the cathepsin pathways not the MMP expression in the tissue[261].

1.7 Diagnostic imaging

Imaging of aneurysms has been carried out using a variety of techniques. The early techniques such as computer tomography provided anatomical detail, whilst more recently developed and used functional imaging techniques provide an analysis of the biological processes that are on going in the aortic wall.

1.7.1 Chest radiography

Many asymptomatic TAA are first detected on chest x-rays. Ascending aortic enlargement produces convex contouring of the right superior mediastinum. If the aneurysm is in the aortic root only, then the cardiac silhouette may obscure it. Aneurysms need to be large and AAA is not delineated (Fig 1.13).

Fig 1.13 Chest radiograph of thoracic aortic aneurysm

Typical chest x-ray finding of mediastinal widening demonstrating a large thoracic aortic aneurysm

1.7.2 Ultrasonography and echocardiography

Ultrasound and enhanced scanning for abdominal and echocardiography for thoracic aneurysmal disease are relatively portable tools that allows cheap, non-invasive diagnosis of acute aortic disease. In case of TAA, aortic valve pathology and detection of complications such as AD and IMH can be made. Transoesophageal echo (TOE) is the most accurate and reliable method of echocardiography for the thoracic aorta. It is limited by the views obtained, as only the aortic root and proximal ascending aorta can be reliably imaged (Fig 1.14).

Fig 1.14 Transthoracic echocardiogram of ascending aortic aneurysm

Long axis view of the left ventricular outflow tract showing the dilatation of the aortic root and the proximal ascending aorta (Ao). The leaflets of the bicuspid aortic valve are visible (arrows).

1.7.3 Computer tomography (CT)

This is a widely used method for imaging of the vascular tree. It provides a quick and anatomically detailed assessment of the aortic size, extent and location of aneurysmal disease. Modern 256-slice scanners can acquire high-resolution full body 0.7mm slice images in a single breath hold. Not only do they help define the nature of the aneurysm, but they also diagnose any complications and development of acute aortic syndrome. Computer software programmes allow 3-dimensional (3D) reconstruction of the images that aid the surgeon in operative and endovascular planning, as the scans can be used to manufacture bespoke aortic endografts for the patients. The main disadvantage of CT is the need for intravenous contrast agent for optimal

spatial resolution. This may be contraindicated in patients who have contrast allergy or at a high risk of developing contrast induced renal failure. There is also the problem of radiation exposure form the scans. A single chest CT is equivalent to 400 chest x-rays, whereas an abdominal CT has the same radiation exposure as 500 x-rays. For an aortic CT scan the radiation exposure is 9.9mSV (millisievert) with the average background exposure in the UK being 1-3mSv per year.

1.7.4 Magnetic resonance imaging (MRI)

1.7.4.1 Basic principles

This technique is based on the principle of electromagnetic activity (EMA) of atomic nuclei. The nuclei contain protons and neutrons that have specific spins. When the spin of neutrons and protons does not cancel each other fields, we are able to detect EMA. When performing a clinical MRI we utilize the protons in the hydrogen nucleus in water molecules. The quantity of water alters in various tissues with varying physiology and in pathological conditions. The hydrogen nuclei rotate around their own axis. A small magnetic field is created as a result of this rotation and called a magnetic moment. When we place a strong external magnetic field we align the hydrogen protons either in parallel or antiparallel directions to the z-axis of the field. The magnetic moments by themselves cancel each other out. There is however alignment of hydrogen nuclei after redistribution so that a greater proportion of the protons are aligned parallel to the field. This is the moment of the nuclei are magnatised. During this interaction the spinning nuclei wobble or precess. This occurs at a frequency that can be calculated by Larmor equation. At each particular frequency we can change the spin of the protons in the magnetic field allowing the signal to change.

MR signal is generated because magnetization is a field with a vector quantity. This has a longitudinal component along the z-axis and transverse component along the XY-axis. The transverse magnetization processes around a receiver

coil induces a current (as per the Faraday principle of induction) and this current becomes the MR signal. It is therefore the transverse magnatisation field that produces the MR signal. As the radiofrequency (RF) energy source is removed, the magnetization vector realigns with the axis of the external magnetic field and the spins of the protons returns the dynamic equilibrium. This time interval during which the longitudinal magnatisation increases or recovers is referred to as the T1 relaxation time (T1R denoted in milliseconds (ms)). The transverse magnetization delay is referred to as the T2 relaxation time. Individual tissues have different T1 and T2 values. For example water has a relatively long T1 and T2, whereas fat has shorter T1 and T2.

1.7.4.2 T1 and T2 relaxation

The longitudinal magnetization recovers as spinning nuclei release energy during the T1 relaxation. This phenomenon is also referred to as the spin lattice relaxation principle. The transverse magnetisation is dephased as the interaction between the spinning nuclei and their magnetic fields during T2 relaxation. This principle is referred to as spin-spin relaxation. In case of T2, the magnetic field can be dephased as a result of inhomogenities that occur in the field. The magnetic field is not exactly the same everywhere as there is differential interaction of air, metals or indeed limitations of magnetic construction. This decay of the transverse magnetisation as a result of these factors is referred to as T2* decay. While T2 is due to random motion of hydrogen nuclei moving within the moving water molecules. The T2* is the resultant field as the source is static but there are magnetic field inhomogeneities within the MR scanner. The T2* decay is therefore shorter than T2 and occurs rapidly in fat and water.

1.7.4.3 Repetition time and echo time

The tissue contrast created on the MRI is as a result of the differences in T1, T2 and the proton densities. The creation of the MR image is due to the parameters referred to as a repetition time (TR) and echo time (TE). The TR is

defined as the interval between the two RF pulses (ms). TE is time between application of the RF pulse and the peak of the echo detection after this. The TR and TE affect the relaxation times in the different tissues allowing anatomical delineation.

1.7.4.4 MR signal localization

An MRI gradient is the application of linear variation in the magnetic field to detect a 3D location of the signal. This process is achieved by passing electric currents through specific 'gradient coils'. This leads to protons within a region being excited by the RF pulse. The information that is detected about the phase shifts in spinning protons is stored within the MR system referred to as the 'k-space'. Their location can be calculated using mathematical modeling using the inverse Fourier transform.

1.7.4.5 Generation of MR sequences

The pulse sequences formed as a result of the coil gradients and RF pulses are used to form a MR image. There is an RF pulses for each x-, y- and z- gradients. MR sequence generation is based on spin echo or gradient echo sequence. These can be 2-dimensional or 3-dimensional with volume of multiple sections that are obtained at a signal acquisition time.

1.7.4.6 MR T1 and 3D T1-mapping

Longitudinal relaxation time (T1) for each pixel (T1-mapping) has been hypothesised to provide additional information about the characteristics of the aortic wall[262,263]. Inversion recovery (IR) sequence is the gold standard sequence for T1 measurement. This needs a long acquisition time and is therefore clinically limited in utility. A modified Look-Locker sequence can be used to speedup the 3D T1-mapping. The importance of T1 quantification in detecting change in pathophysiology and directing therapy also needs further investigation.

1.7.4.7 MRI in aortic imaging

MRI allows excellent contrast between soft tissues and blood flow can be visualised in the heart and aorta. Magnetic resonance angiography (MRA) requires the use of a paramagnetic contrast agent such as gadolinium or a technique called “flow-related enhancement”. The latter uses signal generated as a result of the movement of blood. Axial and sagittal oblique T1 weighted fast spin echo (FSE), axial “bright blood” gadolinium enhancement 3D MRA that is ECG-trigger gated is ideal. The advantages of MRA are that there is no nephrotoxic contrast agents or ionising radiation. The disadvantage of this modality is that it is not as rapid as a CT. Even the fastest scans take 10-15mins compared with a single breath hold for a CT. 3D MRA can be rapid, however it does not provide information on aortic wall itself, therefore axial images are needed to delineate intramural dissections, wall thickening and other acute vascular pathology i.e. PAU, haematoma, adenopathy. The scanners are noisy and very narrow a large minority of patients do not tolerate the scan. The need to remain still to reduce motion artifact in an elective compliant patient is not a problem, but in an acute clinical setting with critically ill patient that needs complex monitoring the scan is not possible. The presence of any ferric metallic prosthetics material in the patient also precludes from MRA.

1.7.5 Positron emission tomography (PET)

PET is a nuclear imaging technique that creates a 3D image of functional processes that occur in the body. The system detects pairs of gamma rays emitted indirectly from a positron-emitting radionuclide (tracer) that is introduced into the body on a biologically active molecule. Two photons result from the disintegration of the positron and are emitted in opposite directions (i.e. at 180 degrees from each other) and recorded in coincidence by the detectors surrounding the subject. A 3D image is created at the same time as the PET scan with the use of CT.

Depending on the radionuclide, a wide variety of physiological and pathological processes can be studied at the molecular level. However, in routine clinical practice, in the vast majority of PET studies, the most commonly used biologically active molecule for PET is fluroride-18 (^{18}F) labelled deoxyglucose, creating the tracer fluorodeoxyglucose (^{18}F-FDG). ^{18}F-FDG is injected into the body where it may accumulate in the tissues with high metabolic activity. During the positive beta decay of ^{18}F, a positron is emitted. This travels in tissue for typically less than 1mm during which time it loses energy and interacts with an electron. The encounter annihilates the electron and positron, releasing gamma photons that move in opposite directions. These are captured by a scintillator generating a burst of light that is detected by photomultiplier tubes.

FDG is a glucose analogue, transported into cells using glucose transporters (GLUTs). Once inside the cells, FDG is phosphorylated to FDG-6-phosphate that cannot be hydrolysed by the enzymes of the glycolytic chain, and therefore accumulates in the cell. FDG-PET recognises increased metabolic activity and is mainly used for cancer imaging. Cellular glucose metabolism is significantly increased in most types of cancers because of increased expression of membrane transporters or increased hexokinase activity. Increased uptake is observed in many non-neoplastic physiological and pathological conditions. For example, when inflammatory cells are activated they have an increase in glucose metabolism and uptake[264-267]. This has been evaluated in various experimental settings, including induced inflammatory states, activation of T lymphocytes in bacterial abscesses or in B-lymphocytes after viral infection[264,266-268]. The lack of specificity for tumours provides a powerful tool for using PET to evaluate inflammatory and infectious conditions including monitoring of vascular graft infection[268-270].

The amount of ^{18}F-FDG uptake correlates to metabolic activity measured by an indexed value – SUV (standardised uptake value)[270-274]. Therefore, rapidly dividing cells, active infection and inflammation will all be sites of high PET

tracer uptake. It is believed that proteolytic and inflammatory processes are at work in the development and propagation of aortic aneurysms and acute aortic syndrome. There is therefore a scientific basis to use these scans for determining aortic activity and predicting aneurysm behaviour. It should be noted, however, that ^{18}F-FDG uptake is often seen in the arterial wall, in the absence of any known inflammatory vascular disease[269-271].

^{18}F-FDG-PET/CT has already an established role in oncology diagnosis confirmation and assesses response to therapy. It has also been used to assess stability of atherosclerotic plaques[265,271-273]. High SUV in the setting of atherosclerotic plaques has been linked to cardiovascular risks, levels of inflammatory markers and macrophage infiltration into tissue[271-274].

Glucose uptake within cell in the aortic wall *via* facultative passive GLUT transporters is varied. The glycolytic activity in the aneurysmal versus normal aortic wall might be different. There have been data reported to suggest that glucose metabolism is increased in AAA patients related to MMP9 activity[275]. GLUT1 is the major isoform in most cells, whilst GLUT 3 is responsible for increased energy utilization as has high affinity for glucose. It is also the main GLUT subtype in immune cells such as neutrophils and macrophages[276-278]. Hence energy utilization by the aortic wall is a reflection of the various cells composing the aortic wall and their glycolytic activity. In AAA models the GLUT3 synthesis is dependent on MMP9 levels and this might be a reflection on macrophage aortic wall content. In ApoE$^{-/-}$ angiotensin II infused animals the expression of GLUT1 decreases in the aortic wall and GLUT3 increases which might be a reflection of immune cell infiltration (monocyte-macrophages) in aortic wall[279]. GLUT10 deficiency is associated with upregulation of TGFβ pathway in the arterial wall, a finding in Loeys-Dietz syndrome and arterial tortuosity syndrome (an autosomal recessive disorder characterized by tortuosity, elongation, stenosis and aneurysm formation with elastic fibre disruption in aortic media. The identification of GLUT transporter

gene involved in arterial dilatation denotes a link between GLUT, aneurysm development and type 2 diabetes[280].

1.7.6 Single photon emission computer tomography (SPECT)

This technique is very similar to PET, in its use of a radioactive tracer and detection of gamma rays. However, the tracer used emits gamma rays that are directly measured. During a PET scan the emissions or the coincident events provide more radiation events per unit of tissue therefore providing greater information on tracer uptake. PET therefore provides higher resolution than SPECT (which has a resolution of 1cm). SPECT is, however, quicker with a total scan time of 15-20 mins (compared with 60-90 mins for a PET scan) as two gamma camera's can be rotated around the patient varying the angle by 3-6^{o} with a full 360^{o} rotation for a complete reconstruction. It has been validated in myocardial perfusion scanning with the use of ^{99m}Tc-sestamibi or ^{99m}Tc-tetrofosmin as a tracer. SPECT conducted after a stress stimulus reveals areas with relatively low blood flow when compared to previous images[264,274,281,282]. This technique is now being applied to aortic aneurysms in experimental work with novel tracers that are though to accumulate in inflammatory areas in the aorta[264,274,282-286].

1.8 Predicting aortic aneurysm behavior

Clinical symptoms and aortic diameter dictate intervention for aortic aneurysms[287-289]. Multivariate regression analysis looking at factors responsible for increased risk of aneurysm rupture or dissection demonstrate that size above 5.5cm for abdominal and ascending aortic aneurysm and a size above 6.5cm for descending thoracic aortic and aortic arch are associated with a five to ten fold increase in complications[21,22,25,290]. Female sex, connective tissue disease, smoking and COPD are all negative predictors of outcomes. The risk of rupture with time is 11 times worse with aortic size of 5.0 to 5.9 cm and nearly 27 times worse with size of 6.0 cm or higher when compared to aneurysms less than 4cm diameter. Larger aneurysms have higher wall shear stress as dictated

by Laplace's law. Leading to high rupture risk. It is also long been recognised that the presence of symptoms indicates an 'unstable aortic wall' that is likely to rupture[291,292]. Apart from these two parameters originally described 45 years ago there is at present, no other way to predict the biological events going on in the aortic wall that are likely to represent aortic aneurysm expansion, rupture or dissection. Functional imaging aims to provide a mechanism to study the cellular and molecular events ongoing in the aortic wall that are likely to lead to a better understanding of aortic wall behaviour.

1.9 Biological pathways for molecular imaging

The main mechanisms that have been studied in human aneurysm development are aortic inflammation, angiogenic response, haemorrhage, elastin synthesis, proteolysis and thrombosis. The presence of inflammatory infiltrates (characterised by a mononuclear cell infiltrate that differentiates to tissue resident macrophages) and neovessels in complicated plaques were reported as early as the 1930s[286-289,293]. These neo-capillaries develop in complicated plaques at the interface of the lipid core, the cap and the media with ingress from the adventitia. They are thought to allow leukocyte diapedesis and accumulation of other inflammatory mediators into the aortic media. The development of these neo-vessels from the vasa vasora is linked to the extent of inflammation that follows, with subsequent haemosiderin deposition, propagation of inflammation and weakening of aortic wall[144,293]. In aneurysms, the breakdown of collagen, elastin, proteoglycan matrix is linked to an inflammatory cascade, vascular oedema and adventitial neoangiogensis[144,294,295]. It is this proteolytic injury that weakens the aortic wall and leads to rupture[113,294,295]. ILT is generated at the blood luminal interface[114,296-298]. Luminal platelet activation and fibrin formation activates leukocytes propagating the aortic matrix degradation. These biological pathways explain the initiation, propagation and development of acute complications of aortic aneurysms. Any new imaging modalities will have to

specifically target the cells and molecules involved in these pathways to study aneurysm clinical expression.

1.9.1 Activity based probes

MMPs produced by macrophages, VSMCs and the endothelial cells are important in regulation of the ECM in the aortic wall. MMPs are also responsible in cardiac remodelling. MMPs can be coupled to ^{123}I, ^{99m}Tc, ^{18}F or gadolinium to enable imaging using SPECT-CT, PET and MRI[296-300]. Other molecular probes could depend on the enzymatic activity rather than simple expression of their targets. This allows for amplification of imaging signals. For example, an MMP probe that contains a substrate for MMP 2, MMP 3, MMP 9 or MMP 13 conjugated to cyanine 5.5 for near infra-red fluorescence [131,287,288]. If there is no MMP activity, the fluorescence is absent as the molecules are close together. If, however, there is peptide substrate that can be cleaved by MMP it leads to liberation of cyanine 5.5 leading to an up to 200 fold increase in signal[137,261,300]. The sites to which the probes are localised reflect sites of enzyme activity and therefore might represent metabolically active aortic wall.

Similarly cathepsins that possess cysteine protease activity in lysosomes are important in ECM regulation. Normal human aorta has minimal cathepsin expression, however diseased aortic tissue expresses cathepsin S and K[261,292,301,302]. Attaching cyanine 5.5 to generate a probe that can be image using fluorescence tomography might allow cathepsin localisation in tissue[301-304]. Near infra-red fluorescence localises to sites of disrupted elastin fibres in association with inflammatory cells expressing cathepsin[302,303]. This has been used in atherosclerotic plaques and in carotid artery atherosclerosis[304,305].

1.10 Hypothesis

Functional imaging of aortic aneurysms with existing and novel PET and MRI agents can predict aneurysm behaviour.

1.11 Aims

1) To elucidate the association between ^{18}F-FDG uptake and inflammatory cell composition of the aneurysmal wall

2) To characterise the relationship between ^{18}F-FDG uptake and of a novel elastin specific MR contrast agent (ESMA) to inflammatory cell composition in aneurysm wall in the ApoE$^{-/-}$ ATII model, and to use these to predict aneurysm behaviour

3) To use the ApoE$^{-/-}$ ATII model to determine the efficacy of treatment with an antagomir to microRNAs that regulate elastin turnover

4) To investigate the interaction between tissue-derived inflammatory cells and VSMC function in order to determine whether specific inflammatory cell types induce a pro-aneurysmal phenotype in smooth muscle cells

Chapter 2: Optimization of PET-CT, use laser scintigraphy and creation of 3D masks for aortic aneurysm biopsy

2.1 Introduction

PET creates high-affinity three-dimensional tomographic images of the distribution of positron emitting radionuclides that are injected into the body. These can be radiolabelled ligands, substrates, antibodies, drugs and other biomolecules that are tracers for specific biological processes. The resultant images are 'functional' as they demonstrate biochemical and/ or physiological activity of the underlying tissues. The initial and currently used PET study protocols focus on cerebral, myocardial and oncological metabolism. The most widely used substrate being flurodeoxyglucose (^{18}F-FDG) as a marker of glycolysis. However FDG uptake is non-specific and is positive in any highly metabolically active cell. Within tumours and inflammatory lesions it is taken up by macrophages and other blood cells. It remains to be seen if ^{18}F-FDG PET-CT would provide useful information for the investigation of aortic aneurysms. In order to provide clinical utility the PET is coupled with a CT scan to provide anatomical information on the vasculature. The accurate image fusion to generate a precise three-dimensional map of the aorta with the PET uptake is vital for locating the aortic wall with the specific PET FDG uptake. The subsequent process is to translate this data into a 3D phantom that would allow the precise biopsy of the sites with varying FDG uptakes to be carried out at surgery.

2.2 Aims

1) Develop a protocol for performing aortovascular PET scans using ^{18}F-FDG that would allow the most optimal vascular tracer uptake in the aortic wall;
2) Develop an imaging software protocol to allow accurate image fusion of PET and CT data to generate hybrid fused PET-CT images to guide surgical biopsy;
3) Develop an anatomically patient specific and precise 3-dimensional segmentation of the aortic vasculature with the PET data overlay;
4) Develop a methodology to carry out accurate aortic biopsies from sites of known ^{18}F-FDG uptake using laser scintagraphy;
5) Validate the aortic masks for accuracy using phantom scanning and retrograde image reconstruction.

2.3 Methods

2.3.1 Patient preparation

It is imperative to minimise the tracer uptake in normal tissues whilst maintaining a high uptake in target structure (aortic wall). Patients were therefore not allowed to consume glucose prior to the scan. Adequate hydration is important to ensure low ^{18}F-FDG concentration in urine (as a radiation safety precaution post procedure) and therefore up to one litre of water was given 2hrs prior to the scan. The patients were kept seated post ^{18}F-FDG injection to prevent increased mobilisation of ^{18}F-FDG in the muscles.

Patients who were diabetic or those with impaired renal function with creatinine clearance of < 30mls/min/1.7m^2 were admitted 12hrs prior to the scan for intravenous (IV) hydration. This was discontinued 4hrs prior to the scan. The scan was carried out late morning and the blood glucose values were normalised as much as clinically possible. All patients had their blood glucose

measured and if value was >7mmol/l the scan was rescheduled for another day. Care was also taken for patients on metformin that were due to get iodinated IV CT contrast medium. They required further IV hydration post scan and a baseline and post procedure renal function check prior to discharge. Patients were provided with patient information sheet that detailed the procedure as per the ethics, research and development protocols (appendix 1, page 333).

2.3.2 Positron emission tomography

As with PET scans carried out for investigating oncological, inflammatory and infectious processes, the patients were starved for at least 6hrs prior to the scan. This was to minimise background uptake from the gastrointestinal track that would obscure the abdominal aortic ^{18}F-FDG uptake. Additionally when investigating inflammatory processes glucose loading significantly decreases glucose transporters expression and ^{18}F-FDG uptake in inflammatory lesions.

A net 3% accuracy of ^{18}F-FDG activity was verified by the user. ^{18}F-FDG (300-400 MBq, 2.5 MBq/kg body weight ±10%) was injected through an indwelling catheter 60mins before the acquisition of the scan. This is normally 90mins for oncological studies but was reduced for vascular imaging as this optimal vascular signal to background uptake. Images are then acquired with an emission scan photons collected from the patient and transmission scan (using an external gamma source). We carried out a classical acquisition from the skull base to the femoral heads over 30mins (Table 1 and 2, appendix 2, page 343). The effective radiation dose being 0.025mSev/MBq. The sequences were recorded at each couch position for 3mins. Coronal, sagittal and transaxial images were based on ordered subset expectation maximisation iterative reconstruction algorithm with post-injection segmented attenuation.

2.3.3 Computer Tomography

The CT scan of the thoracic, abdominal or thoracoabdominal aorta was carried out using 64 x 3.75mm detectors, a pitch of 1.5 and 5mm collimation (150kVp and 30mA in 0.8s), using a Philips Brilliance 64 scanner (Philips Inc. US). A scout CT scan was carried out with helical CT from the region of interest namely aortic arch to femoral head. A non-contrast and contrast CT scan was carried out following the administration of intravenous contrast agent. The initial CT was solely carried out for correction of attenuation, scatter and co-localisation. The optimal tube current, voltage, slice thickness, rotation time and pitch were chosen to minimise radiation exposure for the patient. The diagnostic contrast CT was carried out post PET scan. We ensured that the patient was within the CT-AC field of view (FOV) and in the same position as during emission scanning. The breathing pattern and rate was monitored as deep inspiration at chest causes misintegration and artifacts compared to normal breathing. If CT quality was deemed not of diagnostic quality by the radiologist a repeat scan was carried out. The CT angiogram range is determined by the location of the aneurysm. The patient set-up, scan margins are outlined in Table 3 (appendix 2). The CT parameters used are outlined in Table 4 and the CTA parameters in Table 5 and 6 (appendix 2, page 343).

2.3.4 Image acquisition

The integrated PET/CT system allowed sequential acquisition of corresponding PET and non-contrast CT images with both data sets intrinsically co-registered providing that the patient did not move during or between the acquisitions. Both the CT and PET data sets were subsequently fused using the Hermes software system (Hermes Medical Solutions Ltd, UK). This allowed fused PET+CT data to be seen over the complete data set. A further IV contrast CT scan was acquired for aortovascular anatomical delineation. This data set was fused with the PET imaging using the Hermes or OsiriX software packages.

2.3.4.1 PET image reconstruction

PET emissions information is corrected for detector efficiency and the geometric response, system dead time, scatter and attenuation, hence normalisation is carried out to account for these variables. Some of these corrections are carried out during the reconstruction process. This was done to obtain the quantitative information from the scan. The data present in 3D mode used to perform 3D reconstructions or rebinned in 2D format for slice-by-slice display. We used the iterative reconstruction algorithms to perform the reconstruction with and without attenuation correction. This corrects for possible reconstruction artifacts that arise due to CT based attenuation correction. The reconstructed 3D volume data set is seen in transaxial, coronal and sagittal planes. Minimum and maximal intensity projections are also generated. All data sets were standardised at reconstruction to obtain the SUV_{max} and comparable resolutions. This is important, as the SUV values need to be interchangeable between the patients.

2.3.4.2 CT image reconstruction

Filter backed projection algorithm was used for image reconstruction. The images were in 0.625mm slice thickness. The slice overlap and filter were constant. The reconstruction kernels used modulate image characteristics within the slices such as spatial resolution, edge enhancement and signal to noise ratio. Longitudinal z filters were used to change the slice sensitivity profiles. The attenuation values were normalised to water density to assign device and time independent numerical value to the reconstruction. The z-dimension is almost as high as transaxial resolution allowing high affinity image visualisation in coronal and sagittal views. The CT values were calculated as:

CT value = Hounsfield unit = 1000 (μ-μ water)/ μ water

2.3.5 Laser Scintagraphy

This technique is used to fabricate a highly accurate scale model of the aortic aneurysm using three-dimensional computer aided design data. The PETCT DIACOM data sets were used to generate a 1mm manual segmentation of the aortic profile in Amira 5.3.3® software (Visage Imaging Inc. San Diego, CA). The PET data was overlaid on the mask to generate fenestrations corresponding to regions with varying ^{18}F-FDG uptake as represented by $SUV_{max.}$ The SUV_{max} ranges varied from patient to patient and upto 10 fenestrations were placed per aortic mask. These data files were transferred to be used in Magic v7.5 (very-large-scale-integration layout tool, Magic Software Enterprises, US). This allows the files with the aortic model and the fenestrations to be subtracted to generate the final aortic model. This was given various thickness ranging from 100 to 500µm, to best try the model that would allow aortic biopsies to be undertaken. To optimize process flows, laser sintering is carried out using the Formiga P100 (Eos GmbH, Germany), which can generate individualized masks of the aorta from a polyamide polymer. This material has high strength and good flexibility, is chemically inert and malleable. The turnover time for the production of this mask is less than 12hrs. The masks generated are washed and steam sterilized for 15mins at 121°C before use.

2.3.6 Phantom generation and validation

The aortic masks that were generated using the laser scintigraphy technique were tested for accuracy. PET and CT scans were carried out on the masks with sites of specific ^{18}F-FDG uptake as points of fenestration marked with surface tracers. The tracers contained the CT contrast agent (Omnipaque350™, GE Healthcare, Canada), as well as 10MBq of ^{18}F-FDG. The process was used to compare the accuracy of the mask generated and the sites selected from the fused PET-CT as fenestration points at sites of varying ^{18}F-FDG uptake. This process acted as a validation tool; as once the mask was generated using the fused PET-CT DIACOM data sets, it was rescanned with the fenestrations

marked out and the image overlaid onto the previous PET-CT to “backtrack” for resolution and accuracy.

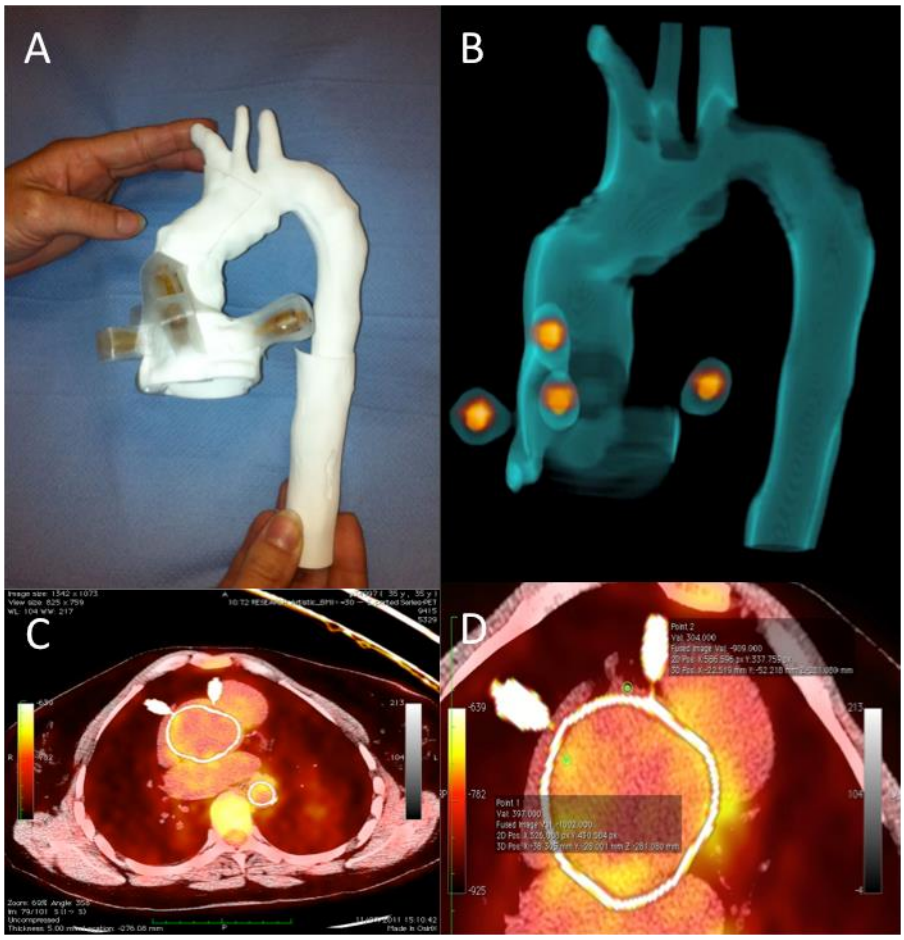

Fig 2.0 Aortic mask generation and phantom testing

A) Aortic mask generated for a patient used to place phantom radiotracer markers. B) Locating the radiotracers in 3-dimensional imaging of the aorta on PETCT scanning. C and D) Fused PETCT DIACOM dataset used to align and co-localise the tracer to specific areas of the aortic wall.

2.3.7 Image analysis

All the human images were pre-operatively analysed and reported by a senior nuclear medicine physician and a vascular radiologist on Hermes Medical Solutions platform (Nuclear Diagnostics AB, Stockholm, Sweden). All the scan data was also reconstructed and processed by the researcher in Hermes, OsiriX software (OsiriX Inc. San Antonio, Texas) and Amira 5.3.3® (Visage Imaging Inc. San Diego, CA). The slices were indexed at 3mm intervals with the PET data (Fig

2.1). Image registration was carried out with data fusion and the images were analyzed in axial, coronal and sagittal planes. Additionally, reformation of the data was carried out in 2-dimensional orthogonal multi-planar reconstructions (MPR) and 3-dimensional image reconstructions (Fig2.1 and Fig 2.2).

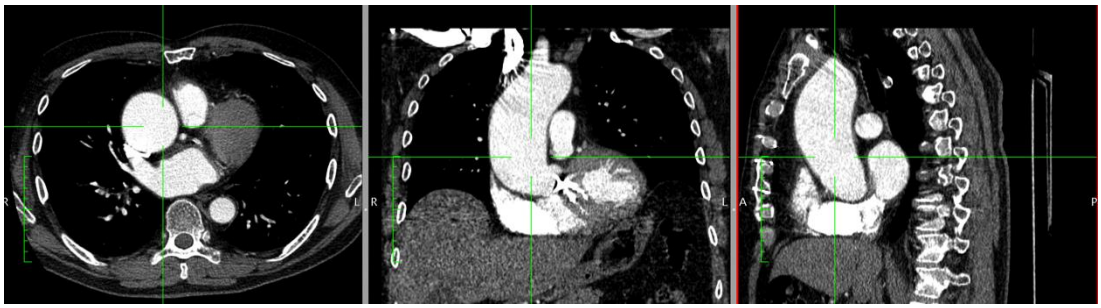

Fig 2.1 2D orthogonal multi-planar reconstructions of ascending aortic aneurysm

Axial, coronal and sagittal views of IV contrast aortic scan. Reconstructions were performed to assess the aortic morphology accurately prior to 3D reconstructions.

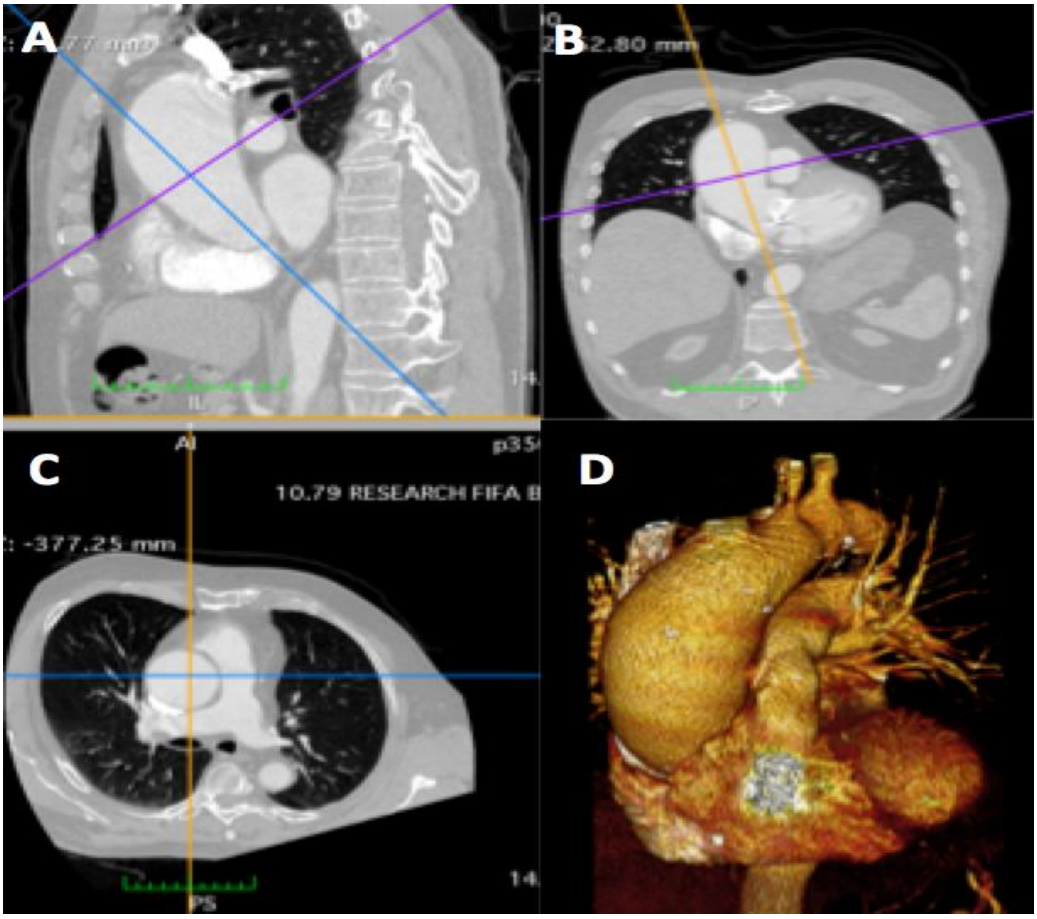

Fig 2.2 3D multi-planar reconstructions of ascending aortic aneurysm

A) Sagittal B) Coronal C) Axial D) 3D volume rendered reconstruction of the ascending aortic aneurysm.

For human scans aortic CT data was used for manual segmentation of the aortic outline. This was done in the aneurysmal segments between two fixed anatomical landmarks. For ascending aortic/arch aneurysms the coronary arteries and the right brachiocephalic trunk formed the boundaries. For AAA, the renal arteries and the iliac bifurcation formed limits of segmentation. The PET scan data was superimposed on the segmented aortic phantom to generate a contour map demonstrating various areas of uptake. For the manual aortic segmentation the luminal and aortic wall boundaries were semi-automatically segmented using the region growing method that utilises the perimeter of the lumen by seeking pixels of a selected range of intensities. The data was pre-processed using Gaussian filters to improve the signal-to-noise

ratio and improve the clarity. The segmented lumen and aortic wall contours were assembled in three dimension and the surfaces were constructed using cubic B splines (a mathematical function that provides minimal support with respect to a given degree, smoothness and domain partitions).

To produce the aortic model this final surface underwent smoothing using the transformer manipulator. The volume rendered 3D projection was rechecked for accuracy with the PETCT data using the Canny Edge Detector tool and canny filtration applied for each label field. The surfaces generated would allow for finite element analysis of the aortic model as the statistical feature detection allows computational triangulation to be applied to the mesh of the surface generated.

For the patients with abdominal aortic aneurysms that had intraluminal thrombus (ILT), this was also reconstructed. The presence of IV contrast agent in the lumen enabled clear delineation of the aortic wall, thrombus and lumen interfaces. The segmentation was carried out for each 0.625mm CT scan on a slice-by-slice basis. The segmented aortic masks were used as a basis to generate the high affinity aortic model with laser scintagraphy (videos 1 and 2).

For each period of dynamic PET imaging, the mean maximum activity concentration (that is corrected for decay) was recorded and used to determine maximum standardised uptake value (SUV_{max}) that was inturn normalised to body weight of the patient. This is calculated using the formula below:

$$SUV = \frac{\text{ROI decay – corrected activity (kBq/ tissue (mL)}}{\text{Injected } ^{18}\text{F-FDG dose (kBq/body weight (g)}}$$

The associated standard error (SE) (SD/√4) was calculated. This calculation is repeated in the patients to ensure that the mean SUV_{max} for the aortic wall and the lumen and the target-to-background (TAR) ratio is calculated.

2.3.8 Statistical analysis

Analysis was carried out using ANOVA of repeated measures when comparing the uptake across the time points and using the Kolmogorov-Smirnov testing for normality. For paired data sets a 2-tailed *t* test was used to compare the differences in between the variables obtained at the time points and the alpha was set at 0.05 for statistical significance testing.

2.4 Results

The PET scan protocol that was followed allowed images to be obtained at resolution accuracy to within 3mm. This data was fused with the 0.625mm CT scan slices. For accuracy testing the phantoms were created from the hybrid PET-CT scan in 3 patients and over 30 biopsy sites were used of varying ^{18}F-FDG uptake. In all patients ^{18}F-FDG uptake was present in the aortic wall. The mean aortic wall SUV_{max} ranged from 1.0 to 3.38$\pm$0.44 (SE 0.11). The mean aortic lumen SUV_{max} was 1.0-1.62$\pm$0.4 (SE 0.1). The mean wall-to-lumen ratio (TBR) was 0.95-1.01$\pm$0.16 (SE 0.06). A significant difference in aortic wall SUV_{max}, luminal SUV_{max} and TBR (repeated measures ANOVA, P=0.02 and P=0.001) were observed (Fig 2.3 and 2.4, video 3).

The image co-registration and manual segmentation of PET and CT data was within 1-3mm of the fenestration points. Each point was triangulated from three known fixed anatomical landmarks (e.g. coronary ostia, brachiocephalic branch, renal or iliac bifurcation). The validation of the phantom rescan showed a resolution accuracy of 1.5$\pm$0.55mm (range 1.3-1.7, 95% CI0.2-0.51). (Video 2, 3 demonstrating the fused anatomical PET aortic topography and generated co-registered aortic model).

For SUV_{max} the voxel with maximum uptake was determined. Considering the volume of interest (VOI) equal to voxel with highest uptake in the aortic wall. The maximal uptake was defined on the original reconstructed PET images, without additional rebinning, resampling or smoothing. 2D peal ROI/VOI was used as well as the SUV_{max}. Hence the VOI was 1.2cm diameter fixed size circle containing the ROI that was 3-5mm in size. The 3D ROI/VOI was then determined where the 1.2cm diameter VOI was focused on the area with the maximal uptake. The 3D isocontouring was adapted for minimal, maximal pixel value, background uptake and the value best corresponding to aortic wall value to luminal blood was taken. It is important to note that when the aortic wall was adjacent to areas of high PET uptake there was a spill over effect from

the heart where there is a high background uptake. All these areas are visually checked close to or adjacent to the aortic wall (Fig 2.1, video 1). If the VOIs are non-correspondent visually to the aortic wall sites, than SUV_{max} was based on manual VOI and 2D SUV peak value.

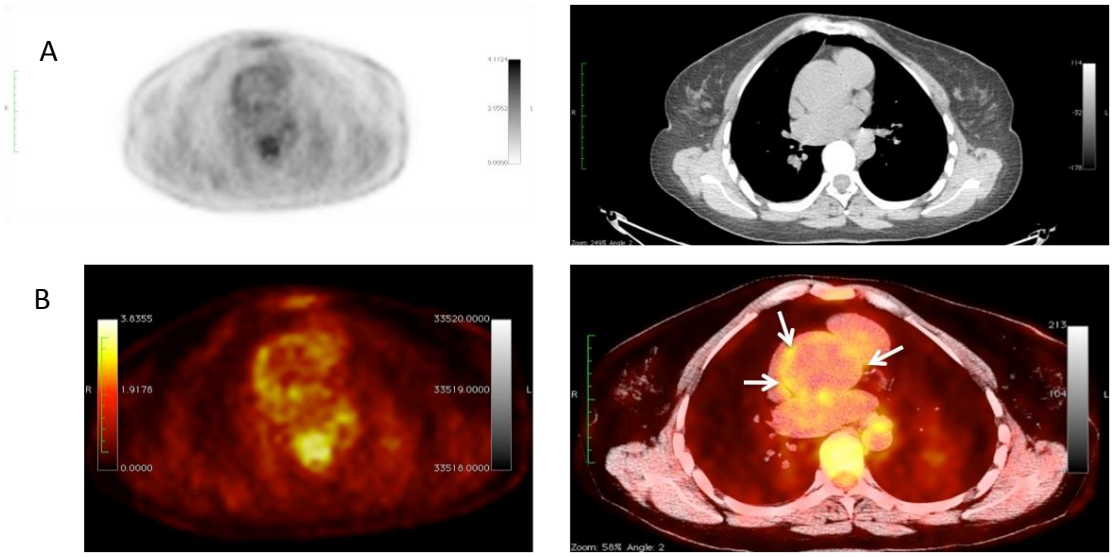

Fig 2.3 Fused aortic PET-CT

A) A single slice PET image from the ascending aorta at the level of the pulmonary trunk with the corresponding non-contrast CT scan of the ascending aortic aneurysm both in the dynamic grey scale range. B) A fixed colour scale is added from SUV = 0 to 10, for interpretation of the co-registered images. Arrows mark the sites of moderate-high SUV uptake (Aortic wall SUV max 2.5-3.5 in this case).

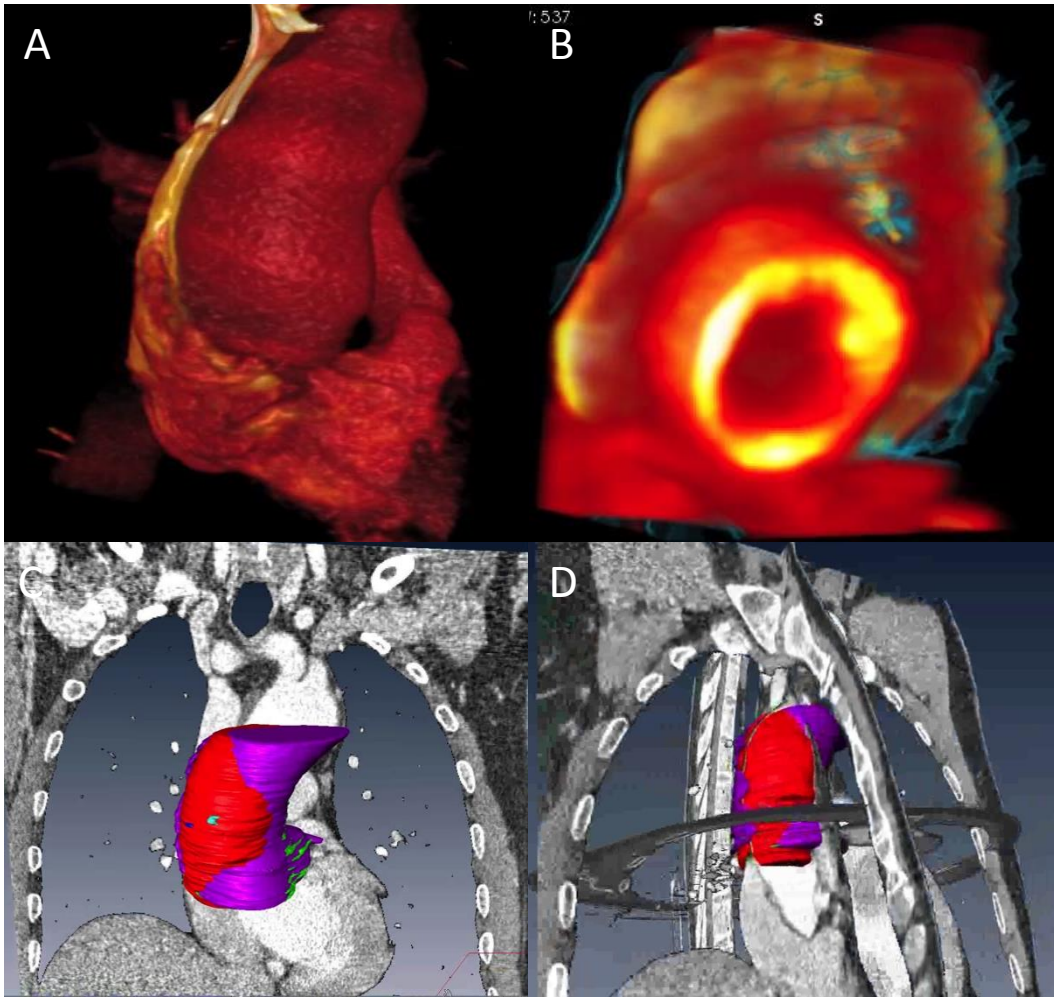

Fig 2.4 Image overlay of 3D fused PET-CT

A) 3-dimensional reconstruction of a patient with aortic root and ascending aortic aneurysm. The 3D reconstructions allowed branch point identification and mapping aortic morphology to help plan the operative placement of the aortic mask. B) Topographical map of the myocardium and aorta demonstrating ^{18}F-FDG uptake in the left ventricle and the aortic wall. C) Anterior aspect of the 3D aortic segmentation on Amira® demonstrating varying areas of ^{18}F-FDG uptake that have been marked as spots for fenestration in the aortic model that would be generated from this DIACOM dataset. D) Posterolateral aspect of the aortic wall demonstrating two different SUV_{max} that has been marked. The mask is generated within 1mm accuracy for CT data and 5mm resolution for PET scan. (Video 2 and 3 for 3D fly-through of aortic tomogram and 3D segmented aortic model)

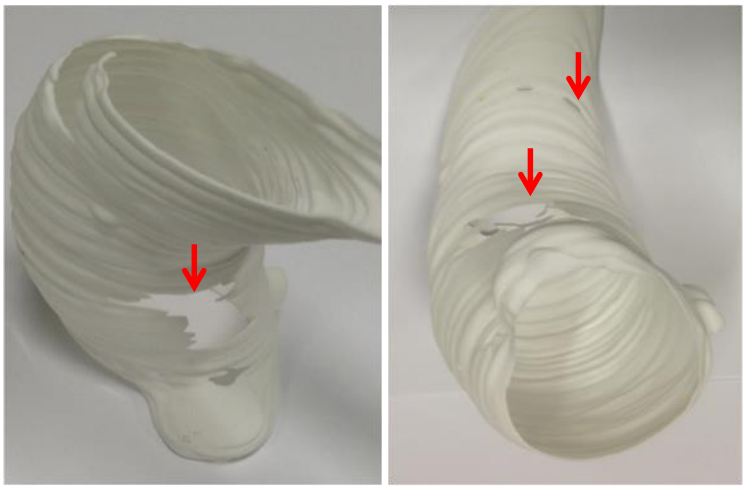

Fig 2.5 A bespoke aortic mask

An ascending aortic mask (200μm) produced using laser scintigraphy. The fenestrations were marked out on the mask at the sites that represent different levels of tracer uptake and where aortic biopsies were to be taken.

On validation of the model with backtrack scanning and image overlay on the previous fused PET-CT, the image accuracy at fenestrations was 1mm±0.62mm at all sites ($R^2$0.88, P<0.05). All models tested at the same accuracy with high correlation to the initial scan used for model generation. The final model produced by laser scintagraphy as seen above was generated to be applied to each patient's aorta to undertake the biopsy for analysis.

2.5 Discussion

^{18}F-FDG uptake occurred within aortic wall and it was best quantified using the SUV_{max}. There was minimal uptake in the aortic lumen and ILT. Uptake was higher in thoracic aortic aneurysms than in abdominal aortic aneurysms. The optimal time to image vascular inflammation with ^{18}F-FDG PET-CT was when a scout CT is performed to demonstrate the anatomical landmarks, followed by a non-contrast helical CT scan with a region of interest defined as aortic arch to femoral head. This was followed by a 60min post injection whole body ^{18}F-FDG PET scan and an IV contrast CT. Our previous data from multiple time point PET of arterial ^{18}F-FDG suggests that uptake dose not significantly change at 3hrs compared with earlier imaging. There were also minimal differences in the arterial wall SUV_{max} at 1 and 3hrs. The blood pool activity was significantly different and did not influence the TBR. There was therefore a minimal 'spill over' effect from ^{18}F-FDG uptake in the blood to the aortic wall value. Given that we were using ^{18}F-FDG uptake to assess vascular inflammation in the aortic wall, this is relevant to get accurate reading form the aortic wall alone. Delayed imaging of ^{18}F-FDG uptake in the arterial wall results in increased variability because of tracer decay and a subsequent increase in noise [306]. Therefore, although the time interval chosen was acceptable to patients, the benefits of delayed imaging are counter balanced by increasing noise and variable SUV_{max} measurements. As we were investigating low-level subtle changes in ^{18}F-FDG uptake these factors might have influenced the outcome of results. The rationale for using the 60min protocol was influenced by the results of previous work that showed a decrease in the aortic wall uptake of FDG after 2hrs[281,282,307].

Although the PET scan is sensitive it is limited in its spatial resolution. The addition of CT (in the hybrid PET/CT) for image acquisition improves spatial resolution and allows anatomical determination of the ^{18}F-FDG. This is important when evaluating the precise biological correlates from the aortic wall analysis from the site of ^{18}F-FDG uptake. Clinically, it aids decision-making

regarding the management of the aneurysm. The intravenous contrast agent used to enhance the CT on arterial phase imaging allows the differentiation of the arterial wall uptake from the uptake in adjacent structures such as the lumen. This allows placement of ROIs, reduction of partial volume effects and calculation of SUV_{max} at precise anatomical sites. In the literature there has been inconsistent use of methodology when performing PETCT vascular studies. These differences in protocol and timings reflect numerous factors, such as logistical constraints, camera availability, radiotracer provision and local scanning personnel. Our protocol was determined using criteria that would allow optimal vascular imaging to guide clinical treatment of the patients and yield highly precise anatomical information.

We also developed a novel methodology to reconstruct and generate a 3D volumetric model of the aorta that was segmented to allow construction of a patient specific aortic phantom. This was validated in phantom testing by back scanning the model and using radiomarkers to check the accuracy of the fenestrations placed at sites of known ^{18}F-FDG uptake. This demonstrated that the model generation was highly accurate in-terms of aortic anatomy and tracer resolution to allow site-specific aortic biopsies to be taken at surgery.

Chapter 3: ^{18}F-FDG uptake in human aneurysms and biological correlates

3.1 Introduction

The cells responsible for the uptake of ^{18}Flurodeoxyglucose in aortic aneurysms are not known. It is not clear what the purpose of these rapidly dividing or highly metabolically active cells would be in the aortic wall. From what is known about the aortic wall biology, the vast majority of cellular milieu is composed of VSMCs that are very slow growing in adults. These cells maintain a stable baseline metabolic activity, as they are responsible for maintaining the ECM in the tunica media.

Multiple small retrospective clinical studies have demonstrated capability of ^{18}FDG-PET-CT to outline specifically the aortic wall in certain patients[264,281,306]. It might be that this is because of insulin-independent glucose uptake of activated lymphocytes and macrophages in diseased aortic segments that are responsible for the ^{18}FDG signal specifically originating from aortic wall[264,281,282,306-308]. As chronic inflammation is known to be important in the development of aortic aneurysms and inflammatory cells are metabolically active, rapidly dividing and differentiating cells, we aimed to focus on these in the context of PET imaging. It is likely that the aortic signal for ^{18}FDG uptake originates from the up regulated activity, synthetic function and division of these cells. As already discussed in section 1.5 (page 45) inflammatory cell activity is important in aneurysm development and the complex interaction of these cells lead to the cellular events that are responsible for aneurysm initiation, propagation and rupture. If the ^{18}FDG uptake signifies inflammatory cell activity and function then accurate determination of the cellular events occurring in the aortic wall at sites of high compared with low ^{18}F-FDG uptake could be informative of the likelihood of aneurysmal dilatation at those sites or

increased risk of rupture or dissection. This information would guide clinical decision making for surgical repair.

3.2 Aims

1) Use the bespoke aortic mask generated using laser scintagraphy to obtain biopsies from areas of low and high ^{18}F-FDG uptake in the aortic wall patients with aneurysms
2) Isolate, quantify and characterise the immune cell populations in normal aorta *vs.* aortic aneurysms in areas of low and high ^{18}F-FDG uptake
3) Determine the location of these cells within the aortic wall

3.3 Methods

3.3.1 Patients

Patients coming to St Thomas' Hospital with aortic aneurysms that require open surgery were candidates for this study. Research committee approval was obtained (Ethics reference number 10/H0711/56). Patients were consented for a PET-CT scan at least 2-weeks prior to surgery for their aneurysm. All patients aged 18-75yrs were included. Pregnancy was the only exclusion criteria for this study. 15 patients were recruited for the study and their aortic wall analysed.

3.3.2 Human aortic biopsy

At time of open surgery for aneurysm repair, the mask was placed on the aneurysm after exposure and clamping of the aorta (distal aortic clamping for thoracic aortic repair and proximal and distal aortic clamping for AAA). The mask was fixed in place with Prolene® sutures using the anatomical landmarks of the coronary arteries proximally and aortic arch distally for the thoracic aorta (Fig 3.0A-B). The renal arteries and iliac bifurcation formed the fixed anatomical landmarks for the abdominal aorta (Fig 3.0C). In some instances the aortae were marked at points of fenestrations whilst in-situ, the aorta was resected and the biopsies taken ex-vivo with the aorta laid out within the mask. The fenestrated aortic sites were biopsied from the aorta and immediately stored in 0.9% saline on ice until the tissues were processed (within 1-hr). Prior to processing the aortic wall was thoroughly washed with sterile 0.9% saline at 4°C to remove any blood contamination. Biopsies of the artery wall (typically 4mm x 4mm) were obtained from regions with different SUV_{max}. Biopsies were processed for either flow cytometric analysis, fixed in 10% formalin (or snap frozen in liquid nitrogen for frozen sectioning) for histological analysis or immunohistochemistry.

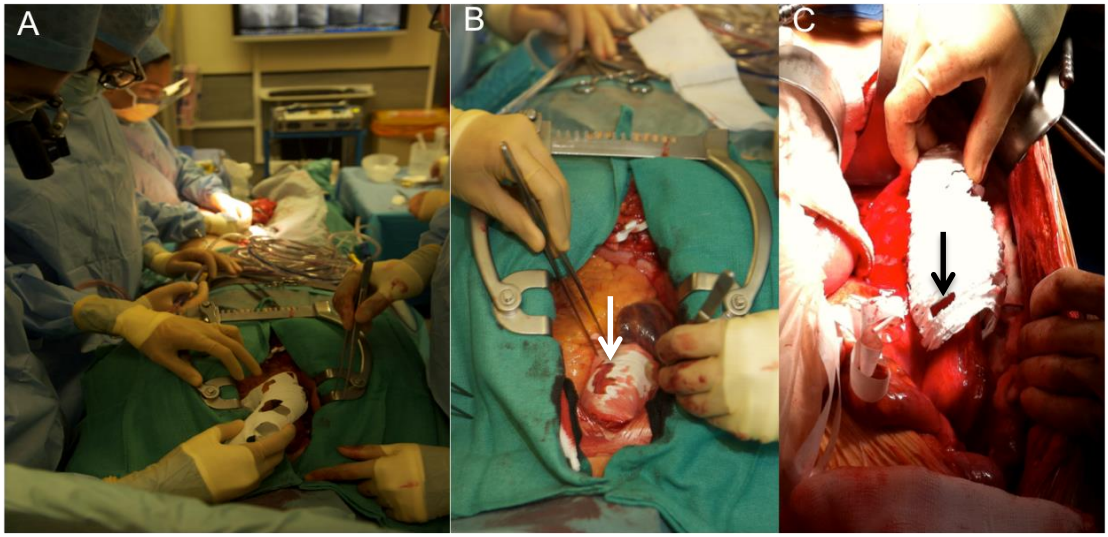

Fig 3.0 Aortic biopsies taken at open surgery for thoracic and abdominal aneurysm repair

A) Aortic model generated using laser scintagraphy being used. Measurements are made to the fixed anatomical landmarks at replacement of ascending aorta B) Aortic mask applied onto the patients ascending aorta confirming to the aneurysm morphology and biopsies from the ascending and C) abdominal aorta are taken at open aneurysm repair. The mask is fixed between the renal arteries and the iliac bifurcation. Fenestration seen in the mask to allow biopsies to be taken (arrows) (Courtesy of Mr Young, Mr Bapat and Professor Taylor)

3.3.3 Isolation of tissue resident inflammatory cells for flow cytometry

Human specimens underwent enzymatic degradation and cell harvest protocol. Tissue was cut into 2x2mm segments from each biopsy site and incubated in phosphate buffered saline (PBS, without calcium and magnesium), pH7.4 containing 0.5% bovine serum albumin (BSA), 1mM ethylenediaminetetraacetic acid (EDTA) with 1mg/ml collagenase D, 100units/ml DNAase I and 500units/ml hyaluronidase IV-S (all Sigma Aldrich, UK). Incubation was at 37°C for 45mins. The sample was then filtered through a 100µm strainer (Falcon BD) into a 6-well plate and the undigested tissue mechanically dissociated in the enzyme suspension, using a plunger from a 10ml syringe. The remnant tissue was washed with 5mls of PBS containing 0.5%BSA and 1mM EDTA (PBS-BE). The cells were washed and centrifuged twice at 320g and 4°C with the supernatant discarded and the pellet resuspended in 1ml PBS-BE and incubated on ice for cell counting with

haemocytometer. The cells were fixed in 4% paraformaldehyde (appendix 3, page 347) for 10mins and subsequently washed and suspended in PBS-BE and stored at 4°C for up to 48hrs prior to staining for flow cytometry.

3.3.4 Antibody staining of human inflammatory cells for flow cytometry

The immune cell content of aortic tissue from sites of varying ^{18}F-FDG uptake was quantified using flow cytometry. This was carried out in the following manner. Cell suspension in FACS buffer (500µl PBS with 1%BSA, 10% sodium azide, pH7.4, PBS-BA) from each aortic biopsy site was incubated with 20µl of human FcR blocking reagent (Miltenyi Biotec, 103-059-901) at 4-8°C for 15mins in a 15ml Falcon tube. The cell suspension was incubated with anti inflammatory cell type antibodies (Table 3.0) at 4°C for 30mins. To expose intracellular epitopes, 500µl of cell suspension from each aortic biopsy site was also permeabilised with 20% saponin (BD Perm/Wash buffer, BD Bioscience, 554723) for 10mins at 4°C. The permeabilised cells were washed twice in the BD Perm/Wash buffer (1ml/wash) and re-suspended in 500µl of BD Perm/Wash buffer containing a pre-determined optimal concentration of a fluorochrome-conjugated antibody or appropriate negative control to detect the macrophage marker CD68+, the macrophage phenotype marker HLA-DR, and the neutrophil marker CD16+.

Table 3.0 Primary flow cytometric antibodies for human immune cell typing

(All antibodies were obtained from BD Biosciences)

Cell	Cell surface marker	Fluorophores	Concentration	Code
Leukocyte	**CD45**	**APC-H7**	**3µg/ml**	**560178**
NK	**CD56**	**PE**	**6.25µg/ml**	**555516**
T-cell	**CD3**	**FITC**	**15µg/ml**	**555339**
B-cell	**CD19**	**PeCy7**	**6µg/ml**	**557835**
Macrophage	**CD68**	**PE**	**6µg/ml**	**556078**
Macrophage	**HLA-DR**	**PeCy7**	**15µg/ml**	**335830**
Neutrophil	**CD16**	**APC-647**	**5µg/ml**	**557710**

After incubation with antibody, the cells were washed twice with x1 BD Perm/Wash buffer (1ml/wash for staining in tubes) and resuspended in 1ml BD staining buffer prior to flow cytometric analysis. All the wash steps were carried out with centrifugation at 400g for 5mins. For non-permeabilised samples the cells were washed and kept in PBS containing 1%BSA. The permeabilised cells were always kept in the BD wash/perm buffer. Analysis was carried out using a FACS Canto II flow cytometer (BD Biosciences, UK). Leukocytes were selected according to forward (size) and side (granularity) scatter properties and final gating performed on CD45+, CD3+ and CD19+ leukocytes.

3.3.5 Antibody staining for human lymphocyte subset markers

The cell suspension sample from each aortic biopsy site was divided into three 500µl aliquots in PBS-BA. Each 500µl of cell suspension in FACS buffer (PBS-BA) was incubated with 20µl of human FcR blocking reagent (Miltenyi Biotec) at 4-8°C for 15mins. Cell suspensions were then incubated with combinations of fluorescently tagged antibodies against a variety of B/B-regulatory cell, T-cell and T regulatory cell surface markers (Table 3.1).

Table 3.1 Primary flow cytometric antibodies for human immune cell subtyping

(All antibodies were obtained from BD Biosciences)

Cell	Surface marker	Fluorophores	Concentration	Code
Early T-cell	CD2 (T11/Leu-5, LFA-2, LFA-3)	PE	6.25µg/ml	561760
Common T-cell	CD3	V500	10µg/ml	561416
T helper cell	CD4	PerCP-Cy5.5	0.2µg/ml	560650
Active antibody producing B-cells	CD5	PE-Cy7	6µg/ml	348810
Active T-cell	CD7	APC	25µg/ml	561604
Cytotoxic T-cell	CD8	V450	50µg/ml	560347
Highly activated T-cells	CD14	APC-H7	10µg/ml	641394
Highly activated T-cell	CD16	APC-H7	20µg/ml	560195
Common B-cell	CD19	PerCP-Cy5.5	6.25µg/ml	561495
Common B-cell	CD20	PerCP-Cy5.5	6.25µg/ml	340955
Plasma B-cell	CD24	PE	12.5µg/ml	555428
T regulatory cell	CD25 (IL2)	PE	12.5µg/ml	555432
Memory B-cell	CD27	V450	50µg/ml	560448
Active B-cells	CD38	APC	6.25µg/ml	555462
Common leukocyte antigen	CD45	FITC	6.25µg/ml	555482
Memory T-cell and T regulatory cell	CD127	Alexa Fluor® 647	6.25µg/ml	558598
Active synthetic B-cell	Anti IgD	PE-Cy7	10µg/ml	561314

3.3.6 Flow cytometric analysis

The samples were analysed using a BD Canto II flow cytometer equipped with either a two (red and blue lasers with excitation wavelengths of 633nm and 388nm respectively) or three lasers (red, blue and violet lasers with excitation wavelengths of 633nm, 388nm and 405nm respectively). Giving an option of either 6 or 9 colour cytometry. Florescence minus one (FMO-1) controls, in which one antibody at a time is left out of a particular antibody cocktail reaction was carried out for every experiment (gating controls), as well as single stain controls (compensation controls). Experimental controls were fully stained biopsy analyses from various sites with the patient sample (comparing areas of no, low, moderate and high tracer activity). Leukocyte content was gated according to their forward and side scatter and expression of the pan leukocyte marker, CD45. Doublets were excluded before the cells were phenotyped into subtypes and quantified. Unstained, fully stained and FMO's were carried out to delineate populations and set gates for each sub-population. Cell content was determined as either a percentage of the total $CD45^+$ population or as an absolute number of CD45+ cells expressing sub phenotype markers per milligram-wet weight of biopsy. Data for all flow cytometric acquisitions was analysed using FlowJo v7.6.5 software (Tree Star Inc, USA).

The number of cells was quantified using CountBright™ Absolute Counting Beads (Invitrogen, UK). The bead mixture was allowed to come to room temperature. The suspension was vortexed and 50µl was added to the stained cells. The number of cells before the addition was noted. The sample was run on the flow cytometer with the forward scatter threshold low enough to include the microspheres on the forward scatter *vs.* linear side scatter plot (Fig 3.1D). The beads were verified as on the highest scatter gate. When using $CD45^+$ *vs.* log side scatter gating, the counting beads are easily distinguished as a separate population from the gated cells. Calculation of cell concentration is made using the following equation:

A/B x C/D = concentration of sample as cells/µl

Where:

A = number of cell events

B = number of bead events

C = assigned bead count of the lot (beads/50µl)

D = volume of sample (µl)

3.3.7 Tinctorial histology

3.3.7.1 Sample preparation

Biopsies were fixed in 10% formal saline (BDH, UK) for 24hrs and processed for paraffin impregnation using a VIP SE-F2 tissue processor (Tissue-Tek, UK). The tissues were then embedded in wax blocks and transverse sections (5µm) cut at 250µm intervals throughout their entire length. Sections were placed on salinized glass slides and placed in an incubator at 40^{o}C overnight to bake the sections to the glass.

3.3.7.2 Aneurysm general morphology by haematoxylin and eosin (H&E) staining

Sections were warmed for 30mins at 60^{o}C to soften the wax and de-paraffinised in 2x5min xylene washes (BDH, UK). Sections were rehydrated through graduated alcohol (industrial methylated spirit, IMS, Genta, UK) washes (100% [x2], 95%, 70%, 50%) and rinsed in tap water for 5mins. Sections were incubated in Mayers haematoxylin (Clin-Tech, UK) for 5mins followed by 5mins washing in running tap water. Staining was differentiated by incubation in 1% acetic acid: 99% ethanol for 3secs followed by a further 5min wash in running tap water. Sections were stained in eosin (Clin-Tech, UK) for 2mins. Sections were washed for 30secs in running tap water prior to dehydration through graduated alcohol, cleared in 2x5min xylene washes, mounted with cover slips in DPX medium (BDH, UK) and allowed to dry overnight.

3.3.7.3 Picrosirius red staining for collagen content

Paraffin sections were rehydrated as described in 3.3.7.2, page 106. Picrosirius red staining was carried out as directed by the manufacturers instruction (Polysciences, USA). In brief sections were incubated with aqueous phosphomolybdic acid hydrate 0.2%(w/v) for 2mins and washed in distilled water for 5mins. Sections were incubated in 0.4%(w/v) Direct Red 80 diluted in a saturated picric acid solution for 1hr at room temperature, washed in 0.1M hydrochloric acid (HCL) for 2mins and subsequently dehydrated through gradated alcohols. Sections were cleared in two 5min xylene washes, mounted with cover slips in DPX medium and allowed to dry overnight.

3.3.7.4 Accustain Trichrome Stains (Masson) for collagen

Sections were deparaffinised and rehydrated as described in 3.3.7.2, page 107. Slides were rinsed in distilled water and placed. Mordant in preheated Bouin's solution (Sigma-Aldrich, Inc. UK), at 56^{o}C for 15mins. The slides were cooled in tap water in a coplin jar. The slides were washed in running tap water to remove the yellow colour from sections. The slides were placed in working Weigert's iron Hematoxylin Solution (mixing equal volumes of Weigert's Iron Hematoxylin A and Weigert's Iron Hematoxylin B) for 5mins. They were washed in running tap water for 5mins. Rinsed in deionised water and stained in Biebrich Scarlet-Acid Fuchsin for 5mins. Rinsed in deionised water before being placed in working phosphotungstic/ phosphomolybdic acid solution (1 part phosphotungstic acid and 1 part phosphomolybdic acid with 2 parts deionised water) for 5mins. The slides were placed in Aniline Blue solution for 5mins placed in 1% acetic acid for 2mins, rinsed in tap water, dehydrated through alcohol to xylene and mounted in DPX medium (BDH, UK).

3.3.7.5 Verhoeff van Gieson staining for elastin

Sections were deparaffinised and rehydrated as described in 3.3.7.2, page 107, placed in working elastin stain for 10mins (appendix 3, page 347). Rinsed in de-ionised water and differentiated in working ferric chloride solution (appendix 3, page 347). Sections were rinsed in tap water and checked microscopically, and if over differentiated returned to working elastin stain. This was followed by a rinse in 95% alcohol to remove excess iodine (present in the working elastin solution) and rinsed in de-ionised water. Sections were then stained in Van Gieson solution for 2mins, rinsed in 95% alcohol, 100% alcohol and finally xylene before mounting in DPX medium (BDH, UK).

3.3.8 Immunohistochemistry (IHC)

3.3.8.1 IHC analysis of leukocyte distribution in paraffin sections

Sections were deparaffinised and rehydrated as described in 3.3.7.2. Endogenous peroxidase activity was blocked by incubating sections in 1%H_2O_2 in methanol (3ml of 30% H_2O_2 in 87ml of 100% methanol) for 30mins. Antigen retrieval was carried out using citrate based retrieval solution at pH6.0 (Menarini, UK) placed in a MenaPath access retrieval unit (Menarini, UK), for 30secs at 125^{o}C and 2secs at 90^{o}C. The reservoir containing the sections was immediately placed on ice and the slides transferred to DPBS at room temperature. Sections were prepared for IHC, by removing from them one at a time (flicking off remaining DPBS), removing DPBS from around each section and drawing a ring around the section with a hydrophobic Pen (DakoCytomation, DAKO, UK). Each section was then quickly covered with Novocastra IHC blocking reagent (10min at room temperature) (Leica Microsystems, UK), placed in moisture box to prevent drying and immediately stained. Care was taken not to allow any section to dry prior to application of the antibody reagent.

Sections of human tonsil were used as a positive control for leukocyte staining. A negative antibody control experiment was carried out each time using species-specific serum or isotype control IgG as negative controls. For the positive control staining, sections were retrieved by heat mediated antigen retrieval at 125°C for 1min in 10mM sodium citrate buffer (pH6.0) and then at 80°C for 10mins.

3.3.8.2 Co-localisation of leukocyte subtypes in aneurysm wall

The antibody staining was carried out as per manufacturers instructions using EnVision™ Doublestain System, Rabbit/Mouse (DAB+/Permanent Red, Dako Inc. UK). Briefly, excess blocking reagent was removed from the slide by tapping off and wiping around the wax line surrounding each section before application of Dual Endogenous Enzyme Block (5mins at room temperature). The sections were rinsed gently with Tris-buffered saline wash buffer solution, pH7.6 (TBS see appendix 3, page 347). Care was taken to use buffer from a wash bottle (not focused directly on tissue) and the sections placed in a fresh wash buffer bath for 5mins. The sections were then incubated with antigen-specific biotinylated-mouse or -rabbit primary antibodies (Table 3.2), appropriate negative IgG controls, or species-specific serum, for 10mins at room temperature.

Table 3.2 Primary anti-human antibodies used for IHC

Primary Antibody	Marker	Species	Dilution factor	Final conc. (μg/ml)	Manufacturer
Anti-tropoelastin	Tropoelastin	Rabbit	1:200	1μl/ml	Abcam, USA
Anti-CD3	Common T-cell	Rabbit	1:500	1μl/ml	Leica, UK
Anti-CD20	Common B-cell	Rabbit	1:1000	4μl/ml	Dako, UK
Anti-CD45	Pan leukocyte	Rabbit	1:100	1μl/ml	Abcam, USA
Anti-CD56 (NCAM1)	Natural killer cells	Mouse	1:100	1μl/ml	Antibodies online, Germany
Anti-Mac-2 (Galectin 3)	Macrophages	Mouse	1:1000	4μl/ml	BioLegend, USA
Anti-CD68	Macrophages	Mouse	1:500	2μl/ml	Dako, UK

Sections were washed in TBS (2x5min). Excess TBS was removed and sections incubated for 10mins at room temperature with the Envision Polymer/Horseraddish peroxidase reagent (extravidin-HRP complex), after which the sections were washed in TBS (2x5mins) and then incubated in DAB+ chromogen (1mL of Substrate Buffer with 1 drop of DAB+, 25-30µl) for 15mins at room temperature. The section was washed in deionised water (2x5mins).

To stain for the second leukocyte antigen, excess water was tapped off and tissue sections incubated with Doublestain Block for 3mins at room temperature, followed by 2x5min rinse in TRIS buffer. Optimally diluted mouse or rabbit primary antibody or negative control reagent (same concentration as the primary antibody) was used to cover specimen for 10sec. Excess wash buffer was tapped off and the slides wiped as before. Rabbit/mouse (LINK) was used to cover the specimen for 10mins followed by wash in TBS 2x5mins on. Excess wash buffer was tapped off and the slides wiped as before. Polymer/Alkaline Phosphatase (extravidin-AP) was used to cover the specimen for 10mins. Excess buffer was tapped off and slides wiped before Permanent Red substrate (100 parts of Permanent Red Substrate Buffer with 1 part of Permanent Red chromogen) was applied for 20mins. Specimen was washed 2x5mins in deionised water. The specimen was immersed in hematoxylin for 5mins for counterstaining followed by a rinse in deionised water. Tissue slides were immersed into a bath of 37mmol/L ammonia water and rinse gently in deionised water for 2-5mins. The sections were dehydrated in graded alcohols and finally xylene. Slides were mounted using DPX. Slides were left to dry for at least 12hrs in room temperature before imaging.

NB. All washes were carried out with gentle shaking on the Belly Dancer (Sorvall).

3.3.8.3 Image acquisition and analysis of histology

Slides were visualised using a light microscope (Leitz, Leica, UK) and images captured using a microscope-mounted camera (EXi Blue, QImaging). The complete slide surface area was digitised and the histological sections were captured and processed using image analysis software (Image Pro-plus, Media Cybernetics). Aneurysm cross-sectional area (mm^2) was measured on van Geison and trichrome stained sections by computerized planimetry (ImageJ, NIH). Computer-assisted colour image analysis was used to quantify the area of staining in tinctorially stained sections for collagen (trichrome stain) and elastin (Verhoeff-Van Gieson), as well as IHC-stained sections. All staining was expressed as a percentage of the total aneurysm cross sectional area. Positively stained cells (DAB+/ Permanent Red Chromogen+) were in each section were counted and expressed as a percentage of total number of cells/section. Two independent observers carried out all image quantification and the inter-observer results correlated for agreement.

3.3.9 Statistical Analysis

Data was analysed in SPSS v21 (IBM Corporation, Data Collection, USA) and Prism v5.0 (GraphPad Inc., USA). Data are represented as mean ± standard error (SE). Parametric data was analysed using Student's Paired T-test. Non-parametric data was analysed using Mann–Whitney U or Wilcoxon rank sum tests. ANOVA was used for analysis of multiple grouped variables comparing two or more means and Bonferroni post-hoc test used to measure differences between specific groups. Where applicable univariate linear regression analysis was performed to model the relationship between a scaled dependent variable and one or more explanatory variables denoted. Correlations were carried out using linear regression and Pearson correlation coefficient analysis and represented as the R^2 value. Alpha was determined to be <0.05 for significance testing.

3.4 Results

15 patients with aortic aneurysms were recruited into the study. This allowed analysis of 152 aortic biopsy sites each representing a distinct SUV_{max} and hence varying ^{18}F-FDG uptake. The patient co-morbidities and demographics are outlined (Table 3.3).

Table 3.3 Demographics for patients involved in PET-CT imaging of the aortic aneurysms

Number of participants	**N=15**
Mean age (years) **Median age** **Range**	65.5 (35-75) 63 35-75
Thoracic aortic aneurysm (TAA) diameter (median, range) **Abdominal aortic aneurysm (AAA) diameter (median, range)** **Male**	6.8 (5.0-8.4) 8.2 (7.4-10.5) 11 (73.3%)
Co-morbidities **I.Hypertension** **II.Hypercholesterolemia** **III.Current smoking** **IV.Ischemic heart disease** **V.Aortic valve regurgitation** **VI.Connective tissue disease**	 15 (100%) 12 (80%) 6 (40%) 1 (6.6%) 9 (60%) 2 Marfans Syndrome 2 Bicuspid aortic valve
Aortic pathology	10 Degenerate thoracic aortic aneurysms 2 Degenerate juxtrarenal aortic aneurysms 1 Mucoid medial degeneration 2 Chronic type A aortic dissection

3.4.1 Flow cytometry

Sites with the highest SUV_{max} had increased number of B-cells (331±52, P<0.0001, 95%CI0.21-0.40) and T-cells (61±15.0 $x10^2$, P<0.0001, 95%CI0.2-0.50) vs. sites of moderate SUV_{max} B-cell (145±31 $x10^2$, P<0.0001, 95%CI0.32-0.44) T-cell (38±17 $x10^2$, P<0.0001, 95%CI0.10-0.64) and low SUV_{max} B-cell (18±15 $x10^2$, 95%CI0.11-0.92) T-cell (16±18 $x10^2$, 95%CI0.05-0.97). (Fig 3.2-3.3)

Aneurysmal tissue had a greater B and T-cell content compared with normal aortic wall in the same patients. 58 biopsies were taken from normal aortic tissue and compared to aneurysm wall with no ^{18}F-FDG uptake; B-cells number was 1±6 $x10^2$ vs. 18±15 $x10^2$, P<0.0001 95%±0.92 and T-cells count was 1±7 $x10^2$ vs. 16±18 $x10^2$, P<0.0001, 95%CI0.23-0.97 respectively.

The number of NK cells was also significantly increased from aortic biopsy sites at varying SUV_{max}. At high (SUV_{max} >4.0) the NK cells numbers were 46±34 $x10^2$, p<0.001, 95%CI0.15-0.25. At moderate uptake (SUV_{max} 2.6-3.9) 26±34 $x10^2$, p<0.001, 95CI0.13-0.76 and at low SUV_{max} >2.5 the number of NK cells was 19±12 $x10^2$, p<0.001, 95%CI0.24-0.92. (Fig 3.3-3.4)

(The individual patient cell counts are summarised in Appendix 3, page 349. All patients are included in the appendix to show overall cell profiles for patients with thoracic and abdominal aortic aneurysms.)

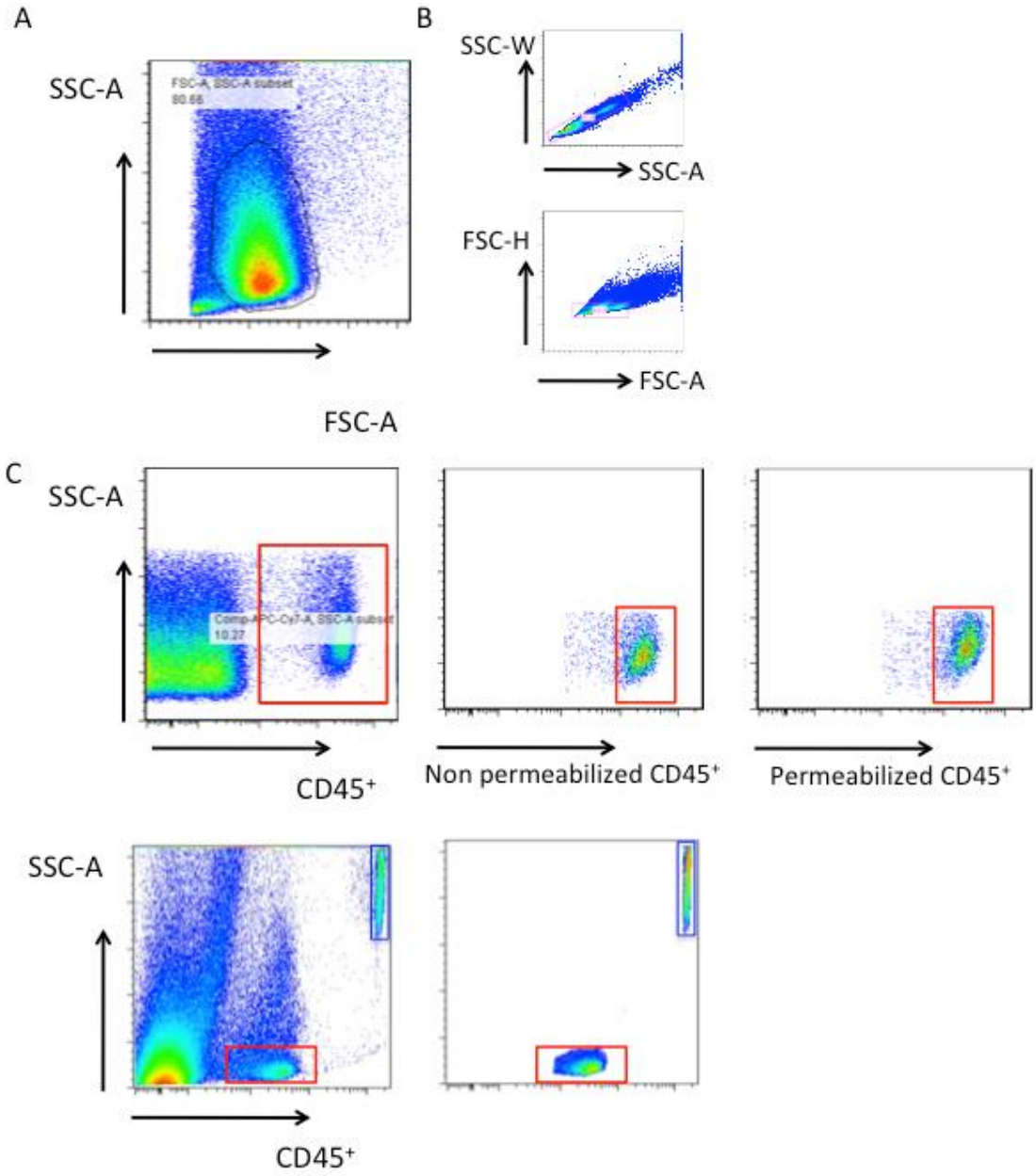

Fig 3.1 Flow cytometry of aortic wall

A) Gating analysis of unstained aortic wall resident cell content on forward and side scatter profile. B) Doublet exclusion was done to remove adherent cell populations and debris and provide a clear cell population for analysis. C) Gating was carried out on $CD45^+$ leucocyte cell fraction with exclusion of all other cellular types. One sample was run without permeabilization and the cell surface markers analysed. The second sample run was a sample permeabilsed with Saponin. This was necessary to stain the intracellular markers for monocyte/ macrophages linage such as $CD68^+$, HLA-DR staining. With and without permeabilisation there was no overall difference in the extracted $CD45^+$ population and the cellular staining profile. D) The cells re counted using CountBright™ beads (Invitrogen, UK) these appear in the top right corner of the flow dot-plot. Calculation of cell concentration can be carried out as outlined in the methods section 3.3.6, page 106).

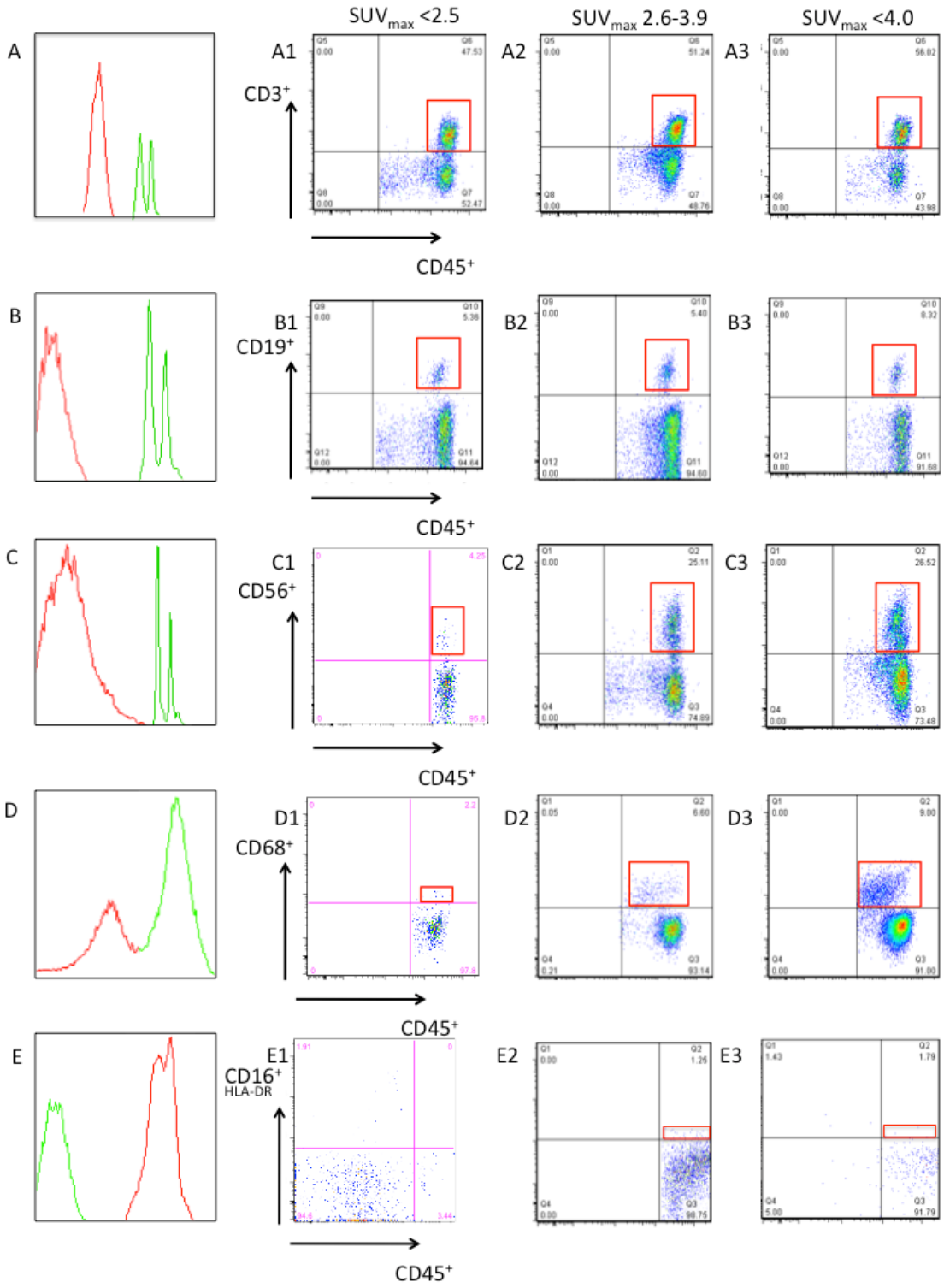

Fig 3.2 The flurophore spectral pattern and dot-plots analysis for CD45$^+$ cells

A-D) The first panels demonstrate differential flurophore patterns without overlap thus each immune cell phenotyped population could be determined accurately. There was no spectral overlap. A1-A3) Typical examples of flow cytometric dot plots of T lymphocytes (CD3$^+$), B1-B3) B-lymphocytes (CD19$^+$), C1-C3) natural killer cells (CD56$^+$), D1-D3) macrophages (CD68$^+$) and E1-E3) neutrophils (CD16$^+$/HLA-DR$^+$). The first dot-plot panel down (A1-E1) is from aortic wall biopsy site with low (SUV$_{max}$ <2.5). The second dot-plot panel down (A2-E2) is from moderate

(SUV_{max} 2.6-3.9). The third dot-plot panel down (A3-E3) is from site of high ^{18}F-FDG uptake (SUV_{max} <4.0). The differential cell numbers are apparent in the dot-plots. The specific cell types are expressed as a percentage of total $CD45^+$ leukocyte fraction. The cells from the different regions of the aortic aneurysm wall were therefore enumerated as a percentage/ fraction of the $CD45^+$ cell population and additionally absolute cell numbers counted using the counting beads. This would allow us to determine the correlation between the cell populations and the SUV_{max} for discrete aortic biopsy sites for thoracic aortic and abdominal aortic aneurysms.

Strong positive correlation was present between ^{18}F-FDG uptake (SUV_{max}) and aortic wall resident $CD3^+$ T lymphocytes (R^2=0.85, P<0.0001), $CD19^+$ B lymphocytes (R^2=0.86, P<0.001) and $CD56^+$ natural killer cells (R^2=0.75, P<0.001). There were very weak correlations between ^{18}F-FDG uptake and aortic wall resident $CD68^+$ macrophages (R^2=0.15, P=0.01) and $CD16^+$/HLA-DR^+ neutrophils (R^2=0.005, P=0.01).

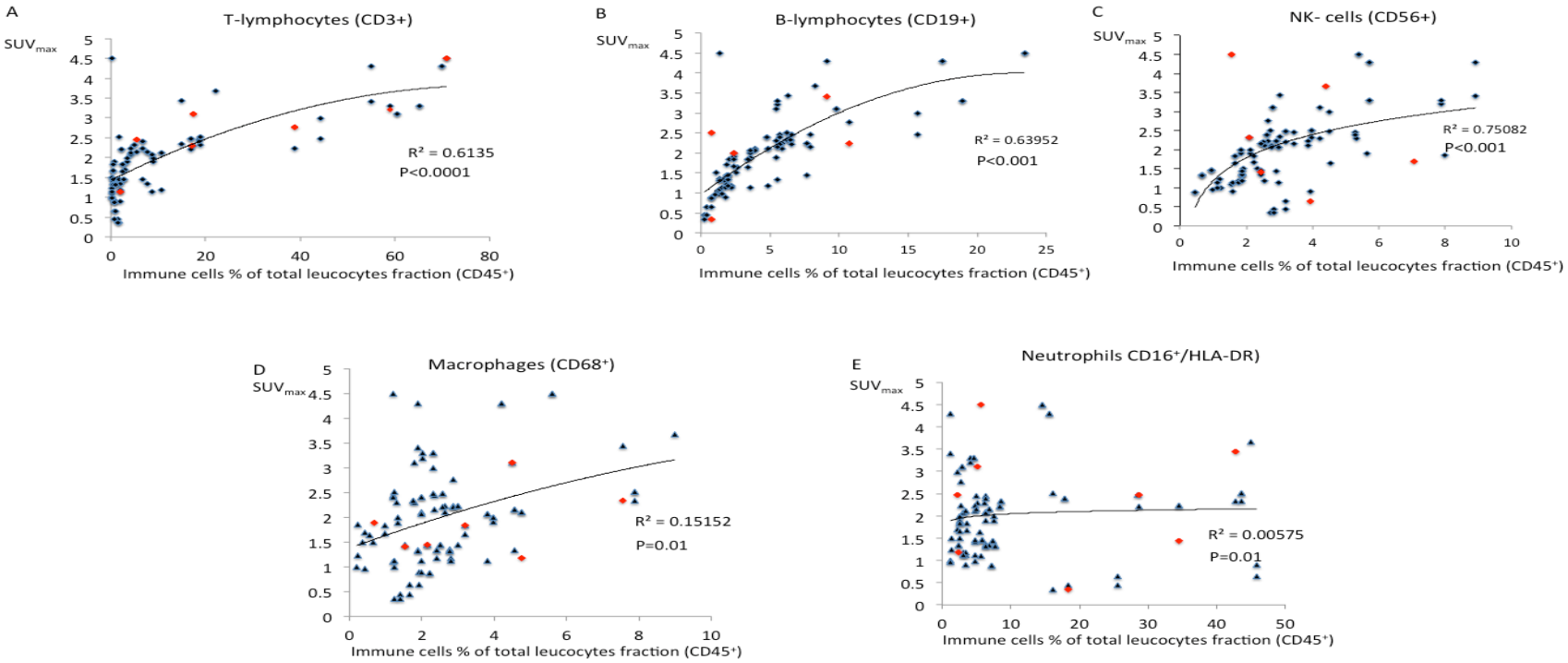

Fig 3.3 Correlations between ^{18}F-FDG and leukocyte content of aneurysmal aorta

A) Strong positive correlations were found between ^{18}F-FDG uptake (SUV_{max}) and aortic wall resident $CD3^+$ T lymphocytes (R^2=0.85, P<0.0001)

B) $CD19^+$ B lymphocytes (R^2=0.86, P<0.001) C) $CD56^+$ NK cells (R^2=0.75, P<0.001)

D) Weak correlations between ^{18}F-FDG uptake and aortic wall residenT-cells were found for both macrophages (R^2=0.15, P=0.01)

E) neutrophils (R^2=0.005, P=0.01) Black diamonds represent thoracic aneurysm wall biopsy sites and red diamonds are abdominal aneurysm wall.

N= 68 biopsies from 7 subjects (Two way ANOVA with post hoc Bonferroni correction). SUV_{max} = Maximal standardised uptake value.

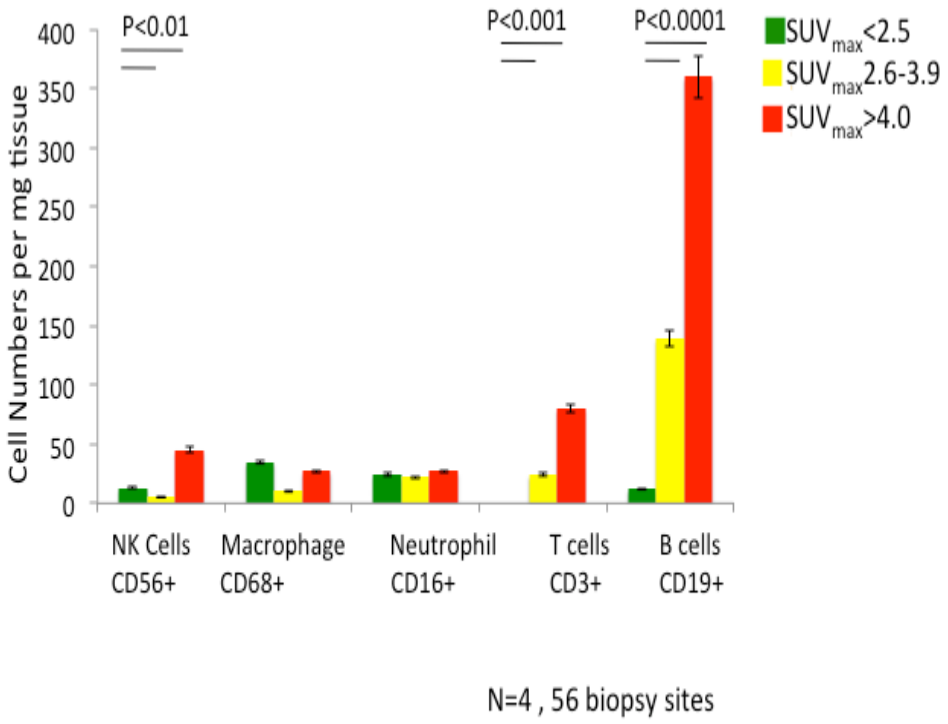

Fig 3.4 Flow cytometric analysis of absolute human leukocyte counts (per mg^{-1} of tissue) using CountBright™ counting beads

Cells were initially gated on $CD45^{+}$ leukocyte cell fraction. There was a significant up-regulation in the aortic wall of resident B-lymphocytes with increase in SUV_{max}, ($P<0.001$, between the low moderate and high SUV_{max} values) and T lymphocyte numbers ($P<0.001$, between the low moderate and high SUV_{max} values). There was a smaller increase in the NK cell population at sites of moderate and high SUV_{max} ($P<0.01$). There were no statistical differences when the macrophage and the neutrophil cell populations were analysed.

N=4, 56 biopsy sites analysed, two way ANOVA with post hoc Bonferroni correction. Mean counts ± SEM (bars).

Lymphocyte populations were further subtyped into specific lineages according to the cell surface markers (table 3.4). The cell surface subtyping markers allowed the T-cells to be sutyped early T-cells ($CD2^+$), naïve T-cell (Th0 cell), helper T-cells ($CD4^+$), cytotoxic T-cells ($CD8^+$), mature activated phenotypes ($CD7^+$, $CD25^+$, $CD38^+$) or T regulatory cells ($CD25^+$, $CD127^+$). B-cell phenotypes were subtyped to common B-cells ($CD19^+$), memory B-cells ($CD27^+$), class switched/ synthetically active B-cells (IgD), activated cells/ plasmablasts ($CD38^+$).

84 biopsies of aortic aneurysms, with a range of ^{18}F-FDG uptake, were taken from of 8 patients. The cells were stained for surface markers as delineated below. The gating profile and cell populations are as outlined in Fig 3.5 for T lymphocytes, Fig 3.6 for T regulatory cells and Fig 3.8 for B-cells including B regulatory cells.

Table 3.4 The stained cell surface lymphocytic markers and the putative phenotype that the epitopes confer.

Cell Marker	Cellular phenotype conferred
CD2 (T11/Leu-5, LFA-2, LFA-3)	**Early T-cell (thymic)/ NK cells**
CD3	**Common T-cell antigen**
CD4	**T helper cell**
CD7	**B-T cell interaction**
CD8	**Cytotoxic T cell**
CD19/20	**Common B-cell antigen**
CD24	**Plasma cell**
CD25	**Activated T-B-cells; T regulatory cells**
CD27	**Memory B-cell**
CD38	**Activated B-T-cells**
CD127	**T regulatory cell**
IgD	**Synthetic B-cell**

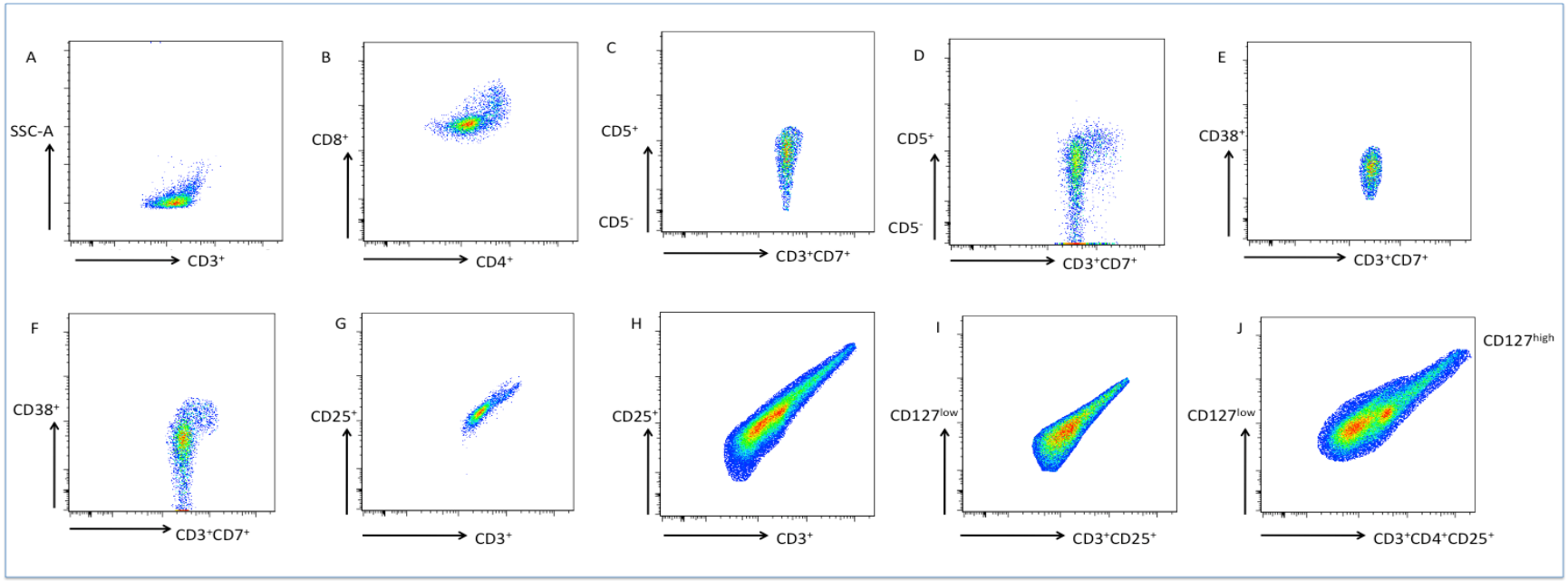

Fig 3.5 Flow cytometry for T-cell subtyping

A) The cells are gated on pan T lymphocyte marker CD3 and side scatter profile. After doubled exclusion as before, the CD3 population is gated upon and the T lymphocytes phenotyped. B) Staining for T helper cells ($CD4^+$) against T cytotoxic ($CD8^+$) cell populations. C-D) The cells expressing $CD3^+CD7^+CD5^-$ and $CD3^+CD7^+CD5^+$ are likely to represent metabolically active cells responsible for B-T cell interaction which are either alpha beta or gamma delta phenotype. E) T-cells modulating active inflammation express $CD3^+CD7^+CD38^+$ F) Increase in $CD38^+$ expression delineates likely differentiation to NK type phenotype and antigen presentation. G) Human $CD25^{+low}$ vs. F) $CD25^{+high}$ cells are likely to represent T regulatory phenotype. I) $CD3^+CD25^+$ cells are further subtyped into $CD127^+$ and $CD127^-$ T regulatory phenotype of cells. J) Two distinct populations, CD127low and $CD127^{high}$ cells can be seen.

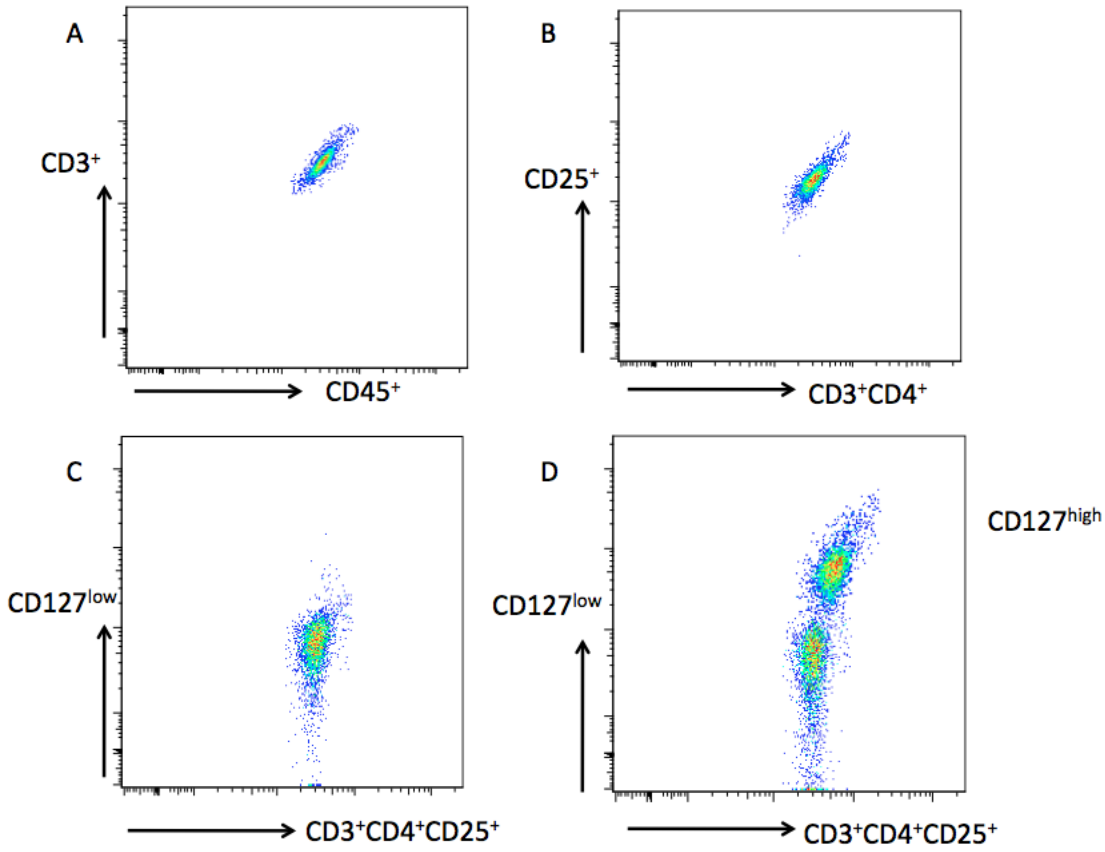

Fig 3.6 T regulatory lymphocytes from human aortic aneurysm wall analysed by flow cytometry

A) Cells were gated on the $CD45^+$ (leukocyte) and $CD3^+$ (pan T-cell marker). B) The cells were selected to ensure that they were $CD4^+$. This is likely the T regulatory cell population in the tissue. However due to unreliability in human T regulatory cell mapping we further looked for the expression of $CD127^{high/low}$ populations C) The CD3+CD4+ $CD127^{low}$ and D) $CD127^{high}$ populations are determined to effectively phenotype the IL7R T regulatory cells.

At sites of no ^{18}F-FDG uptake or at sites of low ^{18}F-FDG uptake cytotoxic ($CD8^+$) and helper T-cell ($CD4^+$) populations were predominantly resident (Fig 3.6 and 3.7). There was a drop in their population at sites of increased ^{18}F-FDG uptake ($P<0.001$). At sites of moderate to high ^{18}F-FDG uptake there was a switch to activated T-cells, memory and effector T-cell types. The highest fold change increase was for T regulatory cells phenotypes ($P<0.001$), followed by activated T-cells and memory T-cells (Fig 3.7).

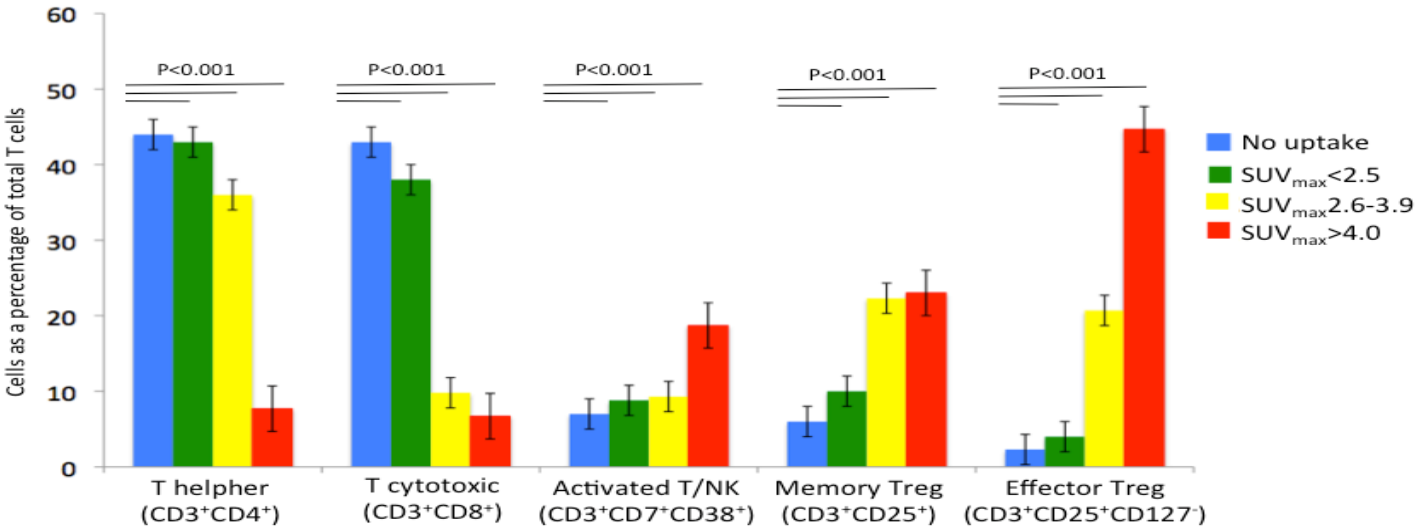

Fig 3.7 The T-cells subtype distribution in the aortic wall in association with the ^{18}F-FDG uptake

The aortic aneurysm wall from sites of no ^{18}F-FDG uptake had T lymphocytes expressing T helper ($CD4^+$) and cytotoxic ($CD8^+$) markers. There was a drop in these populations at sites of high ^{18}F-FDG uptake. There is up-regulation of activated T-cells typified by activation markers $CD7^+$ and $CD38^+$, the effector and memory T regulatory cells that express $CD25^+$ and $CD127^+$. These are the key subtypes influence adaptive immunomodulation to inflammatory responses. (N=8, 84 biopsy sites, 2 way ANOVA with post hoc Bonferroni correction.)

The B-cells populations were gated for the common B-cell ($CD19^+$), synthetically active $CD38^+$ cells that may produce antibodies (IgD/ IgM) and/or interact with T-cells, $CD19^+CD24^+$ cells that are plasma type involved in cell-cell adhesion and $CD27^+$ cells that represent differentiated memory type cells (Fig 3.8, 3.9).

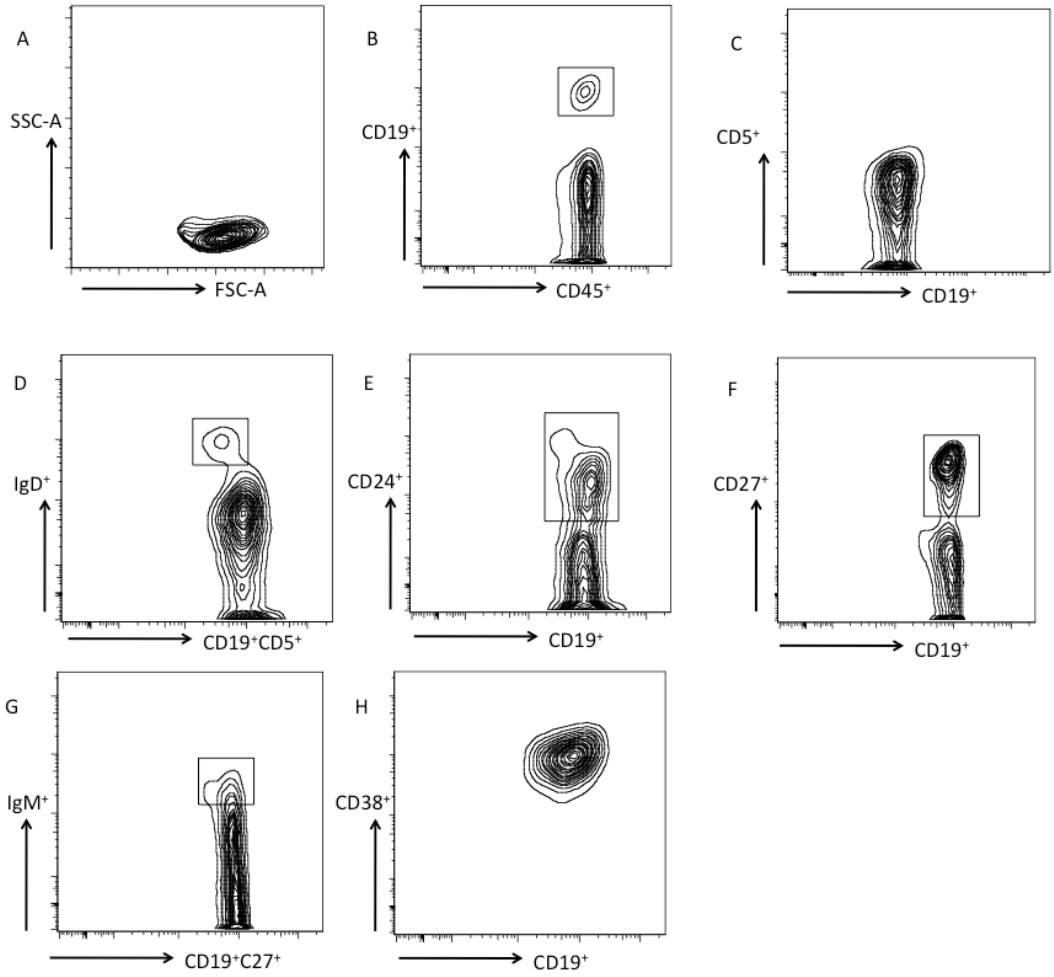

Fig 3.8 B-lymphocytes subsets phenotyped by flow cytometry

A) The cells population on forward and side scatter profiles was identified B) Gating performed on $CD45^+$ $CD19^+$ cells. C) After doubled exclusion the $CD19^+$ cells expressing CD5 were identified. These denote B1 cells the subset likely to secrete IgM and are synthetically active. D) The $CD19^+CD5^+$ cells were also assessed to the ability to stain for IgD expression, which constituted less than 5.5% of this population. E) The expression of $CD24^+$ denotes cell adhesion ability for plasma cells. F) The $CD27^+$ cells are differentiated memory B-cells. G) The memory B-cells were phenotyped as IgM producing cells. H) Activation marker CD38 was phenotyped to delineate active B-cells that interact with T lymphocytes.

At no or low ^{18}F-FDG uptake the common B-cell antigen was expressed with very low level expression of activation, mature B-cell and memory B-cell markers with these populations accounting for less than 10% of the overall B-cell fractions (P<0.001). However at sites of high ^{18}F-FDG uptake there was a 2-3-fold increase in the populations of mature CD19^{+}CD24^{+} cells, memory CD19^{+}CD127^{+}IgM producing cells and IgD expressing likely small B regulatory cell population.

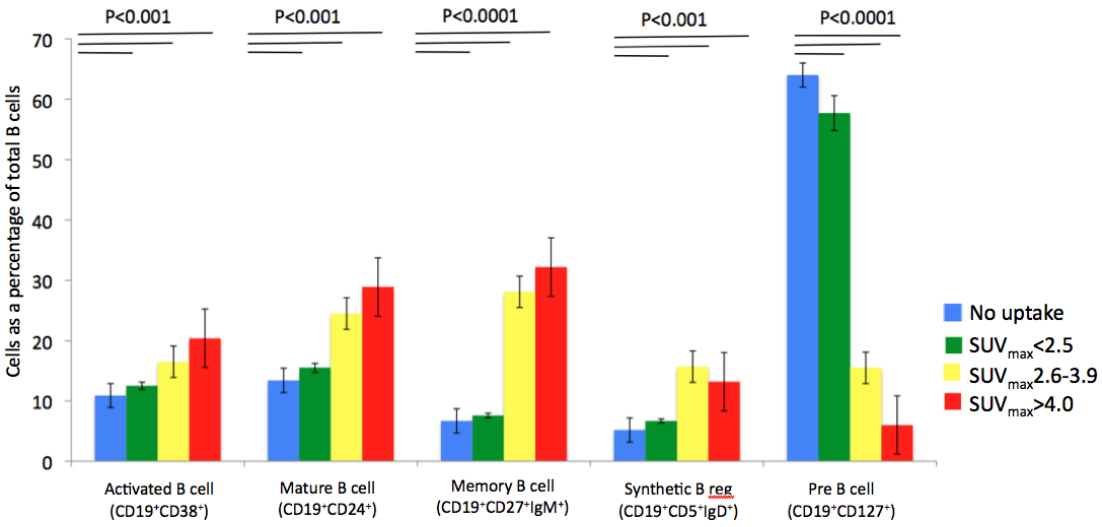

Fig 3.9 B-cell subtype distribution in the aneurysmal aortic wall in association with the ^{18}F-FDG uptake

The aortic aneurysm wall from sites of no ^{18}F-FDG uptake had pre B-cell markers mostly being CD19^{+}CD127^{+} lymphocytes. As the ^{18}F-FDG uptake increased there was an increase in the synthetic B regulatory cell population CD19^{+}CD5^{+}IgD^{+} along with activated phenotypes expressing CD38^{+} epitopes as well as mature B-cells (CD24^{+}) and memory B-cells that express CD27+ and IgM. (N=7, 68 biopsy sites, 2 way ANOVA with post hoc Bonferroni correction).

3.4.2 Tinctorial histology and IHC

The aortic aneurysms from a range of SUV_{max} were stained for elastin, collagen and presence of tropoelastin. Initially all aortic tissue was stained with H&E to determine aortic morphology (Fig 3.10). The EvG stained tissue can be seen to delineate the elastin fibers in the aortic wall and the degree of organisation of the fibres can be analysed (Fig 3.11). This is for fibre organisation, lamellar structure, number of fibre breakages, degree of staining with EvG and the fibre surface area when compared to the total aortic wall surface area (Fig 3.11-3.12).

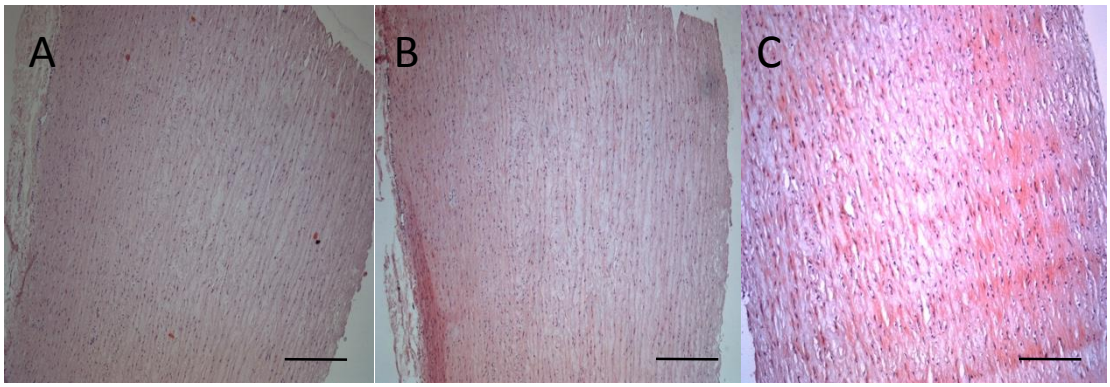

Fig 3.10 Haematoxylin and eosin stained aortic wall

A) Normal aortic wall with preserved aortic architecture and morphology B) The aortic aneurysm wall from low ^{18}F-FDG uptake showing predominantly preserved aortic architecture. Early features of ECM degradation C) Aneurysm wall from high ^{18}F-FDG uptake demonstrating increased vacuolation of the aortic wall and ECM deterioration throughout the tunica media and adventitia. Scale bar 100μm.

There is predominately preserved aortic architecture in the H&E stained sections with only sites of highest ^{18}F-FDG uptake having disrupted aortic media and adventitia. On EvG staining the normal aortic architecture is typified by 60-70 lamellar units of elastin in the tunica media and adventitia. These are break free (Fig 3.11 A1, A2). On IHC analysis with tropoelastin specific antibody (Fig 3.11 B1) there is increased tropoelastin synthesis at discrete sites in the tunica media. Tropoelastin synthesis is highest at the tunica media adjacent to the adventitia in the perivascular zone (Fig 3.11 B2). When this is compared to an aneurysm wall biopsy site that is from the same patient but a high SUV_{max}>4.5 (C1) there is a marked loss of the elastin in the aortic wall with haphazard EvG staining. Loss of lamellar structure, weak staining, that is

predominantly in the tunica media (Fig 3.11 C2). The elastin fibres are no longer in the lamellae and the internal and external elastic lamellae are lost. The corresponding tropoelastin stained sections can be seen to stain extremely highly for tropoelastin (Fig 3.11 D1) with dense regions of tropoelastin staining present in the tunica media adjacent to the adventitia. There is marked increase in the capillary density in the aortic adventitia. There is concomitant staining for Mac-2 expressing macrophages demonstrate that these cells are present in the adventitial vasa vasorum.

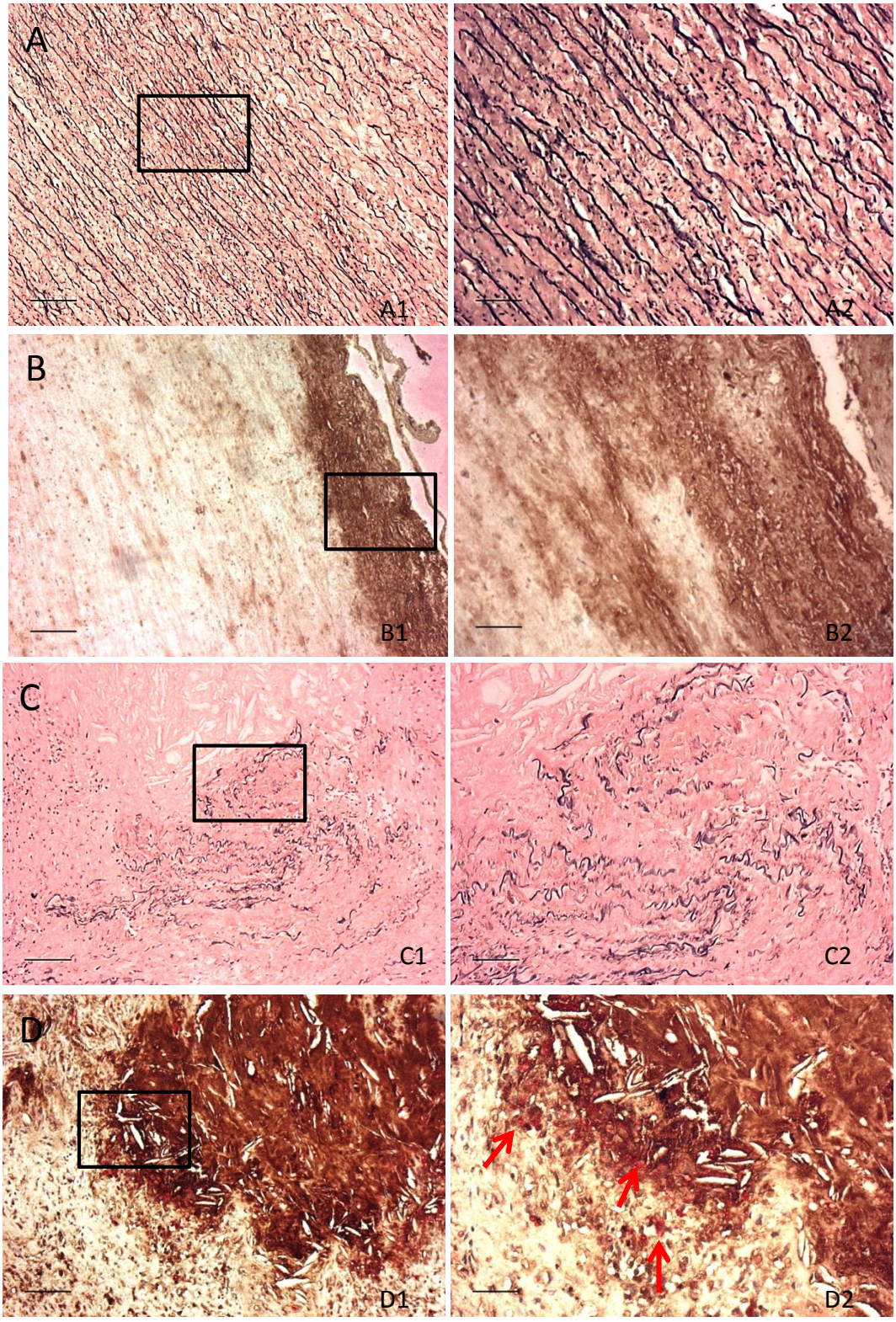

Fig 3.11 Staining for elastin and tropoelastin in aortic aneurysm wall

A) The aortic aneurysm wall from site with low ^{18}F-FDG uptake (SUV_{max} <2.5). The near normal elastin architecture seen at low magnification (A1), the break-free lamellar structure with well-

organised elastin in the tunica media and adventitia is seen (A2). A few breaks become visible in the elastin (A2). B) IHC analysis of tropoelastin in aneurysm wall from area of low tracer uptake (B1). The tropoelastin content is highest in the tunica media adjacent to the adventitia and in the adventitia (black box). The increased magnification (B2) demonstrated the perivascular zone at this site with regions high in tropoelastin content. C) Elastic architecture in aneurysm wall with high tracer uptake (SUV_{max}>4.5) in the same patient (C1) there was a marked loss of the elastin in the aortic wall with haphazard EvG staining. Loss of lamellar structure, weak staining, that was predominantly in the tunica media (C2). The elastin fibres are no longer in the lamellae and the internal and external elastic lamellae are lost. D) The corresponding tropoelastin stained sections can be seen to stain strongly for tropoelastin (D1) with dense regions of tropoelastin staining present in the tunica media adjacent to the adventitia. Concomitant staining for Mac-2 expressing macrophages demonstrates that these cells are present in the adventitia (red stained cells, red arrows) at the sites where there is increased tropoelastin present (D2). Bars represent 50μm and 100μm

The elastin surface area markedly decreased from 39.8% of total aortic wall area to 25.8% at moderate aortic ^{18}F-FDG uptake. The elastin expression decreased to 15.6% of surface area at sites of highest ^{18}F-FDG uptake ($P<0.007$, ANOVA). The tropoelastin uptake followed an inverse pattern with an increase in tropoelastin expression from low to high ^{18}F-FDG uptake. The expression levels increased from 9.8%, 17.8%, 21.9% and 36.8% of vessel wall surface area ($P<0.007$, two-way ANOVA). 35 biopsy sites analysed from aortic aneurysms in 7 patients. The mean coverage in sections taken at 4 different levels per biopsy (a total of 140 sections) was analysed by two independent observers.

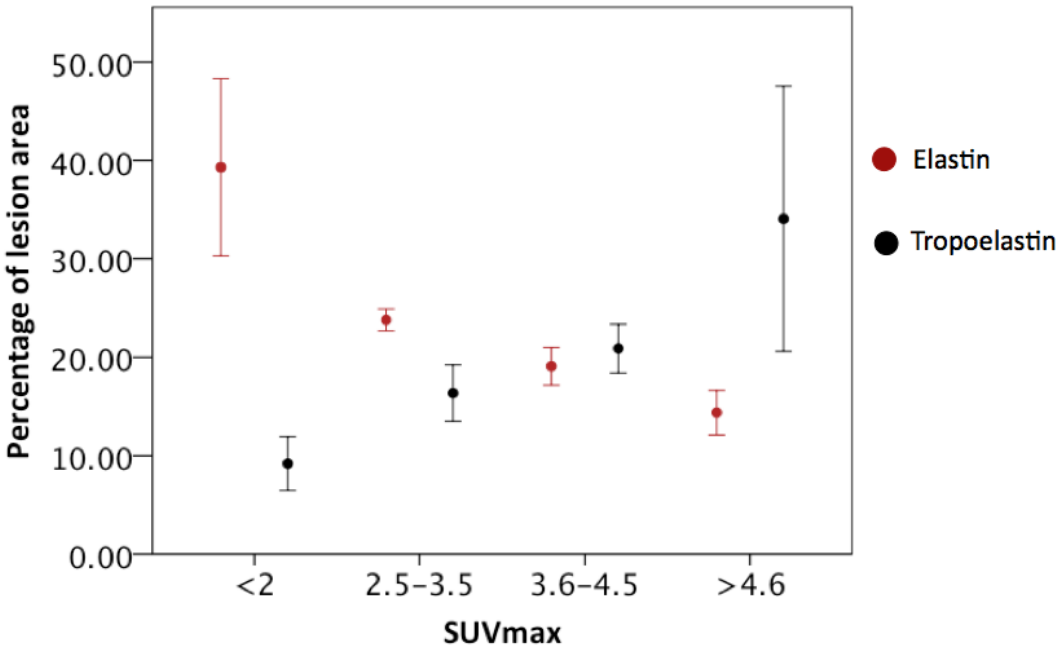

Fig 3.12 Histomorphometric quantification of the aortic aneurysm stained for elastin and tropoelastin stained aortic aneurysm wall.

There is a decrease in the elastin content with increasing SUV_{max} with an increase in collagen content, P<0.007 Two-way ANOVA, with post-hoc Bonferroni test P<0.04.

On analysis of the aortic wall collagen content the histomorphometric assessment demonstrates an increase in collagen content in the tunica media as the ^{18}F-FDG uptake increases. The mean level of collagen content increased from low to high SUV_{max} (Fig 3.14). Mean collagen percentage area increased from 19.8% to 67.6%. There was a significant upregulation of collagen content in the aortic wall, P<0.04, 95%CI1.2-1.65, OR 0.34 (Two-way ANOVA, with post-hoc Bonferroni test).

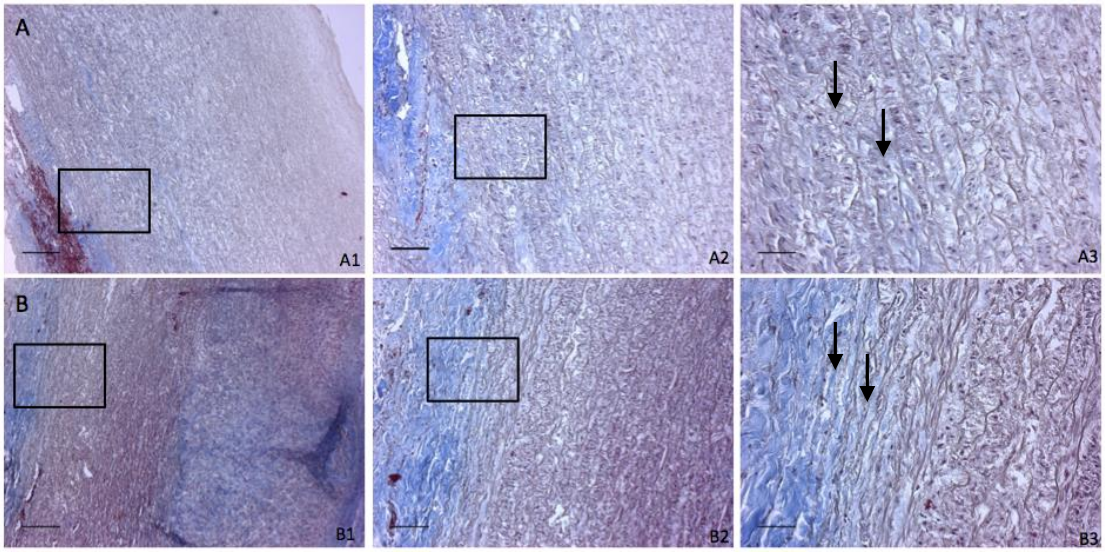

Fig 3.13 Collagen staining (Massons Trichrome) of aneurysmal wall (blue stain)

A) Low ^{18}F-FDG uptake aortic wall (A1) demonstrating collagen expression (blue) predominantly in the tunica media/ adventitia boundary. At 100x magnification the collagen expression is seen with early fragmentation of the aortic ECM (arrows). At 200x (A3) there is low-level expression of collagen seen in between the elastin fibres. B) High ^{18}F-FDG uptake aortic wall (B1) demonstrating increased collagen in the ECM. This is present in the tunica media (B2) despite the increased breakdown of the aortic wall. At 200x the increased expression of collagen is visible in the aortic wall between the elastin fibres. N=7, 35 biopsy sites analysed with 4 sections per biopsy; 140 slides analysed at high power field with complete slide area covered by two independent observers.

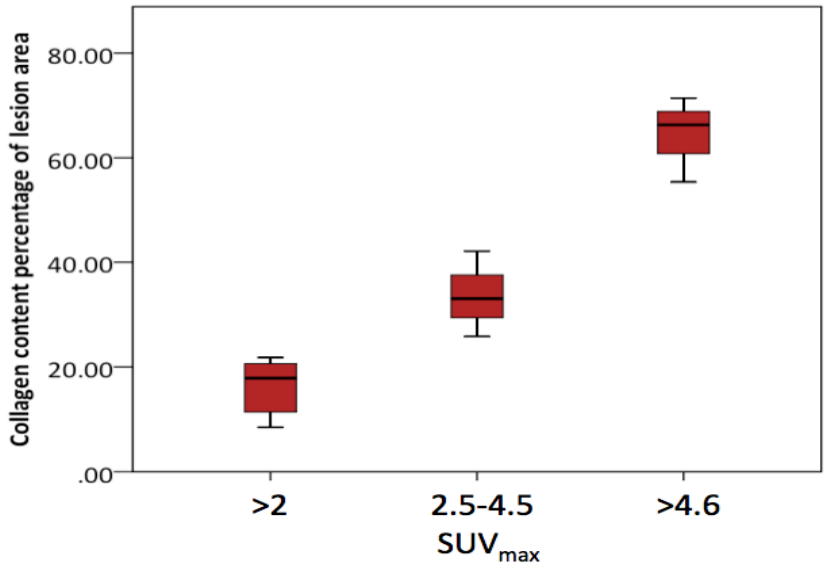

Fig 3.14 Histomorphometric quantification of collagen content in the aortic aneurysm wall in association with ^{18}FDG uptake

There is an increase in the vessel wall collagen content as a percentage of wall surface area and this is statistically significant ($P<0.07$ across the SUVmax, two-way ANOVA, with post hoc Bonferroni test <0.01)

The immunohistochemical analysis of immune cell infiltration in aortic aneurysm wall from varying ^{18}F-FDG uptakes demonstrated increase in the number of $CD3^+$ T-cells and uptake of this tracer in the aneurysm wall ($P<0.001$, paired T-test). The greatest T-cell numbers was found in wall at $SUV_{max}>4.5$, with >175cells/mm^2 aortic wall, compared with >70cells/mm^2 at $SUV_{max}<4.5$, $P<0.001$. The cells were particularly prevalent at the aortic media/ adventitial boarder at sites of perivascular infiltration (Fig 3.15). Mac-2 expressing macrophages were also co-located to these sites. The number of mac-2 expressing cells was highest in aortic wall with highest SUV_{max} ($P<0.05$, paired T-test).

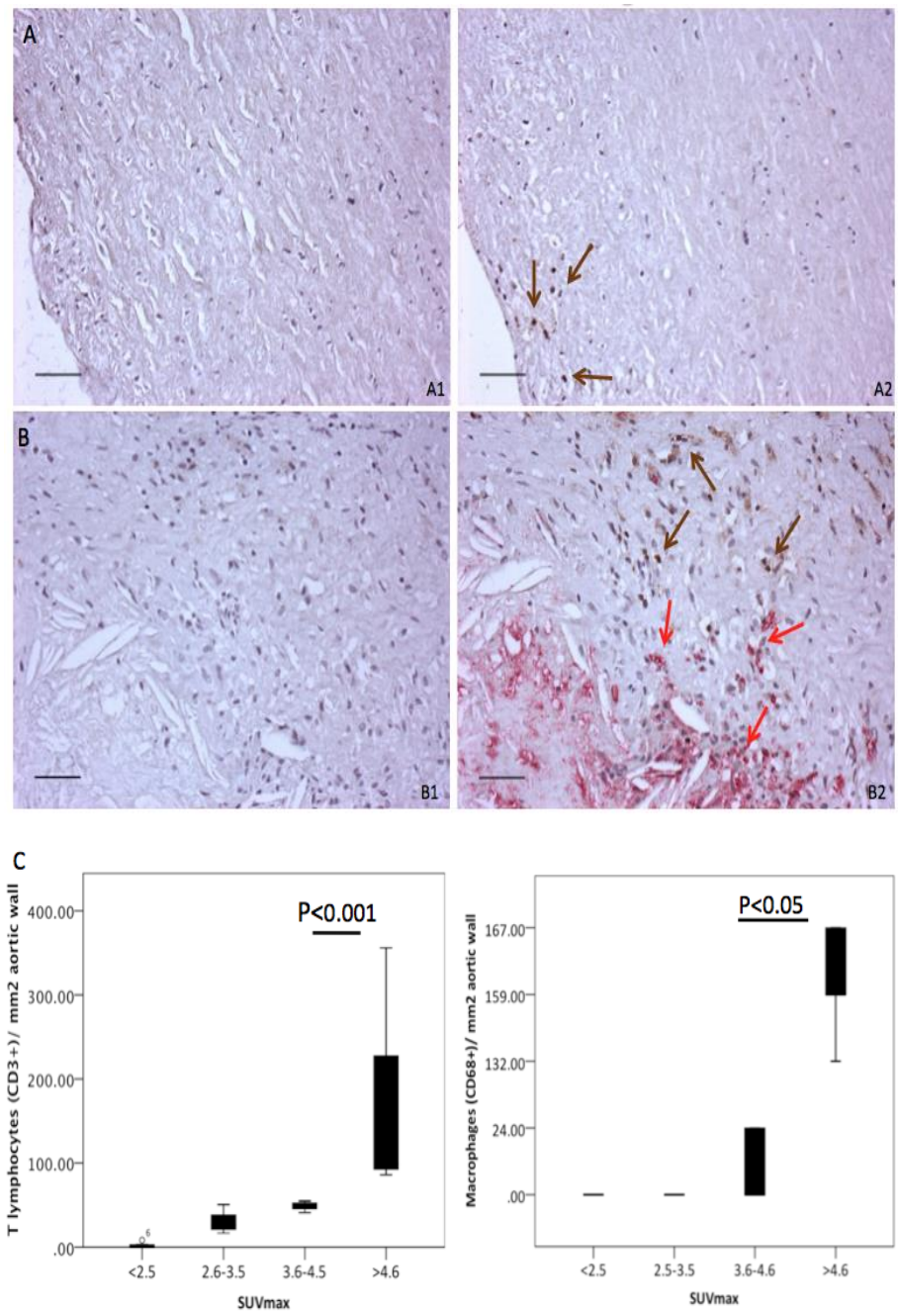

Fig 3.15 Immunohistochemical staining for CD3$^+$ T lymphocytes and Mac-2$^+$ macrophages in association with ^{18}F-FDG uptake

A) Low ^{18}F-FDG uptake (SUV_{max}<2.5) aortic aneurysm wall with IgG negative control staining (A1). CD3$^+$ T lymphocytes stained brown with DAB staining present (brown cells, brown arrows) in the aortic adventitia in the perivascular zone (A2). CD3+ cells were present focally in the adventitia and the outer media ingressing into the aortic wall. There was no macrophage (CD68) staining visible in aortic wall with low ^{18}F-FDG uptake. B) Aortic aneurysm wall from high ^{18}F-FDG uptake (SUV_{max}>4.5) in the same patient. Control IgG staining (B1) and the corresponding CD3$^+$-stained T-cells (B2, brown DAB stained cells, brown arrows) and CD68$^+$ macrophage staining (red cells and arrows). The cells were present in an infiltrative pattern in

the tunica media and tunica adventitia, predominating in the perivascular zone, rich in vasa vasorum. They were present and surround arterioles infiltrating in from the adventitia into the media. C) There were significantly more T lymphocytes (P<0.001) and macrophages (P<0.05) in the aortic wall with SUV_{max} >4.5 (mean of 4 sections per biopsy from 40 biopsies obtained from 10 aneurysms – a total of 160 slides analysed by two independent observers).

The $CD3^+$ T-cells were co-localised with $CD19^+$ B lymphocytes. Both lymphocyte subsets were co-located within the outer third of the tunica media and tunica adventitia at sites of increased neovascularisation. The B-cell numbers were linearly related to ^{18}F-FDG uptake.

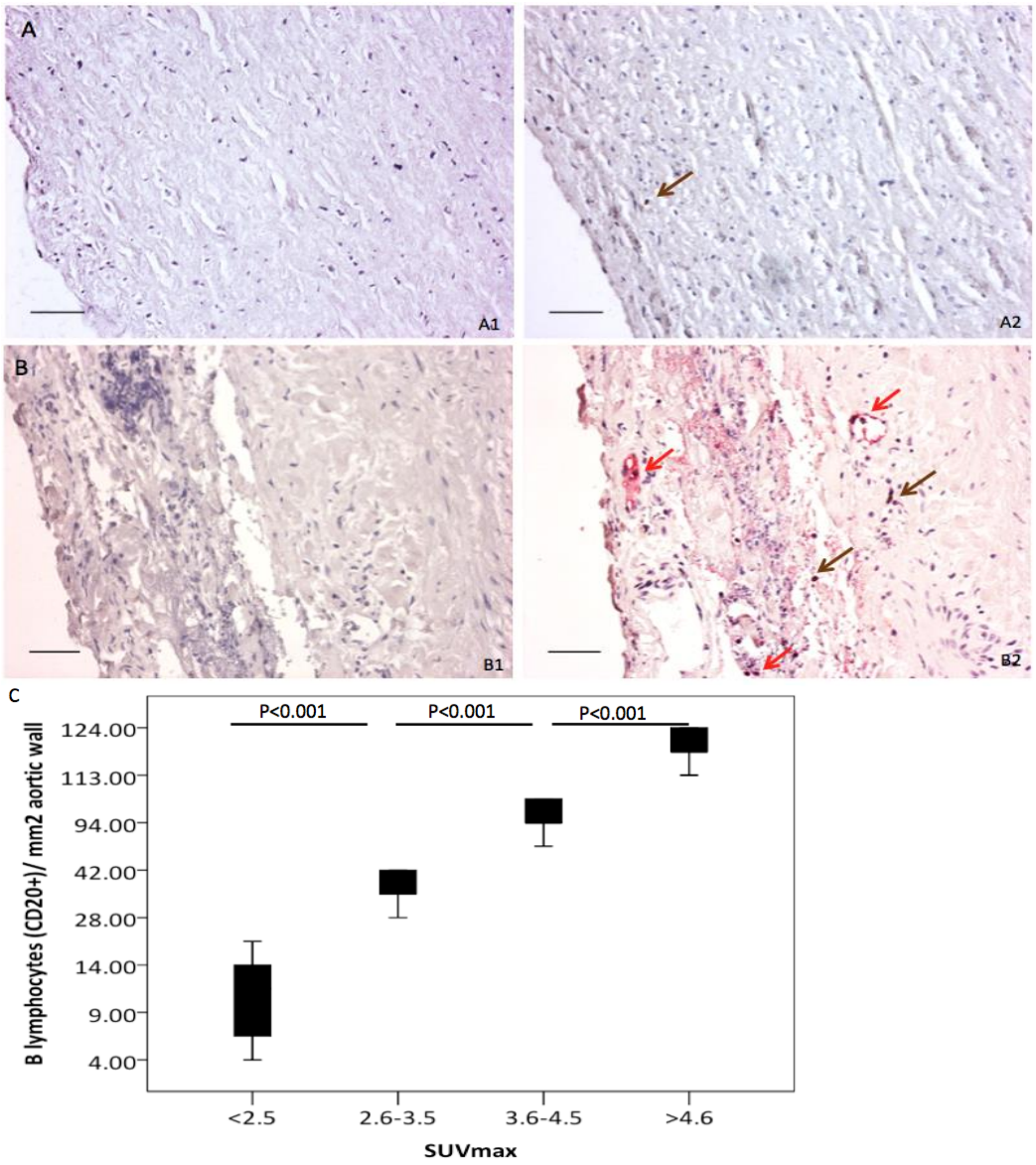

Fig 3.16 IHC staining for $CD3^+$ T lymphocytes and $CD20^+$ B lymphocytes

A) Low ^{18}F-FDG uptake (SUV_{max}<2.5) aortic aneurysm wall stained with negative control with IgG (A1). Aneurysm wall section stained for $CD3^+$ T lymphocytes (brown cell and brown arrow).

These cells were found mainly in perivascular zones in the adventitia, with some ingress into the media (A2). No B lymphocytes were found in wall with low ^{18}F-FDG uptake.

B) Aortic aneurysm wall from high ^{18}F-FDG uptake (SUV_{max}>4.5) in the same patient. The negative IgG staining control is seen in (B1). $CD3^+$ T-cell (brown cells and arrows) and $CD20^+$ B lymphocyte staining (red cells and arrows) (B2). The cells were present in an infiltrative pattern in the tunica media and tunica adventitia, predominating in the perivascular zone, rich in vasa vasorum. Cells were found around what morphologically looks like arterioles infiltrating in from the adventitia into the media. C) On quantification of the cells by cell counting there was a significant increase in the number of B lymphocytes ($P<0.001$) in the aortic wall with increasing SUV_{max} (mean of 4 sections per biopsy from 40 biopsies obtained from 10 aneurysms – a total of 160 slides analysed by two independent observers). Two-way ANOVA <0.001, with post hoc Bonferroni correction.

3.5 Discussion

3.5.1 ^{18}F-FDG uptake in the aneurysmal wall

We have shown that there is focal uptake of ^{18}F-FDG in the aneurysmal wall and that this is heterogeneous in nature (i.e. highly variable from site to site in the aortic wall). Regions of aortic wall within millimeters of each other can have highly variable ^{18}F-FDG uptake. This confirms existing data from longitudinal retrospective human studies that shows episodic focal uptake at different sites in the aortic wall[281,306,309]. This uptake changes over time at the same anatomic site in the aortic wall.

To date, few studies have examined the long-term outcomes of patients with increased vascular ^{18}F-FDG uptake, with most studies having small numbers and described as pilot or early feasibility studies. The ^{18}F-FDG uptake seen in the majority of these studies may be influenced by their patient selection. For instance, in order to carry out a PET/CT scan one needs an optimal time window of at least 2-3hrs between injections of the tracer and scans. This lengthy time and the geographical separation of the scanners in most institutions, gives rise to pre-selection bias of patient groups that are medically stable and compliant, with clinically unstable patients or patients requiring immediate therapy being excluded from the study. It is this precise group who need appropriate, timely investigation and intervention to improve outcomes. Future development of a range of more bespoke PET tracers that are specific for biological processes on going in the aorta wall is needed to facilitate rapid, accurate, specific and sensitive scanning, thus enabling PET/CT examination of acutely unwell or haemodynamically unstable patients.

Another limitation of PET is that despite its sensitivity it has limited spatial resolution, making it difficult to accurately localize the radiotracer uptake in the aortic wall. The addition of CT hybrid techniques for image fusion and registration has sought to circumvent this problem. The anatomical information on ^{18}F-FDG uptake helps differentiate the wall uptake from the

uptake by adjacent tissues such as luminal blood or surrounding soft tissue. The use of ROI, reduction of partial volume effects, SUV_{max}, mean SUV and TBR all allow for correction of this problem. An unenhanced CT scan is technically more difficult to interpret as intraluminal thrombus (ILT) in the abdominal aorta and soft tissue artifact make arterial wall distinction difficult. There is difficulty in delineating the aortic wall from the luminal blood. Intravenous contrast is therefore essential to enhance the image; followed by the PET scan timed at least 1-3hrs post tracer injection. Before there is widespread application of this technique in evaluating patients with aneurysms and with AAS, there needs to be agreement on the visual assessment of FDG uptake (absolute SUV_{max}, SUV thresholds and TBR). The imaging times need to be consistent and a uniform methodology developed for arterial ^{18}F-FDG studies. A recent study on ^{18}F-FDG PET advocates dual time point imaging[264,274,270,281,308], which provides better lesion to background reading on PET visual assessment. This involves identifying the most intense area of aortic wall uptake and drawing regions of interest around the wall and lumen. The maximum activity concentration for each area is then recorded in each 2min frame. For each period of dynamic imaging (4 x 2min frames), the mean maximum activity concentration (decay corrected) is then recorded and converted to SUV_{max} that is normalized to body weight.

Once optimisation of the technical aspects of the fused PET/CT scan has been considered the next problem to overcome is clinical presentation. The protocol that we developed for the PET-CT study was designed to optimize the anatomical detail that the CT scan provided for operative planning, with accurate ^{18}F-FDG localization in the aortic wall to facilitate tissue biopsy of regions of varying tracer uptake. Symptomatic aneurysms are reported to have higher tracer uptake compared with aneurysms in asymptomatic patients and healthy controls[131,264,275,288]. These findings are in keeping with the fact that aneurysm formation and rupture are active metabolic processes that are highlighted by ^{18}F-FDG uptake. There was however no correlation between aneurysm size and uptake. This could be partly explained by the small patient

sample size in these studies. Another possible explanation would be that aneurysm growth is not linear with rapid growth followed by quiescent phases. Hence the ^{18}F-FDG uptake would vary from week to week and over time in the same site in the same patient. We sought again to evaluate this in the murine model of aneurysm development. We additionally aimed to correlate the tracer uptake with aneurysm expansion and growth rates, rather then a static diameter reading. Of the two patients who had chronic aortic dissection, there was increased ^{18}F-FDG uptake in the flap tissue suggesting metabolically active immune cell content in the dissected aortic wall.

3.5.2 Biological correlates of ^{18}F-FDG uptake

The results of this study also show that there is a relationship between specific inflammatory cell subtypes and ^{18}F-FDG uptake in aneurysmal thoracic and abdominal aortic wall. ^{18}F-FDG uptake was strongly, positively correlated with a B, T and NK cell infiltrates. This is contrary to reported observational data which postulated that monocyte/ macrophage infiltrates were responsible for ^{18}F-FDG uptake[136,264,308-310]. It is possible that these biological correlates are specific to large degenerate aneurysms, as these were the aneurysms that were amenable to open repair and were therefore included in this study. All patients included in the study were asymptomatic and the aetiology of the aneurysms was degenerate aneurysms, connective tissue disease and complicated chronic aortic dissection in an aneurysmal aorta. There was more ^{18}F-FDG uptake in the thoracic aortic wall compared to abdominal aortic wall in the patients, however the uptake correlated to the same cell populations in the aortic wall. The intensity and range of ^{18}F-FDG uptakes was no different in the thoracic and abdominal aneurysms.

^{18}F-FDG-PET has been used to assess atherosclerotic plaque in the vascular tree[311-313] where it has been reported that unstable atherosclerotic carotid plaque takes up ^{18}F-FDG and this correlates with levels of circulating matrix metalloproteinase 1 (MMP-1). Others show that the level of ^{18}F-FDG tracer uptake into at risk atherosclerotic plaque increases with degree of plaque

instability [311,312]. It has been suggested that monitoring metabolic activity as a surrogate of inflammatory activity in plaques may be used to assess the efficacy of drugs aimed at modifying the stability of plaques. This postulation is supported by the finding that assessment by ^{18}F-FDG PET-CT is informative of the beneficial effects of statins in limiting atherosclerotic plaque inflammation and attenuating aneurysm formation in animals [311-314]. Increased ^{18}F-FDG tracer uptake is associated with macrophage numbers in plaque, with tracer accumulation in the regions of the plaque with the highest density of macrophages[311,312]. ^{18}F-FDG uptake is well-recognised in inflammatory vasculitis. Takayasu's arteritis and giant cell arteritis both show significant metabolic activity[314,315]. Furthermore, ^{18}F-FDG uptake has been found in mycotic aneurysms that are metabolically active as a result of infection and inflammation[130,314-317].

The processes on-going in the aortic wall that delineates ^{18}F-FDG uptake in the aneurysm are, however, not known. The presences of inflammatory cells (B and T lymphocytes and NK cells in the adventitia might be implicated as suggested by our current work. The underlying biological mechanism for the presence and role of inflammatory cells remains to be elucidated and will form part of further work in this project. Intimal atheroma and adventitial inflammation are features of aortic aneurysms that have been previously described. In almost half the patients with aneurysms lymphoid follicles are observed in the adventitia along with B-cells[101, 107-111,134]. Other authors have placed T-cells with increase CD4/CD8 ratio in aneurysmal tissue and CD19 B-cells in all pathological cases[101,107,134,135,316]. The intensity of the inflammatory immune response has led some authors to consider if aneurysmal disease is a reaction to local aortic wall damage. Initial wall shear stress and mechanical load leads to aortic wall injury that could expose antigens, such as oxidised LDL and cellular proteins, which is then followed by an immunophenotypic response to elastin fragments, collagen fibres and ECM proteins leading to aneurysm formation[107,108,126,320-324].

Characterisation of the T and B-cell subtypes in the aortic aneurysms was based on expression of pan B-cell markers (CD19/20) and T-cell marker (CD3). $CD8^+$ cytotoxic T-cells predominated, with $CD4^+$ T-helper cells in the aneurysm wall. As the ^{18}F-FDG uptake increased there was an increased preponderance of $CD25^+$, $CD38^+$, $CD25^+CD127^+$ cells. This represents an activated cell phenotype that is responsible for T-B interactions, further complex immunomodulation and T regulatory cell function. Previous studies have not found T lymphocytes that demonstrate this phenotype in the aortic wall [96,306]. Some authors have shown T-cells that demonstrate memory phenotype $CD45RO^+$ $CD45RA^-$ indicating T-cells are migrating in the aortic wall in response to a yet unknown antigenic trigger[107,324,326-328]. The B-cells in these studies have been defined as a $CD5^-$ population. This is a polyclonal B-cell type that produces and expresses kappa and lambda chains[107,318]. Additionally these B-cells expressed $CD27^+$ for the $CD19^+$ population which represents a specific memory cell phenotype[319]. Also expression of the surface Ig heavy chains expresses memory status onto these B-cells. In the aortic aneurysm wall there has been a large amount of IgA expression described in certain studies. This is predominantly in AAAs. The reason for this might be due to mucosa associated gut priming of B-lymphocytes[319-320]. Interestingly there might also be differential expression of adhesion molecules on the aneurysm surface. These include the β1, β2, β7 integrin subfamily, members of the Ig super family, and CD44[320,321].

Vast majority of AAAs have been also shown to have B-cell rich infiltrates in the adventitia that are not an autoimmune response to limited repertoire of tissue antigens[128]. There is a presence of lymphoid follicles and plasma cells in the adventitia with expression of immunoglobulin heavy chains[133]. The inflammatory changes were non-specific and macrophages and B-cells were present. Same studies identified gelatinase A, MMP2 and MMP9 activity to be increased in aortic aneurysms[322]. The recruitment of the B-cells into the adventitia with subsequent elaboration of the MMPs including gelastinase A and B may contribute to rapid growth and rupture of large aneurysms[322].

The initiation, development and propagation of aneurysms is complex and several biological processes may be involved including lipid deposition, coagulation, tissue hypoxia and angiogenesis, and protease activity (all of which are involved in atherosclerosis, a disease that occurs concomitantly with aneurysmal disease). Specifically novel tracers could target these processes. It may be possible, for example, to target endothelial epitopes associated with leukocyte transmigration, leukocyte adhesion molecules, angiogenic growth receptors, tissue hypoxia and bespoke synthetically designed radiotracers that are coupled to enzymes or their respective inhibitors (for instance MMPs and TIMPS). These may provide better targets to study aneurysm development and their potential to rupture[322,323].

Novel 4D PET-CT tracer targeting macrophages has been used in clinical trial to identify chronic inflammation in the asymptomatic abdominal aortic aneurysms[324-325]. No aortic uptake was recorded on the visual inspection, neither with [(11)C]-PK11195 nor with [(11)C]-d-deprenyl (the two agents used).

One of the main criticisms of ^{18}F-FDG is that its uptake may vary within the same patient with time as a result of the non-linear growth of aneurysms. The inherent weakness of any imaging modality assessing metabolic activity is that it may miss the rapidly expanding phase, which may last from days to weeks at a time[326]. New animal data suggests that there are other molecular imaging compounds that might be better at identifying vulnerable areas of aortic wall. It is important to consider the interaction of intraluminal thrombus with aortic wall. Autopsy studies have demonstrated that most aortic ruptures occur at site of ILT under the aortic wall[321,326,327]. These sites may be thinner and weaker with increase inflammatory cell infiltrate, proteolysis and ECM breakdown[327,328]. The relationship between size of ILT and risk of aneurysm expansion is controversial[146,326-328]. It might be that increased thrombus volume in expanding aneurysms leads to rupture but it could be that large aneurysms have increased risk of rupture and contain thrombus[140,317,318].

Studies indicate that annexin V it may be able to determine the development of ILT in aneurysms thus providing a new potential diagnostic marker to image aneurysm development and expansion as ILT increases. Annexin V binds to activated platelets and apoptotic cells and ^{99m}Tc-annexin-V has been used for SPECT in humans and animals to demonstrate acute and chronic thrombi. Using platelet activation induced fibrin formation, ^{99m}Tc-annexin-V may mark the interface between aortic wall and ILT and therefore represent biologically active aneurysms[329-332]. The role of ILT in AAA progression has been suggested by links between plasma markers of thrombotic thrombin-antithrombin complexes [332] and fibrinolytic plasmin-antiplasmin activity[332]. The ILT is biologically active component with continuous turnover linked to platelets and phosphatidylerine in the luminal part of the thrombus[333]. This stores PMNLs that are responsible for cellular apoptosis and adhesion[332,333]. The PS exposure on platelet membranes is the mediator linking platelet vesicles to thrombin formation and fibrinolysis[329,334].

Abdominal aortic aneurysms (AAA) are structurally characterized by parietal extracellular matrix degradation attributable to activated matrix metalloproteinases,[46] cell disappearance[334,336] and presence of a mural thrombus[333,334]. The role of the thrombus in aneurysm progression has been suggested by early observations of a link between plasma markers of thrombotic (thrombin-antithrombin complexes)[333] and fibrinolytic (plasmin-antiplasmin) activities[336,337] and aneurysm evolution[338]. Furthermore, this relationship has been documented at the tissue level[334,338-340]. Recently, the AAA thrombus was found to be biologically active involving permanent renewal linked to platelet activation and phosphatidylserine exposure in the luminal part at the interface with the circulating blood[329,341,342]. The luminal part of the thrombus stores polymorphonuclear leukocytes (PMN), which spontaneously disappear by apoptosis after adhesion; in this context of arterial mural thrombus, phosphatidylserine exposed on platelet membranes is the mediator linking platelet vesicles to thrombin generation and fibrinogenesis [329,341-343].

Annexin V specifically binds with nanomolar affinity to PS, which is exposed to the surface of activated platelets and apoptotic cells[329]. Therefore, radiolabeled 99mTc-annexin-V (ANX) has been previously used for in vivo scintigraphic imaging of both apoptotic cells in animals and humans, and acute platelet-rich thrombi in animals[329,344-346]. Nevertheless, the ability of ANX to assess renewal activity in chronic mural thrombus, at the interface between circulating blood and mural thrombus has not yet been reported.

Another novel compound called lacadherin may be able to mark out platelets and cell apoptosis by binding to αvβ5 and αvβ3 integrins. Its role as a novel marker remains to be determined. Other proposed tracers include ^{99m}Tc-Apcitide as this ligand binds to the platelet GPIIb/IIIa receptor[331,347,348]. The platelet infiltration of the intraluminal thrombus might positively modulate the immune cell infiltration into the aortic wall and thus dictate aortic aneurysm behavior and expansion[349].

The studies that have investigated the role of ^{18}F-FDG PET-CT in acute aortic syndrome (AAS), have yielded significantly higher tracer levels at sites of penetrating aortic ulcers, intramural haematoma and aortic dissections[143,310,347,348]. ^{18}F-FDG seemed to correlate to unfavourable clinical outcomes. The pathophysiological changes that characterise these arterial wall changes are degeneration of the elastic fibres in the tunica media, loss of collagen and accumulation of fibrin, loss of vamps, adventitial hypertrophy and accumulation of a pro-inflammatory infiltrate and proteolytic enzymes. It is believed that these immune cells surround areas of medial degradation and with the involvement of MMP's, lyse aortic proteoglycan matrix. Several studies report higher ^{18}F-FDG uptake correlated to immune cell content (mainly macrophages) in the aortic wall[138,309]. ^{18}F-FDG accumulation in aortic dissection may stem from increased macrophage density indicating aortic inflammation and correlation with worse short term outcomes for aortic dissection.

One third of patients with AAS had ^{18}F-FDG uptake suggesting active inflammatory activity[348,349]. There was a trend to an association between higher uptake of radiotracer and poorer clinical outcomes. Other studies demonstrate that in patients with aortic aneurysm, given the SUV mean cut-off value of greater than 3, ^{18}F-FDG PET had a substantial predictive value for discriminating unfavourable from favourable aortic dissection patients[108,347,348]. These authors also report, macrophages in the aortic media in both patients with aortic dissection and aneurysms. However, greater numbers of macrophages are present in the dissection patients, accounting for differential uptake between aneurysms and dissection.

The classically known determinants of aortic dissection are the aortic aneurysm diameter, female sex, older age, partial thrombosis of a false lumen. Identification of an aorta before it ruptures or dissects is the ultimate goal for non-invasive vascular inflammatory imaging. ^{18}F-FDG uptake and its association to AD is unknown. Functional data on aortic wall will determine the usefulness of ^{18}F-FDG PET-CT for risk stratification among aortic dissection patients. Indeed the one patient that had chronic type A dissection in this study demonstrated a high ^{18}F-FDG uptake in the aortic dissection flap. Analysis of this flap tissue on flow cytometry demonstrated intense B and T-cell infiltrate. This suggests that the flap is a metabolically active tissue with immune cell infiltration that is modeling and interacting with the aortic wall.

Performing ^{18}F-FDG PET-CT imaging provides a snapshot of immune cell activity in the aneurysm wall at a specific time. We are unable to tell how the immune cell activity and content changes with aneurysm growth, at various aortic diameters and if there is a variation within the same aneurysm with time. An aneurysm model would allow better characterisation of the biological correlates of the immune cell content in the aortic wall. We aimed to carry this out next.

Chapter 4: ^{18}F-FDG uptake in murine aneurysms and biological correlates

4.1 Introduction

Angiotensin II is the primary bioactive peptide of the renin angiotensin system that plays a critical role in cardiovascular pathology. Subcutaneous injection of angiotensin II into ApoE$^{-/-}$ mice leads to the development of aortic aneurysms[62,153,279,349,359]. Similar to human aortic aneurysms, the angiotensin II-exposed mice exhibit progressive aortic wall changes and clinical complications of aortic aneurysm dissection and rupture[352] as well as the development of intraluminal thrombosis[353]. Angiotensin II-induced mice develop aneurysms in the suprarenal aorta, which differs from the most common locations of aneurysms (the thoracic and abdominal aorta) in humans. The reason for this is unknown, but the peri-aortic tissue around the suprarenal aorta in mice contains an abundant source of leukocytes and pro-inflammatory cytokine following angiotensin II infusion that might be responsible for the development of an aortic aneurysm in this location[352]. Also the haemodynamically induced wall shear stress is different in the murine model and may influence the site of aneurysm development. This model of aneurysm development is thought to accurately recapitulate the disease in man with aneurysm development associated with inflammation, tissue modeling, up-regulation of matrix-degrading proteinases, ECM degeneration, altered VSMCs function, formation of ROS and thus aneurysms[350, 352,353, 354]. Using the ApoE$^{-/-}$ATII model we sought to investigate the relationship between ^{18}F-FDG uptake and aortic wall expansion, maximum aortic diameter, rupture risk and early aortic death. We also sought to understand the biological events on-going in the aortic wall at sites of high ^{18}F-FDG uptake.

4.2 Aims

1) Generate aortic aneurysms in ApoE$^{-/-}$ animals by angiotensin II (ATII) infusion and to determine the natural history of aneurysm progression in this model
2) Carry out contrast enhanced ^{18}F-FDG PET-CT in the ApoE$^{-/-}$-ATII model and determine the natural history of aneurysm progression with ^{18}F-FDG uptake
3) Determine the association between aneurysm growth rate, aortic diameter and risk of rupture to ^{18}F-FDG uptake in aortic wall
4) To characterise the immune cell infiltrate associated with ^{18}F-FDG uptake in murine suprarenal aneurysms
5) Quantify the immune cell populations and define the subtypes present in the normal aorta *vs.* aortic aneurysms *vs.* aortic aneurysms from different ^{18}F-FDG uptake sites
6) Determine the location of these cells within the aortic wall

4.3 Methods

4.3.1 Murine ApoE$^{-/-}$-ATII model of aortic aneurysms

All procedures on animals were carried out under a project license from the ANIMALS SCIENTIFIC PROCEDURES ACT 1986 (PPL 70/7097) and personal license (PIL 70/22677) granted by the Home Office. ApoE$^{-/-}$ mice mutant strain (Jackson Laboratory, Bar Harbor, ME, USA) were used for the aortic aneurysm model. The animals were housed in a 12-hr light/12-hr dark cycle at 18-23^{o}C with 40-60% humidity. The ApoE$^{-/-}$ mice were given normal chow 8-11% fat with water available at all times (SDS, Essex, UK).

Alzet osmotic mini-pumps (Durect Corporation, Cupertino, CA, USA) loaded with 107µl of a 12µg/µl Angiotensin II (Sigma-Aldrich, Saint Louis, MO, USA) solution in sterile normal saline. Under 4% isoflurane anesthesia, the pumps were implanted subcutaneously in the dorsal region of 12-14 week-old male ApoE$^{-/-}$ mice, to achieve a delivery rate of 1µg/kg/minute over the course of 6-weeks as previously described[62,153,279,349,359]. The skin was closed with 4/0 polydiaxonone (Ethicon, UK). Buprenorphine (2µg/g body weight) was administered subcutaneously for post-operative analgesia. An aortic aneurysm was defined as a 2-fold increase in the aortic diameter from the baseline. Abdominal aortic aneurysms in the supra renal and descending thoracic aorta were generated (Fig 4.0).

4.3.2 Detection and quantification of ^{18}F-FDG on PET-CT

The animals previously implanted with the subcutaneous pumps for angiotensin II release were anesthetised with isoflurane/oxygen 4% *via* a face-mask at a constant flow rate of 1.5L/min. One of tail veins was cannulated with a 30-gauge needle. Exitron Nano1200 (Miltenyi Biotec, GmbH, Germany) was used as a blood pool contrast agent delivered through a 100µl injection. ^{18}F-FDG was injected at a dose of 10MBq at the same sitting. CT scan images were acquired at 60mins post injection and the PET images at 90mins without

moving the animals on the gantry. Haemodynamic parameters for the animal were monitored using telemetry system that informed of pulse and respiratory rate. Animals were continuously monitored visually whilst in the scanner. At the end of the scan session animals were allowed to recover in the preparation room in a warm dim environment. The animals were recovered for imaging at later time points in a longitudinal fashion; or animals were culled using exsanguination (direct cardiac puncture). The spectral Nano PET/CT scanner (Medisco, Bioscan Inc. Washington, US) was used for image acquisition. The PET detector comprised of 12 arrays of 85x39 LYSO crystals on 1.12x1.12x13mm^3 at a packing fraction of 92%. The helical CT scan allowed data acquisition at 1.2mm CFOV with a 250-750keV window. CT scan images were acquired from the aortic arch to the iliac bifurcation at maximum FOV, 360 projections at 1600ms, voltage setting of 65keV with 1:4 binning at a pitch of 0.5 (Fig 4.1-4.2). The PET and CT system shared the same axis of rotation enabling real time accurate image fusion without the errors of quantification or due to partial volume effects. This also allowed minimisation of the artifacts caused due to non-uniform sampling from the field of view (Fig 4.2).

Viscover™ ExiTron™ nano (Milteny Biotec, Bergisch-Gladbach, Germany) was used as the intravenous alkaline earth metal–based nanoparticulate (110nm) contrast agent for the preclinical CT imaging. On intravenous injection, ExiTron nano circulated in the bloodstream till finally taken up by the reticuloendothelial system. The ExiTron nano 12000 gave density of 12,000 HU. 100µl was injected per mouse (25g) corresponding to a dose of 1200 mg iodine/kg body weight. The imaging was typically performed 60mins post injection of the contrast agent.

4.3.3 Image analysis of PET scans

The scans were analysed using the Hermes, OsiriX software (OsiriX Inc. San Antonio, Texas) and Amira 5.3.3® (Visage Imaging Inc. San Diego, CA) software as for human scans described in section 3.3. Additionally the murine scans

directly transferred and analysed at a dedicated workstation using Bioscan InvivoScope™ imaging suite. This allowed PET-CT fusion and image registration to be performed. Images were reconstructed to give the maximal field of view (FOV) and co-locate ^{18}F-FDG into aortic tissue (Fig 4.3).

4.3.4 Murine aortic biopsy

Mice had induction anesthesia with 3% isoflurane, which was maintained with 1% isoflurane at 2l/min of oxygen. Aseptic techniques were used throughout the time of open surgery: a median sternotomy and midline laparotomy was carried out to expose the entire length of aorta. The aorta was dissected from the aortic root, along with the aortic arch vessels down to the iliac bifurcation using an operating microscope (Leica Microsystems ltd, UK). The entire aorta was harvested and sectioned into ascending, aortic arch, descending thoracic, suprarenal and infra-renal aortic segments. The affected aneurysmal segment was removed and segmented as per imaging data for analysis. Prior to processing the aortic wall was thoroughly washed with sterile normal saline at 4°C to remove any blood contamination. Aortic segments were obtained from regions with different SUV_{max} (^{18}F-FDG uptake). Biopsies were processed for either flow cytometric analysis, homogenised for PCR/ELISA analysis, or fixed in 10% formalin/snap frozen in liquid nitrogen for histological analysis.

4.3.5 Isolation of tissue resident inflammatory cells for flow cytometry

Murine aortic specimens underwent same enzymatic degradation and cell harvest protocol as in section 3.3.3. Tissue was cut into 1x1mm segments from each site and incubated at 37°C for 30mins in phosphate buffered saline (PBS, without calcium and magnesium) containing 0.5% bovine serum albumin (BSA), 1mM ethylenediaminetetraacetic acid (EDTA) with 1mg/ml collagenase D (Sigma Aldrich, UK), 100units/ml DNAase I (Sigma Aldrich, UK) and 500units/ml hyaluronidase IV-S (Sigma Aldrich, UK). The tissue and dissociated cells was

filtered through a 100µm strainer (Falcon BD) into a 6-well plate and the undigested tissue mechanically dissociated in the enzyme suspension-using plunger from a 10ml syringe. The remnant tissue was washed with 5mls of PBS (0.5%BSA, 1mM EDTA). The cells were washed and spun twice at 320g at 4°C with the supernatant discarded and the pellet resuspended in 1ml PBS/BSA/EDTA and incubated on ice. The cells were fixed in 4% paraformaldehyde for 10mins at room temperature, washed (x1) and suspended in PBS (0.5%BSA, 1mMEDTA) and stored at 4°C for 48hrs prior to staining for flow cytometry.

4.3.6 Antibody staining for murine inflammatory cell markers

Murine samples (normal and aneurysmal) were obtained at 5, 10, 15, 25 and 33 days post-aneurysm induction. For the murine PET-CT experiments n=15 (3 from each time point) tissue samples were obtained at each time interval. Aortic samples were segmented according to anatomical location to ascending aorta including aortic arch, descending thoracic aorta, suprarenal abdominal aorta and infra-renal abdominal aorta. The aneurysmal segment was divided into segments depending on the degree of tracer uptake. The complete aneurysmal segment was excised and cut into anterior, posterior, lateral and medial aortic wall segments as per regional tracer uptake. Tissue underwent enzymatic degradation and cell harvest protocol as described in Section 4.3.5.

Inflammatory cell content of tissue resident cells from murine aortic wall was quantified using flow cytometry. This was carried out in the following manner. 500µl of cell suspension in FACS buffer (PBS with 1%BSA, 10% sodium azide) from each aortic biopsy site was incubated with the antibodies resulting in the following concentrations (Table 4.0).

Analysis was carried out using a FACS Canto II flow cytometer (BD Biosciences, UK). Leukocytes were selected according to forward (size) and aide

(granularity) scatter properties and final gating performed on CD45+, CD3+ and CD19+ leukocytes.

Table 4.0 Primary flow cytometric antibodies for murine immune cell typing

(All antibodies obtained from BD Biosciences)

Cell	Cell surface marker	Fluorophores	Concentration	Code
Leukocyte	**CD45**	**PE**	**0.25 µg/ml**	**553081**
NK	**NK1.1**	**APC-Cy**	**0.1 µg/ml**	**560618**
T-cell	**CD3**	**PE-Cy**	**0.1 µg/ml**	**552774**
B-cell	**CD19**	**APC**	**0.25 µg/ml**	**550992**
Monocyte	**CD11b**	**APC-Cy**	**0.25 µg/ml**	**557657**
Macrophage	**F4/80**	**PE-Cy**	**0.5 µg/ml**	**123114**
Neutrophil	**Ly6c**	**FITC**	**0.25 µg/ml**	**553126**

4.3.7 Antibody staining for murine lymphocyte subset markers

The cell suspension sample was split into three subsets for staining. These were for B-cell, T-cell and T regulatory cell surface markers. Each subset contained 500µl of cell suspension in FACS buffer from each aortic biopsy site that was incubated with the antibodies resulting in the following concentrations (Table 4.1). Flow cytometric analysis was carried out as outlined in Section 3.3.6.

Table 4.1 Primary flow cytometric antibodies for murine immune cell subtyping

(All antibodies were obtained from BD Biosciences)

Cell	Cell surface marker	Fluorophores	Concentration	Code
Common T-cell	**CD3e**	**PerCP-Cy5.5**	**0.2µg/ml**	**551163**
T helper cell	**CD4**	**APC-H7**	**0.2 mg/ml**	**560181**
Active antibody producing B-cells	**CD5 (Ly-1)**	**FITC**	**0.5 mg/ml**	**553020**
Cytotoxic T-cell	**CD8a (Ly-2)**	**FITC**	**0.5 mg/ml**	**553030**
Common B-cell	**CD19**	**PerCP-Cy5.5**	**0.2 mg/ml**	**561495**
Common B-cell	**CD20**	**APC-H7**	**0.2 mg/ml**	**641396**
Plasma B-cell	**CD24**	**PE-Cy7**	**0.2 mg/ml**	**560536**
T regulatory cell	**CD25 (IL2)**	**PE**	**0.2 mg/ml**	**558642**
Memory B-cell	**CD27**	**V450**	**0.2 mg/ml**	**560448**
Active B-cells (B-T interaction/ adhesion)	**CD38**	**APC**	**0.2 mg/ml**	**555462**
Common leukocyte antigen	**CD45**	**V450**	**0.25 mg/ml**	**560501**
Active B plasma cell	**CD138 (syndecN-1)**	**APC**	**0.2 mg/ml**	**558626**
Active synthetic B-cell	**Anti IgD**	**PE**	**0.2 mg/ml**	**553511**
Synthetically active B-cell	**Anti IgM**	**PerCP-Cy5.5**	**0.2 mg/ml**	**550881**
Highly active T-cell	**CD14**	**APC-H7**	**0.2 mg/ml**	**641394**
Highly active T-cell	**CD16**	**APC-H7**	**0.2 mg/ml**	**560195**

4.3.8 Tinctorial histology and immunohistochemistry

This was carried out as described in Sections 3.3.7, page 107 and 3.3.8, page 109, using the primary anti-mouse antibodies described in Table 4.2 and the same secondary antibody staining system.

Table 4.2 Primary anti-mouse antibodies used for murine immunohistochemistry

Primary Antibody	Marker	Species	Final concn (μg/ml)	Manufacturer
Anti-CD3	Common T-cell	Rabbit	1μl/ml	Leica Biosystems, UK
Anti-CD20	Common B-cell	Rabbit	1μl/ml	Millipore, UK
Anti-CD56 (NCAM1)	Natural killer cells	Mouse	1μl/ml	Antibodies Online, Germany
Anti-Mac-2 (Galectin 3)	Macrophages	Mouse	4μl/ml	BioLegend, USA
Anti-tropoelastin	Tropoelastin	Rabbit	1μl/ml	Abcam, MA

4.3.9 Statistical analysis

Data was analysed in SPSS (IBM Corporation, Data Collection, USA). Data are represented as mean ± standard deviation (SD). Parametric data was analysed using Student's Paired T-test. Correlations were carried out using linear regression and Pearson correlation coefficient analysis and represented as the R^2 value. Alpha was determined to be <0.05 for significance testing.

4.4 Results

The $^{-/-}$ApoE/angiotensin II murine model was used to evaluate the ^{18}F-FDG uptake in 15 animals that underwent 20 scans in total at 5 time points (day 5, 10, 25, 25, 33). Some animals developed aortic dissection and rupture as complications in this model (20% of number used, Fig 4.0).

The model mimicked not only the characteristic development of aortic aneurysm but also all the complications that can arise as a consequence of aneurysm development, namely aortic rupture and/ or dissection. To image the aorta at various stages of aneurysm development computer tomography (CT) was used to delineate the aorta. The non-contrast CT as in humans was not helpful as lack of intraluminal vascular contrast agent meant aortovascular anatomy could not be seen compared to surrounding tissues (Fig 4.1). This was the case when assessing mediastinal and abdominal vasculature and it was technically challenging to follow the aortic tree in the abdomen with Hounsfield unit reading similar to surrounding structures.

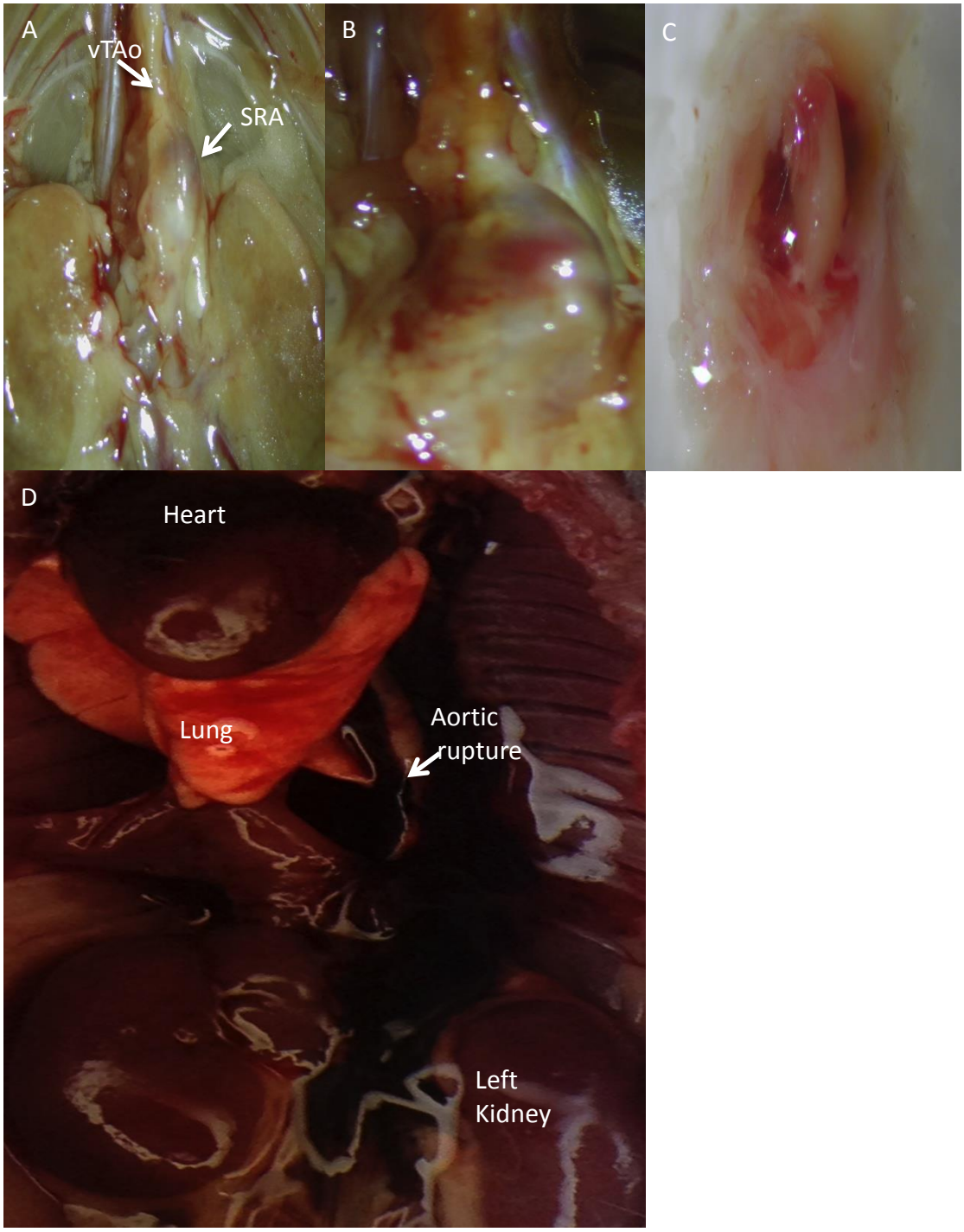

Fig 4.0 ApoE$^{-/-}$-ATII infused animals at day 35 with suprarenal aortic aneurysms (SRA)

A) The supra-renal aorta can be seen to dilate to more than x4 its normal diameter in this animal with a normal thoracic aorta (TAo). The aneurysm typically terminates above the renal arteries B) This ApoE$^{-/-}$-ATII animal developed an aortic dissection and died at day 14. The haemorrhagic change can be seen in the adventitia of the SRA C) This SRA at day 35 had ILT present around the aortic wall when opened up longitudinally. This typically characterises an advanced aortic aneurysm. D) ApoE$^{-/-}$-ATII infused animal developed acute aortic rupture of the thoracoabdominal aorta and was found dead at day 15. A post-mortem examination showed haematoma in the left pleural space and the retroperitoneum.

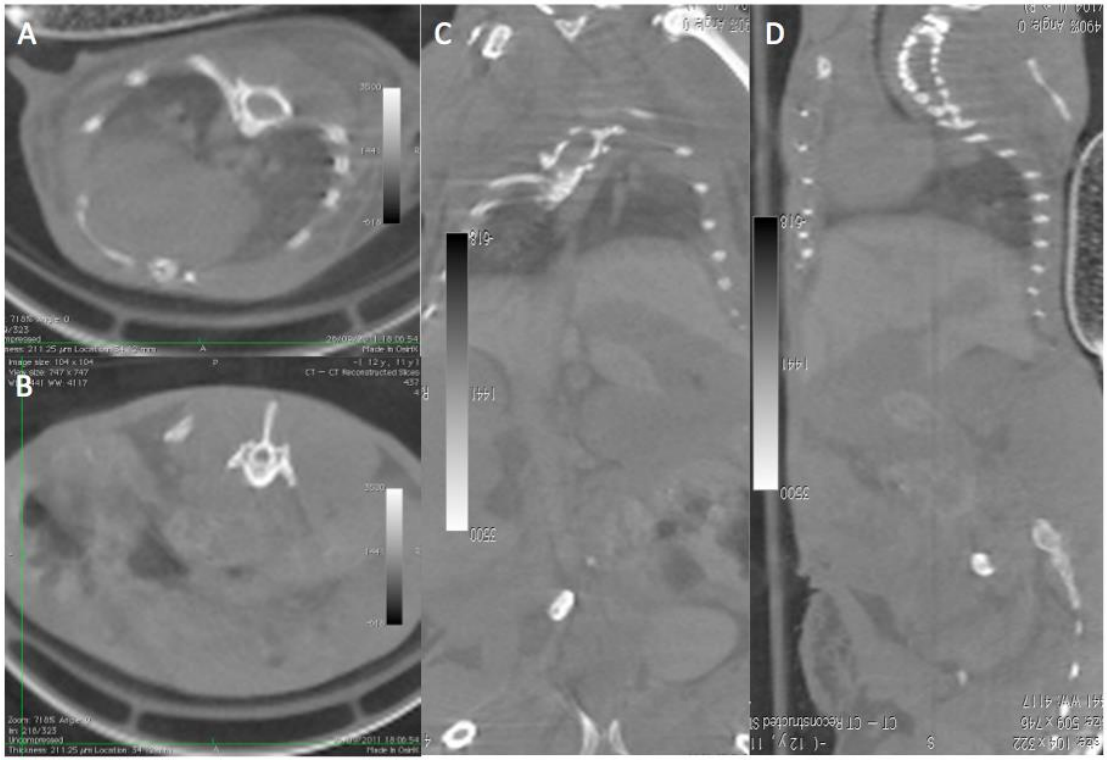

Fig 4.1 Non-contrast enhanced murine CT

A) A transverse slice taken through the mid-thoracic section of the chest where the heart is visible in the middle mediastinum. The aorta or the cardiac structures cannot be delineated clearly due to lack of contrast. B) The transverse section taken through the abdominal aorta at the level of the liver. There is unclear soft tissue opacification and none of the vascular structures seen. C) This is a coronal section through the murine chest and abdominal cavities. The soft tissue and solid organs are just visible. Lungs appear as dark opacities in the upper half of the image with the live seen under the diaphragm. D) A sagittal section through the chest and abdomen again delineating poorly the heart and the aortovascular details are absent

The intravascular contrast agents were therefore used to determine the aortovascular tree. After intravenous administration of ExiTron nano 12000 (Miltenyi Biotech, Bergisch-Gladbach, Germany), the alkaline earth metal-based nanoparticulate contrast agent specifically circulated within the vascular tree and maximally delineated the aortic vascular tree 60mins post intravenous injection. The blood pool agent is eventually taken up by the Kupffer cells and renal excreted but till then allowed excellent intravascular visualisation of the aorta (Fig 4.2). This allowed aortic wall lumen to be delineated and thoracic and abdominal aortic aneurysms to be visualised (Fig 4.2) as well as all the thoracic, visceral, renal arterial branches and the vascular arcades.

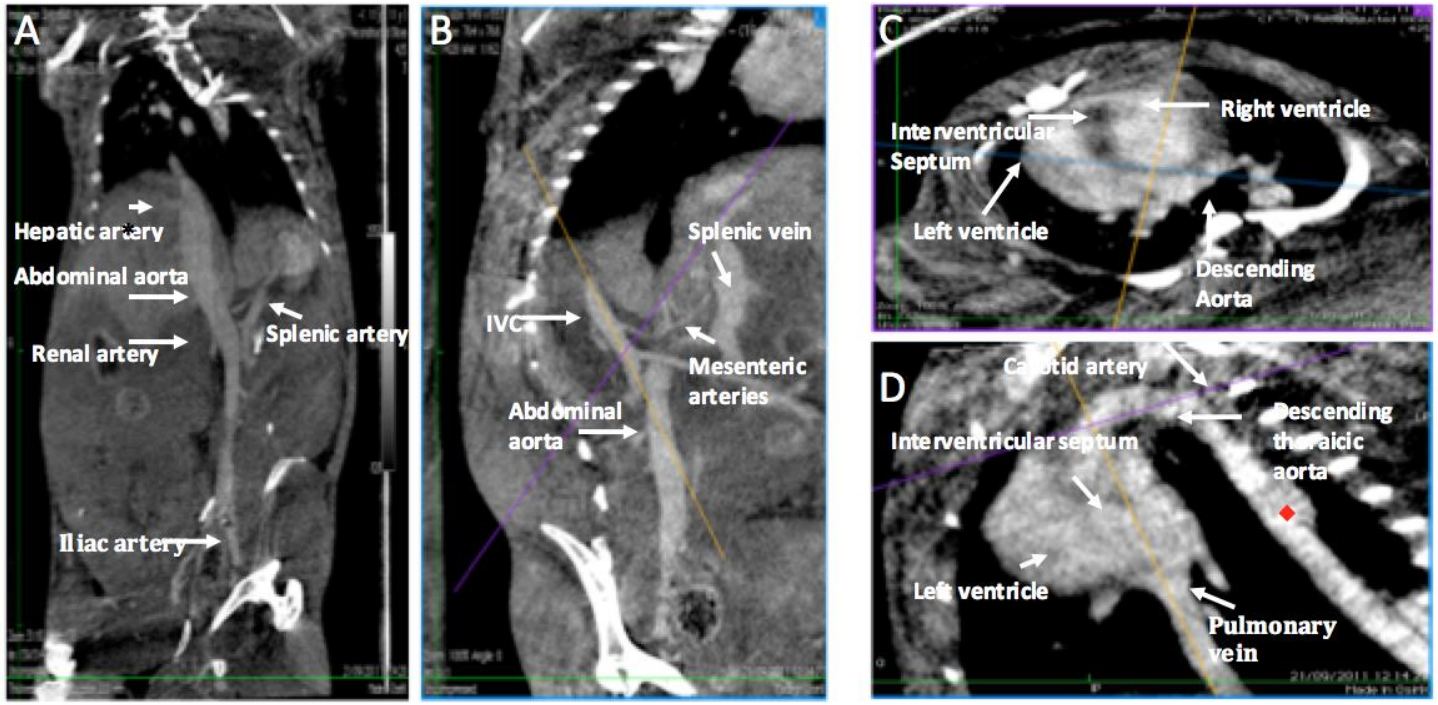

Fig 4.2 Contrast CT scan performed 60mins after intravenous blood pool agent ExiTron nano 12000

A) The coronal section shows the thoracoabdominal aorta and its branches in a day 7 $ApoE^{-/-}$-ATII mouse. Early dilatation of the suprarenal segment can be seen (*) B) Sagittal section MPR showing the abdominal aorta, IVC, and visceral branches. C) Transverse mid-thoracic section demonstrating cardiac chambers. D) Ascending, arch and descending thoracic aorta with arch branches seen. Proximal descending thoracic aneurysm (red diamond).

The PET scan using ^{18}F-FDG was performed 90min after the radiotracer injection (Fig 4.3). Extremely high metabolic activity was seen in the myocardium, followed by the kidneys and increased renal pelvic washout of the ^{18}F-FDG into the urinary bladder. The ^{18}F-FDG uptake varied heterogeneously within the murine model. Overall there was an increased uptake of the ^{18}F-FDG in the animals over the time course of the experiment with a statistically significant higher uptake when day 5 animals were compared to day 15 ($P<0.01$). However there were no differences between the groups when compared on weekly basis. The uptake was localised to certain sites but was heterogeneous (Fig 4.3B) and plateaued in its intensity from day 15 to day 33. Uptake was predominately present in the aneurysmal segments compared to the normal aortic wall. There was no correlation between aneurysm size or growth and the ^{18}F-FDG uptake (Fig 4.4). Uptake varied from site to site at various time intervals within the same animal when serially imaged and the equivalent sequences and slices were compared.

A cohort of serially imaged ApoE$^{-/-}$ATII (n=16) allowed determination of the natural history of aneurysm development. 70% of the cohort developed an aortic aneurysm and off these 20% developed aortic dissection or rupture within the time course of the study. The mean aortic diameter was 210μm±38.3μm and this increased in all animals with time. The maximum aortic diameter reached was x5 the baseline diameter at 1012μm (Fig 4.4).

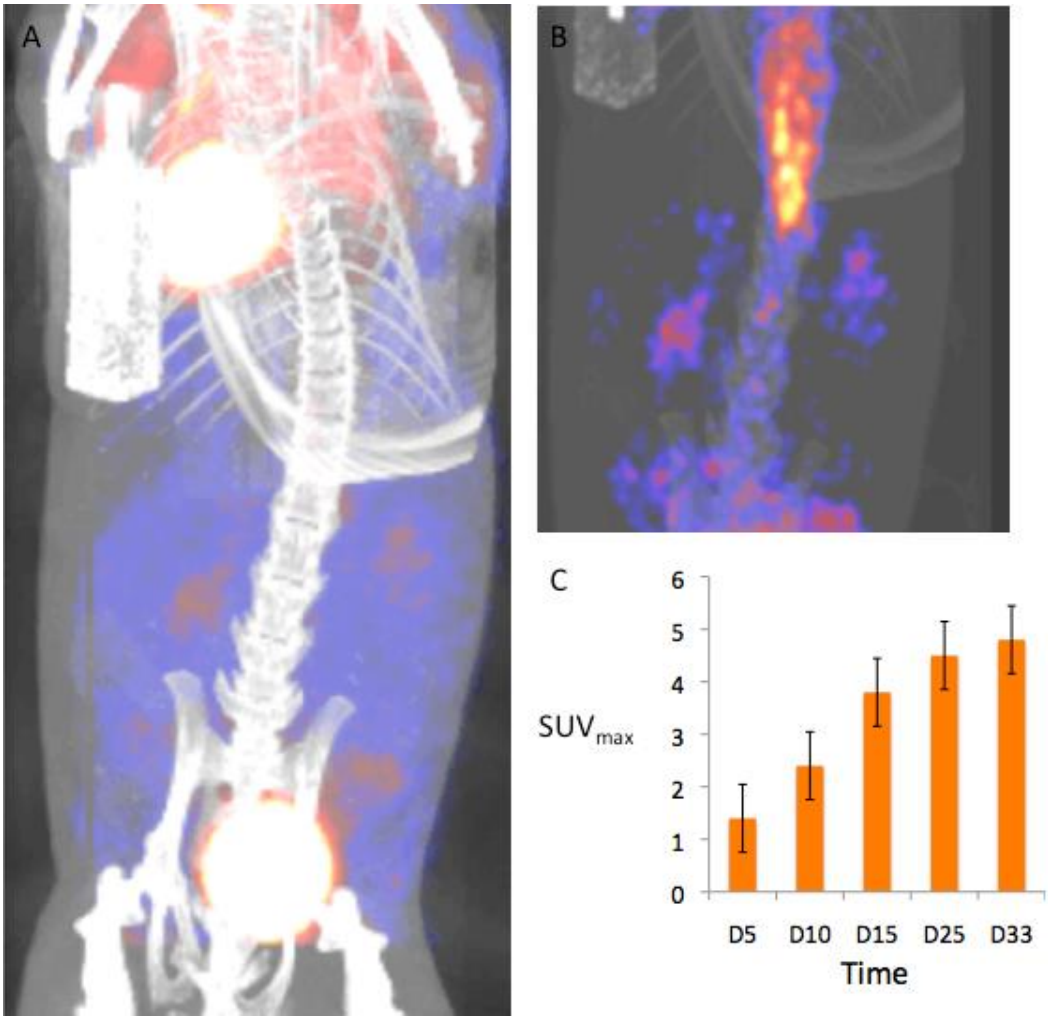

Fig 4.3 A fused PET-CT image, CT scout and ^{18}F-FDG uptake

A) The increased uptake of the ^{18}F-FDG can be seen in the myocardium and the urinary bladder. There is minimal ^{18}F-FDG uptake in the aorta in this animal. B) This is an example of focal but heterogeneous uptake of the ^{18}F-FDG in the suprarenal aortic wall of an aneurysm at day 15. The SUV_{max} ranged upto 4.5 in this instance. The renal outline can be seen at the lower pole of the aneurysm. C) The SUV_{max} represented in the suprarenal aortic aneurysm with time in any specific region of interest selected in the SRA wall. There is significantly more ^{18}F-FDG uptake in the aortic wall at day 5 compared with day 15 ($P<0.01$, paired T test n=9). Thereafter there are no statistically significant differences between the uptakes at the time points out to day 33. Thus there was plateau of ^{18}F-FDG uptake within the aortic wall at difference sites from 15 days after SRA induction.

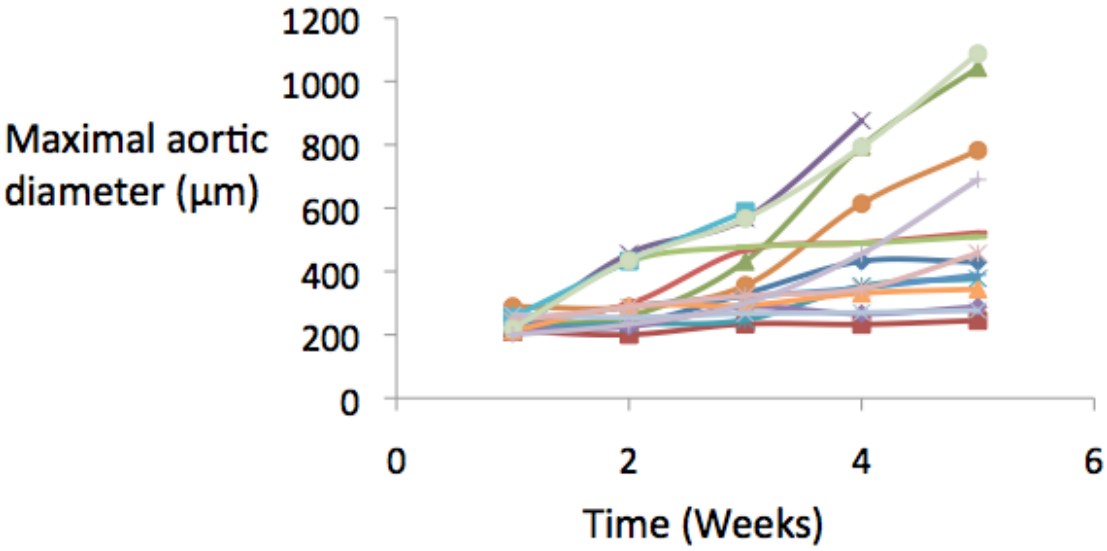

Fig 4.4 The individual growth rates of the ApoE$^{-/-}$ATII aneurysms

The growth rates of individual animals (depicted by a different graph colour) are plotted in a longitudinal temporal manner for n=16 animals. The mean aortic diameter at 5days after ATII infusion was 210±38.3µm and this increased in 70% of animals over time to 812±250.8µm at 35 days. The rate of aneurysm induction was 70%. Of the animals that developed aortic aneurysms the risk of complications increased with time. There was a 20% mortality associated in the group with aneurysms resulting from aortic rupture or dissection.

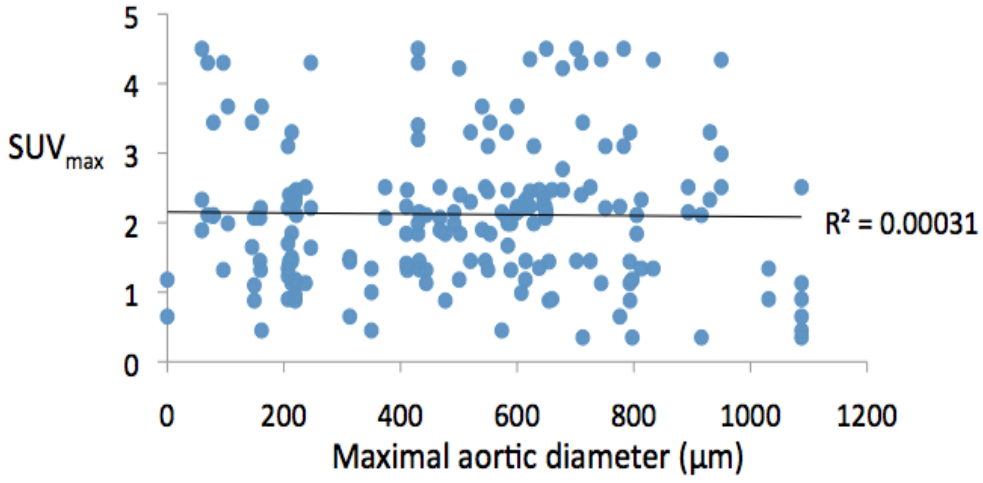

Fig 4.5 No correlation between the maximal aortic diameter on IV contrast CT and the SUV_{max} on PET scan

There was no correlation between maximal aortic diameter and the ^{18}F-FDG uptake (n=16) R^2=0.0003. Multiple murine aortic diameters taken from all the time points were compared to the SUV_{max} readings taken for those aneurysms. There was an intense focal uptake at certain sites in all aneurysms even at small aortic diameters. The SUV_{max} varied from site to site at all the varying time intervals. Different sites had intense ^{18}F-FDG uptake followed by quiescent phase, independent of increase in aortic diameter.

The extracted cell suspensions from sites of specific ^{18}F-FDG uptake were used for flow cytometric analysis to determine the immune cell content and correlate this to radiotracer SUV_{max}. The immune cell content was gated according to their forward and side scatter properties (Fig 4.6) and further gating was performed on CD45 expression. The immune cell content was quantified in all samples (Fig 4.6). Aortic tissue from sites of varying ^{18}F-FDG uptake was quantified according to SUV_{max} (Fig 4.3). Cellular content was quantified per microgram of tissue (Fig 4.6-4.8). Sites with the highest SUV_{max} had increased number of B, T lymphocytes and NK cells (Table 4.3).

Table 4.3 Immune cell content as assessed by flow cytometry at sites of varying SUV_{max}
(N=10, 50 biopsy sites, two way ANOVA with post hoc Bonferroni correction)

Immune cell	Mean cell number per mg wet wt. Aorta ± S.E.M			95%CI±	P
	SUV_{max}<2.5	SUV_{max}2.5-3	SUV_{max}>3.1		
B-cell	77±42	258±85	550±51	0.38	<0.001
T-cell	35±20	170±75	330±70	0.43	<0.001
NK cell	10±8	23±14	74±23	0.45	<0.01
Macrophages	6±25	10±23	11±18	0.22	0.12
Neutrophils	12±8	14±16	16±19	0.13	0.10

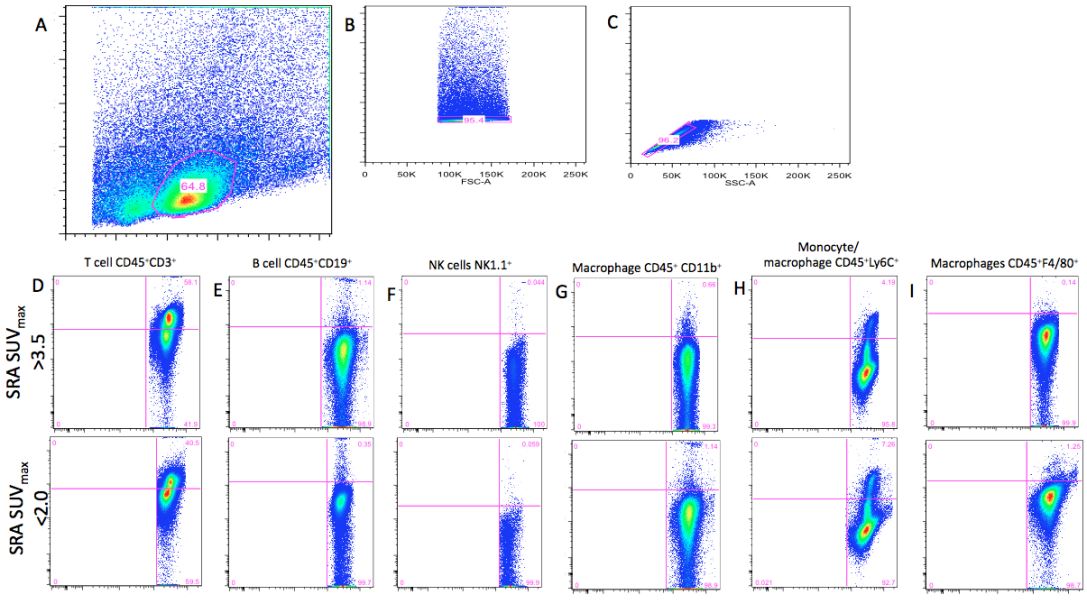

Fig 4.6 Examples of flow cytometric analysis of the suprarenal aortic aneurysm at site of low SUV_{max} and high SUV_{max}

A) The over all cell distribution when gating is performed of $CD45^+$ leukocyte fraction against SSA. B and C) After doublet exclusion on FSC and SSA the cell population subsets are analysed for immune cell quantification. D-I) Upper panels demonstrates the suprarenal aortic aneurysm (SRA) with high ^{18}F-FDG uptake characterised by SUV_{max} >3.5 in the aortic wall compared to the bottom panels where SUV_{max} <2.0. There is increased expression of T lymphocytes ($CD3^+$), B lymphocytes ($CD19^+$), NK cells (Nk1.1), slight increase in macrophages ($F480^+$), but not neutrophils (CD11b/Ly6C). (N=10 patients and 50 biopsy sites).

Once the high expression of lymphocytes was determined at sites of high SUV_{max}. These cells were subtyped according to the cell surface markers to determine the lymphocyte population resident in the aortic aneurysm wall (Fig 4.7). The cells were subtyped according to $CD45^+$ expression, and the leukocyte fraction further gated on the common T-cell antigen ($CD3^+$). The $CD3^+$ T-cell fraction was subtyped to T helper $CD4^+$, cytotoxic $CD8^+$ cell fraction, activated T-cells $CD25^+$ that interact with B-cells and T regulatory cells $FoxP3^+$ with $CD127^+$ expression.

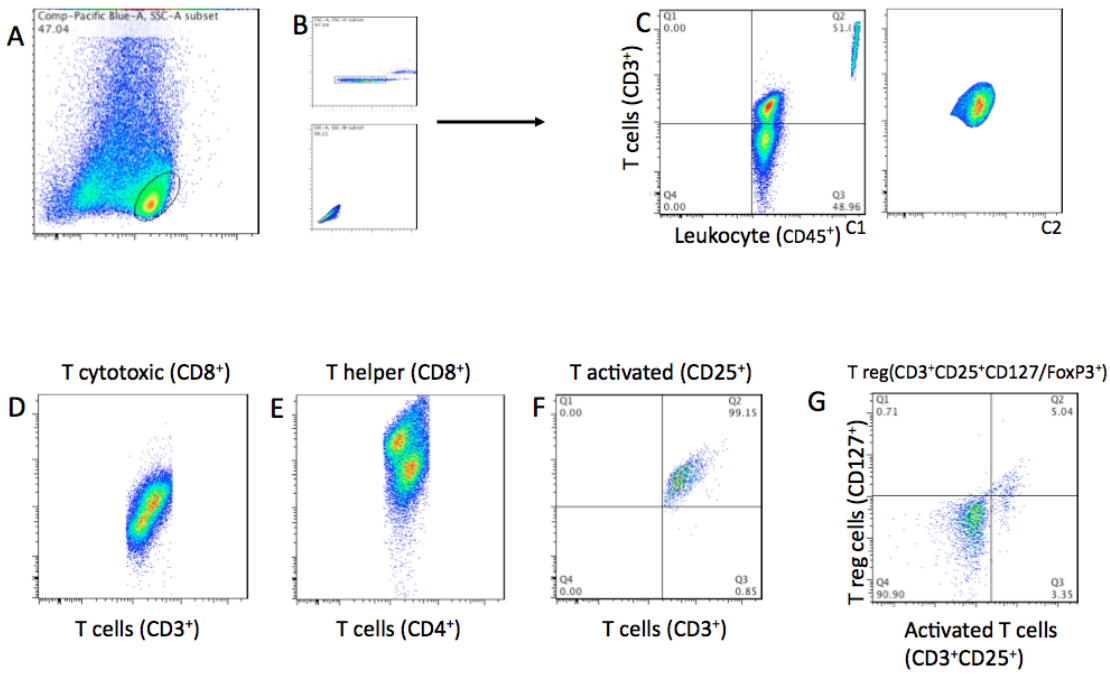

Fig 4.7 Flow cytometry immune sub-typing of the CD45$^+$CD3$^+$ T-cell population

The cells extracted from the normal and aneurysm sites with varying SUV_{max} were characterised on FSC and SSA profiles. B) After doublet exclusion gating. C) The CD45$^+$CD3$^+$ cells were gated and counted (C1) with CountBright^{TM} beads (Invitrogen, UK). This population (C2) and sub-typed as D) the CD8$^+$ cells as expressed a high and low expression group. E) The CD4$^+$ T helper cells along with CD8$^+$ cytotoxic T-cells. F) The activated cell phenotypes expressing CD25$^+$ cell surface marker and G) the identification of T regulatory cell population as CD3$^+$CD25$^+$FoxP3$^+$CD127$^{high/low}$ cells, as seen on the gating strategy.

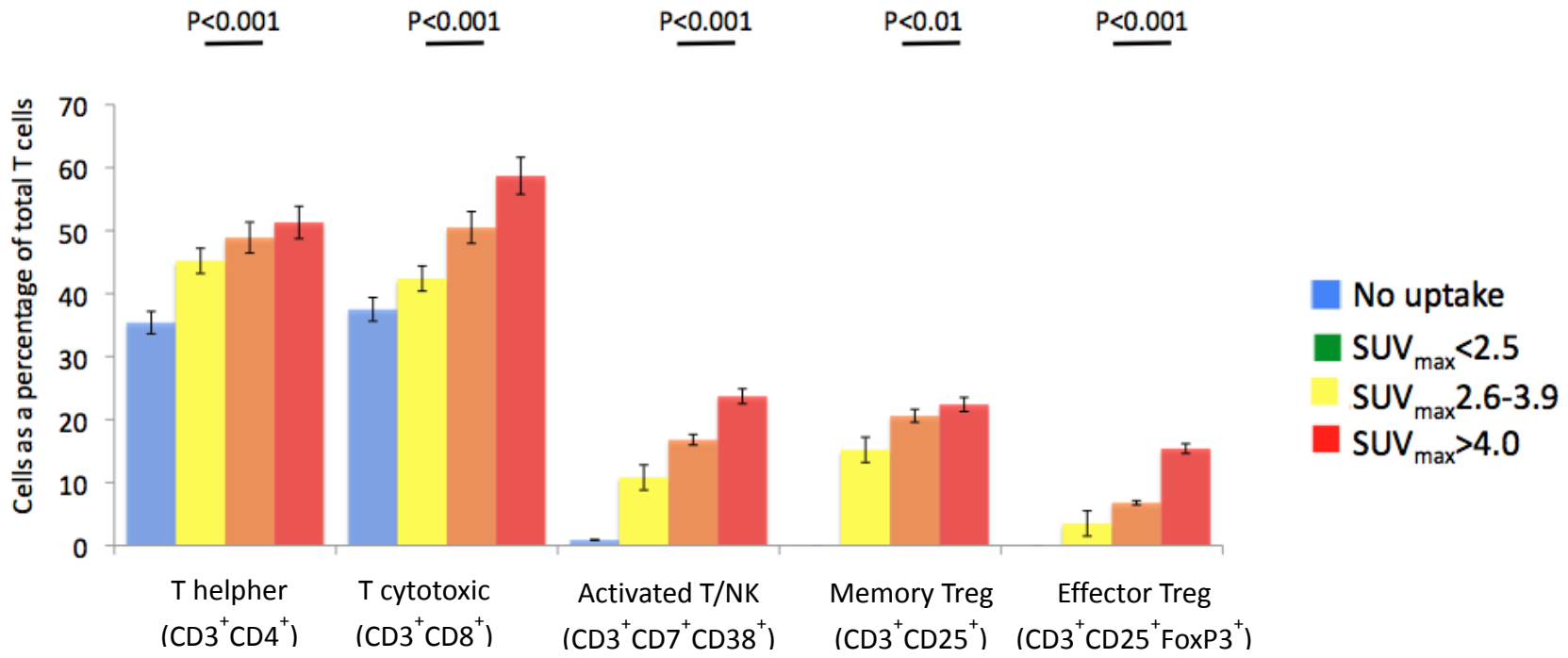

Fig 4.8 Flow cytometric analysis of T-cell fractions as a percentage of total $CD3^+$ cells. (N=6, 32 aortic segments with P<0.001, 2-way ANOVA and post hoc Bonferroni correction as above)

B-cells were subtyped after initially gating on the CD45$^+$ leukocyte population. The cells were gated on the common B-cell antigen CD19$^+$. The cells were subsequently typed according to the presence activated B-cells CD25$^+$, synthetically active plasma cells that produce IgD and IgM producing populations (Fig 4.9).

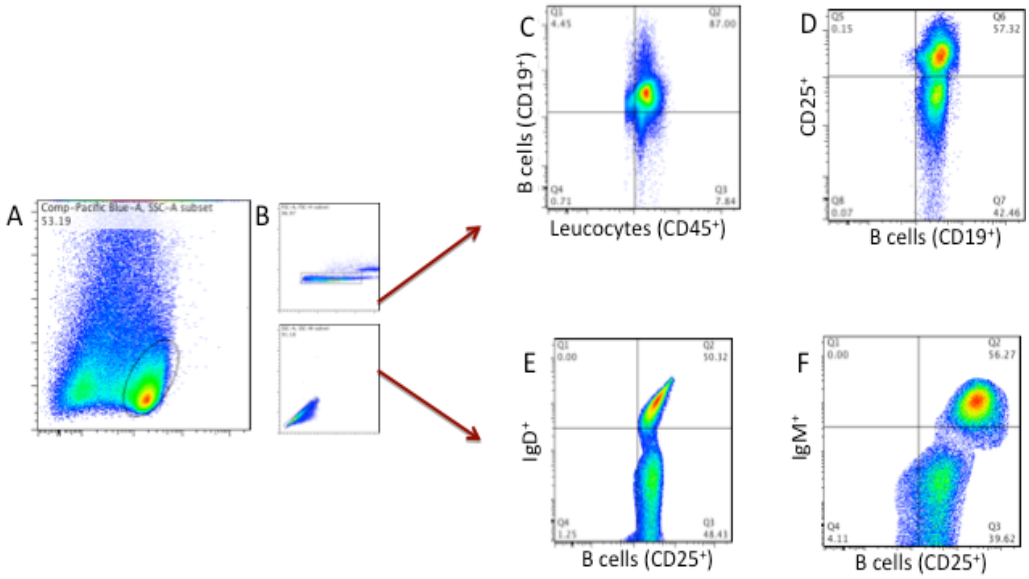

Fig 4.9 B-lymphocytes subsets were phenotyped on flow cytometry

A) The cells population on CD45$^+$ and side scatter profiles was identified. B) Doublet exclusion gating. C) Gating on CD45$^+$ CD19$^+$ B-cells. D) The CD19$^+$CD25$^+$ synthetically active population of B-lymphocytes. E) The expression of CD25$^+$IgD denotes cell adhesion ability for plasma cells. F) The memory B-cells were phenotyped to IgM synthetically active IgM producing cell type.

Site of no ^{18}F-FDG uptake only expressed CD19/20$^+$ pre-B-cells (Fig 4.10). Increasing tracer uptake was associated with increase in the mature B-cell phenotype with CD24$^+$ expression. This was across the biopsy sites with the SUV_{max} increase from low, moderate to high levels. The proportion of CD27$^+$IgM$^+$ and CD5$^+$IgD$^+$ memory and active B-cells increased markedly compared to the no uptake sites ($P<0.001$). There were no statistically significant differences between the no, low, moderate uptake sites; however, when there was very high SUV_{max} there was up-regulation of the cells expressing CD27$^+$, CD5$^+$ and IgM ($P<0.001$).

The flow cytometric cell presence was confirmed and the cellular histomorphometric location determined on immunohistochemistry. T-cells ($CD3^+$), B-cells ($CD19^+$), macrophages ($Mac2^+$) were found in the outer two-thirds of the tunica media co-localising in the same regions and in the tunica adventitia. There was a smaller infiltration with NK cells (NCAM1) at this site. The immune cell content could only be seen in immunohistochemical analysis of aortic wall with the highest SUV_{max} (Fig 4.11).

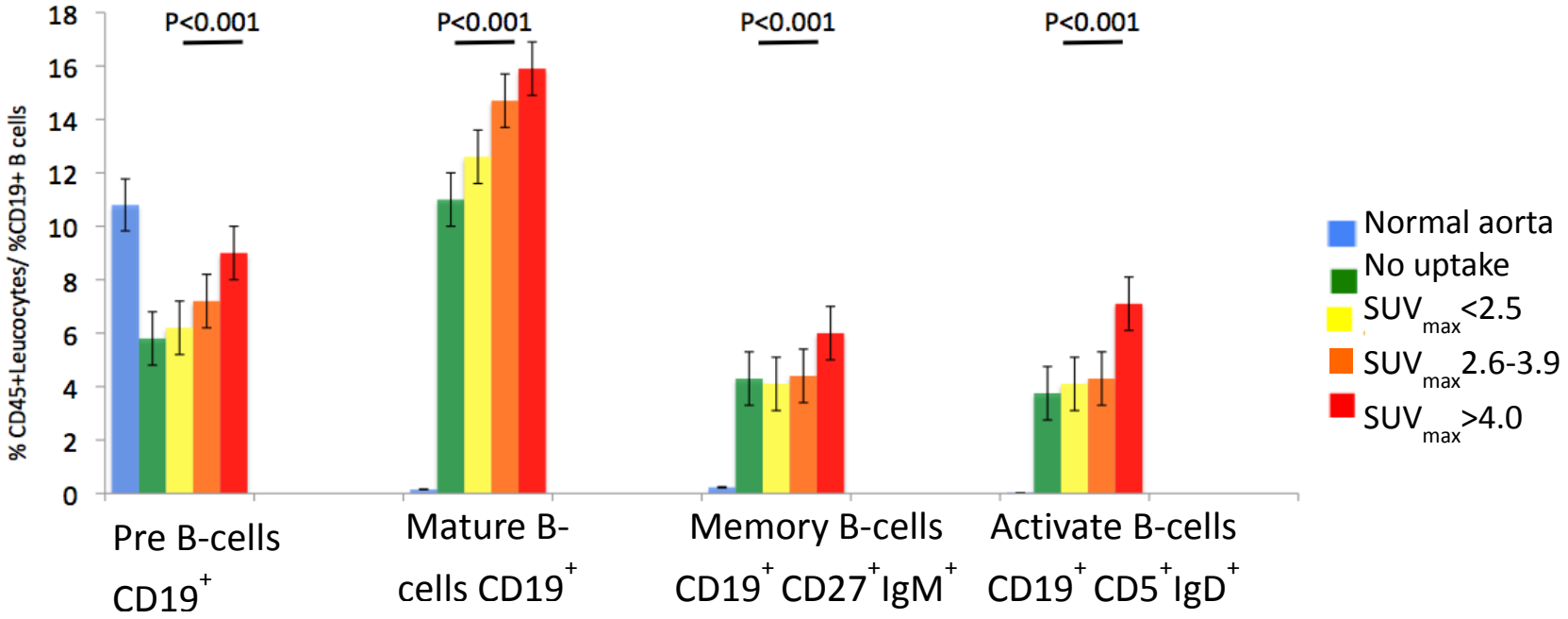

Fig 4.10 The immune cells phenoytped to B-cell subsets from aortic wall with varying ^{18}F-FDG uptake

(N=6, 32 aortic segmented sites, P<0.001 Two way ANOVA with post hoc Bonferroni correction as above between the highest two SUVmax values)

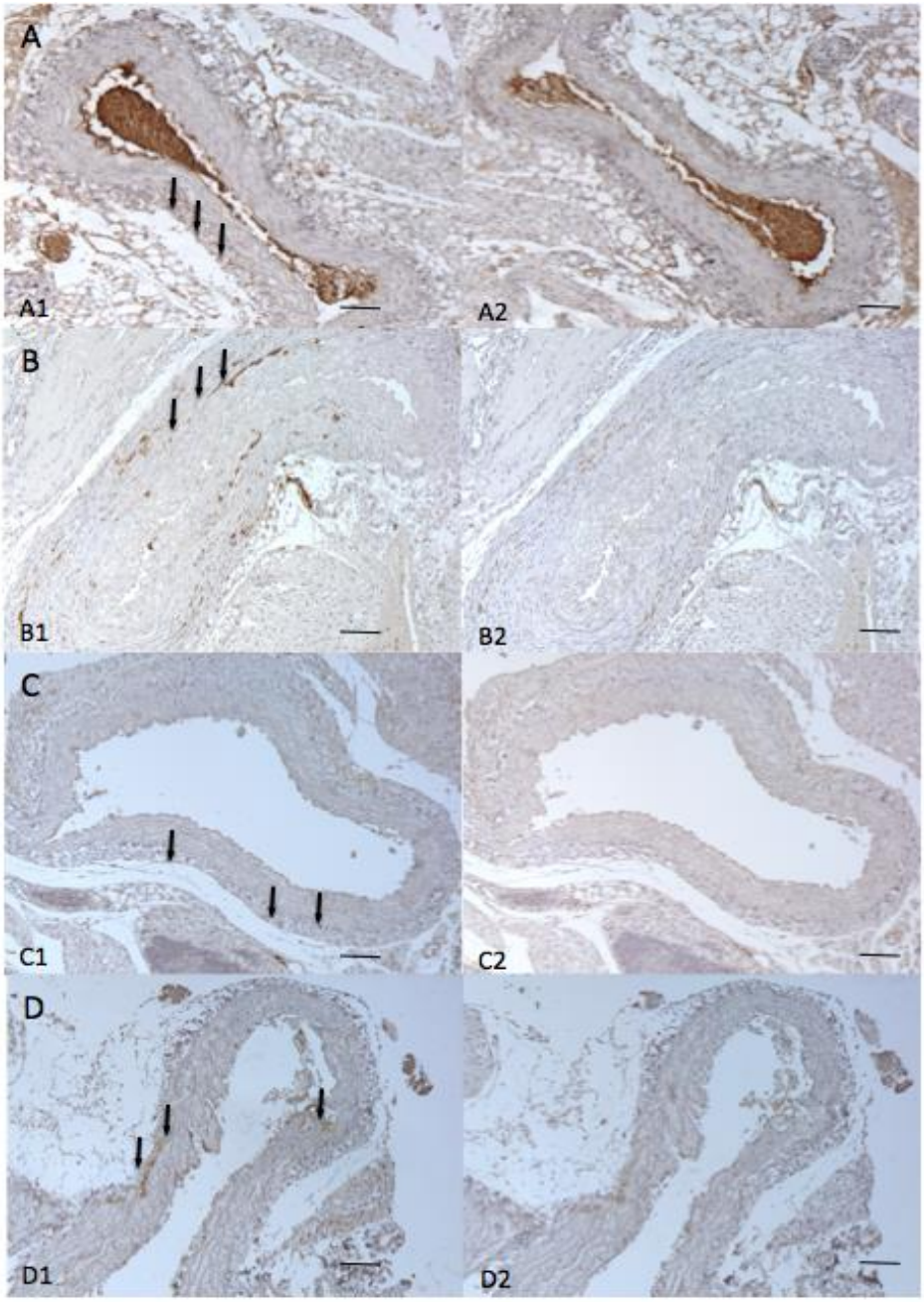

Fig 4.11 The immunohistochemistry of immune cell content in the aneurysm wall

A) T-cells ($CD3^+$) from site of high SUV_{max}>3.5. A1) There are T-cells in media and adventitia (brown stained cells, black arrows); A2) The negative control sample has absent staining B) B-cells ($CD19^+$) at high SUV_{max}>3.5. B1) There is B-cell infiltration in the aortic adventitia and media (brown stained cells, black arrows); (B2) The negative control sample has absent staining. C) NK cells (NCAM1) at high SUV_{max}>3.5. C1) There is little NK cell staining in the aneurysm in the tunica media; C2) The negative control sample has absent staining. D) Macrophages (Mac-2) at high SUV_{max}>3.5. D1) Macrophage staining in the aortic wall is adjacent to the lymphocyte staining at the same sites increasing from the adventitia to the tunica media; D2) The negative control sample has absent staining.

Aortic aneurysm progression was associated with a breakdown of the extracellular matrix (ECM) and decrease in the elastin lamellar content. There were increased breaks seen in the elastin fibers with increased vacuolation of the aortic tunica media, suggesting VSMC loss from the aortic wall. There was no correlation between the immune cellular infiltrate and the ECM degeneration that was more pronounced in aortic wall from larger aneurysms harvested at later time-points (Fig 4.12-4.13). As early as day 5 there were certain animals that had segments of aortic wall with decreased elastin staining, loss of lamellar structure of the tunica media with progresses through to the time-point at day 33. There is increased vacuole formation in the tunica media that represents loss of VSMCs. There is a loss of collagen in the aortic wall at certain sites (Fig 4.12B) however there are regions of the aortic wall in advanced aneurysms where there is a corresponding increase in the collagen content as assessed with masons trichrome staining (Fig 4.12C). These sites might represent active aortic remodelling response to the injury. The complications of loss of aortic matrix are seen (Fig 4.13A) where there is an aortic dissection. The lower aortic wall has normal aortic lamellar structure with intense black staining within the tunica media (black arrows). The upper aortic wall has decreased staining throughout. There are multiple areas with breaks in the elastic lamellae (red arrows) with a start of vacuole formation signifying loss of the homeostatic VSMCs. There are two aortic lumens, a clear true lumen that has been washed of from blood contamination and a partially thrombosed false lumen, that stains red due to fibrin and organized matrix deposition in the clotted lumen. The intimal flap (green arrows) is seen. As aneurysms progress there is generally thinning of the aortic wall with a global decrease in elastin content, decreased lamellae, lamellar breaks, vacuole formation (Fig 4.13B) and that would eventually lead to aortic rupture. This matrix degradation was thus present as common final consequence of inflammatory cell wall changes across all aneurysms.

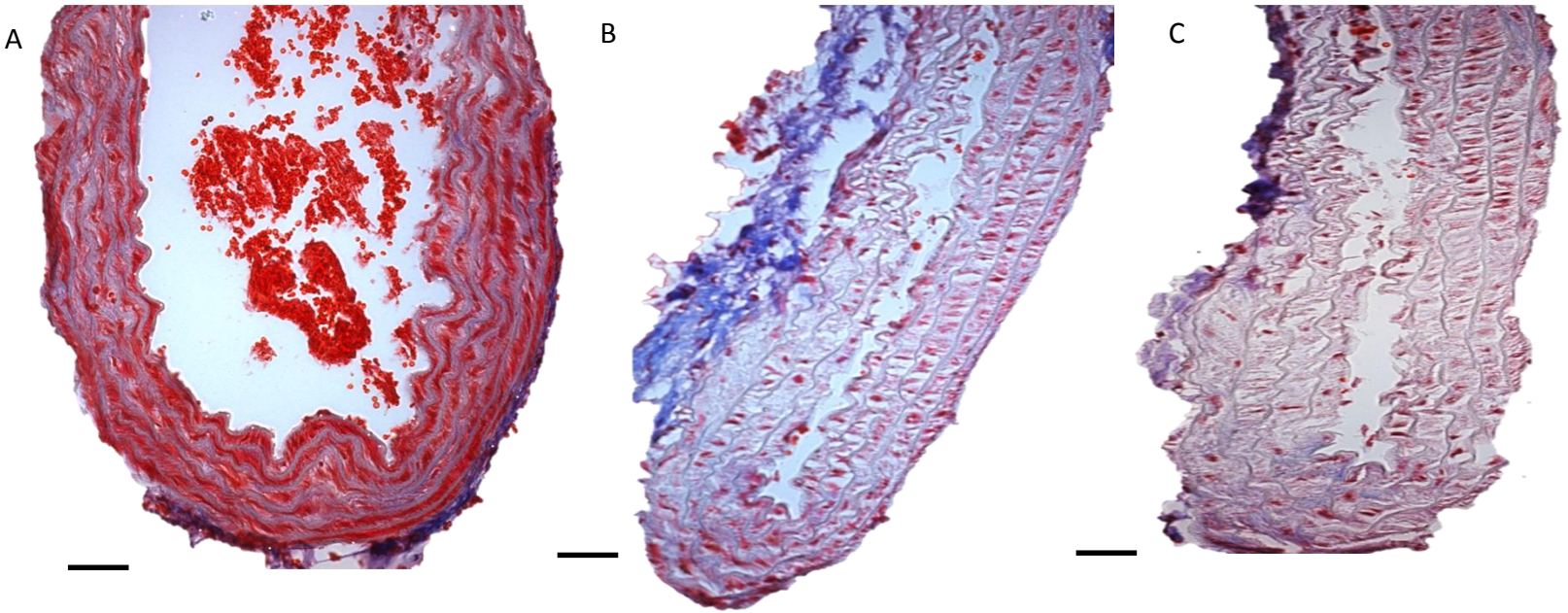

Fig 4.12 Massons Trichrome stained aortic aneurysm wall

A) Day 5 suprarenal aortic wall with organized lamellae of thick elastin bands (red) with organized collagen (blue) in between. B) Day 15 suprarenal aortic aneurysm with thinning of the aortic wall, increased vascoulation, decreased number and thickness of the elastin in the lamellae and loss of collagen staining. C) Day 33 suprarenal aorta with haphazard aortic wall architecture and elastin degradation. There is increased collagen present at this stage as compensatory mechanism to modulate aortic wall. (20x; Scale bar 50µm)

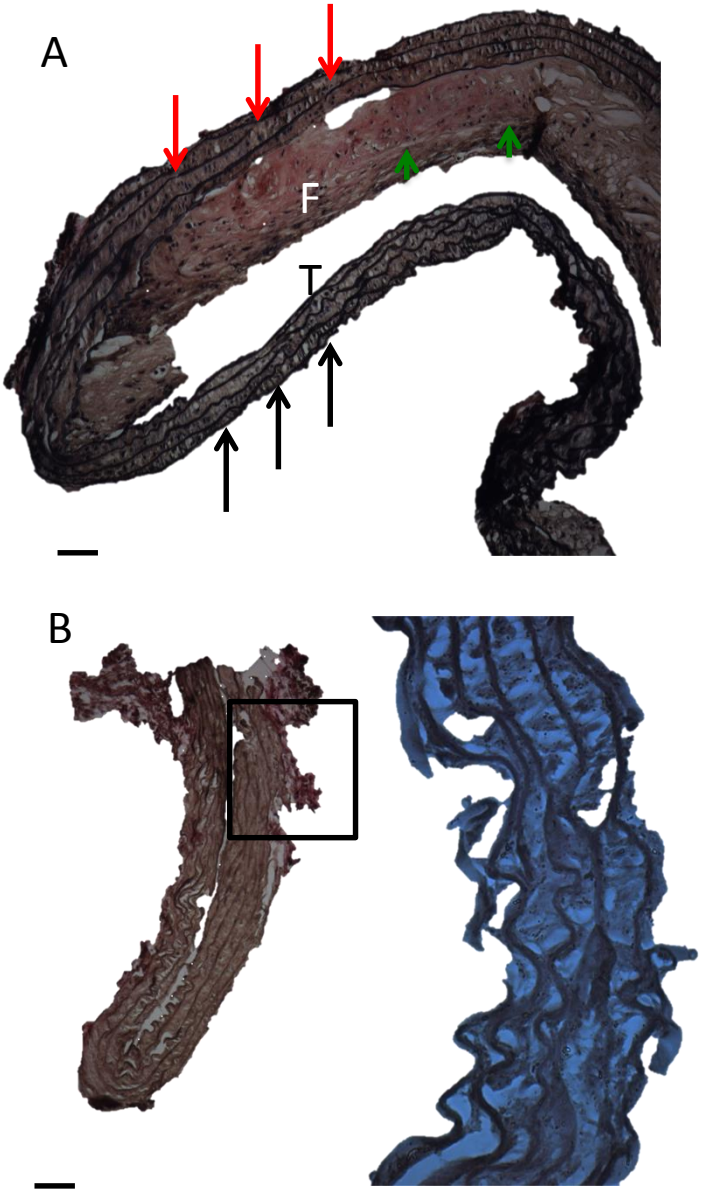

Fig 4.13 Verhoff van Geison stained aortic wall

A) Day 5, there is preserved segments of the aortic wall (black arrows) where the elastic lamellar structure is preserved in the tunica media. The opposing wall is thinner with increased breaks in the elastic lamellae (red arrows) and decreased elastin staining. There is an aortic dissection present with a true lumen (T) and a partially thrombosed false lumen (F). The green areas mark the intimal flap (20x) B) Day 33, aortic aneurysm with marked loss of elastin staining with multiple breaks in the lamellar structure. (Scale bar 50µm)

4.5 Discussion

The mouse model of aortic aneurysms was highly reproducible with (>70%) aneurysm induction and a mortality rate of 20% caused by aortic dissection or rupture. The aneurysms generated were similar in structure and composition to the human aneurysms. The natural history of aneurysm development was analysed with longitudinal serial CT scanning of the aorta. This allowed us to determine the mean growth rate, maximal aortic diameter and volume with time. This was subsequently compared to metabolic uptake using ^{18}F-FDG. By day 10 over 50% of the animals have aortic aneurysms and the maximal aortic diameter reached was 5 times normal aortic diameter. The growth rates were non linear and varied widely as in humans. The mean growth rate in the suprarenal segment was 26µm/day. There was however no correlation between aortic aneurysm diameter or growth rate to aortic wall metabolic activity (SUV_{max}). The ^{18}F-FDG uptake was focal at certain sites within the aortic wall at any one time point. It varied from site to site over the course of serially imaging the animal to different sites within the aneurysm. It was thus heterogeneous and varied widely within an animal and from animal to animal. Although there was an overall trend to increased individual ROI SUV_{max} readings at later time-points there was no statistical significance between the SUV_{max} readings obtained from day 10 onwards till the termination of the experiment where the majority of the animals had large advanced aneurysms. The ^{18}F-FDG uptake was higher in the aneurysm wall compared to normal aorta at all time points.

The focal aortic wall tracer uptake is a novel finding in the murine model as there are few previous studies to have used ^{18}F-FDG in this model to assess aneurysm formation[136,281,282]. We confirmed in our murine studies that there are spurts of highly heterogeneous increased ^{18}F-FDG uptake that occur whilst the aneurysms grow and expansion. This is in contrast with some human studies, which have shown an inverse trend between ^{18}F-FDG uptake and human aneurysm expansion[281-283].

The murine model allows investigation of the aneurysm through the stages of initiation, propagation and expansion, as well as the development of complications. It allows comparison of aneurysm size to aortic wall biochemical activity. It is, however, unlikely that the animal model of aortic aneurysms truly replicates the conditions that lead to aneurysm development in humans. The ApoE$^{-/-}$ATII aneurysm develops over the course of 3-6weeks, while in man the natural history of the disease is usually over many years to decades [10,22,279,340,358]. Other models use mechanical injury, direct enzymatic wall destruction and photochemical injury to generate aortic aneurysms [358,359] and have their own limitations. This the murine ApoE$^{-/-}$ATII model provides the most physiologically and pathologically related model to assess human aortic wall behaviour. The immune cell infiltrates that are identified in the human and murine aortic wall are very similar in relation to metabolic uptake as assessed by flow cytometry including subtype analysis of the precise lymphocyte populations. The histomorphometric location of the immune cells was also identical in the aortic wall in the model and human aortic wall, along with the changes seen in the pattern of ECM degeneration.

When we analysed the biological correlate of the ^{18}F-FDG uptake in the aortic wall, it was clear that immune cells present at the sites of highest metabolic activity had a different cellular signature when compared to sites of moderate or low activity. Analysis of these immune infiltrates in the mouse model reveals that the proportion of B and T-cells accounting for the total immune cell content of aorta is greater in 5-10-fold greater in aneurysmal wall with the highest metabolic uptake compared with wall from low uptake regions. Normal aorta had very low levels if non existent population of inflammatory cells. This is a finding that is recapitulated from our human data. In the aortic aneurysm with no metabolic activity there is a preponderance CD4$^+$ T helper and CD8$^+$ cytotoxic populations. These are virtually absent at sites of high metabolic activity with a clonal shift to mature activated CD7$^+$CD38$^+$ T-cells and the rarer population of CD25$^+$CD127$^+$FoxP3$^+$ T regulatory cells. Mature activated Th17 lineage of CD4$^+$ cells is typically responsible for proinflammatory cytokine

signal and classic inflammatory aortic wall degradation[360-367]. IL-17A produced by activated T-cells is a marker of Th17 lineage and induced Th17 $CD4^+$ activated T-cells are responsible for tissue destruction. The large number of the activated T-cells seen might be involved in immune mediated vascular inflammation and an autoimmune component of aneurysm development[364-366]. αβTCR+CD4+ T-cells are the best investigate source of IL-17A, other cell populations such as γδTCR+ cells, NK and NKT-cells also produce IL-17[364,365]. In vitro studies have previously shown that combination of cytokines produced by the activated T-cells including IL-1, IL-6 and TGFβ in mice and humans[361,366,367]. At the same time as the activated T-cell populations $CD4^+$ $CD7^+$ $CD38^+$, the subset signal is from the T regulatory cells. These have not been previously recognised to be present in the aortic aneurysm wall. $FoxP3^+$ T regulatory cells are known to be a major modulator of immune regulation and homeostasis by immunosuppressive function. The have opposing action to the activated T-cell subtypes from which they clonally arise[368]. IL-17$FoxP3^+$ cells resemble the IL17 cells but under complex cytokine signaling and simulation have pleiotropic functions including positive and negative gene transcription[368]. T regulatory cells have suppressive function that dampens the immune response[368]. The T regulatory populations in-vitro can inhibit the activated T-cell phenotypes thus providing a mechanism of self-regulation and self-tolerance[369-370]. We sought to differentiate between the $CD127^{high}$ vs. $CD127^{low}$ as this is a negative Treg marker for IL-7 receptor. $CD25^+$ expressed by $CD4^+FoXP3^+$Tregs is a marker for functional Tregs. The aortic wall resident population would be *induced* Tregs (iTregs). These upregulate in the periphery following antigen exposure and stimulation by TGFβ[359]. These cells can alter gene transcription and perform numerous epigenetic modifications to alter overall T and B-cell function[372,373].

This immune inhibitory role could be through contact dependent cell surface receptor inhibition, competition for finite growth factors with the metabolically active $CD4^+CD25^+$ populations, hydrolysis of the extracellular nucleotides (CD39, CD73) and specific induction of apoptosis or zymogenic secretion[374,37563]. The iTeg populations can in specific niche microenvironments

skew the complete expression profile of T effector cells. This transcriptional regulation permits homing to a specific inflammatory mediator. The transcription factors such as T-bet, Irf3, STAT3 modulate the iTeg suppression of Th1, Th2 and Th17 mediated inflammation[372-373].

Importantly, there was also evidence of B-cell activation and production of IgM. These B-cell(s) are responsible for B-T interaction and chemotactic attraction of cytotoxic T-cells and NK cells to the tissues they are resident in [376-378]. This phenotype might also confer a memory B-cell phenotype that might be resident in the aortic wall after an antigenic trigger. The immunoglobulin's production and IgM hexamer formation might affect VSMC synthetic activity and therefore influence ECM production. Tissue resident B-cell populations can be similar to T-cells very heterogeneous and constantly changing phenotype. The B-cells expressing $CD19^{+}CD27^{+}$ constitute memory B-cells. This is a population of cells with an extremely long life span, which when stimulated are primed for rapid response on repeated exposure to the antigen. These cells are normally resident in the lymphoreticular system or the bone marrow. They have a high affinity for surface immunoglobulins and this enables their activation by lower levels of cognate antigen compared to the naïve B-cells. $CD24^{+}CD38^{+}IgM^{high}$ cell population could represent an extremely differentiated Bregulatory cell population. This would depend on the cytokine signal given by the cells as Bregs would produce IL-10 and TGFß as pose inhibitory function in immune modulation[378,380]. There might be an additional population of Breg cells that are phenotyped as $CD24^{hi}CD27^{+}$ that is related to memory B-cells[381]. This population has however never been previously described in the aortic wall. The accurate characterisation of the B-cell populations is difficult as there are numerous shared cell surface and transcription markers[381]. The role in the aortic tissue could be pathogenic if the cells are producing antibodies leading to targeted tissue damage[382]. However the autoantibodies that are made may have a protective role in the protection of the aortic wall by removing apoptotic cells and decrease autoantigens that have been produced locally in the microenvironment[383]. B-cell populations can act as antigen presenting cells

leading to activation and amplification of the naïve and activated $CD4^+$ T-cells[372-374]. There is increasing evidence that the B-cells can modulate a B effector 1 response with the T-cell interactions and lead to either Th1 associated proinflmmatory cytokines to be expressed including TNFα, IFNγ and IL12. Conversely B effector 2 responses would be responsible for Th2 activation with production of IL-4 and IL-13[377]. However B-cells that illicit IL10 or TFGß might lead to immunological inhibition of inflammation. The two Breg subsets can produce IL10 that suppresses the production of Th1 cells (IFNγ and TNF-α)[378,379]. It has also been shown that the longer the contact time between $CD4^+CD25^+$ cells and the IL-10 producing B-cells, the T-cell responses are altered[380]. Also IL4 and IL12 production by B-cells has been shown to alter the balances between Th1 and Th2 cellular responses[381-383].

Breg populations are shown to interact with iTreg populations when treated with CD40 to effectively induce $CD4^+CD25^+FoxP3^+$ cells and suppress the cytotoxic $CD4^+CD25^-$ T-cells[389]. This might explain the lymphocyte population subsets in the metabolically active aortic wall. Other authors have also shown that CD40L stimulation of the lymphocytes induces a $CD19^+CD24^{hi}CD38^{hi}$ B-cell population that inturn suppresses Th1 differentiation, implicating CD40 in Breg activation mechanisms[390-391]. As well as Th1/Th2 responses the Breg population modulates FoxP3 and IL-17 Th populations and thus Tregs[392-395]. Bregs have recently been shown to decrease pulmonary inflammation by modulating Treg responses[396]. Also IL-10 producing B-cell deficient murine model has increased activation of the Th1/Th17 pro inflammatory cells and decreased levels of Th17 and Treg populations[390,397]. There is likely complex interaction between the B and T-cell sub-populations that constantly modifies and modulates responses in the aortic wall microenvironment. There are always competing populations of cells that are homeostatically balancing pro and anti-inflammatory activities.

We aim to further study, characterize and elucidate the B-T cell interactions that are responsible for the VSCMC modulation, ECM degradation and aortic wall function. These influences are important in not only understanding the

pathophysiology of aneurysm generation but might provide future targeted therapeutic targets. For instance, the pro-inflammatory state is known to be responsible for activation of the JNK pathway in the VSMCs with down stream phosphorylation to p-JNK[114]. Inhibition of c-Jun N-terminal kinase has been shown to cause regression of AAA in murine models[399,400].

Further studies in this thesis will focus on determining the possible role of the lymphocytic infiltrate in the areas of high tracer uptake in the aortic wall. The final aim being to delineate the downstream signaling pathway responsible for the highly metabolically active cell infiltrates in the aortic wall.

Chapter 5: Magnetic resonance imaging (MRI) of novel elastin peptide uptake in mouse model

5.1 Introduction

Elastin is an abundant ECM component of the aortic wall and its degradation through inflammatory processes is thought to be involved in the pathogenesis of various cardiovascular diseases including aortic aneurysm and atherosclerosis[88,401-405]. The process of elastogenesis is complex, involving an orchestration of a number of proteins, with VSMCs as the key regulators. Elastin deposition occurs early during embryogenesis and the process is nearly complete by postnatal life[204,406-408]. Elastin is a stable protein with a low turnover rate. Its concentration remains predominantly unchanged in adult life, which makes it an attractive molecule to target in longitudinal imaging studies[409,410].

Increased expression of elastin is however seen during atherosclerotic plaque development[399,400] and this has resulted in its use as target for imaging plaques by MRI. Plaque burden can be characterised on the basis of the different elastic fiber ratios[256].

MRI represents an attractive investigative tool, as it is non-invasive (no radiation exposure) and allows delineation of soft tissue detail in high resolution. It enables detection of subclinical disease and arterial remodelling[412]. Numerous studies have used MRI to determine aortic wall dimensions and wall thickness, most using black blood sequences[414-414]. Long-term and recurrent imaging has been affected by long scan times even if slice gaps are present in the imaging protocol[414]. 'Molecular' or 'functional' MRI is a technique that allows the detection and quantification of specific targeted probes with high resolution in the aortic wall. The recently used novel gadolinium based elastin specific magnetic resonance contrast-agent (ESMA) is

an example of this[268,269,417]. This agent is currently only available for use as a research tool and we sought to investigate the biological correlates of the of ESMA tracer uptake in ApoE$^{-/-}$ATII murine model of aortic aneurysms.

5.2 Aims

1) To characterise the temporal uptake of EMSA using the ApoE$^{-/-}$ATII infusion model to characterize the natural history of aneurysm progression.

2) Determine the association between aneurysm growth rate, aortic diameter and risk of rupture and ESMA in aortic wall.

3) To characterize the cell populations resident in the aortic wall at sites of high and low ESMA uptake by flow cytometry and immunohistology.

5.3 Methods

5.3.1 Murine ApoE$^{-/-}$ATII infusion model of aortic aneurysms

This was as described in section 4.3.1 on page 146.

5.3.2 Magnetic resonance imaging of murine aortic aneurysm

5.3.2.1 *In-vivo* MRI protocol at 3T

In vivo MR imaging of aneurysms was carried out using a 3T Philips Achieva MR scanner (Philips Healthcare, Best, The Netherlands) equipped with a clinical gradient system (30mT m^{-1}, 200mT/m/ms) and a single–loop surface coil (diameter = 47 mm). Anesthesia was induced with 5% and maintained with 1 - 2% isoflurane during the MRI experiments. Mice were imaged in prone position at 5, 9, 12, 19, 26 and 33 after angiotensin II infusion. Following a 3D GRE scout scan, arterial and venous time of flight angiography (TOF) as follows: arterial TOF with TR=40ms, TE=6.2ms, flip angle=60º, FOV=20x33x17mm, acquired matrix=68x110, slice thickness=0.6mm, resolution=0.3x0.3mm, reconstructed resolution = 0.1x0.1mm, slice number=50, averages=2, duration=7.5min and venous TOF with TR=50s, TE=6.2ms, flip angle=60º, FOV=20x33x17mm, acquired matrix=68x110, slice thickness=0.3mm, resolution=0.3x0.3, reconstructed resolution=0.13x0.13mm, slices=50, averages=2, duration=9min. The maximum intensity projection images were used to visualize the abdominal aorta, the renal and iliac bifurcations (Fig 5.0). These images were used for planning of the subsequent magnetization transfer, diffusion weighted, and delayed-enhancement scans.

A 2D-Look-Locker sequence planned perpendicular to the ascending aorta, was used to determine the optimal inversion time (TI) for blood signal nulling. Acquisition parameters were: TR=19, TE=8.2ms, FOV=30x30mm, acquired matrix=76x75, slice thickness=2mm, resolution=0.39x0.40, reconstructed resolution=0.27x0.27mm, TR between subsequent IR pulses=1000ms, and flip angle=10°. Subsequently, an inversion-recovery-3D-fast-gradient echo sequence (IR) was acquired before and 2h post intravenous injection of the

elastin-targeted gadolinium contrast agent (8 µg/kg, tracer) and was used for DE-MRI and visualization of contrast uptake. Imaging parameters were: TR=28ms, TE=8.2ms, flip angle=30°, FOV=30x30x8mm, acquired matrix=304x304, slice thickness=0.5mm, resolution=0.1x0.1mm, reconstructed in-plane resolution=0.06x0.06mm, slices=32, averages=2. TR between subsequent IR pulses=1000ms. T1 mapping was performed using a sequence that employs two non-selective inversion pulses with inversion times ranging from 20ms to 2000ms, followed by 8 segmented readouts for 8 individual images. The two imaging trains result in a set of 16 images per slice with increasing inversion times. For T1 mapping the acquisition parameters were: TR=9.0, TE=4.6ms, flip angle=10°. FOV=36x22x10mm, acquired matrix=180x102, measured slice thickness=0.5mm, resolution=0.2x0.2, reconstructed in-plane resolution=0.1x0.1mm, slices=20, averages=1. A 3-dimensional T1 mapping sequence was acquired with two-inversion recovery prepared modified look-locker sequence. The sequence started with a non-selective inversion pulse using specific inversion times followed by eight segmental read outs for eight images. Inversion time (T1) is the time from preparation pulse to acquisition of the k0 profile in k space. Low-high k space ordering with 500ms delay between image acquisition was performed to minimise the saturation effects and allow accurate quantification of T1 values. The imaging planes were acquired at FOV = 18 x 36mm, matrix = 180 x 151, measured voxel size 0.2 x 0.2 x 0.5mm, TR/TE = 9.8/5.1ms, flip angle = 8° and acquisition window = 157ms. T1 values were computed pixel-wise with a three-parameter curve fitting procedure of the longitudinal magnetization Mz(TI) including a T1 correction [418].

$$Mz(TI) = M0^{*}- (M0+M0^{*})e-(TI((1/T1)-(1/TR)\ln(\cos \alpha)))$$

T1 then can be calculated as described previously in [417,418]

$$T1 = T1^{*} (((M0+M0^{*})/(M0^{*})) – 1)$$

M0 is the equilibrium of magnetization; this is sampled during the recovery, as

the recovery is affected by constant RF-pulses that leads to apparent relaxation time T1* (T1* < T1; RI=1/T1; 1/T1=T/T1+1/T1looklocker) and decreased equilibrium magnetization M0*.

5.3.2.2 Gadolinium bound elastin specific magnetic resonance agent (ESMA)

The ESMA agent (Lantheus Medical Imaging, North Billerica, Massachusetts) is a low-molecular-weight contrast agent (molecular mass, 855.95 Da)[262,419]. It is a D-phenylalanine linked to gadolinium diethylenetriamine pentaacetic acid (Gd-DTPA) chelate. This agent specifically binds to elastin and has a short half-life comparable to the current gadolinium based MR contrast tracers. The contrast uptake in the aortic wall in the setting of the atherosclerotic model shown to be specific and low in other areas such as heart, lungs and muscles with a rapid removal from the body[262]. Like all gadolinium-based agents, the contrast is metabolised and cleared by the kidneys, whilst the hepatic concentrations remain low. The agent is known to have a longitudinal relaxivity of 15.1 $mM^{-1}s^{-1}$ when imaged in rabbit aortic wall at 1.5T thus yielding a high target to background signal ratio. The vessel wall ESMA uptake has a favourable pharmacokinetic arterial wall profile making it suitable for aortic wall imaging[262].

In order to make sure that the signal arose from the specific ESMA rather than gadolinium scans were initially carried out using intravenously administered MAGNEVIST® (Gadopentetate dimeglumine, Bayer, UK). Injection is the N-methylglucamine salt of the gadolinium complex of diethylenetriamine pentaacetic acid (Fig 5.1). MAGNEVIST Injection contained a 0.5-mol/L solution of 1-deoxy-1-(methylamino)-D-glucitol dihydrogen [N,N-bis[2-[bis(carboxymethyl)amino]ethyl] glycinato (5-)] gadolinate(2-)(2:1) with a molecular weight of 938, an empirical formula of C28H54GdN5O20, and has the following structural formula:

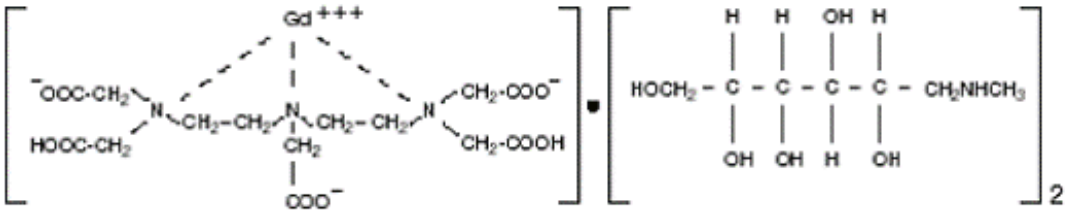

5.3.2.3 Image analysis of MRI scans

MR images were analyzed using Osirix (OsiriX Foundation, Geneva, Switzerland). MRI slices spanning through the region of blood obstruction, as seen on the TOF arterial- angiography, were used for the analysis. Regions of interest (ROI) encompassing the aneurysm were manually segmented on the images acquired without MT pre-pulse and then propagated on the images acquired with the MT-prepulse, and the diffusion weighting. The mean signal intensity (SI) and area (cm^2) of each ROI was recorded. Aortic aneurysm maps were generated based on formula using an Osirix plug-in for visualization of the areas protein-rich within the aneurysm. The same ROIs were used to calculate the apparent diffusion coefficient (ADC) based on the equation $ADC=\ln (S_0-S_1)/b_1-b_0$ (mm^2/s). T1 values were computed on a pixel-by-pixel basis using an in house Matlab software[420-422].

5.3.3 Histological analysis

Aneurysm cross-sectional area (mm^2) was measured on trichrome stained sections by computerized planimetry (ImageJ, NIH). Computer-assisted color image analysis was used to quantify the collagen area on trichrome stained sections and the positive areas for elastin on Verhoeff-Van Gieson and immunohistological sections, which were expressed as percentages of the total aneurysm cross sectional area.

For registration of the *in vivo* MR images and histological sections, the distance of the proximal end of each segment, the gross morphology, and internal aneurysmal landmarks visible on both the MR images and histology were used as references.

5.3.4 Isolation and staining of tissue resident inflammatory cells for analysis by flow cytometry

16 animals underwent MRI using the elastin peptide at 6 time points totaling 18 scans (day 5, 9, 12, 19, 26 and 33). 4 animals also underwent control MRI contrast scan using gadolinium based contrast medium. Murine aortic specimens underwent same enzymatic degradation and cell harvest protocol (Section 4.3.5, page 149).

Flow cytometry Murine aortic tissue from areas of no, low, moderate and high elastin peptide uptake was obtained at day 5, 9, 12, 19, 26 and 33 (n=12, 2 from each time point). Aortic samples were segmented according to anatomical location to ascending aorta including aortic arch, descending thoracic aorta, suprarenal abdominal aorta and infrarenal abdominal aorta. The aneurysmal segment was divided into segments depending on the degree of tracer uptake. The complete aneurysmal segment was excised and cut into anterior, posterior, lateral and medial aortic wall segments as per regional tracer uptake. Tissue underwent enzymatic degradation and cell harvest protocol as mentioned immediately post harvest. Inflammatory cell content of tissue resident cells was quantified using flow cytometry using antibodies and protocols described in section 4.3.5, page 148 and 4.3.6 page 149).

5.3.5 Tinctorial histology and immunohistochemistry

This was carried out as described in section 3.3.7, 3.3.8 and 4.3.8 pages 107, 109 and 153.

5.3.6 Statistical analysis

Data were presented as mean±standard deviation (SD), standard error or the mean (SEM) and analysed in SPSS v21 (IBM Corporation, Data Collection, USA). Parametric data were analysed using Student's Paired T-test. Correlations were carried out using linear regression with Pearson correlation coefficient analysis and represented as the R^2 value. Alpha was determined to be <0.05 for significance testing.

5.4 Results

There was no delineation of the aortic wall on gadolinium (gadopentetate dimeglumine; Magnevist®, Bayer, UK) only scan. The aortic wall and lumen could be clearly visualised in all animals with ESMA. The aortic diameter, aortic volume and aortic wall thickness was determined for each animal at each time point (Fig 5.0).

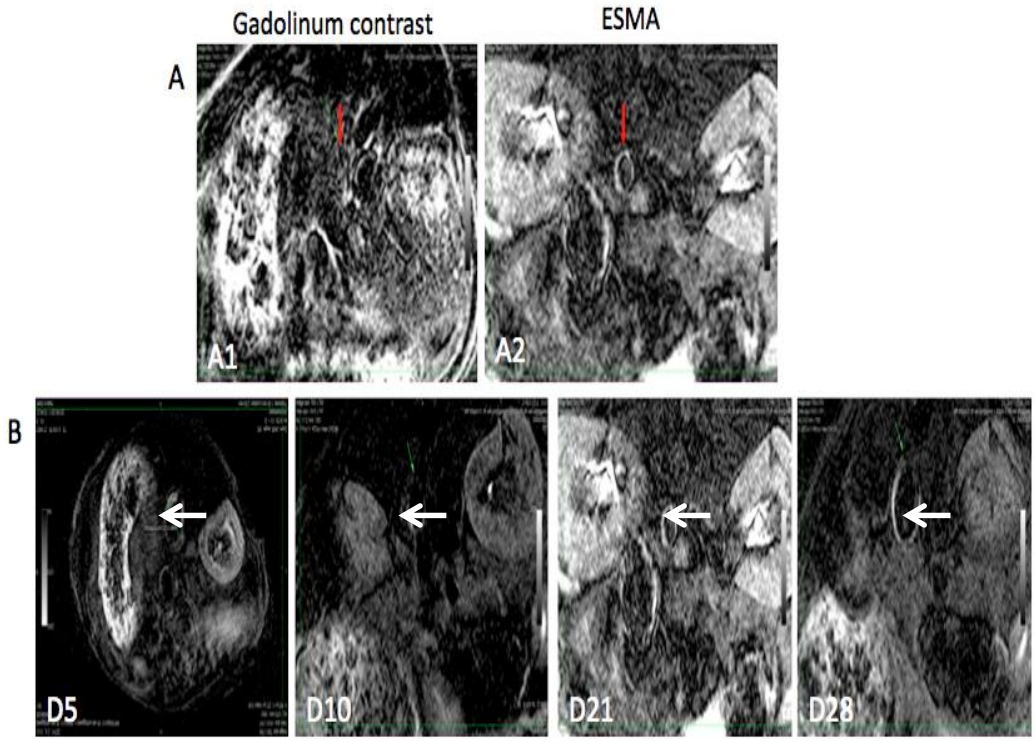

Fig 5.0 Comparison of MRA with MAGNAVIST® and ESMA

The aorta was not visible with MAGNAVIST (A1, red arrow), but is clearly visible with the suppression of the blood pool signal with ESMA (A2). The aortic diameter could be measured and the aortic dimensions followed longitudinally (days 5-33) with the aneurysm development (B). Along with the increase in aortic diameter the aortic wall thickness and therefore elastin content could be monitored.

5.4.1 Assessment of the aortic wall dimensions using ESMA

Imaging of aneurysms in ApoE$^{-/-}$-ATII infused animals was carried out at days 5, 9, 12, 19, 26 and 33 (n=24, Fig 5.0). Continuous infusion of ATII at 1000 ng/kg/min) resulted in the formation of typical aneurysms in ApoE$^{-/-}$ mice. The aneurysms were clearly visualised using MRA (Fig 5.0). This is the region known to generate aneurysms and is therefore the region that we performed the detailed scan, followed by the thoracic aorta in certain animals. In order to make sure that the signal arose from the specific ESMA rather than gadolinum we initially performed scans using IV MAGNEVIST® (Gadopentetate dimeglumine, Bayer, UK). Injection is the N-methylglucamine salt of the gadolinium complex of diethylenetriamine pentaacetic acid (Fig 5.1A).

On the magnetic resonance angiogram and TOF images high-resolution anatomical detail was visualized to see the renal, visceral vessels and the aortic termination. This allowed the correct supra renal segment for detailed MRI. (Fig 5.1) The transverse sections showing the aortic lumen on the angiogram allowed measurement of the maximal aortic diameter, aortic volume and determination of growth rates.

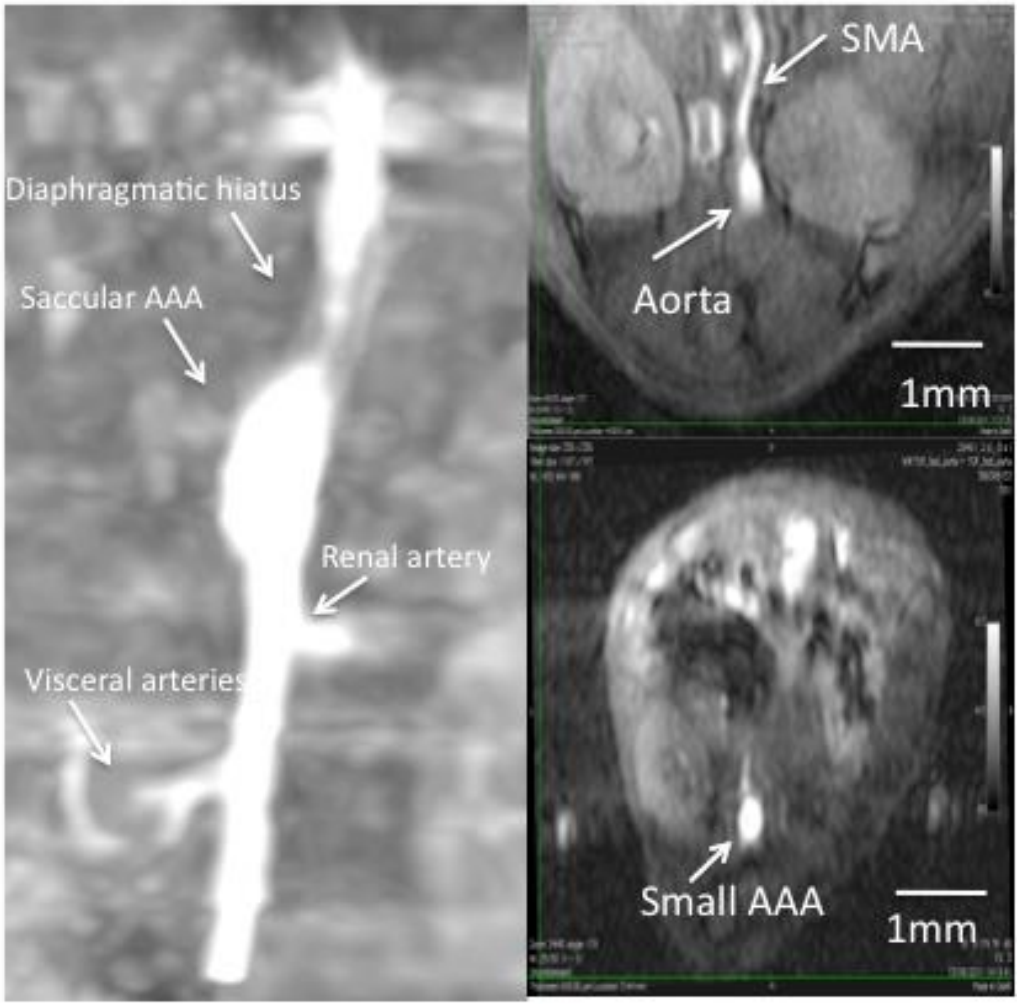

Fig 5.1 MRA of a suprarenal aortic aneurysm in a 5-day post ATII infused ApoE$^{-/-}$animal

The images were reconstructed using 3D MPR, MIP and volume rendered reconstructions created (Fig 5.2). Aortic diameter, volume, aneurysm morphology and aortic wall thickness were calculated.

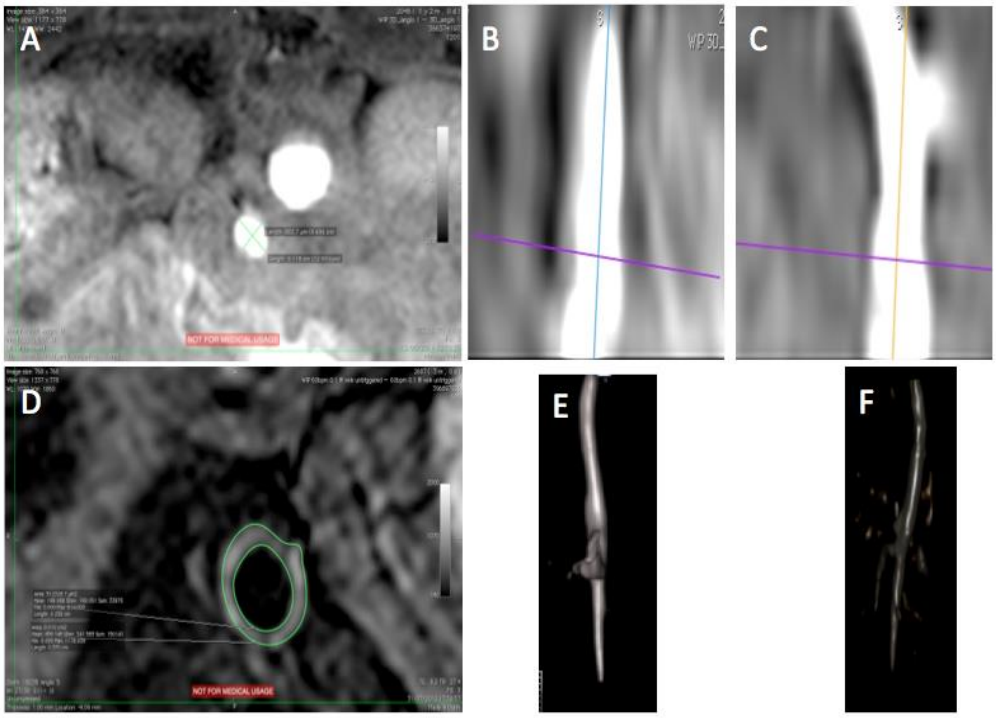

Fig 5.2 2-dimensional cross section imaging of the aorta, multi-planar reconstruction (MPR), minimal intensity projections (MIP) and 3-dimensional reconstructions

Transverse section through single slice aortic MRA sequence to visualise the maximal aortic luminal diameter (A). The MPR images (B) allowed sagittal and coronal reconstructions (C) of the aortic aneurysm for determination of aortic volume. The aortic wall could be delineated on the ESMA scan with suppression of the blood pool signal (D) and the level of aortic wall elastin tracer uptake in the aortic wall calculated as the area between the inner diameter and outer diameters drawn. The 3D volume rendered reconstructions that allowed the aortic morphology to be determined and differentiated between aneurysms (E, F).

5.4.2 *In vivo* detection of the aortic disruption sites and aortic repair processes

The quantification of the ESMA aortic wall uptake in normal aortic wall segments and aortic aneurysms was visualised using image fusion protocols that allowed addition of false colour per pixel value of the ESMA activity on magnified aortic aneurysm luminal views (Fig 5.3). This allowed visualisation of breaks in the aortic wall.

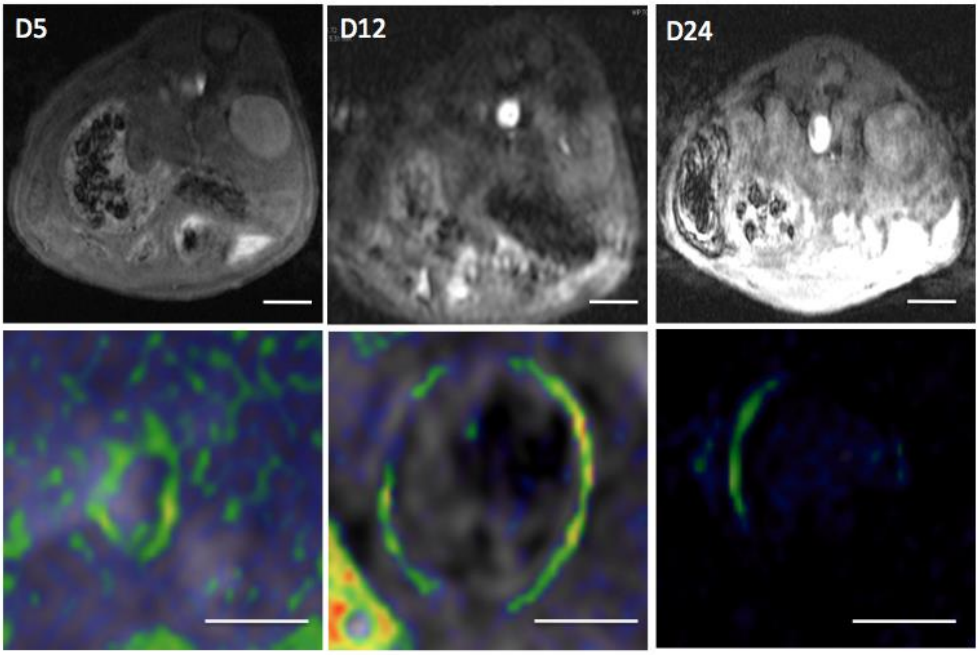

Fig 5.3 Determining maximal aortic diameter and vessel wall ESMA content

(A) Aortic luminal diameter expanding with time from day 5 through to a small aneurysm at day 12 and a large aneurysm at day 24 with increase in diameter by up to 5-fold. (B) The corresponding ESMA fusion images demonstrate a near uniform low-level uptake of the agent in the aortic wall at day 5. By day 12 when the aneurysm was present there was increased signal in different regions of the aortic wall, and increased numbers of breaks in ESMA uptake. These breaks increased in size and distribution so that by day 24 ESMA very low ESMA uptake was present (seen in the 9-11o'clock position). (Upper Scale bars 1mm, lower scale bar 250μm)

There was increased aortic wall remodelling as shown by increased EMSA uptake in the area proximal to aortic aneurysm development, with adventitial tissue remodelling clearly visualised in the proximal aneurysm sequences on the magnified transverse sections of the aorta (Fig 5.4). Increased aortic luminal expansion was seen the continuous AT II infused groups and a corresponding steady and significant increase in adventitial tissue remodelling in the regions proximal to the areas of luminal expansion on the ESMA image fusion sequences. As the maximal aortic diameter increased the ESMA uptake increased at certain sites in large aortic aneurysms. There was focal high ESMA activity surrounded by regions of the aortic wall with no ESMA uptake. We

compared the MR elastin content in the vessel wall to histologically assessed elastin and tropoelastin content in the aortic wall at all time points.

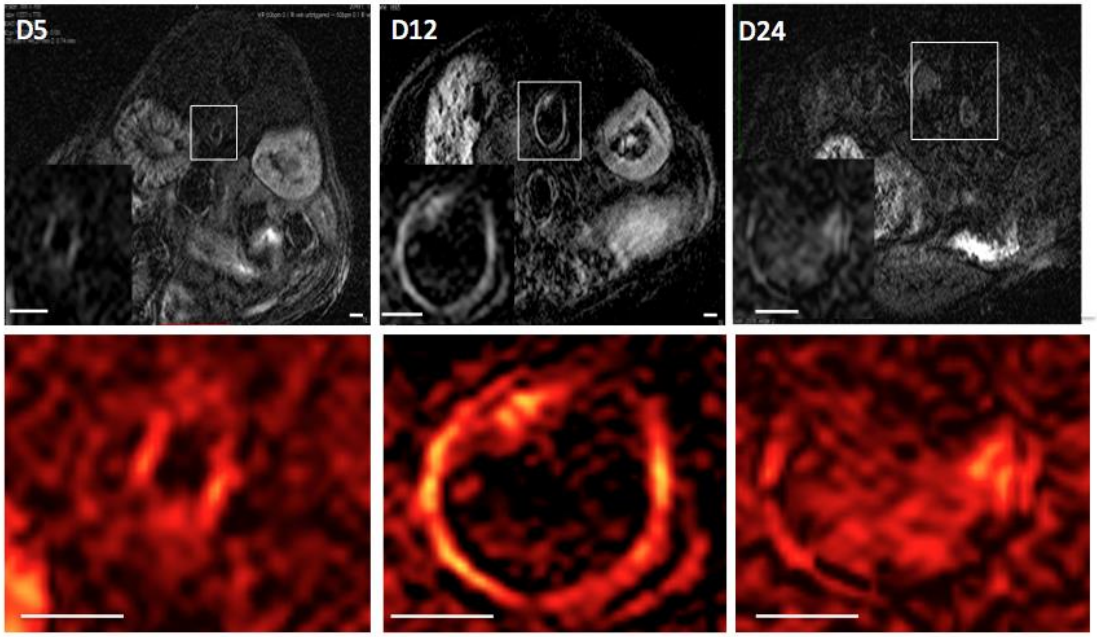

Fig 5.4 Determining the maximal aortic diameter, elastin breaks and ESMA up-regulation
A) T2 blood pool suppression ESMA images for the corresponding TOF angiogram sequences (given in Fig 5.3). The vessel wall ESMA content was visualised on the magnified non-colour enhanced sequences. B) The same transverse slices as shown in panel A, with enhancement on the false colour fusion reconstruction software that allows equal pixel voxel colour coding of ESMA uptake. Increasing deposition of elastin in the aortic wall with the increased aortic aneurysm diameter at day 12. This active aortic remodelling and increased ESMA signifies increased elastin and tropoelastin content in the aortic wall. By day 24 there was loss of ESMA aortic wall at certain sites signifying loss of elastin/tropoelastin. (Upper scale bars 1mm, lower scale bar 250µm**)**

The focal but heterogeneous nature of aortic aneurysm development was apparent on functional imaging. When the complete aortic aneurysm was analysed on slice-by-slice basis there was large aortic wall variation in the ESMA uptake seen from segment to segment as demonstrated in Fig 5.5. As the aortic aneurysm progresses the aortic wall ESMA uptake increases at certain sites. This is likely to represent active positive remodelling. The areas that have decreased ESMA uptake are likely to represent sites of active

inflammatory aortic wall degradation and decreased ECM content. This pattern on ESMA uptake fits the natural history of aortic aneurysm development with episodes of positive aortic remodelling (characterised with high ESMA uptake) followed by periods of quiescence and sites of no ESMA uptake signifying increased water content in the aortic wall (inflammatory immune cell infiltrate) and decreased elastin.

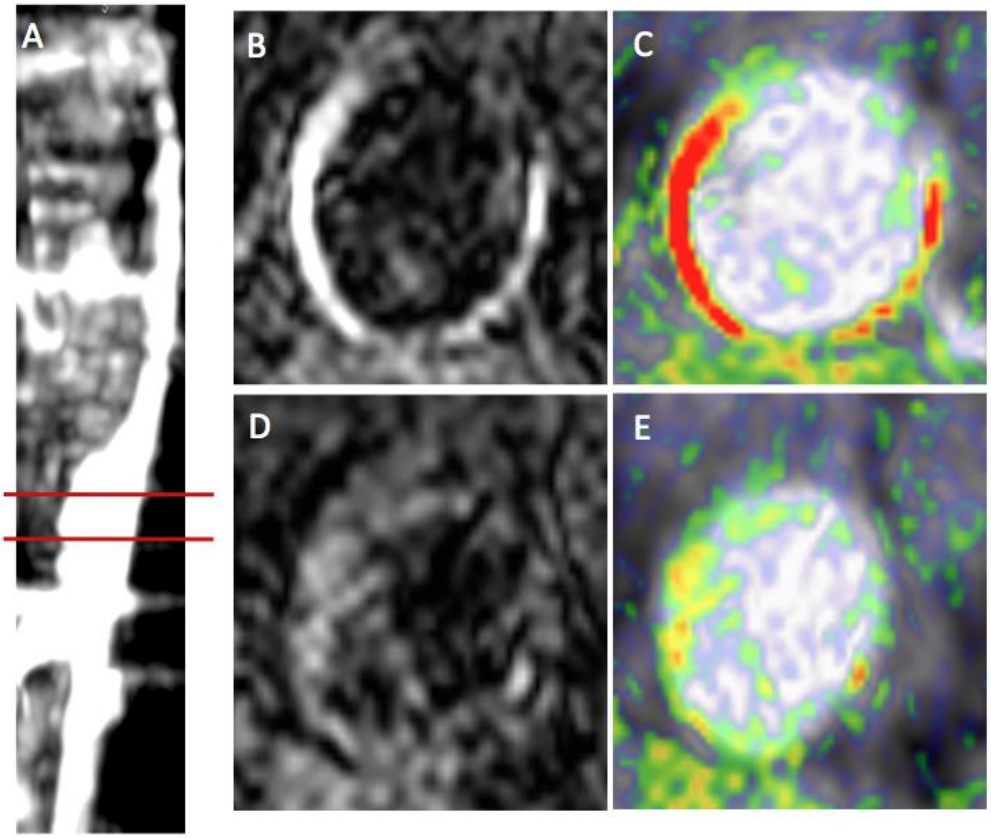

Fig 5.5 MRA demonstrating the heterogeneous nature of aortic wall ESMA content

A) TOF angiogram fly through of the aortic aneurysm. The red lines represent imaging plane of two different transverse planes atleast 50μm apart. B) The first transverse slice taken demonstrates high specific aortic wall ESMA uptake on the blood pool suppressed sequences. 86% of the aortic wall surface area is seen on the transverse section. C) The image fusions sequence with the angiogram now allows determination of the aortic diameter and the aortic wall thickness and elastin content. D) The transverse slice taken shows a similarly dilated aortic wall but at this level there is decreased aortic wall ESMA content at this level in the aortic aneurysm. E) The corresponding fusion ESMA sequences with the angiographic views show little or no ESMA in the aortic wall of the aortic aneurysm. 23% of the aortic wall contains ESMA tracer in this slice.

5.4.3 Aortic aneurysm diameter, ESMA content and T1 mapping

The increase in aortic diameter is noted with time across the ApoE$^{-/-}$ATII aneurysm on the MRA. After administration of ESMA, a gradual increase in R1 values was measured in the aortic wall starting from week one to four of ATII infusion (Fig 5.6-5.8). The temporal association in T1 and R1 values were in agreement with the quantification of elastin and tropoelastin in the aortic wall sections (Fig 5.6-5.8).

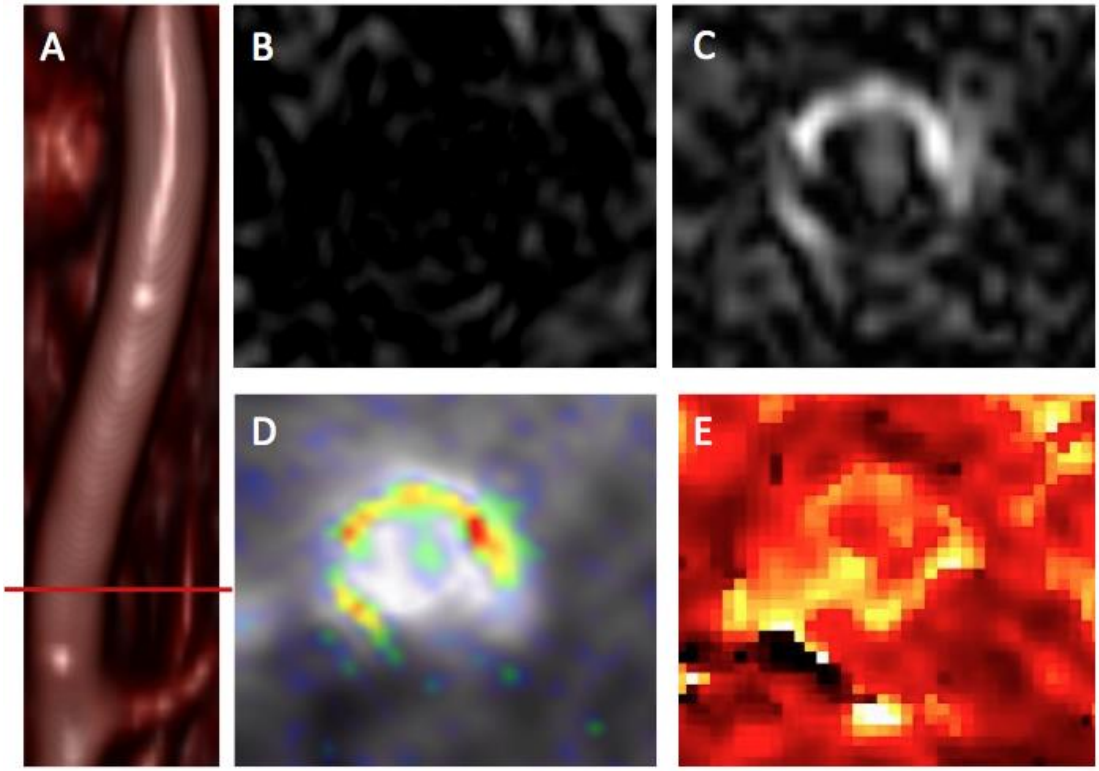

Fig 5.6 Aortic aneurysm assessment using ESMA MRA

A) The aortic diameter is not increased at day 5 imaging with a baseline level of 162±33μm in the supra renal aortic segment. The red line represents a typical single transverse slice taken at that specific level for the purposes of illustration B) Transverse aortic wall segment taken on pre-contrast imaging before the Gd-ESMA tracer is given. The aortic wall is not visualised. C) 60mins post IV injection of the Gd-ESMA tracer, the aortic wall is clearly seen with near uniform uptake of the ESMA specifically in the aorta. There is no luminal blood pool signal that is suppressed and minimal signal to noise artifacts. D) The ESMA fusion sequence where the blood pool suppression T2 image is overlaid onto the TOF angiogram to allow determination of the aortic wall luminal diameter and the ESMA uptake in the aortic wall. E) The corresponding T1 map of the transverse aortic slice that allows numeric quantification of the ESMA uptake in the aorta.

Using ESMA along with increased maximal aortic diameter we can image the aortic wall ECM (elastin and tropoelastin) composition, content and the presence of acute immune cell infiltrate in the aortic wall (sites where there is no ESMA signal). The calculation of the T1 values allows numeric quantification of the relaxivity and this can be correlated to the aortic wall ECM. Certain aneurysms loose the aortic wall ESMA signal at an earlier rate with multiple breaks in the aortic wall and this correlates to histological changes in the matrix content (elastin and tropoelastin) in the aortic wall. (Fig 5.7-5.8)

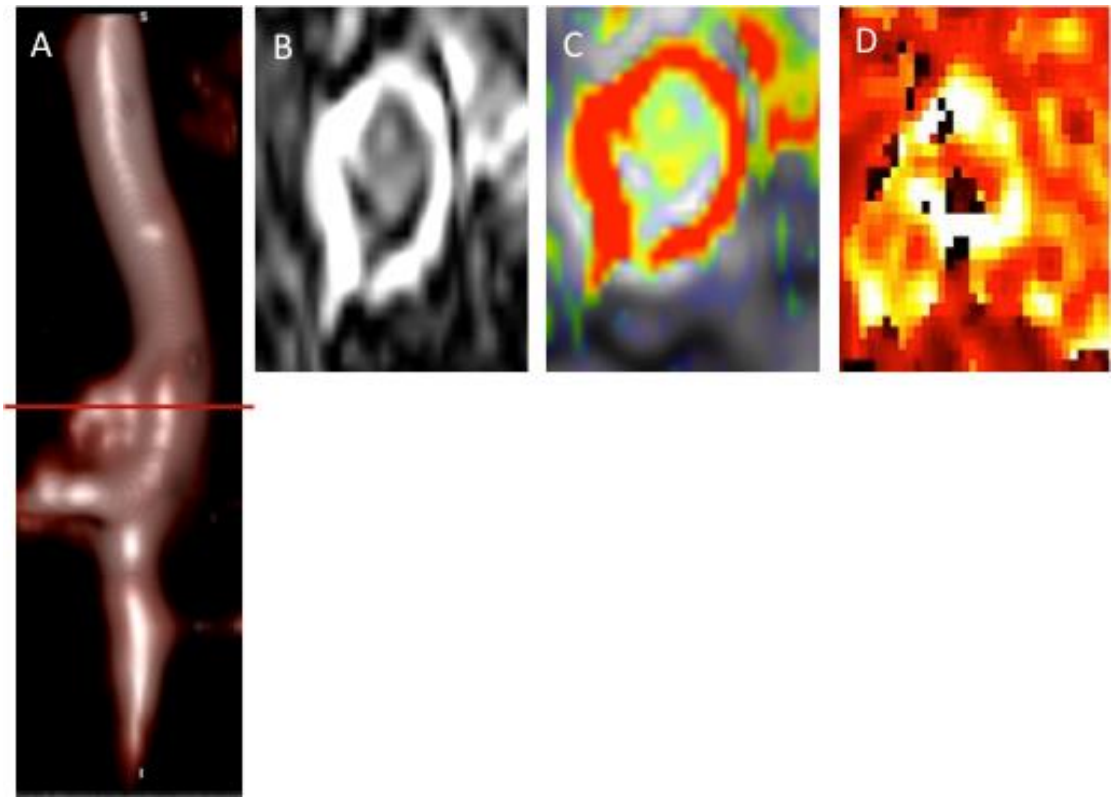

Fig 5.7 *In vivo* assessments of aortic disruption sites with aortic dilatation in a day 24 aortic aneurysm

A) Three dimensional MR angiogram volume rendered reconstruction of the murine aorta from the taken at day 24. The red line represents an example of transverse slice taken for analysis through the middle of the aneurysm. B) This demonstrated the aortic wall delineated using ESMA and near uniform high level of ESMA in the aorta. There is a small site at 6 o'clock position where there is a break in the ESMA uptake C) Axial fusion image of the contrast angiogram demonstrating the presence of ESMA in the same position suggesting an aortic break with likely decreased elastin/ tropoelastin content at a single site on that slice. D) Measurement of T1 relaxation times of the aortic wall to determine the quantification of the ESMA uptake.

In some cases (n=6) aortic disruptions of ESMA uptake were seen prior to dilation of the aorta.

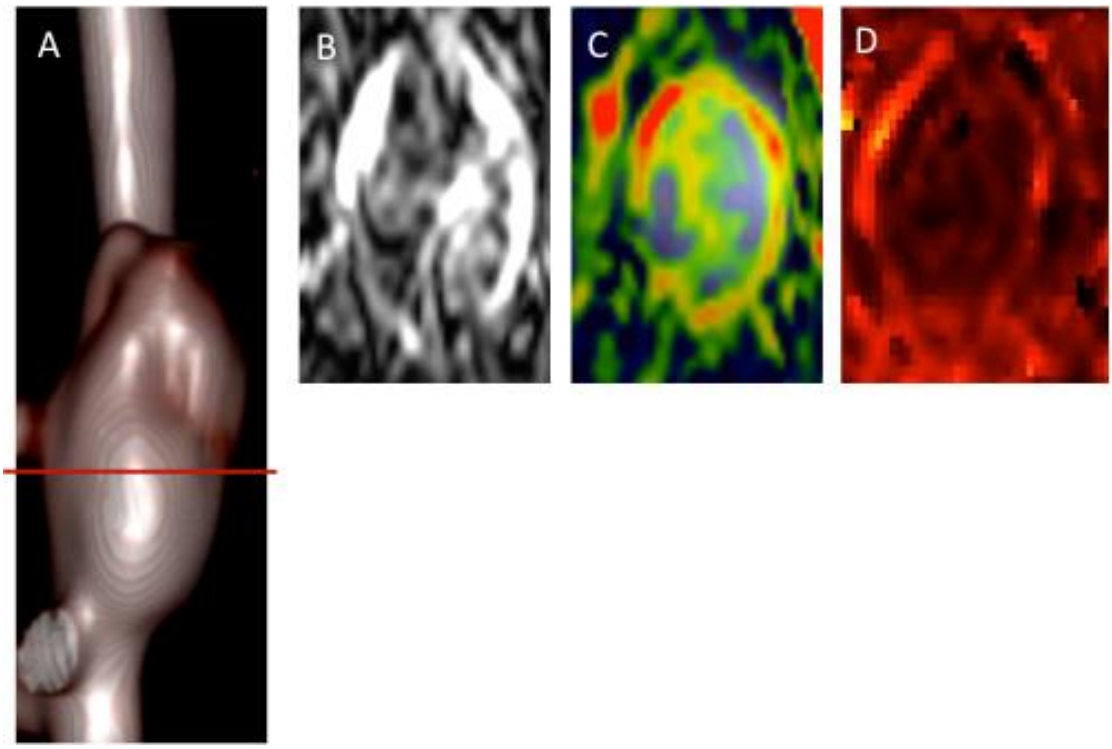

Fig 5.8 In vivo assessments of aortic disruption sites with aortic dilatation in a day 33 aortic aneurysm

A) Three dimensional magnetic resonance angiogram volume rendered reconstruction of the murine aorta from the control group taken at day 33. The red line represents an example of transverse slice taken for analysis through the middle of the aneurysm. B) Transverse section taken through the aortic wall using ESMA showed a decrease in the aortic wall tracer content from 6 o'clock to 9 o'clock position with a further break at the 12 o'clock site. C) Axial fusion image of the contrast angiogram demonstrating the presence of ESMA in the same position suggesting multiple areas of aortic breaks with likely decreased elastin/ tropoelastin content at a the 6 o'clock to 9 o'clock position. D) Measurement of T1 relaxation times of the aortic wall to determine the quantification of the ESMA uptake.

Aortic aneurysm propagation and maturation therefore depend on a continuous homeostatic balance between ECM degradation and formation, with tropoelastin synthesis and elastin fibre organisation being the key regulatory steps in maintaining aortic wall stability. Histologically there is increased elastin expression in the periadventitial regions of the aortic wall in

correlation with ESMA uptake whereas at sites where there is no ESMA present there is marked loss of EvG elastin staining (Fig 5.9).

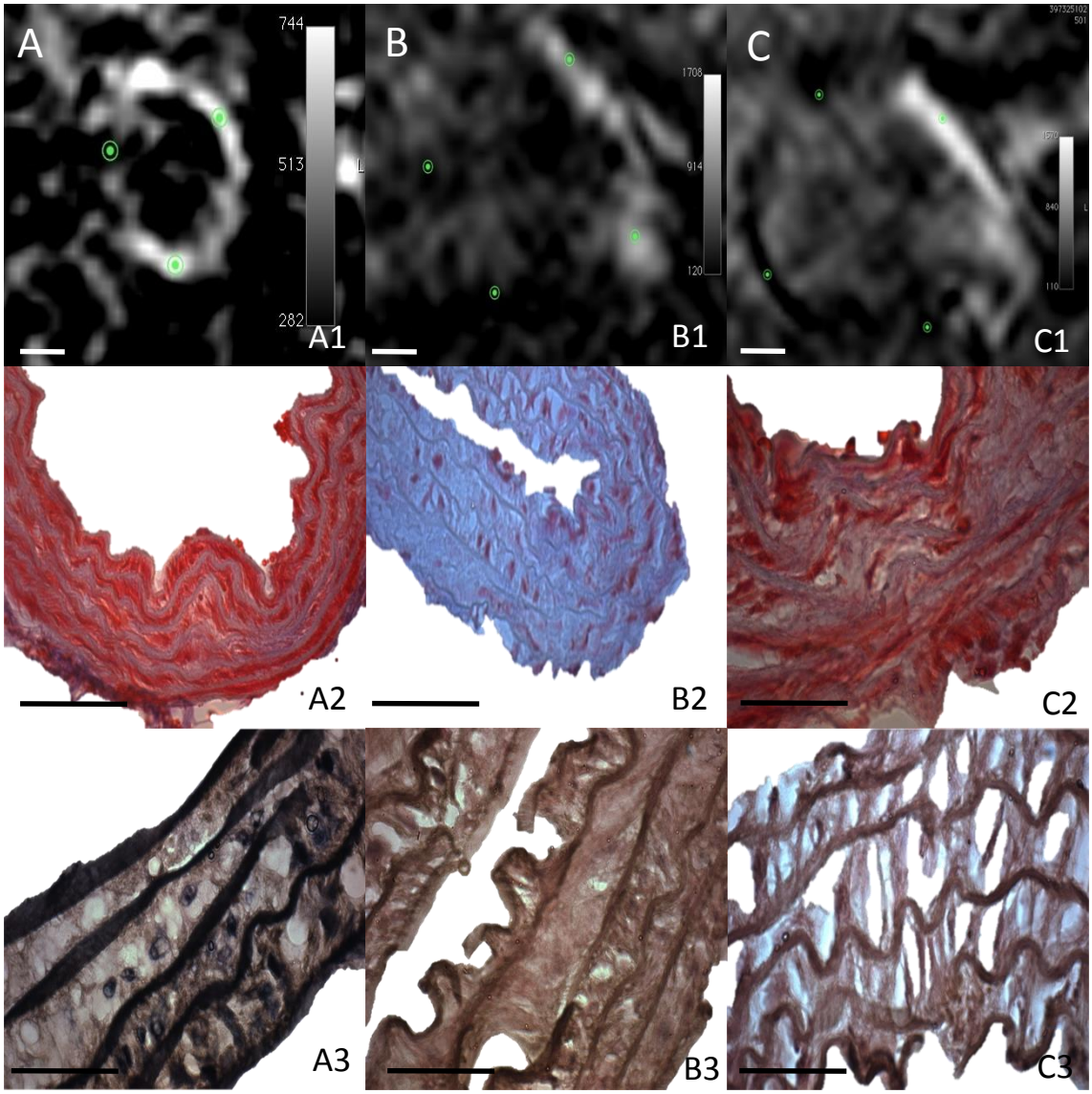

Fig 5.9 Histomorphometric assessment of the aortic wall on Gd-ESMA MRA and its correlation to elastin and collagen content

A) The Gd-ESMA uptake in the aortic wall at day 5 (A1). Collagen content (Masson's Trichrome) (A2). There was high vessel wall collagen content in sections taken from the aortic wall at day 5. The vessel wall elastin content was analysed from sites of high ESMA uptake and high EvG staining (A3) was seen with organised elastic lamellar structure. B) On analysis of the aortic wall at sites of moderate ESMA staining at day 12 (B1) there was reduced collagen staining (B2) and decreased EvG staining with loss of the lamellar structure (B3) C) Aortic wall analysis from larger aneurysms with no ESMA uptake in the aortic wall at day 24 showed increased collagen uptake (C2) and little elastin content on EvG staining. There was loss of elastic lamellar structure, increased breaks in the elastin lining and fragmentation of the aortic wall with vacuolation and disorganised haphazard matrix. (Upper scale bar 250µm, histology scale bars 50µm, 40x magnification).

5.4.4 Comparison of *in vivo* and *ex vivo* aortic aneurysm wall ESMA, elastin and tropoelastin content

The histomorphometric assessment of the aortic wall showed that after day 12 there was progressive maturation of aneurysm with increased elastic fibres *in* and *ex vivo*. The active aortic remodelling response to aneurysm generation adjacent to the lumen is likely to represent compensatory mechanism to enable stabilisation of the aortic wall. This process could be visualized and quantified both *in vivo* on ESMA-MRI and *ex vivo* on corresponding histological sections. At late stages of aortic aneurysm development there is either a very strong signal at extremely specific sites or a complete loss of the signal. It is likely that this will be the site of the aorta that will be the site of rupture or dissection.

There was a significant positive correlation between EMSA uptake and elastin content of the vessel wall as measured by histology. On aortic wall imaging prior to administration of ESMA (pre-contrast) and after administration of ESMA (post-contrast) the R1 values from T1 maps in the aortic wall in all mice was observed (Fig. 5.10). After administration of ESMA, a gradual increase in R1 was measured in the aortic wall. The trends R1 were in agreement with quantification of elastin on histological sections (Fig. 5.10). To exclude contrast effects resulting from Gd-DTPA in the second imaging session, additional pre-contrast scans were performed in 2 mice on day 5 and 9. No significant difference ($P>0.05$) in vessel wall enhancement was measured between pre-contrast scans on day 5 and 9 and pre-contrast scans previously.

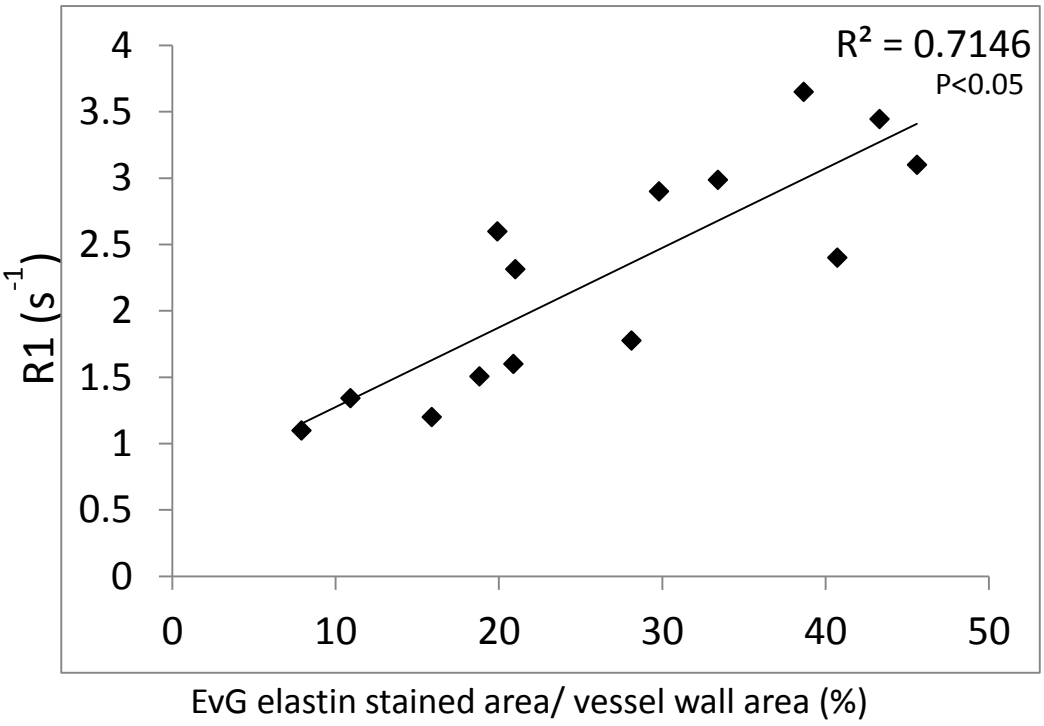

Fig 5.10 The relationship between EMSA uptake and elastin content in the aneurysmal wall on EvG staining

Respective average R1 values derived from T1 maps after ESMA administration and correlation with EvG-stained histological sections.

The percentage area *ex vivo* when assessed using tropoelastin specific antibody staining for aortic wall tropoelastin content that increased with the aneurysms increasing diameter on *in vivo* imaging (P<0.05). There was a strong positive correlation of the R1 values (ESMA uptake) and the corresponding vessel wall tropoelastin content. R^2=0.78, P<0.05 correlation coefficient (Fig 5.11).

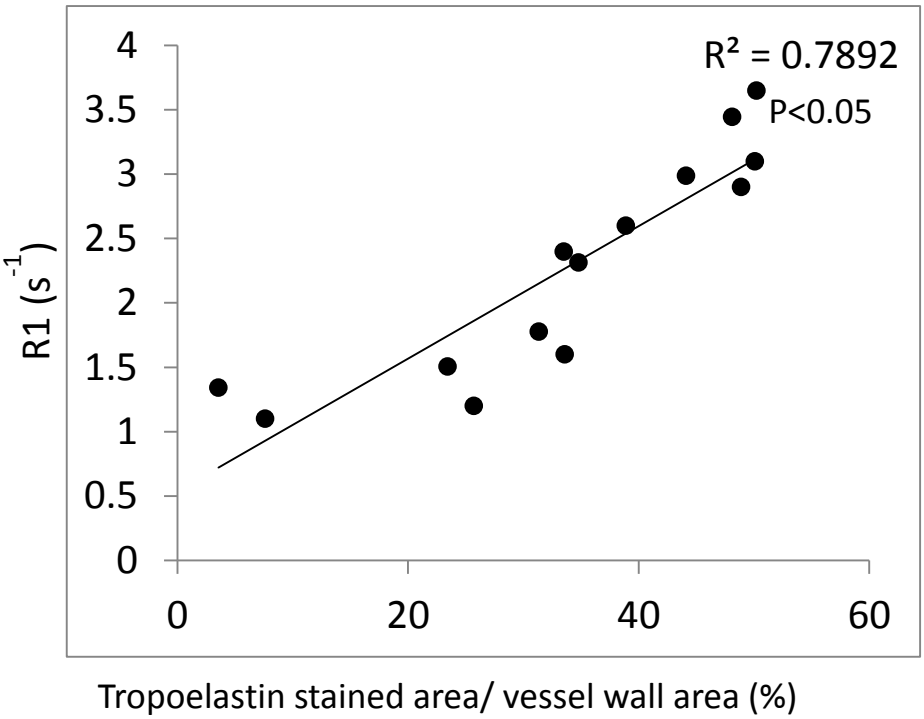

Fig 5.11 The relationship between EMSA uptake and tropoelastin content in the aneurysmal wall on IHC staining

Respective average R1 values derived from T1 maps after ESMA administration and correlation with tropoelastin-stained area on histological sections.

5.4.5 Immunohistochemical assessment of the aortic wall immune cell content in aortic aneurysms with varying ESMA uptake

Immune cell content was assessed from sites of aortic aneurysm wall that had ESMA uptake *vs.* sites of no ESMA uptake. When stained for $CD3^+$ T-cells, $CD19^+$ B-cells, $NCAM1^+$ NK cells and Mac-2^+ macrophages there was increased uptake suggesting immune cell infiltration in the aortic wall at the tunica media and tunica adventitial boarder in the periadventitial vascular zone. Similarly there was expression of immune cells in the tunica media at sites of no ESMA uptake. The immune cell infiltration seems to arise from the vasa vasora from the outside of the vessel wall and move in. The cells were morphologically typical of lymphocytes and macrophages along with staining for the specific antibodies (Fig 5.12).

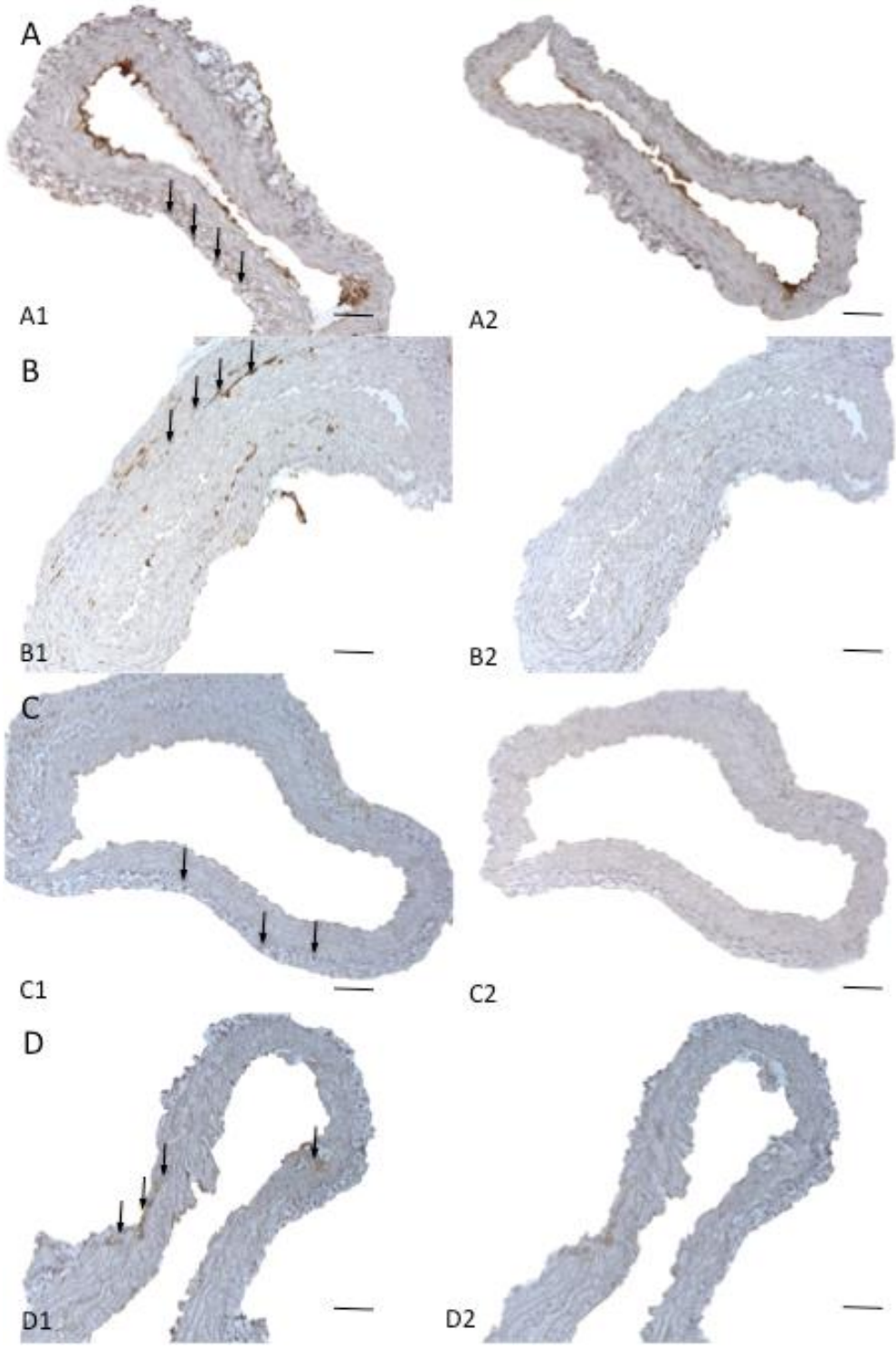

Fig 5.12 Aortic wall immunohistochemical analysis from sites of no ESMA uptake

A) On staining for $CD3^+$ T lymphocytes (A1) there is cell infiltration in the aortic adventitia (DAB+ brown cells, black arrows). Negative control (A2) B) On $CD19^+$ B-cell staining there are B lymphocytes in the aortic adventitia (brown cells, black arrows) infiltrating into the tunica media. (B2) Negative controls. C) NK cells, NCAM1 (brown cells, black arrows) (C1) staining in the aortic wall adventitia. Negative control staining (C2). D) Macrophage (Mac2) staining in the aortic wall (DAB^+ brown cells, black arrows). Negative staining (D2). (Scale bars 50µm).

When IHC analysis was similarly carried out at various sites in the aortic wall when there was a clear signal from the ESMA in the complete section of the aorta, there were occasional immune cells. Almost all immune cell markers tested for were negative apart from the presence of B-cells (Fig 5.13).

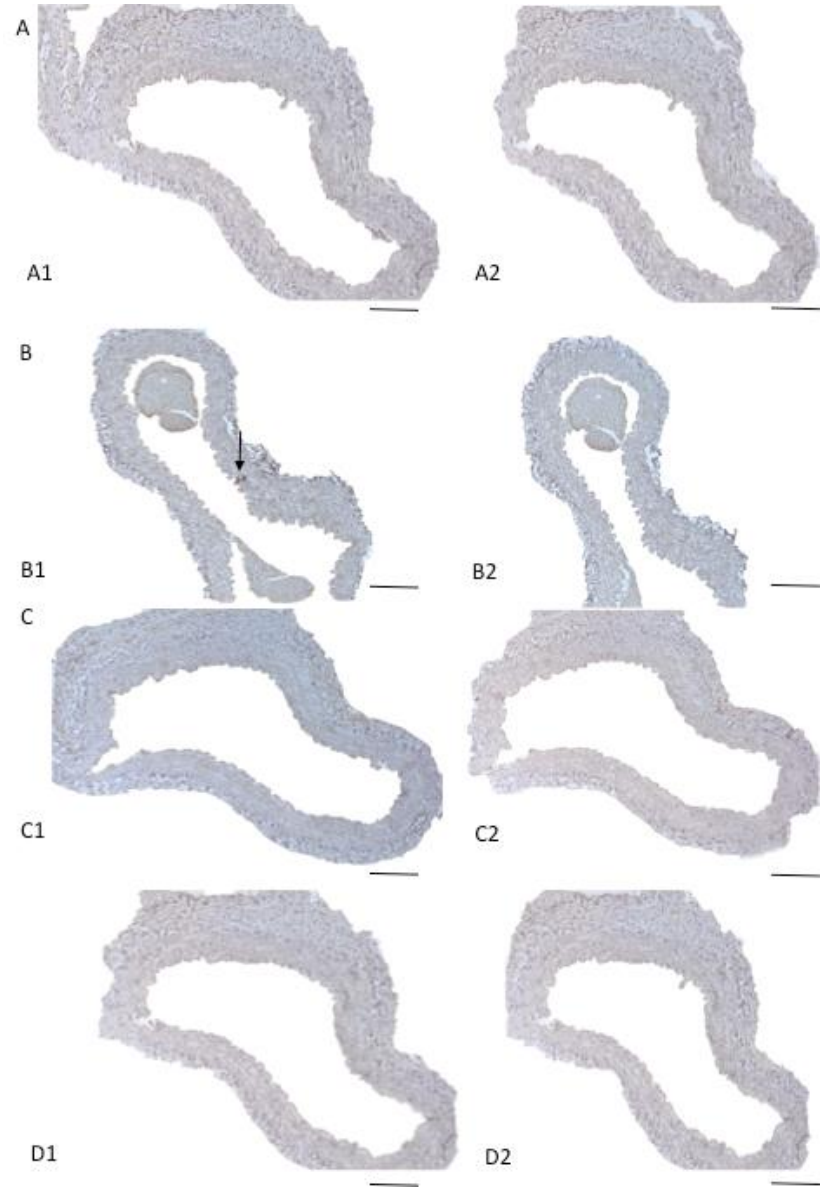

Fig 5.13 Aortic wall immunohistochemical analysis from sites of ESMA uptake

A) On staining for $CD3^+$ T lymphocytes (A1) there are no cells seen (A2) Negative control B) On $CD19^+$ B-cell staining there are occasional B-cells in the aortic adventitia (brown cells, black arrow) infiltrating into the tunica media. (B2) Negative control. C) NK cells, NCAM1 (C1) no staining in the aortic wall media or adventitia. (C2) Negative control staining. D) Macrophage (Mac2) no staining in the aortic wall. (D2) Negative staining. (Scale bars 50μm).

On semi-quantitative analysis there is an increase in the T, B, NK and Macrophage number in relation to the absence of the ESMA signal in the aortic wall (Fig 5.14).

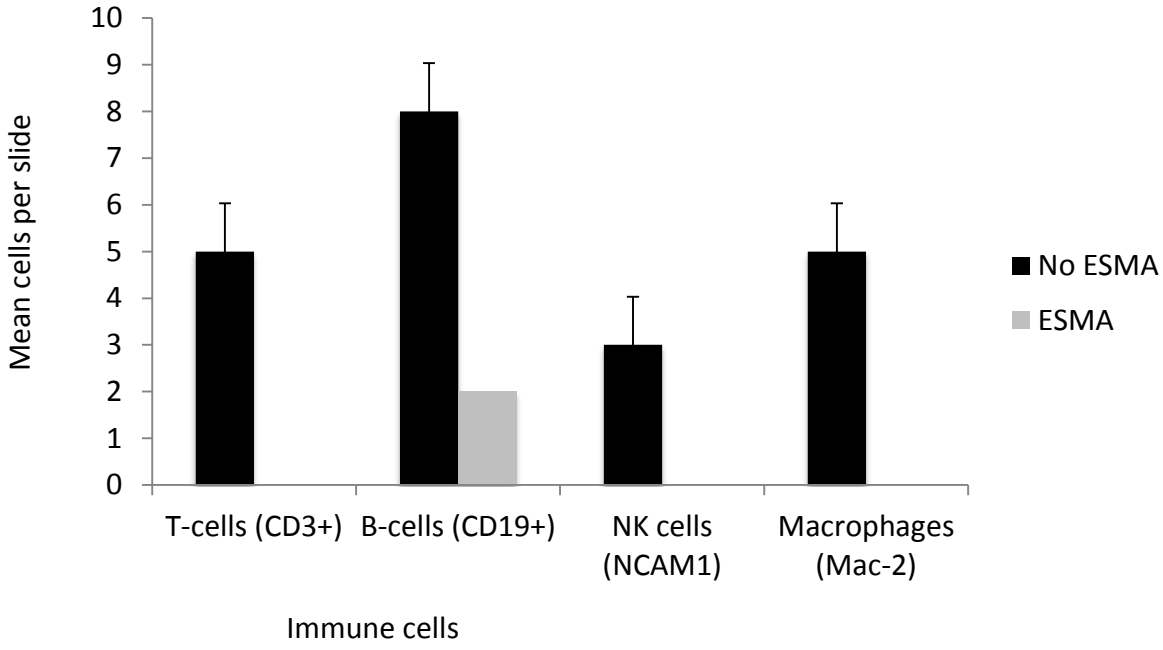

Fig 5.14 IHC quantification of immune cells

The immune cell quantification on immunohistochemistry dependent on EMSA uptake in aortic aneurysms. There is an immune cell infiltration in aneurysm wall when there is no ESMA uptake (P<0.001, paired T-test for all cell types comparing no ESMA to ESMA uptake)

5.4.6 Flow cytometric assessment of the aortic wall and aneurysm immune cell content at sites of high *vs.* no ESMA uptake

The immune cell content was quantified in all samples from high and no ESMA uptake (Fig 5.15). Aortic tissue from sites of varying elastin uptake was quantified according to T1 relaxation times. Cellular content was quantified per microgram of tissue. At regional aortic wall sites in the absence of the ESMA uptake there was an increased number of B-cells (63.8±13.0, P<0.001, 95%CI0.54-0.66) and T-cells (82±9.8, P<0.001, 95%CI0.24-0.64) *versus* sites of ESMA binding where there was a low expression for B-cell (19.4±14.1, P<0.001, 95%CI0.54-0.78) and T-cell (57.8±8.9, P<0.001, 95%CI0.64-0.73). The number of NK cells, was not significantly altered across the two sites. There was an inverse correlation for the macrophage lineage of cells that were statistically

significantly higher in the ESMA uptake group compared to the no ESMA uptake group (93.8±4.8 *vs.* 81.7±4.0, P<0.01, 95%CI0.2-1.2) (Fig 5.15, 5.17, 5.18).

When normal aortic wall was compared to ectatic or aneurysm wall, there was minimal immune cell activity in the aortic wall with 10.3-14.4% of the total cell fraction being $CD45^+$. This was in marked contrast to aneurysmal aorta which typically had >50% $CD45^+$ cell fraction and these predominantly were of T and B-cell linkage, smaller proportion of NK cells and macrophages (Fig 5.16-5.17).

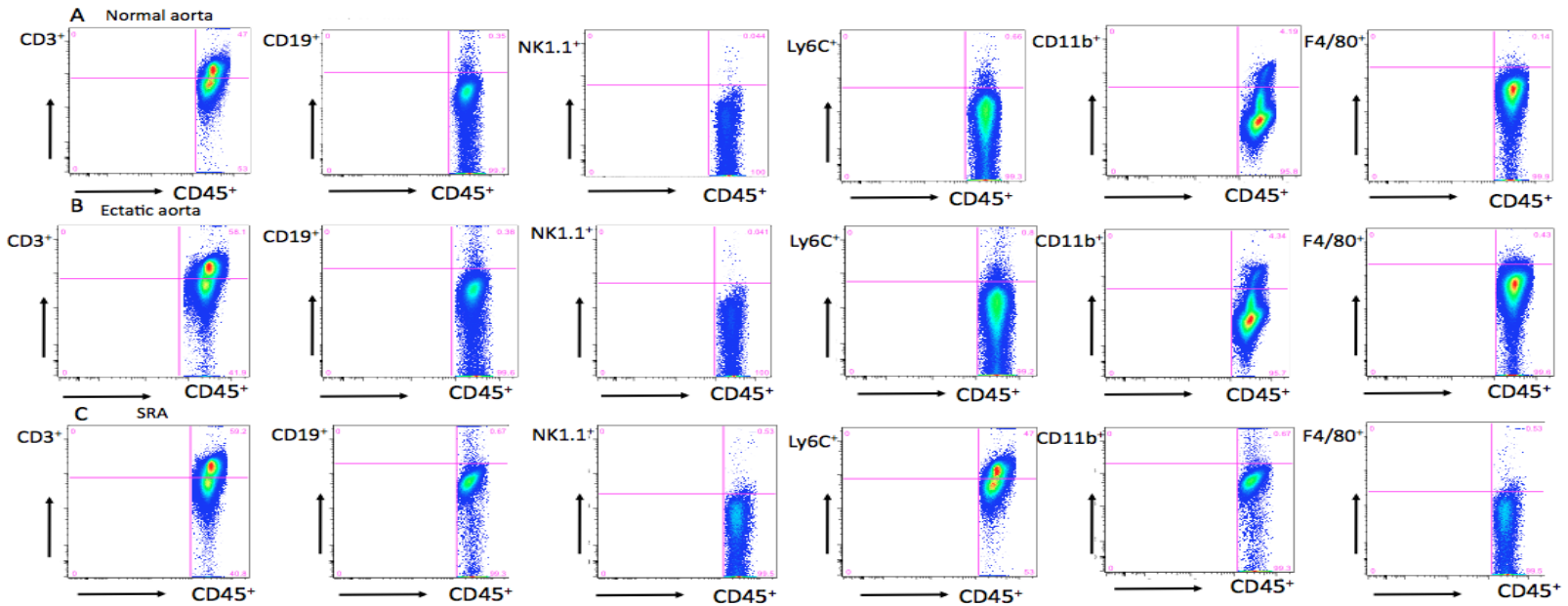

Fig 5.15 Representative flow cytometric assessment of the normal, ectatic aorta and aneurysmal aortic wall for immune cell content

A) Aortic wall was segmented into either normal aorta typically the thoracic aortic segment or infra-renal aortic segment and analysed here at day 24 where there was a markedly low expression of B, T lymphocytes and NK cells. The proportion of macrophages and neutrophils was exceptionally low B) Ectatic suprarenal aorta was defined as an increase in diameter to 1.5x normal diameter and this occurred at typically day 5-12. This suprarenal aortic wall followed an intermediate phenotype with increasing degrees of lymphocyte and NK cell infiltration in the aortic wall. C) Supra renal aortic segment taken at day 24 post ATII infusion when the aorta is over twice the normal starting diameter, typically over 5x normal aortic diameter. As the severity of the aortic aneurysm increases there is increased vessel wall immune cell infiltration in the aortic wall characterised by T, B-lymphocytes, NK cells and macrophages.

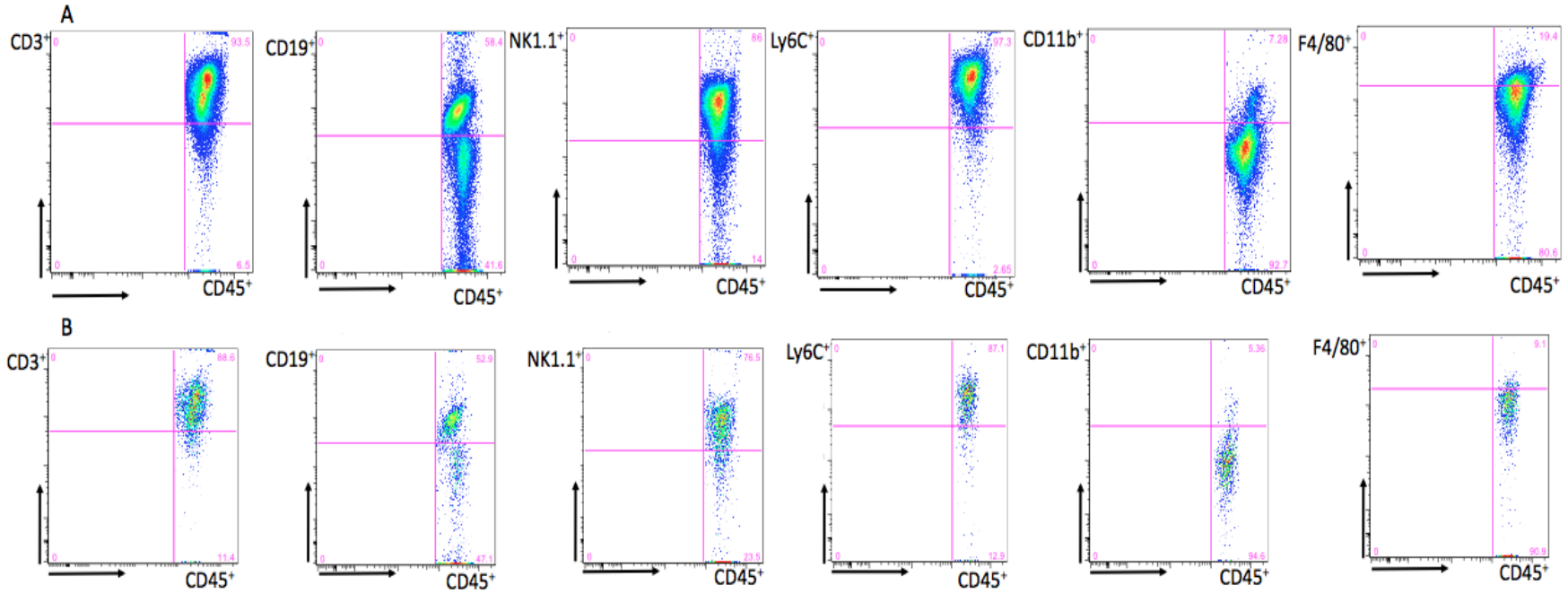

Fig 5.16 Representative flow cytometric assessment of the aortic wall immune cell content in aneurysms with and without ESMA uptake

Aortic aneurysm was segmented into A) without ESMA uptake B) with ESMA uptake. There was marked difference in the immune cell content of the aortic wall. Increased immune cell content was present typified by B ($CD19^+$) and T ($CD3^+$) lymphocytes, NK cells (NK 1.1) and macrophages (Mac-2) at sites of no ESMA uptake compared to sites of ESMA uptake.

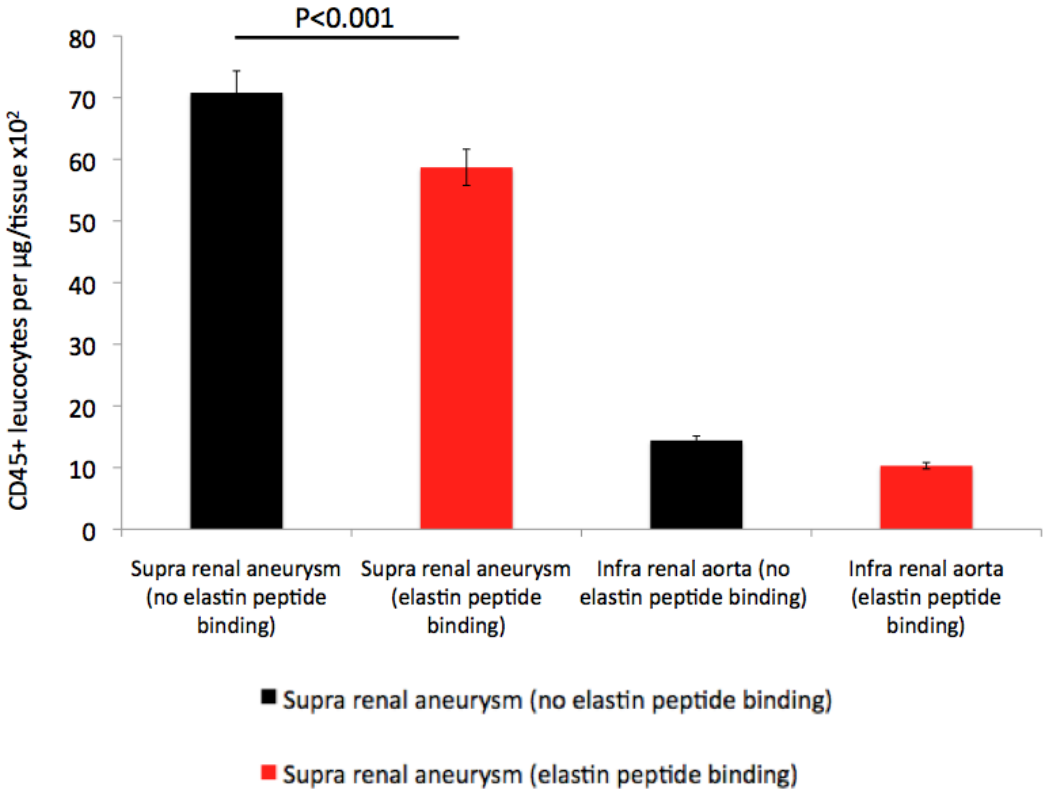

Fig 5.17 Flow cytometric aortic wall analysis from suprarenal aortic aneurysms with and without ESMA uptake

The SRA sites without ESMA uptake had higher total leukocyte content compared to SRA with ESMA uptake (P<0.001). There was no difference in the normal aortic leukocyte content ($CD45^+$) expression with overall low level of immune cells present in the aortic wall. (N=16, 48 aortic segments with 2-way ANOVA P<0.001 and post hoc Bonferroni correction as above).

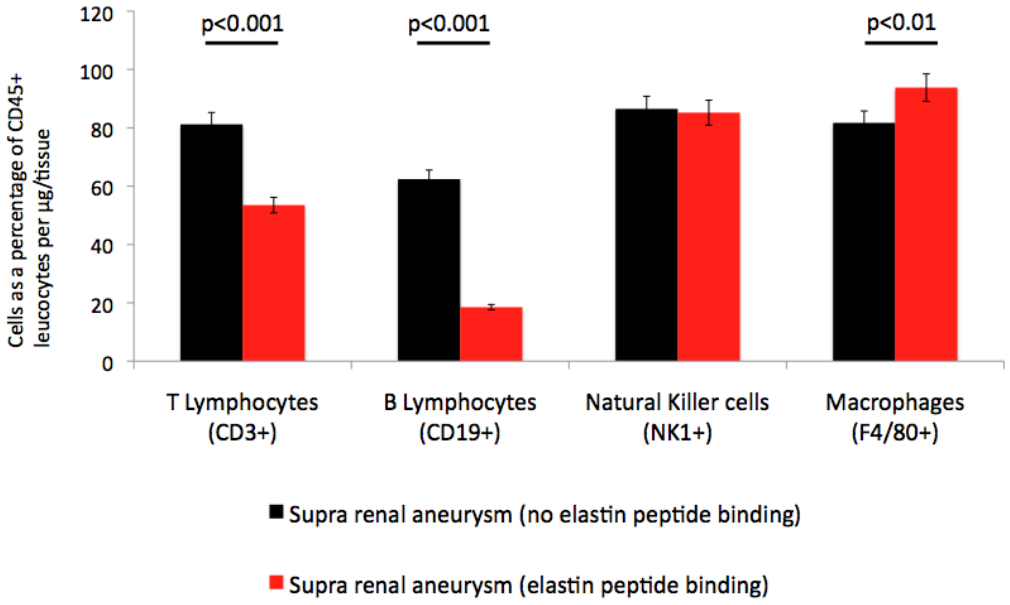

Fig 5.18 Flow cytometric analysis of suprarenal aortic aneurysm with immunophenotyping

When the $CD45^+$ fraction is analysed according to SRA ESMA uptake, sites of low ESMA uptake had higher T-cells ($CD3^+$), B-cells ($CD19^+$), ($P<0.001$) and macrophages ($F4/80^+$) had an inverse pattern ($P<0.01$). There was no difference in the NK cell-staining pattern (N=16, 48 aortic segments with 2-way ANOVA $P<0.01$ and post hoc Bonferroni correction as above).

5.5 Discussion

Our MRI studies have shown specific uptake of a gadolinium bound elastin tracer in aortic wall in the murine model of aortic aneurysm. This elastin tracer uptake was focal but heterogeneous in the aortic wall and occurred at sites with the highest concentration of elastin and tropoelastin. There were increasing breaks in the ESMA uptake in the aortic wall associated with an increase in diameter of the aorta and at sites preceding the aneurysm expansion. Flow cytometric analysis of the aortic wall confirmed a high immune cell infiltrate in the regions that had no ESMA. This was typified by $CD45^+$ leucocytes that are predominantly B-cells ($CD19^+$), T lymphocytes ($CD3^+$) and NK cells ($NK1.1^+$). Macrophages ($F4/80^+$) were conversely more likely to be present at sites of higher ESMA activity. This immune cell expression pattern was confirmed on immunohistochemial staining for the specific cell marks with the immune cell infiltrate localised to the tunica adventitia and tunica media. Specifically histological assessment of the extracellular components including elastin, tropoelastin and collagen demonstrated a highly significant correlation between elastin and tropoelastin content and the aortic wall ESMA uptake (calculated with the expression of the R1 value). At specific aortic wall segmentation from regional areas with and without ESMA uptake demonstrated a decrease in the aortic wall elastin and tropoelastin content at sites of no ESMA uptake. There was however increased tropoelastin turnover seen at other sites as aneurysms progressed.

It is likely that the functional imaging with ESMA is delineating two processes ongoing in the aortic wall. At sites of no ESMA uptake the aortic wall is undergoing inflammatory cell infiltration and decrease in the ECM in the vessel wall. This is followed by expansion and reparative phases where there is an attempt to stabilise the aortic wall. This is demonstrated by the ESMA signal in aneurysm wall. It is clear that the aetiology of the signal is the ESMA binding to elastin fibres and tropoelastin in the aortic wall.

The MR techniques can monitor aneurysms through morphological measurements, assessment of the thrombus (its organisation and structure) and leukocyte uptake with specific contrast agents (SPIO/USPIO). MR has been validated to show adequate morphological detail when compared with CTA [403,413,422,423]. Along with this anatomical detail, MR allows evaluation of tissue composition. In the absence of macroscopic accumulation of fat in the thrombi, it is suggested that fibrinolysis or haemorrhage occur in the aortic wall and this correlates with high levels CD66b (neutrophils), CD68 (macrophages), MMP-2, MMP-9 and pro-MMP-9 activity that are known markers of proteolysis in the aortic wall[281-283,437]. MRI T2 images in the same study showed multilayered thrombus suggesting that it had formed in stages in line with aneurysm growth cycles. This was particularly clear on T2 relaxation imaging, while SPIO uptake resulted in significant signal reduction in the subluminal layer and deeper thrombus tissue[252,328,341,343]. This suggests that functional imaging with MR is picking up leukocytes (likely macrophages) trapped in thrombus and therefore represents an unstable aortic wall that is expanding and is prone to rupture[418,437]. From the clinical point of view the utility of MR lies in assessment of aneurysms morphological properties and correlating these to the biological data obtained from ILT. The use of contrast agent further enhances this by deeper assessment of ILT aortic wall interaction. The use of paramagnetic iron particles does, however, have limitations. These include clearance of these particles by the liver that might reduce their sensitivity and lead to a relatively poor uptake in vasculature. It is not possible to quantify these particles in the inflammatory cells, as the leukocyte turnover at the luminal surface of ILT is unknown. The variable time interval between imaging and treatment results in uncertainty in location of the SPIO engulfing macrophages. Also, because of the small number of patients in these studies it is unclear as to the precise nature of the relationship between MR signal and intensity of cellular infiltration and a cut off value of noise to signal in ILT. The analysis of SPIO uptake will be further complicated as the ILT is heterogeneous with varying ages of thrombus present that takes up SPIO in differential layers. The subluminal thrombus may have

low signal intensity and with the increase in circulating blood pool signal with SPIO injection means that signal measurement might be biased.

The clinical utility of the MR data is from providing the biological correlates to the anatomical data and the likely proteolysis changes occurring in the aortic wall as aneurysms develop. MR has the advantage of exposing the patient to no ionising radiation. Serial imaging with MR using these contrast agents is needed to characterise the natural history of aneurysm growth. Therefore MR could provide clinically critical information on risk of rupture. Currently it is predicted that SPIO uptake signifies high-risk aneurysms that have abundant inflammatory cells, proteolysis and this implies an unstable aortic wall.

T2 weighted imaging along with Gold-DTPA enhancement on T1 imaging to visualise the fibrous cap and ILT correlate with cellular changes in the aneurysm wall[322,426-427]. The authors concluded that MR could identify plaques that are vulnerable to rupture. There is a need for validation of these findings in larger studies as MR may be critical in assessing risk of rupture and therefore influence clinical decision-making.

Imaging that can better predict the progression of aneurysms and development of complications would be of great clinical benefit. Additionally if we understand the chronic inflammatory processes that underlie the pathophysiology of aneurysm development we could target specific drugs to augment aneurysm growth. The development of novel radiotracers and MR agents allows functional imaging of aortic aneurysms to yield potential physiological, biochemical and cellular correlates to events occurring in the aortic wall as aneurysms progresses. The main immune signal is from the B and T lymphocytes. From characterisation of the lymphocyte subtypes we have defined two different overall populations. The synthetically active lymphocytes express $CD5^+$, $CD24^+$, $CD25^+$, IgD and IgM phenotypes. It is possible that as yet unknown antigenic trigger activates the B-cells to be attracted to aortic wall and produce immunoglobulins. Through MHC class II peptide antigen

presentation $CD4^+$ T-helper cells would be recruited to the region. These would in turn activate $CD8^+$ cytotoxic T-cells that are responsible for cytokine release and further interaction with B-cells to produce plasma cells[427,522]. There is subsequent recruitment of macrophages in the aortic wall as a result of lymphocyte activation and B-T interaction. The role of T and B regulatory cells in the pathogenesis of aneurysm is as yet not elucidated. The interaction between B and T lymphocytes and their influence VSMC's is yet not fully understood. This is a second population of immune cells that are present in the aortic wall and are likely involved in remodelling responses to the aortic wall. This B and T memory cells and regulatory cells are likely responsible for dampening the inflammatory response followed up by upregulation of tropoelastin content in the aortic wall.

It is known that pro-inflammatory cytokines, mechanical stress and oxidative state activates the c-Jun N terminal kinase (JNK) pathway that increases activation of activating protein (AP-1), increases expression of matrix metalloproteinase's (MMPs), and decreases expression of matrix synthesis enzymes (lysyl oxidase (LOX) and prolyl 4-hydroxylase (P4H) leading to decreased deposition and increased degradation of elastin[108,268,269,417]. These form putative *in-vitro* targets that be studied to delineate the nature of the interaction between lymphocytes and VSMCs.

Another possible way to investigate any direct connection between immune cells and aneurysm development/growth is to selectively knock B and T-cell function using pharmacotherapy (e.g. cyclosporine to inhibit T-cell function or selective monoclonal antibodies i.e. Rituximab against B-cells (anti CD20 chimeric antibody) and Muromonab against T-cells (anti CD3 monoclonal antibody). This selective knock out would allow investigation on the putative roles of these immune cells in aortic wall tissue to investigate how this augments aneurysm expansion and behaviour on MR imaging.

There are numerous other novel agents that have been used in animal studies and may provide attractive biological markers of aortic wall instability. These include MMP's and their inhibitors (TIMP's), tropoelastin, oxidised LDL receptors, and other markers of platelet activity, apoptosis, inflammation and angiogenesis. Along with USPIO/SPIO other nanoparticles have been used to determine macrophage content. These include integrins (alpha nu beta 3 (amb3)), matrix metalloproteinase (MMPs), micelles labeled with macrophage receptors or products (neutrophil gelatinase associated lipocalin (NGAL), peripheral cannabinoid receptors (CBR-2)[251,468,522]. Although many retrospective and small prospective studies demonstrate a link between functional imaging and clinical outcomes, there needs to be large prospective studies to evaluate this whilst also looking at the effects of anti-inflammatory therapies on aortic wall. The effectiveness of lifestyle modification on cholesterol and statins to reduce arterial wall inflammation has been studied with metabolic alterations in the aorta and carotid wall[74,75,262]. Similar studies have been conducted with MR to study aortic disease progression. Presently animal studies are en route to develop functional imaging to aid delivery of drugs. For instance targeted therapy geared towards angiogenesis inhibition or anti-inflammatory treatments targeted to vascular wall[253,255,421,422].

ESMA therefore allows non-invasive determination of aortic disruption site with ECM loss that precedes aortic wall dilatation. This is followed by *in vivo* assessment of aortic wall remodelling with subsequent increase in ESMA content at certain sites in aortic wall as it expands. The changes in the aortic wall elastin and tropoelastin content can be followed in a longitudinal manner and quantified with aneurysm growth. The MRI signal intensity following ESMA correlates with arterial wall elastin density (EvG staining) and tropoelastin level (specific antibody). The *in vivo* R1 values were in good agreement with the histomorphometric wall assessment of elastin and tropoelastin. ESMA also demonstrates regions of aortic wall immune cell content and sites where active inflammation is occurring (sites of no ESMA activity). This level of aortic wall biological assessment is currently not available in humans but would be

integral to provide additional predictive parameters as to which aneurysms will expand at which sites and are likely to progress to rupture.

Recent data suggests numerous novel microRNA networks that are involved in tropoelastin synthesis and elastin formation[428-431]. It might be that modulating the microRNA networks involved could up-regulate ECM content in the aortic wall and change aortic phenotype. The ESMA MRI would form an ideal imaging modality to assess the response of the aortic aneurysm wall to this novel therapeutic modulation and study the aortic wall immune cell changes. This aortic modeling response that stabilises the aortic wall endogenously in response to dilatation is critical in aortic wall stabilisation and this reinforces the importance of ESMA imaging.

MRI allows marked higher resolution compared to other investigative modalities and therefore the aortic wall can be investigated. Although there is high relaxivity of the contrast agents, to provide soft tissue detail, the metabolic information remains limited compared to PET and SPECT imaging. One way to circumvent this is to combine the two modalities to a hybrid MRI-PET system. MRI yields superb soft-tissue contrast, functional information, and potential biological data with use of bespoke tracers, allowing assessment of perfusion, diffusion, or metabolism. PET will enable visualization of molecular tracers with picomolar sensitivity, providing information about cell metabolism and targeted receptor status[432,433].

In the clinical setting the only predictor of aneurysm behaviour to decide management are symptoms and maximal aortic diameter. ESMA could potentially allow determination of the initial aortic disruption sites prior to dilatation in early aneurysms. It would allow assessment of aortic wall ECM content and the aortic remodelling processes that are on going to repair the aortic wall that is undergoing inflammatory cell degradation at certain focal aortic sites. ESMA MRI would therefore provide accurate risk assessment of

the patients risk of developing an expanding aneurysm and if it is likely to dissect or rupture.

Compared to the other MR imaging studies in aortic aneurysm models ESMA has the advantage of being able to image using a clinical 3T scanning system. This is the relaxation, rotational correlation and signal properties of ESMA are unchanged to traditionally used Gd-based agents. The small molecular weight of the ESMA makes adverse affects less likely when compared to more immunologically active nanoparticle imaging or using antibodies. The agent is rapidly cleared renally and there is minimal blood and background contamination. The next steps would be the clinical translation of this functional imaging modality to determine its utility in man. It would also be valuable to look at aortic phenotype therapeutic change in response to altering microRNA networks to study differences in elastogenesis in the aortic wall.

Chapter 6: Investigating the effect of altering microRNA networks associated with elastin synthesis on aneurysmal growth

6.1 Introduction

Aneurysm development is characterised by infiltration of the arterial wall by inflammatory cells, typified by B and T lymphocytes, NK cells, macrophages and mast-cells[90,146,152]. These cells produce pro-inflammatory cytokines such as IL-1ß, 6, 12, TNFα and IFNγ[44,91], leading to extracellular matrix (ECM) degradation through the up-regulation of matrix metalloproteases (MMP-2, -3, -12, -13)[84,238,476], cathepsins C, S, K[254,255] and down regulation of the tissue inhibitors of matrix metalloproteinase (TIMPS)[43,434]. The key regulator through which the immune cells have the effector actions are the VSMCs that perform the homeostatic role of ECM maintenance in the aortic wall. Of the ECM components, elastin is a major component and elastolytic degradation with production of elastin peptides (EP) is a strong predictor of aneurysm expansion and rupture[435,436]. There are complex interactions at the transcriptional and translational levels that lead to elastogenesis.

The production of elastin is finely regulated at a variety of levels, including the catalyses of pre-mRNA by RNA polymerase II to create mRNA followed by translation of the mRNA, which can be modulated by post-transcriptional regulators called microRNAs (miR). ELN is expressed before birth with the vast majority of elastin synthesis and deposition occurring before birth and within the first few years of life[171-173]. From a young age there is a reduction in the elastin synthesis with extremely low-level expression by middle age. Thereafter, there is a slow turnover of elastin in tissues, with small amounts being deposited in response to degradation in various tissues. Elastin is therefore a highly durable and stable structural protein with a biological half-life of approximately 74-years in man[173]. In pathological states such as

degenerative aortic aneurysm elastin degradation is the final consequence of pro-inflammatory state. Elastin loss triggers an aortic remodelling response where there is attempted repair of the aortic wall with increased synthesis of tropoelastin and organisation in elastin fibers[401,408]. There is data to suggest that collagen synthesis is preferential to elastin providing adaptive stability, but both are upregulated[402,438,439]. Elastin provides the elastic recoil in the artery and progressive stiffening due to increased collagen in a larger diameter aorta leads to the increased risk of eventual dissection or rupture[407,411,439].

6.1.1 MiRs

MiR's are small (~20-25 nucleotides long), non-coding RNAs that post-transcriptionally regulate gene expression by acting on mRNA[441-445]. They are important in cellular activities[444,445], in diseases such as atherosclerosis[445] and cancer[446]. MiRs are highly evolutionarily conserved nucleotides suggesting an important role in biological processes. They are generated in the nucleus by transcription of nascent pri-miRNA transcripts that are initially processed to ~70 nucleotide pre-miRNAs by Drosha in the nucleus. Then processed by RNase-III to form precursor miRs[440,447]. These are transported into the cytoplasm by Exportin 5, where the miRs are processed by ribonuclease dicer into small 20-23 oligonucleotide duplexes, which are then incorporated into RNA-induced silencing complexes (RISC) to silence gene expression at the post translational level by targeting mRNAs. This is done by degrading mRNA leading to protein repression[448,449]. Dicer also processes long double stranded DNA to small interfering RNA (siRNA) duplexes. The miRs act in extensive networks to silence mRNA *via.* translational repression or mRNA cleavage (Fig 6.0).

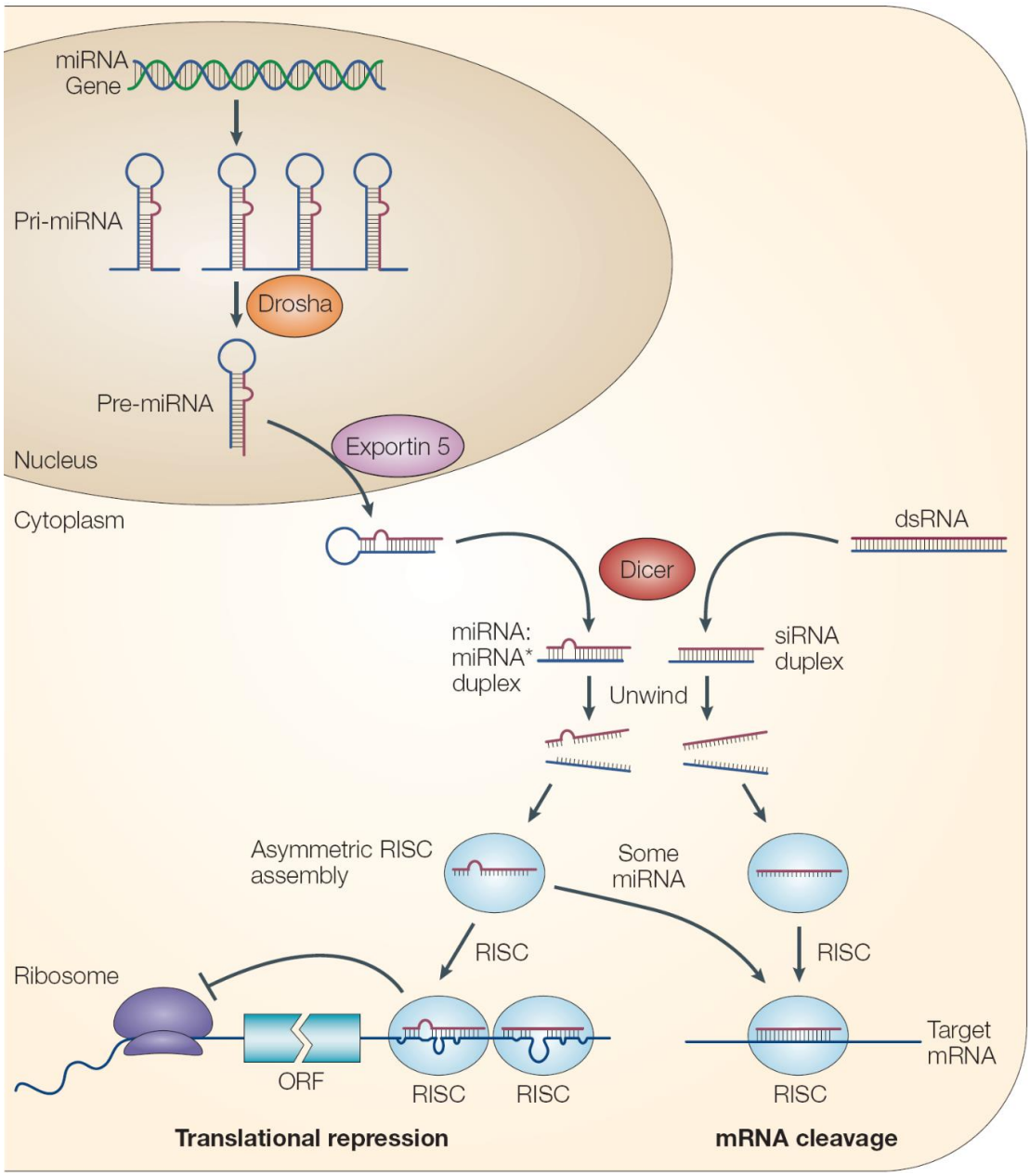

Fig 6.0 The current paradigm of miRNA synthesis and post-translational suppression[451]

Extracellular miRs can be found in the peripheral circulation in patients with cardiovascular disease[452,453]. MiRs are stable in serum as they exit bound to proteins, lipids, lipoprotein complexes i.e. exosomes or microvescicles. MiRs are not single oligonucleotide but sequences of numerous oligonucleotides that interact to form networks of functionally related transcripts[453-456].

6.1.2 MiR expression patterns in aortic aneurysm

The miR expression profile in human aortic aneurysms is different from normal aortic wall tissue. There are differences in the expression profiles of endothelial (miR-20a, -21, -27, -92a, 126, -221 and -222), inflammatory (miR-124a, -146a, -155, and -223) and fibrosis related miRs (miR29b)[444]. Vessel wall related and inflammatory cell derived miRs are upregulated in aortic aneurysm tissue. The miR signatures are correlated to increase in inflammatory cytokines expression and activity, including TNFα, TGFβ and MCP1[457-458]. The circulating plasma concentrations of these miRs are reduced in aneurysm patients compared with tissues resident levels for the miRs[457,459-461].

MiRs such as miR-21 seem to control VSMC proliferation and apoptosis. These are important processes in the development and growth of aneurysms. The regulation of apoptosis might be through phosphatase production, tensin homology, regulation of a tumour suppressor gene PTEN and control of programmed cell death protein 4 (PDCD4)[462]. The phosphoinositide-3 kinases and Akt pathways are also important in these processes. PDCD4 expression is decreased by miR-21 and this might induce VSMC apoptosis through activation of its target molecules (activator protein 1)[462]. MiR-21 has been shown to be an important regulator of VSMC apoptosis in a murine model of aortic aneurysm[456,462-465].

There is increasing evidence that certain miR networks might be important in augmenting vascular inflammation. For instance, miR-126 inhibits expression of vascular cell adhesion molecule-1 (VCAM-1) that mediates leukocyte adherence to endothelial cells[466]. A decrease in miR-126 would increase VCAM-1 expression and leukocyte adhesion and thereby promote leukocyte infiltration into the wall. Other miRs such as miR-223 regulate haematopoietic progenitor cells proliferation, granulocyte differentiation and activation[467,468]. IKKα is targeted by miR-223, during monocyte–macrophage differentiation, and decreased expression of this miRNA along with miR15/16 may prevent

macrophage hyperactivation and recruitment to tissues[468-470]. MiR-146 is present in macrophages and can be induced in the cells by bacteria and proinflammatory cytokines in a nuclear factor κβ dependent manner[471,472]. It is therefore a NFκβ transactivation target that negatively regulates IRAK1 and TRAF6, providing a negative feedback loop to control IL8 and RANTES thus regulating T-cell expression and secretion. Thus modulating innate immune responses through a variety of T-cell mediated effects[471,472]. MiRs involving miR-126, -223, -15, -16 and -146 may therefore be part of larger interconnected network responsible for inflammatory cell activity in the aortic wall. These along with other miRs might indirectly predict aortic wall inflammation.

miR-29 family promotes cardiac fibrosis[462] and other validated targets include elastin (ELN), collagen and fibrillin-1 (FBL-1)[7,430,452,473-476]. MMPs 2 and 9, associated with aortic aneurysms and may also be targets for miR29b[475]. Tissue levels of miR29b levels are elevated in patients with aortic aneurysms[429], whilst inhibition of miR29b down-regulates murine aneurysm development[429-431,465]. MiR29b is important in early aneurysm development in ascending aorta of Marfan mice[430].

MiR-195 is part of another miR network thought to be involved in cardiac fibrosis and alters VSMC phenotype and function[477]. MiR-195 inhibits cell cycle progression and proliferation of cancer cells[451,478-479]. It forms part of the miR15 family of highly conserved miRs (namely miR15, miR15b, miR16, miR16-2, miR195 and miR497). Of these the expression profile for miR195 and miR497 is altered in human aortic dissections[481].

6.1.3 Modulation of miRs

MiR activity can be inhibited *in vivo* using synthetic complementary oligonucleotide sequences (antagomirs) 8-25 base pairs in length, against the seed sequences of the miR. These bind to the miR and last for the duration of

miR activity. Normally nucleic acids are rapidly degraded and thus chemical modifications are required to increase binding efficiency and cellular uptake. These include 2'-O-methyl-modified oligonucleotides (OMe) and locked nucleic acid (LNA)-modified oligonucleotides, where the 2-oxygen is connected to the 4-position by a methylene linker leading to a tight bond that is locked into a C3-endo (RNA) conformation[482-483]. The balance between phosphodiester and phosphorthioate linkages is important leading to improved stability of the synthetic nucleotides[484]. In addition adding a cholesterol construct can improve the cellular uptake of the sequence[441]. LNA modification of oligonucleotides results in thermodynamically very stable duplex formation with complementary RNA. For example, delivery of the unconjugated LNA-antagomir can silence miR-122 in mice and non-human primates [485,486]. This technique is now under clinical investigation in phase I and II clinical trials in treating patients with hepatitis C[486].

Adding a cholesterol construct can improve the cellular uptake of the sequence[441]. The first mammalian knockdown of miR was reported using cholesterol conjugated antagomirs to inhibit liver specific miR, miR-122[483]. Knockdown miR expression has been reported in cardiac tissue after intravenous injection[483]. Various other miR sequences have been inhibited used specific antagomir target in studying cardiac hypertrophy (antagomir to miR-133) and against fibroblasts (antagomir to miR-21)[441,485]. Other strategies to stabilise the antagomirs and effectively knockdown miR function include the use of miR erasers or sponges. This involves deploying vector constructs that can bind multiple miR binding sites where the miR of interest can bind to its intended target[486].

As well as silencing miRs, their actions can be amplified. A miR-mimic consists of a double-stranded oligonucleotide including the miR sequence and the complementary passenger strand. Improved chemical stabilization, conjugation and targeted delivery of the miR mimic are needed to have the desired biological effect[487,489]. MiR levels can also be augmented by delivering

miRs packaged in adeno-associated viruses[489]. Viral delivery of selected miRs can be enriched in specific tissues. Cytoplasmic RNA viruses of positive polarity can lead to mature miRs (virtrons) within the cytoplasm[490-492]. The additional advantage of using a viral vector is that the miR of interest can be continually expressed in the tissue of choice, to replace the downregulated miR. The increased number of adeno-associated viruses (AAV) make tissue specificity due to natural tropism, towards different organs likely. Recent work has used AAV delivery of miR26a to blunt tumour growth of liver cancer[481]. In this case targeted arrest of cell cycle by acting on cyclin D2 and E2 inhibited cancer growth.

6.1.4 MiR therapeutics, pharmacokinetics and delivery

The majority of the antagomirs are water-soluble and can be injected in water/ saline solutions into the intravascular compartment. Intraperitoneal injections of cholesterol-based antagomirs or LNA-based compounds have also been used to silence miRs[494-496]. Studies have demonstrated intravenous, intraperitoneal and subcutaneous delivery of cholesterol bound antagomirs to achieve high level inhibition of various miRs upto 14 days in different tissues [497-498]. There is differential delivery of antagomirs into various tissues. Tissues such as liver, kidney, plasma and heart demonstrate a much higher concentration of antagomir activity then for instance the aorta[429]. The limited penetration into certain tissues can, however, be overcome by increasing the dose and repeated dosing strategy[498].

AmiRs provide an attractive potential for therapeutics. They are specific for a miR, with a known sequence that is often completely conserved among species. This makes it attractive from a drug development point-of-view. Therapeutic mimic of miRs using synthetic RNA duplexes designed to mimic endogenous functions of the miR of interest can be used. These can be synthesized for stability and increased cellular uptake. This method would replace miRs lost in the disease process and there would be limited

modifications possible to the miR as the cell has to recognize it as such. Viral vector mediated delivery has therefore sought to continually express miRs in the target tissue of interest. Antagomir's however remain the most developed and potent method at present to *in vivo* influence miR networks at present.

Selective knockdown of miR21 with antagomirs has been shown to blunt cardiac myocyte hypertrophy by inhibiting and reversing interstitial fibrosis[442]. This effect was thought to be due to regulation of MAPK signaling in cardiac fibroblasts through miR21 targeted Spry1, a negative regulator of MAPK signaling[440]. However gene deletion of miR21 and anti-miR based inhibition failed to result in a phenotypic change and did not alter cardiac remodeling[449,499].

miR15 family including miR195 are thought to be involved in cell cycle regulation and cell survival. Global gene profiling studies and argonaute-2 immunoprecipitation, has shown miR195 to regulate cell cycle genes including checkpoint kinase 1 (Chek 1). LNA modified knockdown of miRs lead to increased number of mitotic cardiomyocytes and derepression of Chek 1[496,497,500]. miR15 family inhibition has been shown to reduce infarct size and improve cardiac function[501].

6.2 Aims

1) To assess the effect of treatment with antagomirs to miR29b and miR195 on the aortic phenotype and ECM content in the ApoE$^{-/-}$-ATII infusion model of aneurysms

2) Study the effect of miR29b and miR195 antagomir treatment on the haemodynamics and cardiac phenotype in the ApoE$^{-/-}$-ATII infusion model

3) To determine the down stream effects of antagomir inhibition of miR29b and miR195 in the aortic wall

6.3 Methods

6.3.1 Laboratory animals and experimental protocol

Homozygous ApoE-knockout male mice 10wks old (C57Bl/6J background, $ApoE^{-/-}$) were obtained from Charles River (Edinburgh, UK). Housing, care and maintenance of animals was carried out in accordance with the regulations of the UK Home Office as previously described in section 4.3.1, page 147.

The experimental protocol used in these experiments is illustrated in Fig 6.1. After acclimatisation for 1wk and prior to osmotic pump implantation, the animals (n=32) were imaged by MRI using 0.4mmol/kg of ESMA (elastin specific magnetic resonance agent)[262,263] in order to obtain baseline aortic parameters using the 3T MTI. A separate 9.4T MRI was performed to determine the baseline cardiac parameters. An osmotic pump (model 2004, Alzet, Durec Corp) containing angiotensin II (1µg/Kg/min, Sigma Aldrich) was then implanted into each mouse. The mice were divided into 4 treatment groups:

1) AntagomiR29b
2) Antagomir-195
3) Control antagomir sequence
4) No injection control

The antagomirs were administered intraperitoneally (i.p.) at a dose of 80mg/kg/day on days 1, 2 and 3 day after osmotic pump implantation. MRI scans and haemodynamic assessment was carried out at weekly intervals until the animals were sacrificed at day 35 for histology, IHC, RT-PCR and bioinformatics analysis.

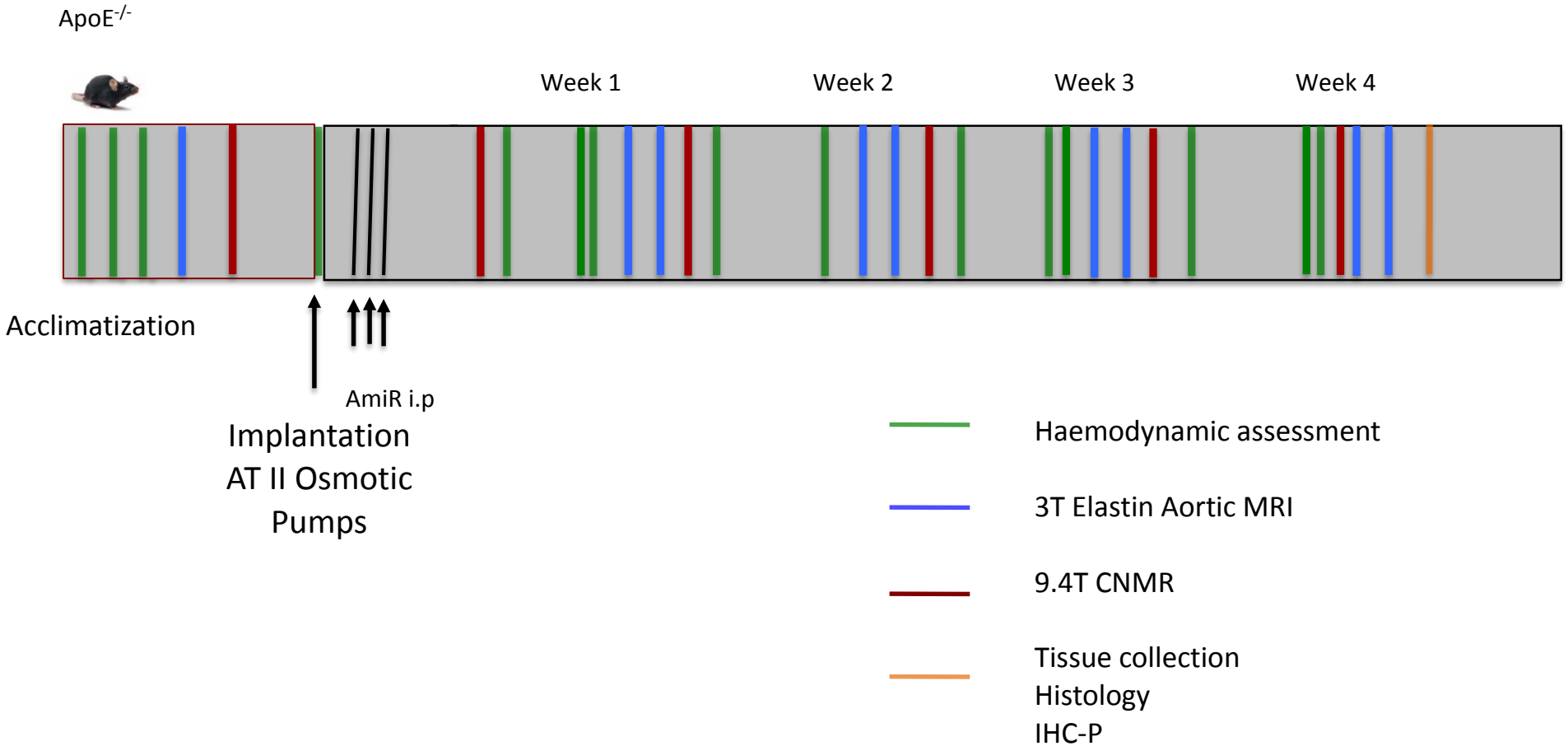

Fig 6.1 The experimental protocol used to investigate the effects of AmiR29b and AmiR195

6.3.2 Systemic silencing of miR in ApoE$^{-/-}$ATII

Cholesterol bound antagomiR constructs from Fidelity Biosystems were resuspended in sterile PBS at 37°C and stored at -20°C. The sequences of the antagomiR constructs were the following: Control AntagomiR: 5` A*A*GGCAAGCUGACCCUGAA*G*U*U* Chol*T-3', AntagomiR-195: 5`G*C*CAAUAUUUCUGUGCU*G*C*U* Chol*T-3', AntagomiR29b: A*A*CACUGAUUUCAAAUGGUG*C*U*A*-Chol*T-3'.

6.3.3 Anesthesia and euthanasia for tissue harvest

Animals were anesthetised by induction with 5% isoflurane and maintained with 1% to 2% isoflurane during pump implantation and MRI. Terminal exsanguination was performed by direct cardiac puncture and aspiration of blood. This was followed by continuous infusion with PBS into the left ventricle to wash out blood contamination, the outlet being the right ventricle. The complete arterial tree was dissected out and excised using an operating microscope (Leica S6D, Leica, UK). Lungs, thymus, heart, liver spleen and kidneys were also harvested. Tissues were either snap frozen in liquid nitrogen and then stored at -80°C pending further processing, or fixed in 10% formal saline for 24hrs before embedding in paraffin (See section 3.3.7.1, page 107) for immunohistochemical analysis.

6.3.4 Non-invasive haemodynamic monitoring

Tail cuff systolic, diastolic pressures were measured and the mean arterial pressure calculated using VPR non-invasive blood pressure monitoring system CODA-6 (Kent Scientific, Torrington, CT) at weekly intervals after acclimatisation of the animals. The protocol followed for the measurements was as previously described[502]. Briefly, 100 waveforms were analysed per animal per sitting. The heart rate and waveform amplitude was measured before cuff inflation. 10 initial readings were unrecorded. These were necessary to warm the mouse-tail and get mouse acclimatised to that session.

We carried out 5 days of training in order to accustom the animals to the procedure. The rapid appearance of a waveform to the tail-cuff procedure as judged by software for first 10 readings were excluded and likewise any waveforms deemed not to fall within the appropriate wave pattern. A single investigator from 1000-1800hrs weekly carried out and recorded the measurements. Each session included 2 sets of 10 measurements; therefore 60-100 measurements were used for BP analysis in each mouse at each time point. For inclusion of each set of measurements for individual animals, we required the software to recognise at least 6 of the 10-trial run of measurements.

6.3.5 Elastin specific magnetic resonance agent (ESMA)

Vessel wall elastin content was assessed using the novel elastin specific contrast agent, ESMA (Lantheus Medical imaging, North Billerica, Massachusetts) as described previously in Chapter 5 and by the authors studying the porcine vascular tree[263] and atherosclerotic plaques in ApoE$^{-/-}$ mice[262].

6.3.6 Magnetic resonance imaging

6.3.6.1 In vivo MRI protocol at 3T

The imaging was performed as described in section 5.3.2.1 on page 181.

6.3.6.2 In vivo MRI protocol at 9.4T

Cardiovascular MR images (n=4 per group) using a horizontal MR scanner (Varian Inc, Palo Alto, CA) with mice positioned in the prone position. The gradient coil had an inner diameter of 12 cm, a gradient strength of 1000 mT/m, and a rise time of 120µs. A quadrature transmit/receive coil (RAPID Biomedical GmbH, Würzburg, Germany) with an internal diameter of 39 mm was used. Anesthesia was achieved as described above, and body temperature was maintained at 37°C with the use of a warm air fan (SA Instruments, Stony

Brook, NY). ECG gating was achieved *via*. 2 metallic needles placed subcutaneously in the anterior chest wall, and a pressure transducer was placed on the abdomen for respiratory gating (SA Instruments). The data was pressure transduced and gated with synchronous acquisition with ECG and to compensate for respiratory motion. Simultaneous ECG triggering and respiratory gating was carried out to minimise the motion artifacts. The typical heart rate was between 350-550bpm (cycle length 110-160ms) with a fluctuation of ±50bpm (12ms) per cardiac cycle. The respiratory rate was 40±10 resp/minute (1500±500 ms) per respiratory cycle.

Cine-FLASH was used to acquire the dynamic short axis images of the heart. The gradient echo technique was used for maintaining steady state. Spoiler gradients of 1ms duration and 100mT/m strength were used after each data acquisition readout to diphase transverse magnetisation before the application of the next radiofrequency (RF) excitation pulse. Cine-FLASH was performed with ECG and respiratory gating. Optimised imaging parameters were, TR=RR-interval, TE=1ms, FOV 20x25mm, matrix size=128x128, slice thickness=1mm; flip angle=40º, 2 averages for the gating, 1 k-space line/frame, 10 frames per cardiac cycle to study the dynamic short axis view. The acquisition time was 10±0.5mins. The trigger was at peel QRS complex, with phase encoding to obtain the end systolic and diastolic frame. Ejection fraction (EF), stroke volume (SV), Cardiac output (CO) and LV mass were calculated.

6.3.6.3 MR image analysis

Analysis of vessel wall luminal diameter, wall thickness and aortic growth rate was performed using OsiriX (OsiriX Foundation, Geneva, Switzerland). Co-registration was performed of the TOF images with the high-resolution DE-MRI images. The morphometric measurements were performed on high-resolution DE-MRI angiography images, which were taken after administration of ESMA. The signal intensity measurements, regions of interest (ROIs) were defined as areas of enhancement on high-resolution DE-MRI images that co-localised to

aortic aneurysms. The T1 values were calculated on a pixel-by-pixel basis using the Matlab software[261].

6.3.7 Histological analysis

The washed normal thoracic and infra renal aortic segments and suprarenal aortic aneurysms were fixed in 10% formalin, and embedded in paraffin (described in section 3.3.7.1, page 107). Serial 5µm thick sections were stained with hematoxylin and eosin to detect cellular components. Elastin was stained using Verhoeff van Gieson stain (EvG) (as described in section 3.3.7.5, page 109). Computer assisted contour tracing was used to determine the aortic elastin content. Leukocyte and tropoelastin content was estimated by IHC as described in sections 3.3.8, page 109 and 4.3.8, page 153.

6.3.8 Genomics and proteomics

6.3.8.1 MicroRNA target prediction

The prediction of miR29b and miR195 putative targets was performed with the miRWALK algorithm (http://www.umm.uni-heidelberg.de/apps/zmf/mirwalk). The MiRNA targets on the 3' UTRs of all known genes in mouse were identified using 8 established miRNA prediction programs (RNA22, miRanda, miRDB, TargetScan, RNAhybrid, PITA, PICTAR and Diana-microT).

6.2.8.2 MegaPlex reverse transcription

To determine the level of miR in cells 100ng of RNA from the 25µl eluate were reverse transcribed using the Megaplex Primer Pools (Rodent Pool A v.2.0) from Life Technologies. The reaction was performed as per manufacturers guidelines. (0.8µl of Pooled Primers were combined with 0.2µl of 100mmol/L dNTPs with dTTP, 0.8µl of 10x Reverse-Transcription Buffer, 0.9µl of MgCl2 (25mmol/L), 1.5 µl of Multiscribe Reverse- Transcriptase and 0.1 µl of RNAs in (20U/µl) to a final volume of 7.5 µl. The RT-PCR reaction was set as follows:

16°C for 2min, 42°C for 1min and 50°C for 1sec for 40 cycles and then incubation at 85°C for 5min using a Veriti thermocycler (Life Technologies). The RT reaction products were diluted to 1ng/µl corresponding RNA and stored at -20°C.

6.3.8.3 Taqman qPCR assay

Taqman assays were used with Taqman probes designed by Roche Molecular Systems, Inc for Life Technologies, USA to determine the individual miR expression profiles. 2.25 ng of Megaplex reverse transcription product were combined with 0.25 µl of Taqman miRNA Assay (20X) (Life Technologies) and 2.5µl of the Taqman Universal PCR Master Mix No AmpErase UNG (2X) to a final volume of 5µl. QPCR was performed on an Viia7 thermocycler at 95°C for 10 min, followed by 40cycles of 95°C for 15sec and 60°C for 1min. U6 was used as a normalization control.

6.3.8.4 Plasma RNA extraction, reverse transcription and preamplification

miRNeasy kit (Qiagen, Valencia, CA) was used to extract the miRs. 3µl of the 25µl RNA eluate was used as input for reverse transcription (RT) reactions [500,501]. miRs were reverse transcribed using Megaplex Primer Pools (Human Pools A v2.1, Life Technologies). The RT reaction products were amplified using Megaplex PreAmp primers (Primers A v2.1). The Taqman miR assays were utilised to determine the expression of the miRs, 0.5µl diluted pre-amplification product were combined with 0.25µl Taqman miRNA Assay (20x) (Life Technologies) and 2.5µl Taqman Universal PCR Master Mix to AmpErase UNG (2x) up-to a final volume of 5µl. All samples were processed and run as duplicates, with the qPCR being performed on a Life Technologies 7900HT thermocycler at 95°C for 10min, followed by 40 cycles of 95°C for 15 sec and 60°C for 1min. Relative quantification using the software SDS2.2 (Life Technologies) was performed and the exogenous miRNA (cel-miR-39) was used

as a spike-in normalization control as described previously[500,501]. All the RT and preamp products were stored at -20°C.

6.3.9 In-vitro studies

6.3.9.1 Cell extraction for co-culture

Murine aortas were harvested from ApoE$^{-/-}$ATII mice at day 35. The normal aortas and suprarenal aneurysms were processed separately as described previously in section 4.3.5, page 149. The final aortic wall tissue obtained was filtered through a 100µm cell strainer (Falcon BD), incubated with 100µl of Annexin V beads (Miltenyi Biotec, UK) for 15mins at room temperature for removal of dead cells. The cell suspension was applied to a MACS MS column (Miltenyi Biotec, UK) and the effluent collected as a live cell fraction. Live cells were pelleted, re-suspended in 80µl of PBS supplemented with 1% BSA and 2mM EDTA and incubated with 10µl of biotinylated anti-CD3ε for 15mins at 4°C. Cells were washed, pelleted and re-suspended in 20µl of anti-biotin microbeads and incubated for 15mins at 4°C. The cell suspension was applied to the MACS MS column and unbound cells washed away with buffer. Bound CD3^{+} cells were collected from the column by applying the plunger supplied with the column. The remaining unbound cells were pelleted, re-suspended in 90µl of buffer and incubated with 10µl of CD19^{+} microbeads for 15mins at 4°C. CD19^{+} cells were collected as described above. Cells were counted using a haemocytometer and viability determined by trypan blue exclusion.

6.3.9.2 In vitro co-culture system

Mouse vascular smooth muscle cells (mVSMCs, Cell Biologics, USA) grown in DMEM containing 1g/l D-glucose, 10% FCS, 1% antibiotics and 1% L-glutamine. Passage 4-5 mVSMCs were plated at 2x10^{4} cells in 12well plates and incubated for 24hrs at 37°C, in 5% CO^{2}. T-cells (5.5±1.4 x10^{5}) and B-cells (3.9±4.8 x10^{5}) were cultured in 0.4µm cell culture inserts (placed above the mVSMCs in the 12 well plates) with RPMI medium supplemented with 10%FCS,

1%penicllin/streptomycin and 1%L-glutamine. Lymphocytes were co-cultured with the mVSMCs as pure $CD3^+$T-cells, $CD19^+$B-cells, or a combination of T and B-cells in a 1:1 ratio. A mVSMC well, to which RPMI only was present in the insert acted as a control in each experiment. At day 3, DMEM medium was replaced and additional RPMI medium added to the lymphocytes. Cells were lifted off with 1% trypsinisation for analysis at day 5. Normal aortic wall derived and aneurysm derived lymphocytes were incubated with mVSMC's with and without 0.2µg/ml Antagomir-miR29b (AmiR29b) in the culture medium through out the duration of the experiment.

6.9.3.3 RNA extraction from mVSMCs

At day 5, total mRNA was extracted from mVSMCs using the RNAeasy MicroKit (Qiagen, Valencia, CA). Briefly, 700µl of QIAzol lysis reagent was added to cell culture wells containing 1ml culture medium and the lysate vortexed for 1min to homogenize the cells. 140µl of chloroform was added to the homogenate, centrifuged for 15mins at 12,000g and 4°C and the upper aqueous phase transferred to a fresh RNAse free collection tube. 525µl of 100% ethanol was added and transferred to RNeasy MinElute spin column before centrifugation at 8000g for 15sec at room temperature. The eluate was discarded and the above procedure repeated after each addition of 700µl of buffer RWT, 500µl of RPE and 500µl of 80% ethanol. The column was placed in a 2ml collection tube and centrifuged at full speed for 5mins. 14µl of RNase-free water was added to the centre of the spin column and centrifuged at 16,000g for 1min at room temperature to elute the RNA which was stored at -20°C till the RT-PCR.

6.9.3.4 RT-PCR for cell cultures

Each sample was diluted 1:60 with nuclease free water. A further 10-fold dilution series was carried out to produce 1:10, 1:100: 1:1000 dilutions of each sample. A nuclease free water negative control was also used. All samples were further diluted 1:5 with nuclease free water to produce enough cDNA for analysis of 10 genes. Top standard was made using 1µl from each sample into a

single well and diluting using nuclease free water to the final volume of 60µl. cDNA was transferred to a 96-well plate (5µl/well) for each gene to be analyzed. 1030µl of Taqman Fast Advanced Mastermix (Invitrogen) and 700µl of nuclease free water was added to 100µl of assay gene/housekeeping gene (Invitrogen). An automated robotic system (Beckman Coulter) was used to transfer 50µl of mastermix to each well of to the cDNA samples. Samples from the 96-well plates were then scaled up to a 384-well plate for analysis of 4 replicates of each sample. The plate was run on the RT-PCR system (7900HT Fast Real Time PCR system Applied Biosystems) and data acquired using SDS (Invitrogen, UK) The data was analysed using DataAssist software v3.01. The cT values of each sample were normalized to the housekeeping genes and then expressed as fold changes relative to the control samples of each experiment using DataAssist™ software v3.1 (Invitrogen, UK). The average fold change was calculated and logged to allow an interpretation of gene regulation.

6.3.9.5 Cytokine Bead Array (CBA)

Day 3 and 5, conditioned DMEM media was collected from mVSMCs co-cultures centrifuged at 300g for 5mins and the supernatant collected, snap frozen in liquid nitrogen and stored at -80°C. Conditioned media from both days were pooled to increase the final concentration of the cytokines for each incubated co-culture condition. A 10K Amicon Ultra-2 centrifugal filter devices (Millipore, UK) used to concentrate the 2ml sample to 100µl. Samples were pipetted into the centrifugal filter device and spun for 25mins at 4000g. To recover the concentrated solute, the filter device was inverted and centrifuged again for 2mins at 1000g to transfer the concentrated sample to the collection tube.

The BD CBA Mouse Th1/Th2/Th17 Cytokine kit (BD Biosciences), in which the cytokine capture beads of known size and fluorescence were conjugated to specific cytokine antibodies, was used to measure the concentrations of IL-2, IL-4, lL-6, IFN-γ, IL-17A, TNF-α and IL-10 protein in the conditioned media

concentrates. The standard stock solution, 5000pg/ml was reconstituted with assay diluent and a double dilution series carried out to produce standards of 20-2500pg/ml and a blank control of 0pg/ml. Beads were briefly vortexed and 10μl of each capture bead suspension added to a single tube. 50μl of mixed capture beads were added to all assay tubes followed by 50μl of Mouse Th1/Th2/Th17 PE Detection reagent and incubated for 2hrs at 21 °C. Wash buffer (1ml) was added, samples centrifuged at 200g for 5mins and the supernatant discarded. A further 300μl of wash buffer was added to resuspend each bead pellet. The fluorescence signals from each bead were acquired on a two-laser BD flow cytometer and analysed using FCAP Array software v3.0.1 (BD, UK).

6.3.10 Statistical analysis

Data was analysed using SPSSv21 (IBM Inc, US). Graphpad Prism 5 has been used for selective graphical analysis. Data is presented as mean and standard error of the mean (SEM) or standard deviations (SD) when specified. Paired student's t-test was used when comparing parametric data. For multiple variables a two-way ANOVA with post-hoc Bonferroni was used. An alpha value of 0.05 was considered significant. Correlations were analysed using Pearson's correlation coefficient. Inter-observer variability was assessed using Cohen's kappa coefficient. All cell culture data was normalised to control co-culture systems where there was mVSMCs present without any lymphocytes.

6.4 Results

6.4.1 *In vivo* effects of AmiR29b and AmiR195 treatment on aortic dilatation and rupture

Aneurysm development was inhibited by treatment with miR29b compared with control antagomir ($P<0.01$ 2-way ANOVA) or controls with ATII infusion ($P<0.01$, 2-way ANOVA), while the effect of AmiR195 was not statistically significant (Fig 6.2). The Kaplan Meier survival analysis for the AmiR groups demonstrates the survival advantage of AmiR29b over AmiR195 and the controls (Fig 6.2). The survival advantage following AmiR29b treatment represents an absolute risk reduction of 37.5%, with HR 1.75, $P<0.01$ compared with the controls.

The control groups started to developed aneurysms by day 5 post AngII infusion, whereas aneurysm development in the AmiR29b group was delayed until day a mean of day 15. There was a significantly lower aortic diameter in AmiR29b group (n=8) compared to the control antagomir and control groups (n=16) (Fig 6.3).

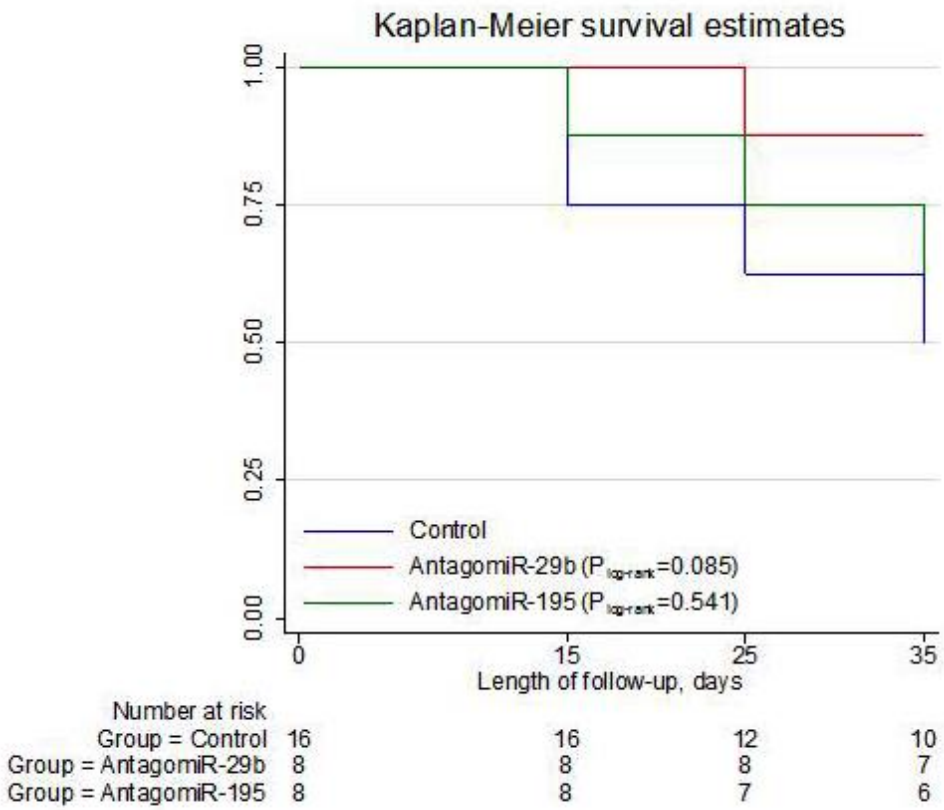

Fig 6.2 The Kaplan Meier survival analysis and cumulative frequency table for the AmiR29b and AmiR195 group and the control groups

There is a significant lowering of the mortality with the miR29b treatment compared to miR195 or the control group.

6.4.2 *In vivo* assessment of the aortic diameter and aortic wall elastin content and continuity

Aortic morphology was assessed by magnetic resonance TOF-angiography (Fig 6.3A, day 15) and used to determine the maximal aortic diameter on transverse aortic sections (Fig 6.3).

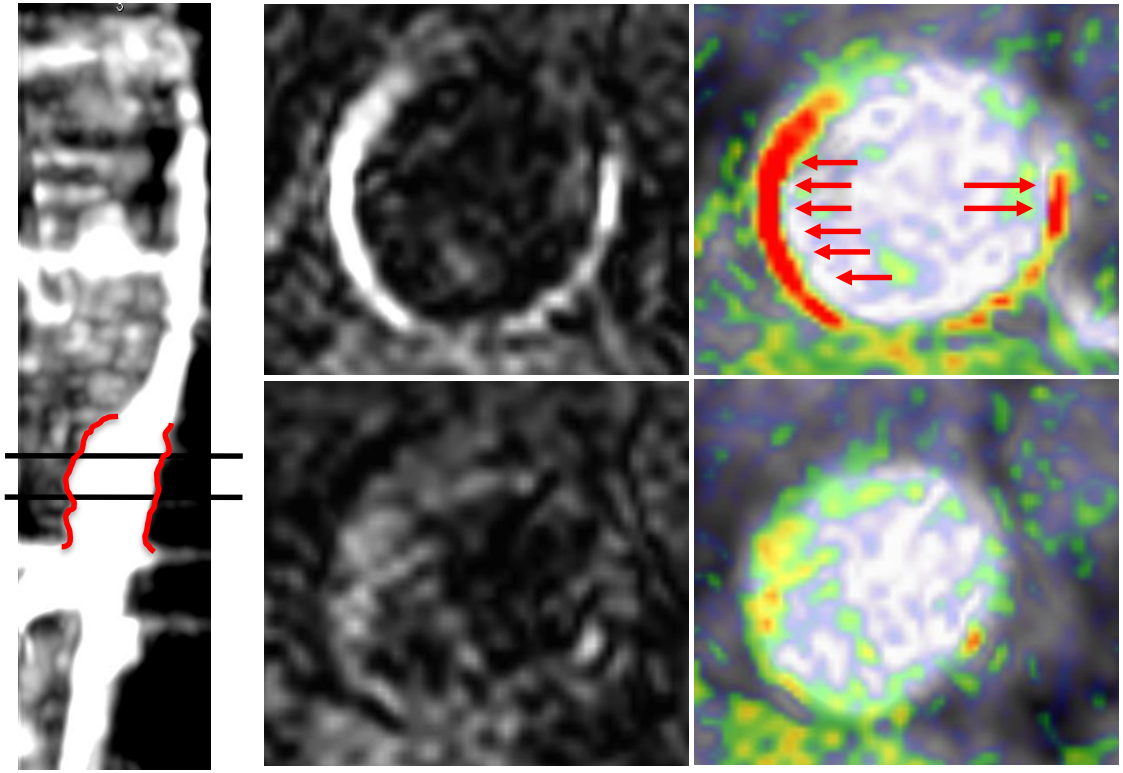

Fig 6.3 In vivo assessments of the aortic aneurysm diameter, volume and elastin content

The black lines represent the imaging plane of subsequent performed axial MRI sequence slices. The two axial slices taken 20 μ m apart. The false colour fused maps of axial slices and the angiogram allowed determination of the vessel wall ESMA content throughout the aneurysm (red arrows). The upper panel shows measurement of the aortic diameter on the fusion angiogram with the aortic wall thickness. The outer and inner aortic wall can be delineated due to the presence of ESMA. This varied according to the axial slice analysed throughout the aneurysm. The lower panel represents aortic outline further down and demonstrates heterogeneity within the aortic wall as to the presence of ESMA. An overall value for the complete aneurysm was obtained through analysis of all the axial sections through the suprarenal aorta. The aortic aneurysm volume was also determined as all the transverse section diameters were taken and the overall aneurysm three-dimensional volume determined.

AmiR29b significantly inhibited aneurysm development (reduction in the maximal aortic diameter) compared with the controls and AmiR195 (P<0.001 each, Fig 6.4). At end point analysis AmiR195 was also at a lower aortic diameter compared to the control groups, P<0.001.

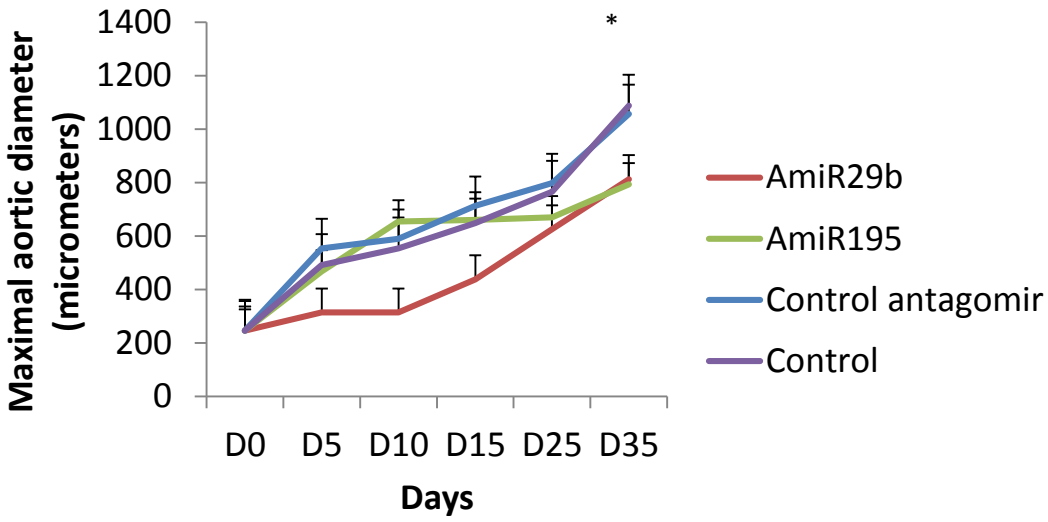

Fig 6.4 Temporal change in suprarenal aortic aneurysm maximal diameters following treatment with AmiR29b, AmiR195, control AmiR or vehicle control

N=8/group for the time points, error bars represent S.E.M. *P<0.001 at end-point analysis between AmiR29b, AmiR195 and control groups, two-way ANOVA, post hoc Bonferroni correction.

The overall aortic volume measured over the complete suprarenal aortic segments was also significantly lower in the AmiR29b compared with control groups at end-point analysis at final time point (P<0.001, 2-way ANOVA, post hoc Bonferroni) (Fig 6.5).

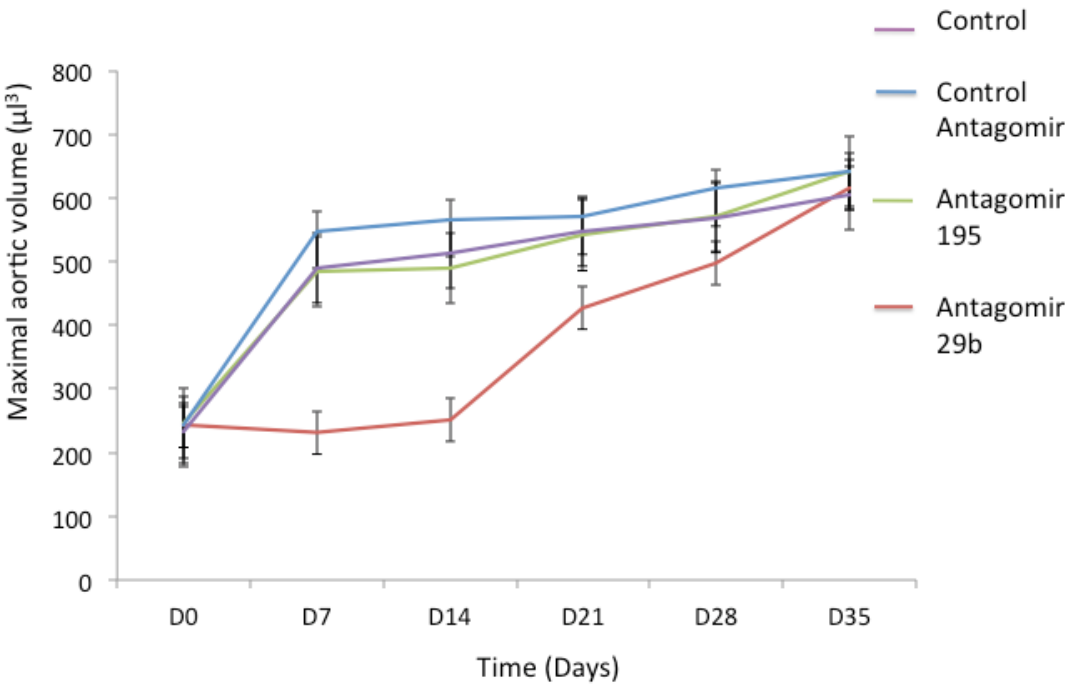

Fig 6.5 The aortic volume from the MRI of the suprarenal aneurysm

N=8/group for the time points, error bars represent S.E.M. At end-point analysis there is significant reduction in aortic volume in miR29b group *vs.* control groups, P<0.001, two-way ANOVA, post hoc Bonferroni test.

When the growth velocity is calculated as proportional fold change in the maximal aortic diameters there is a clear difference in the AmiR29b group with a much lower proportional aortic diameter, which is 2 to 4-fold lower compared with the AmiR195 (P<0.01) and the control groups (P<0.01, Fig 6.6).

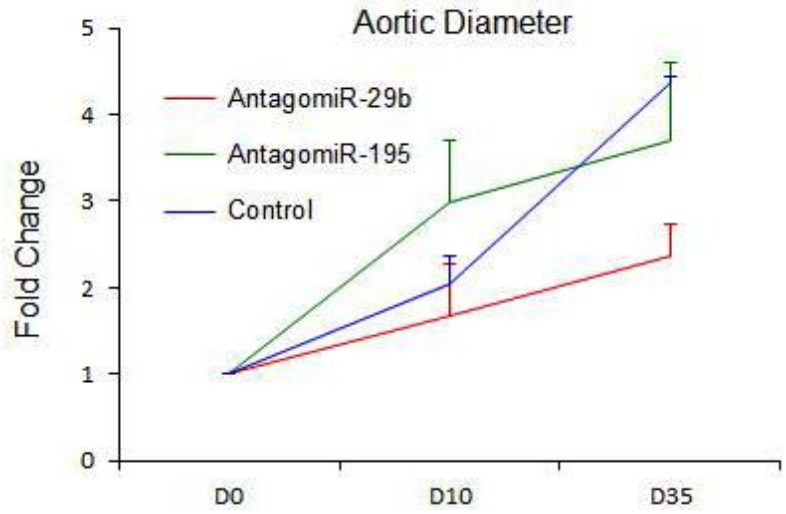

Fig 6.6 Fold changes in the maximal transverse aortic diameter in the suprarenal aortic aneurysm

N=8/group for the time points, error bars represent S.E.M, P<0.01 for AmiR29b group compared to the AmiR195 and control group. (Two-way ANOVA, post hoc Bonferroni correction).

Aortic wall thickness measured, as ESMA content was greatest in the AmiR195 group followed by the AmiR29b group compared with the controls from day 0 till day 10, (P<0.001 at specific time point analysis for AmiR195 *vs.* controls). After day 15 the level of ESMA uptake in the AmiR195 group was not statistically significantly different from the other groups (Fig 6.7). There were no differences in the AmiR29b at any time-point compared to the control group.

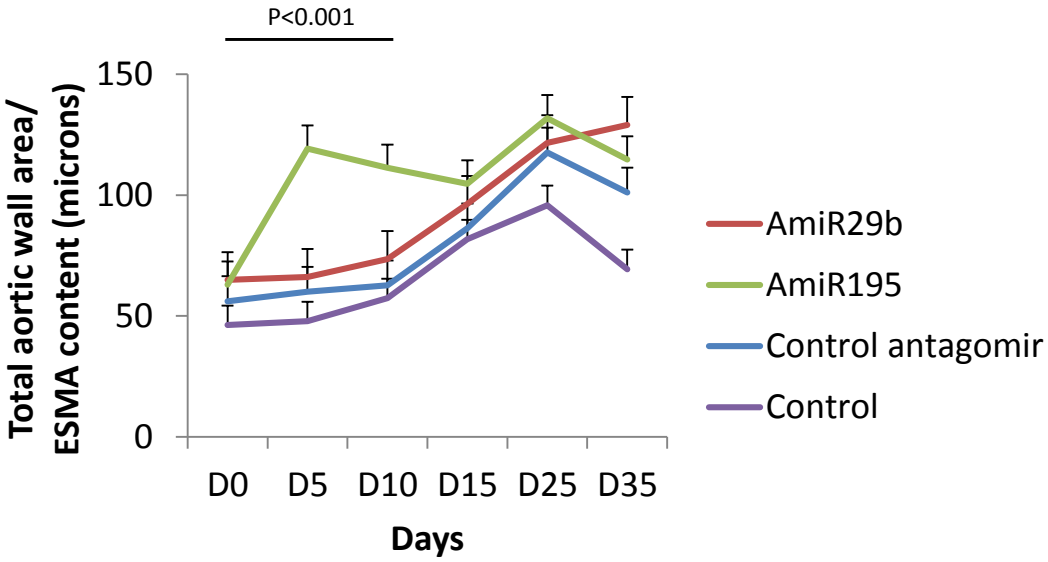

Fig 6.7 Total aortic wall thickness (ESMA content) of supra-renal aortic aneurysm following treatment with AmiR29b and AmiR195

N=8/group for the time points, error bars represent S.E.M. At specific time point analysis there was a significant difference between AmiR195 and the control groups from days 0-10 (P<0.001, paired T-test); thereafter there were no significant differences between the groups on statistical analysis.

The aortic aneurysms from the AmiR29b group had decreased maximal aortic diameters, decreased aortic volume and lowest fold change in the aortic dimensions, and on detailed morphometric analysis, the aortic architecture was markedly altered (Fig 6.8). On overall aneurysm wall ESMA quantification there was no difference in the AmiR29b group compared to the controls but axial slices consistently demonstrated increase in intensity of ESMA in the axial slices which correspondingly matched increased R1 relaxivity values on T1 mapping. This also correlated to histological increase in the elastin and tropoelastin staining from the aortic wall (Fig 6.8).

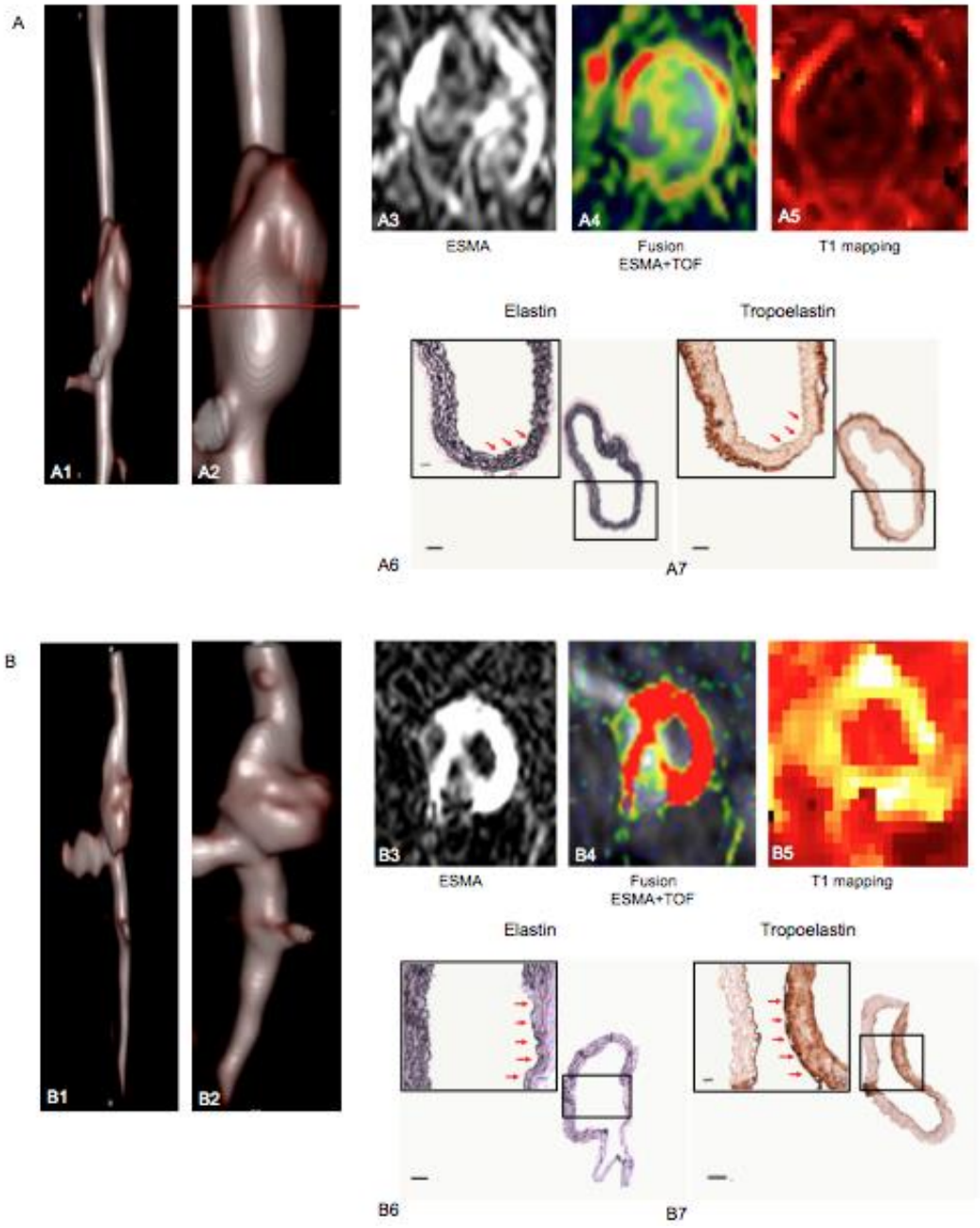

Fig 6.8 *In vivo* assessments of aortic potential disruption sites with aortic dilatation and *ex vivo* histomorphometric assessment of elastin and tropoelastin content

A) Three dimensional magnetic resonance angiogram volume rendered reconstruction (A1) of the murine aorta from the control group taken at day 35. Close up anterior view of the aneurysm (A2). The red line represents an example of axial slice taken for analysis through the middle of the aneurysm. This demonstrated the aortic wall delineated using ESMA (A3) and the absence of ESMA at the 6 o'clock and 9 o'clock positions in the aorta (A4): Axial fusion image of the contrast angiogram demonstrating the absence of ESMA in the same position suggesting an aortic break with likely decreased elastin/ tropoelastin content. Measurement of T1 relaxation times (A5) of the aortic wall to determine the quantification of the ESMA uptake. (A6) The histology on EvG stained aortic section from the aneurysm at the same site as the

scan image demonstrating reduced elastic lamellar units at sites of decreased elastin content in the aortic wall (red arrow) (A7) Decreased aortic wall tropoelastin content (red arrow) at the same site on immunohistochemical assessment using tropoelastin specific antibody. It is likely that the aneurysm will expand/ rupture at a site such as this due to marked loss of elastin/ tropoelastin. (B) Three dimensional magnetic resonance angiogram volume rendered reconstruction (B1) of the murine aorta from the AmiR29b taken at day 35. Close up anterior view of the aneurysm (A2). The red line represents an example of axial slice taken for analysis through the middle of the aneurysm. This demonstrated the aortic wall delineated using ESMA (A3) and the abundance of ESMA throughout the aortic wall. (A4) Axial fusion image of the contrast angiogram demonstrating the high ESMA uptake suggesting an aortic wall has high elastin/ tropoelastin content. Measurement of T1 relaxation times (B5) of the aortic wall to determine the quantification of the ESMA uptake. Compared to control group the higher T1 times were observed (B6) The histology on EvG stained aortic section from the aneurysm at the same site as the scan image demonstrating reduced elastic lamellar units at certain sites (red arrow). However the majority of the wall has high homogeneous elastin staining (B7) Markedly increased aortic wall tropoelastin content (red arrow) at the same site on immunohistochemical assessment using tropoelastin specific antibody (n=6). It is likely that the aneurysm is actively remodelling with up regulation of tropoelastin in response to elastin breakdown.

As the aortic aneurysms develop and enlarge there was disruption of the internal and external elastic laminae in the tunica media that could be observed in all aneurysms. The location of the aortic disruption was seen on the ESMA-MRI and ex vivo on histological sectioning (Fig 6.8, 6.9). Complete aortic wall disruptions were only seen in the control groups (6/8 animals in each group) compared with 0/8 (i.e. total elastin continuity per axial aortic section) seen in the wall of animals in the AmiR9b group (Fig 6.8, 6.9). Intraluminal thrombus was seen the aorta in aneurysms at day 35 in the control groups (5/8 in control antagomir and 3/8 control), but this was absent (0/8) in the AmiR29b group ($P<0.05$).

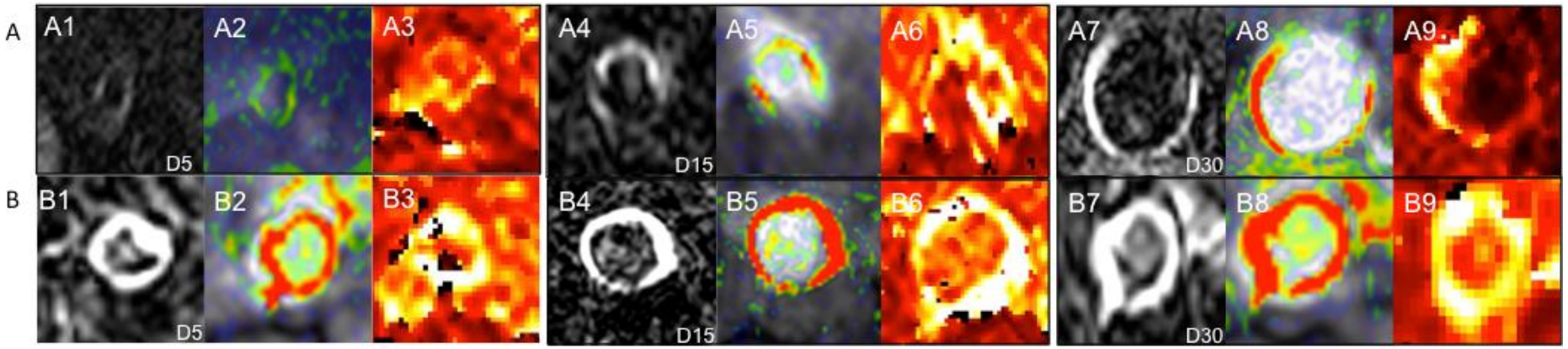

Fig 6.9 Temporal changes in vessel wall elastin content

Increased aortic wall elastin signal (B1) (ESMA uptake) was seen at day 5 throughout the vessel wall (A1-2 *vs.* B1-2) from the endothelium to the adventitia and this was demonstrated on T1 mapping studies (A3 *vs.* B3). At days 15 and 30 ESMA uptake was maintained in the face of increased aortic diameters (B4-9) compared with lower and less homogenous uptake in the control wall (A4-9).

6.4.3 *Ex vivo* assessment of aortic wall composition

The aortic wall architecture and composition was assessed histologically (Fig 6.10, 6.11). The vessel wall elastin content (EvG staining) and tropoelastin content (tropoelastin specific monoclonal antibody) was greater in the AmiR29b group compared with the control groups ($P<0.01$) (Fig 6.10, 6.11). When the elastin and tropoelastin content are correlated to the maximal aortic diameters there is a positive aortic remodelling response that is seen and is more pronounced in the AmiR29b groups.

When the immune cell content is analysed on IHC the AmiR29b treatment was associated with a lower content of T lymphocytes, NK cells and macrophages in the aortic media, $P<0.01$ (Fig 6.12).

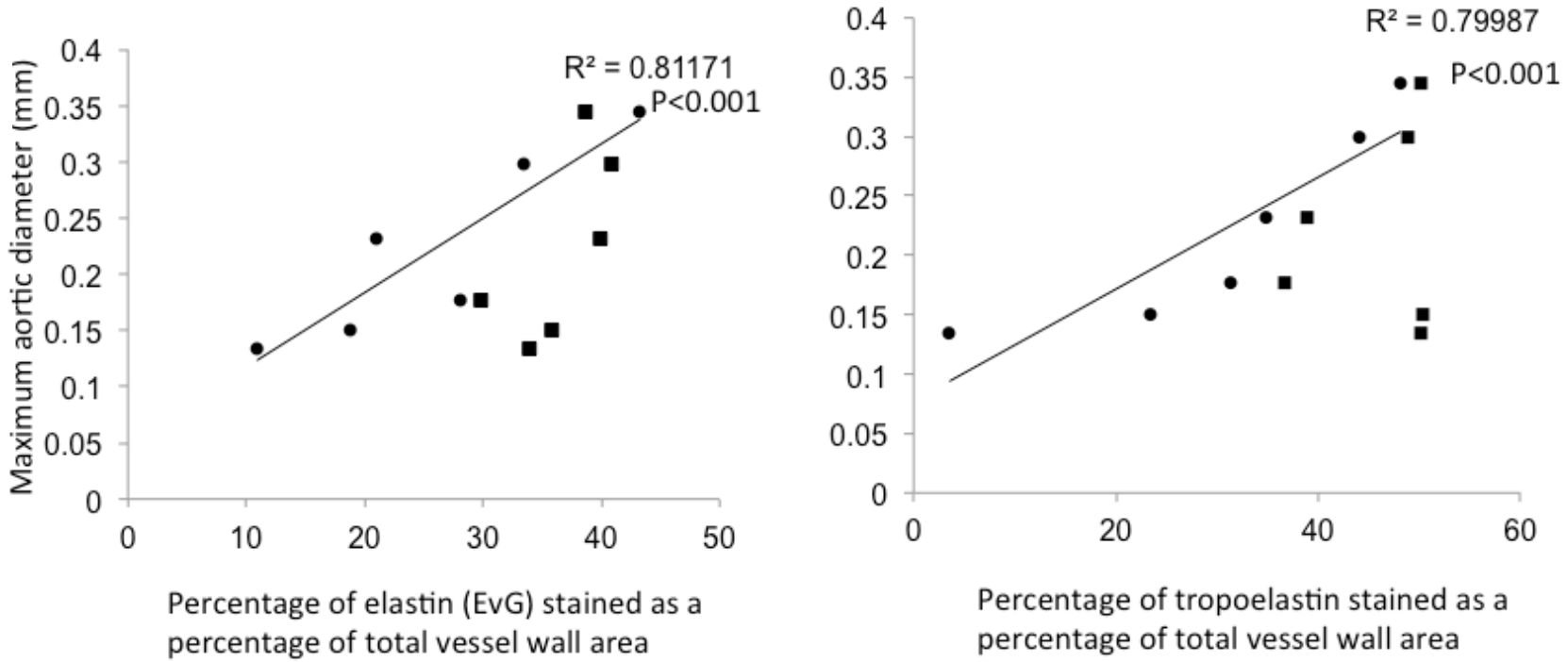

Fig 6.10 Correlation between the maximum aortic diameters and the histological percentage staining area for elastin and tropoelastin as percentage of overall slide area

There is a proportional relationship between the maximal aortic diameter and the percentage of aortic wall elastin content that normally increases with time (black circles). This is a positive aortic remodelling response seen to an expanding aortic lumen (black circles; $R^2$0.81, P<0.001). When the AmiR29b is plotted on this graph (black squares), the vessel wall elastin content (EvG) can be seen to be higher at all aortic diameters. Hence the proportional relationship is now skewed positively with EvG upregulation. Similarly there is normally a positive correlation between tropoelastin content (black circles and the aortic diameter, $R^2$0.79, P<0.001). This correlation is skewed and lost within the AmiR29b group (black squares) that has a higher tropoelastin aortic wall content. (N=16, persons correlation coefficient, two-tailed T-test P<0.001)

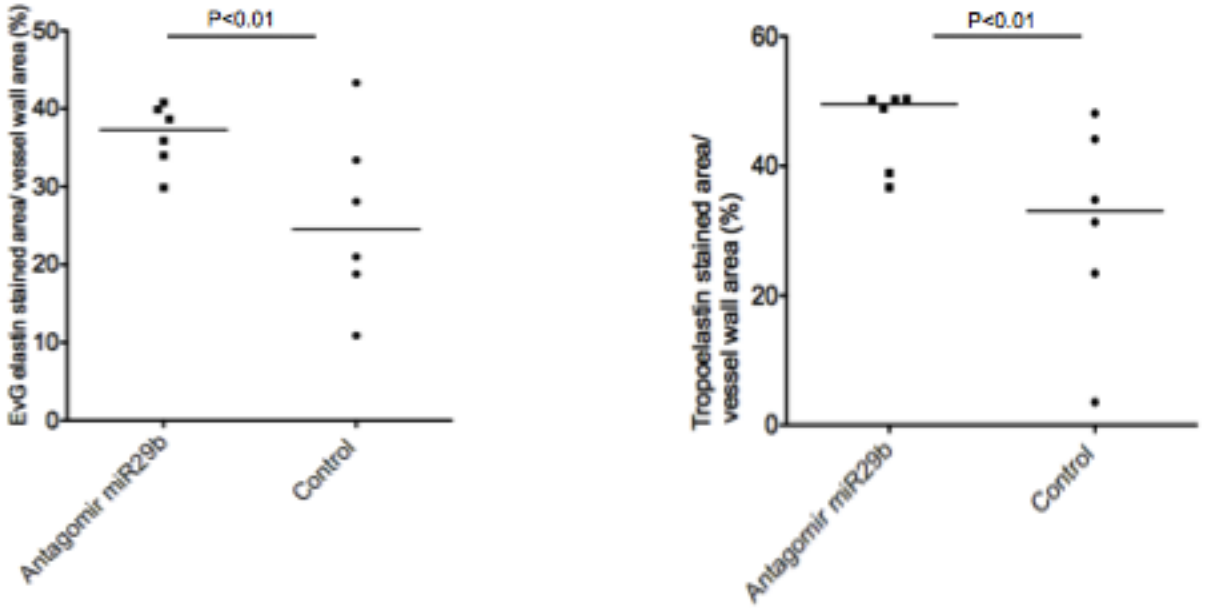

Fig 6.11 Histological assessment of the aortic wall elastin and tropoelastin content

The histological vessel wall elastin content for the control aorta *versus* AmiR29b, demonstrates significantly higher elastin content in the AmiR29b group, P<0.01 (paired two-tailed, T-test). The histological vessel wall tropoelastin content for the control aorta *versus* AmiR29b demonstrates significantly higher tropoelastin content in the AmiR29b group, P<0.01(paired two-tailed, T-test). N=6, 30 slides analysed

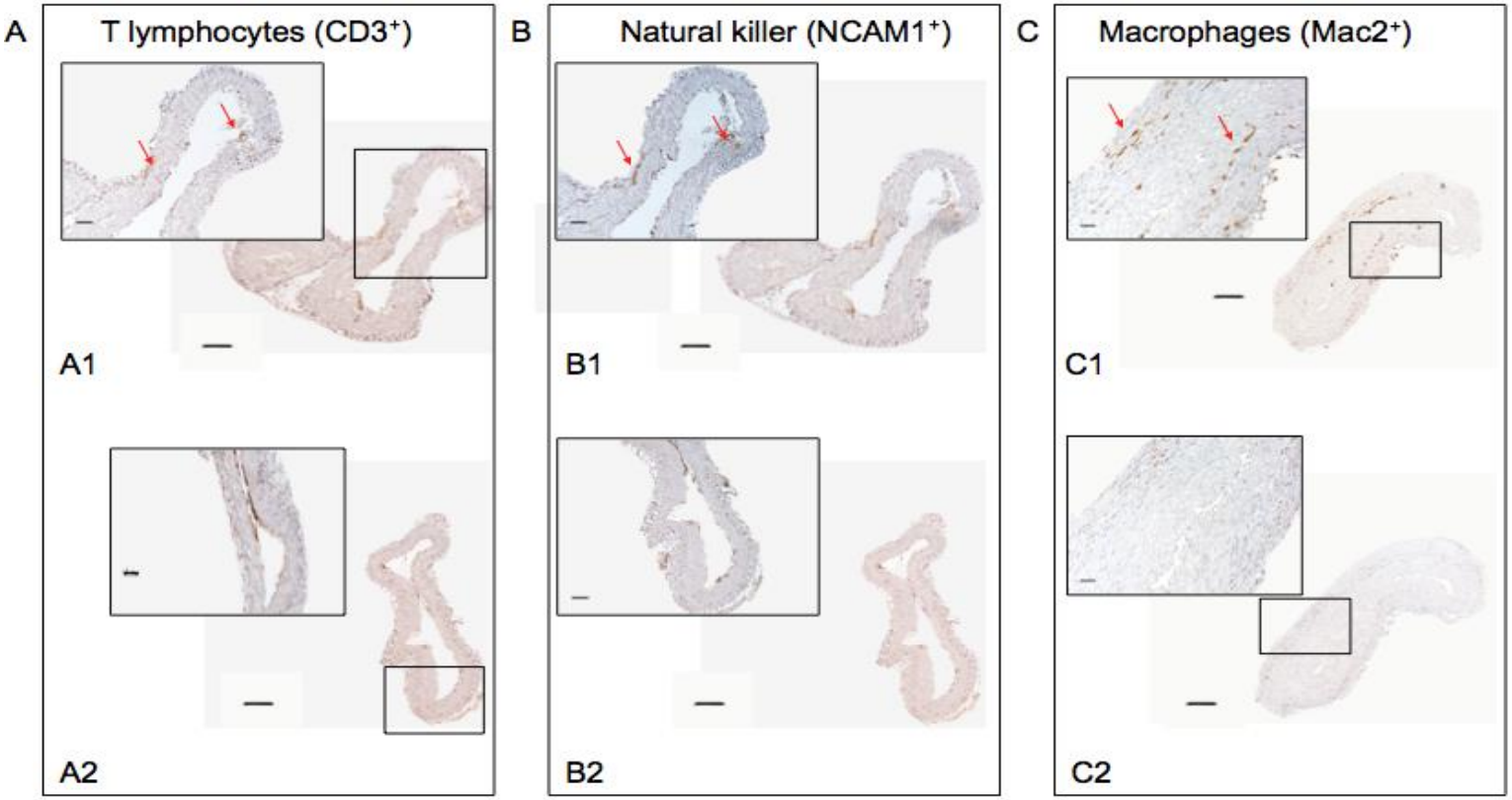

Fig 6.12 Histological assessment for aneurysm wall immune cell content

AmiR29b aortic aneurysms (A2-C2) had a reduced number of T-, B-cells and macrophages compared to the control antagomir group (A1-C1). These apprear as brown (DAB+) staining cells for the immune cell specific cell markers.

On semi-quantitative analysis the number of T-cells (D1, P<0.01), NK cells (D2, P<0.01) and macrophages (D3, P<0.01) infiltrating the tunica media/adventitia was higher in the control ApoE$^{-/-}$ATII. Cell counts given as percentage area of total aneurysm wall stained for specific leukocyte markers (mean±SEM, students T-test).

D1

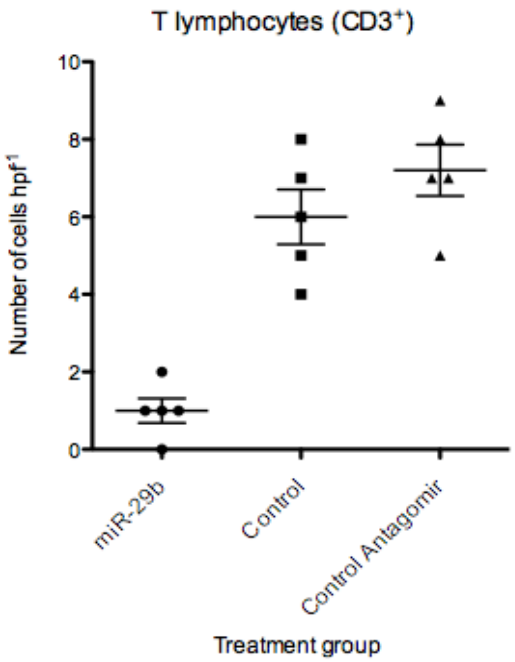

D2

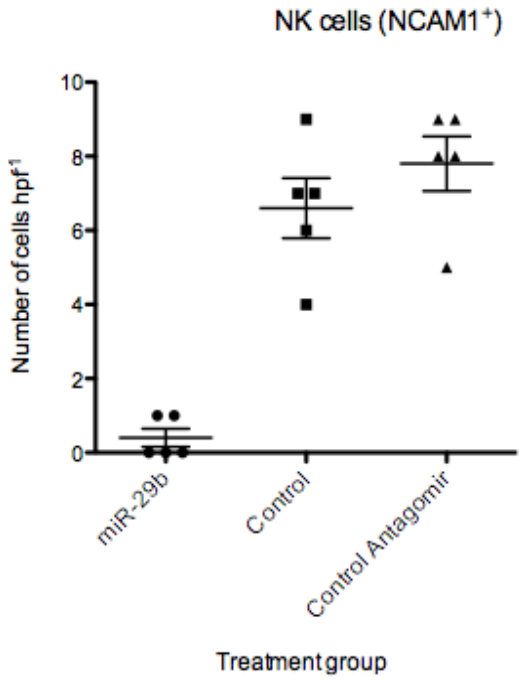

D3

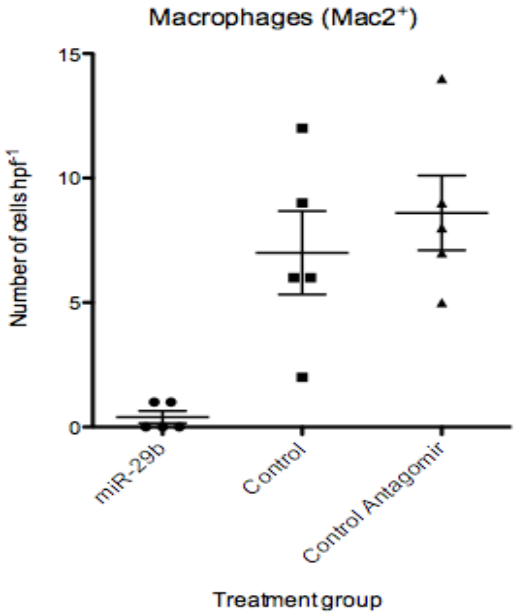

6.4.4 AmiR29b and AmiR195 effects on blood pressure

The baseline mean systolic pressure was similar in all the groups (control 102.1mmHg, control antagomir 94mmHg and AmiR29b 100mmHg, P>0.05) Fig 6.13. Similarly the diastolic baseline blood pressure was the similar across the groups (control 66.7mmHg, control antagomir 71.9mmHg, AmiR29b 69mmHg, P>0.05) Fig 6.14. The mean arterial pressure was similar across the groups (control 78.3mmHg, control antagomir 74.4mmHg, AmiR29b 84.2mmHg) Fig 6.15. There was a statistically significant divergence in systolic blood pressure in all the groups compared to the baseline from day 5 onwards to mean systolic pressure of 145mmHg (P<0.01) Fig 6.13. Elevated systolic pressures were maintained upto day 35 (Fig 6.13). There was a statistically significant difference in the diastolic pressures between the control/ control antagomir groups and the AmiR29b group (P<0.01) (Fig 6.14). There was no difference in the MAP across the groups (P>0.05). The MAP increased in the control and control antagomir from baseline by day 5 (control 92.8mmHg, control antagomir 88.2mmHg). Due to a drop in diastolic pressures in the AmiR29b group the MAP was lower in the AmiR29b group on day 5 compared with the control and control antagomir group (P<0.01), thereafter there were no differences in the groups from day 10 till termination of the experiments, Fig 6.14.

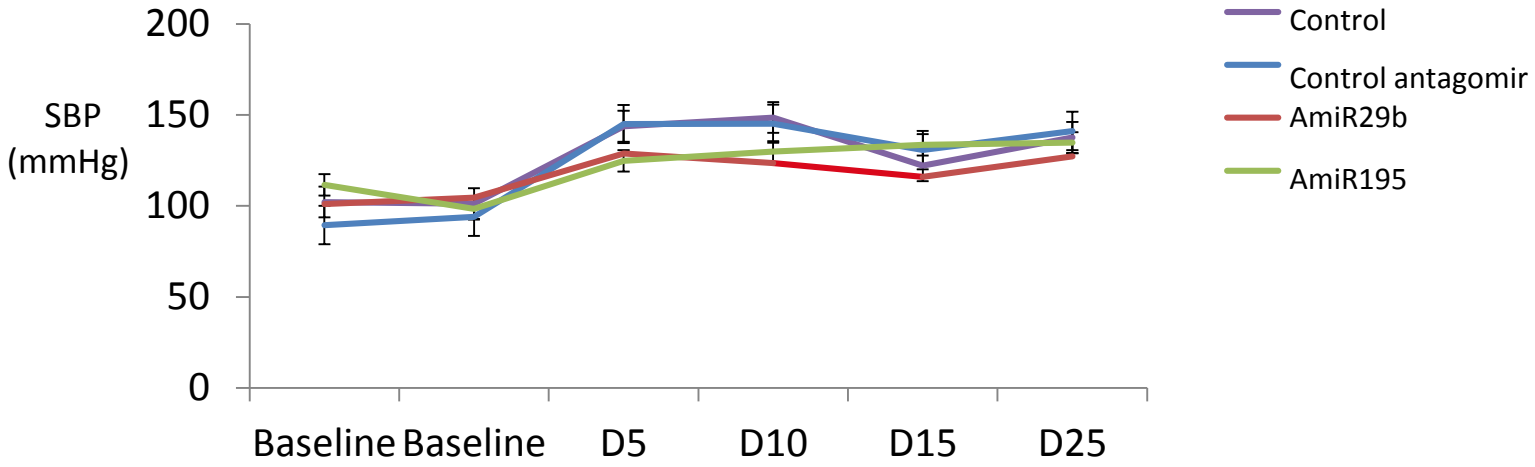

Fig 6.13 Non-invasive systolic blood pressure measurements taken at weekly intervals for all ApoE$^{-/-}$ATII groups

There was an increase in the systolic pressures across all the groups compared with baseline (mean SBP of 101±27 mmHg to mean SBP 145±18 mmHg, P<0.01), showing that AII infusion consistently caused hypertension in all groups. There were no differences between the groups (Two-way ANOVA post-hoc Bonferroni correction)

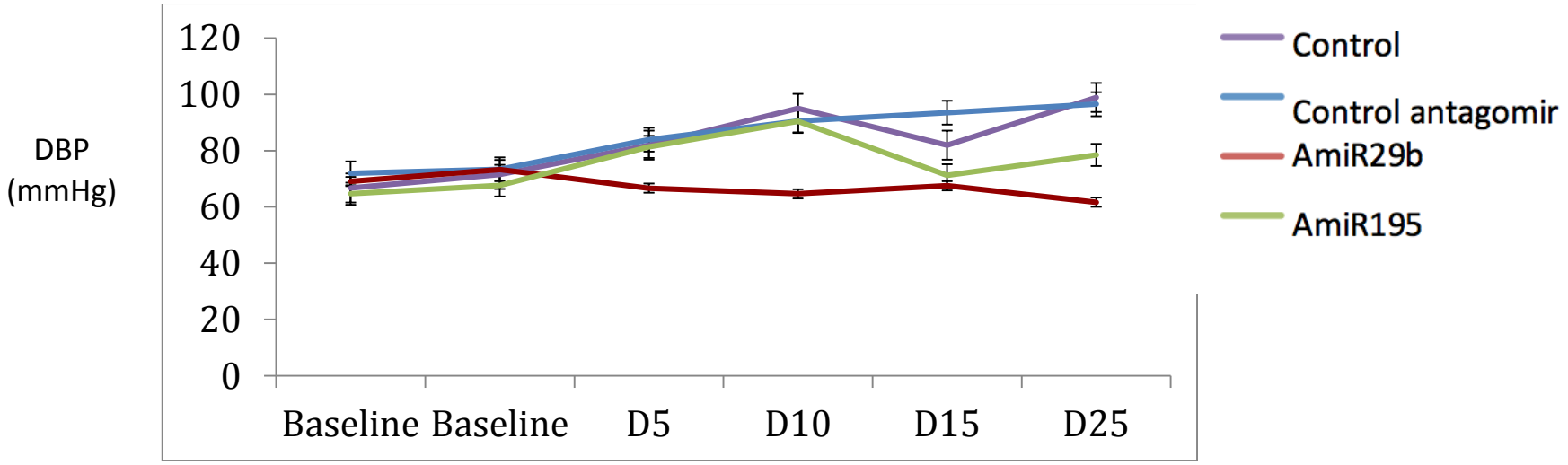

Fig 6.14 The non-invasive haemodynamic assessment of the diastolic blood pressure

The diastolic blood pressure was reduced in the AmiR29b group from day 5 to the end of the study at specific time point analysis, $P<0.01$. This could be due to mVSMCs vasodilator effect on the overall vascular tone. There were no other statistical differences between the groups on Two-way ANOVA post-hoc Bonferroni correction testing.

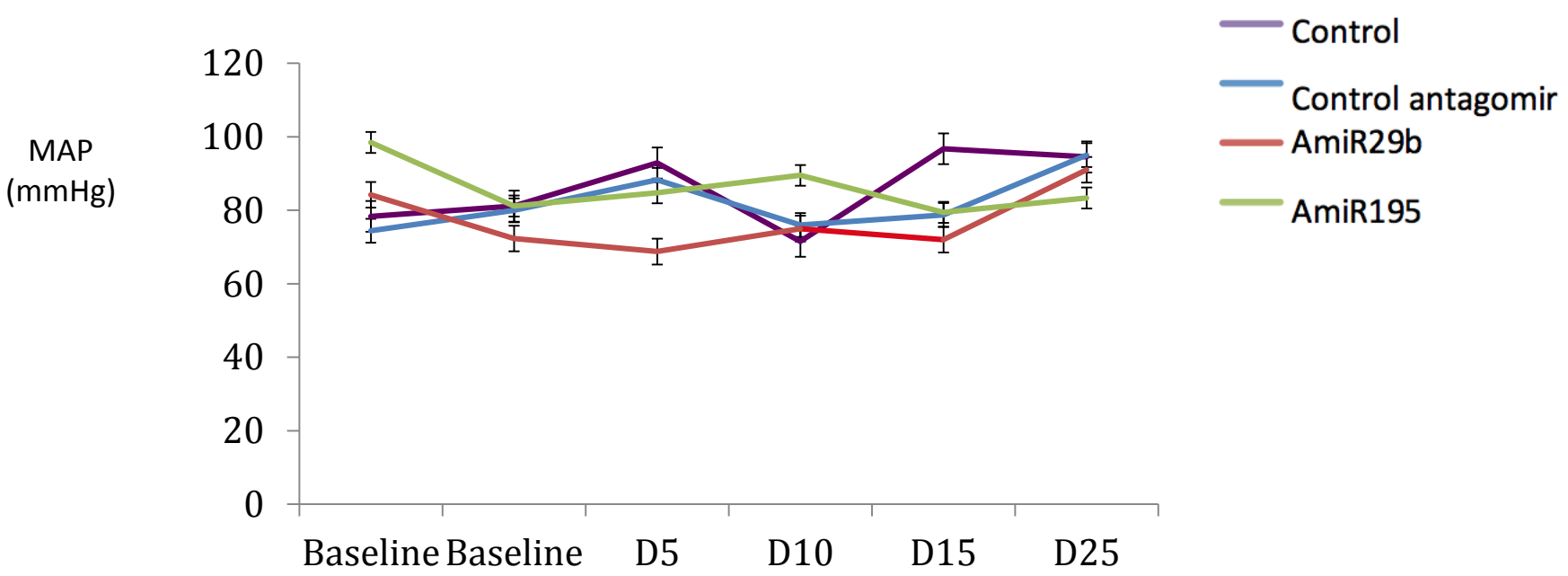

Fig 6.15 The non-invasive mean arterial pressure was not significantly altered continuously across the time course of the study

There were transient decreases in the MAP in AmiR29b group at day 5 and 15 but these were not maintained. There were no significant differences in between the groups. (Two-way ANOVA post-hoc Bonferroni correction)

6.4.5 Cardiac MRI left ventricular cardiac remodelling and haemodynamics

The left ventricular end-systolic and diastolic volumes were lower in the AmiR29b treated group compared with control anatagomir ($P<0.01$) and control ($P<0.01$) over a period of 4weeks (Fig 6.16). However, the left ventricular muscle mass and the derived cardiac haemodynamic parameters were not significantly different between any of the groups (Fig 6.17, 6.18).

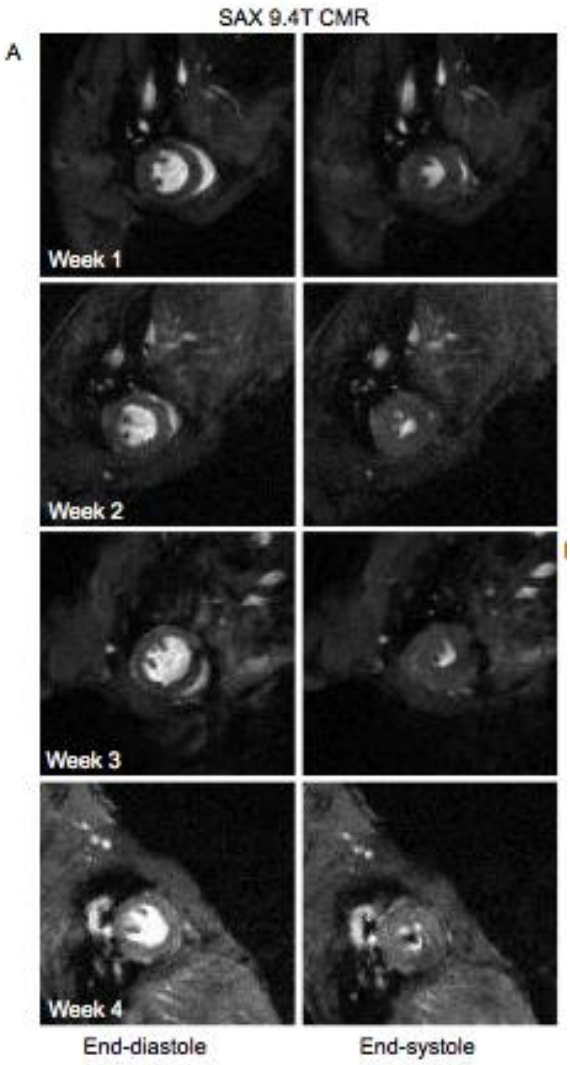

Fig 6.16 ECG gated cardiac magnetic resonance angiogram of the left ventricle in short axis view (SAX) using the 9.4Tesla MRI scanner

A) Images above displayed demonstrating LVES dimension in first panel and LVED dimension in the second panel. Cardiac parameters calculated from the data obtained in these sequences. LVES; left ventricular end-systolic; LVED left ventricular end diastolic

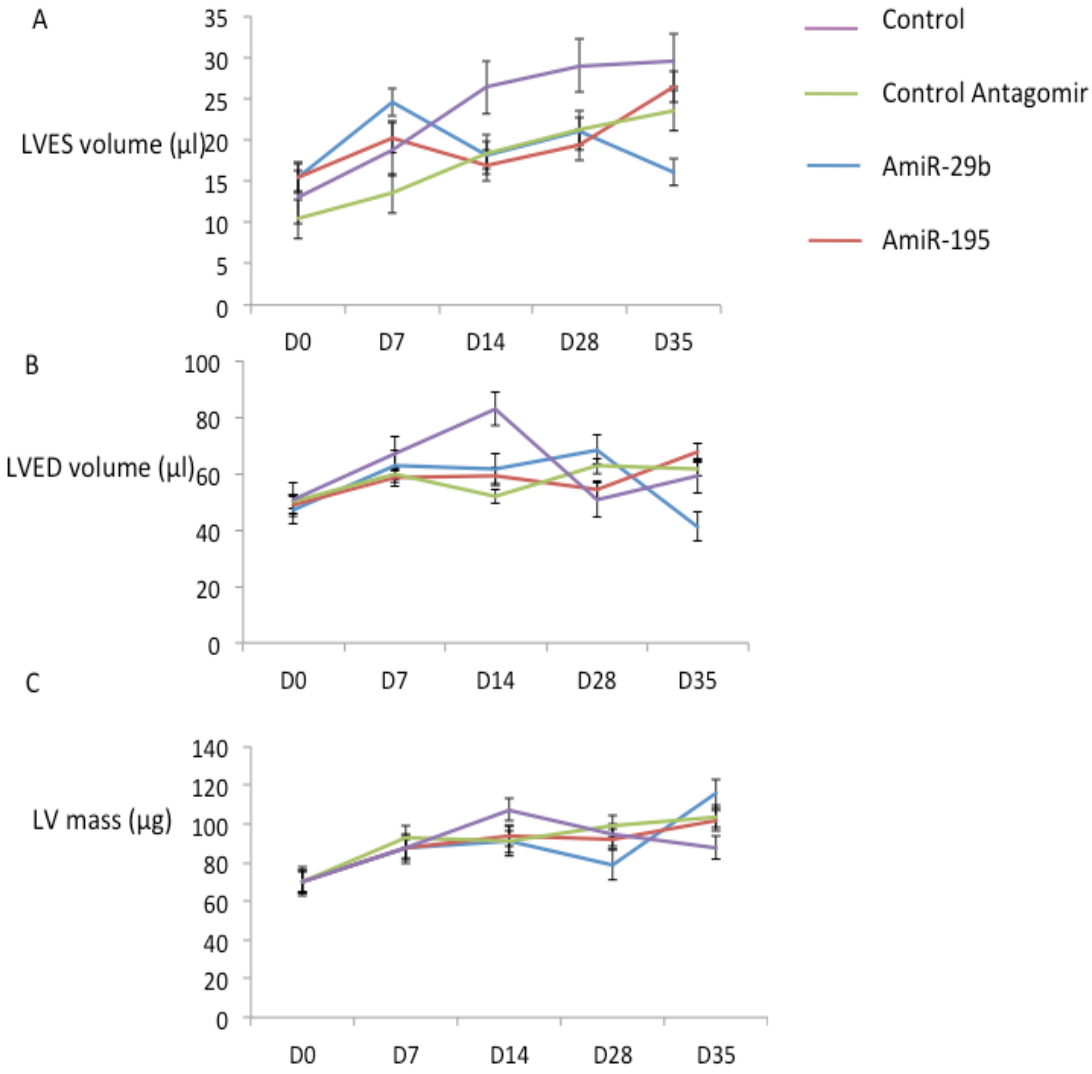

Fig 6.17 Cardiac indices

At specific time point analysis of the indices there are differences in the aortic and ventricular dimension that could be due to an alteration in the aortic vessel wall due to aortic remodelling and mVSMC responses. A) The LVES starts from a similar baseline value however there is a divergence of the LVES beyond day 7 with a decrease of LVES in the AmiR29b cohort compared to the control groups with the effects maximal at day 35 ($P<0.01$). B) The LVED starts from a similar baseline across the groups with a non-significant decrease in dimensions at around day 14. At day 35 the LVED is decreased in the AmiR29b vs. control groups ($P<0.01$). C) The LV muscle mass trended to be slightly lower in the AmiR29b group till day 28, however this was not statistically significant. (Two-way ANOVA $P>0.05$, post hoc Bonferroni test)

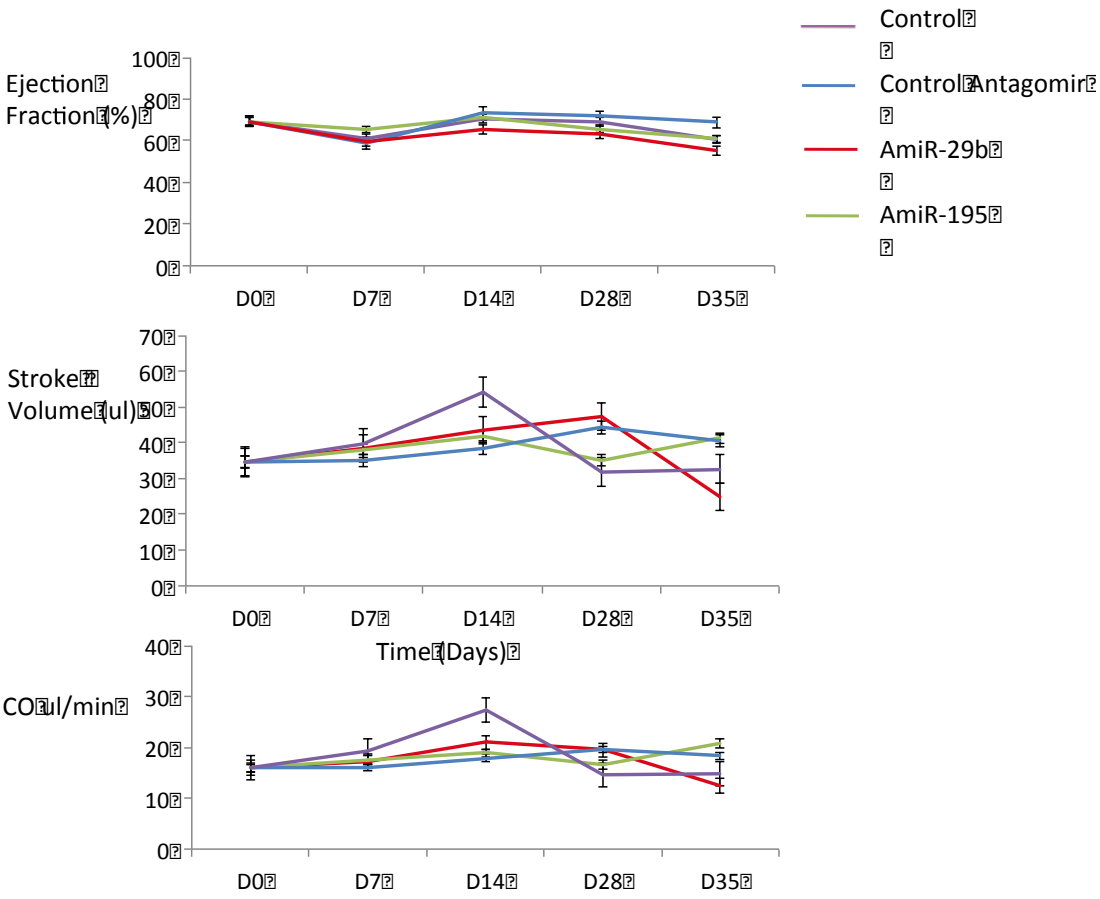

Fig6.18 The cardiac parameters calculated from echocardiograms

The calculated cardiac indices that represent alteration in cardiac physiology did not show any significant differences across the various treatment groups. The percentage left ventricular ejection fraction (LVEF) remained similar across the animals at 60% throughout the course of the study. The left ventricular stroke volume and cardiac output what transient variations within the groups but there were no statistically significant discernable differenced between the control groups and the miR cohorts.

6.4.6 Inhibition of miR-29 and 195 *in vivo* in the ApoE$^{-/-}$ATII

There was marked inhibition of the miR29b activity in the liver and with a decreased efficiency of inhibition in the aorta (Fig 6.19A). Accordingly, an upregulation of elastin expression and other ECM genes was detected in the liver of AmiR29b injected mice (Fig 6.19B). The genes for collagen were up-regulated (Fig 6.19C).

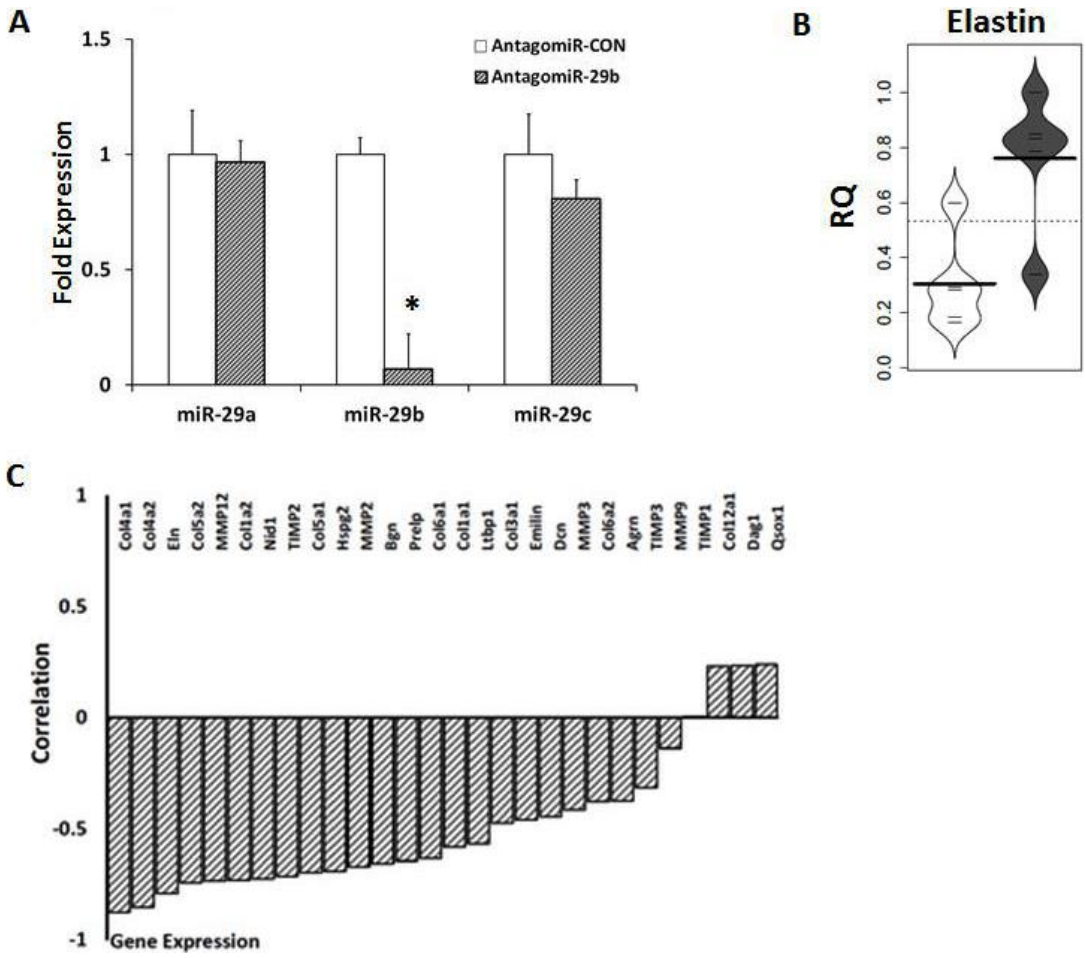

Fig 6.19 The regulation of the ECM microenvironment by miR29b in liver

A) Expression levels of the miR-29 family in the liver following AmiR29b administration. MiR expression was normalized to U6. P<0.05 compared to control antagomir B) Elastin expression in the liver following antagomiR treatment. C) Correlation between the efficiency of miR29b knockdown and the derepression of ECM genes as quantified by QTPCR. Gene expression was normalized to b-actin

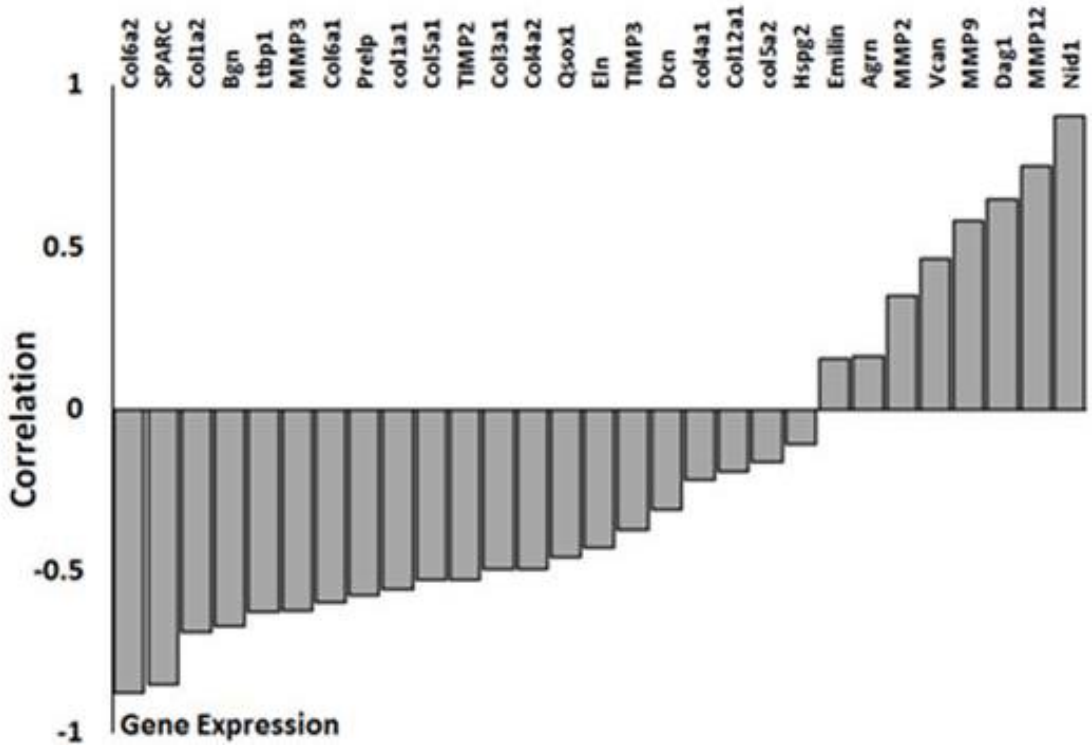

Fig 6.20 The gene expression profiling in aorta following AmiR195 administration Correlation between the efficiency of miR-195 knockdown in the aorta (n=4) and the derepression of a panel of 30 ECM genes on Day10 after AngII infusion. Expression levels were normalised to b-actin.

Following AmiR195 administration there are mild downregulated affects on elastin, fibrillin and collagen genes, whereas upregulation of certain MMPs, notably 2, 9 and 12.

4.6.7 Inhibition of miR29b *in vivo* mVSMCs co-culture system

AmiR29b addition to the mVSMC media during co-culture with normal aortic wall specific $CD3^+$ T lymphocytes resulted in up regulation of TFGβ expression in the mVSMCs (Fig 6.21, $P<0.01$). The $CD3^+$ aortic aneurysm derived lymphocytes demonstrated an up regulation of TGFβ expression and LOX (Fig 6.21, $P<0.01$ and $P<0.05$). There were no significant differences in gene expression of Cttk, FBN, and MMP2 in this group. These effects were specific

to the co-culture set-up with isolated $CD3^+$ cells. The genetic changes were not seen in the $CD19^+$ or the $CD3^+/CD19^+$ groups (Fig 6.21).

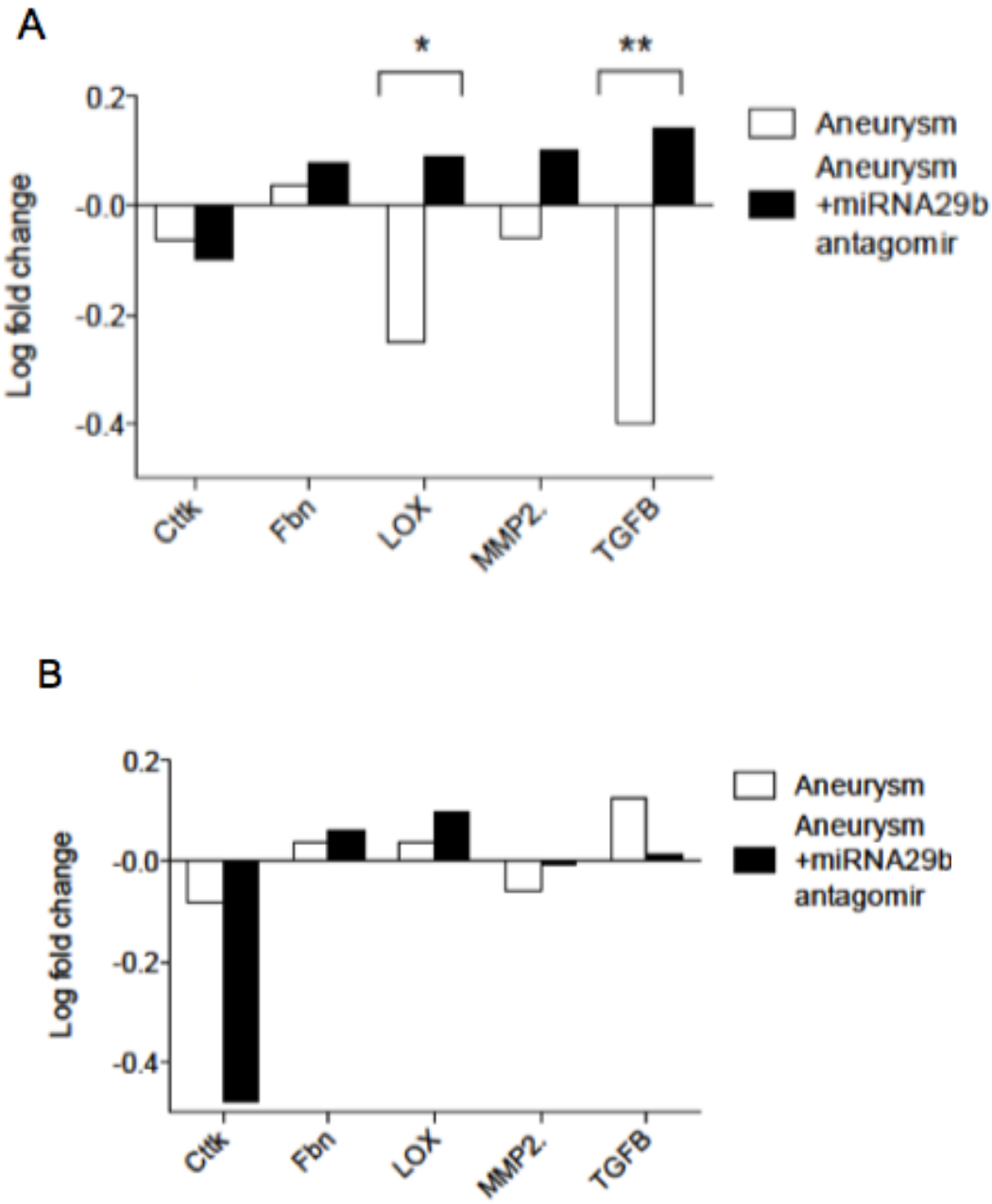

Fig 6.21 RT- PCR data showing average log fold change differences in gene expression of CttK, FBN, LOX, MMP-2 and TGFβ

A) Average log fold change differences in expression of CttK, FBN, LOX, MMP-2 and TGF-β in AmiR29b treated mVSMCs co-cultured with T lymphocytes ($CD3^+$) derived from aortic aneurysm from $ApoE^{-/-}$ATII. There is significant up regulation of TGFβ gene along with LOX in

the mVSMCs (**P<0.01, *P<0.05). B) Average log fold change differences in expression of CttK, FBN, LOX, MMP2 and TGFβ in AmiR29b treated mVSMCs co-cultured with B lymphocytes ($CD19^{+}$) derived from the supra renal aortic aneurysm from $ApoE^{-/-}$ATII infused group. There is no statistical change in cellular gene expression pattern.

C

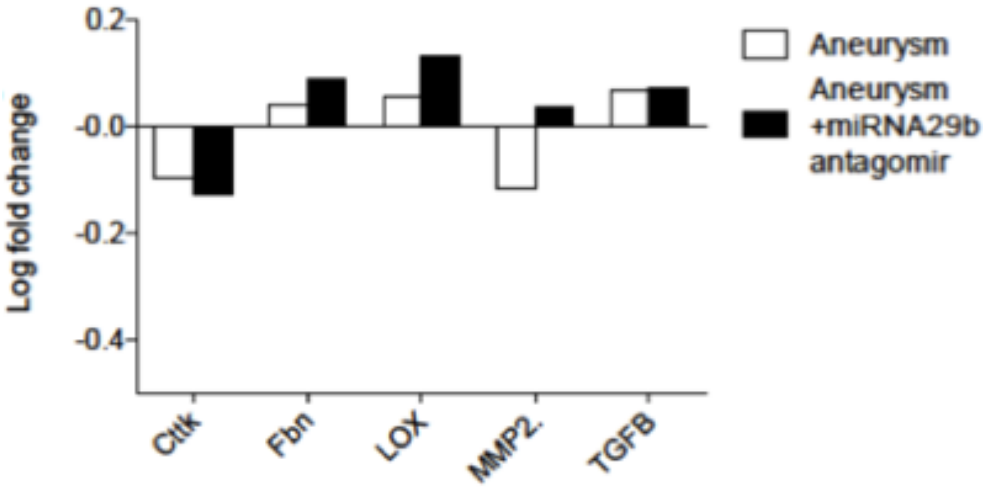

D

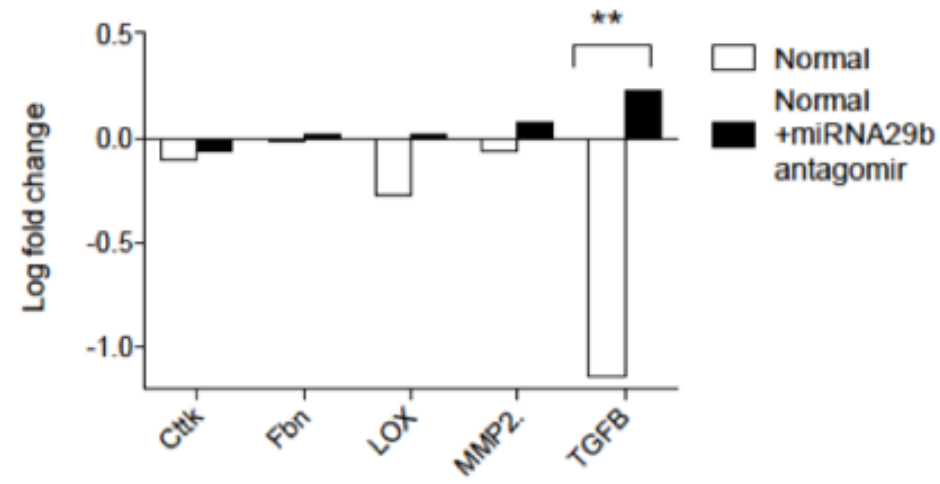

C) Average log fold change differences in expression of CttK, FBN, LOX, MMP2 and TGFβ in AmiR29b treated mVSMCs co-cultured with B and T lymphocytes ($CD3^{+}$ and $CD19^{+}$) derived from the suprarenal aortic aneurysm from $ApoE^{-/-}$ATII infused group. There is no statistical change in cellular gene expression pattern. D) Average log fold change differences in expression of CttK, FBN, LOX, MMP2 and TGFβ in AmiR29b treated mVSMCs co-cultured with

T lymphocytes ($CD3^+$) derived from the normal aorta from the $ApoE^{-/-}$ATII infused group. There is up-regulation of the TGFβ genes to a greater degree in the normal aortic wall derived lymphocyte incubated mVSMCs in the AmiR29b group compared to controls (**P<0.05).

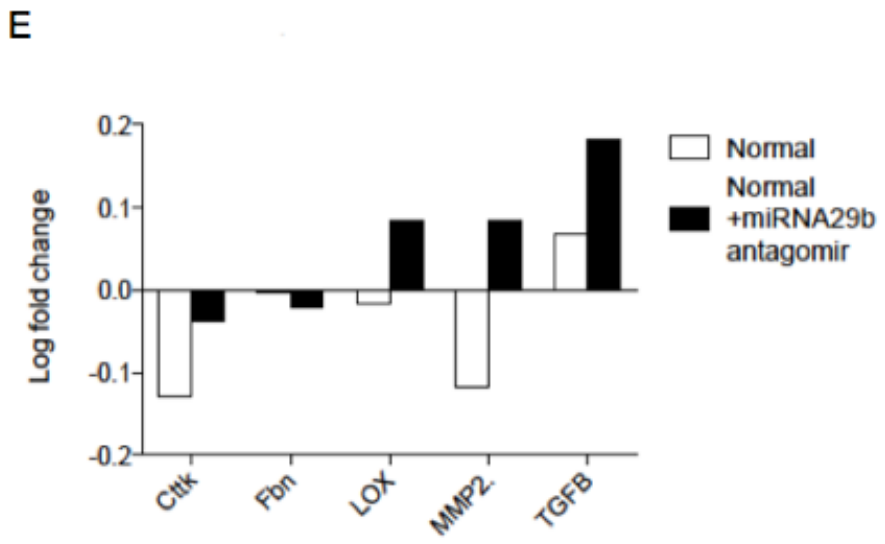

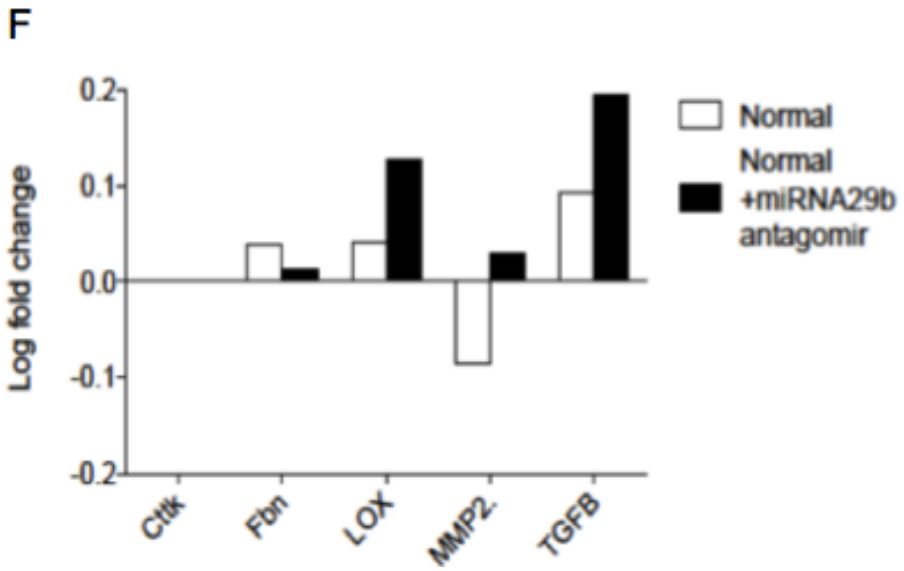

E) Average log fold change differences in expression of CttK, FBN, LOX, MMP2 and TGFβ in AmiR29b treated mVSMCs co-cultured with B lymphocytes ($CD19^+$) derived from normal aortic wall from $ApoE^{-/-}$ATII infused group. There is no statistical change in cellular gene expression pattern. F) Average log fold change differences in expression of CttK, FBN, LOX,

MMP2 and TGFβ in AmiR29b treated mVSMCs co-cultured with T and B lymphocytes ($CD3^+$ and $CD19^+$) derived from normal aortic wall from $ApoE^{-/-}$ATII infused group. There is no statistical change in cellular gene expression pattern.

6.5 Discussion

6.5.1 MiR29b

MiR29b is a critical regulator of elastin turnover in aortic wall by modulating several genes and pathways responsible for ECM composition, dynamics and inflammatory interactions. In murine aortic aneurysms inhibition of miR29b lead not only to decrease in the in the incidence of aortic aneurysms, their speed of progression, maximal eventual aortic diameter and therefore rupture risk. The extensive aortic remodelling response seen on MRI using ESMA, demonstrated aortic wall composition was significantly altered with the antagomir. The increase in wall thickness and up regulation in elastin being laid down within the tunica media was responsible for high wall signal in the AmiR29b group compared to the controls. This correlates with histological preservation of the elastic lamellae in the tunica media. Moreover the tropoelastin synthesis in the aortic wall was significantly elevated on immunohistochemistry staining with tropoelastin specific antibody. This represents up regulation of the elastin synthesis pathway possibly with increased up regulation of lysyl oxidase and TGFβ production. Concomitantly the aortic wall histomorphometric analysis reveals a decrease in inflammatory cell infiltration in AmiR29b inhibited wall is decreased compared to controls. The number of T lymphocytes ($CD3^+$), natural killer cells (NCAM1) and macrophages (Mac2) were down regulated in the antagomir group.

Lysyl oxidase is responsible for catalysing an oxidative de-amination of lysine and hydroxylysine residues to peptidyl a-aminoadipic-semialdehydes in aortic wall. These highly reactive semialdehydes can spontaneously condense to form intra- and intermolecular covalent bonds that assure ECM stability [502]. Additionally lysyl oxidase has been demonstrated to suppress secretion of MCP-1 in cultured VSMCs [503,504]. In murine models of aneurysms enhanced

lysyl oxidase activity has demonstrated decreased macrophage infiltration and aneurysm progression [502]. Furthermore inactivation of the lysyl oxidase gene LOX leads to aortic aneurysms, cardiovascular dysfunction and perinatal death in mice [172]. Hence the up regulation of LOX expression in miR29b inhibited group in our aneurysm co-culture system demonstrates a protective phenotype in VSMCs. Similarly in the normal aortic co-cultured lymphocytes with VSMCs there is a marked up regulation of TGFβ gene expression. TGFβ has been shown to increases LOX expression activity in the VSMCs [115,505]. TGFβ concomitantly increases collagen synthesis in VSMCs and known to enhance peptidoglycan and fibronectin production in rat aortic models [494].

TGFβ activity protects against inflammatory aortic aneurysm progression and complications in the ApoE$^{-/-}$ATII infusion model [113]. Treatment with TGFβ1, a known regulator of miR29b expression and a profibrotic stimulant, has been reported to significantly decrease miR29b expression in human aortic adventitial fibroblasts but not in human aortic smooth muscle cell lines [432,507]. Function of TGFβ in aortic aneurysm formation remains controversial. Hyperactive signaling of TGFβ is associated with Marfans syndrome and has been shown to stimulate multiple signaling molecules including Smad2/3, RhoA and MAP kinases in FBN1 mutant mice [508]. However, other studies suggest TGF-β has a protective role in aortic aneurysms. Neutralization of TGFβ prevents the resistance of normocholesterolemic C57BL/6 mice to angiotensin-II induced aneurysm formation [113]. Increased TGFβ by endovascular gene delivery in rats has been associated with diameter stabilization, decreased inflammatory infiltration, reduced MMP-2 and MMP-9 expression and reduced elastin degradation [114].

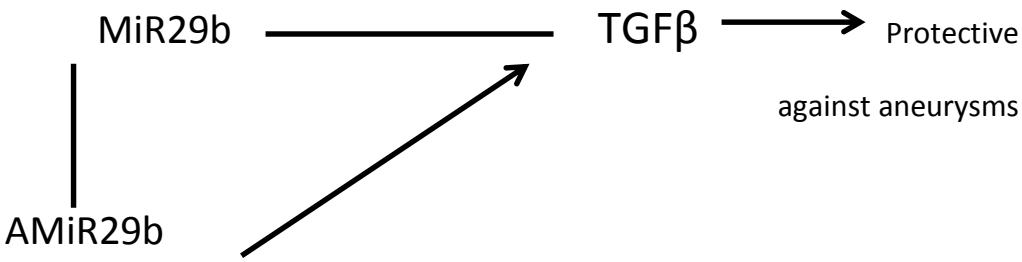

miR29b has been shown to down regulate TGFβ in aneurysms. AmiR29b can be protective by regulating VSMC targeted TGFβ expression. We demonstrate augmentation of TGFβ gene expression following miR29b inhibition supporting its protective role in aortic aneurysm development by altering VSMC phenotype to elastosythetic type. In the aneurysm group the addition of a miR29b inhibitor reversed the pattern of gene expression across all genes investigated, with the exception of Cttk, which was upregulated compared to the control. *In vivo* administration of the AmiR29b decreased expression of miR29b and increased expression of its target genes: LOX. AmiR29b can increase synthesis of ECM synthesis genes to leading to positive aortic remodelling response, stabilize aneurysm lesions and prevent aortic dilatation and rupture.

MiR29 in human thoracic aortic aneurysmal disease is up regulated [417], whereas in a small group of abdominal aortic aneurysm patients there is a decrease in miR29b expression [504,505]. Other authors have found no difference in the expression of miR29b in thoracic aneurysms [509], however they describe a drop in miR29a levels compared with controls. The likely explanation of such variations in the results is highly anatomically specific differences between sites in the aortovascular tree. Hence we specifically and accurately removed the suprarenal aortic aneurysm section and divided any normal remaining aorta into thoracic descending or infrarenal abdominal aorta for analysis.

There were no aneurysms with thrombus in our samples from the miR29b groups or substantial atherosclerotic plaques as the aneurysms were away from the major aortovascular branch points at which traditionally plaques are described in this model [262]. Inhibition of miR29a alters ELN expression in different human cells [510] and our work using ESMA *in vivo*, histomorphometric assessment of aortic tissue, genomic and proteomic alteration of targets and *in-vitro* co-culture studies support this supposition.

The cardiac manifestations of AmiR29b with reduction in LVES and LVED dimensions might be the result of regulation of cardiomyocyte fibrosis with augmentation caused by ATII induced BP changes [511]. Cardiac fibroblasts communicate in a paracrine manner with the myocytes allowing modulation of ECM and cell-cell interactions [512]. MiR29b suppresses the expression level of collagens and ECM proteins and is normally down regulated in myocardial infraction and cardiac disease models of LV hypertrophy, contributing to scar formation and cardiac fibrosis [442,474,499]. Treatment with AmiR29b could, therefore, result in increased production of collagens in the myocardium to prevent changes in cardiac dimensions in response to hypertension in the ApoE$^{-/-}$ATII model.

6.5.2 MiR195

In this study we report decreased miR195 in vivo, but no effects on aortic phenotype in the ApoE$^{-/-}$ATII model of aneurysms. MiR195 is a member of the miR15 family and as such ubiquitously expressed miR with and highly conserved seed region. This implies overlap in the miR targets between different members of the family [512]. miR195 plays a critical role in the cell cycle with active post-transcription changes to proliferation and apoptosis previously reported. miR195 can regulate WEE1, CDK6, Sirt1 and Bcl2 expression [502-505]. Within the cardiovascular system miR195 is upregulated in

the heart after transverse aortic constriction or expression of activated calcineurin. miR195 overactive and expression leads to cardiomyocyte hypertrophy and heart failure in transgenic animals [474]. Embryonic forced expression of miR195 lead to ventricular hypoplasia and ventricular septal defects [517,518]. This was due to cell cycle arrest in the development of βmyosin heavy chain [517,518]. Chek1 as a direct regulator of mitosis was identified to be under the control of miR195 [517,518]. miR195 have been shown to effect ECM deposition [519]. There was a decrease in damage to renal mesangial cells with decreased apoptosis in early diabetic renal injury in mice when miR195 was inhibited [520]. Inverse association between miR195 expression and INFβ induced hepatic fibrosis has been reported [479]. Prior to our study the role of miR195 within the vasculature was not known. We have demonstrated that AmiR29b is far more effective than AmiR195 in reducing aortic diameter, volume and mortality from aortic aneurysms. There are increases in the vessel wall elastin content earlier on with AmiR195 but by day 15, these changes are reversed. Consistent with the *in vivo* data, the *in vitro* data suggests that AmiR19b has a more robust effect on ECM deposition by VSMCs than AmiR195. These apparent differences for AmiR29b might be due to its protective effects on the aortic wall in addition to the effects on elastin homeostasis, namely the effects on TGFβ and other ECM proteins such as collagen.

Future work needs to focus on the mechanism of miR29b-mediated effects on VSMCs through expression changes in LOX and TGFβ activity. Analysis of the other ECM components and how these might be affected by AmiR29b to explain the changes in the aortic phenotype.

Chapter 7: The effect of immune cells on vascular smooth muscle cell phenotype

7.1 Introduction

The functional imaging data from the ^{18}F-FDG and ESMA *in vivo* studies has shown that lymphocytes infiltrate the aneurysm wall in large numbers and that these may act locally to affect the capacity of vascular smooth muscle cells (VSMCs) to regulate the turnover of ECM proteins such as elastin that is vital for aortic wall integrity.

i) Lymphocyte infiltration - The presence of T- and B-cells in the aneurysm wall suggests they can directly alter VSMC viability, proliferation and synthetic ability [138,428,521]. The immune composition of the aortic wall is dynamic and changing. The predominant immune cell types within the aorta are $CD3^+$ T-cells and $CD20^+$ B-cells with fewer $CD68^+$ macrophages[520,521].

When T-cell function is assessed using intracellular staining and flow cytometry, 15.7% of T-cells are shown able to progress to the proliferative phase of the cell cycle. T-cells also differentiate down the $CD4^+$Th1 phenotype characterized by the production of TNF-α and IFN-γ, variable amounts of IL-5 and IL-6 and no production of the Th2-type cytokines IL-4 or IL-10. In human studies, T-cells produce IFN-γ, in pro-inflammatory states, with these effects predominating over IL-4, reflecting a Th1 cytokine response [110,138]. Quantitative RT-PCR has shown increased IFN-γ transcript levels in the aorta compared with IL-2 and IL-4[110,138]. However advanced human aneurysms have also been shown to be associated with Th2 expression with IL-4 and IL-10 levels increasing[522]. As these cytokines inhibit the macrophage expression of MMP9, they may have a role in protecting the aorta from degradation.

There is currently no evidence that Th17 or T-regulatory cells (T-regs) are present in the aortic wall and if present what their role would be (potentially for dampening the pro-inflammatory response and leading to a more protective remodelling phenotype). Our work has suggested the presence of activated T-cells, memory T-cells and T-reg cells in the aneurysm compared to an absence of these cells in the normal aortic wall. It is intriguing to investigate which T-cell phenotype(s) predominate and a possible role for these cells in the expansion of the aortic wall.

B-cells infiltrating the wall of aortic aneurysms and express immunoglobulin heavy chains[123]. The ratio of tissue resident $CD19^+$ B-cells compared to peripherally circulating $CD19^+$ B-cells was greater in human AAA patients[96]. On phenotyping the surface expression of light chain, $kappa^+$ and $lambda^+$ with k/λ ratio was maintained in patients AAA and peripheral circulation[96]. The isotype of surface Ig expressed by infiltrating B cells is different from circulating B cells with fewer B cells expressing IgD+IgM+ phenotype; if not the secretory phenotype there might be other populations present in tissue.

The antigenic triggers that stimulate these cells to enter the aortic wall, and remain there, are unknown. We have demonstrated that memory B-cells, synthetically active B-cells (producing IgM/IgD and a specialised subset of B-regs are present in the aneurysm wall). These cells are absent in the normal aortic wall. The B-regs are known to interact and modulate T-cell activity and expression[368,523], but the biological role of these B-cells in the aortic wall remains unclear.

ii) VSMC activity – These cells are the key biological determinants of aortic wall function and its metabolic activity. When compared with normal aortic wall, aneurysm derived VSMCs produce a higher level of MMP2 and MM9[524-526]. This may contribute to ECM degeneration and aortic wall weakness. It is

not known why this occurs[527]. The effect of immune cells on VSMC activity and has not yet been elucidated.

VSMCs are responsible for aortic wall ECM maintenance, with a continuous low-level production of tropoelastin (that is cross-linked by lysyl oxidase to form elastin) and separate pathways to form collagen[400,408,440]. During *in-vitro* studies with decellularised porcine aortas seeded with macrophages and lymphocytes, the induced pro-inflammatory changes are reversed by seeding the decellularised porcine xenografts with healthy VSMCs, thus preventing aneurysm development[108]. VSMCs repair aortic wall damage through increased proliferation, migration and gene expression for ECM proteins, partly through elastosynthetic enzyme systems[515,516]. During the late stages of aneurysm development there is increased apoptosis of VSMCs with loss of the repair mechanisms to maintain ECM in the aortic wall[528]. There is an increased expression of p53 and p21 in the aortic aneurysm wall and this correlates to decreased levels of VSMCs and ECM content[529,530]. VSMCs have a key regulatory role in maintain aortic wall ECM homeostasis.

TGFβ seems to be a key regulatory of VSMC behaviour. Increased TGFβ signaling is associated with aortic aneurysms in Marfans syndrome as already discussed in Chapter 1. It is worth noting again that TGF-β antagonists such as the angiotensin II type 1 receptor blocker, losartan prevents aortic root dilatation in fibrillin-1 mutant mice[508,509]. TGFβ1 is able to inhibit VSMC proliferation and induce apoptosis by arresting the cells in G1 phase of the cell cycle[532]. Increased TGFβ expression is associated with increased VSMC density at regions of aortic dilatation with an increased VSMC TUNEL staining, decreased $Ki67^{+}$ staining and decreased cell proliferation[508]. There are some studies that however suggest TGFβ expression can confer a protective phenotype against inflammatory aortic aneurysm disease[113]. Neutralization of

TGFβ prevents the resistance of normocholesterolemic C57BL/6 mice to ATII induced aneurysms[113]. Anti-TNFβ antibody enhanced monocyte activity and MMP12 activity and levels leading to aneurysm progression[46,84,113,234]. There was no affect on aneurysm progression by IL4, IL6, TNFα, IFNγ inhibition but genetic deletion of T-and B-cells results in partial protection to development of aneurysms[113]. The lymphocyte interaction with VSMCs and TGFβ signaling may therefore be important in the pathogenesis of aneurysms.

7.2 Aims

The aims of this part of the study were to determine the effect of lymphocytes isolated from normal and aneurysmal human and murine wall on VSMC activity.

1) Isolate $CD3^+$ T-cells and $CD19^+$ B-cells from human and murine aortic aneurysm tissue and normal aortic wall

2) Develop an *in vitro* co-culture system with VSMCs and tissue-derived lymphocytes to study the affect of lymphocyte populations on human and murine VSMC proliferation, viability and synthetic capacity

3) Determine the alteration of the immune cell phenotype when interacting with VSMCs

7.3 Methods

A schematic diagram of the experimental layout below to summarise the techniques used to study the interaction between lymphocytes and VSMCs.

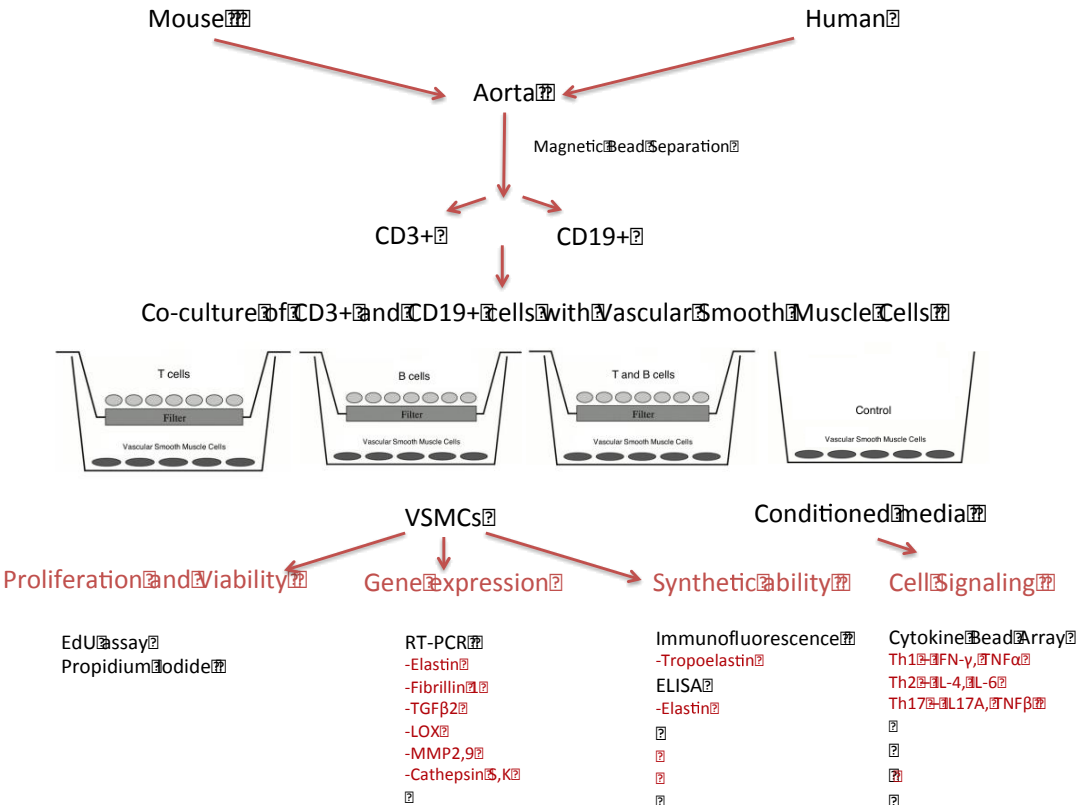

Fig 7.0 Experimental layouts for studying the interaction between tissue-derived lymphocytes on VSMC genotype and phenotype

The $CD3^+$ T lymphocytes and $CD19^+$ B lymphocytes isolated from normal and aneurysmal murine and human aortic wall were co-cultured with VSMCs for 5days. Thereafter the VSMCs were analysed for proliferative capacity, viability and synthetic activity. VSMCs were also assessed for their extracellular matrix remodeling capacity using RTPCR and ELISA. VSMC conditioned media analysed for inflammatory cytokine content.

7.3.1 Human aortic samples

Aortic aneurysm samples were collected from patients undergoing elective surgical repair (n=5). Three were thoracic aortic aneurysms and two abdominal aortic aneurysms. Normal aged and sex matched control aortic biopsy specimens were collected from patients undergoing other cardiac operations such as coronary artery bypass surgery where the ascending the aorta was exposed and clamped allowing tissue biopsy to be taken (n=9). The tissue collection was under the ethics protocol as described previously in section 3.3.1, page 101.

7.3.2 Murine ApoE$^{-/-}$-ATII infusion model of aortic aneurysms

This was carried out as described in section 4.3.1 on page 147.

7.3.3 Lymphocyte extraction

7.3.3.1 Human aortic wall processing

Aortic biopsies were transferred in cold 0.9% saline and processed within 1hr of harvesting. The aortic wall was thoroughly washed in cold PBS to remove all blood contamination. The EC layer was scrapped off with a scalpel and the aorta finely sectioned manually. Approximately 4g of tissue was incubated in 15mls of PBS containing 0.5%BSA and 1mM EDTA with 1 mg/ml collagenase D, 100 units/ml DNAase I and 500 units/ml hyaluronidase IV-S at 37°C for 30mins. Samples were filtered through a 100µm cell strainer, washed x2 at 450g in PBS and pelleted. The final resuspension in PBS was incubated with 100µl of Annexin V microbeads (dead cell removal) for 15mins at room temperature (Miltenyi Biotec, Bergisch Gladbach, Germany). Annexin V microbeads bound phosphatidylserine on the outer-membrane of dead cells. The cell/bead suspension was applied to a MACS MS column (Miltenyi Biotec) placed in the magnetic field of a magnetic bead separator (Miltenyi Biotec),

and the effluent collected as a live cell fraction. Live cells were pelleted, re-suspended in 80µl of wash buffer (PBS supplemented with 1% BSA and 2mM EDTA) and incubated with CD3ε Biotin (10µl per 10^7 total cells) (Miltenyi Biotec) for 15mins at 4°C. Cells were washed with wash buffer, pelleted and re-suspended in anti-biotin microbeads (20µl per 10^7 total cells) (Miltenyi Biotec) and incubated for 15mins at 4°C. The cell suspension was applied to a MACS MS column and unbound cells washed away with wash buffer. $CD3^+$ cells were collected from the column using a plunger. The remaining unbound cells were pelleted, re-suspended in 90µl of buffer and incubated with $CD19^+$ microbeads (10µl per 10^7 total cells) (Miltenyi Biotec) for 15mins at 4°C. $CD19^+$ cells were collected as above. Cells were counted using a haemocytometer and viability determined using trypan blue. The purity of $CD3^+$ and $CD19^+$ lymphocyte populations was determined by $CD3^+$ and $CD19^+$ staining using flow cytometry.

7.3.3.2 Murine aortic harvest

This was done as outlined in section 4.3.4 on page 149. Prior to processing the aortic wall was washed additionally with PBS and excess connective tissue and periaortic fat was meticulously dissected away using an operating microscope (Leica Microsystems ltd, UK). The endothelial cell layer was scraped off after the aorta was opened longitudinally and the aorta digested as previously described in section 4.3.5 on page 149. Thereafter the extracted cells in suspension were treated in the same manner as human cells. 20µl anti human $CD3^+$, $CD19^+$ beads were used (Miltenyi Biotec, Bergisch Gladbach, Germany). The purity of $CD3^+$ and $CD19^+$ lymphocytes was determined by $CD3^+$ and $CD19^+$ staining by flow cytometry.

7.3.4 Flow cytometry

Cells were centrifuged at 300g for 10mins and re-suspended in FACS buffer (PBS, 1%BSA, 2mM EDTA) and incubated in FcR block (Miltenyi Biotec) for 15mins at 4°C. Staining was performed with the following primary antibodies:

Table 7.0 Primary flow cytometric antibodies for immune cell typing

(All antibodies were obtained from BD Biosciences)

Murine				
Cell	**Cell surface marker**	**Fluorophores**	**Concentration**	**Code**
Leukocyte	**CD45**	**PE**	**0.25 µg/ml**	**553081**
T-cell	**CD3**	**PE-Cy7**	**0.1 µg/ml**	**552774**
B-cell	**CD19**	**APC**	**0.25 µg/ml**	**550992**
Monocyte	**CD16**	**APC-647**	**5 µg/ml**	**558636**
Human				
Leukocyte	**CD45**	**APC-H7**	**3µg/ml**	**560178**
T-cell	**CD3**	**FITC**	**15µg/ml**	**555339**
B-cell	**CD19**	**PeCy7**	**6µg/ml**	**557835**
Monocyte	**CD16**	**PE**	**5 µg/ml**	**555407**

Flow cytometric sample processing and analysis was carried out using the Canto II as described previously in sections 3.3.4, 3.3.6, pages 103 and 106.

7.3.5 *In-vitro* co-culture studies

Human mature aortic VSMCs (obtained and maintained after removal and cultured from patients donated aortae) were plated at passage 5 and human umbilical arterial VSMCs plated at passage 11 (Cell Biologics, Chicago IL, USA), and grown in DMEM (1g/l D-glucose, containing 10% FCS, 1% streptomycin,

1% penicillin and 5% L-glutamine). Murine VSMCs were used at passage 5 (Cell Biologics, Chicago IL, USA) and grown in DMEM (1g/l D-glucose, containing 10% FCS, 1% streptomycin, penicillin and L-glutamine). All VSMCs were plated at $2x10^4$ in 12 well adherent plates (Greiner Bio-one, UK) and incubated for 24hrs at 37°C, 5% CO_2 prior to the co-culture. Lymphocytes were cultured in 0.4μm cell culture inserts (Greiner Bio-one, UK) with RPMI medium (supplemented with 10% FCS, 1% streptomycin, 1% penicillin and 5% L-glutamine). Lymphocyte populations were co-cultured with VSMCs as $CD3^+$ T-cells, $CD19^+$ B-cells or a combination of $CD3^+CD19^+$ T and B-cells. Control VSMCs wells were grown without lymphocyte co-culture (Standard errors were obtained from n=6 experiments). The cells were incubated for 5days. All experiments were terminated on day 5 to carryout the various analyses. The plating densities are given in Table 7.1.

Table 7.1 VSMC plating density

Murine			
Cell	**Marker**	**Tissue**	**Number**
T-cells	**$CD3^+$**	**Normal aorta**	**$5.3x10^5 \pm 6.2x10^4$**
B-cells	**$CD19^+$**	**Normal aorta**	**$2.4x10^5 \pm 2.3x10^4$**
T-cells	**$CD3^+$**	**Aneurysm**	**$5.5x10^5 \pm 1.4x10^5$**
B-cells	**$CD19^+$**	**Aneurysm**	**$3.9x10^5 \pm 4.8x10^4$**
T and B-cells	**$CD3^+CD19^+$**	**Aneurysm**	**$1.6x10^5 \pm 3.6x10^5$**
Human			
T-cells	**$CD3^+$**	**Normal aorta**	**$1.14x10^6 \pm 2.9x10^5$**
B-cells	**$CD19^+$**	**Normal aorta**	**$5.58^6 \pm 1.9x10^5$**
T-cells	**$CD3^+$**	**Aneurysm**	**$1.17x10^6 \pm 5.4x10^5$**
B-cells	**$CD19^+$**	**Aneurysm**	**$1.34x10^6 \pm 5.9x10^5$**
T and B-cells	**$CD3^+CD19^+$**	**Aneurysm**	**$1.9x10^6 \pm 3.6x10^5$**

7.3.6 Assessing cellular proliferation and viability

7.3.6.1 5-Ethynyl-2-deoxyuridine (EdU) and propidium iodide assay

The VSMCs were plated on collagen coated 24-well coverslips (Sigma-Aldrich, Poole, UK). 5000 cells were co-cultured per well with the lymphocyte densities mentioned above. The VSMCs were incubated with 10µm EdU (Click-iT EdU Imaging Kit, Invitrogen, UK) 48hrs later. 5 days after the initial plating the cells were fixed in 4% paraformaldehyde (appendix 3, page 347) for 15mins. The cells were subsequently washed with PBS (3% BSA) and permeabilised in PBS (0.1% Triton X-100) for 20mins. Cells were washed again in PBS (3% BSA) and incubated in 100µl/well Click-iT reaction cocktail (1x click-it reaction buffer, $CuSO_4$, Alexa Fluor azide, reaction buffer additive) for 30mins at room temperature. Final wash with PBS (3%BSA) was performed and coverslips were mounted to glass slides using vectashield-mounting medium with DAPI (Vector Labs CA) containing 50µg/ml propidium iodide (BD Biosciences). Light microscope (Leitz, Leica, UK) was used with a microscope-mounted camera (Coolpix, Nikon, UK) along EXi Blue (QImaging), to capture light microscope and fluorescent images. Analysis of captured images was performed using Pro Plus software (Media Cybernetrics, USA) and Image J as described previously [532,533]. Proliferating cells were calculated as number of EdU stained cells/DAPI stained cells expressed as a percentage.

7.3.7 Gene analysis

7.3.7.1 RNA extraction

RNA was extracted using the RNAeasy MicroKit (Qiagen, Valencia, CA). Cell culture media was removed on day 5 and 700µl of QIAzol lysis reagent added. Lysate was vortexed for 1min to homogenize the cells and 140µl of chloroform was added to the homogenate, with centrifugation for 12,000g at

4°C for 15mins. Upper aqueous phase was transferred to a new collection tube and 525µl of 100% ethanol was added and transferred to an RNeasy MinElute spin column before centrifugation at 800g at room temperature for 15mins. The flow through was removed and discarded. The above steps were repeated after adding 700µl of buffer RWT, 500µl of RPE and 500µl of 80% ethanol independently. The column was placed in a new 2ml collection tube and centrifuged at full speed for 5mins. 14µl of RNase-free water was added to the center of the spin column and centrifuged at full speed for 1min to elute the RNA. RNA concentration was measured using a Nanodrop and the samples stored at -20°C.

7.3.7.2 cDNA synthesis

RNA was synthesized to cDNA using a high capacity RNA-to-CDNA kit (Applied Biosystems, Foster City, CA). All the RNA samples were normalised to the lowest concentration; murine VSMC normalised to 13.3ng/ml, human VSMC normalised to 15.8ng/ml. 2X reverse transcriptase buffer and 20x enzyme mix was added to each sample and the volume made up to 20µl using nuclease-free water. The plate was centrifuged and incubated at 37°C for 60mins. The reaction was stopped by heating to 95 °C for 5mins and cooling to 4°C.

7.3.7.3 RT-PCR

Each sample was diluted 1:60 with nuclease free water. A further 10 fold dilution series was carried out to produce 1:10, 1:100: 1:1000 dilutions of each sample. A nuclease free water negative control was also used. All samples were further diluted 1:5 with nuclease free water to produce enough cDNA for analysis of 10 genes. cDNA was transferred to a 96 well plate (5µl/well) for each gene to be analyzed. 1030µl of Taqman Fast Advanced Mastermix (Invitrogen) and 700µl of nuclease free water was added to 100µl

of assay gene/housekeeping gene (Invitrogen). An automated robotic system (Beckman Coulter) was used to transfer 50µl/well of mastermix to the cDNA samples. Samples from the 96-well-plates were then scaled up to a 384 well plate to make 4 replicates of each sample. The plate was run on the RT-PCR system (7900HT Fast Real Time PCR system Applied Biosystems) and data acquired using SDS (Invitrogen, UK) The data was analysed using DataAssist™ software v3.01. The cT values of each sample were normalized to the housekeeping genes and then expressed as fold changes relative to the control samples of each experiment using DataAssist™ software v3.1 (Invitrogen, UK). The average fold change was calculated and logged to allow an interpretation of gene regulation.

7.3.8 Assessment of VSMC synthetic ability

7.3.8.1 Immunofluroscence microscopy

5000 VSMCs/well were plated onto collagen coated 24-well coverslips and co-cultured with lymphocytes as previously described in section 7.3.6. Cells were fixed in 4% paraformaldehyde for 10mins, washed x1 in PBS and permeabilised in PBS (0.1% Triton X-100) for 3mins. The cells were placed for 45mins in protein block (Dako, Cambridgeshire, UK). The cells were incubated with the primary antibodies (Table 7.2) at room temperature for 1hr, followed by 2 washes in PBS for 5min and incubation in secondary antibodies (Table 7.3) for 45mins.

Table 7.2 Primary immunofluorescence antibodies

Primary Antibody	Marker	Species	Final concentration (μg/ml)	Code	Manufacturer
Anti-tropoelastin	Tropoelastin	Rabbit	1μl/ml	Ab21600	Abcam, MA
Anti-α-actin	α-smooth muscle actin	Mouse	1μl/ml	C6198	Sigma, UK

Table 7.3 Secondary immunofluorescence antibodies

Secondary Antibody	Fluorophore	Species	Final concentration (μg/ml)	Code	Manufacturer
Anti-rabbit	Alexa Fluor 488	Donkey	1μl/ml	711-546-152	Jackson Immunoresearch

The cells were washed in PBS x1 and coverslips mounted onto glass slides with vectashield mounting medium with DAPI (Vector Labs, CA). Slides were imaged on a Leica Leitz DMRB fluorescent microscope. Sequential images were taken of the complete cover slip with atleast 5 quadrants covered per coverslip and the fluorescent intensity measured using Image-J software (NIH, US).

7.3.8.2 ELISA

Elastin levels were measured using an elastin (ELN) ELISA Kit (USCN Life Science Inc, China). VSMCs were cultured at a density of $2x10^4$ and co-cultured with lymphocytes as described previously in section 7.3.5, page 279.

At day 5 the cells were lysed with RIPA lysis buffer (ThermoFisher Scientific) containing protease inhibitor 100ul-200µl. The standard stock solution of 120ng/ml was diluted to 30ng/ml with standard diluent and a double dilution series performed to produce standards ranging from 0.47 to 30ng/ml along with a blank standard at 0g/ml all at 100µl. Standards, blank and samples were added to the ELISA plate in duplicate and incubated at 37°C for 2hrs. The solution was removed, and the plate washed 5x with PBS of Detection Reagent A (100µl) was added and the plate incubated at 37°C for 1hr. The solution was removed, wells washed x3 with PBS and 100µl of Detection Reagent B added and incubated at 37°C for 30mins. Wells were washed x5 in PBS and 90µl of substrate solution added and incubated for 25mins at room temperature. The reaction was stopped on addition of 50µl of Stop Solution. The optical density of the solution in each well was measured on microplate reader (SpectraMax, Molecular Devices, USA) at 450nm.

7.3.9 Cytokine bead array (CBA) for cell signaling

This was carried out as previously described in section 6.3.9.5, page 235.

7.3.10 Statistical analysis

All results were normalised to the control group, which had no lymphocyte co-cultures. A Kolmogorov-Simonov test was used to test for normality. Data was analysed using SPSSv21 (IBM Inc, US). Graphpad Prism 5 has been used for selective graphical analysis. Data is presented as mean and standard error of the mean (SEM) or standard deviations (SD) when specified. Paired student's t-test was used when comparing parametric data. Non-parametric data was analysed using a Mann Whitney U test. For multiple variables a two-way ANOVA with post-hoc Bonferroni or Newman-Keuls correction was used. An alpha value of 0.05 was considered significant.

7.4 Results

7.4.1 Human

7.4.1.1 Aortic aneurysm formation

Three thoracic aortic aneurysms and two abdominal aortic aneurysms from patients undergoing elective surgical repair were obtained (n=5). Normal aged and sex matched control aortic biopsy specimens were collected from patients undergoing other cardiac operations (Table 7.4). There were no differences in the demographics between the thoracic and abdominal aortic aneurysm patients, with patients presenting with degenerate aortic aneruysms.

Table 7.4 Demographics of the patient population for the *in-vitro* aortic analysis

	Aneurysm N=5	Control N=9	P
Age	66	68	ns
Sex	4M:1F	7M:2F	ns
Hypertension	5	7	ns
Smoking	4	7	ns
Hyperlipidemia	5	9	ns

7.4.1.2 Verification and quantification of lymphocyte phenotypes(s) isolated from normal and aneurysmal wall

98.5% of live cells eluted from the T-cell column were $CD3^+$ (Fig 7.1) and 98% of live cells eluted from the B-cell column were $CD19^+$ (Fig 7.2). All the cells isolated from the normal human aortic wall were $CD45^+$ (leukocytes), but $CD16^-$ (demonstrating absence of monocyte lineage).

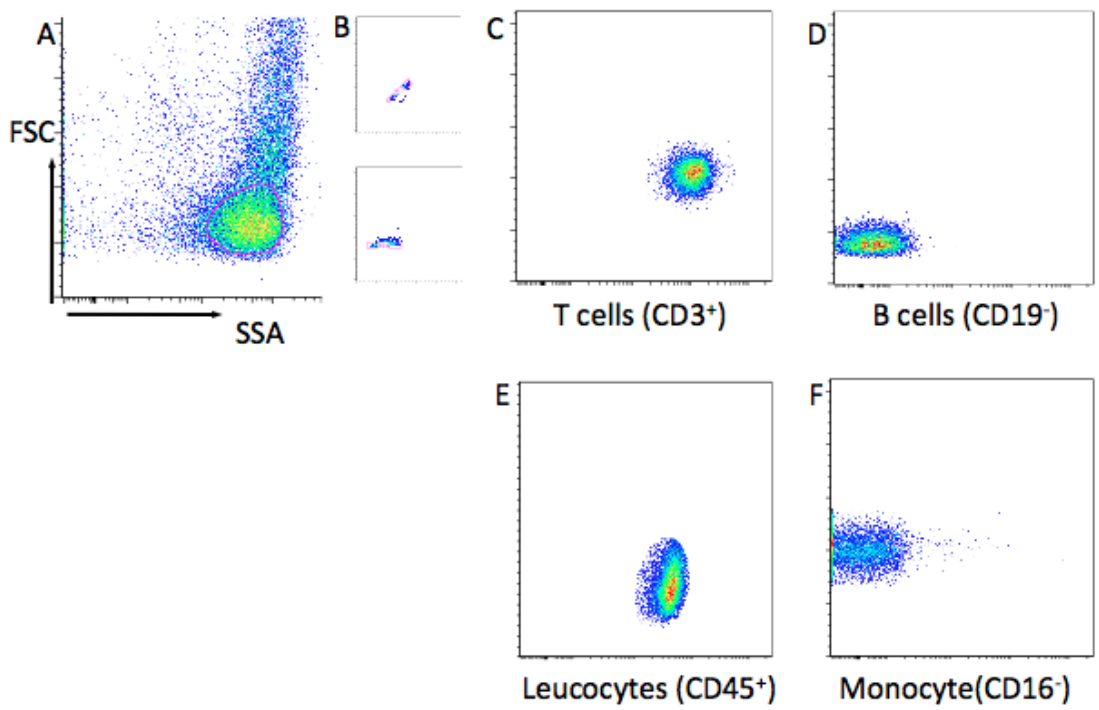

Fig 7.1 Flow cytometric analysis of T-cells isolated from normal human aortic wall by anti-CD3 linked magnetic beads

A) The cells population gated on forward and side scatter properties, clear population to gate on seen B) Doublet exclusion performed C) Gating on $CD3^+$ T lymphocytes that are extracted as a clean discrete population. D) The sample was stained and was negative for B-cell marker $CD19^+$ E) The cells in this population all stained positive for $CD45^+$ hence belonged to leukocyte fraction. F) The cells stained negative for $CD16^-$ demonstrating absence of monocytic lineage. (98.5% of $CD3^+$ cells were live with $12x10^3 \pm 8.5\ x10^3$ cells/mg tissue, N=4, 20 biopsy sites analysed).

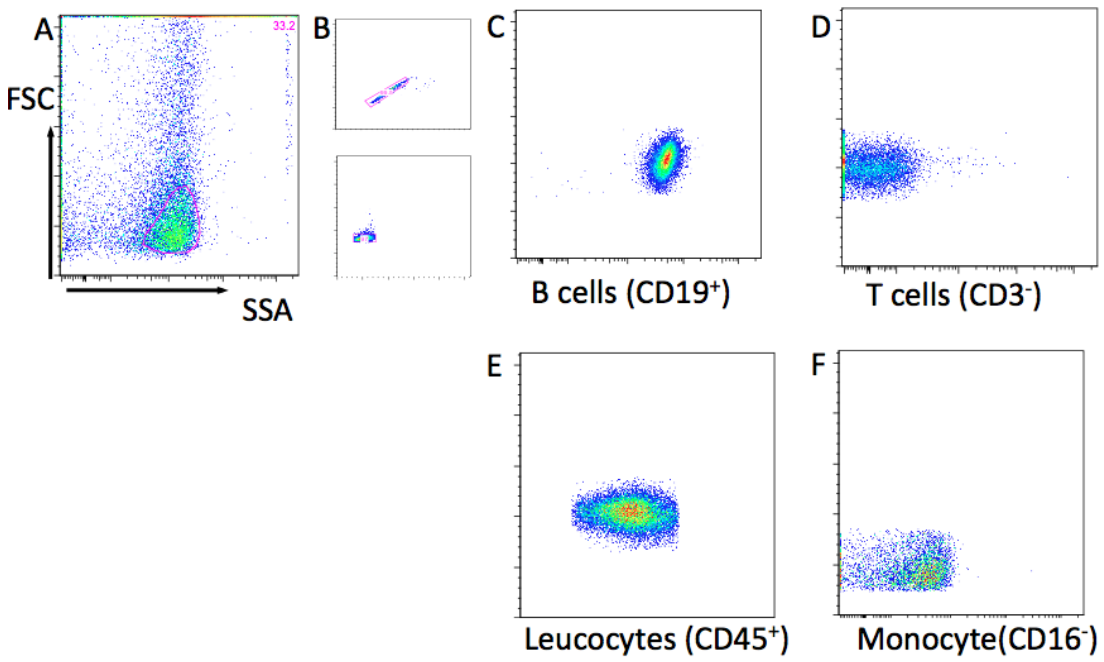

Fig 7.2 Flow cytometric analysis of B-cells isolated from normal human aortic wall by anti-CD19 linked magnetic beads

A) The cells population gated on forward and side scatter properties, clear population to gate on seen B) Doublet exclusion performed C) Gating on $CD19^+$ B lymphocytes that were extracted as a clean discrete population. D) The sample was stained and was negative for T-cell marker $CD3^-$. E) The cells in this population all stained positive for $CD45^+$ hence belonged to leukocyte fraction. F) The cells stained negative for $CD16^-$ demonstrating absence of monocytic lineage. (97% of $CD19^+$ cells were alive with $16x10^3 \pm 5.8\ x10^3$ cells/mg tissue, N=4, 20 biopsy sites analysed).

Flow cytometric analysis was carried out for $CD3^+CD19^+$ population and 98.5% of $CD3^+$ and 96% of $CD19^+$ cells were alive with $12\text{-}20x10^3$cells/mg tissue. The cells were $CD45^+$, $CD16^-$ (Fig 7.3). Annexin V bead separation of cells was performed and samples were run on the flow cytometer with and without Annexin V beads. This demonstrated a clear distinct difference in the populations with reduction in cellular debris and removal of dead cells (Fig 7.4).

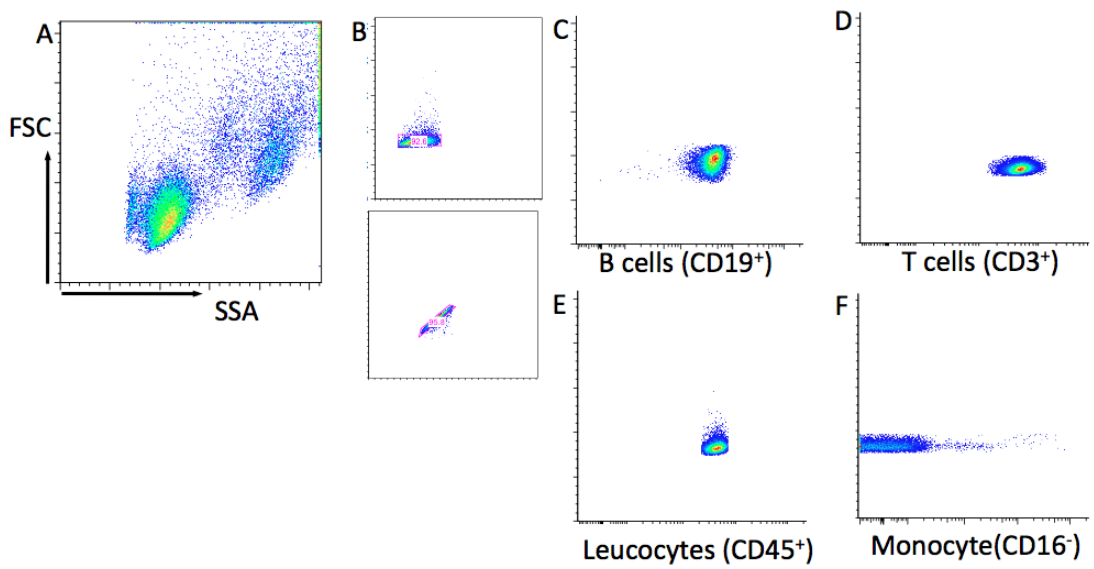

Fig 7.3 Flow cytometric analysis of B and T lymphocytes isolated from human aortic aneurysm wall by antibody-coated magnetic bead separation

A) The cells population gated on forward and side scatter properties, clear population to gate on seen B) Doublet exclusion performed C) Gating on $CD19^+$ B lymphocytes that are extracted as a clean discrete population. D) The sample was then gated for $CD3^+$ T lymphocytes. E) The cells in this population all stained positive for $CD45^+$ hence belonged to leukocyte fraction. F) The cells stained negative for $CD16^-$ demonstrating absence of monocytic lineage. (98.5% of $CD3^+$ and 96% of $CD19^+$ cells were live with 12-20x10^3±8.9 x10^3cells/mg tissue, N=4, 20 biopsy sites analysed).

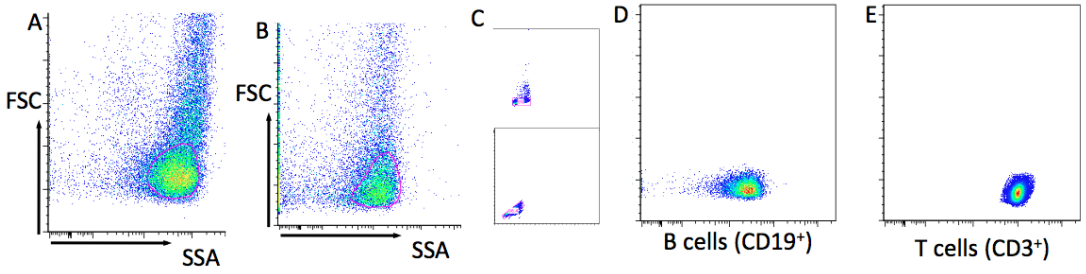

Fig 7.4 Representative flow cytometric analysis of anti-annexin V magnetic bead separated B and T lymphocytes

A) Pre and B) Post anti Annexin V bead extraction complete cell population on forward and side scatter properties. C) Doublet gating exclusion strategy D) clear $CD19^+$ B lymphocyte E) $CD3^+$ T lymphocyte populations extracted for human aortic aneurysm biopsy site.

7.4.1.3 Co-culture of VSMCs and lymphocyte

VSMC lymphocyte culture was set up as described with the pating densities and cell numbers. The final ratio of incubation for VSMC: T-cells was 1:50; VSMC: B-cells 1:10 and VSMC:T-B-cell 1:60. Lymphocyte viability was >96% in all experiments. The VSMCs were morphologically typical on light microscopy. There were no phenotypical differences between the groups on visual inspection at day 5 or when compared to the controls.

7.4.1.4 Proliferation/Viability

7.4.1.4.1 Assessment of VSMC proliferation

Fluorescent images show EdU staining of human vSMCs co-cultured with $CD3^+$, $CD19^+$ or $CD3^+/CD19^+$ lymphocytes isolated from aneurysm tissue (Fig 7.5).

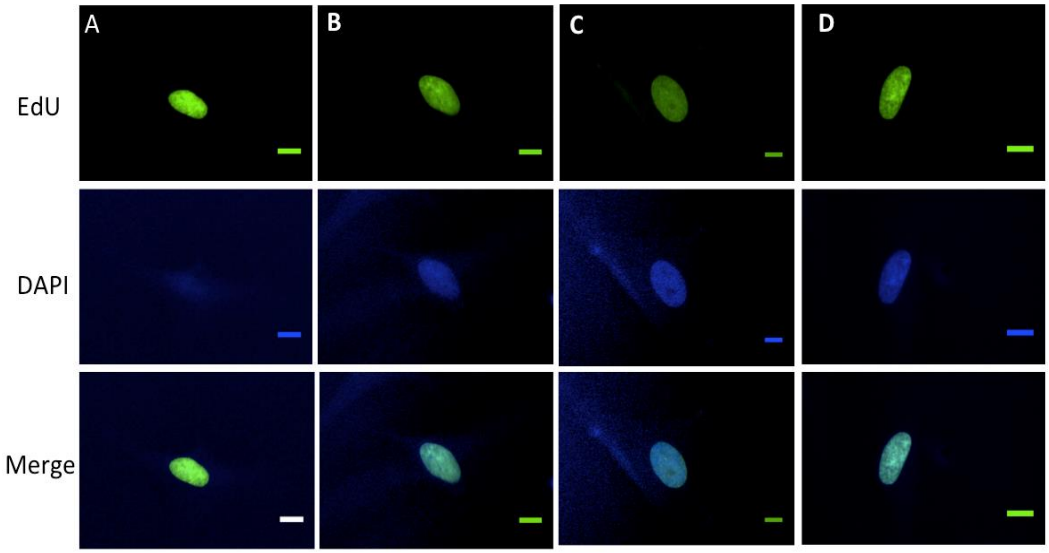

Fig 7.5 Proliferation of human VSMCs co-cultured with lymphocytes isolated from aortic aneurysm tissue

A) VSMCs co-cultured with $CD3^+$ T-cells B) VSMCs co-cultured with $CD19^+$ B-cells C) VSMCs co-cultured with T- and B-cells D) VSMCs alone. Images are representative of 3 independent experiments n=5, 20 isolates. Scale bar 10µm.

VSMC proliferation was higher when cells were co-cultured with lymphocytes from aneurysm aorta than normal aortic lymphocytes. All aneurysm lymphocyte subtype populations increased VSMC proliferation compared to the normal group (Fig 7.6). The results were not statistically significant despite showing a higher trend. The cell proliferation counts are normalized to control samples of VSMC wells.

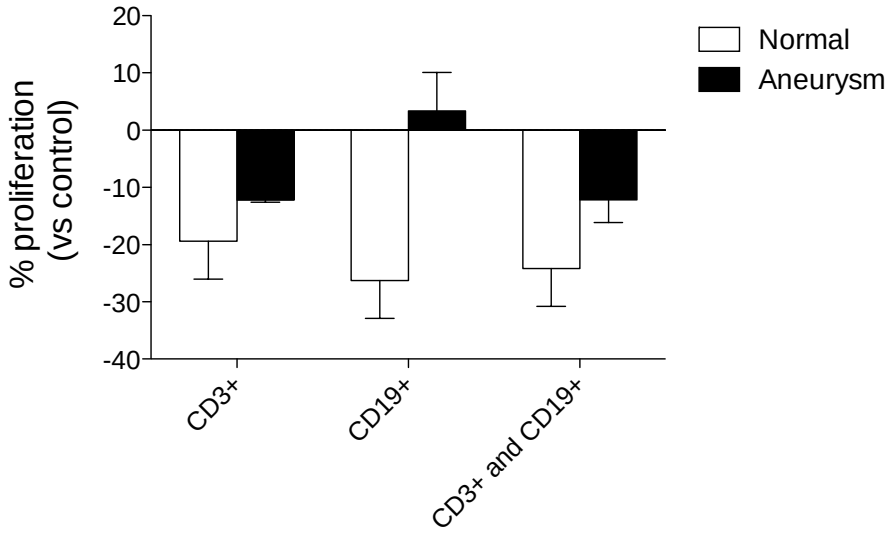

Fig 7.6 Percentage of proliferating human VSMCs co-cultured with lymphocytes isolated from aneurysm and normal aortic wall

Percentage of proliferating human VSMCs co-cultured with $CD3^+$, $CD19^+$ or $CD3^+/CD19^+$ lymphocytes. 3 independent experiments (n=5, 20 isolates)

7.4.1.4.2 Cell death - propidium iodide (PI) staining

Staining with PI (Fig 7.7) revealed that co-culture with lymphocytes regardless of sub-type resulted up to 30% death of human VSMCs. This applied to co-cultures with lymphocytes isolated from both aneurysm and normal tissue. There were no differences between the groups in the percentage of dead cells (Fig 7.8).

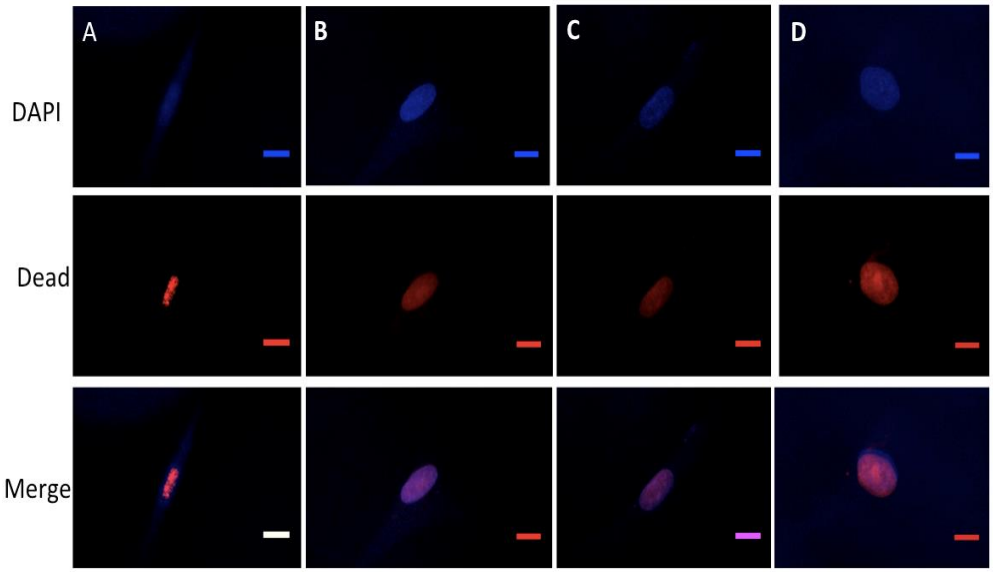

Fig 7.7 Representative micrographs of PI staining to show cell death of human VSMCs after co-culture with aortic wall derived lymphocytes

A) VSMCs co-cultured with $CD3^+$ T-cells B) VSMCs co-cultured with $CD19^+$ B-cells C) VSMCs co-cultured with T and B-cells D) VSMCs alone. Images are representative of two independent experiments n=5, 20 isolates. Scale bar 10μm.

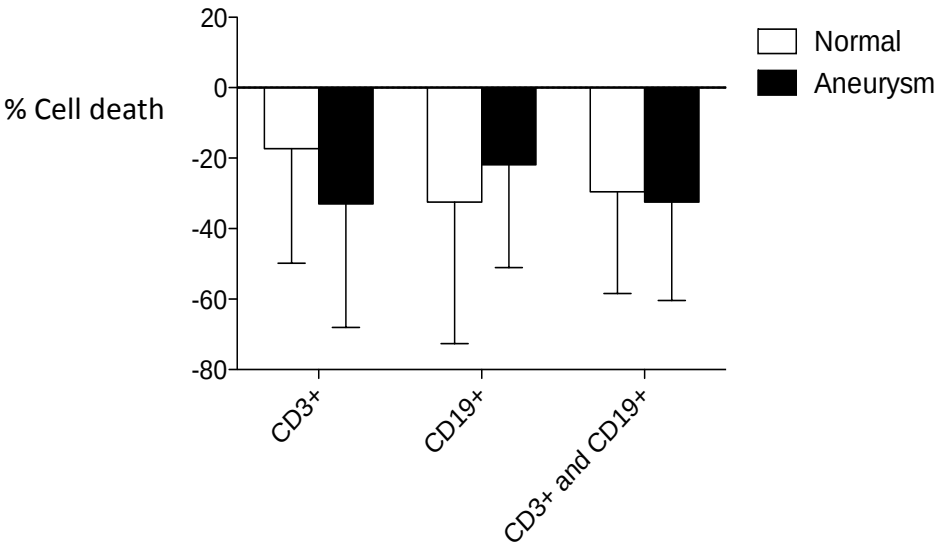

Fig 7.8 Percentage of dead human VSMCs following co-culture with lymphocytes isolated from aneurysm and normal aortic wall.

Results are from 2 independent experiments (n=5, 20 isolates) normalized to the control group.

7.4.1.5 Synthetic ability

7.4.1.5.1 Assessment of tropoelastin staining in VSMCs co-cultured with $CD3^+$, $CD19^+$ or $CD3^+/CD19^+$ lymphocytes

There was no apparent difference in VSMC tropoelastin staining (intensity or numbers of cells) between cells co-cultured with the different lymphocyte sub-populations in either the normal or aneurysmal wall (Fig 7.9) groups.

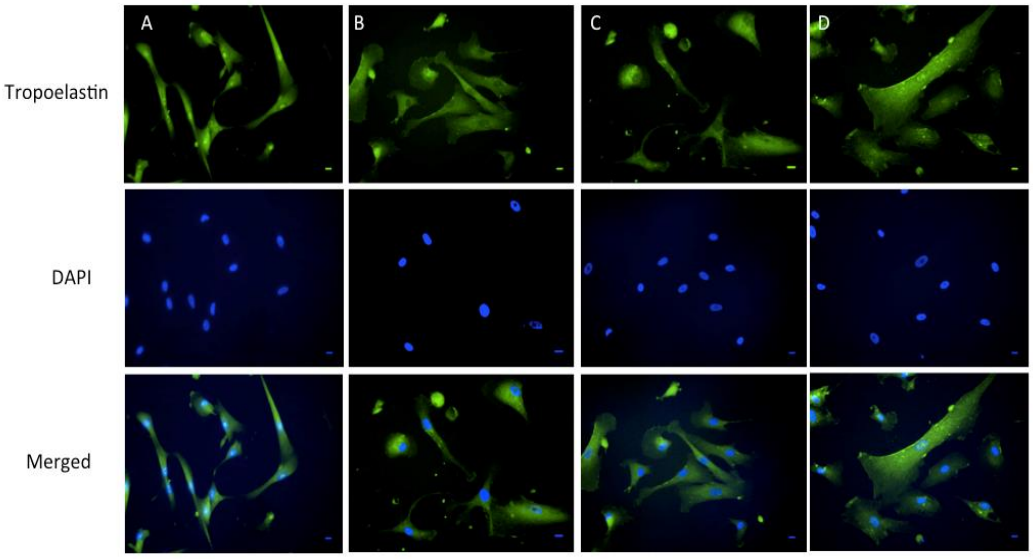

Fig 7.9 Representative immunostaining for tropoelastin at 5 days in human VSMCs co-cultured with aortic aneurysm lymphocyte populations

A) VSMCs co-cultured with $CD3^+$ T-cells B) VSMCs co-cultured with $CD19^+$ B-cells C) VSMCs co-cultured with T and B-cells D) VSMCs alone. Images are representative of 3 independent experiments with 6 co-culture experiments, n=5, 24 isoaltes. Scale bar 10µm.

For each experiement a negative control isotype to the primary antipbody was used. (Fig 7.10).

Fig 7.10 IgG anti-rabbit negative control. A) DAPI B) FITC C) Merge. Scale bar 10µm

All cells expressed alpha-actin, verifying their smooth muscle phenotype (Fig 7.11).

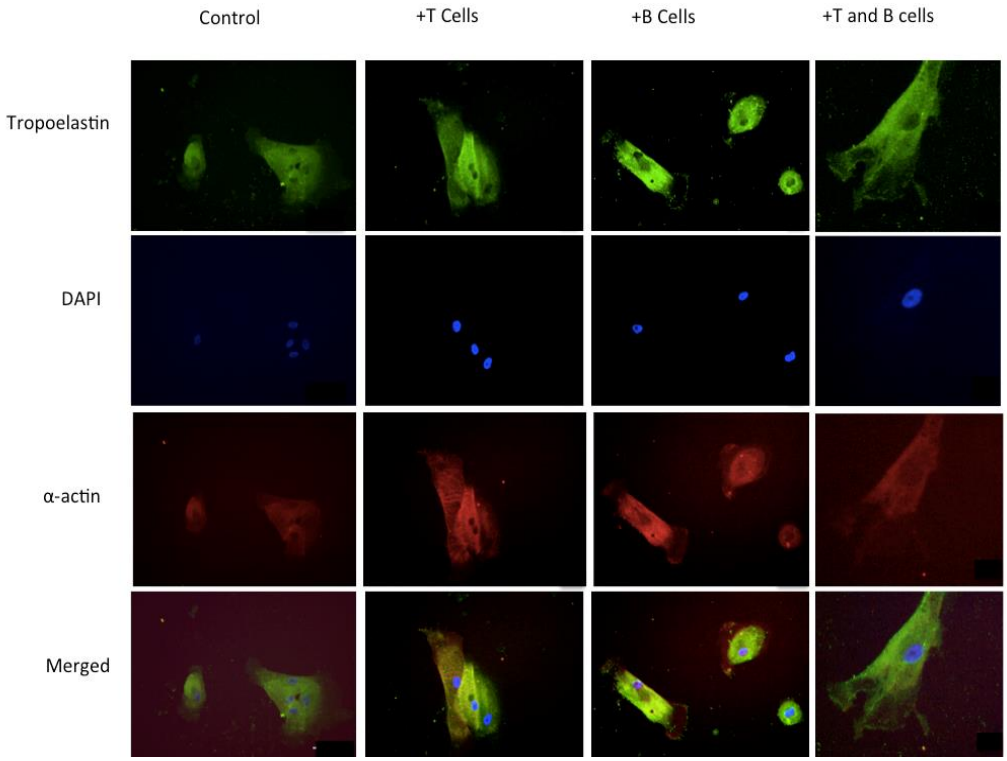

Fig 7.11 Tropoelastin and αSMA expression in human vSMCs co-culture with aortic aneurysm lymphocytes at 5 days

Images are representative of three independent experiments where 6 co-culture experiments were set-up n=5, 30 isolates.

There was an a greater number of number of tropoelastin expressing VSMCs co-cultured across all lymphocyte populations from aneurysmal aorta compared with normal aortic wall, $P<0.01$, Mann-Whitney U test (Fig 7.12).

Addition of the $CD19^{+}$cells to $CD3^{+}$ cells leads to reduction in the percentage of tropoelastin expressing cells (P<0.01).

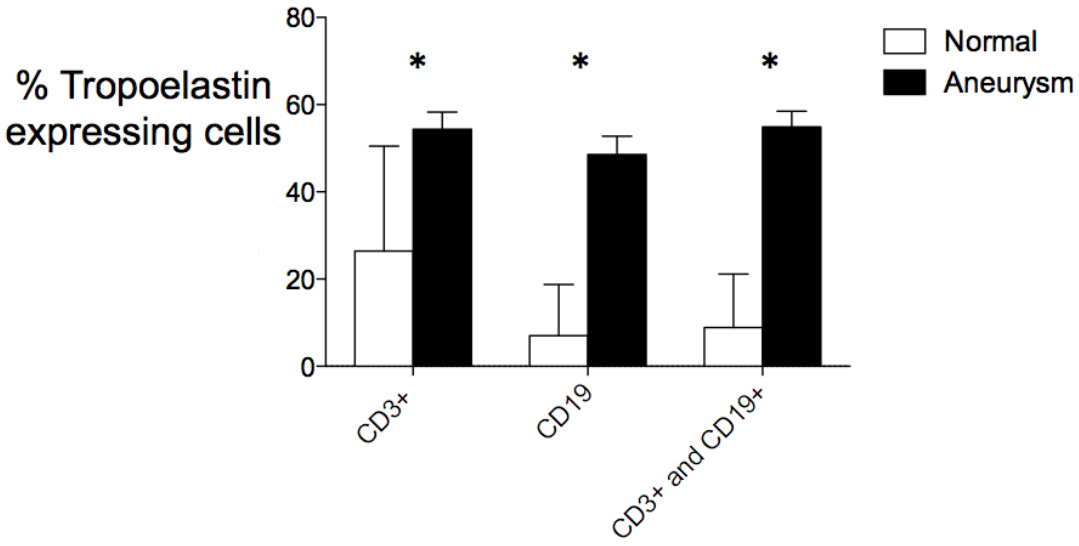

Fig 7.12 Percentage of tropoelastin expressing human VSMCs co-cultured with lymphocytes isolated from aneurysm and normal tissue

All results normalized to the control group with VSMCs without co-culture set-up. A) Normal aorta *vs.* aortic aneurysm tropoelastin expression B) Percentage of tropoelastin expressing vSMCs co-cultured with CD3+, CD19+ or CD3+ and CD19+ lymphocytes.*P<0.01 (n=5, 24 isolates).

There is upregulation of tropoelastin expression across all lymphocyte population co-cultures from the aneurysm wall when compared to the normal aortic wall P<0.01, (two way ANOVA, with post hoc Bonferroni correction P<0.01).

7.4.1.5.2 Elastin ELISA

Identical standards and standard curve were applied. Total mean elastin content of human VSMCs co-cultured with aneurysm $CD3^+$ lymphocytes was 1.49±0.20ng/ml, $CD19^+$ lymphocytes 1.51±0.15ng/ml and with $CD3^+/CD19^+$ lymphocytes, 1.45±0.26ng/ml. There were no static (Fig 7.13; n=5, two-way ANOVA, Bonferroni post hoc test, P>0.05).

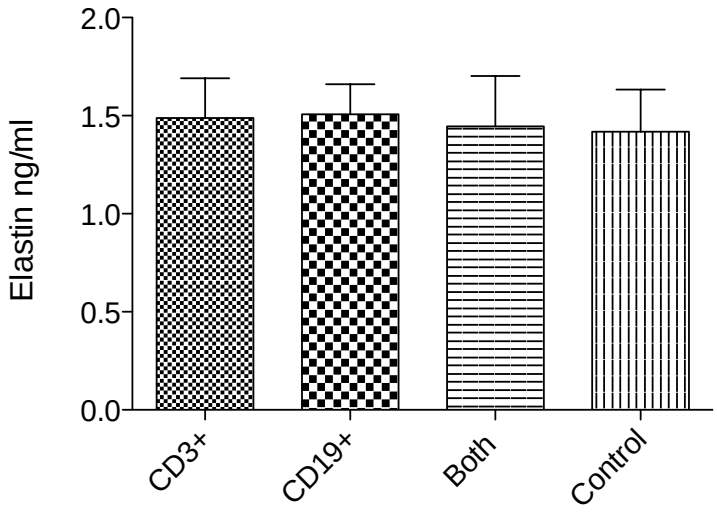

Fig 7.13 Total elastin content of human VSMCs co-cultured with lymphocytes isolated from aortic aneurysms

There were no differences in the elastin content across the different groups P>0.05 n=5 experiments, 20 co-culture sets.

7.4.2 Murine

7.4.2.1 Aortic aneurysm formation

ApoE$^{-/-}$ mice were fitted with an osmotic mini pump containing AT II as described before (n=24). In this cohort of the model, aneurysms developed in 75% of the animals by day 28. The normal aorta and aneurysms were harvested at this time point. 10% of animals were lost due to aortic aneurysm rupture or aortic dissection.

7.4.2.2 Verification of murine lymphocyte phenotypes

95% of live cells eluted from the T-cell column were CD3^{+}. 96.8% of live cells eluted from the B-cell column were CD19+. All the cells isolated from the columns stained for CD45^{+} leukocytes, but CD56^{-}CD16^{-} demonstrating absence of natural killer, monocyte/macrophage lineage (Fig 7.14). The remaining cell suspension was run to test the efficacy of the magnetic bead separation. This was to ensure that minimal cell loss occurred due to the extraction through the MS column (Fig 7.15).

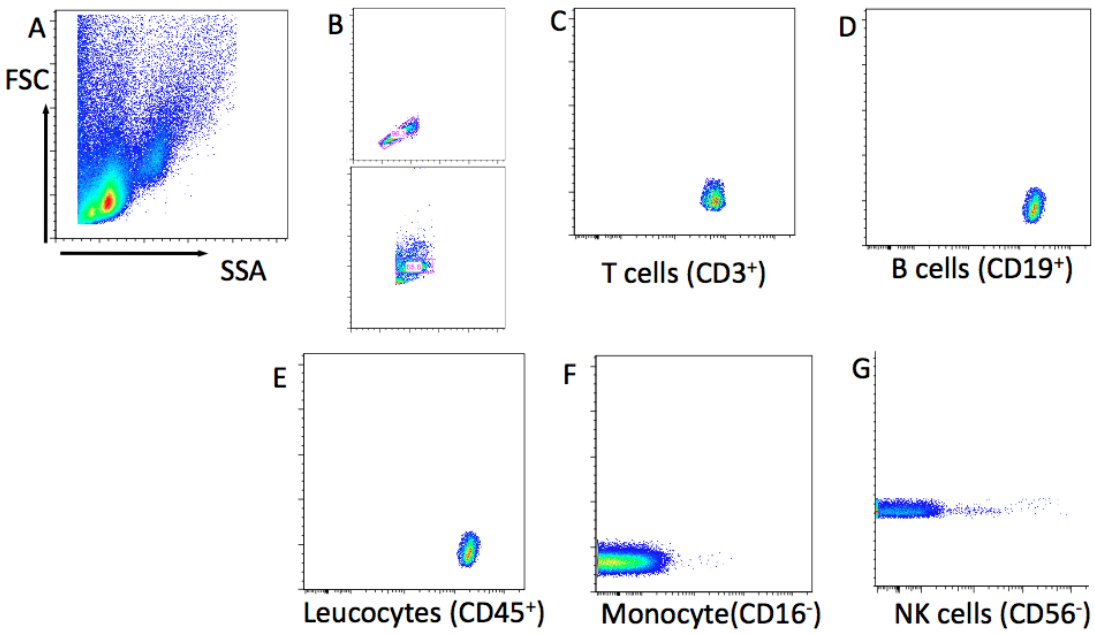

Fig 7.14 Normal aortic wall extracted lymphocytes post magnetic bead separation for B and T-cells

A) The cells population gated on forward and side scatter properties, clear population to gate on seen B) Doublet exclusion performed C) Gating on $CD3^+$ T lymphocytes that are extracted as a discrete population. D) The sample was subsequently gated for $CD19^+$ B-cells that are seen as a discrete extracted population. E) The cells in this population all stained positive for $CD45^+$ hence belonged to leukocyte fraction. F) The cells stained negative for $CD16^-$ demonstrating absence of monocytic lineage. G) The cells stained negative for $CD56^-$ demonstrating absence of NK cells. (95% of $CD3^+$ cells and 97% of B-cells were live, N=6, 12 biopsy sites analysed).

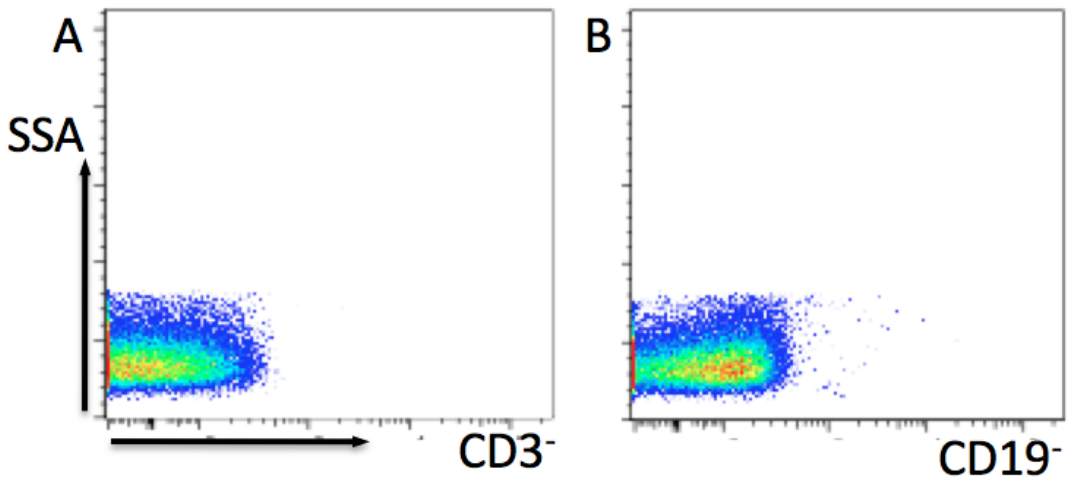

Fig 7.15 Flow cytometry of the cell suspension remaining following $CD3^+$ and $CD19^+$ cell extraction A) The cells that passed through the selection column are seen to be negative for T-cells $CD3^-$ and B) B lymphocytes ($CD19^-$). This implies near 100% efficiency of cellular extraction from the samples for the $CD3^+$ and $CD19^+$ cells.

7.4.2.3 Co-culture of VSMCs and lymphocyte

$CD3^+$ T-cells were incubated with VSMC in a ratio of 1:50. $CD19^+$ B-cells were incubated with VSMC in a ratio of 1:10 or as T and B-cell combined incubation at 1:60. Lymphocyte viability was >96% in all experiments. The cells were imaged using light microscopy on the first and last day of the co-culture experiment to look at the differences in the VSMC phenotype. Typical VSMC shape and morphology was seen across the groups at day 5 with no visual differences. Mouse VSMCs were cultured alone as a control sample.

7.4.2.4 Proliferation/Viability

7.4.2.4.1 Assessment of proliferation

An EdU assay (Click-iT EdU Imaging Kit, Invitrogen, UK) was used to determine the proliferative capacity of the VSMCs. The intensity of fluorescent signal determined the proliferation rate (Fig 7.16). Only bright, highly proliferating cells were counted as dividing cells.

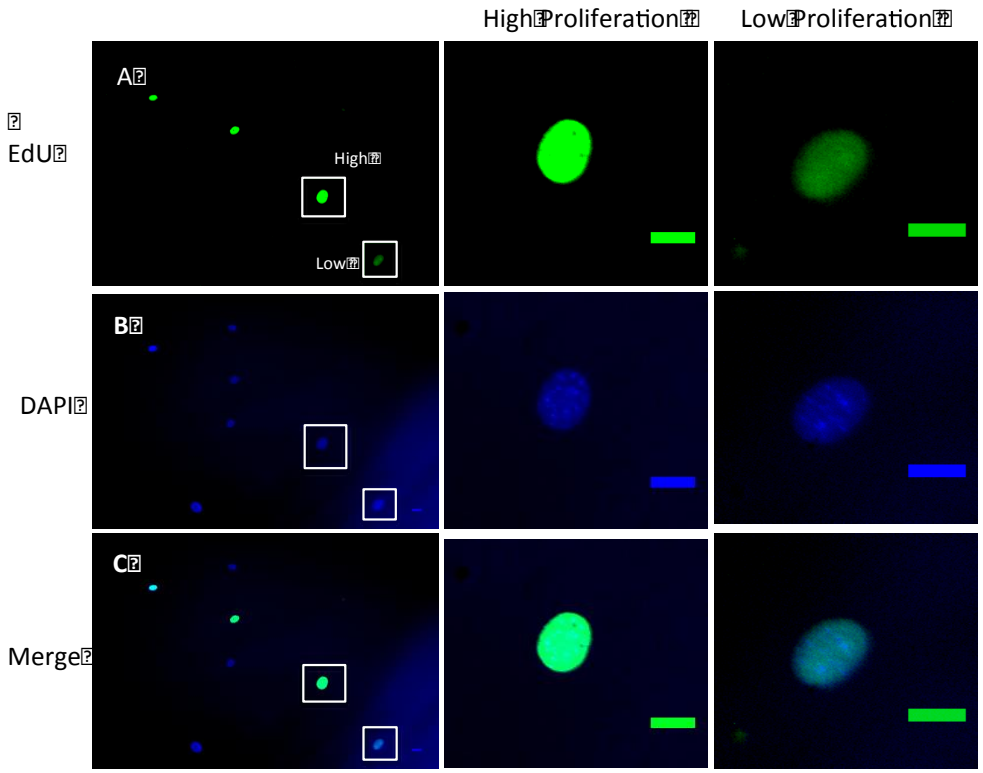

Fig 7.16 Proliferation of mouse VSMCs using the EdU assay

A) EdU incorporated cells (1µm, 72hrs) were fixed and detected with click reaction using AlexaFluor488. B) DNA was counterstained with DAPI. (C) Images were merged using ImageJ, to demonstrate nucleated cells expressing the EdU. Scale bar 10µm.

The EdU positive cells were counted as a proportion of the total cell number and finally normalized to the control well that only contained the VSMCs, thus the cellular proliferation is normalized to background VSMC proliferation rate.

VSMC proliferation was greater when cells were co-cultured with lymphocytes from aneurysm aorta than normal aortic lymphocytes (Fig 7.17). The most pronounced effect was in the $CD3^{+}CD19^{+}$ group lymphocytes from the aneurysm aorta that cause marked proliferation of VSMCs, $P<0.01$.

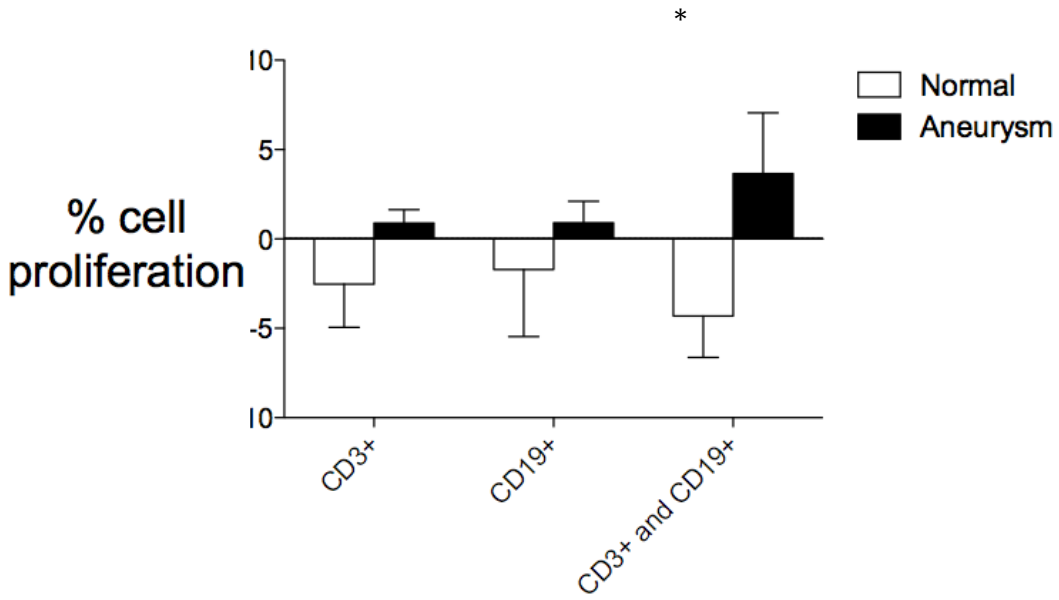

Fig 7.17 Percentage of proliferating mouse VSMCs co-cultured with lymphocytes isolated from aneurysmal and normal aorta

The percentage of proliferating cells was calculated as number of EdU stained cells/DAPI stained cells x100 and normalized to the control VSMC wells. Results are from 3 independent experiments (n=9, 36 sets of isolates). *P<0.01 Kruskal-Wallis.

7.4.2.4.2 PI staining

There were no differences between the normal aortic or aneurysm derived lymphocyte population in term of the PI staining of VSMCs (Fig 7.18) to demonstrate a panel examples of PI staining when lymphocyte co-cultures are set-up with VSMCs.

1.

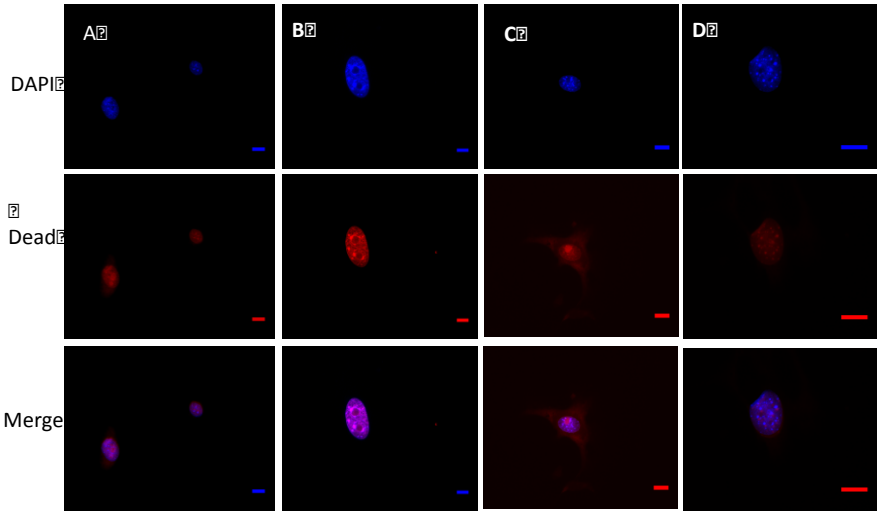

2.

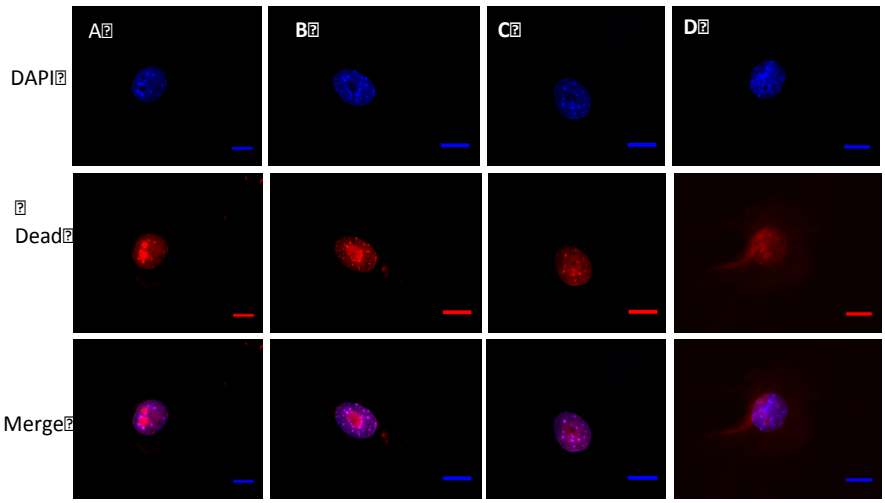

Fig 7.18 Micrographs of propidium iodide (PI) stained murine VSMCs following co-culture with 1) normal aortic or 2) aneurysmal wall lymphocyte isolates to assess cell viability

50ng/ml PI was added to vecatshield mounting medium containing DAPI and cells imaged

immediately. A) VSMCs co-cultured with $CD3^+$ T-cells B) VSMCs co-cultured with $CD19^+$ B-cells C) VSMCs co-cultured with T and B-cells D) VSMCs alone. Images are representative of two independent experiments (isolates from n=6 wall samples from each condition) Bar=10μm.

There was a greater VSMC loss when co-cultured with $CD3^+$ and $CD3^+/CD19^+$ lymphocytes derived from aortic aneurysms compared to VSMCs co-cultured with normal aortic lymphocytes (Fig 7.19). VSMCs co-cultured with $CD19^+$ B-cells had decreased cell death (results were not statistically significant P>0.05, Mann-Whitney U test).

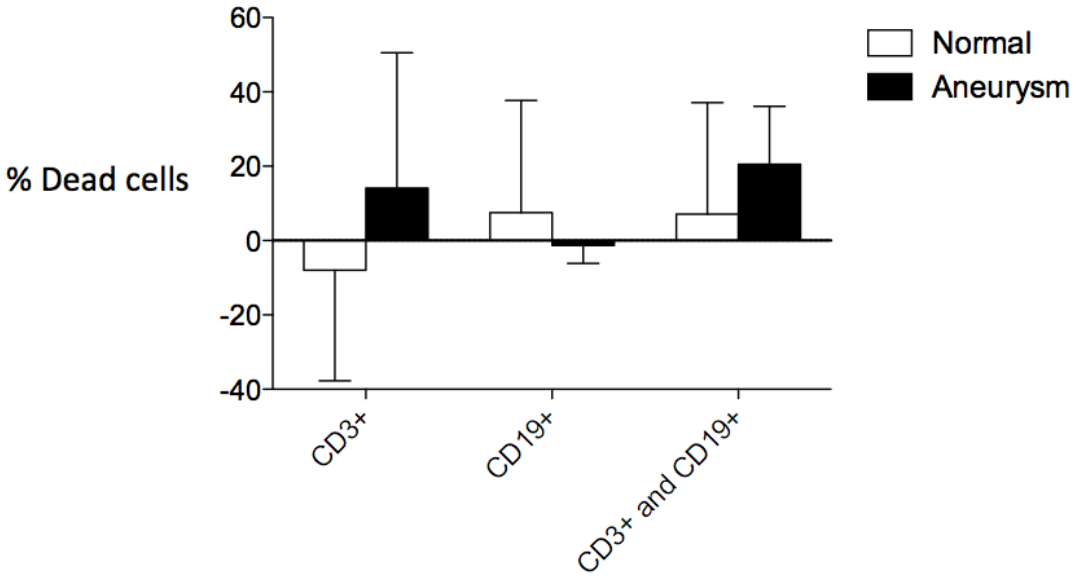

Fig 7.19 Cell viability of murine VSMCs following co-culture with lymphocytes isolated from aneurysm and normal aortic wall as determined by PI staining

The percentage of dead was calculated as number of PI stained cells/DAPI stained cells x100. Results were normalised to the control group. Data are from 2 independent experiments (isolates from n=6 wall samples from each condition). P>0.05, Mann-Whitney U test.

7.4.2.5 Synthetic ability

7.4.2.5.1 Tropoelastin Staining

There were no differences in the tropoelastin expression on fluorescent imaging of the VSMCs cross the different lymphocyte incubation conditions. Fig 7.20 demonstrates a representative staining pattern for cellular staining. All cells expressed αSMA, verifying their smooth muscle cell phenotype.

1.

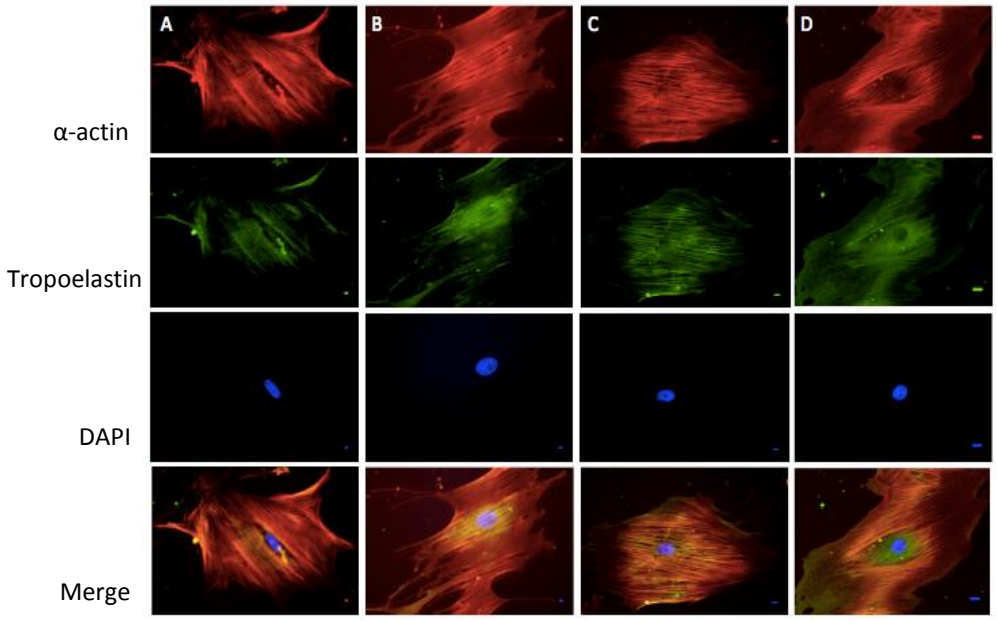

2.

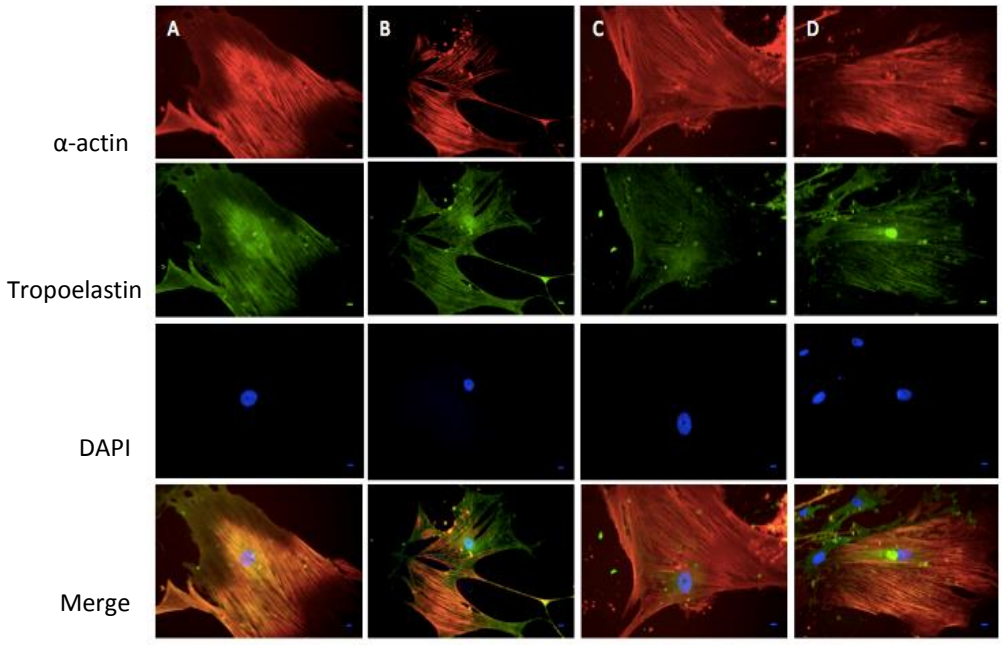

Fig 7.20 Tropoelastin and αSMA expression in mouse VSMCs co-cultured with 1) aortic aneurysm AND 2) normal aortic T- and B-cells for 5days

A) VSMCs co-cultured with $CD3^+$ T-cells B) VSMCs co-cultured with $CD19^+$ B-cells C) VSMCs co-cultured with T and B-cells D) VSMCs alone. Images are representative of three independent experiments n=9, 36 isolates. Scale bar 10 μ m.

A negative control IgG anti-rabbit antibody secondary was used for each experiment alongside staining for tropoelastin and αSMA staining (Fig 7.21).

Fig 7.21 IgG anti-rabbit negative control for tropoelastin staining

A) DAPI B) FITC C) Merge. Scale bar 10μm

There were increased numbers of tropoelastin expressing VSMCs co-cultured with $CD19^+$ B-cells from aneurysm wall compared with normal aorta (Fig 7.31; Mann-Whitney U test $P<0.001$). There was also an increase in the number of tropoelastin VSMCs co-cultured with $CD3^+/CD19^+$ cells from aneurysm wall compared with normal aorta (Fig 7.22; Mann-Whitney U test $P<0.01$). There was no statistically significant difference in the tropoelastin expression of VSMCs co-cultured with $CD3^+$ lymphocytes from normal and aneurysm aortic wall (Fig 7.22; Mann-Whitney-U $P>0.05$). Lymphocyte populations from normal aortic wall behaved differently from aneurysm wall, where they cause a more profound increase in the tropoelastin expression from VSMCs.

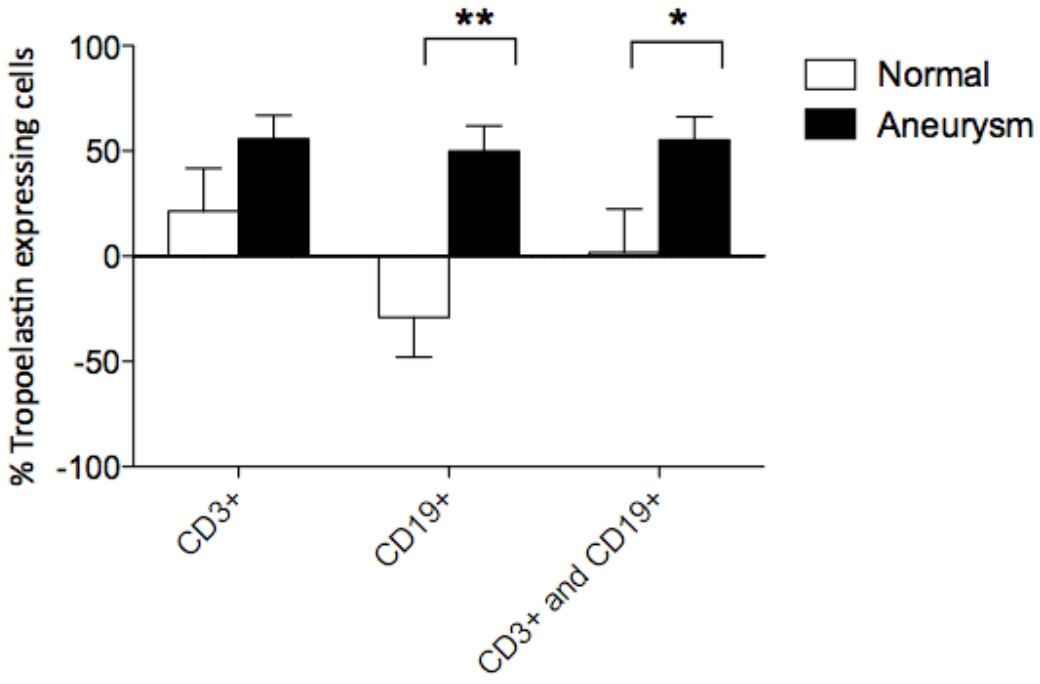

Fig 7.22 Percentage of tropoelastin expressing mouse VSMCs co-cultured with lymphocytes isolated from aneurysm and normal tissue at day 5

The percentage of tropoelastin expressing cells is expressed as a percentage of the total number of αSMA^{+} VMCs. All results normalized to the control group with VSMCs grown alone. (n=9, 27 co-culture experiments $P<0.01$ $^{**}P<0.001$, Mann- Whitney U test).

7.4.2.5.2 Elastin ELISA

A typical standard curve plot can be seen in Fig 7.23.

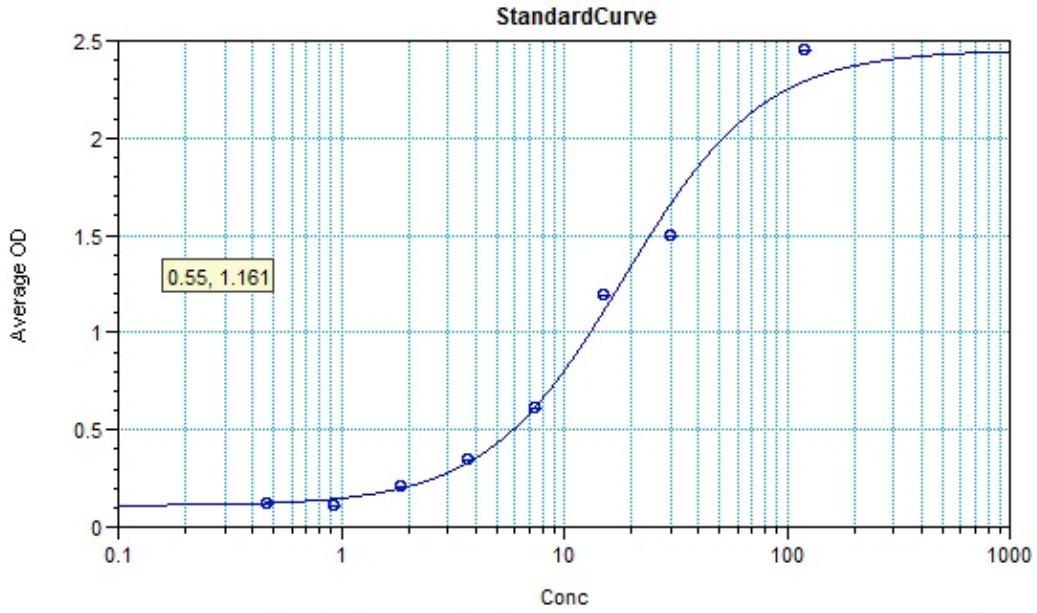

Fig 7.23 Standard curve for elastin ELISA

Total mean elastin content of mouse VSMCs co-cultured with combined lymphocyte populations was greater in the aneurysm group than untreated controls, but this did not reach statistical significance (Table 7.5, Fig 7.24; two-way ANOVA, Bonferroni post hoc test, $P<0.08$).

Table 7.5 Elastin ELISA results for mouse VSMCs

Tissue	Lymphocyte subset added	Elastin content (ng/ml ±SEM)
VSMCs alone	**none**	**1.56±0.11**
Normal aorta	**$CD3^+$**	**1.5 ±0.04**
	$CD19^+$	**1.64±0.02**
	$CD3^+/CD19^+$	**1.39±0.34**
Aortic aneurysm	**$CD3^+$**	**1.56±0.04**
	$CD19^+$	**1.75±0.16**
	$CD3^+/CD19^+$	**1.78±0.11**

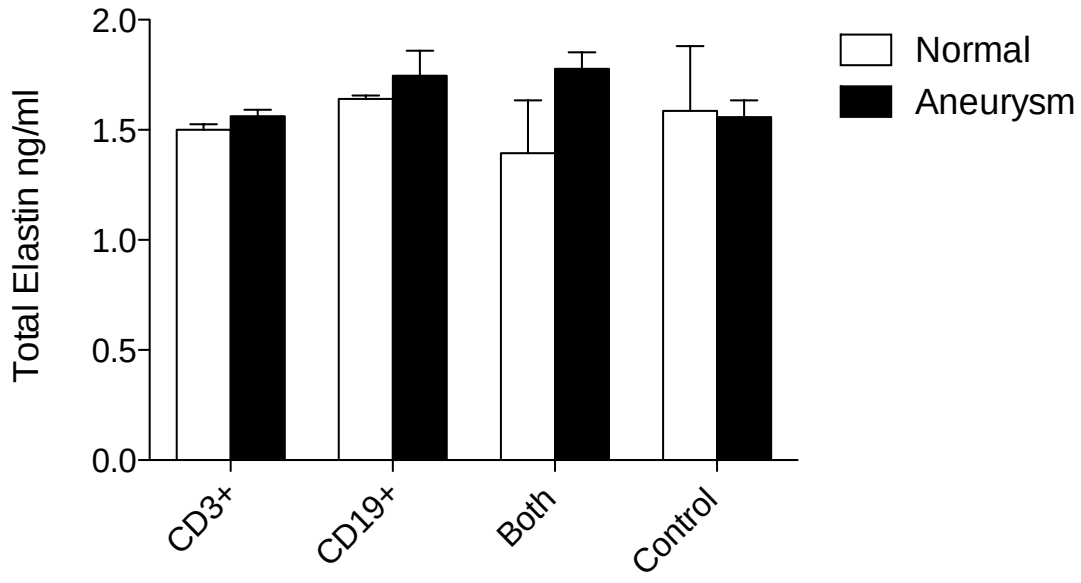

Fig 7.24 Total elastin content in murine VSMCs co-cultured with normal aortic and aortic aneurysm derived lymphocytes

There was an increase in elastin content in the aneurysm group in all the co-cultured vSMCs with lymphocytes. This however, did not reach statistical significance P<0.08 (2-way ANOVA) n=6, 24 cell isolates.

7.4.2.6 Gene expression

Real-time PCR was used as described previously (section 6.3.9.4, page 235) to quantify mRNA levels and determine the effect that lymphocyte co-culture has on VSMC gene expression. Genes investigated include those regulating extracellular matrix turnover - cathepsin S (Ctts), cathepsin K (Cttk), elastin (ELN), fibrillin (FBN), lysyl oxidase (LOX), matrix metalloproteinase-2 (MMP-2), matrix metalloproteinase-9 (MMP-9) and transforming growth factor-β (TGF-β). All results were normalized to the housekeeping genes, peptidylprolyl isomerase B (PPIB, Cyclophilin B) and 50S ribosomal subunit protein (RPLP0).

The slope of the standard curve indicates PCR efficiency and should be between 90-100% i.e. −3.6 ≥ slope ≥ −3.3 (efficiency=10(-1/slope)-1. The R^2

value of the standard curve gives an indication of the quality of the results. A value of 0.9 and higher indicates good precision. Analysis of these parameters shows the assays for; Ctts, ELN and MMP-9 had poor PCR efficiency and low precision and therefore were eliminated from further analysis (appendix 4, page 349). The remaining genes had good PCR efficiency and precision (appendix 4, page 349). A summary of the slope value and efficiency is presented in table 7.6

Table 7.6 RT-PCR efficiency (slope values) and precision ($R^2$0 values from the standard curves of all assay genes. Ctts, ELN and MMP9 were excluded from further analysis.

Gene	Slope Value	Efficiency	R^2
Cttk	**-3.42**	**96.1%**	**0.99**
Ctts	**-0.89**	**1229.2%**	**0.68**
ELN	**-1.81**	**256.9%**	**0.20**
FBN	**-3.57**	**90.6%**	**0.99**
LOX	**-3.47**	**94.2%**	**0.99**
MMP-2	**-3.18**	**106.3%**	**0.99**
MMP-9	**-2.589**	**143.4%**	**0.83**
TGF-B	**-3.11**	**109.7%**	**0.97**
PPIB	**-3.91**	**80.2%**	**0.99**
RPLP0	**-2.848**	**124.5%**	**0.98**

The standard surves for all the genes are given in Appendix 4, page 349. The cT value (threshold cycle) represents the intersection between the amplification curve and the threshold line. It is a measure of the concentration of gene target in the sample (Fig 7.25). The linear portion of the curve is the exponential phase of PCR, where the amount of product doubles after each cycle (Fig 7.25).

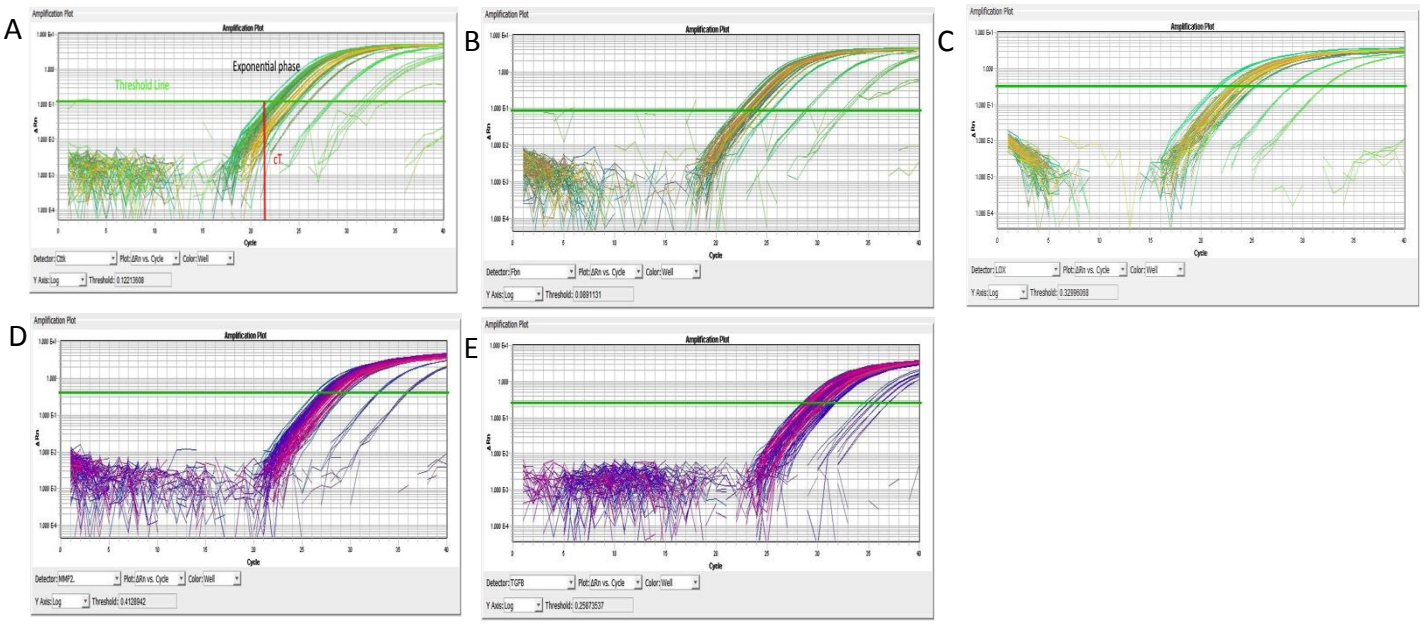

Fig 7.25 RT-PCR amplification plots of assay genes that meet the slope efficiency and precision criteria

The cT value is the intersection between the amplification curve and the threshold reaction. The amount of PCR product doubles after each cycle. (A) Cttk K (B) FBN (C) LOX (D) MMP-2 (E) TGF-β.

Analysis of the different lymphocyte populations derived from the normal aorta demonstrated significant down-regulation of TGFβ expression in VSMCs co-cultured with $CD3^+$ cells compared with $CD19^+$ cells (Fig 7.26; two way ANOVA, Bonferroni post hoc test P<0.01). There was also significant down-regulation of TGFβ expression in the VSMCs co-cultured with $CD3^+$ cells compared to $CD3^+/CD19^+$ cells (Fig 7.26; two way ANOVA, Bonferroni post hoc test P<0.01). There were no significant differences in gene expression of Cttk, FBN, LOX and MMP-2 in VSMCs co-cultured with different lymphocyte subtypes.

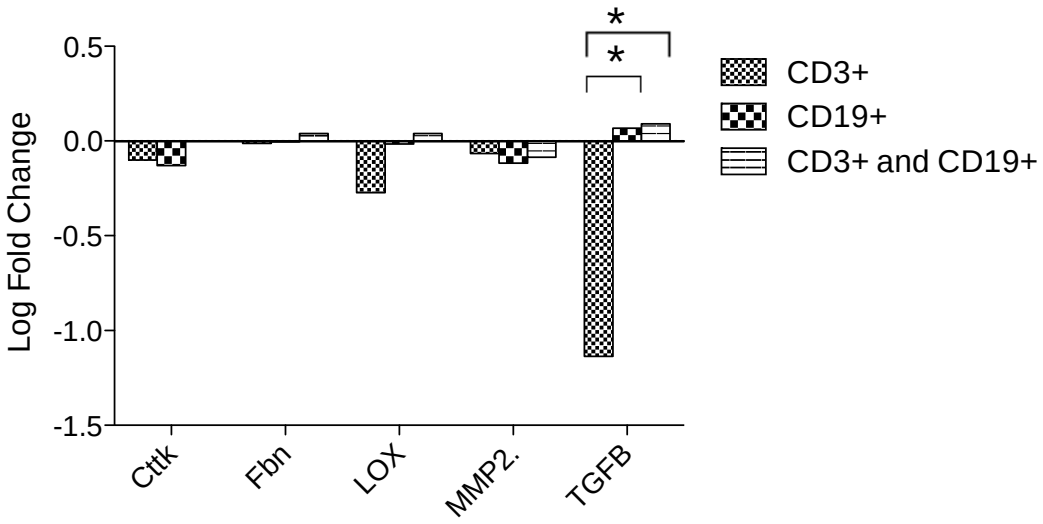

Fig 7.26 Gene expression profiling of VSMCs co-cultured with normal aortic wall-derived lymphocytes

Average log-fold differences in gene expression of CttK, FBN, LOX, MMP-2 and TGF-β in mouse VSMCS co-cultured with $CD3^+$, $CD19^+$ and $CD3^+/CD19^+$ lymphocytes from normal aorta using real time PCR (RT-PCR) n=9 wall biopsies measured in triplicate (27 co-culture conditions, 81 wells), *P<0.01, two way ANOVA, post hoc Bonferroni correction P<0.001.

Analysis of the aneurysm derived lymphocyte populations showed there was down-regulation of LOX and TGFβ expression in the VSMCs co-cultured with $CD3^+$ cells compared to $CD19^+$ cells (Fig 7.27; two way ANOVA, Bonferroni

post hoc test P<0.01). There was also significant down-regulation of TGFβ and LOX expression in the VSMCs co-cultured with $CD3^+$ cells compared to $CD3^+/CD19^+$ cells (Fig 7.27; two way ANOVA, Bonferroni post hoc test P<0.01).

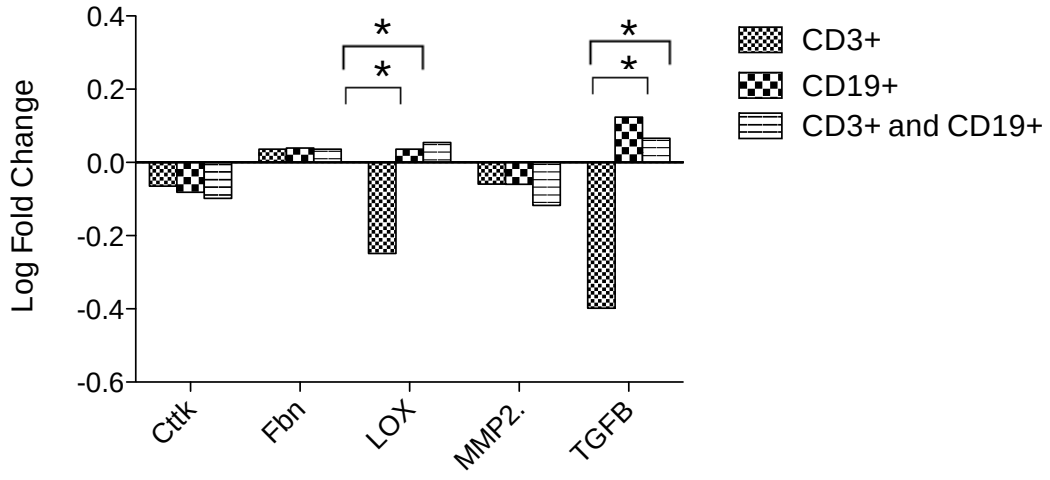

Fig 7.27 Gene expression profiling of VSMCs co-cultured with aneurysmal wall-derived lymphocyte

Average log-fold change differences in expression of CttK, FBN, LOX, MMP-2 and TGF-β in mouse VSMCS co-cultured with $CD3^+$, $CD19^+$ and $CD3^+/CD19^+$ lymphocytes from aneurysms. Three independent experiments n=9 *P<0.01, two way ANOVA, post hoc Bonferroni correction P<0.001.

7.4.2.7 Cytokine Bead Array

The BD Cytometric Bead Array (CBA) was used to determine the concentrations of IL-2, IL-4, IL-6, IFN-γ, TNF-α, IL-17A and IL-10 in the conditioned media of mVSMCs co-cultured with lymphocyte populations. All results have been normalized to control samples. This would allow Th phenotyping of the $CD3^+CD4^+$ cells. Amongst the cytokines there was upregulation of IL-10, TNF-α, and Il-6. There was significant up-regulation of IL-10 (Fig 7.28; two way ANOVA; P<0.001). There was down-regulation of IL-17a, IFN-γ, IL-4 and IL-2 (Fig 7.28-7.29). IL-10 and IL-6 were the most highly expressed cytokines in conditioned media of VSMCs co-cultured with

lymphocytes normal aortic tissue. Conditioned media of VSMCs co-cultured with lymphocytes from aneurysm aortic tissue had down-regulation of IL-10, Il-17a, TNF-α, Il-6 and IL-2 compared to the control. IFN-γ is slightly upregulated compared to the control (Fig 7.28-7.29).

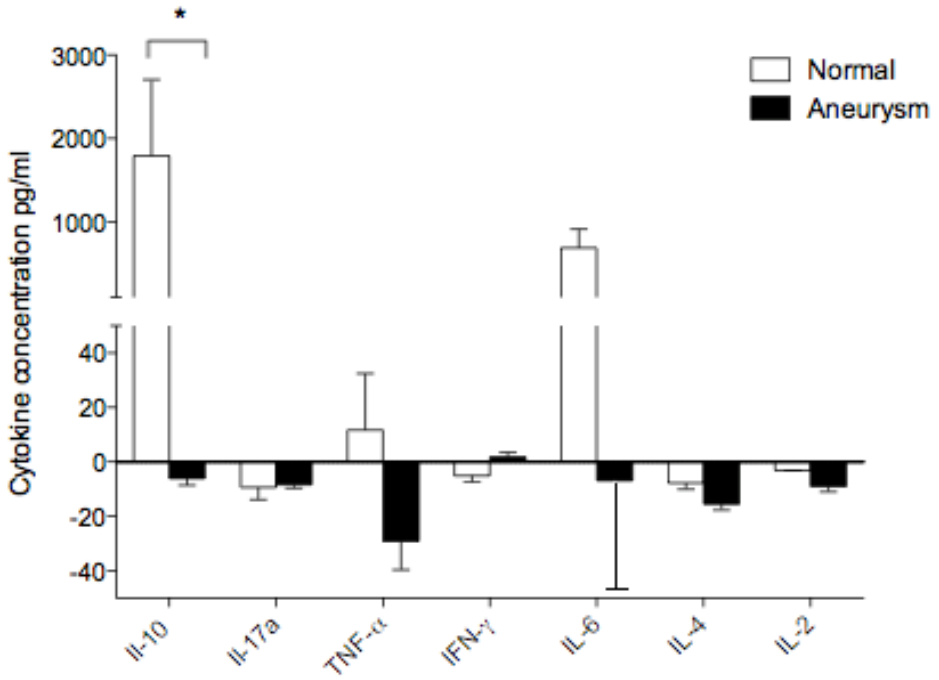

Fig 7.28 Cytokine bead array for mVSMC conditioned with normal or aneurysm derived B and T lymphocytes

6 independent experiments, 12 co-culture set-ups, n=22. Results are normalised to the control VSMC alone wells. *P<0.001, two-way ANOVA, post hoc Bonferroni correction. Mean±SEM

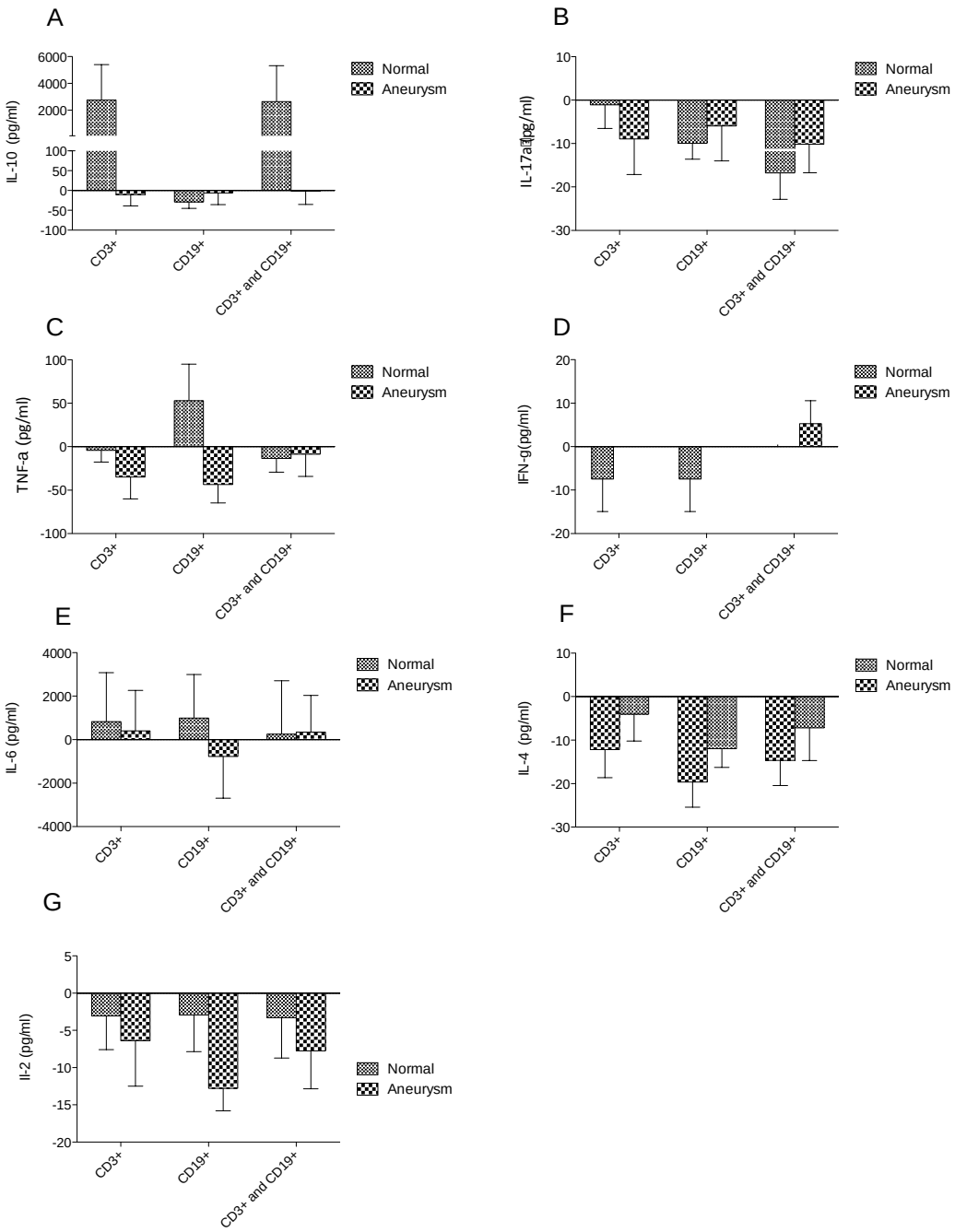

Fig 7.29 Cytokine expression profiles of VSMCs and lymphocyte co-cultures

A) IL-10 (B) IL-17a (C) TNF-α (D) IFN-γ (E) IL-6 (F) IL-4 (G) IL-2. Data is from six independent experiments 12 co-culture set-ups with n=22.

Table 7.7 Cytokine bead array data summary

Cytokine	Co-culture condition	Lymphocytes derived from normal Aorta	Lymphocytes derived from aneurysm aorta
IL10	$CD3^+$	↑	↓
	$CD19^+$	↓	↓
	$CD3^+CD19^+$	↑	↓
Il-17a	$CD3^+$	↓	↓
	$CD19^+$	↓	↓
	$CD3^+CD19^+$	↓	↓
TNF-α	$CD3^+$	↓	↓
	$CD19^+$	↑	↓
	$CD3^+CD19^+$	↓	↓
IFN-γ	$CD3^+$	↓	-
	$CD19^+$	↓	-
	$CD3^+CD19^+$	-	↓
IL-6	$CD3^+$	↑	↑
	$CD19^+$	↑	↓
	$CD3^+CD19^+$	↑	↑
IL-4	$CD3^+$	↓	↓
	$CD19^+$	↓	↓
	$CD3^+CD19^+$	↓	↓
Il-2	$CD3^+$	↓	↓
	$CD19^+$	↓	↓
	$CD3^+CD19^+$	↓	↓

7.5 Discussion

We studied the *in-vitro* effects of specific aortic wall derived lymphocytes on VSMCs to determine the effects of proliferation, synthetic ability, gene expression and cytokine production.

7.5.1 VSMC Proliferation and death

There was marked increase in proliferation in murine and human VSMCs in the lymphocyte group compared with controls. Specifically $CD3^+$ and $CD3^+/CD19^+$ cells from the aneurysm wall increased the proliferation rate most. It could be that the increased proliferation is to compensate for increased cell death as PI staining tended to be also higher in this group compared to the normal aortic wall derived lymphocyte group. Previous work has shown that Ki67 expression and apoptotic markers are higher at the site of aortic aneurysms[534]. It has also been suggested $CD3^+CD4^+$ T-cells enhance VSMC stability by causing VSMC proliferation when there is cell-cell contact[535]. The mechanism responsible for this effect is unknown but it is unaffected by blocking V-Cam, I-CAM or CD40[535]. The role of p53 in VSMC proliferation and regulating the cell cycle checkpoints is thought to play a critical role in aortic remodelling[534]. Overall VSMC density is reduced in upto 74% in aortic aneurysms compared to normal aortic wall[536]. Upto a third of the cells that are αSMA positive are apoptotic[536]. It has been postulated that lymphocytes might causes VSMC death in the aortic wall by mediation through death proteins such as Fas ligand and perforin[36]. Binding of Fas to its ligand would lead to the activation of a series of proteases and caspases the initiate cell death. Double TUNEL staining of human αSMA expressing cells has shown that there is increased DNA fragmentation and apoptosis that is correlated with cytotoxic T lymphocytes that are thought to produce Fas and perforin [36]. $CD4^+$ are also able to produce TNF related apoptosis inducing

ligand (TRAIL) that can bind and trigger transmembrane proteins with activation of death signaling induced pathways. Anti-TRAIL antibodies to immunodeficient murine human aorta's prevents VSMC apoptosis[537].

In contrast to our murine model data the human VSMCs demonstrated less cell death in the lymphocyte groups derived from normal and aneurysm tissue compared to control VSMCs. This suggests that $CD3^+$ lymphocytes that are derived from the aortic wall and not blood confer a protective phenotype that promotes cell proliferation and decreased apoptosis. This would be in keeping with our earlier subtyping phenotype data that suggests that the aortic wall resident $CD3^+$ lymphocytes tend to be the T-regulatory and memory phenotype cells that are acting as an anti-inflammatory modulator to VSMCs. This is further supported as discussed below when we assess the synthetic capacity of the VSMCs. This is increased in the lymphocyte group compared to controls.

7.5.2 VSMC synthesis of ECM

VSMCs are the key mediator of elastogenesis. This is a complex post-translational extracellular process that begins with tropoelastin formation, anchoring into the microfibrillar scaffold. Cross-linking steps with LOX and production of an insoluble elastin fibre that is linked to desmosine and isodesmosine[58,538,539]. Our data shows increase in tropoelastin synthesis in the murine $CD19^+$ and $CD3^+/CD19^+$ group and in all the human aneurysm derived lymphocyte groups compared to controls. There is upto a 50% increase in tropoelastin expression in $CD3^+/CD19^+$ cell incubated VSMCs. Earlier preliminary work in human aneurysm segments showed a five fold increase in tropoelastin with increased presence of macrophages along with tropoelastin mRNA[538]. We did not investigate macrophages as a source of the tropoelastin in aneurysms we instead have strong evidence to suggest the importance of lymphocytes in modulating VSMC behaviour into producing

more elastin. It is likely that the presence of macrophages in tissue is a causal association as inflammatory processes are ongoing in the aortic wall. Indeed when we perform histology in the aortic aneurysm wall there is increased Mac2 staining in the regions of the tunica media with specific tropoelastin antibody staining. It might be that there is aortic degradation at these sites associated with elastin breakdown and there is a corresponding increase in tropoelastin synthesis that is mediated through the lymphocytic up-regulation of VSMC activity. Human lymphocytes are able to express elastin-laminin receptor, which when activated by elastin peptides triggers the release and synthesis of elastases[540,541]. This ability to modulate tropoelastin synthesis in aortic aneurysms is important part of the aortic remodelling response. Tropoelastin synthesis has been demonstrated in aortic aneurysms using an adenoviral vector transfected into aortic VSMCs that were perfused into rat aneurysm[542]. The adenoviral transcripts were able to reverse aneurysmal change and there was increased elastic fibre formation in the aortic wall[542]. Tropoelastin is a key component that is responsible for providing aortic wall its strength and prevent further aortic dilatation and aortic rupture. The ELISA studies showed very little increase in the elastin expression in VSMCs co-cultured with aneurysm-derived lymphocytes across human and murine derived cells. Although the results did not reach statistical significance in the studies the trend was to see higher elastin levels. It might be that termination of the experiment was far too early at day 5 to allow enough mature elastin to be laid down in the co-culture plate. Under normal physiological conditions in adults elastin deposition is a slow processes occurring over many weeks and months. The reason for terminating the experiment at day 5 is that we wanted to investigate the true effects of all vessel wall derived lymphocytes on VSMCs. Lymphocytes are known to alter their phenotype after 5 days in culture[96,101,110,543]. It is also known that other structural proteins are needed (fibrillin1/2, laminin and emilin) in the

formation of mature structured elastin fibres[58,175,176,184]. The cross-linking of tropoelastin requires fibulin and LOX activity. It might be that although there is increase tropoelastin levels the necessary post translational proteins are not present and functional to allow the elastin fibre formation. *In vitro* co-cultures have their limitations and growing VSMCs in plastic wells might not facilitate the required microenvironment with necessary signaling molecules for elastin fibre organisation and ECM formation. 3D collagen gels/ matrices might be more appropriate for future studies into ELN generation by the VSMCs[544,545].

7.5.3 VSMC gene expression profile

When we studied gene expression we characterised the elastogenic processes looking at expression for elastin (ELN), fibrillin (FBN), lysyl oxidase (LOX) and TGFβ. For elastolytic processes we characterised MMP2, MMP9, cathepsin S (Ctts) and cathepsin K (Cttk). The assays for Ctts, ELN and MMP9 were not analysed due to late amplification with poor RT-PCR quality. The main difference was an up regulation of fibrillin and down regulation of all the other remaining genes when comparing the lymphocyte groups compared to VSMCs alone. When analysed by lymphocyte subgroups there were significant differences in the TGFβ levels that were down regulated by T lymphocytes derived from normal and aneurysm aortic wall *vs.* B-cell and B/T-cell groups. This suggests an isolated T-cell effect that is neutralised by the B-cells. Increased TGFβ signaling is associated in Marfans syndrome and is shown to increase signaling with Smad2/3, RohA and MAP kinases in FBN1 mutant models[546]. Neutralisation of the TGFβ prevents the resistance of normocholesterolemic C57Bl/6 mice to ATII induced aneurysm formation[113]. TGFβ over-expression by endovascular gene delivery in rat models has been associated with diameter stabilisation, decreased inflammation, decreased MMP2/MMP9 expression and reduced ECM degradation[114]. There was

down-regulation of LOX in the aneurysm derived T-cell group compared to the B and B-T cell cohorts. It is likely that the down regulation of the LOX genes in the $CD3^+$ group would mean decreased elastin fibre formation. There is emerging evidence that $CD4^+$ T-cells are involved in ECM remodelling through modulation of LOX expression[547]. It is known that T lymphocytes orchestrate fibrotic response through an array of cytokines[548,549]. TGFβ has shown to increase LOX mRNA but also LOX activity in VSMCs[538]. Also TNFα, ILβ have been implicated in LOX induction[550,551]. Several studies have suggested that pro-inflammatory cytokines such as TNFα, IL1β and TGFβ1 are involved in modulation and expression of MMP's that inturn affect the ECM *via.* LOX activity[552,554].

7.5.4 Cell cytokine profile

The cytokine bead array data showed a significant up regulation of IL10 and IL6 in the conditioned media of VSMCs co-cultured with lymphocytes from normal aortic tissue and down regulation of IL10 and IL6 in the aneurysm group. In normal aortic tissue the high concentrations of IL10 and IL6 implies a Th17 phenotype. IL10 is an anti-inflammatory cytokine and inhibits the production of INFγ[522,554,555]. IL10 is produced by T-regulatory cells and leads to expression of transcription factor $FOXP3^+$ that reduces the activity of other inflammatory cells[556]. It is likely that the Tregs are dampening the inflammatory response. This could explain low expression of pro-inflammatory cytokines IL2, IL4, IL17a and IFNγ. When aortic tissue explants are analysed there is uniform increase in pro-inflammatory cytokines (IL6 and IL10)[556]. Comparison between tissue extracts of aneurysm wall and *in-vitro* co culture aren't directly comparable as the cell concentrations, inflammatory cell content and therefore the cytokine profile are different. The other important difference in the co-culture set-up was that the cells were not stimulated with PMA or known inflammatory stimulants. The results are

therefore likely to represent endogenous milieu from the tissue resident lymphocytes. Another study where $CD3^+$ cells were isolated alone or in combination with anti-CD28 (MOPC)[521]. The activation of $CD3^+$ cells with anti-CD3 lead to TNFα and INFγ expression with little IL5, IL6 [521]. Whereas activation of T and B-cells with mitogens such as PMA and Ca^{2+}ionophore leads to increased IL5, IL6, TNFα and a switch to Th1 phenotype. It is likely that the cytokines from $CD3^+$ lymphocytes from the normal aortic wall are more biologically active with production of IL6 and IL10 compared to the aneurysm derived T-cells.

The data shows lymphocytes isolated from aneurysm tissue increase VSMC proliferation and tropoelastin synthesis. There is a trend to increased elastin formation. The effects are maximal in the $CD3^+$ subset with the cytokine profile suggesting a T regulatory phenotype that produces anti-inflammatory cytokines leading to positive aortic remodelling. Lymphocytes may have a protective role in aneurysm formation by increasing VSMC proliferation and tropoelastin synthesis, ECM degradation is reduced, which decreases the chances of aortic dilatation and rupture. Gene expression of TGFβ is down regulated in this group that might additionally offer protective response to VSMC phenotype.

Chapter 8: General Discussion and future work

8.1 General discussion

Imaging that can better predict the progression of aneurysms and development of complications would be of great clinical benefit. Additionally if we understand the chronic inflammatory processes that underlie the pathophysiology of aneurysm development we could target specific drugs to augment aneurysm growth. The development of novel radiotracers and MR agents allows functional imaging of aortic aneurysms to yield potential physiological, biochemical and cellular correlates to events occurring in the aortic wall as aneurysms progresses.

The main immune signal in the aneurysm wall is from the B and T lymphocytes and their interaction with VSMCs. This inturn dictates aortic remodelling behaviour through alteration of the ECM content. It is possible that as yet unknown antigenic trigger activates the B-cells to be attracted to aortic wall and produce immunoglobulins. Through MHC class II peptide antigen presentation $CD4^+$ T-helper cells are recruited to the region. These would in turn activate $CD8^+$ cytotoxic T-cells that are responsible for cytokine release and further interaction with B-cells to produce plasma cells [108,427]. The role of T and B regulatory cells in the pathogenesis of aneurysm is not before reported. We have demonstrated that there are two distinct population subtypes that reside in the aortic wall. This was discovered in the context of functional imaging using ^{18}F-FDG PET-CT in human and murine aortic wall. This was the $CD3^+CD4^+CD25^+$ activated cell population that is likely responsible for the pro-inflammatory cell activity in the aortic wall and the corresponding Treg cell population that expresses $CD4^+CD25^+CD127^-$ (humans) and $CD4^+CD25^+FOXP3^+$ (murine). It is likely that these cells are

responsible for dampening down the inflammatory response and encourage positive aortic remodelling behaviour. The B-cell subtypes that predominated in the metabolically active aortic wall on functional imaging were also the activated B-cell phenotype that expressed $CD19^{+}CD25^{+}IgD/IgM$. This also typifies memory B-cells in the aortic wall as well as cells that expressed $CD27^{+}$. The $CD38^{+}$ B-cells were present that would interact with T-cells and modulate the immune response in the aortic wall. As well as Bregs that form an elusive ever changing population expressing $CD24^{hi}CD27^{+}$ that arise from memory B-cells can produce IL-10 and TGFß leading to inhibitory effects on $CD4^{+}$ T-cells. These B-cell subtypes can go on and express $CD24^{+}CD38^{+}IgM^{high}$ phenotype and alter widespread cytokines responses.

It is the increased metabolic activity of these cells that is being picked up by the functional imaging tracer, as confirmed in the murine studies. However the sites at which these cells are active is focal yet heterogeneous and varies significantly with time. Hence although it informs us of the biological activity at that time in the aortic wall, it is not predictive of aortic wall expansion at the site, or eventual rupture. There was no correlation between ^{18}F-FDG uptake and aortic wall expansion or rupture in the murine studies. These findings have also been reported in small scale human studies[281,281,282]. The interaction between the identified B and T lymphocytes and their influence on VSMCs was not understood. It is known that pro-inflammatory cytokines, mechanical stress and oxidative state activates the c-Jun N terminal kinase (JNK) pathway[169,398,400] in VSMCs that increases activation of activating protein (AP-1), increases expression of matrix metalloproteinase's (MMPs), and decreases expression of matrix synthesis enzymes (lysyl oxidase (LOX) and prolyl 4-hydroxylase (P4H) leading to decreased deposition and increased degradation of elastin[108,251].

We therefore sought to determine how the aortic wall resident B and T-cells would interact from aneurysmal and normal aortic tissue with *in-vitro* co-culture of VSMCs. We further linked the cell signaling (looking at cytokine expression profiles) and gene expression data to VSMC activity, proliferation, viability and cell synthetic capacity (this being a marker of aortic remodelling ability). The aortic aneurysm derived cells that were $CD3^{+}CD4^{+}$Th2 phenotype influenced VSMC death. It is unclear through which mechanism that was induced. Previous work has implicated Fas, perforin and p53 activity as being responsible[36]. The interaction between aneurysm tissue derived lymphocytes and VSMCs confirmed the biological behaviour that was seen from the functional imaging data on flow cytometry and IHC. The lymphocytes are responsible for up-regulation of VSMC mediated increased ECM generation and hence a protective phenotype.

In-vitro studies performed focused on tropoelastin synthesis, and the enzymes and transcription factors involved in regulation of elastin modulation, namely LOX and TFGß. The VSMCs isolated from aneurysms had increased expression of tropoelastin under the influence of B-T lymphocytes. This was independent of antagomir mediated modulation of immune cell and VSMC function. The antagomir mediated miR29b inhibition was responsible for upregulation of LOX gene expression. It has to be remembered that there are other ECM components and enzyme systems apart from the elastogenic and elastolytic pathways. For instance, a disintegrin and metalloprotease domain containing proteins (ADAMs) produced by VSMCs ADAMs 10, 12, 15 and 17 are present in the aortic wall in the absence of immune cell infiltration[558,559]. These have a role in proteolysis, cell adhesion, migration, cell extracellular matrix activation and angiogenesis[558]. TIMPs 1 and 3 counteract ADAMs activity and are found in aortic aneurysms[428,559].

Turning the attention back to novel tracers that might be better able to inform us of aortic aneurysm biology, there are numerous other novel agents that have been used in animal studies and may provide attractive biological markers of aortic wall instability. These include MMP's and their inhibitors (TIMP's), tropoelastin, oxidised LDL receptors, and other markers of platelet activity, apoptosis, inflammation and angiogenesis. Along with USPIO/SPIO other nanoparticles have been used to determine macrophage content. These include integrins (alpha nu beta 3 (amb3)), matrix metalloproteinase (MMPs), micelles labeled with macrophage receptors or products NGAL, and CBR-2[74,75,251]. Although many retrospective and small prospective studies demonstrate a link between functional imaging and clinical outcomes, there needs to be large prospective studies to evaluate this whilst also looking at the effects of anti-inflammatory therapies on aortic wall. The effectiveness of lifestyle modification on cholesterol and statins to reduce arterial wall inflammation has been studied with ^{18}F-FDG uptake in the aorta and carotid wall[74,75,252,253]. Similar studies have been conducted with MR to study aortic disease progression. Presently animal studies are en route to develop functional imaging to aid delivery of drugs. For instance targeted therapy geared towards angiogenesis inhibition or anti-inflammatory treatments targeted to vascular wall[241,249,305,560,561].

Various imaging endpoints can be used to provide surrogate markers of disease development and progression. For instance the intima-medial thickness in the carotid artery is accepted as a phenotypic marker that signifies cardiovascular disease[131,293,309,560,561]. Similarly, it might be possible to use functional imaging end-points as surrogate markers of disease activity and progression. The biomolecular imaging phenotypes would complement current imaging to enhance the process of drug development and discovery. If we can measure and quantify the biological correlates in the aortic wall then we could identify patients that are likely to progress rapidly with the

disease process and therefore require earlier intervention. The imaging would allow us to report on cellular events that reflect the mechanism of disease progression and therefore facilitate evaluation of drugs with novel mechanisms, using these tracers in rapid clinical trials. The imaging phenotype can show us if the drug is having the desired effect that is proposed based on its mechanism of action. If the drug fails to cause a mechanistic change on functional imaging then it could be abandoned earlier. This is especially important in aortic aneurysms, as this is a slowly progressive indolent disease in the earlier stages. Aneurysms expand episodically over many years and it would take decades to see clinical changes in patients with this condition. Additionally ^{18}F-FDG PET-CT provides an assessment of the metabolic pathways as it interacts with glucose uptake. For instance in cancer imaging inhibitors for rapamycin (mTOR) – an important step in nutrient response and phosphoinositide-3 kinase (PI3) – a regulator of serine-threonine kinase Akt that is in turn a key mediator of growth factor and insulin signalling[131,309,560,563]. Changes in ^{18}F-FDG uptake in neoplasia correlate with tumour mass in patients. Therefore ^{18}F-FDG PET-CT might be able to inform us on aortic wall metabolism in aneurysms.

Functional imaging techniques might be used clinically to gain information on aortic wall metabolism, blood flow, regional biochemical and cellular composition. As opposed to anatomical imaging (simple radiography, USS, CT, MRI), functional imaging aims to reveal physiological activities within the tissue with the use of tracers and probes. These are radiolabelled or gadolinium attached molecules that locate to specific sites within the body. To provide clinical utility many of the functional imaging systems are coupled for hybrid imaging that combines two or more modalities to inform us about the anatomical and physiological and/or biochemical composition of the tissues. The biological correlates to the uptake of the specific tracers such as ^{18}F-FDG are not known.

Preliminary pilot retrospective human data postulate that monocyte/macrophage infiltration into the aortic wall is responsible for the ^{18}F-FDG uptake seen in human aneurysms [131,309,558]. However, there has been no direct attempt to determine the biological correlates(s) of ^{18}F-FDG uptake. Examining the meaning of the uptake of currently available 'non-specific' tracers and development of novel tracers that are specific for biological processes (on-going in the aortic wall) could lead to a greater understanding of the mechanisms that underlie aneurysm development, expansion and the development of complications.

From our *in vitro* work we have demonstrated the importance of lymphocyte and VSMC interactions in maintenance of the aortic wall ECM content. The lymphocytes have a key role in proliferation of VSMCs and preventing cell death. There is at the same time increased VSMC death in the lymphocyte groups. It might be that there are two distinct cellular effects at play. We could use anti-Fas ligand and an anti-Perforin antibody to determine the expression within the VSMCs of these proteins. Flow cytometric assessment of the lymphocyte population post VSMC culture could determine the direction in which the lymphocyte population is skewed as a result of the cell-cell interaction with VSMCs. We could also determine the presence of p53, p21, protein kinase C-delta (PKCδ) as key mediators of VSMC apoptosis[550]. PKCδ expression has been previously been shown to be higher in aneurysms compared to normal aorta. PKCδ deficient mice have decreased aneurysm expansion on $CaCl_2$ administration[556]. PKCδ deficient VSMCs have impaired monocyte chemoattractant protein-1 (MCP-1) production[556]. $CD3^+$ T-cells affects *via*. PCKδ mediated VSMC apoptosis could be analysed using western blotting or immunoprecipitation technique.

For the effects on ECM as well as assessing tropoelastin synthesis, we need to be able to assess desmosine and isodesmosine levels. These would be eventually important in determining the elastin content in the aortic wall.

Small levels of desmosine <200pg would be evident with radioimmunoassays and this would provide sensitive method of detection with low number of VSMCs and their interactions with lymphocytes. As the ELISA to detect elastin levels and the ELN gene on RT-PCR were unable to detect any significant differences in the VSMC co-culture experiments, the native cells could be stimulated with ascorbic acid to allow synthesis of ECM[564]. Alternative strategy would be to use [3H] elastin-coated plates and soluble tritium measured to quantify the effect lymphocytes.

The CBA profiling revealed an increased signal from the TGFβ to be important and under the effect of AmiR29b to augment aortic wall homeostasis. These needs to be confirmed with anti-TGFβ antibody mediated inhibition of the signaling pathway and assess the response on VSMC phenotype.

For the complex flow cytometric phenotypic analysis we utilized the multilaser Canto cytometer. If we wanted to not only analyse the cell phenotype in a very niche population of cells but also assess intracytomplasmic proteins such as perforin, fas, micro cytokine levels, microRNAs and intranuclear proteins all simultaneously we could deploy CyTOF® (DVS imaging). This would allow single cell high-speed analysis in a conventional manner to flow cytometry to determine cell type followed by a multi-probe analysis with over 100 metal halide probes with a minimal sign of overlap (as using mass spectroscopy) thus allowing simultaneous phenotyping and functionally profiling of the cells.

8.2 Limitations of the study

Aneurysm patients We had a combination of thoracic and abdominal aortic patients in whom the analyses were carried out. Although the cellular compositions were the same in relation to the functional imaging tracers assessed, the aneurysms that develop in thoracic and abdominal aorta might represent slightly different disease processes with subtle differences in

pathophysiology. Also although the majority of the aneurysm patients had age related degenerated aneurysms, we did have patients with connective tissue disease and chronic aortic dissection leading to aneurysms. Due to limitation in the number of patients coming to open surgery all patients were included in the study.

The aneurysm model The ApoE-/-ATII model of aneurysms provides an excellent model to study the pathophysiology and natural history of the disease. It is however still a model that might not completely recapitulate the ongoing biological processes in the aortic wall as in humans. The small volume of aortic and other tissue has impact on the number of analyses that can be performed and experiments have to be replicated at cost.

^{18}F-FDG PET-CT The radiation dose, time taken to perform the scan, its invasive nature and cost all preclude this imaging modality in its current state from clinical utility for vascular imaging. The poor spatial resolution, difficulties in having appropriate ROIs for vessel wall imaging, no time-of-flight imaging and high-definition fusion would be the limits. However as discussed in detail in chapter 3, we sought out to and resolve some of these problems in aortovascular metabolic imaging. This included standardization of the imaging protocol, reducing noise with image parameter alteration, SUV_{max} assessment for the ROIs targeted on aortic wall, fused IV contrast CT imagining and the 3D image fusion, reconstruction and overlay.

MR T1 mapping The scan time for a mouse takes two hrs. The data processing is considerably longer. The generation of T1 maps being longer still. Bespoke in-house software was used for the analysis. Fused images from commercially available software were exported and slice-by-slice manual segmented analysis of performed of the aortic wall regions to obtain the T1

values. The process requires a considerable learning curve and time to develop expertise in all elements of the data analysis, fusion, measurements and calculations to be performed. The clinical utility of ESMA MRI for use in patients with aortic aneurysm would need to be addressed with refinement of the image processing.

Comparative analysis of MRI and histology We correlated the aortic axial slices on MRI to the histology of the aorta at the termination of the experiment. It was anticipated that the MR image of the aorta could be divided into quadrants and compared to the histology of the aorta. However even when using fixed anatomical landmarks such as the diaphragm, renal arteries, it was difficult to perform robust analysis to match the imaging data to the histological sections. *In vivo* MR images were compared to *ex vivo* histological data on pixel-by-pixel fusion basis, with multiple high numbers of sections taken through the aneurysm wall to get to the sections that would correlate it to MR axial slices. We also performed mean T1 relaxation / R1 time correlations to ECM area analysis for tropoelastin and elastin to circumvent this and additionally analyse large amounts of data points from multiple sections throughout the aneurysm in many aneurysms and animals.

Histological analysis We used histology to confirm the position of the immune cells within the aortic wall and semi-quantified the immune cell content and infiltration in the aorta. However it is known that histological assessment can vary between batches of slides. To minimize this effect, we analysed multiple regions from within the same slide or the complete slide with multiple slides taken through the section of the aneurysm at all levels so the complete aortic profile can be accurately determined. Also batches of slides were analysed at the same time and adequate stain made for the whole study.

8.3 Conclusions

This study has:

i) Defined the role of ^{18}F-FDG imaging in human aortic aneurysms and determined the biological correlates for the imaging tracer in the aortic wall

ii) Determined the utility of ^{18}F-FDG imaging in the ApoE$^{-/-}$ATII model of aortic aneurysms and defined its pattern during the natural history of aneurysm development. We have also determined the biological correlates to ^{18}F-FDG in the murine ApoE$^{-/-}$ATII model

iii) Determined the utility of ESMA MRI in defining the aortic wall extracellular matrix content. We have described the biological correlates to ESMA uptake in the aortic wall and determined the natural history of aneurysm development with ESMA uptake

iv) Determined the role of microRNA network involving miR29b and miR195 *in vivo* on ApoE$^{-/-}$ATII model of aneurysms. We have also determined the mechanisms involved in *in vitro* alteration of VSMC phenotype due to change in AmiR29b activity

v) Demonstrated a change in the aortic and cardiac phenotype in response to alteration of gene and proteomic signaling due to antagomir mediated inhibition of miR29b

vi) Determined the *in vitro* interaction and effects of aortic wall resident T and B-cell subsets involving regulatory cells in modulating the aortic VSMC activity, dampening inflammatory response and explaining the mechanisms in positive aortic remodeling

Appendix 1

Ethics protocol

Version 1.0
Date:03/03/2010

Title

A study of emerging functional imaging techniques in aortic aneurysms.

Background

Aortic aneurysm diameter is an important predictor of risk of rupture[1]. Size is, however, not the only determinant of rupture. Some aneurysms may rupture when small[2], while large aneurysms can grow to a considerable size without rupture. Aortic aneurysm expansion is associated with inflammatory cell infiltration and enzymatic degradation of the vessel wall[3,4]. Increased inflammatory infiltrate, absence of smooth muscle cells and high levels and activity inflammatory cytokines such as metalloproteinases (MMPs) have also been found at the site of aneurysm rupture[3,4].

The PET tracer, ^{18}F-FDG, is used to detect areas of high metabolic activity such as tumours and inflammation. It also accumulates in atherosclerotic plaque, where active macrophage uptake is associated with plaque instability[4,5]. Studies in small numbers of patients show that there is focal uptake of ^{18}F-FDG in the aortic aneurysm wall of patients with large, rapidly expanding or symptomatic aneurysms and suggest that this may be associated with the likelihood of rupture[6,7]. At St Thomas' we reviewed PET-CT fusion scans in 30 patients with abdominal aortic aneurysms (AAA) (median diameter 48mm, range 33-74mm) and graded localized ^{18}F-FDG uptake in the wall. Uptake varied from none (39% of patients), minimal (32%), moderate (14%) and high (14%). The pattern of uptake varied, from patchy to generalised. One patient with high ^{18}F-FDG uptake presented to another hospital with a ruptured aneurysm 6weeks later and died. FDG uptake in AAA wall might reflect inflammation, macrophage or other cellular infiltration, active atherosclerotic plaque or increased vascularity (neovascularisation). Understanding the meaning of uptake would further our knowledge of aneurysm disease progression and possibly reveal novel targets for therapies to reduce expansion or rupture.

Hypothesis

1. Uptake of the PET tracer (^{18}F-FDG) will correspond to aortic wall inflammation, macrophage infiltration indicating active atherosclerotic plaque.

2. Aortic wall with high ^{18}F-FDG uptake will be more likely to expand and/or rupture.

Study design

This will be a prospective study. We will evaluate aortic aneurysms with a PET-CT scan. Patients with a positive scan will have biopsy of aortic wall taken at time of surgery for their aneurysm repair. The patient will be anesthetised. There will be one to three biopsies approximately 5mm each from the aortic wall. This tissue is of no use for the operation and normally gets either completely excised or left to cover the aortic graft. The biopsies will not affect the operation or operative recovery.

Inclusion criteria

Adult patients with aortic aneurysm that need an open operation and who have a positive aortic PET scan.

Exclusion criteria

Any patients with aortic aneurysms that will undergo endovascular repair. Pregnancy.

Consent

Patients will be provided with an information sheet and consent form about the study prior to having the PET-CT and aortic biopsies. The information sheet will clearly explain the purpose and nature of the research. Patients will be given one week to decide about participation in the trial. The information sheet will clearly state that if the patients do not want to participate they would still receive the best available treatment. A contact number for a clinical research fellow would also be available with the information sheet in case the patients are not clear about some point and would like to ask someone about it. Once agreed the patient will sign the consent form which would also be signed by the person taking the consent.

Monitoring

Trial will start only after approval by the ethics and local research and development committee. Recruitment in the study will not disadvantage any patient groups. The recruited patients will be monitored in a usual manner by the consultant who is supported by a team of junior doctors, nursing staff and allied health professionals 24 hrs a day. In case of any specific information

required about this study a contact number for a clinical research fellow will be available to the patients and the clinical staff. The patients will not need any special follow-up for this study.
All patients will be informed of the research outcome through a written letter at the end of the study.

Power Calculation

Considering our categorical data we have used a Nomogram to calculate the sample size. Based on previous studies[6,7] we expect 40% of aortic aneurysms to have PET uptake. At out unit we undertake 200 aortic aneurysm repairs per year. Of these 5% are open repairs. Based on these values we will need 15 patients in this study. To account for subject withdrawal and follow up loss we will target 30 patients.

Statistical analysis

As the comparison for the primary end point is made with an intention to treat, a Kaplan Meier analysis will be used. For continuous variables a Student's t test or Mann Whitney U test will be used. Categorical variables will be compared using Fisher's exact test.

Conflict of Interest

There are no conflicts of interest from any of the researchers. The patients recruited will be given the same treatment as any other patient with similar disease.

References

1. Brown PM et al., J Vasc Surg 2003;37:280-4
2. Limet R et al., J Vasc Surg 1991;14:540-8
3. Choke E et al., Eur J Vasc Endovasc Surg. 2005;30(3):227-44
4. Shimizu K et al., Arterioscler Thromb Vasc Biol 2006;26:987-94
5. Rudd JH et al., J Nucl Med. 2009;50(9):1560
6. Reeps C et al., J Vasc Surg 2008;48:417-24

Patient information sheet

Version 2.6
21/07/2010

PART 1

PATIENT INFORMATION SHEET
(Patients with aortic aneurysms) REC REF: 10/H0711/56
Study Title:
A study of emerging functional imaging techniques in aortic aneurysms.

Invitation:
You are being invited to take part in a research study. Before you decide it is important for you to understand why the research is being done and what it will involve. Please take time to read the following information carefully and talk to others about the study if you wish.

- Part 1 tells you the purpose of this study and what will happen to you if you take part.
- Part 2 gives you more detailed information about the conduct of the study.

Please ask if there is anything that is not clear or if you would like more information. Take time to decide whether or not you wish to take part in our study.

What is the purpose of the study?
You are coming to St Thomas Hospital to attend the out-patients clinic to monitor your aortic aneurysm. You have been under follow-up to monitor the size of the aneurysm as this determines when surgery will take place to repair it. Usually aneurysms only burst when they reach a certain size. This is a very serious complication of aneurysms with a high risk of death. There are some small aneurysms that burst while some patients develop large aneurysms that do not burst. It is still not known why aneurysms behave in this manner.

We intend to study this by looking at the activity of cells in the aneurysm wall by performing a PET-CT scan two weeks before your operation. This scan shows up active cells and is currently used in other clinical areas to detect cases of infection or cancer. The PET-CT involves injection of a radioactive marker (^{18}F-FDG) that can be taken up by aneurysms. If this marker shows up on the scan, then we propose to take a small sample of the aneurysm wall at time of your operation. We will analyze this tissue to determine what tracer uptake in aneurysm wall means, and find out what cells and biochemical processes are involved in aneurysm expansion or rupture.

What is PET scanning?
A PET scan is a special kind of scan that detects the radioactive sugar molecule and then the computers create a picture of where this is in the body. An injection of the radioactive sugar is given before the scan. The scan involves radiation. Extra radiation can increase the chances of developing cancer however the risk from the extra scan in this study is small (1 in 500) compared with the natural lifetime risk of getting cancer (1 in 4).

Why have I been chosen?
You have been chosen because you have an aortic aneurysm that needs an open operation to repair it at St Thomas Hospital.

Do I have to take part?
No. It is up to you to decide whether or not to take part or if you want to participate in some part of the study and not the whole of it. If you do, you will be given this information sheet to keep and be asked to sign a consent form. You are still free to withdraw at any time and without giving a reason. A decision to withdraw at any time, or a decision not to take part, will not affect the standard of care you receive.

Will this affect my treatment?
No, you will receive the same treatment by the same team of doctors and nurses if you were not taking part in the study.

What will happen to me if I take part?
We would like to take the following material when you attend the clinic. You will be invited for a PET-CT scan. You will have to fast prior for at least six hrs prior to the scan. Following the scan, you will be secluded for surgery as usual, and aortic tissue biopsy will be taken at time of operation. This does not influence the duration or the nature of the surgery in any way. The aortic tissue taken is small (approximately 5 millimeters i.e. pea sized) and does not influence the outcome of the repair.
What are genetic tests and will any be done?
No. We do not plan to perform any genetic tests.

What are the side effects of any treatment received when taking part?
The PET-CT scan will require you to be in the hospital for about two hrs longer than normal. It will mean having an additional dose of radiation that carries an added risk of about 1 in 500 compared to normal lifetime risk of cancer that is 1 in 4. For the complete scan the level of radiation dose given in the study corresponds to about 13-18 years of natural background radiation.
Some people may find not eating six hrs before the scan unpleasant and the injection into you arm prior to the scan. This causes minor discomfort (as when having a blood test).

What if I am pregnant?
All women of childbearing age will have a mandatory pregnancy scan prior to the scans. Pregnant women can NOT be involved in this study.

What are the possible benefits of taking part?
There are no direct benefits to you, but we hope that the results will contribute to work that will eventually lead to new treatments for aortic aneurysms.

What if there is a problem?
Any complaint about the way you have been dealt with during the study or any possible harm you might suffer will be addressed. If you have a concern about any aspect of this study, you should ask to speak with the researchers who will do their best to answer your questions (02071880214). If you remain unhappy and wish to complain formally, you can do this through the NHS Complaints Procedure. Details can be obtained from the hospital (02071887188).

Is there someone I can talk to independently about the research trials in general?
You can talk to any of the staff in the cardiovascular unit if you have any concerns about the study or contact the Patient Advice and Liaison Service (PALS).

Will my taking part in the study be kept confidential?
Yes. If you consent to taking part in the study, relevant parts of your medical records will be seen by your surgeon and the doctor who is carrying out the research study. All information including the results of the scan and all other investigations and tests will be kept entirely confidential. No individual patients will be identifiable when the results of the study are published in the medical literature. Your General Practitioner will, however, be informed of your participation in accordance with our usual practice. All the information about your participation in this study will be kept confidential.

What will happen to the results of the study?
In approximately 3 years the results will be analysed and published in an appropriate medical journal and presented at relevant scientific meetings. The results will be available to you at this stage and a copy of the results will be sent to you if you wish. If the scans indicate a need for additional treatment or further scans your surgeon or the clinical research doctor mentioned below will explain this to you.

Contact Details:

Clinical Research Doctor-

Surgery

Mob: 07525857015

Mr Rizwan Attia
Academic Department of

1st Floor, North Wing,
St Thomas' Hospital,
London SE1 7EH
Tel: 0207188021

E-mail: rizwan.attia@kcl.ac.uk

PART 2

What will happen if I don't want to carry on with the study?
If you withdraw from the study it will not affect your treatment.

What if there is a problem?
In the unlikely event that you become unwell after any procedure then you should contact your family doctor. Alternatively you can contact the researchers for advice on the number given above.

Harm:
In the event that something does go wrong and you are harmed during the research study there is indemnity provided by King's College London. This covers both non-negligent and negligent harm.

Will my taking part in this study be kept confidential?
Any information collected about you in the course of the study will be kept strictly confidential at all times. Any personal details will be kept in the Academic Department of Surgery at St Thomas' Hospital. Anonymised data will be stored on King's College London computers in the department, which are password protected to allow access only to authorised researchers. The department is locked and only authorised researchers have access. The Research Doctor involved will be responsible for the data collected.

Tissue samples will be labelled with a code and no identifying details. The data collected (including tissue specimens) will be stored. When the data is no longer needed it will be disposed of securely and confidentially.

Authorised researchers directly involved in the study will have access to the data. Authorised representatives from King's College London and the Research and Development department may need access to the data in order to confirm that the study is being carried out appropriately.

What will happen to any samples I give?
Tissue specimens will be stored anonymously in the locked Academic Department of Surgery at St Thomas' Hospital. They will only be accessible to the authorised researchers. They will be stored until they are used in this or further research studies looking at aneurysm behaviour. Tissues are used until they are depleted as further tests may be helpful over time. If not depleted, they will eventually be disposed of securely.

What will happen to the results of the research study?
The results of the study will be written up as a thesis for a post graduate degree and may be published in scientific journals or presented at scientific meetings. The individual participants involved will remain anonymous at all times.

Who is organising and funding the research?
The research is sponsored and funded by King's College London (KCL). The doctors and scientists carrying out the research are employed by KCL and Guy's and St Thomas' Hospitals to conduct research.

Who has reviewed the study?
This study has been reviewed and received favourable outcome from the research Ethics Committee at Charing Cross Hospital as part of South West Research Network.

You will be given a copy of the information sheet and a signed consent form to keep.
The researchers would like to thank you for taking the time to read this information sheet.

01/03/2010
Version 1.0

Unique patient Identification Number: US/AA/number

CONSENT FORM

Title of Project: A study of emerging functional imaging techniques in aortic aneurysms.

Name of Researcher: Mr Rizwan Attia

Please tick box

1. I confirm that I have read and understand the information sheet dated 21/07/2010 (Version 2.6),for the above study. I have had the opportunity to consider the Information, ask questions and have had these answered satisfactorily. ☐

2. I understand that my participation is voluntary and that I am free to withdraw at any time, without giving any reason, without my medical care or legal rights being affected. ☐

3. I understand that relevant sections of any of my medical notes and data collected during the study, may be looked at by responsible individuals from regulatory authorities or from the NHS Trust, where it is relevant to my taking part in this research. I give permission for these individuals to have access to my records. ☐

4. I agree to allow my samples to be stored in subsequent future research projects related to aortic aneurysms ☐

5. I agree to take part in the above study. ☐

_____ _____
_____
Name of Patient Date Signature

_____ _____
_____
Name of Person taking consent Date Signature
(if different from researcher)

_____ _____
_____
Researcher Date Signature
When completed, 1 for patient; 1 for researcher site file; 1 (original) to be kept in medical notes

Appendix 2

Table 1 Criteria for PET data reconstruction

PET reconstruction parameters			
Reconstruction parameters	Image set description	STH_3D_WB _AC	STH_3D WB NAC
VCT	Output	Image	Image
	Matrix	128 x128	128 x128
	Recon Method	Iterative	Iterative
	Z Filter axis	Standard	Standard
	Subsets	20	20
	Iterations	1	1
	Diameter	70.00	70.00
	Centre L	0.0	0.0
	Centre P	0.0	0.0
	Post filter	Hanning 6.0	Hanning 6.0
	Cutoff_freq	10.9	10.9
	Axial_cutoff	6.5	6.5
	loop filter	5.47	5.47
Corrections	Wellcounter files	Default	Default
	Wellcounter	Sensitivity and Activity	Sensitivity and Activity
	Randoms	Corrections by singles	Corrections by singles
	Normalisation	Default	Default
	Decay	Yes	Yes
	Deadtime	Yes	Yes
	Scatter	Yes	No
	Geometric	---	Yes
Attentuation	Type	Measured	None
	Transmission scan	Most recent	
	Smooth		
	Axial smooth		

Table 2 **PET half body dosing using ^{18}F-FDG**

Group	Number of AFOV in group	Number of AFOV in group	Overlap	Pre scan delay	Towards head	D	Tracer	Nuclide
1	4-7	5min	11	0	No	3|D	F18	FDG

Table 3 **Acquisition technique for CT scan**

Patient setup	Head first Supine Arms up (Arms down if patient is unable to raise Wedge under knees)
Scan Margins	Landmark: Sternal notch ROI for PET scan: Aortic Arch to femoral head (2cm above aortic arch to femoral head or nearest bed step below femoral head) ROI for CT contrast Abdomen aneurysm: renal artery to femoral head Chest aneurysm: Aortic Arch to Diaphragm Thorax aneurysm: aortic arch to femoral head

Table 4 **Parameters used for data reconstruction of images acquired during CT**

CT reconstruction parameters:								
	Thick (mm)	Interval (mm)	DFOV (cm)	R/L cent	A/P cent	Matrix	Recon type	Recon Mode
AC			70.0	0.0	0.0	512	AC	Full w400/wl 40
STD	3.75 1.375:1	3.27	50.00	0.00	0.00	512	Std	Full w400/wl 40
STD 5mm	5.0 1.375:1	5.0	35.0	0.0	0.0	512	Std	Full w400/wl 40
CT angiogram 5mm	0.984	2.5	35.0	0.0	0.0	512	Std	Full w400/wl 40

Table 5 **Parameters used for data reconstruction of the vascular CT angiogram**

CT reconstruction parameters:								
	Thick (mm)	Interval (mm)	DFOV (cm)	R/L cent	A/P cent	Matrix	Recon type	Recon Mode
AC			70.0	0.0	0.0	512	AC	Full w400/wl 40
STD	3.75 1.375:1	3.27	50.00	0.00	0.00	512	Std	Full w400/wl 40
STD 5mm	5.0 1.375:1	5.0	35.0	0.0	0.0	512	Std	Full w400/wl 40
CT angiogra 5mm	0.984	2.5	35.0	0.0	0.0	512	Std	Full w400/wl 40

Table 6 Parameters used for the vascular CTA

CT Helical BMI up to 35 – low dose CT								
Helical CT FULL	Detector coverage	Pitch & Speed (mm/rot)	mA	kV	Helical thickness (mm)	mAs	Rotation time	Beam collimation
0.4sec	40cm	1.375:1 55:00	20	140	2.5	0.9mSv	0.8s	

CT angiogram for patients with a BMI up to 30											
	Scan type	Detector coverage	Pitch speed mm/rot	&Helical thickness	Rotation Time	Interval	kV	mA	Sfov	mAs DLP	Smart prep
VCT	Helical Full 0.4	40mm	0.984:1 39.37	0.625	0.4s	0.625	120	375	large	20.5mSv 1057mGycm	on

Appendix 3

Paraformaldehyde

40grams paraformaldehyde

1-litre distilled water with sodium hydroxide heated to 65°C at pH7.35

Working elastin solution

5% alcoholic hematoxylin	20 ml
10% ferric chloride	8 ml
Weigert's iodine solution	8 ml

Weigert's iodine solution:

Potassium iodide	2 g
Iodine	1 g
Distilled water	100 ml

4 ml of distilled water to dissolve potassium iodide and add iodine; once iodine is dissolved, then the solution is diluted by adding 96 ml of distilled water.

5% alcoholic hematoxylin

Hematoxylin	5 g
100% alcohol	100 ml

Mixed to dissolve with the aid of gentle heat and then filtered.

10% aqueous ferric chloride

Ferric chloride	10 g
Distilled water	100 ml

2% aqueous ferric chloride

10% ferric chloride	10 ml
Distilled water	50 ml

5% aqueous sodium thiosulfate - Van Gieson's counterstain

1% aqueous acid fuchsin	5 ml
Saturated aqueous picric acid	100 ml

TRIS buffer

Sodium chloride	80g
Tris (Tris hydroxymethylamine)	6.06g
1M hydrochloric acid	44ml

1M Hydrochloric acid (HCL)

(85ml HCL/1000ml distilled water) dissolved in 10liters of distilled water and stored at 4^{o}C for up to a month).

Ammonia water (37 mmol/L)

Concentrated Ammonia hydroxide (15 mol/L)	2.5 mL
Deionised water	1l

Appendix 4

Cell composition for each patient's aortic aneurysm wall with varying SUVmax. Cell counts from flow cytometry data obtained as events per mg of wet tissue analysed. These counts are used as e a percentage of the total CD45 positive fraction to obtain correlations between leukocyte content and ^{18}F-FDG uptake in Fig 3.3 from the first 7 patients.

TAA (Marfans)

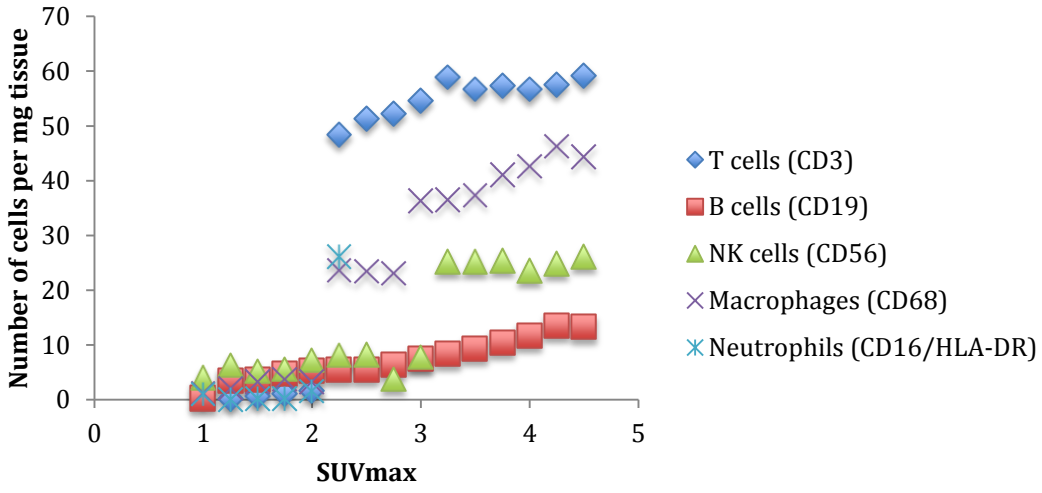

TAA (Degenerative)

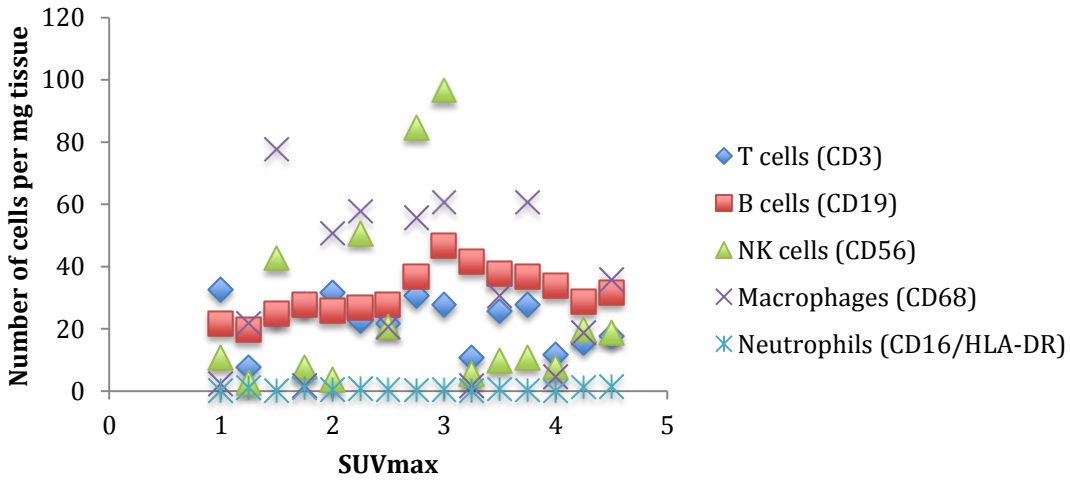

AAA (Juxtra-renal degenerative)

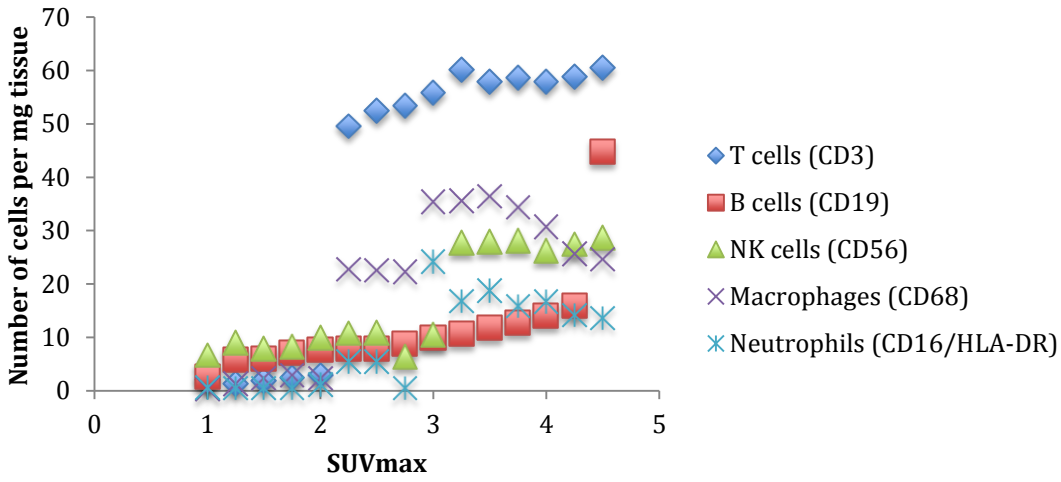

TAA (Degenerative)

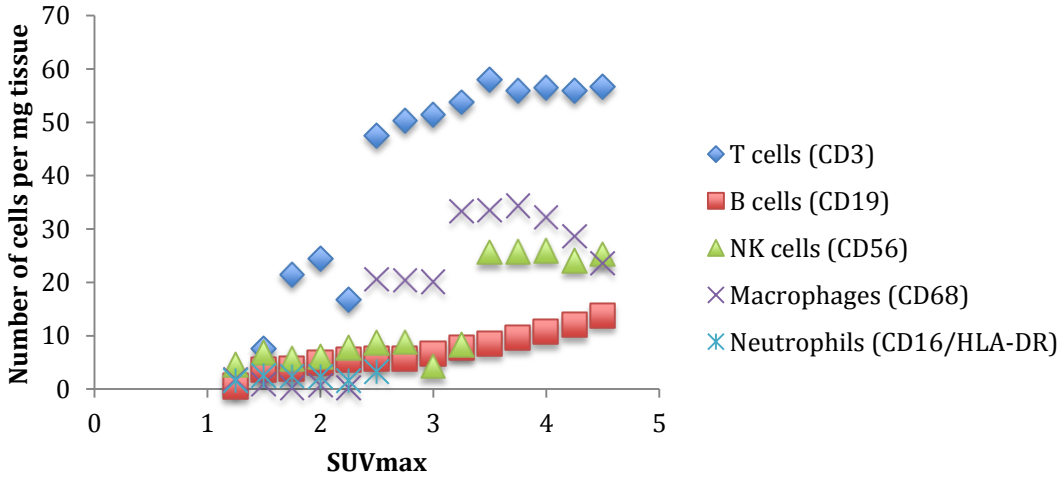

TAA (Degenerative)

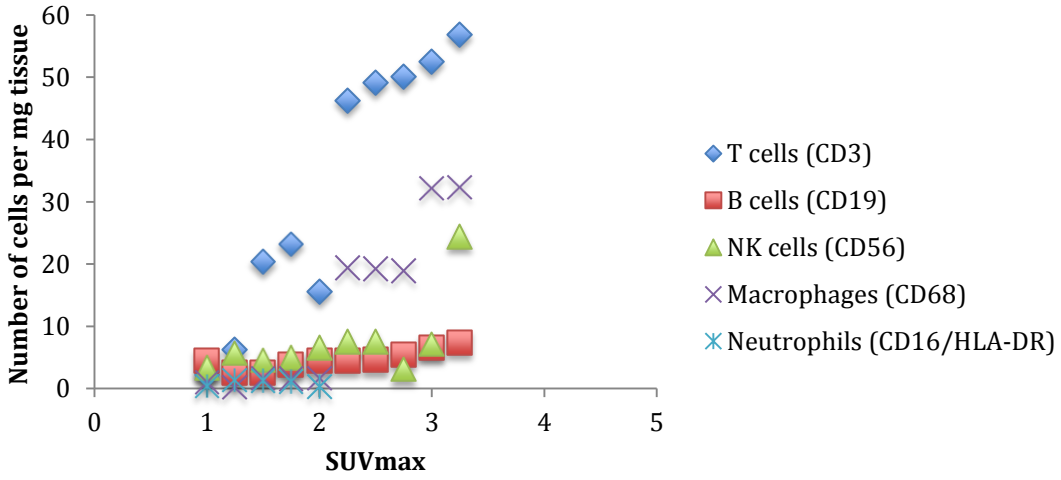

TAA (Degenerative)

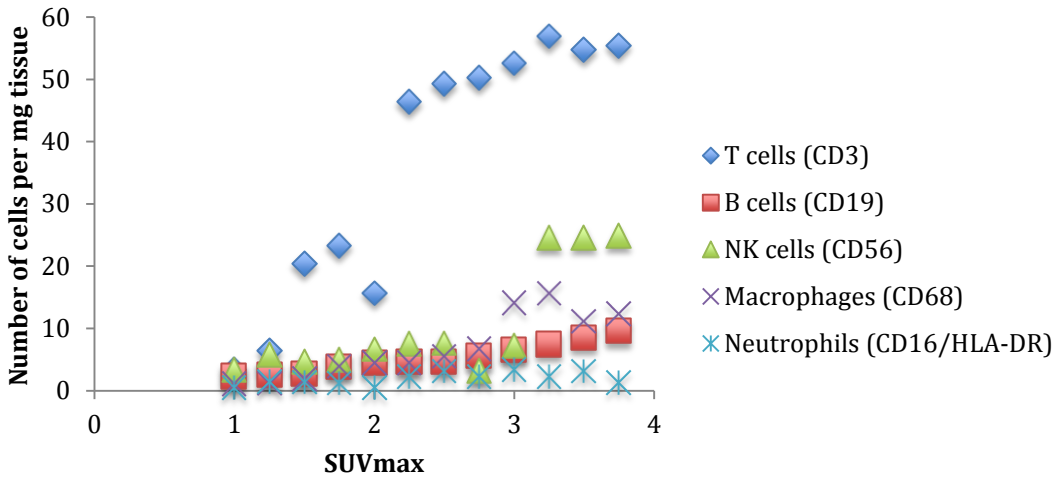

TAA (Degenerative)

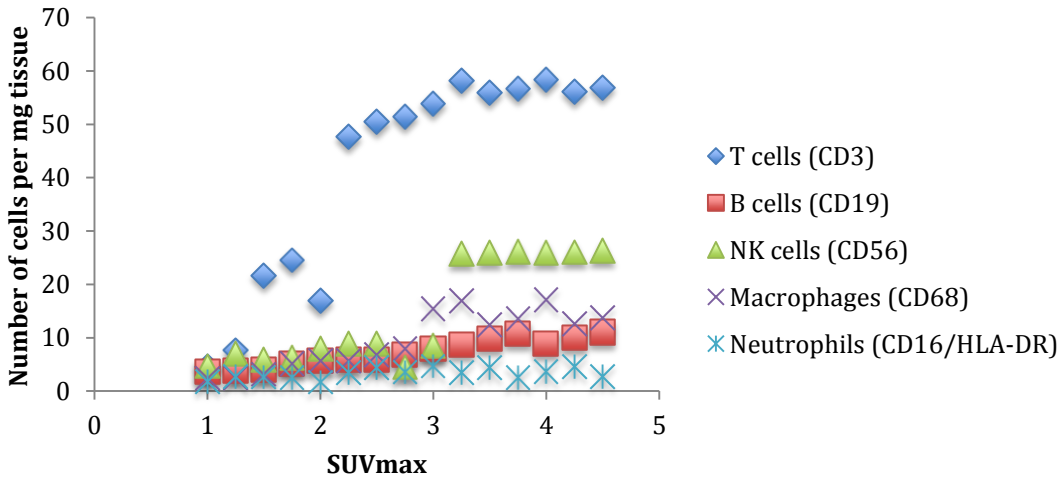

TAA (Chronic Type A dissection)

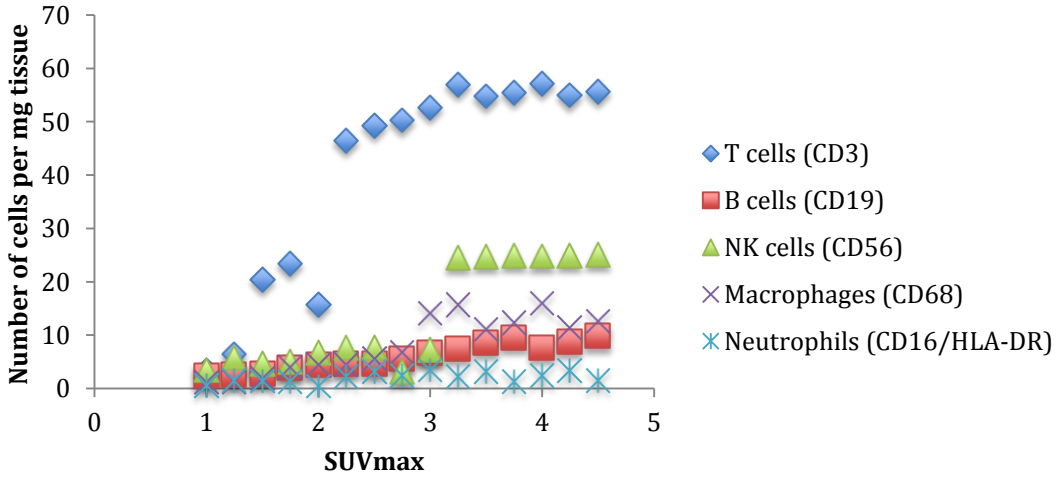

TAA (Degenerative)

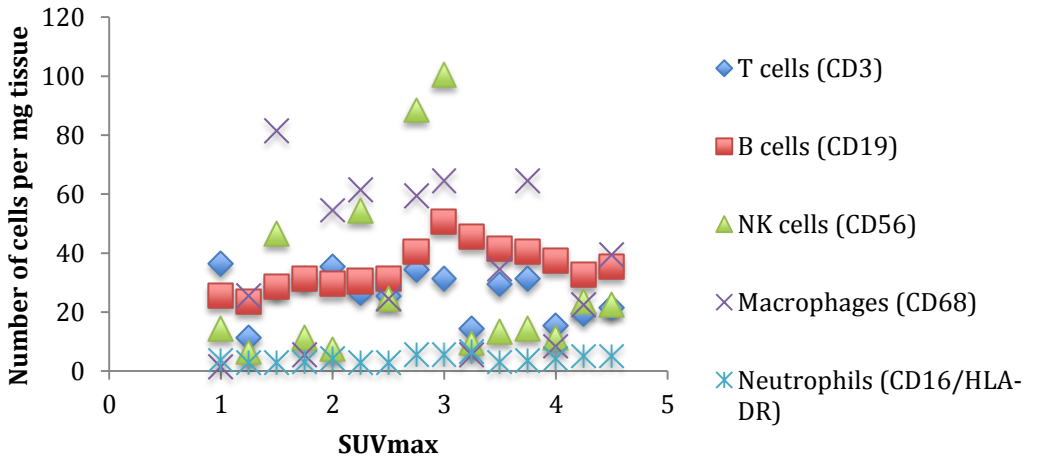

TAA (Degenerative)

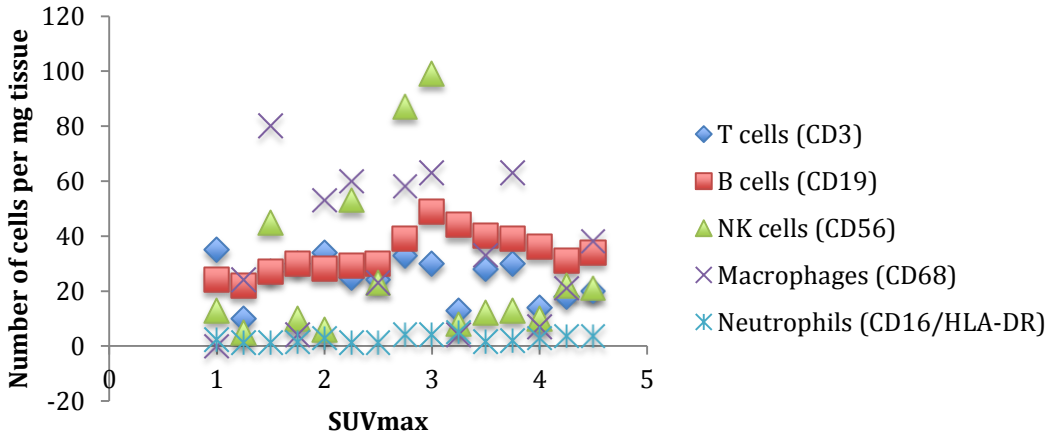

TAA (Chronic Type A dissection)

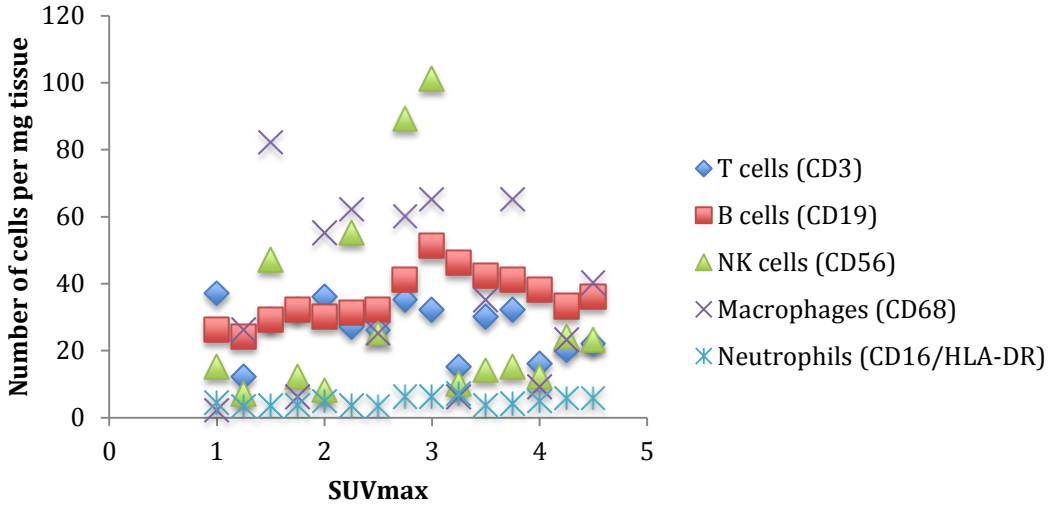

AAA (Juxtra renal degenerative)

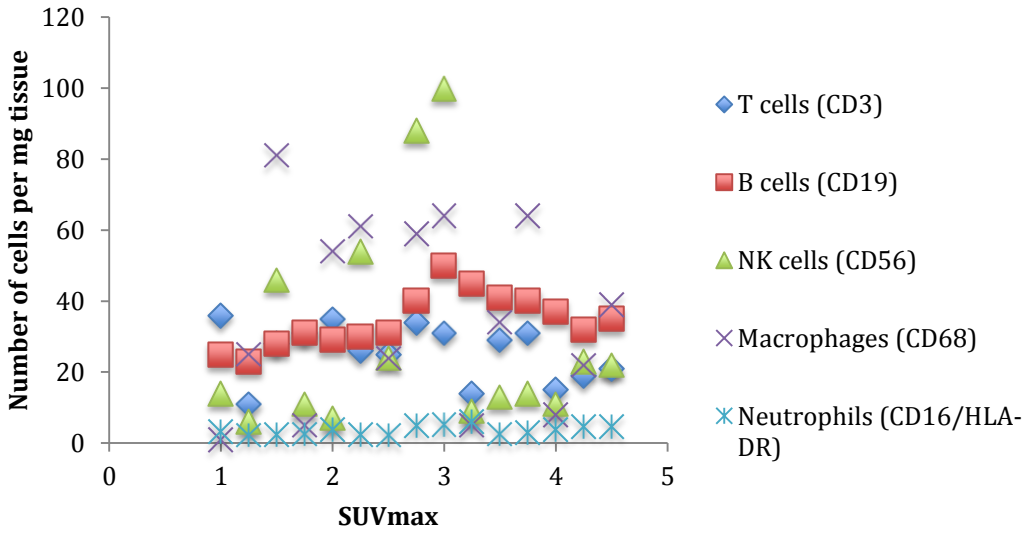

TAA (mucoid degeneration)

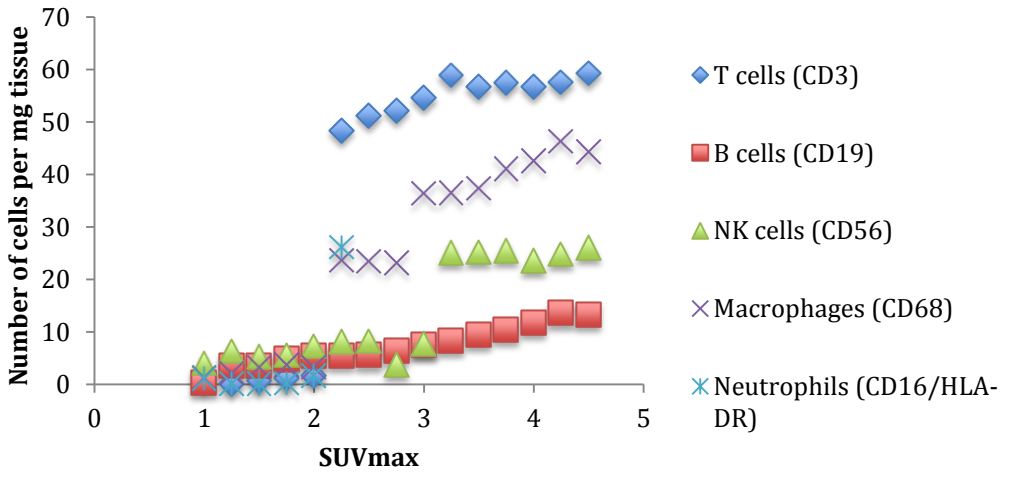

TAA (degenerative)

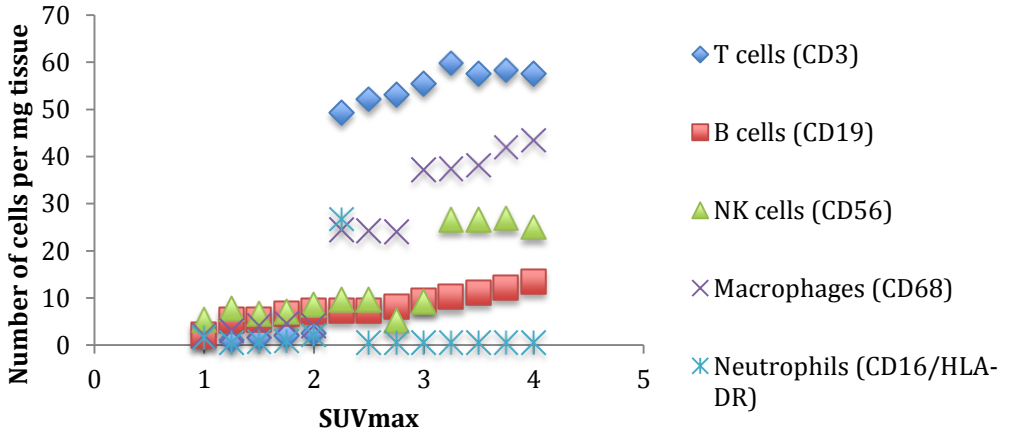

TAA (Degenerative)

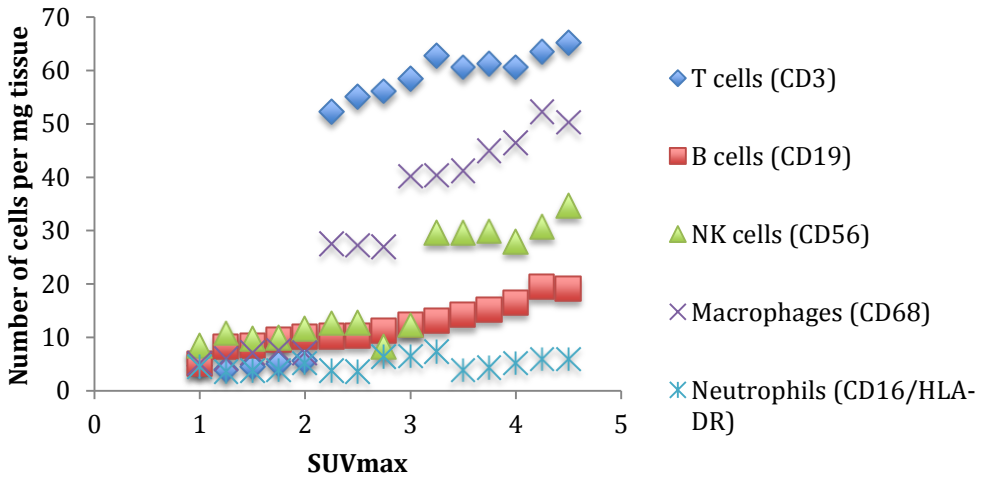

TAA (Degenerative)

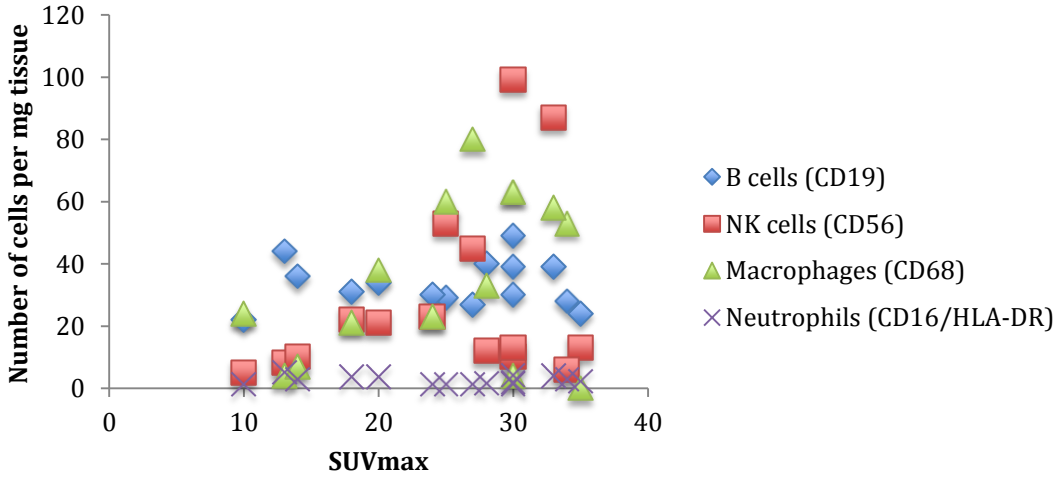

RT-PCR standard curves and slope efficiencies

Murine RT-PCR standard curves

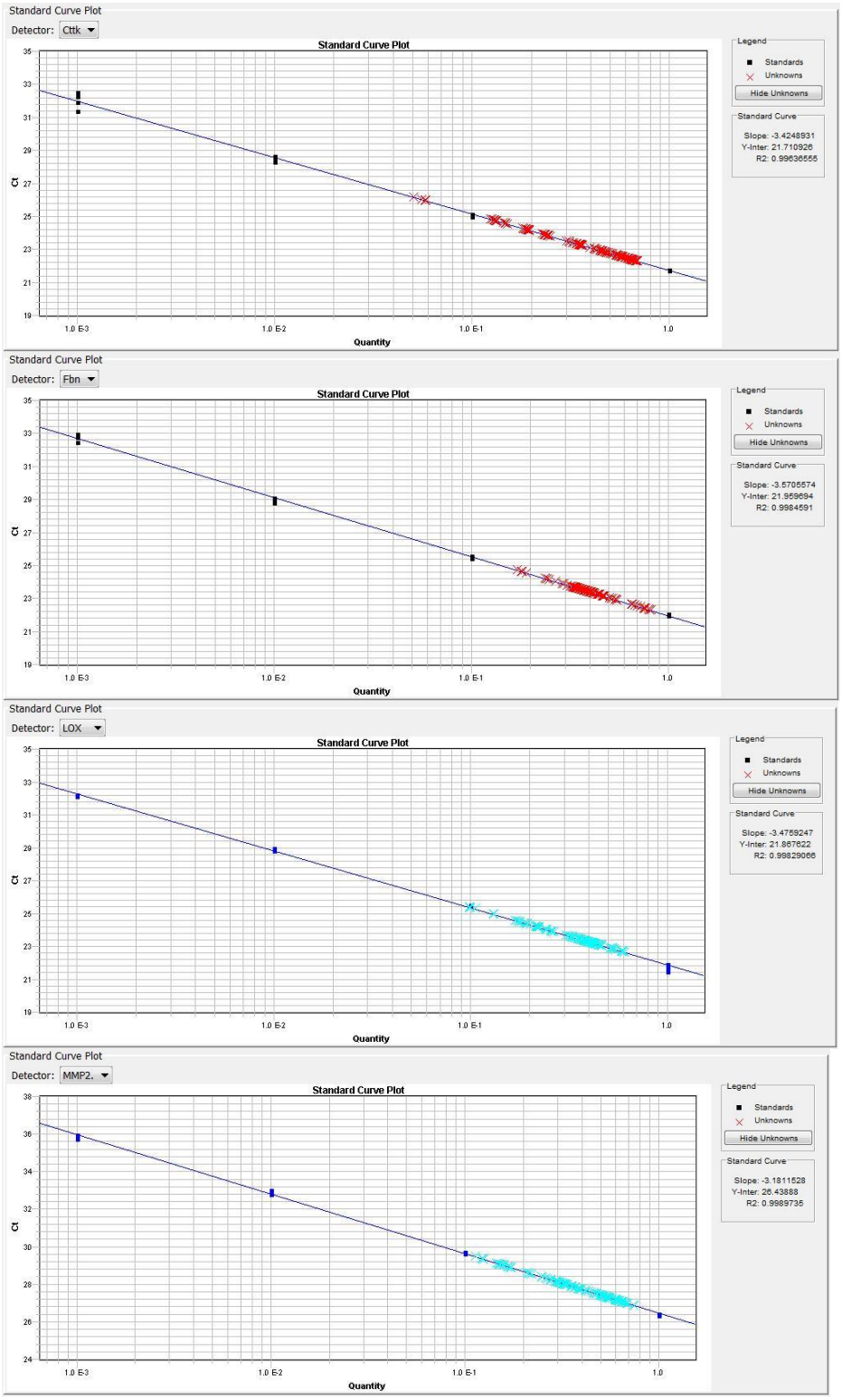

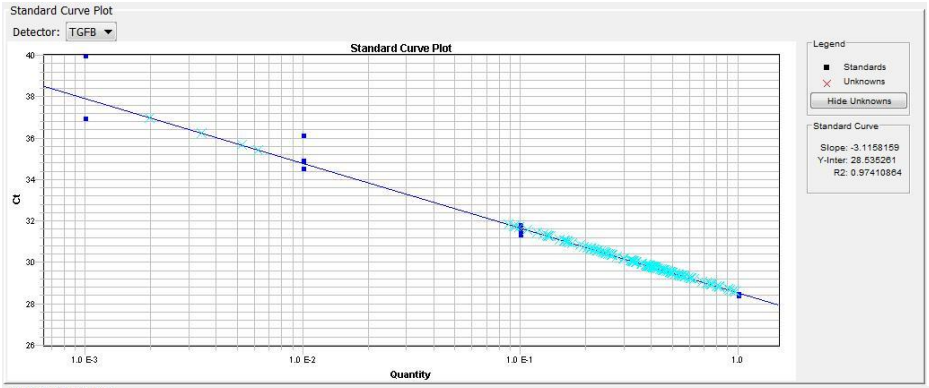
Standard Curve Plot
Detector: TGFB
Standard Curve Plot
Ct
Quantity
1.0 E-3
1.0 E-2
1.0 E-1
1.0
Legend
Standards
Unknowns
Hide Unknowns
Standard Curve
Slope: -3.1158159
Y-Inter: 28.535261
R2: 0.97410864

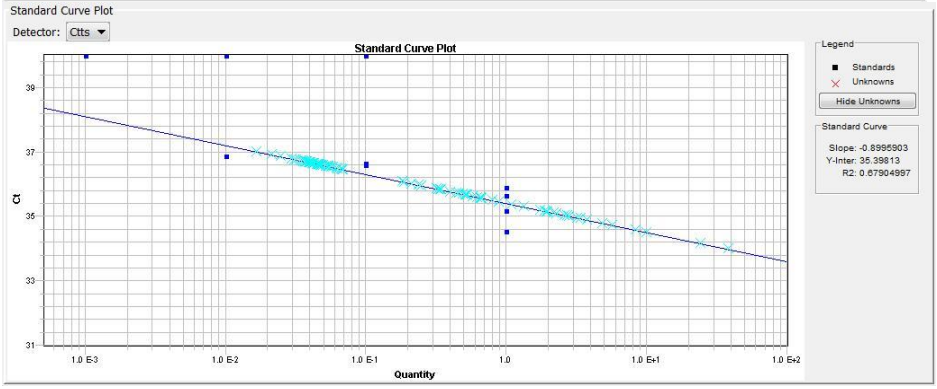
Standard Curve Plot
Detector: Ctts
Standard Curve Plot
Ct
Quantity
1.0 E-3
1.0 E-2
1.0 E-1
1.0
1.0 E+1
1.0 E+2
Legend
Standards
Unknowns
Hide Unknowns
Standard Curve
Slope: -0.8995903
Y-Inter: 35.39813
R2: 0.67904997

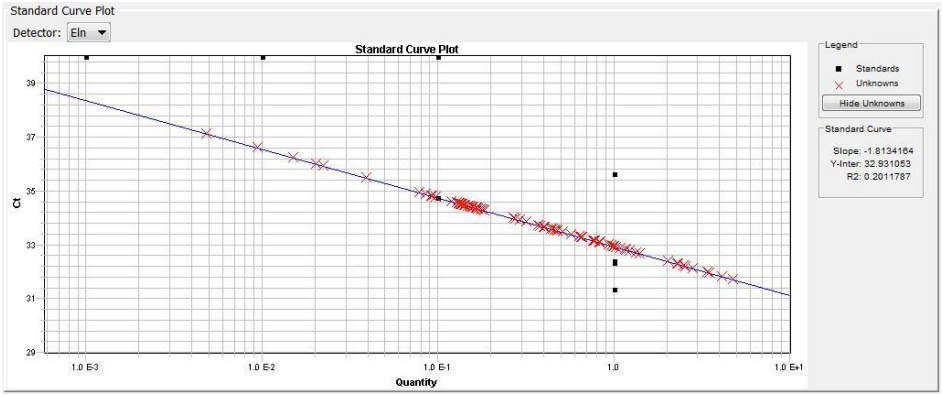
Standard Curve Plot
Detector: Eln
Standard Curve Plot
Ct
Quantity
1.0 E-3
1.0 E-2
1.0 E-1
1.0
1.0 E+1
Legend
Standards
Unknowns
Hide Unknowns
Standard Curve
Slope: -1.8134164
Y-Inter: 32.931053
R2: 0.2011787

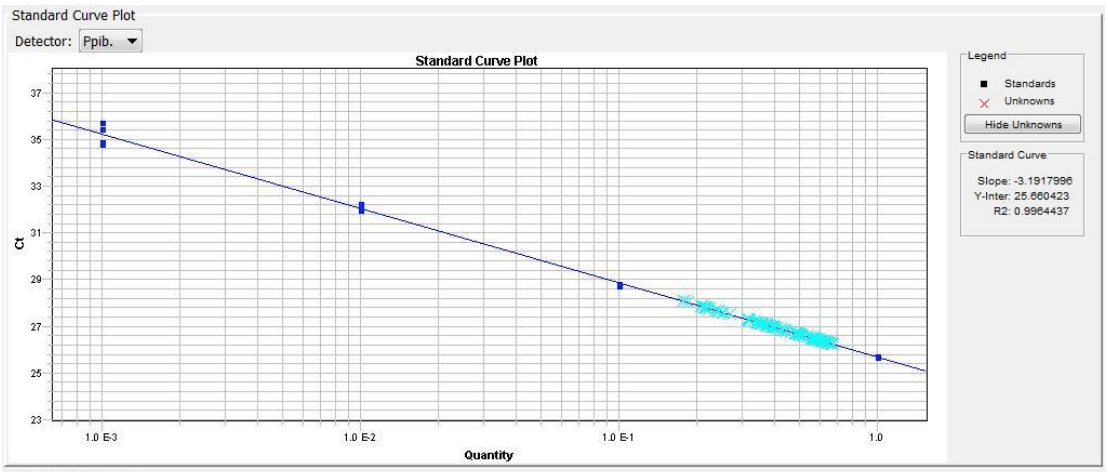
Standard Curve Plot
Detector: Ppib.
Standard Curve Plot
Ct
Quantity
1.0 E-3
1.0 E-2
1.0 E-1
1.0
Legend
Standards
Unknowns
Hide Unknowns
Standard Curve
Slope: -3.1917996
Y-Inter: 25.660423
R2: 0.9964437

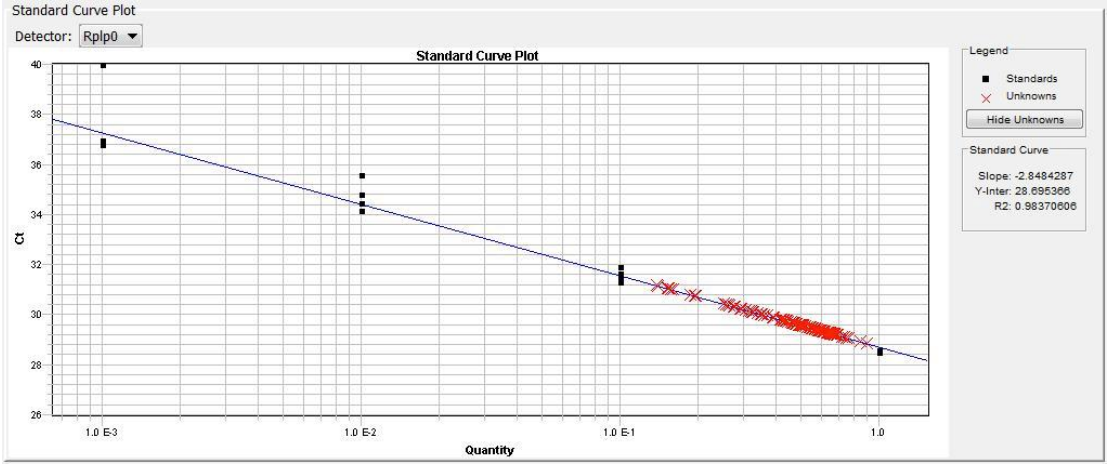
Standard Curve Plot
Detector: Rplp0
Standard Curve Plot
Ct
Quantity
1.0 E-3
1.0 E-2
1.0 E-1
1.0
Legend
Standards
Unknowns
Hide Unknowns
Standard Curve
Slope: -2.8484287
Y-Inter: 28.695366
R2: 0.98370606

References

1. Kampmeier RH. SACCULAR ANEURYSM OF THE THORACIC AORTA: A CLINICAL STUDY OF 633 CASES. Ann Intern Med. 1938;12(5):624-651.

2. Baker WF. The arteries. Press: Silvergirl. 1988. At http://books.google.com/books?id=lp5rp7K9H0kC>

3. Weissmann G. Americans Sweep Nobel Prizes: Thinking Inside and Outside the Box. FASEB. 2007;21(1):1-4

4. Volodos NL, Shekhanin VE, Karpovich IP, et al.: A self-fixing synthetic blood vessel endoprosthesis. Vestn Khir Im I I Grek. 137:123-125 1986

5. Elefteriades JA. Acute aortic disease. Publisher: Informa healthcare. CRC Press. 2007

6. Greenhalgh RM, Brown LC, Kwong GP, Powell JT, Thompson SG; EVAR trial participants. Comparison of endovascular aneurysm repair with open repair in patients with abdominal aortic aneurysm (EVAR trial 1), 30-day operative mortality results: randomised controlled trial. *Lancet.* 2004 Sep 4-10;364(9437):843-8

7. Olsson C, Thelin S, Ståhle E, Ekbom A, Granath F. Thoracic aortic aneurysm and dissection: increasing prevalence and improved outcomes reported in a nationwide population-based study of more than 14,000 cases from 1987 to 2002. *Circulation.* 2006 Dec 12;114(24):2611-8

8. Bickerstaff LK, Pairolero PC, Hollier LH, Melton LJ, Van Peenen HJ, Cherry KJ, Joyce JW, Lie JT. Thoracic aortic aneurysms: a population-based study. *Surgery.* 1982;92(6):1103-8

9. Baliga RR, Nienaber CA, Isselbacher EM, Eagle KA. Aortic dissection and related syndromes. Springer Press. 2007

10. Elefteriades JA. Natural history of thoracic aortic aneurysms: indications for surgery, and surgical versus nonsurgical risks. *The Annals of Thoracic Surgery*. 2002;

11. Brown PM, Zelt DT, Sobolev B. The risk of rupture in untreated aneurysms: The impact of size, gender, and expansion rate. *Jour Vasc Surg*;37(2):280-84

12. Kainulainen K, Karttunen L, Puhakka L, Sakai L, Peitonen. Mutations in the fibrillin gene responsible for dominant ectopia lentis and neonatal Marfans syndrome. *Nature Genetics*;6: 64-69

13. Davies RR, Goldstein LJ, Coady MA, Tittle SL, Rizzo JA, Kopf GS, Elefteriades JA. Yearly rupture or dissection rates for thoracic aortic aneurysms: simple prediction based on size. *Ann Thorac Surg.* 2002;73(1):17-28

14. Brady AR, Thompson SG, Fowkes FG, Greenhalgh RM, Powell JT; UK Small Aneurysm Trial Participants. Abdominal aortic aneurysm expansion: risk factors and time intervals for surveillance. *Circulation.* 2004;110(1):16-21

15. Dapunt OE, Galla JD, Sadeghi AM, Lansman SL, Mezrow CK, de Asla RA, Quintana C, Wallenstein S, Ergin AM, Griepp RB. The natural history of thoracic aortic aneurysms. *J Thorac Cardiovasc Surg.* 1994;107(5):1323-32; discussion 1332-3.

16. Masuda Y, Takanashi K, Takasu J, Morooka N, Inagaki Y. Expansion rate of thoracic aortic aneurysms and influencing factors. *Chest;* 2(2)461-466

17. Miller F. Aortic aneurysms. It is all about the stress. *Arter Thormb Vasc Biol.* 2002;22:1948-1949

18. Bluth EI, Murphey SM, Hollier LH, Sullivan MA. Color flow Doppler in

the evaluation of aortic aneurysms. *Int Angiol.* 1990; 9(1):8-10

19. Nakahashi TK1, Hoshina K, Tsao PS, Sho E, Sho M, Karwowski JK, Yeh C, Yang RB, Topper JN, Dalman RL. Flow loading induces macrophage antioxidative gene expression in experimental aneurysms. *Arterioscler Thromb Vasc Biol.* 2002 1;22(12):2017-22.

20. Hiratzka LF, Bakris GL, Beckman JA, Bersin RM, Carr VF, Casey DE Jr, Eagle KA, LK, Isselbacher EM, Kazerooni EA, Kouchoukos NT, Lytle BW, Milewicz DM, Reich DL, Sen S, Shinn JA, Svensson LG, Williams DM ACCF/AHA/AATS/ACR/ASA/SCA/SCAI/SIR/STS/SVM guidelines for the diagnosis and management of patients with thoracic aortic disease: executive summary. A report of the American College of Cardiology Foundation/American Heart Association Task Force on Practice Guidelines, American Association for Thoracic Surgery, American College of Radiology, American Stroke Association, Society of Cardiovascular Anesthesiologists, Society for Cardiovascular Angiography and Interventions, Society of Interventional Radiology, Society of Thoracic Surgeons, and Society for Vascular Medicine. *J Am Coll Cardiol.* 2010;55(14):1509-1544.

21. Coady MA, Rizzo JA, Goldstein LJ, Elefteriades JA. Natural history, pathogenesis, and etiology of thoracic aortic aneurysms and dissections. *Cardiol Clin.* 1999; 17(4):615-35; vii

22. Mandapati D, Darr U, Kopf GS, Elefteriades JA. What is the appropriate size criterion for resection of thoracic aortic aneurysms? *J Thorac Cardiovasc Surg.* 1997; 113(3):476-91; discussion 489-91

23. Elefteriades JA. Thoracic aortic aneurysm: reading the enemy's playbook. *Curr Probl Cardiol.* 2008; 33(5):203-77

24. Joyce JW, Fairbairn JF 2nd, Kincaid OW, Juergen JL . Aneurysms of the thoracic aorta. A clinical study with special reference to prognosis. *Circulation.* 1964;29:176-81.

25. United Kingdom Small Aneurysm Trial Participants. Long-term outcomes of immediate repair compared with surveillance of small abdominal aortic aneurysms. *N Engl J Med*. 2002; 346(19):1445-52

26. Ashton HA, Buxton MJ, Day NE, Kim LG, Marteau TM, Scott RA, Thompson SG, Walker NM; Multicentre Aneurysm Screening Study Group. The Multicentre Aneurysm Screening Study (MASS) into the effect of abdominal aortic aneurysm screening on mortality in men: a randomised controlled trial. *Lancet.* 2002; 360(9345):1531-9

27. Lederle FA, Johnson GR, Wilson SE, Chute EP, Hye RJ, Makaroun MS, Barone GW, Bandyk D, Moneta GL, Makhoul RG. The aneurysm detection and management study screening program: validation cohort and final results. Aneurysm Detection and Management Veterans Affairs Cooperative Study Investigators. *Arch Intern Med.* 2000; 160(10):1425-30

28. Merali FS, Anand SS. Immediate repair compared with surveillance of small abdominal aortic aneurysms. *Vasc Med.* 2002; 7(3):249-50.

29. Cosford PA, Leng GC, Thomas J. Screening for abdominal aortic aneurysm (Review). *The Cochrane Collaboration.* 2007 Issue 2. Wiley Press.

30. Guo D, Hasham S, Kuang SQ, Vaughan CJ, Boerwinkle E, Chen H, Abuelo D, Dietz HC, Basson CT, Shete SS, Milewicz DM. Familial thoracic aortic aneurysms and dissections: genetic heterogeneity with a major locus mapping to 5q13-14. *Circulation.* 2001; 103(20):2461-8

31. Isselbacher EM. Thoracic and abdominal aortic aneurysms. *Circulation.* 2005; 111(6):816-28

32. Bown MJ, Jones GT, Harrison SC, Wright BJ, Bumpstead S, Baas AF, Gretarsdottir S, Badger SA, Bradley DT, Burnand K, Child AH, Clough RE, Cockerill G, Hafez H, Scott DJ, Futers S, Johnson A, Sohrabi S, Smith A, Thompson MM, van Bockxmeer FM, Waltham M, Matthiasson SE, Thorleifsson G, Thorsteinsdottir U, Blankensteijn JD, Teijink JA, Wijmenga C, de Graaf J, Kiemeney LA, Assimes TL, McPherson R; CARDIoGRAM Consortium; Global BPgen Consortium; DIAGRAM Consortium; VRCNZ Consortium, Folkersen L, Franco-Cereceda A, Palmen J, Smith AJ, Sylvius N, Wild JB, Refstrup M, Edkins S, Gwilliam R, Hunt SE, Potter S, Lindholt JS, Frikke-Schmidt R, Tybjærg-Hansen A, Hughes AE, Golledge J, Norman PE, van Rij A, Powell JT, Eriksson P, Stefansson K, Thompson JR, Humphries SE, Sayers RD, Deloukas P, Samani NJ. Abdominal aortic aneurysm is associated with a variant in low-density lipoprotein receptor-related protein 1. *Am J Hum Genet*. 2011;89(5):619-27

33. Wild JB, Stather PW, Sylvius N, Choke E, Sayers RD, Bown MJ. Low density lipoprotein receptor related protein 1 and abdominal aortic aneurysms. *Eur J Vasc Endovasc Surg.* 2012; 44(2):127-32

34. Deguara J, Burnand KG, Berg J, Green P, Lewis CM, Chinien G, Waltham M, Taylor P, Stern RF, Solomon E, Smith A. An increased frequency of the 5A allele in the promoter region of the MMP3 gene is associated with abdominal aortic aneurysms. *Hum Mol Genet.* 2007; 16(24):3002-7

35. Lesauskaite V, Sinkunaite-Marsalkiene G, Tamosiunas A, Benetis R. Protective effects of angiotensin-converting enzyme I/I and matrix metalloproteinase-3 6A/6A polymorphisms on dilatative pathology within the ascending thoracic aorta. *Eur J Cardiothorac Surg.* 2011; 40(1):23-7

36. Henderson EL, Geng YJ, Sukhova GK, Whittemore AD, Knox J, Libby P. Death of smooth muscle cells and expression of mediators of apoptosis by T

lymphocytes in human abdominal aortic aneurysms. *Circulation.* 1999;99:96–104

37. Acilan C, Serhatli M, Kacar O, Adiguzel Z, Tuncer A, Hayran M, Baysal K. Smooth muscle cells isolated from thoracic aortic aneurysms exhibit increased genomic damage, but similar tendency for apoptosis. *DNA Cell Biol.* 2012; 31(10):1523-34

38. Leeper NJ, Raiesdana A, Kojima Y, Kundu RK, Cheng H, Maegdefessel L, Toh R, Ahn GO, Ali ZA, Anderson DR, Miller CL, Roberts SC, Spin JM, de Almeida PE, Wu JC, Xu B, Cheng K, Quertermous M, Kundu S, Kortekaas KE, Berzin E, Downing KP, Dalman RL, Tsao PS, Schadt EE, Owens GK, Quertermous T. Loss of CDKN2B promotes p53-dependent smooth muscle cell apoptosis and aneurysm formation. *Arterioscler Thromb Vasc Biol.* 2013;33(1):e1-e10.

39. Lee AJ, Fowkes FG, Carson MN, Leng GC, Allan PL. Smoking, atherosclerosis and risk of abdominal aortic aneurysm. *Eur Heart J*. 1997; 18(4):671-6

40. Wang S, Zhang C, Zhang M, Liang B, Zhu H, Lee J, Viollet B, Xia L, Zhang Y, Zou MH. Activation of AMP-activated protein kinase α2 by nicotine instigates formation of abdominal aortic aneurysms in mice in vivo. *Nat Med.* 2012;18(6):902

41. Kaschina E, Scholz H, Steckelings UM, Sommerfeld M, Kemnitz UR, Artuc M, Schmidt S, Unger T. Transition from atherosclerosis to aortic aneurysm in humans coincides with an increased expression of RAS components. *Atherosclerosis*. 2009; 205(2):396-403

42. Ward MR, Pasterkamp G, Yeung AC, Borst C. Arterial remodeling. Mechanisms and clinical implications. *Circulation.* 2000; 102(10):1186-91.

43. Elmore JR, Keister BF, Franklin DP, Youkey JR, Carey DJ. Expression of matrix metalloproteinases and TIMPs in human abdominal aortic aneurysms. *Ann Vasc Surg*. 1998; 12:221–228

44. Newman KM, Jean-Claude J, Li H, Ramey WG, Tilson MD. Cytokines that activate proteolysis are increased in abdominal aortic aneurysms. *Circulation.* 1994;90:II224–7

45. Elmore JR, Keister BF, Franklin DP, Youkey JR, Carey DJ. Expression of matrix metalloproteinases and TIMPs in human abdominal aortic aneurysms. *Ann Vasc Surg.* 1998; 12(3):221-8

46. Wilson WRW, Anderton M, Choke EC, Dawson J, Loftus IM, Thompson MM. Elevated plasma MMP1 and MMP9 are associated with abdominal aortic aneurysm rupture. *Eur J Vasc Endovasc Surg.* 2008; 35:580–584

47. Eriksson P, Jones KG, Brown LC, Greenhalgh RM, Hamsten A, Powell JT. Genetic approach to the role of cysteine proteases in the expansion of abdominal aortic aneurysms. *Br J Surg.* 2004; 91(1):86-9

48. Yasuda Y, Li Z, Greenbaum D, Bogyo M, Weber E, Brömme D. Cathepsin V, a novel and potent elastolytic activity expressed in activated macrophages. *J Biol Chem.* 2004; 279(35):36761-70

49. Abisi S, Burnand KG, Waltham M, Humphries J, Taylor PR, Smith A. Cysteine protease activity in the wall of abdominal aortic aneurysms. *J Vasc Surg.* 2007; 46:1260–1266

50. Moore WS. Vascular Surgery: A comprehensive review. 6th Edition. 2002 Saunders WB

51. Svensson LG, Crawford ES. Cardiovascular and vascular diseases of the aorta. 1997. Saunders WB

52. Johnsen SH, Forsdahl SH, Singh K, Jacobsen BK. Atherosclerosis in abdominal aortic aneurysms: a causal event or a process running in parallel? The Tromsø study. *Arterioscler Thromb Vasc Biol.* 2010; 30(6):1263-8

53. Lenk GM, Tromp G, Weinsheimer S, Gatalica Z, Berguer R, Kuivaniemi H. Whole genome expression profiling reveals a significant role for immune function in human abdominal aortic aneurysms. *BMC Genomics.* 2007; 8:237

54. Treska V, Kocova J, Boudova L, Topolcan O, Molacek J, Tonar Z. Tissue levels of interleukins 6, 8 and of tumor necrosis factor alpha in the wall of ruptured and asymptomatic abdominal aortic aneurysms. *European Surgery.* 2007; 39:307-310

55. Loeys BL, Dietz HC, Braverman AC, Callewaert BL, De Backer J, Devereux RB, Hilhorst-Hofstee Y, Jondeau G, Faivre L, Milewicz DM, Pyeritz RE, Sponseller PD, Wordsworth P, De Paepe AM. The revised Ghent nosology for the Marfan syndrome. *J Med Genet.* 2010; 47(7):476-85

56. Jondeau G, Michel JB, Boileau C. The translational science of Marfan syndrome. *Heart.* 2011; 97(15):1206-14

57. Hutchinson S, Wordsworth BP, Handford PA. Marfan syndrome caused by a mutation in FBN1 that gives rise to cryptic splicing and a 33 nucleotide insertion in the coding sequence. *Hum Genet.* 2001; 109(4):416-20

58. Carta L, Carta L, Pereira L, Pereira L, Arteaga-Solis E, Arteaga-Solis E,

Lee-Arteaga SY, Lee-Arteaga SY, Lenart B, Lenart B, Starcher B, Starcher B, Merkel CA, Merkel CA, Sukoyan M, Sukoyan M, Kerkis A, Kerkis A, Hazeki N, Hazeki N, Keene DR, Keene DR, Sakai LY, Sakai LY, Ramirez F, Ramirez F. Fibrillins 1 and 2 Perform Partially Overlapping Functions during Aortic Development. *J Biol Chem.* 2006;281:8016–8023.

59. Mizuguchi T, Collod-Beroud G, Akiyama T, Abifadel M, Harada N, Morisaki T, Allard D, Varret M, Claustres M, Morisaki H, Ihara M, Kinoshita A, Yoshiura K, Junien C, Kajii T, Jondeau G, Ohta T, Kishino T, Furukawa Y, Nakamura Y, Niikawa N, Boileau C, Matsumoto N. Heterozygous TGFBR2 mutations in Marfan syndrome. *Nat Genet.* 2004;36(8):855-6

60. Forteza A, Evangelista A, Sánchez V, Teixidó G, García D, Sanz P, Gutiérrez L, Centeno J, Rodríguez-Palomares J, Cortina J, García-Dorado D. Study of the efficacy and safety of losartan versus atenolol for aortic dilation in patients with Marfan syndrome. Rev Esp Cardiol (Engl Ed). 2011;64(6):492-8. Heterozygous TGFBR2 mutations in Marfan syndrome. *Nat Genet.* 2004; 36(8):855-60

61. Radonic T, de Witte P, Baars MJ, Zwinderman AH, Mulder BJ, Groenink M; COMPARE study group. Losartan therapy in adults with Marfan syndrome: study protocol of the multi-center randomized controlled COMPARE trial. *Trials.* 2010; 11-3

62. Lu H, Rateri DL, Bruemmer D, Cassis LA, Daugherty A. Involvement of the renin-angiotensin system in abdominal and thoracic aortic aneurysms. *Clin Sci (Lond).* 2012; 123(9):531-43

63. Rughani G, Robertson L, Clarke M. Medical treatment for small abdominal aortic aneurysms. *Cochrane Database Syst Rev*. 2012 Sep 12;9

64. Braiser A, Ju Brooke, Tilton R. Multifaceted role of angiotensin II in

vascular inflammation and aortic aneurysmal disease. edited by Reinhart Grundmann, ISBN 978-953-307-523-5, Published: July 27, 2011 under CC BY-NC-SA 3.0

65. Loeys BL, Chen J, Neptune ER, Judge DP, Podowski M, Holm T, Meyers J, Leitch CC, Katsanis N, Sharifi N, Xu FL, Myers LA, Spevak PJ, Cameron DE, De Backer J, Hellemans J, Chen Y, Davis EC, Webb CL, Kress W, Coucke P, Rifkin DB, De Paepe AM, Dietz HC. A syndrome of altered cardiovascular, craniofacial, neurocognitive and skeletal development caused by mutations in TGFBR1 or TGFBR2. *Nat Genet.* 2005; 37(3):275-81

66. Aalberts JJ, van den Berg MP, Bergman JE, du Marchie Sarvaas GJ, Post JG, van Unen H, Pals G, Boonstra PW, van Tintelen JP. The many faces of aggressive aortic pathology: Loeys-Dietz syndrome. *Neth Heart J*. 2008; 16(9):299-304.

67. Van Hemelrijk C, Renard M, Loeys B. The Loeys-Dietz syndrome: an update for the clinician. *Curr Opin Cardiol.* 2010;25(6):546-51

68. David TE, Armstrong S, Maganti M, Colman J, Bradley TJ. Long-term results of aortic valve-sparing operations in patients with Marfan syndrome. *J Thorac Cardiovasc Surg*. 2009;138(4):859-64; discussion 863-4.

69. Everitt MD, Pinto N, Hawkins JA, Mitchell MB, Kouretas PC, Yetman AT. Cardiovascular surgery in children with Marfan syndrome or Loeys-Dietz syndrome. *J Thorac Cardiovasc Surg.* 2009;137(6):1327-32; discussion 1332-3

70. Lum YW, Brooke BS, Black JH 3rd. Contemporary management of vascular Ehlers-Danlos syndrome. *Curr Opin Cardiol.* 2011;26(6):494-501

71. Gravholt CH, Landin-Wilhelmsen K, Stochholm K, Hjerrild BE, Ledet T, Djurhuus CB, Sylvén L, Baandrup U, Kristensen BØ, Christiansen JS. Clinical and epidemiological description of aortic dissection in Turner's syndrome. *Cardiol Young.* 2006; 16(5):430-6.

72. Matura LA, Ho VB, Rosing DR, Bondy CA. Aortic dilatation and dissection in Turner syndrome. *Circulation.* 2007; 116(15):1663-70.

73. Carlson M, Silberbach M. Dissection of the aorta in Turner syndrome: two cases and review of 85 cases in the literature. *J Med Genet*. 2007; 44(12):745-9

74. Tahara N, Kai H, Ishibashi M, Nakaura H, Kaida H, Baba K, Hayabuchi N, Imaizumi T. Simvastatin attenuates plaque inflammation: evaluation by fluorodeoxyglucose positron emission tomography. *J Am Coll Cardiol*. 2006; 48(9):1825-31

75. Lee SJ, On YK, Lee EJ, Choi JY, Kim BT, Lee KH. Reversal of vascular 18F-FDG uptake with plasma high-density lipoprotein elevation by atherogenic risk reduction. *J Nucl Med.* 2008; 49(8):1277-82

76. Coady MA, Davies RR, Roberts M, Goldstein LJ, Rogalski MJ, Rizzo JA, Hammond GL, Kopf GS, Elefteriades JA. Familial Patterns of Thoracic Aortic Aneurysms. *Arch Surg*. 1999; 134:361–367

77. Sugamura K, Keaney JF Jr. Nicotine: linking smoking to abdominal aneurysms. Nat Med. 2012; 18(6):856-8

78. Schlatmann TJ, Becker AE. Pathogenesis of dissecting aneurysm of aorta. Comparative histopathologic study of significance of medial changes. Am J Cardiol. 1977; 39(1):21-6

79. Golledge J, Norman PE. Atherosclerosis and abdominal aortic aneurysm: cause, response, or common risk factors? *Arterioscler Thromb Vasc Biol.* 2010; 30(6):1075-7

80. Larson EW, Edwards WD. Risk factors for aortic dissection: a necropsy study of 161 cases. *Am J Cardiol.* 1984;53(6):849-55

81. Michelena HI, Desjardins VA, Avierinos JF, Russo A, Nkomo VT, Sundt TM, Pellikka PA, Tajik AJ, Enriquez-Sarano M. Natural history of asymptomatic patients with normally functioning or minimally dysfunctional bicuspid aortic valve in the community. *Circulation.* 2008;117(21):2776-84

82. Abdulkareem N, Smelt J, Jahangiri M. Biscuspid aortic valve aortopathy: genetics, pathophysiology and medical therapy. *Inter Cariovasc and Thorac Surg.* 2013; 17:554-559

83. Della Corte A, Body SC, Booher AM, Schaefers HJ, Milewski RK, Michelena HI, Evangelista A, Pibarot P, Mathieu P, Limongelli G, Shekar PS, Aranki SF, Ballotta A, Di Benedetto G, Sakalihasan N, Nappi G, Eagle KA, Bavaria JE, Frigiola A, Sundt TM; International Bicuspid Aortic Valve Consortium (BAVCon) Investigators. Surgical treatment of bicuspid aortic valve disease: knowledge gaps and research perspectives. *J Thorac Cardiovasc Surg*. 2014;147(6):1749-57

84. Prakash SK, Bossé Y, Muehlschlegel JD, Michelena HI, Limongelli G, Della Corte A, Pluchinotta FR, Russo MG, Evangelista A, Benson DW, Body SC, Milewicz DM; BAVCon Investigators. A roadmap to investigate the genetic basis of bicuspid aortic valve and its complications: insights from the International BAVCon (Bicuspid Aortic Valve Consortium). J Am Coll Cardiol. 2014; 26;64(8):832-9

85. Bavaria JE, Komlo CM, Rhode T, Vallabhajosyula P. Can the bicuspid

aortic valve be spared? The con position, with caveats and nuances. Tex Heart Inst J. 2013;40(5):544-6

86. Nishimura RA, Otto CM, Bonow RO, Carabello BA, Erwin JP 3rd, Guyton RA, O'Gara PT, Ruiz CE, Skubas NJ, Sorajja P, Sundt TM 3rd, Thomas JD; ACC/AHA Task Force Members. 2014 AHA/ACC Guideline for the Management of Patients With Valvular Heart Disease: executive summary: a report of the American College of Cardiology/American Heart Association Task Force on Practice Guidelines. Circulation. 2014; 129(23):2440-92

87. He R, Guo DC, Estrera AL, Safi HJ, Huynh TT, Yin Z, Cao SN, Lin J, Kurian T, Buja LM, Geng YJ, Milewicz DM. Characterization of the inflammatory and apoptotic cells in the aortas of patients with ascending thoracic aortic aneurysms and dissections. *J Thorac Cardiovasc Surg.* 2006; 131(3):671-8

88. Arnaud L, Haroche J, Mathian A, Gorochov G, Amoura Z. Pathogenesis of Takayasu's arteritis: a 2011 update. *Autoimmun Rev.* 2011; 11(1):61-7

89. Sakalihasan N, Delvenne P, Nusgens BV, Limet R, Lapière CM. Activated forms of MMP2 and MMP9 in abdominal aortic aneurysms. *Journ Vasc Surg.* 1996; 24:127–133

90. Sakalihasan N, Limet R, Defawe OD. Abdominal aortic aneurysm. *The Lancet.* 2005; 365:1577-1589

91. Ra HJ, Parks WC. Control of matrix metalloproteinase catalytic activity. *Matrix Biol.* 2007; 26(8):587-96

92. Madala SK, Pesce JT, Ramalingam TR, Wilson MS, Minnicozzi S, Cheever AW, Thompson RW, Mentink-Kane MM, Wynn TA. Matrix metalloproteinase 12-deficiency augments extracellular matrix degrading

metalloproteinases and attenuates IL-13-dependent fibrosis. *J Immunol.* 2010; 184(7):3955-63

93. Hellenthal FAMVI, Buurman WA, Wodzig WKWH, Schurink GWH. Biomarkers of abdominal aortic aneurysm progression. Part 2: inflammation. *Nat Rev Cardiol*. 2009;6:543–552

94. Dawson J, Cockerill G, Choke E, Loftus I, Thompson MM. Aortic aneurysms as a source of circulating interleukin-6. Ann N Y Acad Sci. 2006; 1085:320-3

95. Dawson J, Cockerill G, Choke E, Choke E, Loftus I, Thompson MM, Thompson MM. Circulating Cytokines in Patients with Abdominal Aortic Aneurysms. *Ann N Y Acad Sci*. 2006; 1085:324–326

96. Szekanecz Z, Shah MR, Pearce WH, Koch AE. Human atherosclerotic abdominal aortic aneurysms produce interleukin (IL)-6 and interferon-gamma but not IL-2 and IL-4: the possible role for IL-6 and interferon-gamma in vascular inflammation. *Agents Actions.* 1994;42:159–162

97. Szekanecz Z, Shah MR, Harlow LA, Pearce WH, Koch AE. Interleukin-8 and tumor necrosis factor-alpha are involved in human aortic endothelial cell migration. The possible role of these cytokines in human aortic aneurysmal blood vessel growth. *Pathobiology.* 1994;62(3):134-9.

98. Holmes DR, Wester W, Thompson RW, Reilly JM. Prostaglandin E2 synthesis and cyclooxygenase expression in abdominal aortic aneurysms. *J Vasc Surg*. 1997; 25(5):810-5

99. Holmes DR, Liao S, Parks WC, Thompson RW. Medial neovascularization in abdominal aortic aneurysms: a histopathologic marker of aneurysmal degeneration with pathophysiologic implications. *J Vasc Surg.* 1995; 21(5): 761-71; discussion 771-2

100. Walton LJ, Franklin IJ, Bayston T, Brown LC, Greenhalgh RM, Taylor GW, Powell JT. Inhibition of prostaglandin E2 synthesis in abdominal aortic aneurysms: implications for smooth muscle cell viability, inflammatory processes, and the expansion of abdominal aortic aneurysms. *Circulation.* 1999 Jul 6;100(1):48-54.

101. Ocana E, Bohórquez J-C, Pérez-Requena J, Brieva JA, Rodríguez C. Characterisation of T and B lymphocytes infiltrating abdominal aortic aneurysms. *Atherosclerosis* 2003; 170:39–48

102. Koch AE, Haines GK, Rizzo RJ, Radosevich JA, Pope RM, Robinson PG, Pearce WH. Human abdominal aortic aneurysms. Immunophenotypic analysis suggesting an immune-mediated response. *Am J Pathol.* 1990; 137(5):1199-213

103. Shi GP, Lindholt JS. Mast cells in abdominal aortic aneurysms. *Curr Vascular Pharmacol.* 11, 314–326 (2013)

104. Cohen JR, Parikh S, Grella L, Sarfati I, Corbie G, Danna D, Wise L. Role of the neutrophil in abdominal aortic aneurysm development. *Cardiovasc Surg.* 1993; 1(4):373-6

105. Eliason JL, Hannawa KK, Ailawadi G, Sinha I, Ford JW, Deogracias MP, Roelofs KJ, Woodrum DT, Ennis TL, Henke PK, Stanley JC, Thompson RW, Upchurch GR Jr. Neutrophil depletion inhibits experimental abdominal aortic aneurysm formation. *Circulation.* 2005 Jul 12;112(2):232-40

106. Bai Z, Bai Z, Cai L, Cai L, Umemoto E, Umemoto E, Takeda A, Takeda A, Tohya K, Tohya K, Komai Y, Komai Y, Veeraveedu PT, Veeraveedu PT, Hata E, Hata E, Sugiura Y, Sugiura Y, Kubo A, Kubo A, Suematsu M, Suematsu M,

Hayasaka H, Hayasaka H, Okudaira S, Okudaira S, Aoki J, Aoki J, Tanaka T, Tanaka T, Albers HMHG, Albers HMHG, Ovaa H, Ovaa H, Miyasaka M, Miyasaka M. Constitutive Lymphocyte Transmigration across the Basal Lamina of High Endothelial Venules Is Regulated by the Autotaxin/Lysophosphatidic Acid Axis. *J Immunol*. 2013; 190:2036–2048

107. Umemoto E, Hayasaka H, Bai Z, Cai L, Yonekura S, Peng X, Takeda A, Tohya K, Miyasaka M. Novel regulators of lymphocyte trafficking across high endothelial venules. *Crit Rev Immunol.* 2011; 31(2):147-69

108. Tsuboi K, Hirakawa J, Seki E, Imai Y, Yamaguchi Y, Fukuda M, Kawashima H. Role of high endothelial venule-expressed heparan sulfate in chemokine presentation and lymphocyte homing. *J Immunol.* 2013; 191(1):448-55

109. Stem cells: scientific progress and future research directions. NIH.US. 2001

110. The age of insight. The quest to understand the unconscious in art, mind and brain. Random House LLC, 2012

111. Schönbeck U, Sukhova GK, Gerdes N, Libby P. T(H)2 predominant immune responses prevail in human abdominal aortic aneurysm. *Am J Pathol.* 2002; 161(2):499-506

112. Piccirillo CA. Regulatory T-cells in health and disease. Cytokine. 2008; 43(3):395-401

113. Thompson RW. Aneurysm treatments expand. *Nat Med*. 2005; 11:1279–1281

114. Kuivaniemi H, Platsoucas CD, Tilson MD 3rd. Aortic aneurysms: An immune disease with a strong genetic component. *Circulation*. 2008;

117(2):242-52

115. Galle C, Schandené L, Stordeur P, Peignois Y, Ferreira J, Wautrecht J-C, Dereume J-P, Goldman M. Predominance of type 1 CD4+T cells in human abdominal aortic aneurysm. *Clin Exp Immunol*. 2005;0:051006055454003.

116. Reiner SL. Development in motion: helper T cells at work. *Cell.* 2007;129(1):33-6

117. Murphy KM, Reiner SL. The lineage decisions of helper T cells. *Nat Rev Immunol.* 2002; 2(12):933-44

118. Wang Y, Ait-Oufella H, Herbin O, Bonnin P, Ramkhelawon B, Taleb S, Huang J, Offenstadt G, Combadière C, Rénia L, Johnson JL, Tharaux P-L, Tedgui A, Mallat Z. TGF-beta activity protects against inflammatory aortic aneurysm progression and complications in angiotensin II-infused mice. *J Clin Invest*. 2010;120:422–432

119. Dai J, Dai J, Losy F, Guinault A-M, Pages C, Anegon I, Desgranges P, Becquemin J-P, Allaire E. Overexpression of Transforming Growth Factor- 1 Stabilizes Already-Formed Aortic Aneurysms: A First Approach to Induction of Functional Healing by Endovascular Gene Therapy. *Circulation*. 2005; 112:1008–1015

120. Shanley CJ, Gharaee-Kermani M, Sarkar R. Transforming growth factor-β 1 increases lysyl oxidase enzyme activity and mRNA in rat aortic smooth muscle cells. *J Vasc Surg.* 1997; 25(3):446-52

121. Bettelli E, Korn T, Kuchroo VK. Th17: the third member of the effector T cell trilogy. *Curr Opin Immunol.* 2007; 19(6):652-7

122. Afzali B, Lombardi G, Lechler RI, Lord GM. The role of T helper 17 (Th17) and regulatory T cells (Treg) in human organ transplantation and

autoimmune disease. *Clin Exp Immunol.* 2007; 148(1):32-46

123. Piccirillo CA, d'Hennezel E, Sgouroudis E, Yurchenko E. CD4+Foxp3+ regulatory T cells in the control of autoimmunity: in vivo veritas. *Curr Opin Immunol.* 2008; 20(6):655-62

124. Haribhai D, Williams JB, Jia S, Nickerson D, Schmitt EG, Edwards B, Ziegelbauer J, Yassai M, Li SH, Relland LM, Wise PM, Chen A, Zheng YQ, Simpson PM, Gorski J, Salzman NH, Hessner MJ, Chatila TA, Williams CB. A requisite role for induced regulatory T cells in tolerance based on expanding antigen receptor diversity. *Immunity.* 2011; 35(1):109-22

125. Laurence A, O'Shea JJ. T(H)-17 differentiation: of mice and men. *Nat Immunol.* 2007; 8(9):903-5

126. Bobryshev YV, Lord RS. Vascular-associated lymphoid tissue (VALT) involvement in aortic aneurysm. *Atherosclerosis.* 2001; 154(1):15-21

127. Bobryshev YV, Lord RS, Pärsson H. Immunophenotypic analysis of the aortic aneurysm wall suggests that vascular dendritic cells are involved in immune responses. *Cardiovasc Surg.* 1998; 6(3):240-9

128. Walton LJ, Powell JT, Parums DV. Unrestricted usage of immunoglobulin heavy chain genes in B cells infiltrating the wall of atherosclerotic abdominal aortic aneurysms. *Atherosclerosis*. 1997;135:65–71

129. Nagasawa T. Microenvironmental niches in the bone marrow required for B-cell development. *Nat Rev Immunol.* 2006; 6(2):107-16

130. Brophy CM, Reilly JM, Smith GJ, Tilson MD. The role of inflammation in nonspecific abdominal aortic aneurysm disease. *Ann Vasc Surg.* 1991; 5(3):229-33

131. Capella JF, Paik DC, Yin NX, Gervasoni JE, Tilson MD. Complement activation and subclassification of tissue immunoglobulin G in the abdominal aortic aneurysm. *J Surg Res.* 1996; 65(1):31-3

132. Immunobiology: The Immune System in Health and Disease. Charles Janeway, Paul Travers. *Current Biology,* Immune system 1 Jan 1997

133. Bendelac A, Savage PB, Teyton L. The biology of NKT cellsT-cells. *Annu Rev Immunol.* 2007; 25:297-336

134. Lindeman JH, Abdul-Hussien H, Schaapherder AF, Van Bockel JH, Von der Thüsen JH, Roelen DL, Kleemann R. Enhanced expression and activation of pro-inflammatory transcription factors distinguish aneurysmal from atherosclerotic aorta: IL-6- and IL-8-dominated inflammatory responses prevail in the human aneurysm. *Clin Sci (Lond).* 2008; 114(11):687-97

135. Shimizu K, Mitchell RN, Libby P. Inflammation and cellular immune responses in abdominal aortic aneurysms. *Arterioscler Thromb Vasc Biol.* 2006; 26(5):987-94

136. Nahrendorf M, Keliher E, Marinelli B, Leuschner F, Robbins CS, Gerszten RE, Pittet MJ, Swirski FK, Weissleder R. Detection of Macrophages in Aortic Aneurysms by Nanoparticle Positron Emission Tomography-Computed Tomography. *Arterioscler Thromb Vasc Biol*. 2011;31:750–757

137. Nahrendorf M, Pittet MJ, Swirski FK. Monocytes: protagonists of infarct inflammation and repair after myocardial infarction. *Circulation.* 2010; 121(22):2437-45

138. Tazume H, Miyata K, Tian Z, Endo M, Horiguchi H, Takahashi O, Horio E, Tsukano H, Kadomatsu T, Nakashima Y, Kunitomo R, Kaneko Y, Moriyama S, Sakaguchi H, Okamoto K, Hara M, Yoshinaga T, Yoshimura K, Aoki H, Araki K, Hao H, Kawasuji M, Oike Y. Macrophage-derived angiopoietin-like protein 2

accelerates development of abdominal aortic aneurysm. *Arterioscler Thromb Vasc Biol.* 2012; 32(6):1400-9

139. Hans CP, Koenig SN, Huang N, Cheng J, Beceiro S, Guggilam A, Kuivaniemi H, Partida-Sánchez S, Garg V. Inhibition of Notch1 signaling reduces abdominal aortic aneurysm in mice by attenuating macrophage-mediated inflammation. *Arterioscler Thromb Vasc Biol.* 2012; 32(12):3012-23

140. Tsunemi K, Takai S, Nishimoto M, Yuda A, Hasegawa S, Sawada Y, Fukumoto H, Sasaki S, Miyazaki M. Possible roles of angiotensin II-forming enzymes, angiotensin converting enzyme and chymase-like enzyme, in the human aneurysmal aorta. *Hypertens Res.* 2002; 25(6):817-22

141. Mäyränpää MI, Trosien JA, Fontaine V, Folkesson M, Kazi M, Eriksson P, Swedenborg J, Hedin U. Mast associate with neovessels in the media and adventitia of abdominal aortic aneurysms. *J Vasc Surg.* 2009; 50(2):388-95; discussion 395-6

142. Ait-Oufella H, Wang Y, Herbin O, Bourcier S, Potteaux S, Joffre J, Loyer X, Ponnuswamy P, Esposito B, Dalloz M, Laurans L, Tedgui A, Mallat Z. Natural regulatory T-cells limit angiotensin II-induced aneurysm formation and rupture in mice. *Arterioscler Thromb Vasc Biol.* 2013; 33(10):2374-9

143. Yin M, Zhang J, Wang Y, Wang S. Deficient CD4+ CD25+ T regulatory cell function in patients with abdominal aortic aneurysms. *Arterioscler Thromb Vasc Biol.* 2010; 30(9):1825-31

144. Fontaine V, Touat Z, Mtairag el M, Vranckx R, Louedec L, Houard X, Andreassian B, Sebbag U, Palombi T, Jacob MP, Meilhac O, Michel JB. Role of leukocyte elastase in preventing cellular re-colonization of the mural thrombus. *Am J Pathol.* 2004; 164(6):2077-87

145. Satta J, Läärä E, Juvonen T. Intraluminal thrombus predicts rupture of an abdominal aortic aneurysm. *J Vasc Surg.* 1996; 23(4):737-9

146. Carrell TW, Burnand KG, Booth NA, Humphries J, Smith A. Intraluminal thrombus enhances proteolysis in abdominal aortic aneurysms. *Vascular.* 2006; 14(1):9-16

147. Strieter RM, Kasahara K, Allen R, Showell HJ, Standiford TJ, Kunkel SL. Human neutrophils exhibit disparate chemotactic factor gene expression. *Biochem Biophys Res Commun.* 1990; 173(2):725-30.

148. McCain RW, Dessypris EN, Christman JW. Granulocyte/macrophage colony-stimulating factor stimulates human polymorphonuclear leukocytes to produce interleukin-8 in vitro. *Am J Respir Cell Mol Biol.* 1993; 8(1):28-34

149. Sun J, Sukhova GK, Yang M, Wolters PJ, MacFarlane LA, Libby P, Sun C, Zhang Y, Liu J, Ennis TL, Knispel R, Xiong W, Thompson RW, Baxter BT, Shi GP. Mast cells modulate the pathogenesis of elastase-induced abdominal aortic aneurysms in mice. *J Clin Invest.* 2007; 117(11):3359-68

150. Herron GS, Unemori E, Wong M, Rapp JH, Hibbs MH, Stoney RJ. Connective tissue proteinases and inhibitors in abdominal aortic aneurysms. Involvement of the vasa vasorum in the pathogenesis of aortic aneurysms. *Arterioscler Thromb.* 1991; 11(6):1667-77

151. Choke E, Choke E, Thompson MM, Dawson J, Wilson WRW, Sayed S, Loftus IM, Cockerill GW. Abdominal Aortic Aneurysm Rupture Is Associated With Increased Medial Neovascularization and Overexpression of Proangiogenic Cytokines. *Arterioscler Thromb Vasc Biol*. 2006; 26:2077–2082.

152. Thompson RW, Geraghty PJ, Lee JK. Abdominal aortic aneurysms: basic mechanisms and clinical implications. *Curr Probl Surg.* 2002; 39(2):110-230

153. Blomkalns AL, Gavrila D, Thomas M, Neltner BS, Blanco VM, Benjamin SB, McCormick ML, Stoll LL, Denning GM, Collins SP, Qin Z, Daugherty A, Cassis LA, Thompson RW, Weiss RM, Lindower PD, Pinney SM, Chatterjee T, Weintraub NL. CD14 directs adventitial macrophage precursor recruitment: role in early abdominal aortic aneurysm formation. *J Am Heart Assoc.* 2013; 2(2):e000065

154. Alkiviadis T, Krawiec JT, Vorp DA. Elastin and collagen fibre microstructure of the human aorta in ageing and disease: a review. *J R Soc Interface.* 2013; 10(83):20121004

155. Nicosia RF, Zorzi P, Ligresti G, Morishita A, Aplin AC. Paracrine regulation of angiogenesis by different cell types in the aorta ring model. *Int J Dev Biol.* 2011; 55(4-5):447-53.

156. Wilson WR, Anderton M, Schwalbe EC, Jones JL, Furness PN, Bell PR, Thompson MM. Matrix metalloproteinase-8 and -9 are increased at the site of abdominal aortic aneurysm rupture. *Circulation.* 2006; 113(3):438-45

157. Hamano Y, Zeisberg M, Sugimoto H, Lively JC, Maeshima Y, Yang C, Hynes RO, Werb Z, Sudhakar A, Kalluri R. Physiological levels of tumstatin, a fragment of collagen IV alpha3 chain, are generated by MMP-9 proteolysis and suppress angiogenesis via alphaV beta3 integrin. *Cancer Cell*. 2003; 3(6):589-601

158. Cockerill GW, Gamble JR, Vadas MA. Angiogenesis: models and modulators. *Int Rev Cytol.* 1995; 159:113-60.

159. Rundhaug JE. Matrix metalloproteinases and angiogenesis. *J Cell Mol Med.* 2005; 9(2):267-85

160. Sakamoto A, Kawashiri M, Ishibashi-Ueda H, Sugamoto Y, Yoshimuta T, Higashikata T, Ogino H, Tada H, Konno T, Hayashi K, Yamagishi M.

Expression and Function of Ephrin-B1 and Its Cognate Receptor EphB2 in Human Abdominal Aortic Aneurysm. *Int J Vasc Med.* 2012; 2012:127149

161. Pasquale EB. Eph receptors and ephrins in cancer: bidirectional signalling and beyond. *Nat Rev Cancer*. 2010; 10(3):165-80

162. Almine JF, Bax DV, Mithieux SM, Nivison-Smith L, Rnjak J, Waterhouse A, Wise SG, Weiss AS. Elastin-based materials. *Chem Soc Rev.* 2010; 39(9):3371-9

163. Daamen WF, Veerkamp JH, van Hest JC, van Kuppevelt TH. Elastin as a biomaterial for tissue engineering. *Biomaterials.* 2007; 28(30):4378-98

164. Debelle L, Alix AJ. The structures of elastins and their function. *Biochimie.* 1999; 81(10):981-94

165. Bashir MM, Indik Z, Yeh H, Ornstein-Goldstein N, Rosenbloom JC, Abrams W, Fazio M, Uitto J, Rosenbloom J. Characterization of the complete human elastin gene. Delineation of unusual features in the 5'-flanking region. *J Biol Chem.* 1989; 264(15):8887-91

166. Indik Z, Yoon K, Morrow SD, Cicila G, Rosenbloom J, Rosenbloom J, Ornstein-Goldstein N. Structure of the 3' region of the human elastin gene: great abundance of Alu repetitive sequences and few coding sequences. *Connect Tissue Res.* 1987;16(3):197-211

167. Indik Z, Yeh H, Ornstein-Goldstein N, Kucich U, Abrams W, Rosenbloom JC, Rosenbloom J. Structure of the elastin gene and alternative splicing of elastin mRNA: implications for human disease. *Am J Med Genet.* 1989; 34(1):81-90

168. Mithieux SM, Weiss AS. Elastin. *Adv Protein Chem.* 2005; 70:437-61

169. Wise SG, Weiss AS. Tropoelastin. *The Int Journ Biochem & Cell Biol.*

2009; 41(3):494-497

170. Wirtschafter ZT, Cleary EG, Jackson DS, Sandberg LB. Histological changes during the development of the bovine nuchal ligament. *Journ Cell Biol.*1967;33:481–488

171. Jackson DS, Cleary EG. The determination of collagen and elastin. *Methods Biochem Anal.* 1967;15:25–76

172. Jacob MP, Sauvage M, Osborne-Pellegrin M. [Regulation of elastin synthesis]. *J Soc Biol*. 2001;195(2):131-41

173. Shapiro SD, Endicott SK, Province MA, Pierce JA, Campbell EJ. Marked Longevity of Human Lung Parenchymal Elastic Fibers Deduced From Prevalence of D-Aspartate and Nuclear-Weapons Related Radiocarbon. *Journ Clin Invest.* 1991;87:1828–1834

174. Alternative splicing of human elastin mRNA indicated by sequence analysis of cloned genomic and complementary DNA. 1987; **84,** 5680–5684

175. Satoh K, Nigro P, Matoba T, O'Dell MR, Cui Z, Shi X, Mohan A, Yan C, Abe J-I, Illig KA, Berk BC. Cyclophilin A enhances vascular oxidative stress and the development of angiotensin II induced aortic aneurysms. *Nat Med*. 2009;15:649–656

176. Getie M, Schmelzer CEH, Neubert RHH. Characterization of peptides resulting from digestion of human skin elastin with elastase. *Proteins: Structure, Function, and Bioinformatics*. 2005;61:649–657

177. Klevay LM. Cardiovascular disease from copper deficiency - a history. *Jour Nutr.* 2000;130:489S-494S

178. Mäki JM, Räsänen J, Tikkanen H, Sormunen R, Mäkikallio K, Kivirikko

KI, Soininen R. Inactivation of the lysyl oxidase gene Lox leads to aortic aneurysms, cardiovascular dysfunction, and perinatal death in mice. *Circulation.* 2002;106:2503–2509

179. Menashi S, Campa JS, Greenhalgh RM, Powell JT. Collagen in abdominal aortic aneurysm: typing, content, and degradation. J Vasc Surg. 1987;6(6):578-82

180. Abdominal aortic aneurysm. Report of a meeting of physicians and scientists, University College London Medical School. *Lancet*__1993; 341(8839):215-20

181. Bressan GM, Daga-Gordini D, Colombatti A, Castellani I, Marigo V, Volpin D. Emilin, a component of elastic fibers preferentially located at the elastin-microfibrils interface. *The Journal of cell biology*. 1993; 121:201–212

182. Zanetti M, Braghetta P, Sabatelli P, Mura I, Doliana R, Colombatti A, Volpin D, Bonaldo P, Bressan GM. EMILIN-1 deficiency induces elastogenesis and vascular cell defects. *Mol Cell Biol.* 2004; 24(2):638-50

183. Rosenbloom J, Abrams WR, Mecham R. Extracellular matrix 4: the elastic fiber. *FASEB J.* 1993; **7:**1208–1218

184. Mithieux SM, Wise SG, Raftery MJ, Starcher B, Weiss AS. A model two-component system for studying the architecture of elastin assembly in vitro. *J Struct Biol.* 2005; 149(3):282-9

185. Wise SG, Mithieux SM, Raftery MJ, Weiss AS. Specificity in the coacervation of tropoelastin: solvent exposed lysines. *J Struct Biol.* 2005; 149(3):273-81

186. Yamauchi Y, Tsuruga E, Nakashima K, Sawa Y, Ishikawa H. Fibulin-4 and -5, but not Fibulin-2, are Associated with Tropoelastin Deposition in Elastin-Producing Cell Culture. *Acta Histochem Cytochem*. 2010; 43(6):131-8

187. Vrhovski B, Jensen S, Weiss AS. Coacervation characteristics of recombinant human tropoelastin. *Eur J Biochem.* 1997; 250(1):92-8

188. Debelle L, Tamburro AM. Elastin: molecular description and function. *Int J Biochem Cell Biol.* 1999; 31(2):261-72

189. Daga-Gordini D1, Bressan GM, Castellani I, Volpin D. Detection of elastin by immunoelectronmicroscopy. A comparison of different procedures. *Histochemistry.* 1987;87(6):573-8

190. Daga-Gordini D, Bressan GM, Castellani I, Volpin D. Fine mapping of tropoelastin-derived components in the aorta of developing chick embryo. *The Histochemical journal* 1987;19:623–632

191. Ruoslahti E. RGD and other recognition sequences for integrins. *Annu Rev Cell Dev Biol.* 1996;12:697-715

192. Gibson MA, Leavesley DI, Ashman LK. Microfibril-associated glycoprotein-2 specifically interacts with a range of bovine and human cell types via alphaVbeta3 integrin. *J Biol Chem.* 1999; 274(19):13060-5

193. Pfaff M, Reinhardt DP, Sakai LY, Timpl R. Cell adhesion and integrin binding to recombinant human fibrillin-1. *FEBS Lett.* 1996; 384(3):247-50

194. Nakamura T, Lozano PR, Ikeda Y, Iwanaga Y, Hinek A, Minamisawa S, Cheng CF, Kobuke K, Dalton N, Takada Y, Tashiro K, Ross Jr J, Honjo T, Chien KR. Fibulin-5/DANCE is essential for elastogenesis in vivo. *Nature.* 2002; 415(6868):171-5

195. Swee MH, Parks WC, Pierce RA. Developmental regulation of elastin production. Expression of tropoelastin pre-mRNA persists after down-regulation of steady-state mRNA levels. *J Biol Chem.* 1995; 270(25):14899-906.

196. Antonicelli F, Bellon G, Debelle L, Hornebeck W. Elastin-elastases and inflamm-aging. *Curr Top Dev Biol.* 2007; 79:99-155.

197. Gross J, Nagai Y. Specific degradation of the collagen molecule by tadpole collagenolytic enzyme. *Proc Natl Acad Sci U S A.* 1965; 54(4):1197-204

198. Sonesson B, Malina M, Ivancev K, Lindh M, Lindblad B, Brunkwall J. Dilatation of the infrarenal aneurysm neck after endovascular exclusion of abdominal aortic aneurysm. *J Endovasc Surg.* 1998; 5(3):195-200

199. Fülöp T, Khalil A, Larbi A. The role of elastin peptides in modulating the immune response in aging and age-related diseases. *Pathologie Biologie*. 2012;60:28–33.

200. Varga Z, Kovács EM, Paragh G, Jacob MP, Robert L, Fülöp T. Effect of elastin peptides and N-formyl-methionyl-leucyl phenylalanine on cytosolic free calcium in polymorphonuclear leukocytes of healthy middle-aged and elderly subjects. *Clinical biochemistry*. 1988;21:127–130

201. Brown SL, Busuttil RW, Baker JD, Machleder HI, Moore WS, Barker WF. Bacteriologic and surgical determinants of survival in patients with mycotic aneurysms. *J Vasc Surg.* 1984 Jul;1(4):541-7

202. Fortun A, Khalil A, Gagné D, Douziech N, Kuntz C, Jay-Gerin JP, Dupuis G, Fülöp T Jr. Monocytes influence the fate of T-cells challenged with oxidised low density lipoproteins towards apoptosis or MHC-restricted proliferation. *Atherosclerosis.* 2001;156(1):11-21

203. Hsu RB, Lin FY. Infected aneurysm of the thoracic aorta. *J Vasc Surg.* 2008; 47(2):270-6

204. Hornebeck W, Derouette JC, Roland J, Châtelet F, Bouissou H, Robert

L. Correlation between age, arteriosclerosis and elastinolytic activity of human aorta wall]. *C R Acad Sci Hebd Seances Acad Sci D.* 1976; 282(22):2003-6

205. Hornebeck W, Emonard H. The cell-elastin-elastase(s) interacting triade directs elastolysis. *Front Biosci* (Landmark Ed). 2011;16:707-22.

206. Hinek A. Biological roles of the non-integrin elastin/laminin receptor. *Biol Chem.* 1996; 377(7-8):471-80

207. Dobrin PB, Baker WH, Gley WC. Elastolytic and collagenolytic studies of arteries. Implications for the mechanical properties of aneurysms. *Arch Surg.* 1984; 119(4):405-9

208. Wikby A, Johansson B, Olsson J, Löfgren S, Nilsson BO, Ferguson F.Expansions of peripheral blood CD8 T-lymphocyte subpopulations and an association with cytomegalovirus seropositivity in the elderly: the Swedish NONA immune study. 37, 445–453 (2002). *Exp Gerontol.* 2002; 37(2-3):445-53

209. Fulop T Jr, Larbi A, Fortun A, Robert L, Khalil A. Elastin peptides induced oxidation of LDL by phagocytic cells. 53, 416–423 (2005). *Pathol Biol (Paris)*. 2005; 53(7):416-23

210. Hass GM. 1942. Elastic tissue. II. A study of the elasticity and tensile strength of elastic tissue isolated from the human aorta. *Arch. Path*. 34, 971

211. Faber M, Moller-Hou G. The human aorta. V. Collagen and elastin in the normal and hypertensive aorta. *Acta Pathol Microbiol Scand.* 31, 377–382 (1952)

212. Schlatmann TJ, Becker AE. Pathogenesis of dissecting aneurysm of

aorta. Comparative histopathologic study of significance of medial changes. *Am J Cardiol.* 1977;39(1):21-6

213. John R, Thomas J. Chemical compositions of elastins isolated from aortas and pulmonary tissues of humans of different ages. *Biochem J.* 1972; 127(1):261-9

214. Fujimoto D. Aging and cross-linking in human aorta. *Biochem Biophys Res Commun.* 1982; 109(4):1264-9

215. Paz MA, Keith DA, Traverso HP, Gallop PM. Isolation, purification, and cross-linking profiles of elastin from lung and aorta. *Biochemistry.* 1976; 15(22):4912-8

216. Spina M, Garbin G. Age-related chemical changes in human elastins from non-atherosclerotic areas of thoracic aorta. *Atherosclerosis.* 1976; 24(1-2):267-79

217. Toda T, Tsuda N, Nishimori I, Leszczynski DE, Kummerow FA. Morphometrical analysis of the aging process in human arteries and aorta. 106, 35–44 (1980). *Acta Anat (Basel).* 1980;106(1):35-44

218. Sans M, Moragas A. Mathematical morphologic analysis of the aortic medial structure. Biomechanical implications. *Anal Quant Cytol Histol.* 1993; 15(2):93-100

219. Avolio A, Jones D, Tafazzoli-Shadpour M. Quantification of alterations in structure and function of elastin in the arterial media. *Hypertension.* 1998; 32(1):170-5

220. Greenwald SE. Ageing of the conduit arteries. *J Pathol.* 2007; 211(2):157-72

221. Wolinsky H, Glagov S. Comparison of abdominal and thoracic aortic

medial structure in mammals. Deviation of man from the usual pattern. *Circ Res.* 1969; 25(6):677-86

222. Cheuk BL, Cheng SW. Expression of integrin alpha5beta1 and the relationship to collagen and elastin content in human suprarenal and infrarenal aortas. *Vasc Endovascular Surg.* 2005; 39(3):245-51

223. Oh SP, Kamagata Y, Muragaki Y, Timmons S, Ooshima A, Olsen BR. Isolation and sequencing of cDNAs for proteins with multiple domains of Gly-Xaa-Yaa repeats identify a distinct family of collagenous proteins. *Proc Natl Acad Sci U S A.* 1994; 91(10):4229-33

224. Halfter W, Dong S, Schurer B, Cole GJ. Collagen XVIII is a basement membrane heparan sulfate proteoglycan. 273, 25404–25412 (1998). *Biol Chem.* 1998; 273(39):25404-12

225. Prockop DJ, Kivirikko KI, Tuderman L, Guzman NA. The biosynthesis of collagen and its disorders *N Engl J Med.* 1979; 301(1):13-23

226. Uitto J. Biochemistry of the elastic fibers in normal connective tissues and its alterations in diseases. *J Invest Dermatol.* 1979;72(1):1-10

227. Hatzinikolas G, Gibson MA. The exon structure of the human MAGP-2 gene - Similarity with the MAGP-1 gene is confined to two exons encoding a cysteine-rich region. *J Biol Chem.* 1998; 273(45):29309-14

228. Dobrin PB, Doyle JM. Vascular Smooth Muscle and Anisotropy of Dog Carotid Artery. *Circ Res.* 1970; 27(1):105-19

229. Dobrin PB, Anidjar S. Pathophysiology of arterial aneurysms. *Arch Mal Coeur Vaiss.* 1991;84 Spec No 3:57-62

230. Brown SL, Backstrom B, Busuttil RW. A new serum proteolytic enzyme in aneurysm pathogenesis. *J Vasc Surg.* 1985; 2(3):393-9

231. Annabi B, Shédid D, Ghosn P, Kenigsberg RL, Desrosiers RR, Bojanowski MW, Beaulieu E, Nassif E, Moumdjian R, Béliveau R. Differential regulation of matrix metalloproteinase activities in abdominal aortic aneurysms. *J Vasc Surg.* 2002; 35(3):539-46

232. Carrell TW, Burnand KG, Wells GM, Clements JM, Smith A. Stromelysin-1 (matrix metalloproteinase-3) and tissue inhibitor of metalloproteinase-3 are overexpressed in the wall of abdominal aortic aneurysms. *Circulation.* 2002; 105(4):477-82

233. Longo GM, Buda SJ, Fiotta N, Xiong W, Griener T, Shapiro S, Baxter BT. MMP-12 has a role in abdominal aortic aneurysms in mice. *Surgery.* 2005; 137(4):457-62.

234. Mao D, Lee J, Van Vickle S, Thompson R. Expression of collagenase-3 (MMP-13) in human abdominal aortic aneurysms and vascular smooth muscle cells in culture. *Biochem Biophys Res Commun.* 1999; 261(3):904-10

235. Curci JA, Liao S, Huffman MD, Shapiro SD, Thompson RW. Expression and localization of macrophage elastase (matrix metalloproteinase-12) in abdominal aortic aneurysms. *J Clin Invest*. 1998; 102(11):1900-10

236. Thompson RW, Holmes DR, Mertens RA, Liao S, Botney MD, Mecham RP, Welgus HG, Parks WC. Production and localization of 92-kilodalton gelatinase in abdominal aortic aneurysms. An elastolytic metalloproteinase expressed by aneurysm-infiltrating macrophages. *J Clin Invest.* 1995; 96(1):318-26

237. Longo GM, Xiong W, Greiner TC, Zhao Y, Fiotti N, Baxter BT. Matrix metalloproteinases 2 and 9 work in concert to produce aortic aneurysms. *J Clin Invest*. 2002; 110:625–632

238. Papalambros E, Sigala F, Georgopoulos S, Menekakos C, Giatromanolaki A, Bastounis E, Sivridis E. Immunohistochemical expression of metalloproteinases MMP-2 and MMP-9 in abdominal aortic aneurysms: correlation with symptoms and aortic diameter. *Int J Mol Med.* 2003; 12(6):965-8

239. Borges LF, Touat Z, Leclercq A, Zen AA, Jondeau' G, Franc B, Philippe M, Meilhac O, Gutierrez PS, Michel JB. Tissue diffusion and retention of metalloproteinases in ascending aortic aneurysms and dissections. *Hum Pathol.* 2009;40(3):306-13

240. Tamarina NA, McMillan WD, Shively VP, Pearce WH. Expression of matrix metalloproteinases and their inhibitors in aneurysms and normal aorta. *Surgery.* 1997; 122(2):264-71; discussion 271-2

241. Higashikata T, Yamagishi M, Sasaki H, Minatoya K, Ogino H, Ishibashi-Ueda H, Hao H, Nagaya N, Tomoike H, Sakamoto A. Application of real-time RT-PCR to quantifying gene expression of matrix metalloproteinases and tissue inhibitors of metalloproteinases in human abdominal aortic aneurysm. *Atherosclerosis.* 2004; 177(2):353-60

242. Lim CS, Shalhoub J, Gohel MS, Shepherd AC, Davies AH. Matrix metalloproteinases in vascular disease--a potential therapeutic target? *Curr Vasc Pharmacol.* 2010; 8(1):75-85

243. Thompson AR, Drenos F, Hafez H, Humphries SE. Candidate gene association studies in abdominal aortic aneurysm disease: a review and meta-analysis. *Eur J Vasc Endovasc Surg.* 2008; 35(1):19-30

244. McMillan WD, Patterson BK, Keen RR, Shively VP, Cipollone M, Pearce WH. In situ localization and quantification of mRNA for 92-kD type IV collagenase and its inhibitor in aneurysmal, occlusive, and normal aorta.

Arterioscler Thromb Vasc Biol. 1995;15(8):1139-44

245. McMillan WD, Patterson BK, Keen RR, Shively VP, Cipollone M, Pearce WH. In situ localization and quantification of mRNA for 92-kD type IV collagenase and its inhibitor in aneurysmal, occlusive, and normal aorta. *Arterioscler Thromb Vasc Biol.* 1995; 15(8):1139-44

246. Rouis M, Adamy C, Duverger N, Lesnik P, Horellou P, Moreau M, Emmanuel F, Caillaud JM, Laplaud PM, Dachet C, Chapman MJ. Adenovirus-mediated overexpression of tissue inhibitor of metalloproteinase-1 reduces atherosclerotic lesions in apolipoprotein E-deficient mice. *Circulation.* 1999; 100(5):533-40

247. Burtea C, Laurent S, Murariu O, Rattat D, Toubeau G, Verbruggen A, Vansthertem D, Vander Elst L, Muller RN. Molecular imaging of alpha v beta3 integrin expression in atherosclerotic plaques with a mimetic of RGD peptide grafted to Gd-DTPA. *Cardiovasc Res.* 2008 ;78(1):148-57

248. Allaire E, Forough R, Clowes M, Starcher B, Clowes AW. Local overexpression of TIMP-1 prevents aortic aneurysm degeneration and rupture in a rat model. *J Clin Invest.* 1998; 102(7):1413-20

249. Winter PM, Caruthers SD, Zhang H, Williams TA, Wickline SA, Lanza GM. Antiangiogenic synergism of integrin-targeted fumagillin nanoparticles and atorvastatin in atherosclerosis. *JACC Cardiovasc Imaging*. 2008; 1(5):624-34

250. Baker AH, Edwards DR, Murphy G. Metalloproteinase inhibitors: biological actions and therapeutic opportunities. *J Cell Sci*. 2002; 115(Pt 19):3719-27

251. Zucker S, Cao J, Chen WT. Critical appraisal of the use of matrix metalloproteinase inhibitors in cancer treatment. *Oncogene*. 2000;

19(56):6642-50

252. Gacko M, Głowiński S. Activities of proteases in parietal thrombus of aortic aneurysm. *Clin Chim Acta.* 1998; 271(2):171-7

253. Gacko M, Chyczewski L. Activity and localization of cathepsin B, D and G in aortic aneurysm. *International Surgery* 1997; 82:398–402

254. Sukhova G, Shi G, Simon D. Expression of the elastolytic cathepsins S and K in human atheroma and regulation of their production in smooth muscle cells. *J Clin Invest.* 1998; 102(3):576-83

255. Reddy VY, Zhang QY, Weiss SJ. Pericellular mobilization of the tissue-destructive cysteine proteinases, cathepsins B, L, and S, by human monocyte-derived macrophages. *Proc Natl Acad Sci U S A.* 1995; 92(9):3849-53

256. Puizdar V, Zajc T, Zerovnik E, Renko M, Pieper U, Eswar N, Sali A, Dolenc I, Turk V. Biochemical characterization and structural modeling of human cathepsin E variant 2 in comparison to the wild-type protein. *Biol Chem*. 2012; 393(3):177-86

257. Repnik U, Stoka V, Turk V, Turk B. Lysosomes and lysosomal cathepsins in cell death. *Biochem Biophys Acta.* 2012; 1824(1):22-33

258. Abrahamson M, Alvarez-Fernandez M, Nathanson CM. *Cystatins.* 2003; 70:179-199

259. Qin Y, Cao X, Guo J, Zhang Y, Pan L, Zhang H, Li H, Tang C, Du J, Shi GP. Deficiency of cathepsin S attenuates angiotensin II-induced abdominal aortic aneurysm formation in apolipoprotein E-deficient mice. *Cardiovasc Res.* 2012; 96(3):401-10

260. Lindholt JS, Erlandsen EJ, Henneberg EW. Cystatin C deficiency is

associated with the progression of small abdominal aortic aneurysms. *Br J Surg.* 2001; 88(11):1472-5

261. Sukhova GK, Wang B, Libby P, Pan JH, Zhang Y, Grubb A, Fang K, Chapman HA, Shi GP. Cystatin C deficiency increases elastic lamina degradation and aortic dilatation in apolipoprotein E-null mice. *Circ Res.* 2005; 96(3):368-75

262. Makowski MR, Wiethoff AJ, Blume U, Cuello F, Warley A, Jansen CHP, Nagel E, Razavi R, Onthank DC, Cesati RR, Marber MS, Schaeffter T, Smith A, Robinson SP, Botnar RM. Assessment of atherosclerotic plaque burden with an elastin-specific magnetic resonance contrast agent. *Nat Med*. 2011; 17:383–388

263. Makowski MR, Preissel A, Bary von C, Warley A, Schachoff S, Keithan A, Cesati RR, Onthank DC, Schwaiger M, Robinson SP, Botnar RM. Three-Dimensional Imaging of the Aortic Vessel Wall Using an Elastin-Specific Magnetic Resonance Contrast Agent. *Investigative Radiology*. 2012;47:438–444

264. Reeps C, Essler M, Pelisek J, Seidl S, Eckstein HH, Krause BJ. Increased 18F-fluorodeoxyglucose uptake in abdominal aortic aneurysms in positron emission/computed tomography is associated with inflammation, aortic wall instability, and acute symptoms. *J Vasc Surg.* 2008; 48(2):417-23

265. Mehta NN, Torigian DA, Gelfand JM, Saboury B, Alavi A. Quantification of atherosclerotic plaque activity and vascular inflammation using [18-F] fluorodeoxyglucose positron emission tomography/computed tomography (FDG-PET/CT). *J Vis Exp*. 2012; (63):e3777

266. Karantanis D, Subramaniam RM, Peller PJ, Lowe VJ, Durski JM, Collins DA, Georgiou E, Ansell SM, Wiseman GA. The value of

[(18)F]fluorodeoxyglucose positron emission tomography/computed tomography in extranodal natural killer/T-cell lymphoma. *Clin Lymphoma Myeloma.* 2008; 8(2):94-9

267. Murata Y, Kubota K, Yukihiro M, Ito K, Watanabe H, Shibuya H. Correlations between 18F-FDG uptake by bone marrow and hematological parameters: measurements by PET/CT. *Nucl Med Biol.* 2006; 33(8):999-1004

268. Fukuchi K, Ishida Y, Higashi M, Tsunekawa T, Ogino H, Minatoya K, Kiso K, Naito H. Detection of aortic graft infection by fluorodeoxyglucose positron emission tomography: comparison with computed tomographic findings. *J Vasc Surg.* 2005; 42(5):919-25

269. Wassélius J, Malmstedt J, Kalin B, Larsson S, Sundin A, Hedin U, Jacobsson H. High 18F-FDG Uptake in synthetic aortic vascular grafts on PET/CT in symptomatic and asymptomatic patients. *J Nucl Med.* 2008; 49(10):1601-5

270. Kilk K, Hyhlik-Dürr A, Afshar-Oromieh A, Böckler D. Chronic abdominal aortic graft infection : Detection with 18F-FDG-PET/CT. *Chirurg.* 2010; 81(7):653-6

271. Ben-Haim S, Israel O. PET/CT for atherosclerotic plaque imaging. *Q J Nucl Med Mol Imaging.* 2006; 50(1):53-60

272. Kinahan PE, Fletcher JW. Positron emission tomography-computed tomography standardized uptake values in clinical practice and assessing response to therapy. *Semin Ultrasound CT MR.* 2010; 31(6):496-505

273. Tong S, Alessio AM, Kinahan PE. Image reconstruction for PET/CT scanners: past achievements and future challenges. *Imaging Med.* 2010; 2(5):529-545

274. Kohlmyer SG, Alessio AM, Kinahan PE, Hurley DP. Methods and systems for attentuation correction in medical imaging. *Google patents.* 2010. http://www.google.com/patents/US7729467?dq=kinahan+pe

275. Tsuruda T, Hatakeyama K, Nagamachi S, Sekita Y, Sakamoto S, Endo GJ, Nishimura M, Matsuyama M, Yoshimura K, Sato Y, Onitsuka T, Imamura T, Asada Y, Kitamura K. Inhibition of development of abdominal aortic aneurysm by glycolysis restriction. *Arterioscler Thromb Vasc Biol.* 2012; 32(6):1410-7

276. Ahmed N, Kansara M, Berridge MV. Acute regulation of glucose transport in a monocyte-macrophage cell line: Glut-3 affinity for glucose is enhanced during the respiratory burst. *Biochem J.* 1997 Oct 15;327 (Pt 2):369-75

277. Fu Y, Maianu L, Melbert BR, Garvey WT. Facilitative glucose transporter gene expression in human lymphocytes, monocytes, and macrophages: a role for GLUT isoforms 1, 3, and 5 in the immune response and foam cell formation. *Blood Cells Mol Dis*. 2004;32(1):182-90

278. Simpson IA, Dwyer D, Malide D, Moley KH, Travis A, Vannucci SJ. The facilitative glucose transporter GLUT3: 20 years of distinction. *Am J Physiol Endocrinol Metab*. 2008;295(2):E242-53.

279. Daugherty A, Cassis L. Angiotensin II-mediated development of vascular diseases. *Trends Cardiovasc Med*. 2004; 14(3): 117-20

280. Coucke PJ, Willaert A, Wessels MW, Callewaert B, Zoppi N, De Backer J, Fox JE, Mancini GM, Kambouris M, Gardella R, Facchetti F, Willems PJ, Forsyth R, Dietz HC, Barlati S, Colombi M, Loeys B, De Paepe A. Mutations in the facilitative glucose transporter GLUT10 alter angiogenesis and cause arterial tortuosity syndrome. *Nat Genet*. 2006: 38(4):452-7

281. Kotze CW, Groves AM, Menezes LJ, Harvey R, Endozo R, Kayani IA, Ell PJ, Yusuf SW. What is the relationship between ^{18}F-FDG aortic aneurysm

uptake on PET/CT and future growth rate? *Eur J Nucl Med Mol Imaging*. 2011;38:1493–1499.

282. Menezes LJ, Kotze CW, Agu O, Richards T, Brookes J, Goh VJ, Rodriguez-Justo M, Endozo R, Harvey R, Yusuf SW, Ell PJ, Groves AM. Investigating vulnerable atheroma using combined (18)F-FDG PET/CT angiography of carotid plaque with immunohistochemical validation. *J Nucl Med*. 2011; 52:1698–1703

283. Meirelles GS, Gonen M, Strauss HW. 18F-FDG uptake and calcifications in the thoracic aorta on positron emission tomography/computed tomography examinations: frequency and stability on serial scans. *J Thorac Imaging*. 2011; 26(1):54-62

284. Small GR, Ruddy TD. PET imaging of aortic atherosclerosis: Is combined imaging of plaque anatomy and function an amaranthine quest or conceivable reality? *J Nucl Cardiol.* 2011; 18(4):717-28.

285. Sakalihasan N, Michel JB. Functional imaging of atherosclerosis to advance vascular biology. *Eur J Vasc Endovasc Surg.* 2009; 37(6):728-34

286. Joly L, Djaballah W, Koehl G, Mandry D, Dolivet G, Marie PY, Benetos A. Aortic inflammation, as assessed by hybrid FDG-PET/CT imaging, is associated with enhanced aortic stiffness in addition to concurrent calcification. *Eur J Nucl Med Mol Imaging.* 2009;36(6):979-85

287. Wartman WB. Occlusion of the coronary arteries by hemorrhage into their walls. *American heart journal.* 1938; 15(4):459-470

288. Giessler R, Heberer G. Diagnosis and therapy of a ruptured aneurysm of the abdominal aorta. *Chirurg.* 1967;38(11):514-20

289. Darling RC. Ruptured arteriosclerotic abdominal aortic aneurysms. A

pathologic and clinical study. *Am J Surg.* 1970; 119(4):397-401

290. Powell JT, Brown LC, Forbes JF, Fowkes FG, Greenhalgh RM, Ruckley CV, Thompson SG. Final 12-year follow-up of surgery versus surveillance in the UK Small Aneurysm Trial. *Br J Surg.* 2007; 94(6):702-8

291. Sullivan CA, Rohrer MJ, Cutler BS. Clinical management of the symptomatic but unruptured abdominal aortic aneurysm. *J Vasc Surg.* 1990; 11(6):799-803

292. Tambyraja AL, Raza Z, Stuart WP, Murie JA, Chalmers RT. Does immediate operation for symptomatic non-ruptured abdominal aortic aneurysm compromise outcome? *Eur J Vasc Endovasc Surg*. 2004; 28(5):543-6

293. Michel JB. Contrasting outcomes of atheroma evolution: intimal accumulation versus medial destruction. *Arterioscler Thromb Vasc Biol.* 2001; 21(9):1389-92

294. Comino A, Ciravegna G, Mollo F. Aortic dissection at autopsy: a fifty-four year survey in Torino. *G Ital Cardiol.* 1986; 16(6):510-5

295. Houard X, Touat Z, Ollivier V, Louedec L, Philippe M, Sebbag U, Meilhac O, Rossignol P, Michel JB. Mediators of neutrophil recruitment in human abdominal aortic aneurysms. *Cardiovasc Res*. 2009; 82(3):532-41

296. Su H, Spinale FG, Dobrucki LW, Song J, Hua J, Sweterlitsch S, Dione DP, Cavaliere P, Chow C, Bourke BN, Hu XY, Azure M, Yalamanchili P, Liu R, Cheesman EH, Robinson S, Edwards DS, Sinusas AJ. Noninvasive targeted imaging of matrix metalloproteinase activation in a murine model of postinfarction remodeling. *Circulation.* 2005; 112(20):3157-67

297. Breyholz HJ, Wagner S, Levkau B, Schober O, Schäfers M, Kopka K. A 18F-radiolabeled analogue of CGS 27023A as a potential agent for assessment

of matrix-metalloproteinase activity in vivo. *Q J Nucl Med Mol Imaging.* 2007;51(1):24-32

298. Lancelot E, Amirbekian V, Brigger I, Raynaud JS, Ballet S, David C, Rousseaux O, Le Greneur S, Port M, Lijnen HR, Bruneval P, Michel JB, Ouimet T, Roques B, Amirbekian S, Hyafil F, Vucic E, Aguinaldo JG, Corot C, Fayad ZA. Evaluation of matrix metalloproteinases in atherosclerosis using a novel noninvasive imaging approach. *Arterioscler Thromb Vasc Biol.* 2008;28(3):425-32

299. Chen J, Tung CH, Allport JR, Chen S, Weissleder R, Huang PL. Near-infrared fluorescent imaging of matrix metalloproteinase activity after myocardial infarction. *Circulation*. 2005; 111(14):1800-5

300. Deguchi JO, Aikawa M, Tung CH, Aikawa E, Kim DE, Ntziachristos V, Weissleder R, Libby P. Inflammation in atherosclerosis: visualizing matrix metalloproteinase action in macrophages in vivo. *Circulation.* 2006; 114(1):55-62

301. Chen J, Tung CH, Mahmood U, Ntziachristos V, Gyurko R, Fishman MC, Huang PL, Weissleder R. In vivo imaging of proteolytic activity in atherosclerosis. *Circulation*. 2002; 105(23):2766-71

302. Ntziachristos V, Bremer C, Graves EE, Ripoll J, Weissleder R. In vivo tomographic imaging of near-infrared fluorescent probes. *Mol Imaging.* 2002; 1(2):82-8

303. Jaffer FA, Kim DE, Quinti L, Tung CH, Aikawa E, Pande AN, Kohler RH, Shi GP, Libby P, Weissleder R. Optical visualization of cathepsin K activity in atherosclerosis with a novel, protease-activatable fluorescence sensor. *Circulation.* 2007; 115(17):2292-8

304. Jaffer FA, Vinegoni C, John MC, Aikawa E, Gold HK, Finn AV,

Ntziachristos V, Libby P, Weissleder R. Real-time catheter molecular sensing of inflammation in proteolytically active atherosclerosis. *Circulation.* 2008;118(18):1802-9

305. Tardif JC, Heinonen T, Orloff D, Libby P. Vascular biomarkers and surrogates in cardiovascular disease. *Circulation.* 2006; 113(25):2936-42

306. Menezes LJ, Kotze CW, Hutton BF, Endozo R, Dickson JC, Cullum I, Yusuf SW, Ell PJ, Groves AM. Vascular inflammation imaging with 18F-FDG PET/CT: when to image? *Journ Nucl Med*. 2009; 50:854–857

307. Kotze CW, Menezes LJ, Endozo R, Groves AM, Ell PJ, Yusuf SW. Increased metabolic activity in abdominal aortic aneurysm detected by 18F-fluorodeoxyglucose (18F-FDG) positron emission tomography/computed tomography (PET/CT). *Eur J Vasc Endovasc Surg*. 2009; 38:93–99

308. Defawe OD, Hustinx R, Defraigne JO, Limet R, Sakalihasan N. Distribution of F-18 fluorodeoxyglucose (F-18 FDG) in abdominal aortic aneurysm: high accumulation in macrophages seen on PET imaging and immunohistology. *Clin Nucl Med.* 2005; 30(5):340-1

309. Reeps C, Bundschuh RA, Pellisek J, Herz M, van Marwick S, Schwaiger M, Eckstein HH, Nekolla SG, Essler M. Quantitative assessment of glucose metabolism in the vessel wall of abdominal aortic aneurysms: correlation with histology and role of partial volume correction. *Int J Cardiovasc Imaging*. 2013; 29(2):505-12

310. Kramer CM, Cerilli LA, Hagspiel K, DiMaria JM, Epstein FH, Kern JA. Magnetic resonance imaging identifies the fibrous cap in atherosclerotic abdominal aortic aneurysm. *Circulation.* 2004; 109(8):1016-21

311. Rudd JH, Myers KS, Bansilal S, Machac J, Woodward M, Fuster V, Farkouh ME, Fayad ZA. Relationships among regional arterial inflammation,

calcification, risk factors, and biomarkers: a prospective fluorodeoxyglucose positron-emission tomography/computed tomography imaging study. *Circ Cardiovasc Imaging.* 2009; 2(2):107-15

312. Wu Y-W, Kao H-L, Chen M-F, Lee B-C, Tseng W-YI, Jeng J-S, Tzen K-Y, Yen R-F, Huang P-J, Yang W-S. Characterization of plaques using 18F-FDG PET/CT in patients with carotid atherosclerosis and correlation with matrix metalloproteinase-1. *Journ Nucl Med.* 2007;48:227–233

313. Zhao QM, Feng TT, Zhao X, Xu ZM, Liu Y, Li DP, Li LQ, Su G, Zhang XX. Imaging of atherosclerotic aorta of rabbit model by detection of plaque inflammation with fluorine-18 fluorodeoxyglucose positron emission tomography/computed tomography. *Chin Med J.* 2011; 124(6):911-7

314. Petitpierre S, Bart PA, Leimgruber A, Spertini F, Prior J, Spertini F. [Large vessel vasculitis: giant cell arteritis and Takayasu arteritis]. *Rev Med Suisse.* 2007; 3(108):1056-60, 1062-3

315. Petitpierre S, Bart PA, Leimgruber A, Spertini F, Prior J, Spertini F. Large vessel vasculitis: giant cell arteritis and Takayasu arteritis. *Rev Med Suisse.* 2007; 3(108):1056-60, 1062-3

316. Spacek M, Stadler P, Bělohlávek O, Sebesta P. Contribution to FDG-PET/CT diagnostics and post-operative monitoring of patients with mycotic aneurysm of the thoracic aorta. *Acta Chir Belg.* 2010; 110(1):106-8.

317. Parums DV. The spectrum of chronic periaortitis. *Histopathology.* 1990 ;16(5):423-31

318. Yen HC, Lee FY, Chau LY. Analysis of the T cell receptor V beta repertoire in human aortic aneurysms. *Atherosclerosis.* 1997; 135(1):29-36

319. Agematsu K, Hokibara S, Nagumo H, Komiyama A. CD27: a memory B-cell marker. *Immunol Today.* 2000; 21(5):204-6

320. Fabbri M, Bianchi E, Fumagalli L, Pardi R. Regulation of lymphocyte traffic by adhesion molecules. *Inflamm Res.* 1999; 48(5):239-46

321. Simão da Silva E, Rodrigues AJ, Magalhães Castro de Tolosa E, Rodrigues CJ, Villas Boas do Prado G, Nakamoto JC. Morphology and diameter of infrarenal aortic aneurysms: a prospective autopsy study. *Cardiovasc Surg.* 2000; 8(7):526-32

322. Freestone T, Turner RJ, Coady A, Higman DJ, Greenhalgh RM, Powell JT. Inflammation and matrix metalloproteinases in the enlarging abdominal aortic aneurysm. *Arterioscler Thromb Vasc Biol*. 1995; 15:1145–1151.

323. Schäfers M, Schober O, Hermann S. Matrix-metalloproteinases as imaging targets for inflammatory activity in atherosclerotic plaques. *Jour Nucl Med*. 2010;51:663–666

324. Lucignani G, Schäfers M. PET, CT and MRI characterisation of the atherosclerotic plaque. *Eur J Nucl Med Mol Imaging*. 2010;37:2398–2402

325. Tegler G, Sörensen J, Ericson K, Björck M, Wanhainen A. 4D-PET/CT with [(11)C]-PK11195 and [(11)C]-(D)-deprenyl does not identify the chronic inflammation in asymptomatic abdominal aortic aneurysms. *Eur J Vasc Endovasc Surg.* 2013;45(4):351-6

326. Wolf YG, Thomas WS, Brennan FJ, Goff WG, Sise MJ, Bernstein EF. Computed tomography scanning findings associated with rapid expansion of abdominal aortic aneurysms. *Jour Vasc Surg*. 1994; 20:529–35– discussion 535–8

327. Kazi M, Zhu C, Roy J, Paulsson-Berne G, Hamsten A, Swedenborg J, Hedin U, Eriksson P. Difference in matrix-degrading protease expression and

activity between thrombus-free and thrombus-covered wall of abdominal aortic aneurysm. *Arterioscler Thromb Vasc Biol.* 2005; 25(7):1341-6

328. Speelman L, Schurink GW, Bosboom EM, Buth J, Breeuwer M, van de Vosse FN, Jacobs MH. The mechanical role of thrombus on the growth rate of an abdominal aortic aneurysm. *Jour Vasc Surg*. 2010; 51(1):19-26

329. Sarda-Mantel L, Coutard M, Rouzet F, Raguin O, Vrigneaud J-M, Hervatin F, Martet G, Touat Z, Merlet P, Le Guludec D, Michel J-B. 99mTc-annexin-V functional imaging of luminal thrombus activity in abdominal aortic aneurysms. *Arterioscler Thromb Vasc Biol*. 2006; 26:2153–2159

330. Stratton JR, Dewhurst TA, Kasina S, Reno JM, Cerqueira MD, Baskin DG, Tait JF. Selective uptake of radiolabeled annexin V on acute porcine left atrial thrombi. *Circulation*. 1995; 92(10):3113-21

331. Alberto R, Pak JK, van Staveren D, Mundwiler S, Benny P. Mono-, bi-, or tridentate ligands? The labeling of peptides with 99mTc-carbonyls. *Biopolymers.* 2004; 76(4):324-33

332. Yamazumi K, Ojiro M, Okumura H, Aikou T. An activated state of blood coagulation and fibrinolysis in patients with abdominal aortic aneurysm. *Am J Surg*. 1998;175:297–301

333. Lindholt JS, Jørgensen B, Fasting H, Henneberg EW. Plasma levels of plasmin-antiplasmin-complexes are predictive for small abdominal aortic aneurysms expanding to operation-recommendable sizes. *J Vasc Surg*. 2001;34:611–615

334. Michel J-B, Martin-Ventura JL, Egido J, Sakalihasan N, Treska V, Lindholt J, Allaire E, Thorsteinsdottir U, Cockerill G, Swedenborg J, FAD EU consortium. Novel aspects of the pathogenesis of aneurysms of the abdominal aorta in humans. *Cardiovasc Res*. 2011; 90:18–27

335. Lawrence MB, McIntire LV, Eskin SG. Effect of flow on polymorphonuclear leukocyte/endothelial cell adhesion. *Blood*. 1987; 70:1284–1290

336. Cafueri G, Parodi F, Pistorio A, Bertolotto M, Ventura F, Gambini C, Bianco P, Dallegri F, Pistoia V, Pezzolo A, Palombo D. Endothelial and smooth muscle cells from abdominal aortic aneurysm have increased oxidative stress and telomere attrition. *PLoS ONE*. 2012; 7:e35312

337. Houard X, Rouzet F, Touat Z, Philippe M, Dominguez M, Fontaine V, Sarda-Mantel L, Meulemans A, Le Guludec D, Meilhac O, Michel JB. Topology of the fibrinolytic system within the mural thrombus of human abdominal aortic aneurysms. *J Pathol*. 2007; 212:20–28.

338. Michel J-B, Thaunat O, Houard X, Meilhac O, Caligiuri G, Nicoletti A. Topological determinants and consequences of adventitial responses to arterial wall injury. *Arterioscler Thromb Vasc Biol*. 2007; 27:1259–1268.

339. Borges LF, Gomez D, Quintana M, Touat Z, Jondeau G, Leclercq A, Meilhac O, Jandrot-Perrus M, Gutierrez PS, Freymuller E, Vranckx R, Michel J-B. Fibrinolytic activity is associated with presence of cystic medial degeneration in aneurysms of the ascending aorta. *Histopathology*. 2010; 57:917–932.

340. Thompson RW, Curci JA, Ennis TL, Mao D, Pagano MB, Pham CTN. Pathophysiology of abdominal aortic aneurysms: insights from the elastase-induced model in mice with different genetic backgrounds. *Ann N Y Acad Sci*. 2006;1085:59–73

341. Mower WR, Quiñones WJ, Gambhir SS. Effect of intraluminal thrombus on abdominal aortic aneurysm wall stress. *J Vasc Surg*. 1997;26:602–608.

341. Labruto F, Blomqvist L, Swedenborg J. Imaging the intraluminal thrombus of abdominal aortic aneurysms: techniques, findings, and clinical implications. *J Vasc Interv Radiol*. 2011;22:1069–75– quiz 1075

342. Gasser TC, Auer M, Labruto F, Swedenborg J, Roy J. Biomechanical rupture risk assessment of abdominal aortic aneurysms: model complexity versus predictability of finite element simulations. *Eur J Vasc Endovasc Surg*. 2010;40:176–185

343. Gasser TC, Martufi G, Auer M, Folkesson M, Swedenborg J. Micromechanical characterization of intra-luminal thrombus tissue from abdominal aortic aneurysms. *Ann Biomed Eng*. 2010;38:371–379

344. Koole D, Zandvoort HJA, Schoneveld A, Vink A, Vos JA, van den Hoogen LL, de Vries J-PPM, Pasterkamp G, Moll FL, van Herwaarden JA. Intraluminal abdominal aortic aneurysm thrombus is associated with disruption of wall integrity. *J Vasc Surg*. 2013;57:77–83

345. Sarda-Mantel L, Alsac J-M, Boisgard R, Hervatin F, Montravers F, Tavitian B, Michel J-B, Le Guludec D. Comparison of 18F-fluoro-deoxy-glucose, 18F-fluoro-methyl-choline, and 18F-DPA714 for positron-emission tomography imaging of leukocyte accumulation in the aortic wall of experimental abdominal aneurysms. *J Vasc Surg*. 2012;56:765–773

346. Peker C, Sarda-Mantel L, Loiseau P, Rouzet F, Nazneen L, Martet G, Vrigneaud J-M, Meulemans A, Saumon G, Michel J-B, Le Guludec D. Imaging apoptosis with (99m)Tc-annexin-V in experimental subacute myocarditis. *J Nucl Med*. 2004;45:1081–1086

347. Kuehl H, Eggebrecht H, Boes T, Antoch G, Rosenbaum S, Ladd S, Bockisch A, Barkhausen J, Erbel R. Detection of inflammation in patients with acute aortic syndrome: comparison of FDG-PET/CT imaging and serological

markers of inflammation. *Heart.* 2008; 94(11):1472-7

348. Kato K, Nishio A, Kato N, Usami H, Fujimaki T, Murohara T. Uptake of 18F-FDG in acute aortic dissection: a determinant of unfavorable outcome. *J Nucl Med.* 2010; 51(5):674-81

349. Daugherty A, Cassis L. Complex pathologies of angiotensin II-induced abdominal aortic aneurysms. *J Zhejiang Univ Sci B.* 2011; 12(8):624-8

350. Daugherty A, Manning MW, Cassis LA. Angiotensin II promotes atherosclerotic lesions and aneurysms in apolipoprotein E–deficient mice. *J Clin Invest*. 2000; 105:1605–1612

351. Bruemmer D, Collins AR, Noh G, Wang W, Territo M, Arias-Magallona S, Fishbein MC, Blaschke F, Kintscher U, Graf K, Law RE, Hsueh WA. Angiotensin II–accelerated atherosclerosis and aneurysm formation is attenuated in osteopontin-deficient mice. *J Clin Invest*. 2003; 112:1318–1331

352. Police S, Thatcher S, Charnigo R. Obesity promotes inflammation in periaortic adipose tissue and angiotensin II-induced abdominal aortic aneurysm formation. *Arterioscler Thromb Vasc Biol.* 2009; 29(10):1458-64

353. Schriefl AJ, Collins MJ, Pierce DM, Holzapfel GA. Remodeling of intramural thrombus and collagen in an Ang-II infusion ApoE−/− model of dissecting aortic aneurysms. *Thromb Res.* 2012; 130(3):e139-46.

354. Berk BC, Haendeler J, Sottile J. Angiotensin II, atherosclerosis, and aortic aneurysms. *J Clin Invest*. 2000; 105:1525–1526.

355. Weiss D, Kools JJ, Taylor WR. Angiotensin II–induced hypertension accelerates the development of atherosclerosis in apoE-deficient mice. *Circulation*. 2001; 103(3):448-54

356. Cao RY, Adams MA, Habenicht AJ, Funk CD. Angiotensin II-induced abdominal aortic aneurysm occurs independently of the 5-lipoxygenase pathway in apolipoprotein E-deficient mice. *Prostaglandins & Other Lipid Mediators*. 2007;84:34–42

357. Mell M, White JJ, Hill BB, Hastie T, Dalman RL. No increased mortality with early aortic aneurysm disease. *J Vasc Surg*. 2012; 56(5):1246-51

358. Zaragoza C, Gomez-Guerrero C, Martin-Ventura JL, Blanco-Colio L, Lavin B, Mallavia B, Tarin C, Mas S, Ortiz A, Egido J. Animal Models of Cardiovascular Diseases. *Journal of Biomedicine and Biotechnology*. 2011; 2011:1–13

359. Bruemmer D, Daugherty A, Lu H, Rateri DL. Relevance of angiotensin II-induced aortic pathologies in mice to human aortic aneurysms. *Ann N Y Acad Sci*. 2011; 1245:7–10

360. Vietinghoff von S, Ley K. Interleukin 17 in vascular inflammation. *Cytokine Growth Factor Rev*. 2010;21:463–469

361. Onishi RM, Gaffen SL. Interleukin-17 and its target genes: mechanisms of interleukin-17 function in disease. *Immunology*. 2010;129:311–321

362. Onishi RM, Park SJ, Hanel W, Ho AW, Maitra A, Gaffen SL. SEF/IL-17R (SEFIR) is not enough: an extended SEFIR domain is required for il-17RA-mediated signal transduction. *J Biol Chem*. 2010;285:32751–32759

363. Bettelli E, Korn T, Oukka M, Kuchroo VK. Induction and effector functions of T(H)17 cells. *Nature*. 2008;453:1051–1057

364. Iwakura Y, Nakae S, Saijo S, Ishigame H. The roles of IL-17A in

inflammatory immune responses and host defense against pathogens. *Immunol Rev*. 2008;226:57–79

365. Wilson NJ, Boniface K, Chan JR, McKenzie BS, Blumenschein WM, Mattson JD, Basham B, Smith K, Chen T, Morel F, Lecron J-C, Kastelein RA, Cua DJ, McClanahan TK, Bowman EP, de Waal Malefyt R. Development, cytokine profile and function of human interleukin 17-producing helper T-cells. *Nat Immunol*. 2007;8:950–957

366. Acosta-Rodriguez EV, Rivino L, Geginat J, Jarrossay D, Gattorno M, Lanzavecchia A, Sallusto F, Napolitani G. Surface phenotype and antigenic specificity of human interleukin 17-producing T helper memory cells. *Nat Immunol*. 2007;8:639–646

367. Du R, Zhao H, Yan F, Li H. IL-17+Foxp3+ T-cells: an intermediate differentiation stage between Th17 cells and regulatory T-cells. *J Leukoc Biol*. 2014; 2014 Apr 17. [Epub ahead of print]

368. Ramsdell F, Ziegler SF. FOXP3 and scurfy: how it all began. *Nat Rev Immunol*. 2014;14:343–349

369. Fontenot JD, Gavin MA, Rudensky AY. Foxp3 programs the development and function of CD4+CD25+ regulatory T-cells. *Nat Immunol*. 2003;4:330–336

370. Karim M, Kingsley CI, Bushell AR, Sawitzki BS, Wood KJ. Alloantigen-induced CD25+CD4+ regulatory T-cells can develop in vivo from CD25-CD4+ precursors in a thymus-independent process. *J Immunol*. 2004;172:923–928

371. Singer BD, D'Alessio FR. Regulatory T cell Itch reins in Th2 inflammation. *Cell Mol Immunol*. 2014;11:126–128

372. Singer BD, King LS, D'Alessio FR. Regulatory T-cells as

Immunotherapy. *Front Immunol*. 2014;5:46

373. Shevach EM. Mechanisms of foxp3+ T regulatory cell-mediated suppression. *Immunity*. 2009;30:636–645

374. Tran DQ, Shevach EM. Therapeutic potential of FOXP3(+) regulatory T-cells and their interactions with dendritic cells. *Hum Immunol*. 2009; 70:294–299

375. Mucosal memory B-cells retain the ability to produce IgM antibodies 2 years after oral immunization. *Immunology*. 1995; 86:336–342

376. Production of IgM hexamers by normal and autoimmune B-cells: implications for the physiologic role of hexameric IgM. *J Immunol*. 1998; 161:4091–4097

377. IgM antibodies to apoptosis-associated determinants recruit C1q and enhance dendritic cell phagocytosis of apoptotic cells. *J Immunol*. 2009; 182:6031–6043

378. Mizoguchi A, Bhan AK. A case for regulatory B-cells. *J Immunol*. 2006;176:705–710

379. Yang M, Rui K, Wang S, Lu L. Regulatory B-cells in autoimmune diseases. *Cell Mol Immunol*. 2013; 10:122–132.

380. Iwata Y, Matsushita T, Horikawa M, Dilillo DJ, Yanaba K, Venturi GM, Szabolcs PM, Bernstein SH, Magro CM, Williams AD, Hall RP, St Clair EW, Tedder TF. Characterization of a rare IL-10-competent B-cell subset in humans that parallels mouse regulatory B10 cells. *Blood*. 2011; 117:530–541.

381. Edwards JC, Cambridge G, Abrahams VM. Do self-perpetuating B lymphocytes drive human autoimmune disease? *Immunology*. 1999; 97:188–

196.

382. Shimomura Y, Mizoguchi E, Sugimoto K, Kibe R, Benno Y, Mizoguchi A, Bhan AK. Regulatory role of B-1 B cells in chronic colitis. *Int Immunol*. 2008; 20:729–737.

383. Shlomchik MJ, Craft JE, Mamula MJ. From T to B and back again: positive feedback in systemic autoimmune disease. *Nat Rev Immunol*. 2001; 1:147–153.

384. Rodríguez-Pinto D. B cells as antigen presenting cells. *Cell Immunol*. 2005; 238:67–75

385. Rodríguez-Pinto D, Moreno J. B cells can prime naive CD4+ T cells in vivo in the absence of other professional antigen-presenting cells in a CD154-CD40-dependent manner. *Eur J Immunol*. 2005; 35:1097–1105.

386. Harris DP, Haynes L, Sayles PC, Duso DK, Eaton SM, Lepak NM, Johnson LL, Swain SL, Lund FE. Reciprocal regulation of polarized cytokine production by effector B and T cells. *Nat Immunol*. 2000;1:475–482.

387. Evans JG, Chavez-Rueda KA, Eddaoudi A, Meyer-Bahlburg A, Rawlings DJ, Ehrenstein MR, Mauri C. Novel suppressive function of transitional 2 B cells in experimental arthritis. *J Immunol*. 2007; 178:7868–7878

388. Yang M, Sun L, Wang S, Ko K-H, Xu H, Zheng B-J, Cao X, Lu L. Novel function of B cell-activating factor in the induction of IL-10-producing regulatory B cells. *J Immunol*. 2010; 184:3321–3325

389. Carter NA, Vasconcellos R, Rosser EC, Tulone C, Muñoz-Suano A, Kamanaka M, Ehrenstein MR, Flavell RA, Mauri C. Mice lacking endogenous IL-10-producing regulatory B cells develop exacerbated disease and present

with an increased frequency of Th1/Th17 but a decrease in regulatory T cells. *J Immunol*. 2011; 186:5569–5579

390. Moulin V, Andris F, Thielemans K, Maliszewski C, Urbain J, Moser M. B lymphocytes regulate dendritic cell (DC) function in vivo: increased interleukin 12 production by DCs from B cell-deficient mice results in T helper cell type 1 deviation. *J Exp Med*. 2000; 192:475–482

391. Tu W, Lau Y-L, Zheng J, Liu Y, Chan P-L, Mao H, Dionis K, Schneider P, Lewis DB. Efficient generation of human alloantigen-specific CD4+ regulatory T cells from naive precursors by CD40-activated B cells. *Blood*. 2008; 112:2554–2562

392. Blair PA, Noreña LY, Flores-Borja F, Rawlings DJ, Isenberg DA, Ehrenstein MR, Mauri C. CD19(+)CD24(hi)CD38(hi) B cells exhibit regulatory capacity in healthy individuals but are functionally impaired in systemic Lupus Erythematosus patients. *Immunity*. 2010; 32:129–140

393. Amu S, Saunders SP, Kronenberg M, Mangan NE, Atzberger A, Fallon PG. Regulatory B cells prevent and reverse allergic airway inflammation via FoxP3-positive T regulatory cells in a murine model. *J Allergy Clin Immunol*. 2010; 125:1114–1124.e8

394. Amu S, Gjertsson I, Brisslert M. Functional characterization of murine CD25 expressing B cells. *Scand J Immunol*. 2010; 71:275–282

395. Tedder TF, Matsushita T. Regulatory B cells that produce IL-10: a breath of fresh air in allergic airway disease. *J Allergy Clin Immunol*. 2010;125:1125–1127

396. Tedder TF. Innate and adaptive receptors interact to balance humoral immunity. *J Immunol*. 2010;184:2231–2232

397. Carter NA, Rosser EC, Mauri C. Interleukin-10 produced by B cells is crucial for the suppression of Th17/Th1 responses, induction of T regulatory type 1 cells and reduction of collagen-induced arthritis. *Arthritis Res Ther*. 2012; 14:R32.

398. Yoshimura K, Aoki H, Ikeda Y, Fujii K, Akiyama N, Furutani A, Hoshii Y, Tanaka N, Ricci R, Ishihara T, Esato K, Hamano K, Matsuzaki M. Regression of abdominal aortic aneurysm by inhibition of c-Jun N-terminal kinase. *Nat Med*. 2005; 11:1330–1338

399. Yoshimura K, Aoki H, Ikeda Y, Furutani A, Hamano K, Matsuzaki M. Identification of c-Jun N-Terminal Kinase as a Therapeutic Target for Abdominal Aortic Aneurysm. *Ann N Y Acad Sci*. 2006; 1085:403–406

400. Pratt B, Curci J. Arterial elastic fiber structure. Function and potential roles in acute aortic dissection. *J Cardiovasc Surg (Torino)*. 2010; 51:647–656

401. Lindsay ME, Dietz HC. Lessons on the pathogenesis of aneurysm from heritable conditions. *Nature*. 2011; 473:308–316

402. Hellenthal FAMVI, Buurman WA, Wodzig WKWH, Schurink GWH. Biomarkers of AAA progression. Part 1: extracellular matrix degeneration. *Nat Rev Cardiol*. 2009; 6:464–474

403. Hellenthal FAMVI, Geenen ILA, Teijink JAW, Heeneman S, Schurink GWH. Histological features of human abdominal aortic aneurysm are not related to clinical characteristics. *Cardiovasc Pathol*. 2009; 18:286–293

404. Robert L, Robert AM, Jacotot B. Elastin-elastase-atherosclerosis revisited. *Atherosclerosis*. 1998; 140:281–295

405. Papke CL, Yanagisawa H. Fibulin-4 and fibulin-5 in elastogenesis and beyond: Insights from mouse and human studies. *Matrix Biol*. 2014; pii:

S0945-053X(14)00043-2

406. Tsamis A, Krawiec JT, Vorp DA. Elastin and collagen fibre microstructure of the human aorta in ageing and disease: a review. *J R Soc Interface*. 2013; 10:20121004–20121004

407. Sandberg LB, Soskel NT, Leslie JG. Elastin structure, biosynthesis, and relation to disease states. *N Engl J Med*. 1981; 304:566–579

408. Li DY, Brooke B, Davis EC, Mecham RP, Sorensen LK, Boak BB, Eichwald E, Keating MT. Elastin is an essential determinant of arterial morphogenesis. *Nature.* 1998 May 21; 393(6682):276-80

409. Pasquali-Ronchetti I, Baccarani-Contri M. Elastic fiber during development and aging. *Microsc Res Tech.* 1997; 38(4):428-35

410. Maurice P, Blaise S, Gayral S, Debelle L, Laffargue M, Hornebeck W, Duca L. Elastin fragmentation and atherosclerosis progression: the elastokine concept. *Trends Cardiovasc Med*. 2013; 23:211–221

411. Seyama Y, Wachi H. Atherosclerosis and matrix dystrophy. *J Atheroscler Thromb*. 2004; 11:236–245

412. Makowski MR, Wiethoff AJ, Jansen CH, Botnar RM. Molecular imaging with targeted contrast agents. *Top Magn Reson Imaging*. 2009; 20(4):247-59

413. Litmanovich D, Bankier AA, Cantin L, Raptopoulos V, Boiselle PM. CT and MRI in diseases of the aorta. *AJR Am J Roentgenol.* 2009; 193(4):928-40

414. Roes SD, Westenberg JJ, Doornbos J, van der Geest RJ, Angelié E, de Roos A, Stuber M. Aortic vessel wall magnetic resonance imaging at 3.0 Tesla: a reproducibility study of respiratory navigator gated free-breathing 3D black

blood magnetic resonance imaging. *Magn Reson Med.* 2009; 61(1):35-44

415. Hussain T, Clough RE, Cecelja M, Makowski M, Peel S, Chowienczyk P, Schaeffter T, Greil G, Botnar R. Zoom imaging for rapid aortic vessel wall imaging and cardiovascular risk assessment. *J Magn Reson Imaging*. 2011; 34(2):279-85

416. Makowski MR, Forbes SC, Blume U, Warley A, Jansen CH, Schuster A, Wiethoff AJ, Botnar RM. In vivo assessment of intraplaque and endothelial fibrin in ApoE(-/-) mice by molecular MRI. *Atherosclerosis.* 2011; 222(1):43-9

417. Messroghli DR, Radjenovic A, Kozerke S, Higgins DM, Sivananthan MU, Ridgway JP. Modified Look-Locker inversion recovery (MOLLI) for high-resolution T1 mapping of the heart. *Magn Reson Med*. 2004; 52:141–146

418. Deichmann R, Hahn D, Haase A. Fast T1 mapping on a whole-body scanner. *Magn Reson Med*. 1999;42:206–209

419. von Bary C, Makowski M, Preissel A, Keithahn A, Warley A, Spuentrup E, Buecker A, Lazewatsky J, Cesati R, Onthank D, Schickl N, Schachoff S, Hausleiter J, Schömig A, Schwaiger M, Robinson S, Botnar R. MRI of coronary wall remodeling in a swine model of coronary injury using an elastin-binding contrast agent. *Circ Cardiovasc Imaging.* 2001; 4(2):147-55

420. Thompson MR, Venkatesan R, Kuppusamy K, Celik A, Lin W, Kido DK, Haacke EM. Increased-contrast, high-spatial-resolution, diffusion-weighted, spin-echo, echo-planar imaging. *Radiology.* 1999; 210(1):253-9

421. Haacke MA, Reichenbach JR. Susceptablity weighted imaging in MRI. Basic concents and clinical applications. Wiley J & Sons. 2011

422. Prince MR, Narasimham DL, Stanley JC, Wakefield TW, Messina LM, Zelenock GB, Jacoby WT, Marx MV, Williams DM, Cho KJ. Gadolinium-enhanced magnetic resonance angiography of abdominal aortic aneurysms. *J*

Vasc Surg. 1995 21(4):656-69a

423. Lutz AM, Willmann JK, Pfammatter T, Lachat M, Wildermuth S, Marincek B, Weishaupt D. Evaluation of aortoiliac aneurysm before endovascular repair: comparison of contrast-enhanced magnetic resonance angiography with multidetector row computed tomographic angiography with an automated analysis software tool. *J Vasc Surg.* 2003; 37(3):619-27

424. Nchimi A, Defawe O, Brisbois D, Broussaud TK, Defraigne JO, Magotteaux P, Massart B, Serfaty JM, Houard X, Michel JB, Sakalihasan N. MR imaging of iron phagocytosis in intraluminal thrombi of abdominal aortic aneurysms in humans. *Radiology.* 2010; 254(3):973-81

425. Sadat U, Taviani V, Patterson AJ, Young VE, Graves MJ, Teng Z, Tang TY, Gillard JH. Ultrasmall superparamagnetic iron oxide-enhanced magnetic resonance imaging of abdominal aortic aneurysms--a feasibility study. *Eur J Vasc Endovasc Surg.* 2011; 41(2):167-74

426. Vos AW, Wisselink W, Marcus JT, Vahl AC, Manoliu RA, Rauwerda JA. Cine MRI assessment of aortic aneurysm dynamics before and after endovascular repair. *J Endovasc Ther.* 2003; 10(3):433-9

427. He X, Janeway CA, Levine M, Robinson E, Preston-Hurlburt P, Viret C, Bottomly K. Dual receptor T cells extend the immune repertoire for foreign antigens. Nature immunology. 2002; 3:127–134

428. Boon RA, Boon RA, Seeger T, Seeger T, Heydt S, Heydt S, Fischer A, Fischer A, Hergenreider E, Hergenreider E, Horrevoets AJG, Horrevoets AJG, Vinciguerra M, Vinciguerra M, Rosenthal N, Rosenthal N, Sciacca S, Sciacca S, Pilato M, Pilato M, van Heijningen P, van Heijningen P, Essers J, Essers J, Brandes RP, Brandes RP, Zeiher AM, Zeiher AM, Dimmeler S, Dimmeler S. MicroRNA-29 in Aortic Dilation: Implications for Aneurysm Formation.

Circulation Research. 2011; 109:1115–1119

429. Merk DR, Merk DR, Chin JT, Chin JT, Dake BA, Dake BA, Maegdefessel L, Maegdefessel L, Miller MO, Miller MO, Kimura N, Kimura N, Tsao PS, Tsao PS, Iosef C, Iosef C, Berry GJ, Berry GJ, Mohr FW, Mohr FW, Spin JM, Spin JM, Alvira CM, Alvira CM, Robbins RC, Robbins RC, Fischbein MP, Fischbein MP. miR29b Participates in Early Aneurysm Development in Marfan Syndrome. *Circulation Research*. 2012; 110:312–324

430. Maegdefessel L, Azuma J, Toh R, Merk DR, Deng A, Chin JT, Raaz U, Schoelmerich AM, Raiesdana A, Leeper NJ, McConnell MV, Dalman RL, Spin JM, Tsao PS. Inhibition of microRNA-29b reduces murine abdominal aortic aneurysm development. *J Clin Invest*. 2012; 122:497–506

431. Sauter AW, Judenhofer MS, Pichler BJ. Combined PET/MR imaging--technology and applications. *Technology in cancer res treat.* 2010; ;9(1):5-20.

432. Boss A, Kolb A, Hofmann M, Bisdas S, Nägele T, Ernemann U, Stegger L, Rossi C, Schlemmer H-P, Pfannenberg C, Reimold M, Claussen CD, Pichler BJ, Klose U. Diffusion Tensor Imaging in a Human PET/MR Hybrid System. *Investigative Radiology*. 2010;45:270–274

433. Kyaw T, Kyaw T, Winship A, Winship A, Tay C, Tay C, Kanellakis P, Kanellakis P, Hosseini H, Hosseini H, Cao A, Cao A, Li P, Li P, Tipping P, Tipping P, Bobik A, Bobik A, Toh BH, Toh B-H. Cytotoxic and Proinflammatory CD8+ T Lymphocytes Promote Development of Vulnerable Atherosclerotic Plaques in ApoE-Deficient Mice. *Circulation*. 2013;127:1028–1039

434. Tsarouhas K, Soufla G, Apostolakis S, Zaravinos A, Panagiotou M, Khoury M, Hassoulas JA, Tsatsakis AM, Spandidos DA. Transcriptional regulation of TIMPs in ascending aorta aneurysms. *Thromb Res*. 2010;126:399–405

435. Lindholt JS, Heickendorff L, Henneberg EW, Fasting H. Serum-elastin-peptides as a predictor of expansion of small abdominal aortic aneurysms. *Eur Jour Vasc Endovasc Surg.* 1997;14:12–16

436. Lindholt JS, Ashton HA, Heickendorff L, Scott RAP, Scott RA. Serum Elastin Peptides in the Preoperative Evaluation of Abdominal Aortic Aneurysms. *European Journal of Vascular and Endovascular Surgery*. 2001;22:546–550

437. Baxter BT, Davis VA, Minion DJ, Wang YP. Abdominal aortic aneurysms are associated with altered matrix proteins of the nonaneurysmal aortic segments. *J Vasc Surg.* 1994 ;19(5):797-802; discussion 803

438. Minion DJ, Davis VA, Nejezchleb, Wang Y, McManus BM, Baxter BT. Elastin Is Increased in Abdominal Aortic Aneurysms. *Journal of Surgical Research*. 1994;57:443–446

439. Carmo M, Colombo L, Bruno A, Corsi FRM, Roncoroni L, Cuttin MS, Radice F, Mussini E, Settembrini PG. Alteration of elastin, collagen and their cross-links in abdominal aortic aneurysms. *Eur J Vasc Endovasc Surg*. 2002;23:543–549

440. Thum T, Gross C, Fiedler J, Fischer T, Kissler S, Bussen M, Galuppo P, Just S, Rottbauer W, Frantz S, Castoldi M, Soutschek J, Koteliansky V, Rosenwald A, Basson MA, Licht JD, Pena JTR, Rouhanifard SH, Muckenthaler MU, Tuschl T, Martin GR, Bauersachs J, Engelhardt S. MicroRNA-21 contributes to myocardial disease by stimulating MAP kinase signalling in fibroblasts. *Nature*. 2008;456:980–984

441. Bonauer A, Bonauer A, Carmona G, Carmona G, Iwasaki M, Iwasaki M, Mione M, Mione M, Koyanagi M, Koyanagi M, Fischer A, Fischer A, Burchfield J, Burchfield J, Fox H, Fox H, Doebele C, Doebele C, Ohtani K,

Ohtani K, Chavakis E, Chavakis E, Potente M, Potente M, Tjwa M, Tjwa M, Urbich C, Urbich C, Zeiher AM, Zeiher AM, Dimmeler S, Dimmeler S. MicroRNA-92a Controls Angiogenesis and Functional Recovery of Ischemic Tissues in Mice. *Science*. 2009;324:1710–1713

442. van Rooij E, Olson EN. MicroRNAs: powerful new regulators of heart disease and provocative therapeutic targets. *J Clin Invest*. 2007;117:2369–2376

443. Urbich C, Urbich C, Kuehbacher A, Kuehbacher A, Dimmeler S, Dimmeler S. Role of microRNAs in vascular diseases, inflammation, and angiogenesis. *Cardiovasc Res*. 2008;79:581–588

444. Bartel DP. MicroRNAs: genomics, biogenesis, mechanism, and function. *Cell.* 2004;116:281–297

445. Wang GK, Wang G-K, Zhu J-Q, Zhu JQ, Zhang JT, Zhang J-T, Li Q, Li Q, Li Y, Li Y, He J, He J, Qin Y-W, Qin YW, Jing Q, Jing Q. Circulating microRNA: a novel potential biomarker for early diagnosis of acute myocardial infarction in humans. *Eur Heart J*. 2010;31:659–666

446. Reid G, Kirschner MB, van Zandwijk N. Circulating microRNAs: Association with disease and potential use as biomarkers. *Critical Reviews in Oncology/Hematology*. 2011;80:193–208

447. Lee Y, Ahn C, Han J, Choi H, Kim J, Yim J, Lee J, Provost P, Rådmark O, Kim S, Kim VN. The nuclear RNase III Drosha initiates microRNA processing. *Nature*. 2003;425:415–419

448. deepBase: a database for deeply annotating and mining deep sequencing data. *Nucleic Acids Research*. 2010;38:D123–30

449. Zhao H, Harris RA, Coarfa C, Chen ZJ. MicroRNA transcriptome in the

newborn mouse ovaries determined by massive parallel sequencing. *Mol Hum Reprod.* 2010;16(7):463-71

450. Xu T, Zhu Y, Xiong Y, Ge Y-Y, Yun J-P, Zhuang S-M. MicroRNA-195 suppresses tumorigenicity and regulates G 1/S transition of human hepatocellular carcinoma cells. *Hepatology*. 2009;50:113–121

451. He L, Hannon GJ. MicroRNAs: small RNAs with a big role in gene regulation. *Nature Reviews Genetics*. 2004; 5(7):522-31

452. Simper D, Simper D, Mayr U, Mayr U, Urbich C, Urbich C, Zampetaki A, Zampetaki A, Prokopi M, Prokopi M, Didangelos A, Didangelos A, Saje A, Saje A, Mueller M, Mueller M, Benbow U, Benbow U, Newby AC, Newby AC, Apweiler R, Apweiler R, Rahman S, Rahman S, Dimmeler S, Dimmeler S, Xu Q, Xu Q, Mayr M, Mayr M. Comparative Proteomics Profiling Reveals Role of Smooth Muscle Progenitors in Extracellular Matrix Production. *Arterioscler Thromb Vasc Biol*. 2010;30:1325–1332.

453. Widera C, Gupta SK, Lorenzen JM, Bang C, Bauersachs J, Bethmann K, Kempf T, Wollert KC, Thum T. Diagnostic and prognostic impact of six circulating microRNAs in acute coronary syndrome. *Journal of Molecular and Cellular Cardiology*. 2011;51:872–875.

454. Fichtlscherer S, Fichtlscherer S, De Rosa S, De Rosa S, Fox H, Fox H, Schwietz T, Schwietz T, Fischer A, Fischer A, Liebetrau C, Liebetrau C, Weber M, Weber M, Hamm CW, Hamm CW, Röxe T, Roxe T, Muller-Ardogan M, Müller-Ardogan M, Bonauer A, Bonauer A, Zeiher AM, Zeiher AM, Dimmeler S, Dimmeler S. Circulating MicroRNAs in Patients With Coronary Artery Disease. *Circulation Research*. 2010;107:677–684.

455. Kin K, Kin K, Miyagawa S, Miyagawa S, Fukushima S, Fukushima S, Shirakawa Y, Shirakawa Y, Torikai K, Torikai K, Shimamura K, Shimamura K,

Daimon T, Daimon T, Kawahara Y, Kawahara Y, Kuratani T, Kuratani T, Sawa Y, Sawa Y. Tissue- and Plasma-Specific MicroRNA Signatures for Atherosclerotic Abdominal Aortic Aneurysm. *Journal of the American Heart Association*. 2012;1:e000745–e000745.

456. Maegdefessel L, Dalman RL, Tsao PS. Pathogenesis of Abdominal Aortic Aneurysms: MicroRNAs, Proteases, Genetic Associations. *Annu Rev Med*. 2014;65:49–62.

457. Chen L-J, Lim SH, Yeh Y-T, Lien S-C, Chiu J-J. Roles of microRNAs in atherosclerosis and restenosis. *J Biomed Sci*. 2012;19:79.

458. Goettsch C, Aikawa E. Role of MicroRNAs in Cardiovascular Calcification: focus on targets and extracellular vesicle delivery mechanisms. *Circ Res.* 2013; 112(7):1073-84

459. Goettsch C, Hutcheson JD, Aikawa E. MicroRNA in cardiovascular calcification: focus on targets and extracellular vesicle delivery mechanisms. *Circulation Research*. 2013; 112:1073–1084.

460. Ji R, Ji R, Cheng Y, Cheng Y, Yue J, Yue J, Yang J, Yang J, Liu X, Liu X, Chen H, Chen H, Dean DB, Dean DB, Zhang C, Zhang C. MicroRNA Expression Signature and Antisense-Mediated Depletion Reveal an Essential Role of MicroRNA in Vascular Neointimal Lesion Formation. *Circulation Research.* 2007;100:1579–1588

461. Liu X, Cheng Y, Yang J, Huo Y, Zhang C. Involvement of MicroRNAs in hydrogen peroxide-mediated gene regulation and cellular injury response in vascular smooth muscle cells. *Journ Biol Chem.* 2009; 284(12):7903-13

462. Davis-Dusenbery BN, Wu C, Hata A. Micromanaging vascular smooth muscle cell differentiation and phenotypic modulation. *Arterioscler Thromb Vasc Biol*. 2011;31:2370–2377

463. Davis-Dusenbery BN, Hata A. Smad-mediated miRNA processing. *RNA biology*. 2011; 8(1):71-6

464. Maegdefessel L, Maegdefessel L, Azuma J, Azuma J, Toh R, Toh R, Deng A, Deng A, Merk DR, Merk DR, Raiesdana A, Raiesdana A, Leeper NJ, Leeper NJ, Raaz U, Raaz U, Schoelmerich AM, Schoelmerich AM, McConnell MV, McConnell MV, Dalman RL, Dalman RL, Spin JM, Spin JM, Tsao PS, Tsao PS. MicroRNA-21 Blocks Abdominal Aortic Aneurysm Development and Nicotine-Augmented Expansion. *Science Translational Medicine*. 2012;4:122ra22–122ra22.

465. Harris TA, Harris TA, Yamakuchi M, Yamakuchi M, Ferlito M, Ferlito M, Mendell JT, Mendell JT, Lowenstein CJ, Lowenstein CJ. MicroRNA-126 regulates endothelial expression of vascular cell adhesion molecule 1. *Proceedings of the National Academy of Sciences*. 2008;105:1516–1521

466. Taganov KD, Taganov KD, Boldin MP, Boldin MP, Chang K-J, Chang KJ, Baltimore D, Baltimore D. NF- B-dependent induction of microRNA miR-146, an inhibitor targeted to signaling proteins of innate immune responses. *Proceedings of the National Academy of Sciences*. 2006;103:12481–12486

467. Li T, Morgan MJ, Choksi S, Zhang Y, Kim Y-S, Liu Z-G. MicroRNAs modulate the noncanonical transcription factor NF-kappaB pathway by regulating expression of the kinase IKKalpha during macrophage differentiation. *Nat Immunol*. 2010;11:799–805

468. Li T, Morgan MJ, Choksi S, Zhang Y, Kim YS. MicroRNAs modulate the noncanonical transcription factor NF-[kappa] B pathway by regulating expression of the kinase IKK [alpha] during macrophage differentiation. *Nat Immunol*. 2010; ;11(9):799-805

470. MicroRNAs in NF-kappaB signaling. *J Mol Cell Biol*. 2011;3:159–166

471. Johnnidis JB, Harris MH, Wheeler RT, Stehling-Sun S, Lam MH, Kirak O, Brummelkamp TR, Fleming MD, Camargo FD. Regulation of progenitor cell proliferation and granulocyte function by microRNA-223. *Nature*. 2008;451:1125–1129

472. Perry MM, Moschos SA, Williams AE, Shepherd NJ, Larner-Svensson HM, Lindsay MA. Rapid changes in microRNA-146a expression negatively regulate the IL-1beta-induced inflammatory response in human lung alveolar epithelial cells. *J Immunol*. 2008;180:5689–5698

473. Lovis P, Roggli E, Laybutt DR, Gattesco S, Yang J-Y, Widmann C, Abderrahmani A, Regazzi R. Alterations in microRNA expression contribute to fatty acid-induced pancreatic beta-cell dysfunction. *Diabetes*. 2008;57:2728–2736

474. van Rooij E, van Rooij E, Sutherland LB, Sutherland LB, Thatcher JE, Thatcher JE, DiMaio JM, DiMaio JM, Naseem RH, Naseem RH, Marshall WS, Marshall WS, Hill JA, Hill JA, Olson EN, Olson EN. Dysregulation of microRNAs after myocardial infarction reveals a role of miR-29 in cardiac fibrosis. *Proceedings of the National Academy of Sciences*. 2008;105:13027–13032

475. Cheng J, Wang Y, Wang D, Wu Y. Identification of collagen 1 as a post-transcriptional target of miR29b in skin fibroblasts: therapeutic implication for scar reduction. *Am J Med Sci*. 2013;346:98–103

476. Chen K-C, Chen KC, Wang YS, Wang Y-S, Hu C-Y, Hu CY, Chang WC, Chang W-C, Liao Y-C, Liao YC, Dai C-Y, Dai CY, Juo SHH, Juo S-HH. OxLDL up-regulates microRNA-29b, leading to epigenetic modifications of MMP-2/MMP-9 genes: a novel mechanism for cardiovascular diseases. *The FASEB Journal*. 2011;25:1718–1728

477. Wang YS, Wang Y-S, Wang HYJ, Wang H-YJ, Liao YC, Liao Y-C, Tsai PC,

Tsai P-C, Chen KC, Chen K-C, Cheng H-Y, Cheng HY, Lin RT, Lin R-T, Juo S-HH, Juo SHH. MicroRNA-195 regulates vascular smooth muscle cell phenotype and prevents neointimal formation. *Cardiovasc Res*. 2012;95:517–526

478. Thoracic aortic aneurysm frequency and dissection are associated with fibrillin-1 fragment concentrations in circulation. *Circulation Research*. 2013;113:1159–1168

479. Li D, Li D, Zhao Y, Zhao Y, Liu C, Liu C, Chen X, Chen X, Qi Y, Qi Y, Jiang Y, Jiang Y, Zou C, Zou C, Zhang X, Zhang X, Liu S, Liu S, Wang X, Wang X, Zhao D, Zhao D, Sun Q, Sun Q, Zeng Z, Zeng Z, Dress A, Dress A, Lin MC, Lin MC, Kung HF, Kung H-F, Rui H, Rui H, Liu L-Z, Liu LZ, Mao F, Mao F, Jiang B-H, Jiang BH, Lai L, Lai L. Analysis of MiR-195 and MiR-497 Expression, Regulation and Role in Breast Cancer. *Clinical Cancer Research*. 2011;17:1722–1730

480. Sekiya Y, Ogawa T, Iizuka M, Yoshizato K, Ikeda K, Kawada N. Down-regulation of cyclin E1 expression by microrna-195 accounts for interferon-β-induced inhibition of hepatic stellate cell proliferation. *J Cell Physiol*. 2011;226:2535–2542

481. Liao M, Zou S, Weng J, Hou L, Yang L, Zhao Z, Bao J, Jing Z. A microRNA profile comparison between thoracic aortic dissection and normal thoracic aorta indicates the potential role of microRNAs in contributing to thoracic aortic dissection pathogenesis. *J Vasc Surg*. 2011; 53:1341–1349.e3

482. Elmén J, Lindow M, Schütz S, Lawrence M, Petri A, Obad S, Lindholm M, Hedtjärn M, Hansen HF, Berger U, Gullans S, Kearney P, Sarnow P, Straarup EM, Kauppinen S. LNA-mediated microRNA silencing in non-human primates. *Nature*. 2008; 452:896–899

483. Krützfeldt J, Rajewsky N, Braich R, Rajeev KG, Tuschl T, Manoharan M, Stoffel M. Silencing of microRNAs in vivo with “antagomirs.” *Nature*. 2005;

438:685–689

484. Krutzfeldt J, Krützfeldt J, Kuwajima S, Kuwajima S, Braich R, Braich R, Rajeev KG, Rajeev KG, Pena J, Pena J, Tuschl T, Tuschl T, Manoharan M, Manoharan M, Stoffel M, Stoffel M. Specificity, duplex degradation and subcellular localization of antagomirs. *Nucleic Acids Research*. 2007; 35:2885–2892

485. Faria M, Ulrich H. Sugar boost: when ribose modifications improve oligonucleotide performance. *Curr Opin Mol Ther.* 2008; 10(2):168-75

486. Lanford RE, Lanford RE, Hildebrandt-Eriksen ES, Hildebrandt-Eriksen ES, Petri A, Petri A, Persson R, Persson R, Lindow M, Lindow M, Munk ME, Munk ME, Kauppinen S, Kauppinen S, Ørum H, Orum H. Therapeutic Silencing of MicroRNA-122 in Primates with Chronic Hepatitis C Virus Infection. *Science*. 2010;327:198–201

487. Carè A, Catalucci D, Felicetti F, Bonci D, Addario A, Gallo P, Bang M-L, Segnalini P, Gu Y, Dalton ND, Elia L, Latronico MVG, Høydal M, Autore C, Russo MA, Dorn GW, Ellingsen O, Ruiz-Lozano P, Peterson KL, Croce CM, Peschle C, Condorelli G. MicroRNA-133 controls cardiac hypertrophy. *Nat Med*. 2007;13:613–618

488. Wang Z. The Concept of Multiple-Target Anti-miRNA Antisense Oligonucleotide Technology. In: Methods in Molecular Biology. Totowa, NJ: Humana Press; 2010. p. 51–57

489. MiRNA-miRNA synergistic network: construction via co-regulating functional modules and disease miRNA topological features. *Nucleic Acids Research*. 2011;39:825–836

490. Wang Z. The Guideline of the Design and Validation of MiRNA Mimics. *Methods Mol Biol.* 2011; 676:211-23

491. Hinkel R, Trenkwalder T, Kupatt C. Gene therapy for ischemic heart disease. *Expert Opin Biol Ther*. 2011; 11:723–737

492. Noncanonical cytoplasmic processing of viral microRNAs. *RNA*. 2010; 16:2068–2074

493. Functional microRNA generated from a cytoplasmic RNA virus. *Nucleic Acids Research*. 2010; 38:8328–8337

494. Kota J, Chivukula RR, O'Donnell KA, Wentzel EA, Montgomery CL, Hwang H-W, Chang T-C, Vivekanandan P, Torbenson M, Clark KR, Mendell JR, Mendell JT. Therapeutic microRNA Delivery Suppresses Tumorigenesis in a Murine Liver Cancer Model. *Cell*. 2009;137:1005–1017.

495. da Costa Martins PA, Leptidis S, Salic K, De Windt LJ. MicroRNA regulation in cardiovascular disease. *Curr drug targets.* 2010; 11:900–906

496. da Costa Martins PA, Salic K, Gladka MM, Armand A-S, Leptidis S, Azzouzi el H, Hansen A, Coenen-de Roo CJ, Bierhuizen MF, van der Nagel R, van Kuik J, de Weger R, de Bruin A, Condorelli G, Arbones ML, Eschenhagen T, De Windt LJ. MicroRNA-199b targets the nuclear kinase Dyrk1a in an auto-amplification loop promoting calcineurin/NFAT signalling. *Nature*. 2010; 12:1220–1227

497. Montgomery RL, van Rooij E. Therapeutic Advances in MicroRNA Targeting. *Journal of Cardiovascular Pharmacology*. 2011; 57:1–7

498. Montgomery RL, Montgomery RL, Hullinger TG, Hullinger TG, Semus HM, Semus HM, Dickinson BA, Dickinson BA, Seto AG, Seto AG, Lynch JM, Lynch JM, Stack C, Stack C, Latimer PA, Latimer PA, Olson EN, Olson EN, van Rooij E, van Rooij E. Therapeutic Inhibition of miR-208a Improves Cardiac Function and Survival During Heart Failure. *Circulation*. 2011;124:1537–1547

499. Fiedler J, Fiedler J, Jazbutyte V, Jazbutyte V, Kirchmaier BC, Kirchmaier BC, Gupta SK, Gupta SK, Lorenzen J, Lorenzen J, Hartmann D, Hartmann D, Galuppo P, Galuppo P, Kneitz S, Kneitz S, Pena JTG, Pena JTG, Sohn-Lee C, Sohn-Lee C, Loyer X, Loyer X, Soutschek J, Soutschek J, Brand T, Brand T, Tuschl T, Tuschl T, Heineke J, Heineke J, Martin U, Martin U, Schulte-Merker S, Schulte-Merker S, Ertl G, Ertl G, Engelhardt S, Engelhardt S, Bauersachs J, Bauersachs J, Thum T, Thum T. MicroRNA-24 Regulates Vascularity After Myocardial Infarction. *Circulation*. 2011;124:720–730

500. van Rooij E, Purcell AL, Levin AA. Developing microRNA therapeutics. *Circulation Research*. 2012;110:496–507

501. Liu L, Zhang G, Liang Z, Liu X, Li T, Fan J, Bai J, Wang Y. MicroRNA-15b enhances hypoxia/reoxygenation-induced apoptosis of cardiomyocytes via a mitochondrial apoptotic pathway. *Apoptosis*. 2014;19:19–29

502. Krege JH, Hodgin JB, Hagaman JR, Smithies O. A noninvasive computerized tail-cuff system for measuring blood pressure in mice. *Hypertension.* 1995; 25:1111–1115

503. Zampetaki A, Kiechl S, Drozdov I, Willeit P, Mayr U, Prokopi M, Mayr A, Weger S, Oberhollenzer F, Bonora E, Shah A, Willeit J, Mayr M. Plasma microRNA profiling reveals loss of endothelial miR-126 and other microRNAs in type 2 diabetes. *Circulation Research*. 2010;107:810–817

504. Lucero HA, Kagan HM. Lysyl oxidase: an oxidative enzyme and effector of cell function. *Cell Mol Life Sci*. 2006;63:2304–2316

505. Onoda M, Yoshimura K, Aoki H, Ikeda Y, Morikage N, Furutani A, Matsuzaki M, Hamano K. Lysyl oxidase resolves inflammation by reducing monocyte chemoattractant protein-1 in abdominal aortic aneurysm. *Atherosclerosis*. 2010;208:366–369

506. Gacheru SN, Thomas KM, Murray SA, Csiszar K, Smith-Mungo LI, Kagan HM. Transcriptional and post-transcriptional control of lysyl oxidase expression in vascular smooth muscle cells: effects of TGF-beta 1 and serum deprivation. *Journal of Cell Biochem.* 1997; 65:395–407

507. Fogelgren B, Fogelgren B, Polgár N, Szauter KM, Ujfaludi Z, Laczkó R, Fong KSK, Csiszar K. Cellular Fibronectin Binds to Lysyl Oxidase with High Affinity and Is Critical for Its Proteolytic Activation. *J Biol Chem*. 2005;280:24690–24697

508. Maegdefessel L, Azuma J, Tsao PS. MicroRNA-29b regulation of abdominal aortic aneurysm development. *Trends Cardiovasc Med*. 2014;24:1–6

509. Habashi JP, Habashi JP, Doyle JJ, Doyle JJ, Holm TM, Holm TM, Aziz H, Aziz H, Schoenhoff F, Schoenhoff F, Bedja D, Bedja D, Chen Y, Chen Y, Modiri AN, Modiri AN, Judge DP, Judge DP, Dietz HC, Dietz HC. Angiotensin II Type 2 Receptor Signaling Attenuates Aortic Aneurysm in Mice Through ERK Antagonism. *Science*. 2011;332:361–365

510. Jones JA, Jones JA, Stroud RE, Stroud RE, O'Quinn EC, O'Quinn EC, Black LE, Black LE, Barth JL, Barth JL, Elefteriades JA, Elefteriades JA, Bavaria JE, Bavaria JE, Gorman JH, Gorman JH, Gorman RC, Gorman RC, Spinale FG, Spinale FG, Ikonomidis JS, Ikonomidis JS. Selective MicroRNA Suppression in Human Thoracic Aneurysms: Relationship of miR-29a to Aortic Size and Proteolytic Induction. *Circulation: Cardiovascular Genetics*. 2011;4:605–613

511. Zhang P, Huang A, Ferruzzi J, Mecham RP. Inhibition of microRNA-29 enhances elastin levels in cells haploinsufficient for elastin and in bioengineered vessels—brief report. *Arterioscler Thromb Vasc Biol.* 2012; 32(3):756-9

512. Abonnenc M, Nabeebaccus AA, Mayr U, Barallobre-Barreiro J, Dong X, Cuello F, Sur S, Drozdov I, Langley SR, Lu R, Stathopoulou K, Didangelos A, Yin X, Zimmermann W-H, Shah AM, Zampetaki A, Mayr M. Extracellular matrix secretion by cardiac fibroblasts: role of microRNA-29b and microRNA-30c. *Circulation Research*. 2013;113:1138–1147

513. Kakkar R, Lee RT. Intramyocardial fibroblast myocyte communication. *Circulation Research*. 2010;106:47–57

514. Finnerty JR, Wang W-X, Hébert SS, Wilfred BR, Mao G, Nelson PT. The miR-15/107 group of microRNA genes: evolutionary biology, cellular functions, and roles in human diseases. *J Mol Biol*. 2010;402:491–509

515. He J-F, Luo Y-M, Wan X-H, Jiang D. Biogenesis of MiRNA-195 and its role in biogenesis, the cell cycle, and apoptosis. *J Biochem Mol Toxicol*. 2011;25:404–408

516. Chen Y-Q, Wang X-X, Yao X-M, Zhang D-L, Yang X-F, Tian S-F, Wang N-S. MicroRNA-195 promotes apoptosis in mouse podocytes via enhanced caspase activity driven by BCL2 insufficiency. *Am J Nephrol*. 2011;34:549–559

517. Qi J, Yu J-Y, Shcherbata HR, Mathieu J, Wang AJ, Seal S, Zhou W, Stadler BM, Bourgin D, Wang L, Nelson A, Ware C, Raymond C, Lim LP, Magnus J, Ivanovska I, Diaz R, Ball A, Cleary MA, Ruohola-Baker H. microRNAs regulate human embryonic stem cell division. *Cell Cycle*. 2009;8:3729–3741

518. Zhu H, Yang Y, Wang Y, Li J, Schiller PW, Peng T. MicroRNA-195 promotes palmitate-induced apoptosis in cardiomyocytes by down-regulating Sirt1. *Cardiovasc Res*. 2011;92:75–84

519. MiR-15 family regulates postnatal mitotic arrest of cardiomyocytes. *Circulation Research*. 2011;109:670–679

520. Nelson PT, Wang W-X, Mao G, Wilfred BR, Xie K, Jennings MH, Gao Z, Wang X. Specific sequence determinants of miR-15/107 microRNA gene group targets. *Nucleic Acids Research*. 2011;39:8163–8172

521. Chen YQ, Wang XX, Yao XM, Zhang DL, Yang XF, Tian SF, Wang NS. Abated microRNA-195 expression protected mesangial cells from apoptosis in early diabetic renal injury in mice. *J Nephrol*. 2012;25:566–576

522. Forester ND, Cruickshank SM, Scott DJA, Carding SR. Functional characterization of T cells in abdominal aortic aneurysms. *Immunology*. 2005;115:262–270

523. Davis VA, Davis VA, Persidskaia RN, Persidskaia RN, Baca-Regen LM, Baca-Regen LM, Fiotti N, Fiotti N, Halloran BG, Halloran BG, Baxter BT, Baxter BT. Cytokine Pattern in Aneurysmal and Occlusive Disease of the Aorta. *Journal of Surgical Research*. 2001;101:152–156

524. Yoshizaki A, Miyagaki T, Dilillo DJ, Matsushita T, Horikawa M, Kountikov EI, Spolski R, Poe JC, Leonard WJ, Tedder TF. Regulatory B cells control T-cell autoimmunity through IL-21-dependent cognate interactions. *Nature*. 2012;491:264–268

525. Patel MI, Melrose J, Ghosh P, Appleberg M. Increased synthesis of matrix metalloproteinases by aortic smooth muscle cells is implicated in the etiopathogenesis of abdominal aortic aneurysms. *J Vasc Surg*. 1996; 24(1):82-92

526. Allaire E, Muscatelli-Groux B, Mandet C. Paracrine effect of vascular smooth muscle cells in the prevention of aortic aneurysm formation. *J Vasc Surg.* 2002 Nov;36(5):1018-26

527. Petersen E, Wågberg F, Ängquist KA. Proteolysis of the abdominal aortic aneurysm wall and the association with rupture. *Vascular and*

endovascular surgery. 2002; 23(2):153-7

528. Ailawadi G, Eliason JL, Upchurch GR. Current concepts in the pathogenesis of abdominal aortic aneurysm. *Journ Vasc Surg*. 2003;38:584–588

529. Ailawadi G, Moehle CW, Pei H, Walton SP, Yang Z, Kron IL, Lau CL, Owens GK. Smooth muscle phenotypic modulation is an early event in aortic aneurysms. *The Journal of Thoracic and Cardiovascular Surgery*. 2009; 138:1392–1399

530. Airhart ND, Brownstein B, Schierding W, Cobb P, Arif B, Ennis T, Thompson R, Curci JA. Smooth Muscle Cells from Abdominal Aortic Aneurysms Are Unique and Can Independently and Synergistically Degrade Insoluble Elastin. *J Vasc Surg*. 2013; 57:23S

531. Thompson RW, Liao S, Curci JA. Vascular smooth muscle cell apoptosis in abdominal aortic aneurysms. *Coron Artery Dis*. 1997;8:623–631

532. Fukui D, Miyagawa S, Soeda J, Tanaka K, Urayama H, Kawasaki S. Overexpression of transforming growth factor β1 in smooth muscle cells of human abdominal aortic aneurysm. *European Journal of Vascular and Endovascular Surgery*. 2003; 25:540–545

533. Modarai B, Humphries J, Burnand KG, Gossage JA, Waltham M, Wadoodi A, Kanaganayagam GS, Afuwape A, Paleolog E, Smith A. Adenovirus-mediated VEGF gene therapy enhances venous thrombus recanalization and resolution. *Arterioscler Thromb Vasc Biol*. 2008; 28:1753–1759

534. Humphries J, McGuinness CL, Smith A, Waltham M, Poston R, Burnand KG. Monocyte chemotactic protein-1 (MCP-1) accelerates the organization and resolution of venous thrombi. *J Vasc Surg*. 1999;30:894–899

535. Hyperplastic cellular remodeling of the media in ascending thoracic aortic aneurysms. *Circulation*. 2005; 112:1098–1105

536. Chan WL, Chan WL, Pejnovic N, Hamilton H, Liew TV, Popadic D, Poggi A, Khan SM. Atherosclerotic Abdominal Aortic Aneurysm and the Interaction Between Autologous Human Plaque-Derived Vascular Smooth Muscle Cells, Type 1 NKT, and Helper T-cells. *Circulation Research*. 2005; 96:675–683

537. López-Candales A, Holmes DR, Liao S, Scott MJ, Wickline SA, Thompson RW. Decreased vascular smooth muscle cell density in medial degeneration of human abdominal aortic aneurysms. *The American journal of pathology* 1997;150:993–1007

538. Sato K, Niessner A, Kopecky SL, Frye RL. TRAIL-expressing T-cells induce apoptosis of vascular smooth muscle cells in the atherosclerotic plaque. Journal *of Experimental Medicine* 2006; 203(1)239-250

539. Krettek A, Sukhova GK, Libby P. Elastogenesis in Human Arterial Disease A Role for Macrophages in Disordered Elastin Synthesis. *Circulation.* 2003; 23:582-587

540. Zhang Y, Davarani SZ. Chapter 14: Role of Elastin in Arterial Mechanics. *Multiscale Simulations and Mechanics of Biological Materials.* 2013. Edited by Shaofan Li, Dong Qian. Wiley Press

541. Péterszegi G, Texier S, Robert L. Human helper and memory lymphocytes exhibit an inducible elastin-laminin receptor. *International archives of allergy and immunology*. 1997; 114:218–223

542. Péterszegi G, Mandet C, Texier S, Robert L, Bruneval P. Lymphocytes in human atherosclerotic plaque exhibit the elastin-laminin receptor: potential role in atherogenesis. *Atherosclerosis*. 1997; 135:103–107

543. Xiong J, Wang SM, Chen LH, Lin Y, Zhu YF, Ye CS. Elastic fibers reconstructed using adenovirus-mediated expression of tropoelastin and tested in the elastase model of abdominal aortic aneurysm in rats. *J Vasc Surg*. 2008;48:965–973

544. Smith SH, Haas KM, Poe JC, Yanaba K. B-cell homeostasis requires complementary CD22 and BLyS/BR3 survival signals. *Int Immunol.* 2010; 22(8):681-91

545. Boudreau N, Turley E, Rabinovitch M. Fibronectin, hyaluronan, and a hyaluronan binding protein contribute to increased ductus arteriosus smooth muscle cell migration. *Developmental Biology*. 1991; 143:235–247

546. Weintraub AS, Schnapp LM, Lin X, Taubman MB. Osteopontin deficiency in rat vascular smooth muscle cells is associated with an inability to adhere to collagen and increased apoptosis. *Lab Invest*. 2000; 80:1603–1615

547. Holm TM, Habashi JP, Doyle JJ, Bedja D, Chen Y, van Erp C, Lindsay ME, Kim D, Schoenhoff F, Cohn RD, Loeys BL, Thomas CJ, Patnaik S, Marugan JJ, Judge DP, Dietz HC. Noncanonical TGFβ signaling contributes to aortic aneurysm progression in Marfan syndrome mice. *Science.* 2011; 332(6027):358-61

548. Yu Q, Vazquez R, Zabadi S, Watson RR, Larson DF. T-lymphocytes mediate left ventricular fibrillar collagen cross-linking and diastolic dysfunction in mice. *Matrix Biol.* 2010; 29(6):511-8

549. Yu Q, Watson RR, Marchalonis JJ, Larson DF. A role for T lymphocytes in mediating cardiac diastolic function. *Am J Physiol Heart Circ Physiol*. 2005; 289(2):H643-51

550. Yu Q, Horak K, Larson DF. Role of T lymphocytes in hypertension-induced cardiac extracellular matrix remodeling. *Hypertension.* 2006;

48(1):98-10

551. Shanley CJ, Gharaee-Kermani M, Sarkar R, Welling TH, Kriegel A, Ford JW, Stanley JC, Phan SH. Transforming growth factor-beta 1 increases lysyl oxidase enzyme activity and mRNA in rat aortic smooth muscle cells. *J Vasc Surg.* 1997; 25(3):446-52

552. Rodríguez C, Alcudia JF, Martínez-González J, Raposo B, Navarro MA, Badimon L. Lysyl oxidase (LOX) down-regulation by TNFalpha: a new mechanism underlying TNFalpha-induced endothelial dysfunction. *Atherosclerosis.* 2008; 196(2):558-64

553. Alcudia JF, Martinez-Gonzalez J, Guadall A, Gonzalez-Diez M, Badimon L, Rodriguez C. Lysyl oxidase and endothelial dysfunction: mechanisms of lysyl oxidase down-regulation by pro-inflammatory cytokines. *Front Biosci.* 2008; 13:2721-7

554. Brown RD, Jones GM, Laird RE, Hudson P, Long CS. Cytokines regulate matrix metalloproteinases and migration in cardiac fibroblasts. *Biochem Biophys Res Commun.* 2007; 362(1):200-5

555. Siwik DA, Chang DL, Colucci WS. Interleukin-1beta and tumor necrosis factor- alpha decrease collagen synthesis and increase matrix metalloproteinase activity in cardiac fibroblasts in vitro. *Circ Res.* 2000; 86(12):1259-65

556. Fiorentino DF, Zlotnik A, Vieira P, Mosmann TR, Howard M, Moore KW, O'Garra A. IL-10 acts on the antigen-presenting cell to inhibit cytokine production by Th1 cells. *J Immunol*. 1991;146:3444–3451

557. Murai M, Turovskaya O, Kim G, Madan R, Karp CL, Cheroutre H, Kronenberg M. Interleukin 10 acts on regulatory T-cells to maintain

expression of the transcription factor Foxp3 and suppressive function in mice with colitis. *Nat Immunol*. 2009; 10:1178–1184

558. Vucevic D, Maravic-Stojkovic V, Vasilijic S, Borovic-Labudovic M, Majstorovic I, Radak D, Jevtic M, Milosavljevic P, Colic M. Inverse production of IL-6 and IL-10 by abdominal aortic aneurysm explant tissues in culture. *Cardiovasc Pathol.* 2012; 21(6):482-9

559. Oksala N, Levula M, Airla N, Pelto-Huikko M, Ortiz RM, Järvinen O, Salenius JP, Ozsait B, Komurcu-Bayrak E, Erginel-Unaltuna N, Huovila AP, Kytömäki L, Soini JT, Kähönen M, Karhunen PJ, Laaksonen R, Lehtimäki T. ADAM-9, ADAM-15, and ADAM-17 are upregulated in macrophages in advanced human atherosclerotic plaques in aorta and carotid and femoral arteries--Tampere vascular study. Ann Med. 2009;41(4):279-90

560. Lipp C, Lohoefer F, Reeps C, Rudelius M, Baummann M, Heemann U, Eckstein HH, Pelisek J. Expression of a disintegrin and metalloprotease in human abdominal aortic aneurysms. *J Vasc Res.* 2012; 49(3):198-206

561. Engelman JA, Chen L, Tan X, Crosby K, Guimaraes AR, Upadhyay R, Maira M, McNamara K, Perera SA, Song Y, Chirieac LR, Kaur R, Lightbown A, Simendinger J, Li T, Padera RF, García-Echeverría C, Weissleder R, Mahmood U, Cantley LC, Wong KK. Effective use of PI3K and MEK inhibitors to treat mutant Kras G12D and PIK3CA H1047R murine lung cancers. *Nat Med.* 2008; 14(12):1351-6

562. Wei LH, Su H, Hildebrandt IJ, Phelps ME, Czernin J, Weber WA. Changes in tumor metabolism as readout for Mammalian target of rapamycin kinase inhibition by rapamycin in glioblastoma. *Clin Cancer Res.* 2008;14(11):3416-26

563. Harrington LE, Hatton RD, Mangan PR, Turner H, Murphy TL, Murphy

KM, Weaver CT. Interleukin 17-producing CD4+ effector T cells develop via a lineage distinct from the T helper type 1 and 2 lineages. *Nat Immunol*. 2005;6:1123–1132

564. Churchman AT, Siow RCM. Isolation, culture and characterisation of vascular smooth muscle cells. *Methods Mol Biol*. 2009;467:127–138